MOISTURE REMOVAL FROM AND LIQUEFACTION OF BEULAH ZAP LIGNITE.

K. S. Vorres*, D. Wertz**,
J. T. Joseph***, and R. Fischer***

*Chemistry Div., Bldg. 211, Argonne National Lab., Argonne, IL 60439,
**Dept. of Chemistry, Univ. So. Miss., Hattiesburg, MS, 39406,
***Amoco Oil Co. R&D, Naperville, IL,60566

Keywords: Drying, Liquefaction, Lignite

INTRODUCTION

Lignite reserves represent an important resource for the production of synthetic liquid fuels. The high reactivity of lignite would indicate a high throughput from a given process train. However the moisture content of this material has been a concern for efficient processing into liquid hydrocarbons. Furthermore, drying might introduce irreversible changes to the pore structure which would limit the rates of reaction.

This collaborative study has been undertaken to help understand the role of moisture in the liquefaction and also to understand the kinds of changes that take place in the coal particles during drying.

The physical structure of coal consists an organic matrix and inorganic matter containing an extensive network of pores. The pore network usually contains water. Mraw and Silbernagel (1) suggested that the amount of water present in as-mined coals provides a measure of pore volume. However, Kaji et al. (2) examined the water-holding capacity, specific surface area, and pore volume of 13 coals from various locations, ranging from lignite to anthracite, and found no correlation between the water-holding capacity and the pore volume. Assuming that the total coal oxygen is distributed uniformly through the coal and the functional-group oxygen increases with oxygen content, Kaji et al. found a linear relationship between the hydrophilic sites and the water-holding capacity of coal. The relationship between the total oxygen content of coal and the water-holding capacity may be fortuitous since oxygen-functional groups are not the only hydrophilic sites in coal (3). Moreover, the presence of minerals, especially smectite lattices, and various cations will also strongly influence the coal-water interactions.

Vorres et al. (4) and Vorres and Kolman (5) studied the kinetics of vacuum drying of coal to understand the complex coal-water interactions. From isothermal thermogravimetry analysis, i.e., the weight loss vs. time at fixed temperature, Vorres and his co-workers observed that the dehydration of Illinois No. 6 in the form of a block, -20 mesh, and -100 mesh, follows a desorption kinetics mechanism. Thus, they concluded that the rate controlling mechanism of dehydration is governed by the surface of coal. In addition, Vorres and his co-workers indicated that the particle size and the history of coal also affect the dehydration kinetics of coal. More recently, Abhari and Isaacs (6) used the thermogravimetric analysis (TGA) technique to explore the drying

kinetics of six coals from the Argonne coal-sample series. They used a bulk moisture/pore moisture model to explain the observed drying kinetics for the six coals, in which the order of kinetics, i.e., the order of dehydration showed a strong dependence on the rank of coal. These researchers assumed that water in coal is held by the physisorption process. This assumption is at variance with the temperature dependent NMR results (7) and the contention of Kaji et al. (2). Even more recently, Vorres et al reported the kinetics of drying of lignite in dry nitrogen. They observed a unimolecular mechanism, with a transition after the loss of about 85% of the water present in the original sample (8). The transition resulted in a lower rate with the unimolecular mechanism. Studies with the thermobalance and differential scanning calorimeter indicated the same mechanism and transition (8).

In this paper, we report our recent results on: the kinetics of water's desorption from Beulah-Zap lignite coal, as determined by thermogravimetric analysis (TGA); physical structure changes as observed with x-ray diffraction; and the effects on liquefaction due to drying.

EXPERIMENTAL

Isothermal Thermogravimetry

Coal drying was done with a Cahn model 121 thermobalance attached to an IBM PC/XT microcomputer. Vendor-supplied software was used to monitor the progress of individual runs, and convert data files to a form that could be further studied with Lotus 123.

The data were obtained as files of time, temperature and weight at 10 second intervals. Run times varied from 7-16 hours. Sample sizes varied from about 20-160 mg. Temperatures were varied between 20 and 80 C. The gas velocity past the sample was varied from 20 to 160 cc/min in the 25 mm diameter tube. The sample was placed in either a quartz or a platinum hemispherically-shaped pan. Sample included the two mesh sizes (-100 and -20) of the Argonne Premium Coal Samples and also one or two small pieces which came from lumps which were stored under nitrogen.

Samples were quickly transferred from ampoules which had been kept in constant humidity chambers with water at room temperature ($293^{o}K$). In the thermobalance system a period of about 5 minutes was used to stabilize the system and initiate data acquisition. A condenser was made to replace the usual quartz envelope that surrounds the sample. An antifreeze solution was circulated from a constant temperature bath through the condenser to maintain constant temperature during the experiments. This was more stable than the furnace and provided very uniform temperature control during the experiments.

The gas atmosphere was cylinder nitrogen (99.99%) or "house" nitrogen from the evaporation of liquid nitrogen storage containers used without further purification and passed over the sample at rates of about 20-160 cc/min.

Data were initially analyzed by testing the weight loss as a function of time with 13 different kinetic expressions including geometrical, unimolecular, first and second order diffusion to establish a best fit (8). Regression analysis was used to obtain the kinetic constants. Lotus 123 was used for analysis of individual run data.

Round Robin Sample Preparation

In order to compare the results of drying with the help of several techniques a set of samples was prepared and distributed. A batch of twenty five grams of -100 mesh lignite was dried in a vacuum oven at room temperature. One batch was dried for 4 hours, and the other for 24 hours. The samples were brought to atmospheric pressure under nitrogen, quickly transferred to a nitrogen filled glove bag, and transferred to previously dried screw cap vials. The vials were further sealed with tape around the cap. These samples were distributed to the University of Southern Mississippi for x-ray diffraction studies and Amoco Oil Company for liquefaction studies and comparison with fresh lignite sample.

RESULTS AND DISCUSSION

Isothermal Thermogravimetry

The data were normalized to one gram of starting sample weight. The best fit of the data were obtained with a unimolecular decay kinetic expression. Plots of ln (water left) versus time gave a characteristic shape. The plot indicates a consistent slope for the initial 85% of the moisture loss of the coal. A transition then occurs. The rate is then reduced to about 0.5-0.1 of the earlier rate. Figure 1 shows a typical plot of ln water left (mg/gm sample) as a function of time (10 second intervals).

The rates are similar for different particle sizes if the sample weight and gas velocity are held constant. Table 1 indicates the similarity in rates for 150 mg samples in the hemispherical quartz container. Activation energies are also given for each particle size.

Table 1. Rate Constants for First Segment
(mg water/gm sample/10 sec)

Temperature-->	20 C	40 C	80 C	E_a
Size				Kcal/mole
-100	.00009	.00024	.00099	8.2
-20	.00007	.00024	.00131	10.0
Block	.00010	.00023	.00085	7.3

The activation energy calculated from these data averages 8.5 Kcal/mole.

The rate is a function of the size of the sample and the gas velocity around the sample. The size of the sample affects the depth of the material through which the moisture must diffuse to escape. The normalized rates were inversely proportional to the sample size. The rate is directly proportional to the gas

velocity since the more rapidly moving stream is more effective in removing the water molecules or limiting the opportunity for rehydration.

The effect of temperature is measured through the activation energy from an Arrhenius plot. Figure 2 shows the data plotted for several sets of data representing three different constant gas velocities. The lines are almost parallel and indicate an average activation energy of 8.0 Kcal/mole. The higher gas velocities are able to more effectively remove water molecules and increase the rate of drying.

Varying the sample weight also varies the depth of the sample in the container. Figure 3 indicates the change in rates as the sample weight is changed at different temperatures. The rate in terms of mass of water lost per gram of sample in a given time is greater for the smaller, and therefore thinner samples. The probability of a water molecule recombining with the lignite rather than leave the sample diminishes as the diffusion path is shortened.

The use of vacuum to remove moisture was seen to be capable of much more rapid removal of water than a stream of dry nitrogen. The ratio of the rate coefficients is an order of magnitude greater, and would imply a rate advantage to this technique for engineering for rapid processing of pulverized fuel.

The initial removal of about 85% of the moisture and then a transition to a slower rate of water loss implies a structural rearrangement. It is believed that the pores of the particles are changed after this amount of water is lost in a manner that makes the further loss of water more difficult.

X-RAY DIFFRACTION STUDIES

The X-ray diffraction studies carried out at the University of Southern Mississippi shown in Figure 4 indicate that the physical structure of the coal (not the inorganic material) changes with the drying. Further the reduced "noise" level associated with the diffraction pattern on the recorder indicates that there is a greater regularity in the dried coal than the raw or partially dried material. Further studies of the diffraction data are underway to provide additional insight into the changes that have been observed. The figure indicates the diffractograms from: A. untreated lignite, B. partially dried lignite and C. dried lignite.

The peak at 22^{o} is due to an internal standard that was added. The peak at 14^{o} is due to the 002 plane of graphitic material associated with coal samples. Note that the peak shape for untreated lignite is reasonably symmetrical implying a distribution of spacings about an average value. The partially dried material has a distorted shape for the 002 peak indicating that the larger planar spacings are no longer present in the sample. In the dried sample the peak is again relatively symmetrical.

LIQUEFACTION STUDIES

The oil yield measurements have been carried at Amoco Oil Co. at the Naperville Research Center. Small samples were added to tetralin, and the material heated under hydrogen at 1000 psi to 400 C for four hours. The product gases were recovered and analyzed by gas chromatography. The liquid and residual material were extracted with a series of solvents to give oil, preasphaltene and asphaltene fraction amounts.

The studies indicated that the different coal samples did give different oil yields, as well as preasphaltene and asphaltene yields. The initial data indicate that the raw and partially dried samples gave higher preasphaltene and asphaltene yields than the dried material, with the highest yields for the partly dried sample. Conversely the oil yield was highest for the dried sample, lowest for the partly dried material and the starting material had an intermediate value. The data are given in Table 2. The total of the oil, preasphaltene and asphaltene was almost the same for all samples. The gas yield was the same for the two moist materials and higher than the dried material, suggesting a role for moisture in gas production. Hydrogen diminishes for dried coal, while carbon monoxide increases. Methane and higher hydrocarbons remain about the same for all levels of dryness, suggesting that they are released by some mechanism which is not dependent on moisture, i. e. they may simply be dissolved in the matrix. Carbon dioxide yield increased for the partly dried material and then decreased for the dry material suggesting two competing reactions.

Table 2. Initial Liquefaction Results from Lignite Samples

Coal	Raw	High Moisture	Low Moisture
Moisture:	32.2%	23.9%	0.3%
Products, Wt%			
OIL	24	21	31
ASPHALTENE	24	25	20
PRE-ASPHALTENE	11	13	7
UNCONVERTED	31	31	33
TOTAL GASES	10.5	10.5	8.5
GAS BY TYPE:			
hydrogen	0.209	0.196	0.156
carbon monoxide	0.238	0.276	0.340
methane	0.486	0.474	0.480
carbon dioxide	5.373	5.543	4.849
ethane	0.163	0.166	0.154
propane	0.056	0.055	0.054
propylene	0.011	0.011	0.009

CONCLUSIONS

The lignite drying kinetics follow a unimolecular rate law which is first order in the water in the sample. There are two segments in the dehydration kinetics plots, and each follows a unimolecular rate law. The first drying segment includes about 80-85% of the water loss. The second drying segment includes most of the remaining water and occurs at about half the rate of the first segment. The mechanism is unchanged over the range 20-80°C. The activation energy for the initial moisture loss is about 8 Kcal/mole. The water jacketed heating system provides superior temperature control. The rate of drying is sensitive to the gas velocity over the sample. The rate of drying is dependent on the sample size and the sample depth. Rates are generally similar for -20 and -100 mesh samples. The same mechanism is observed for differential scanning calorimetry measurements. X-ray powder diffraction measurements show structural changes during the drying process. Drying improves the oil yield from lignite samples as a result of hydrogenation.

ACKNOWLEDGMENTS

One of the authors (KSV) gratefully acknowledges the support of the U. S. Department of Energy, Pittsburgh Energy Technology Center for the part of the work dealing with the kinetics of drying.

REFERENCES

1. Mraw, S. C. and B. G. Silbernagel, Am. Inst. Physics Proceedings 70, 332 (1981).

2. Kaji, R., Y. Maranaka, K. Otsuka, and Y. Hishinuma, Fuel 65, 288 (1986).

3. Laskowski, J. S., Am. Chem. Soc. Preprints Fuel Chem. Div. 32 (1), 367 (1987).

4. Vorres, K. S., R. Kolman, and T. Griswold, Am. Chem. Soc. Preprints Fuel Chem. Div. 33 (2), 333 (1988).

5. Vorres, K. S. and R. Kolman, Am. Chem. Soc. Preprints Fuel Chem. Div. 33 (3), 7 (1988).

6. Abhari, R. and L. L. Isaacs, Energy & Fuels 4, 448 (1990).

7. Unsworth, J. F., C. S. Fowler, N. A. Heard, V. L. Weldon, and V. J. McBrierty, Fuel 67 1111 (1988).

8. Vorres, K. S., Molenda, D., Dang, Y. and Malhotra, V. M., Am. Chem. Soc. Preprints Fuel Chem. Div. 36 (1), 108 (1991).

Figure 1, Lignite Dried in N2, 80 C

ND65, −100 mesh, 80 cc/min, 160 mg, rbb

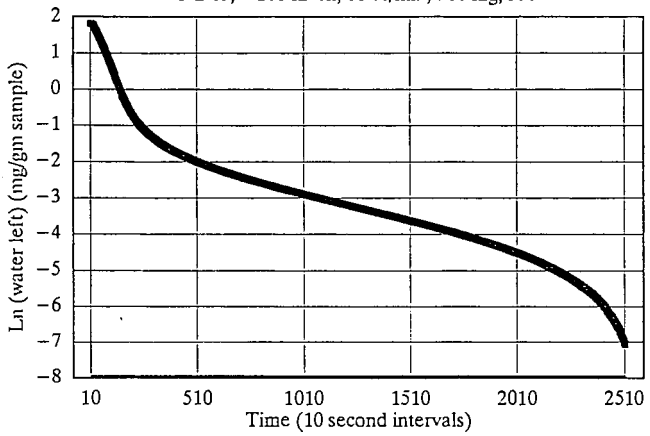

Figure 2, Arrhenius Plot, Lignite Dried in N2
−20 mesh, 150 mg samples, 30,40, 60 C

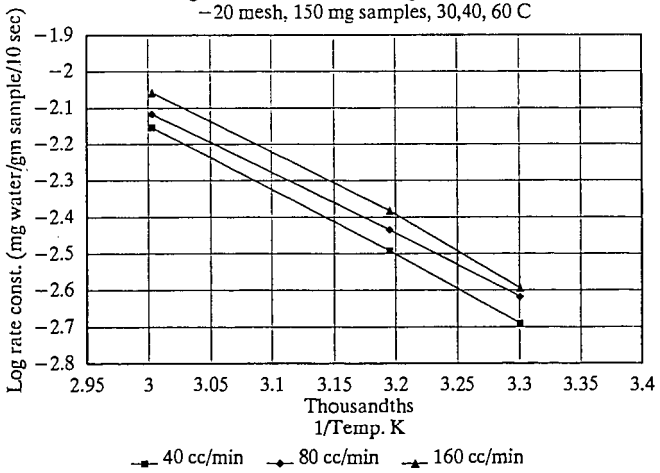

Fig. 3, Rates Change as Sample Weight Changes
75, 150 mg samples, 30,40, 60 C

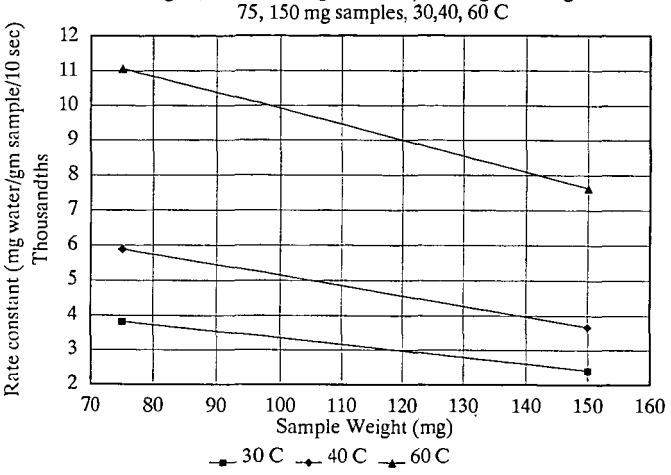

Figure 4, X–Ray Diffractograms of Lignite Samples

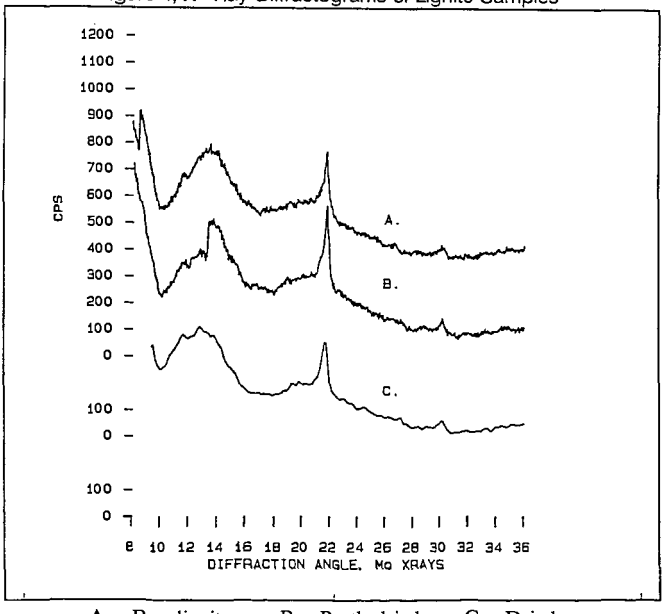

A = Raw lignite B = Partly dried C = Dried

MONITORING THE OXIDATION OF COALS IN STORAGE

David C. Glick, Gareth D. Mitchell and Alan Davis
Energy and Fuels Research Center
Penn State University
205 Research Building E
University Park, PA 16802

Keywords: coal, oxidation, storage

ABSTRACT

Two studies of conventional coal sample storage containers revealed problems with the atmospheric gas composition and preservation of the samples. Heat-sealable polyethylene/aluminum foil laminate bags were evaluated by various methods in two further studies. The first compared preservation of a freshly collected mvb coal in laminate bags to other container types. The second compared Argonne premium coal samples sealed in their original ampoules to those repackaged in laminate bags. Preservation in laminate bags is better than in conventional containers and comparable to glass ampoules. Samples collected after 1988 for the Penn State Coal Sample Bank have been stored exclusively in laminate bags after processing. Monitoring the condition of these samples is an ongoing project.

INTRODUCTION

When coals are stored in a sample bank for use over a period of months or years, it is important to preserve their original properties. If preservation is not achieved, measurements made after the passage of time will not be comparable to those obtained from the fresh sample. Among the properties which may change are pyritic and sulfate sulfur content, calorific value, thermoplastic properties as measured by free-swelling index and the Gieseler plastometer, fluorescence, FTIR spectra, liquefaction yields and products, alkali extraction and methane content. Some changes are purely chemical, many involving oxidation. Others may have a physical component related to relaxation after release of lithostatic pressure in mining and comminution in sample preparation.

STUDIES OF CONVENTIONAL CONTAINERS

The environment of a coal sample in storage differs greatly from its in situ environment prior to mining. Conventional laboratory and bulk materials containers such as barrels, buckets, cans, jars and bags are typically used for storage. The internal atmosphere is often replaced with nitrogen or argon to reduce oxidation.

In the Penn State Coal Sample Bank (1), field collection and bulk sample storage were previously accomplished with 113 L polyethylene barrels (100 kg capacity) and 19 L buckets (16 kg capacity), both fitted with gasketed lids and valves for argon introduction. Smaller splits of samples at -0.85 mm have been stored in heat-sealed argon-filled polyethylene bags sealed in standard #2 steel cans (600 mL, 400 g capacity).

The composition of the atmospheres within barrels and buckets over time was studied using gas chromatography. Different methods of argon introduction were used on three containers of each type:

for 113 L barrels:

1) The lid was sealed, and the container was pumped with a small vacuum pump for approximately 2 minutes, then argon was introduced until a slight positive pressure was reached.

2) Same, except with large vacuum pump.

3) The lid was placed loosely over the container to allow the introduction of a stainless steel wand, through which argon was introduced to the bottom of the container. The wand was gradually withdrawn while the argon flowed for approximately 4 minutes, and the lid was sealed.

for 19 L buckets:

1) The lid was sealed, and the container pumped with a small vacuum pump for approximately 30 seconds, until the bucket began to deform. Argon was introduced until a slight positive pressure was reached.

2) Same, except that the pumping and argon introduction were repeated after 3 hours.

3) A wand was used as in #3, under barrels, above.

The results of monitoring the atmospheric compositions (Fig. 1) showed that some argon introduction methods were more effective but all containers tended to leak so that after one month the argon had escaped.

In another study, splits of 53 coals of varying rank stored in barrels and cans were monitored. Gieseler fluidity, sulfate sulfur and calorific value changed during storage over a period of four years. In the graph of Gieseler fluid range (Fig. 2), lower values after storage indicate oxidation or deterioration of the sample. In the graph of sulfate sulfur (Fig. 3), higher values after storage indicate oxidation of pyritic sulfur to sulfate. Both graphs show that splits stored in cans were better preserved than those in barrels, and that deterioration increases with time. A related study showed buckets to be similar to barrels in their preservation ability.

After initial processing, each of the 53 coals occupied two full barrels (at -25 mm particle size) and one half-full barrel (at -6 mm). Polarographic oxygen analysis was performed on one barrel of each particle size for each coal. Two trends were observed in the results (2). Gaseous oxygen levels in the drums were related to coal rank, with low oxygen values for most low-rank and high-volatile bituminous coals and high values (above 15%) for all medium- and low-volatile bituminous and anthracite coals. This is interpreted as better scavenging of oxygen by low-rank coals. The half-full drums also had higher oxygen levels than the full drums. The coals stored in barrels at -6 mm showed an average decrease in calorific value of only 130 BTU/lb (dry, ash-free basis) (2).

For the bituminous coal samples stored in cans, alkali extraction values (3) were plotted against decrease in Gieseler fluid temperature range (4). For bituminous coals, alkali extraction is a measure of the state of weathering at the time of collection, whereas Gieseler fluidity parameters are sensitive indicators of deterioration during storage. Decreases in fluid temperature range varied from zero to 60°C, with more than half decreasing less than 10°C, while alkali extract transmission of nearly all samples was above 94%. Thus many of the samples stored in cans were judged to be preserved rather well, while a few had deteriorated noticeably.

Although some changes in storage are probably inevitable, it was concluded that the degree of preservation achieved in polyethylene pails and barrels was unsatisfactory. The difference in preservation between cans and larger containers was also considered a problem. When the initial stock of cans of a given sample was depleted, a new batch of cans made from the contents of a bucket would be more deteriorated. Other container types which would better preserve coal samples of varying amounts were sought.

FOIL/POLYETHYLENE MULTILAMINATE BAGS

A study by Sharp (5) reported the use of laminated foil and plastic bags to preserve moisture and calorific value. These bags are constructed of three layers; polyethylene inside allows heat-sealing and shields the contents from the middle aluminum foil layer which provides a barrier to gas transport and light. An outer spun-bonded polyethylene layer resists tears and abrasion. Sealing may be accomplished by manual flushing with inert gas and a manually operated sealer, or an automated vacuum/inert gas sealer as used in the food industry.

EXPERIMENTAL METHODS

Comparison to conventional containers

A study was planned to measure changes in several properties through time for a coal sample stored in different container types. Because fluidity had changed significantly during storage in previous studies, a coal with fluidity was desired for this study. A run-of-mine sample of medium-volatile (mean-max R_o 1.27%) Lower Kittanning seam coal was collected in western Pennsylvania. The sample was immediately taken to Penn State, crushed, split and prepared for analysis. Gieseler fluidity, free-swelling index and alkali extraction results were obtained within 30 hours of the coal being mined. Epoxy-binder pellets for fluorescence microscopy and splits for other analyses were also prepared at this time.

Splits of the sample were packaged in several container types for the study: -6 mm coal in polyethylene buckets and foil laminate bags; -0.85 mm coal in steel cans, foil laminate bags and an open container exposed to the atmosphere. After 4, 16 and 52 weeks containers were opened and samples analyzed as had been done for the original sample.

Comparison to Argonne Premium Coal Sample glass ampoules

Argonne National Laboratory's Premium Coal Sample Program supplies coal samples in flame-sealed, nitrogen-filled glass ampoules (6). Six ampoules of each of the six available bituminous coals were obtained. Two of each were opened and analyzed to obtain initial Gieseler fluidity and alkali extraction values. Two of each were placed in a nitrogen-filled glovebox where they were opened and the contents resealed in foil

laminate bags. Two of each remained unopened. After eight months analyses comparing the coal resealed in foil laminate bags with that in the undisturbed ampoules were performed.

RESULTS

Thermoplastic Properties

Fluid properties (Gieseler plasticity and free-swelling index) are among the most sensitive indicators of deterioration during storage. The fresh Lower Kittanning sample had a maximum fluidity of 1224 ddpm with a fluid range of 100°C. Figure 4 shows that foil laminate bags maintain fluid range better than steel cans and much better than buckets. Maximum fluidity and free-swelling index showed similar trends.

For the Argonne premium samples, Table I shows that samples ANL-101 and -501 repackaged in foil laminate bags and stored for eight months compared well to those stored in their original ampoules. The variation in results for ANL-701 is probably caused by problems with the instrument, and for ANL-301, -401 and -601 the test could not be successfully completed on the amount of coal allocated because multiple repeat runs were required to meet the ASTM precision requirement (7).

Sulfur Forms

Another sensitive indicator of deterioration, particularly in coals with abundant iron sulfide minerals, is the oxidation of sulfides to sulfates. Figure 5 shows that foil laminate bags avoid production of sulfates better than cans and much better than buckets. As with fluid range, the bucket sample was even worse than the sample exposed to the atmosphere. The bucket sample had much higher moisture than the exposed sample, perhaps caused by leakage, trapping of moist air, and subsequent condensation. Surface moisture would accelerate the sulfide to sulfate reaction.

Gaseous Oxygen

Oxygen levels in the containers' internal atmospheres were measured with a polarographic oxygen detector (Fig. 6). Low oxygen levels in the foil bags and cans are assumed to be the principal reason for better preservation of coal samples in these containers.

Fluorescence

Alteration of vitrinite fluorescence intensity is measured with photometric readings taken at regular intervals during a period of constant irradiation with blue light. For freshly mined coal, alteration patterns change from positive in lignites to one showing a dual response (first decreasing then increasing) for high volatile coals and finally becoming negative in medium volatile coals. Recent work has shown that different mechanisms of photochemical oxidation may be responsible for the formation (positive alteration) and destruction (negative alteration) of fluorophoric sites during blue-light irradiation (8). When coal becomes weathered its pattern of alteration changes from dual to positive and the mean fluorescence intensity of vitrinite also decreases (9).

Fluorometric analysis of high volatile coals stored at -6 mm for more than 30 months shows that the positive component of alteration increases and mean fluorescence intensity (F_{1600}) decreases with time. However, the alteration pattern for the medium volatile Lower Kittanning coal in this study is unchanged after 49 weeks of storage, whereas intensity decreases significantly (10). Thus, fluorescence intensity is a more sensitive measure of short-term storage changes in the medium volatile coal than alteration.

Other Properties

The alkali extraction test for oxidation of bituminous coal was performed on all samples. According to this test, all containers of the Lower Kittanning sample allowed oxidation with a narrow range of results; -6 mm coal in foil bags was preserved best and the exposed sample fared worst. For the Argonne samples (Table 1), those repackaged in foil bags compared favorably to those in ampoules, but both readings tended to be lower than those on the original ampoules. The precision of this test has not yet been determined.

Total conversion and product yield were determined from tubing-bomb liquefaction experiments (350°C, 30 min, 1000 psig H_2, 2:1 tetralin to coal ratio) for samples stored for 4 and 16 weeks in foil laminate bags and 4 weeks in a polyethylene bucket. Although conversion ranged from 17.9 - 21.7% and oil yields from 2.5 - 3.3%, no significant difference attributable to storage methods was observed.

Selected samples were examined with FTIR; no significant differences in carbonyl (~1600 cm^{-1}) or aliphatic stretching (~ 2920 cm^{-1}) were found between the foil bag and bucket storage after 4 and 16 weeks.

DISCUSSION

Conventional storage containers can cause sample deterioration. Based on this study and the desire to improve sample preservation in long-term storage, samples collected since December, 1989 for the Penn State Coal Sample Bank are being stored in foil laminate bags after processing. At this time all such samples are designated DECS (Department of Energy Coal Samples).

For field collection and temporary storage prior to processing, steel barrels with high-density gaskets (11) are employed. Samples are processed into -6 mm and -0.85 mm mesh sizes. Coal crushed to -0.85 mm is stored as 300 g splits in 19 x 24 cm foil laminate bags, -6 mm material is stored in either 2 kg or 12 kg splits in larger bags (23 x 38 or 50 x 64 cm). This avoids the problem of poorer preservation of bulk samples caused by storage in a different container type.

REFERENCES

1. Glick, D.C. and A. Davis, in press, Operation and Composition of the Penn State Coal Sample Bank and Data Base, Org. Geochem.
2. Davis, A., D.C. Glick and G.D. Mitchell, 1989, The DOE Coal Sample Bank -- Monitoring of Coal Deterioration, Proc. Direct Liquefaction Contractors' Review Meeting, Pittsburgh, PA, p. 211-222.
3. Lowenhaupt, D.E. and R.J. Gray, 1980, The Alkali-Extraction test as a Reliable Method of Detecting Oxidized Metallurgical Coal, Int. J. Coal Geol., v. 1, p. 63-73.
4. Quick, J.C., A. Davis and D.C. Glick, 1989, Coal Oxidation -- Its Detection and Effects on Thermoplastic Behavior, Extended Abstr. Prog. 19th Cont. on Carbon, University Park, PA, p. 232-233.
5. Sharp, P.A., 1986, Storage of 8 mesh sub-bituminous coal, J. Coal Qual., v. 5, p. 131-132.
6. Vorres, K.S., 1990, The Argonne Premium Coal Sample Program, Energy & Fuels, v. 4, p. 420-426.
7. ASTM, 1989, Standard D 2639-74, Standard Test Method for Plastic Properties of Coal by the Constant-Torque Gieseler Plastometer, 1989 Annual Book of ASTM Standards, ASTM, Philadelphia, p. 270-273.
8. Davis, A., R.F. Rathbone, R. Lin and J.C. Quick, 1990, Observations Concerning the Nature of Maceral Fluorescence Alteration with Time, Adv. Org. Geochem., v. 16, p. 897-906.
9. Quick, J.C., A. Davis and R. Lin, 1988, Recognition of Reactive Maceral Types by Combined Fluorescence and Reflectance Microscopy, Proc. 47th Ironmaking Conf., Toronto, p. 331-337.
10. Mitchell, G.D., A. Davis and R.F. Rathbone, in press, The Use of Vitrinite Fluorescence as a Measure of Changes in Coal Thermoplasticity and Weathering, ISS-AIME Proc., v. 50.
11. Harvey, R.D. and C.W. Kruse, 1988, The Illinois Basin coal sample program: Status and sample characterization, J. Coal Qual., v. 7, p. 109-113.

Table 1. Gieseler Fluidity and Alkali Extraction Data for Argonne Premium Coal Samples

	ANL-101, Upper Freeport, mvb			ANL-301, Illinois #6, hvBb		
Gieseler Fluidity	As Rec'd	Stored in Ampoule	Stored in foil bag	As Rec'd	Stored in Ampoule	Stored in foil bag
max. fluidity, ddpm	29,998	29,934	29,910	72	54	
initial fluidity T, °C	381	376	386	368	367	test
max. fluidity T, °C	456	456	454	418	413	failed
solidification T, °C	507	502	498	447	444	
fluid range, °C	126	126	112	79	77	
Alkali Extraction						
% transmittance	94.5	91.7	87.7	95.3	86.2	91.1

	ANL-401, Pittsburgh, hvAb			ANL-501, Pocahontas #3, lvb		
Gieseler Fluidity	As Rec'd	Stored in Ampoule	Stored in foil bag	As Rec'd	Stored in Ampoule	Stored in foil bag
max. fluidity, ddpm	25,055	17,093		46	39	37
initial fluidity T, °C	386	384	test	453	444	445
max. fluidity T, °C	438	430	failed	486	480	484
solidification T, °C	475	473		515	511	508
fluid range, °C	89	89		62	67	63
Alkali Extraction						
% transmittance	96.4	91.8	91.5	97.9	95.4	95.1

	ANL-601, Blind Canyon, hvBb			ANL-701, Lewiston-Stockton, hvAb		
Gieseler Fluidity	As Rec'd	Stored in Ampoule	Stored in foil bag	As Rec'd	Stored in Ampoule	Stored in foil bag
max. fluidity, ddpm	2	2		112	12	119
initial fluidity T, °C	404	398	test	410	406	409
max. fluidity T, °C	424	415	failed	445	422	437
solidification T, °C	446	438		469	431	463
fluid range, °C	41	40		59	25	54
Alkali Extraction						
% transmittance	96.0	89.9	87.6	95.7	81.7	90.9

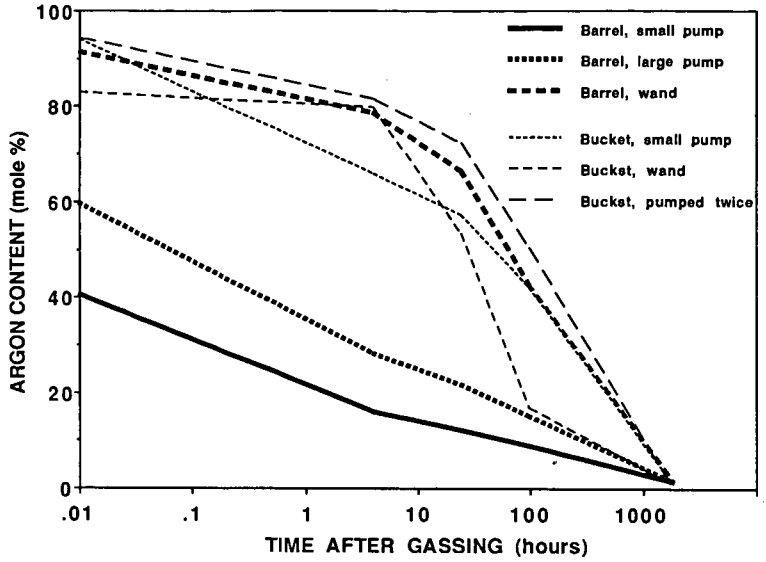

Figure 1. Argon in Barrel and Bucket Atmospheres

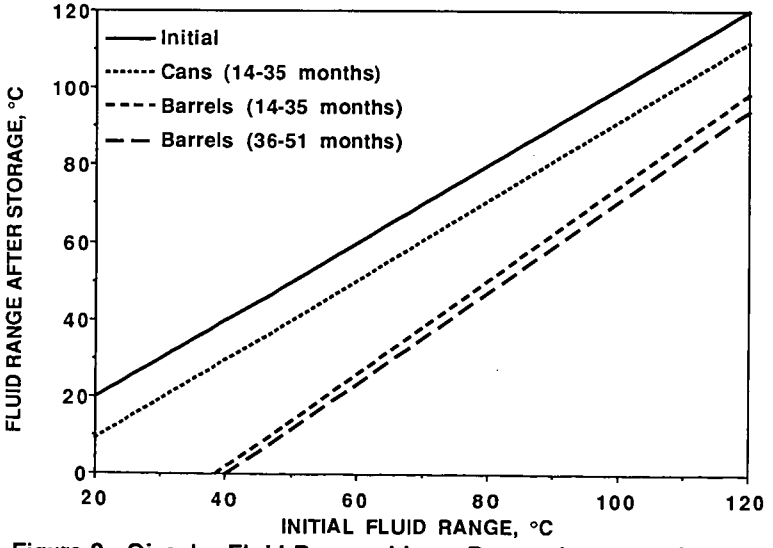

Figure 2. Gieseler Fluid Range: Linear Regression on 28 Samples

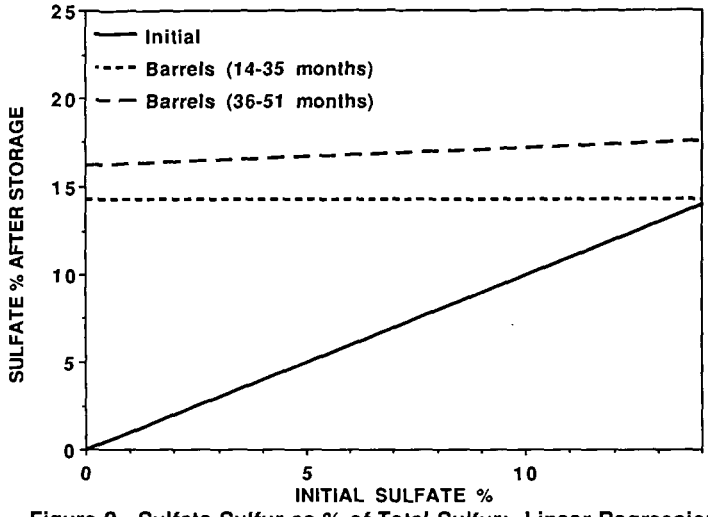

Figure 3. Sulfate Sulfur as % of Total Sulfur: Linear Regression on 53 samples

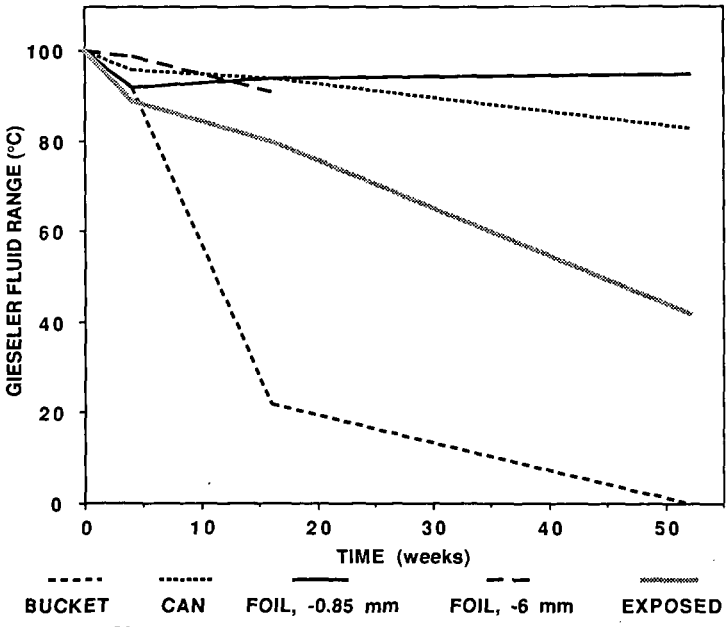

Figure 4. Gieseler Fluid Range of mvb Lower Kittanning Seam Sample

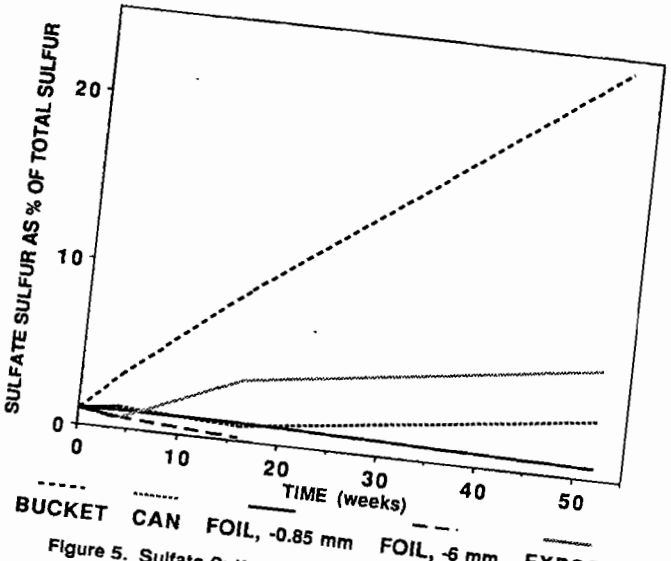

Figure 5. Sulfate Sulfur as % of Total Sulfur in mvb Lower Kittanning Seam Sample

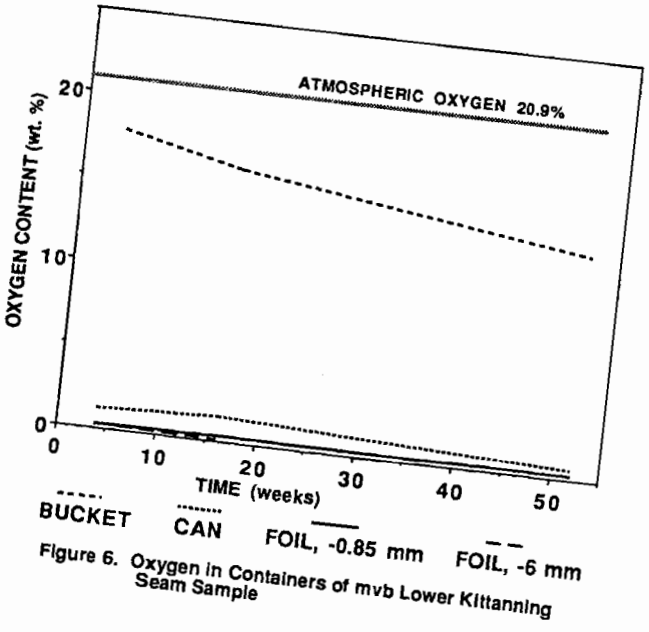

Figure 6. Oxygen in Containers of mvb Lower Kittanning Seam Sample

ORGANIC OXYGEN CONTENTS OF ARGONNE PREMIUM COAL SAMPLES

Bongjin Jung, Shawn J. Stachel, and William H. Calkins*
Center for Catalytic Science and Technology, Department of Chemical Engineering
University of Delaware, Newark, DE19716

Keywords: Organic Oxygen, Flash Pyrolysis, FNAA

ABSTRACT

The organic oxygen content has been determined for the Argonne premium coal samples through fast neutron activation analysis (FNAA) of the dry original coal and low temperature ash (LTA). This is compared with the oxygen-by-difference method using elemental analysis and high temperature ash corrected by the Parr Formula. The total organic oxygen content is compared with oxygen functional group contents as determined by chemical and flash pyrolysis techniques.

INTRODUCTION

The organic oxygen components of coal are important in determining coal structure and reactivity in coal liquefaction and other processes (1). Coal contains substantial amounts of chemically bound oxygen in the organic components in addition to the oxygen associated with mineral matter in coal. The total oxygen content decreases with the rank of the coal (2). The conventional ASTM method (3) used to estimate the organic oxygen content of coal is to subtract from 100 the sum of the percentages of carbon, hydrogen, nitrogen, sulfur, and high temperature ash. All errors in these determinations and errors due to large weight changes in the coal mineral matter in the ASTM high temperature ash method are included in the oxygen-by-difference estimate. This can be corrected to some degree by the modified Parr Formula (4), but the result is only an estimate.

Fast neutron activation analysis (FNAA) has been used to determine organic oxygen of coal directly by several workers (5,6,7). Low temperature ashing instead of ASTM high temperature ash method has been used with fast neutron activation analysis of the ash and the dried coal for the determination of organic oxygen (5,6). Mahajan (7) and others have reported that, during low temperature ashing of coals, mineral matter present in coal undergoes minimal change in composition. Organic oxygen is calculated from the following difference of FNAA determinations of total dry coal oxygen and oxygen in low temperature ash.

$$\% O_{organic} = \% O_{total} - \% O_{LTA} \times g\ LTA/g\ coal$$

The problems involved in determining the organic oxygen content of coal were discussed in detail by Given and Yarzab (8).

Oxygen structures in coal give off water, carbon monoxide or carbon dioxide on pyrolysis, and the temperatures at which these are evolved depend on the functional groups. Pyrolysis together with NMR and other analytical methods may allow us to identify the particular oxygen functional groups in the coal, and correlate this with process studies.

*To whom communications should be sent

There is chemical evidence for the presence of hydroxyl, carbonyl, carboxyl, and methoxy groups in low-rank coals, and for hydroxyl and carbonyl groups in higher rank coals (9, 10). However a certain fraction of the oxygen is not detected by standard chemical analyses and is usually considered to be ether oxygen. It has been speculated that coal liquefaction consists at least in part in the cleavage of ether linkages between aromatic ring clusters (11, 12), leaving free radical ends which are capped by hydrogen transfer from coal or a donor solvent. Cleavage of ether groups might be expected to give more phenolic groups (13). The principal evidence for this is the presence of more phenolic groups after liquefaction than were present in the original coal (12, 14). However, the presence and type of ether groups in coal and the role of oxygen functionalities in coal liquefaction is still obscure (1).

It is to try to provide more information on the oxygen functional groups distribution and organic oxygen species in coal and their roles in coal processes that this work was undertaken. The research described will be an important step toward understanding the chemistry of the coal pyrolysis process. To the extent that it is successful in developing an understanding of coal structure it will also assist in developing an understanding of coal liquefaction and other coal conversion processes.

EXPERIMENTAL

Coals Studied

The eight coals from the Argonne premium coal sample program were studied (see Table1).

Low Temperature Ashing

The low temperature asher (LFE Corp., LTA-302) was operated at around 75-100 W depending on fluctuations in the unit while running. The oxygen flow rate was kept at 100 cc/min. All the samples (approximately 0.2 g) were ashed after being ground under nitrogen for one hour with a mortar and pestle. The samples in the boat were stirred to expose fresh surface for oxidation approximately every 5 hours. Ashing was continued until constant weight of the sample was obtained. All of the low temperature ash samples were sealed in air tight vials in the nitrogen atmosphere of a glove box. In the case of Wyodak and Beulah samples the low temperature ash was measured on both the original and acid forms.

Chemical Methods

The chemical methods of Blom and Schafer (9, 10) were used for analysis of the oxygen functional groups in coal such as carboxyl, hydroxyl, and carbonyl. Ethers (internal and external) were estimated by difference. Kjeldahl nitrogen runs as part of the carbonyl determination were run by Micro Analysis Inc.

Pyrolysis Method

The pyrolysis experiments were conducted on the Beulah-Zap and Wyodak samples at 625-930°C with 74-105 μm fractions in a continuous fluidized sand bed pyrolyzer (described in detail in reference 15). The coals used were ground in a SPEX mill or mortar and pestle in a nitrogen atmosphere, sieved, and then vacuum dried at 104-107°C for approximately 20 hours. The coal particles were entrained into a nitrogen stream in the coal feeder and carried over into the fluidized sand bed at various flash pyrolysis temperatures.

The coal feeder was suspended from a Mettler balance and the change in its weight with time was monitored by a Linseis recorder. Coal was fed at uniform rates of 0.03-0.1 grams/min and approximately 1-2 grams total are fed. Upon entering the pyrolyzer, the coal was rapidly heated to the bed temperature at a rate of approximately 10^4 °C/sec and residence time (assuming full utilization of the expanded fluidized sand bed) was about 0.5 sec. Thermocouple wells in the reactor allow close monitoring of the temperature in the reactor bed and in the region above it. The pyrolysis products exit the pyrolyzer to a set of three cold traps. A side stream after the first trap can be vented to a Panametrics hygrometer for measurement of water content. The gases were collected and analyzed for CO and CO_2 in a Perkin-Elmer Sigma 1B gas chromatograph. The tars were collected in Soxhlet thimbles for later recovery by Soxhlet extraction with methylene chloride and subsequent analysis in an HP5880A gas chromatograph/mass spectrometer.

RESULTS AND DISCUSSION

Organic Oxygen Content: We have run eight Argonne National Laboratory (ANL) premium coal samples in the low temperature asher. The remaining ash, after the sample reached constant weight, was analyzed by Radioanalytical Services of the University of Kentucky for determination of percent oxygen through fast neutron activation. This value was subtracted from the total oxygen content, which was determined in the same manner on the dried coal itself, to give the percent organic oxygen for each sample of coal. Oxygen values reported by FNAA are for at least three replicate analyses of the same sample. The oxygen contents of eight coals and their low temperature ashes are shown in Table 1. A comparison of % low temperature ash of the samples between our experiments and ANL data (16) are generally in close agreement, except for the Beulah-Zap and Wyodak samples which are somewhat higher in this study. The reason for this difference is not apparent. The organic oxygen contents of the dried coals determined by FNAA method are compared in Table 2 with those determined by oxygen-by-difference using elemental analysis and high temperature ash corrected by the Parr Formula. These two values are generally in agreement. Table 3 shows the elemental analysis of samples (16) by direct determination including the contents of low temperature ashes and the total organic oxygen determined by FNAA method. It will be noted that the total of these values are approximate 100 %, except for the Illinois #6 coal which is somewhat high. The reason for this is being investigated.

Low-rank coals contain the large concentration of exchangeable metal ions associated with the carboxyl groups. In the case of Wyodak and Beulah-Zap samples, the comparison of % low temperature ash of the original and acid forms show significant concentrations of associated metal ions, as shown in Table 4.

Chemical Methods: The percent oxygen as carboxyl, hydroxyl, carbonyl, and ether (by difference) in each sample is shown in Table 5. Carboxylic groups are found in considerable concentration in the low-rank coals. The percent oxygen in carboxyl groups decreases with increasing rank and approaches zero for coals of higher rank. The percent oxygen as hydroxyl and carbonyl show similar trend with increasing rank, but carbonyl shows greater variability. There is significant amounts of ether oxygen (by difference) in all samples. Illinois #6 coal, however, seems to be somewhat lower in ether oxygen than might be expected for its rank.

Flash Pyrolysis: The pyrolysis of coal over a range of controlled conditions offers a possible unexploited and independent approach to studying the oxygen species in coal. The structural interpretations of pyrolysis data of coal sample are compared to total organic oxygen contents determined by FNAA and oxygen functional group contents such

as % carboxyl, % hydroxyl, % carbonyl, and % ether (by difference) by chemical methods.

The corresponding oxygen yields of Wyodak subbituminous as a function of pyrolysis temperature are shown in Figure 1. The main oxygen-containing products of the decomposition of oxygen groups of the sample are H_2O, CO_2, and CO. Some water is adsorbed in coal and some may appear through decomposition of chemical structures. Carboxyl content as determined by CO_2 evolution agrees closely with chemical analysis indicating that carboxyl groups pyrolyze quantitatively to CO_2 (17). Water and CO_2 evolution occurs below 700 °C.

CO is a major gaseous product of coal pyrolysis and oxygen yield as CO continues increasing with temperature up to 930 °C. More experimental work is need to confirm the carbon monoxide emissions at temperatures in the range of 950-1000 °C. Based on model compounds studied, hydroxyl and ether groups appear to evolve mainly carbon monoxide and possibly water. Very preliminary work by one of the writers (15) at temperatures in the range of 600-1000 °C tend to confirm those observations and suggest that in our system these carbon oxide emissions may be complete and reasonably quantitative by 950-1000 °C.

Total oxygen yield from oxygen-containing groups increased with temperature. The total organic oxygen contents of the sample determined by flash pyrolysis technique and fast neutron activation analysis are in fairly close agreement.

CONCLUSIONS

The conclusions of this work are as follows

1. The organic oxygen contents of the dried coals determined both by FNAA method and by oxygen-by-difference using the modified Parr Formula on high temperature ash are generally in agreement.

2. The percent carboxyl, hydroxyl, and carbonyl groups of samples decrease with increasing rank. Ethers represent a significant fraction of the organic oxygen in the Argonne coals.

3. Temperatures approaching 1000 °C are required to pyrolyze all the oxygen groups in coal.

4. Carboxyl groups in coal pyrolyze quantitatively to CO_2 below 700 °C.

5. A substantial proportion of the mineral matter in low-rank coals is associated with the carboxyl groups.

ACKNOWLEDGMENTS

The pyrolysis work was sponsored in part by Amoco Oil Company. We are grateful to Dr. Karl S. Vorres for providing the Argonne National Laboratory Premium Coal Samples and Radioanalytical Services of the University of Kentucky for doing the FNAA.

REFERENCES

1. Szladow, A.J. and Given, P.H., ACS Fuel Division Preprints, **23**(4), 161 (1978)
2. van Krevelen, D.W., Coal, Elsevier Scientific, 1981
3. ASTM, "Annual Book of Standards", Part 26 (1976)
4. Parr, S.W., Analysis of Fuel, Gas, Water and Lubricants, McGraw Hill, N.Y., 1932
5. James, W.D., Ehmann, W.D., Hamrin, C.E., and Chyi, L.L., J. Radioanal. Chem., **32**, 195 (1976)
6. Volborth, A., Miller, G.E., Garner, C.K., and Jerabek, P.A., Fuel, **56**, 204 (1977)
7. Mahajan, O.P., Fuel, **64**, 973 (1985)
8. Given, P.H. and Yarzab,F., in "Analytical Methods for Coal and Coal Products" , Karr, C.,Jr., ed., Vol. 2, pp. 3-41, Academic Press, N.Y. (1978)
9. Blom, L., Edelhausen, L., and van Krevelen, D.W., Fuel, **36**, 135 (1957)
10. Schafer, H.N.S., Fuel, **49**, 197 (1970)
11. Takazawa, I., Kajeyama, S., and Tokokawa, G., Fuel, **42**, 291 (1963)
12. Kuhlmann, E., Boerwinkle, E., and Orchin, M., Fuel, **60**, 1002 (1981)
13. Cronauer, D.C. and Ruberto, R.C, EPRI Rept. AF913, March (1979)
14. Ignasiak, B.S. and Gawlak, M., Fuel, **56**, 216 (1977)
15. Calkins, W.H., Hagaman, E., and Zeldes, H., Fuel, **63**, 1113 (1984)
16. Vorres, K.S., Users Handbook for the Argonne Premium Coal Sample Program, Argonne National Lab, October, 1989
17. Schafer, H.N.S., Fuel, **58**, 667 (1979)

Table 1. Organic Oxygen Contents of Argonne Premium Coal Samples (dry, wt %) by Fast Neutron Activation Analysis

Coal	Beulah-Zap	Wyodak-Anderson	Illinois #6	Blind Canyon	Pittsburgh #8	Lewiston-Stockton	Upper Freeport	Pocahontas #3
Rank C(dmmf)	Lig. 74.05	Subb. 76.04	HVB. 80.73	HVB. 81.32	HVB. 84.95	HVB. 85.47	MVB. 88.08	LVB. 91.81
LTA by ANL	8.7	8.7	18.1	5.3	10.9	21.6	15.3	5.5
LTA[a]	11.88	11.51	19.77	5.7	10.05	21.9	15.7	5.8
O_{LTA}[b]	51.3	55.5	37.9	48.0	41.4	49.1	38.4	45.4
O_T[c]	23.3	20.7	14.9	12.5	10.9	16.5	8.93	4.22
O_{org}[d]	17.2	14.31	7.41	9.76	6.74	5.75	2.90	1.59

[a] Low temperature ash in this study

[b] Oxygen content of low temperature ash by FNAA

[c] Total oxygen content of coal by FNAA

[d] Organic oxygen content of coal by % $O_{organic}$ = % O_{total} - % O_{LTA} x g LTA/g coal

Table 2. Comparison of Organic Oxygen Contents of Argonne Premium Coal Samples (dry, wt %) by Fast Neutron Activation Analysis and Oxygen-by-Difference Methods

Coal		Beulah-Zap	Wyodak-Anderson	Illinois #6	Blind Canyon	Pittsburgh #8	Lewiston-Stockton	Upper Freeport	Pocahontas #3
Rank C(dmmf)		Lig. 74.05	Subb. 76.04	HVB. 80.73	HVB. 81.32	HVB. 84.95	HVB. 85.47	MVB. 88.08	LVB. 91.81
ANL[a]	O_{org}[b]	17.01	15.21	8.21	10.29	6.13	5.17	3.98	1.57
Exp.[c]	O_{org}[d]	17.21	14.31	7.41	9.76	6.74	5.75	2.90	1.59

[a] Argonne National Laboratory

[b] Organic oxygen content of coal by difference using elemental analysis and high temperature ash % corrected by Parr Formula

[c] Our experimental data by FNAA

[d] Organic oxygen content of coal by % $O_{organic}$ = % O_{total} - % O_{LTA} x g LTA/g coal

Table 3. Elemental Analysis by Direct Determination of Argonne Premium Coal Samples (dry, wt %)

Coal	Beulah-Zap	Wyodak-Anderson	Illinois #6	Blind Canyon	Pittsburgh #8	Lewiston-Stockton	Upper Freeport	Pocahontas #3
Rank	Lig.	Subb.	HVB.	HVB.	HVB.	HVB.	MVB.	LVB.
C(dmmf)	74.05	76.04	80.73	81.32	84.95	85.47	88.08	91.81
C[a]	65.85	68.43	65.65	76.89	75.50	66.20	74.23	86.71
H[a]	4.36	4.88	4.23	5.49	4.83	4.21	4.08	4.23
N[a]	1.04	1.02	1.16	1.50	1.49	1.25	1.35	1.27
S[a]	0.80	0.63	4.83	0.62	2.19	0.71	2.32	0.66
Cl[a]	0.04	0.03	0.05	0.03	0.11	0.10	0.00	0.19
F[a]	0.00	0.00	0.00	0.00	0.00	0.00	0.00	0.00
O_{org}[b]	17.21	14.31	7.41	9.76	6.74	5.75	2.90	1.59
LTA[c]	11.88	11.51	19.77	5.7	10.05	21.9	15.7	5.8
Total	101.18	100.81	103.10	99.99	100.91	100.12	100.58	100.45

[a] Data from ANL user handbook

[b] Organic oxygen content of coal by $\%\ O_{organic} = \%\ O_{total} - \%\ O_{LTA} \times g\ LTA/g\ coal$

[c] Low temperature ash in this study

Table 4. Metal Ions Associated with Low-Rank Coals

Coal	Beulah-Zap (wt %)	Wyodak-Anderson (wt %)
Low Temperature Ash on Raw Coal	11.88	11.51
Low Temperature Ash on Acid Form	2.87	5.7
Associated Metal Ions	9.01	5.81

Table 5. Determination of Organic Oxygen Contents by Chemical and Pyrolytic Analyses of Argonne Premium Coal Samples (dry, wt. %)

Coal	Beulah-Zap	Wyodak-Anderson	Illinois #6	Blind Canyon	Pittsburgh #8	Lewiston-Stockton	Upper Freeport	Pocahontas #3
Rank	Lig.	Subb.	HVB.	HVB.	HVB.	HVB.	MVB.	LVB.
C(dmmf)	74.05	76.04	80.73	81.32	84.95	85.47	88.08	91.81
Total Organic O by FNAA (1)	17.21	14.31	7.41	9.76	6.74	5.75	2.90	1.59
% O as CO_2H by Chemical Method (2)	*3.81*	*3.33*	0.23	0.23	0.16	0.20	0.14	0.05
% O as CO_2H by Pyrolysis Method	*3.94*	*3.14*						
% O as OH by Chemical Method (3)	9.16	7.68	5.68	5.22	4.32	2.70	1.96	0.98
% O as C=O by Chemical Method (4)	1.96	0.74	0.93	0.63	0.18	0.18	0.44	0.32
% O as Ether by Difference (1) - (2) - (3) - (4)	2.28	2.56	0.57	3.68	2.08	2.67	0.36	0.24

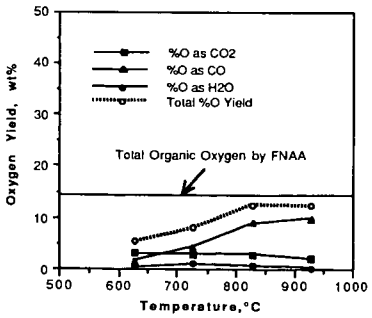

Figure 1. Oxygen Yield from Pyrolysis of Wyodak Subbituminous Coal in Fluidized Bed Pyrolyzer

QUANTITATIVE ^{13}C NMR MEASUREMENTS ON THE ARGONNE PREMIUM SAMPLES AND OTHER COALS

Colin E. Snape and Gordon D. Love
University of Strathclyde, Dept. of Pure & Applied Chemistry,
Thomas Graham Building, 295 Cathedral St., Glasgow G1 1XL, UK

Keywords: Quantitative ^{13}C NMR, aromaticity, Argonne coals.

ABSTRACT

In view of the well-documented inherent problems with cross-polarisation (CP) ^{13}C NMR concerning quantification for coals, the more time-consuming single pulse excitation (SPE) or Bloch decay technique has much to commend it. SPE ^{13}C NMR has been carried out on the Argonne Premium Samples and a selection of UK coals and maceral concentrates at a low field strength (25MHz) to avoid problems with spinning sidebands. In addition to aromaticity measurements, quaternary aromatic carbon concentrations have been determined by SPE dipolar dephasing. As anticipated, much greater proportions of the carbon were obseved by SPE than by CP and the use of tetrakis(trimethylsilyl)silane as an internal standard has indicated that over 90% of the carbon in most of the coals is observed by SPE. Moreover, aromaticity values measured by SPE are consistently higher than those from CP. For anthracite, the concentration of bridgehead aromatic carbon measured by dipolar dephasing SPE is in close agreement with that from elemental analysis.

INTRODUCTION

The combination of dipolar decoupling and magic angle spinning (MAS) with cross-polarisation now enables ^{13}C NMR spectra of carbonaceous materials to be obtained on a routine basis. Although ^{13}C NMR has shown considerable potential for the characterisation of coals, oil shales and other humic materials [1,2], there has been considerable doubt concerning the quantitative reliability of aromaticity and other skeletal parameter measurements using this technique [3]. There is a consensus that significant errors can arise in CP/MAS ^{13}C NMR measurements of aromaticity and other skeletal parameters due to the unfortunate spin-dynamics of carbonaceous materials which typically result in only 50% of the carbon being observed for bituminous coals. Although it is well established that the rate of magnetisation transfer from abundant ^{1}H to dilute ^{13}C spins during CP is slower for quaternary aromatic carbons than for protonated carbons, the major problem for coals is undoubtedly the presence of paramagnetic species which cause ^{1}H spins to relax too quickly during CP, i.e. before polarisation transfer to ^{13}C spins has been achieved. In addition, carbons in the vacinity of paramagnetic centres are not observed due to a combination of shielding effects and rapid relaxation. Thus, in general, there is often a clear discrimination against aromatic carbon . Moreover, additional problems are posed by measurements at high field strengths where either much higher spinning speeds or special pulse sequences (e.g. TOSS) are needed to remove sidebands associated with aromatic peaks.

In view of the well-documented inherent problems with CP ^{13}C NMR concerning quantification for solid fuels [2,3], the use of the more time-consuming Bloch decay or single pulse excitation (SPE) technique has much to commend it, particularly at low field strengths to avoid problems with spinning sidebands. This paper covers the application of SPE ^{13}C NMR to the Argonne Premium Coal Samples, a number of UK coals and maceral concentrates, the results being compared with those reported here and by other workers from CP. In addition to aromaticity measurements, dipolar dephasing has been used with SPE to estimate the quaternary aromatic carbon concentration in an anthracite.

EXPERIMENTAL

All the Argonne Premium Coal Samples were analysed except Pocahontas. The 3 UK bituminous coals investigated where Linby, Gedling (both 83% dmmf C) and Point of Ayr (87% dmmf C),

together with an anthracite (Cynheidre). The maceral concentrates were obtained from a US Kentucky low volatile bituminous coal (88% dmmf C) by density gradient centifugation.

Most of the measurements were carried out at 25MHz on a Bruker MSL100 spectrometer with MAS at 4.5 kHz to give virtually sideband free spectra. For CP, contact times were varied between 0.1 and 15 ms. A relaxation delay of 20s was used in SPE in view of the fact that the few published values of ^{13}C thermal relaxation times for coals are at least 5s [4-6]. No background signal was evident in the SPE spectra from the Kel-F rotor caps. Typically, between 3000 and 4000 scans were accumulated for both the CP and SPE spectra. Dipolar dephasing was carried out with both variable and fixed (50us) dephasing periods. Some spectra were also obtained at high field (75 MHz) with rapid MAS (>10 kHz) using a Varian VXR300 spectrometer. Tetrakis(trimethyl)silane (TKS) was used as an internal standard to determine the proportions of carbon observed in the samples investigated. In experiments with TKS, the acquisition time was extended from 30 to 250 ms to avoid truncating the free induction decay.

RESULTS AND DISCUSSION

Figure 1 shows the 25 MHz SPE spectra of N.Dakota lignite, Pittsburgh No.8 coal and Cynheidre anthracite and indicates that the signal to noise levels are high (50 Hz line broadening routinely used). Moreover, the intensities of the sidebands are below 5% of the central aromatic peaks with MAS at 5 kHz. The 25 MHz SPE and CP spectra of one of the bituminous coals (Gedling) are shown in Figure I and it is evident that significantly more aromatic carbon is observed by SPE. Table 1 compares the aromaticity values derived by SPE and CP for the coals investigated and the same trend is found in most cases. Indeed, differences in the measured aromaticity values by the two methods range from 3 to 10 mole%. For CP, the differences are small between the values obtained with a contact time of 1ms and those obtained by fitting the intensities of the aromatic and aliphatic bands from multiple contact experiments to the form.

$$I_o = I_t \exp(1\text{-}t/T_{CH}).\exp(-t/T_{1\rho})$$

where T_{CH} is the time constant for CP and $T_{1\rho}$ is the ^1H rotating frame relaxation time.

For the Argonne samples, the CP-determined aromaticities are generally in reasonable agreement ($\pm$ 2 mole %) with those reported by Botto and Axelson [5] and Pugmire et al [7]. However, at relatively long contact times (>4 ms), the values obtained were typically 2-3% higher than those from using a contact time of 1ms and multiple contacts (Table 1). Illinois No.6, Pittsburgh No.8, Lewiston-Stockton, Linby, Gedling and Point of Ayr coals all have H/C ratios between 0.76 and 0.78 despite their carbon contents varying between 80 and 87%. Interestingly, their 25 MHz SPE-determined aromaticities fall in the relatively narrow range of 0.77-0.81. Indeed, one of the authors has argued previously that such aromaticities are more consistent with the H/C ratios than the considerably lower CP-determined values of 0.72$\pm$0.04 (Table 1). Of the coals investigated, the lowest proportion of the carbon was observed by SPE for Upper Freeport coal (80%, Table 1) and, with the exception of the anthracite, this was the only coal for which CP and SPE gave the same aromaticity value within the experimental error of about $\pm$1%. From the H/C ratio of 0.67 for this coal and the SPE-determined aromaticities discussed above, a value close to 0.85 would have been anticipated. Indeed, if it is assumed that the 20% of the carbon not observed is aromatic, then the measured value of 0.81 increases to 0.84. Although aromaticities derived from the high-field SPE spectra (Figure 3 shows the 75 MHz spectrum for Linby coal) were less precise due to a combination of the greater sideband intensities, the high-field sidebands overlapping with the aliphatic bands and some background signal being obtained from the Kel-F rotor caps, reasonable agreement was obtained with values from the low-field spectra (Table 1).

Figure 4 shows the SPE spectra for the liptinite, vitrinite and inertinite concentrates and, as anticipated, aromaticity increases in going from liptinite to vitrinite to inertinite. However, as for the whole coals, the respective aromaticity values of 0.60, 0.80 and 0.89 are considerably higher than those determined by CP and over 85% of the carbon was observed.

The concentration of quaternary aromatic carbon was estimated by dipolar dephasing using both CP and SPE for the anthracite. Figures 5 and 6 present the decays of the aromatic carbon intensities with increasing dephasing time for CP (10 ms contact time) and SPE, respectively; it was expedient to obtain

more data points for CP because of the superior signal to noise ratios obtained with the much shorter recycle times. Figure 5 ,in particular, indicates the modulation of the decaying aromatic peak by the MAS. However, in both plots, the expected two component decay is observed. As anticipated with a relatively short contact time (1 ms), the value obtained of about 50 mole % quaternary aromatic carbon was considerably lower than that of 0.67 from the H/C ratio and the SPE-determined aromaticity. Considerably higher values of 67 and 69 mole % C were obtained from Figures 5 and 6 for long contact time CP and SPE, respectively. Moreover, these values are in close agreement with the estimate discussed above from elemental analysis. It should be pointed out that the anthracite investigated here has a slightly higher atomic H/C ratio than that investigated by Gerstein and co-workers [8] and this is consistent with the value obtained with a contact time of 1 ms (50%) being lower than that of about 65% reported in Gerstein's study with a similar contact period. The dipolar dephasing SPE experiment is being extended to the other coals and also being used to estimate methyl concentrations.

CONCLUSIONS

The results clearly demonstrate that, for most coals, aromaticity and other skeletal parameters measured by SPE ^{13}C NMR are quantitatively reliable with typically over 90% of the carbon being observed. The SPE-determined aromaticities of high volatile bituminous coals having H/C ratios of about 0.78 are close to 0.8 and these values are consistently higher than those in the range 0.68-0.75 measured by CP. The development of larger rotors for MAS [6] will help make SPE measurements an even more attractive proposition for quantitative ^{13}C NMR analysis of solid fuels.

REFERENCES

1. Davidson, R.M. Nuclear magnetic resonance studies on coals, ICTIS/TR32, IEA Coal Research, London, 1986.
2. Axelson, D.E., Solid state NMR of fossil fuels, Multiscience, Canada (1985).
3. Snape, C.E., Axelson, D.E., Botto, R.E., Delpuech, J.J., Tekely, P., Gerstein, B.C., Pruski, M., Maciel, G.E. and Wilson, M.A., Fuel, 1989, **68**, 547 and references therein.
4. Palmer, A.J. and Maciel, G.E., Anal. Chem., 1982, **54**, 2194.
5. Botto, R.E. and Axelson, D.E., Prepr. Am. Chem. Soc. Div. Fuel Chem., 1988, **33(3)**, 50.
6. Zhang, M. and Maciel, G.E., Fuel, 1991, **69**, 557.
7. Solum, M.S., Pugmire, R.J. and Grant, D.M., Energy & Fuels, **3**, 187.
8. Murphy, P.D., Cassidy, T.J. and Gerstein, B.C., Fuel, **61**, 1233.

ACKNOWLEDGEMENTS

The authors thank the Science and Engineering Research Council and British Gas plc for financial support (Grant no. GR/F/87264 and a CASE studentship for GDL) and D. Taulbee of the University of Kentucky Centre for Applied Energy Research for supplying the maceral samples.

Table 1 Aromaticity values derived from the 25 MHz spectra of the coals

Sample	% *dmmf* C	Aromaticity values				% of carbon observed by SPE
		CP-1ms	CP-7ms	CP-fit	SPE	
N.Dakota lignite	73	0.66	0.69	0.65 (0.65)	0.76	94
Wyodak sub-bit.	75	0.62	0.65	0.63 (0.63)	0.75	100
Illinois No.6	80	0.70	0.73	0.70 (0.72)	0.78 [0.76]	92
Pittsburgh No.8	83	0.72	0.73	0.72 (0.72)	0.77	89
Blind Canyon	81	0.62	0.62	0.63 (0.63)	0.65	96
Linby	83	0.68	0.72	0.68 (0.68)	0.81 [0.79]	100
Gedling	83	0.68	0.74	0.67 (0.67)	0.78	95
Lewis.-Stockton	84	0.69	n.d.	n.d.	0.79	100
Point of Ayr	87	0.71	0.75	0.71	0.79	92
Upper Freeport	88	0.75	0.79	0.77 (0.80)	0.81	83
Cynheidre anthracite	95	0.96	0.98	0.96 (0.98)	0.99	94

CP-fit = from multiple contact experiments, ( ) = values from fitting aromatic carbon band to two components for T_{CH} and $T_{1\rho}$ which gave much better fits.

[ ] = values from 75 MHz spectra. n.d. = not determined.

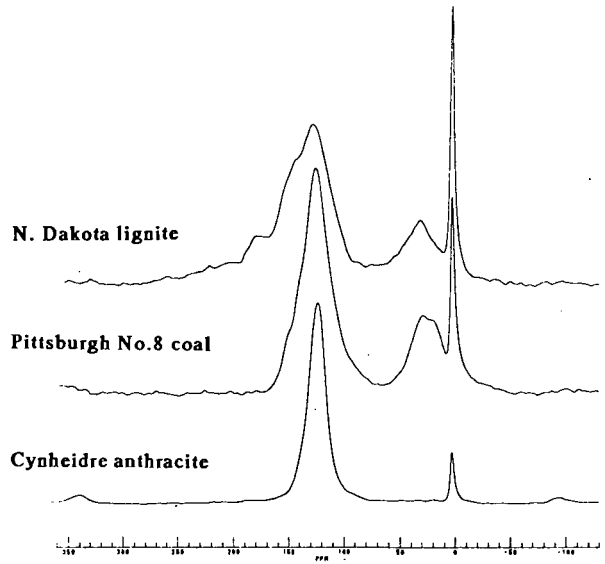

FIGURE 1 25 MHz SPE ^{13}C NMR SPECTRA OF SOME OF THE COALS

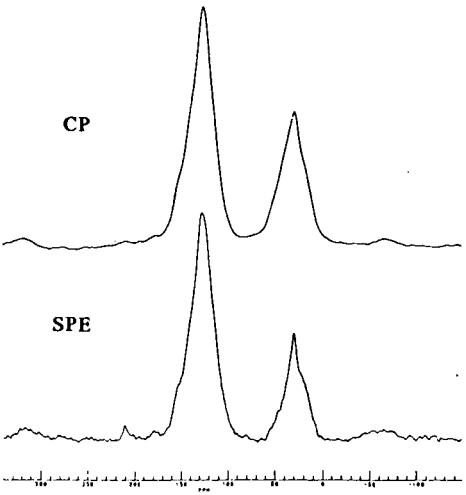

FIGURE 2 25 MHz CP AND SPE ^{13}C NMR SPECTRA OF GEDLING COAL

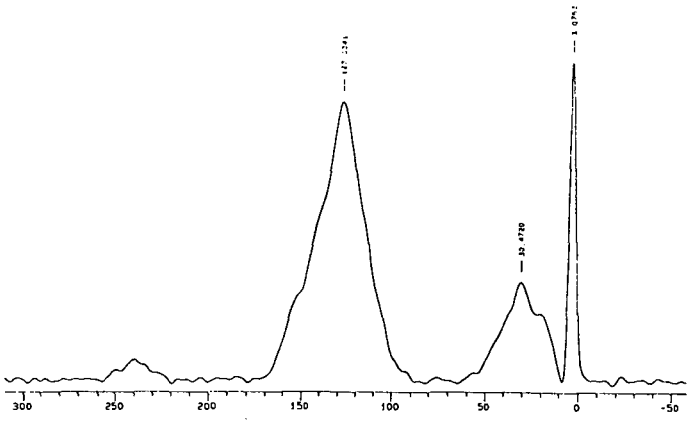

FIGURE 3 75MHz SPE SPECTRUM OF ILLINOIS No. 6 COAL

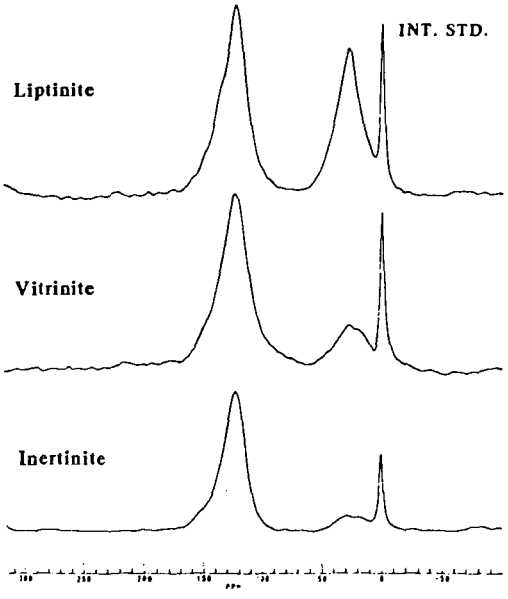

FIGURE 4 25 MHz SPE SPECTRA OF MACERAL CONCENTRATES

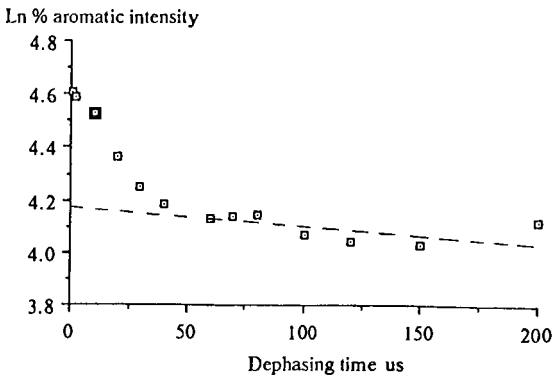

FIGURE 5 AROMATIC CARBON INTENSTIES FROM CP DIPOLAR DEPHASING EXPERIMENT ON THE ANTHRACITE

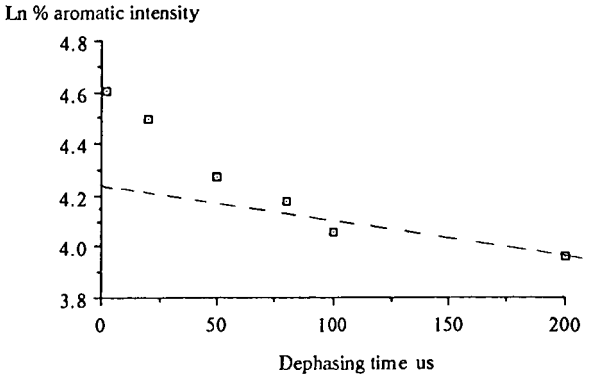

FIGURE 6 AROMATIC CARBON INTENSITIES FROM SPE DIPOLAR DEPHASING EXPERIMENT ON THE ANTHRACITE

HYDROGEN TRANSFER FROM NAPHTHENES TO COAL DURING COPROCESSING

Ruth M. Owens and Christine W. Curtis
Chemical Engineering Department
Auburn University, Alabama 36830

Abstract

Hydrogen transfer from naphthenes to aromatics, coal, resid, and coal plus resid has been investigated at 430°C in a N_2 atmosphere. The reaction of perhydropyrene (PHP) with anthracene (ANT) resulted in the formation of pyrene (PYR) and dihydroanthracene (DHA). The weight percents of the products formed varied according to the ratio of ANT/PHP with a minimum appearing at a 2 to 1 weight ratio. Increased reaction times and high ANT/PHP ratios also yielded tetrahydroanthracene (THA). Reactions of Illinois No. 6 coal from the Argonne Premium Coal Bank with PHP, ANT, and PYR resulted in higher coal conversion with PHP and lower with ANT and PYR. With PHP less retrogressive reactions occurred in the resid than with either PYR or ANT. Apparent hydrogen transfer from coal or resid to ANT and PYR was observed. Combining PHP with ANT or PYR with coal, resid or coal plus resid yielded in higher conversions and less retrogressive reactions. Hydrogen transfer occurred from PHP to ANT or PYR and to the coal and resid as evinced by the increased conversion.

Introduction

The coprocessing of coal with petroleum residuum involves the simultaneous conversion of coal to liquid products and the upgrading of resid to higher quality products. These two feedstocks are quite different in composition with petroleum resid being hydrogen-rich with a hydrogen to carbon (H/C) ratio in the range of 1.4 to 1.6 while coal is hydrogen deficient with a H/C ratio of 0.6 to 0.8. The conversion of coal and the subsequent upgrading of coal liquids requires the transfer of hydrogen to coal. Many different sources of hydrogen are available to coal during typical coprocessing: hydrogen from hydrogen rich portions of the coal, hydrogen from aliphatic, naphthenic or hydroaromatic components in the resid, or hydrogen from the molecular hydrogen present in the reactor. Hydrogen from naphthenic components in the resid would provide a valuable hydrogen resource for coal and alleviate some dependence on molecular hydrogen.

This research investigates the hydrogen transfer from naphthene type structures in the resid to hydrogen acceptors: aromatic species, coal, and the resid itself. Previous research by Clarke et al. (Fuel, 63, 1476, 1984) had pointed to the possibility that hydrogen transfer was occurring between naphthenic components and coal resulting in increased conversion of coal and formation of aromatics from the naphthenes. In this work, a systematic set of experiments was performed using the naphthene perhydropyrene (PHP) reacted with the aromatic pyrene (PYR) or anthracene (ANT) to evaluate hydrogen transfer from naphthenes to aromatics in an inert atmosphere. Reactions were then performed with both naphthenes and aromatics with Illinois No. 6 coal from the Argonne Premium Coal Bank and with Maya resid individually and with the coal and resid combinatorially. Hydrogen transfer from both the naphthene to the coal and resid and from the coal and resid to the aromatic was examined.

Experimental

Materials. The chemicals used in this study included pyrene, perhydropyrene, and anthracene which were obtained from Aldrich Chemical at a purity of 99% or higher. The coal used was Illinois No. 6 from the Argonne National Laboratory Premium Coal Sample Program. The residuum used was Maya Resid from Amoco. The solvents used for the extraction analyses were toluene and THF from Fisher Scientific.

Procedure. Model compound and coprocessing reactions were conducted in small tabular microreactors charged with nitrogen gas. The reaction conditions for the model reactions were temperature of 430°C, N_2 at 400 psig ambient, and reaction times of 60, 90 and 180 minutes. For the single component model reactants, 0.1 gram was charged. For the binary component model reactants, the amount of individual reactant used ranged from 0.1 to 0.6g with the total amount of reactant charged ranging from 0.4 to 1.0g. Following the reaction the products were extracted with THF and analyzed by gas chromatography. The gaseous products from the reaction were analyzed using a Varian 3700 gas chromatograph equipped with a thermal conductivity detector and a molecular sieve column. The liquid products were analyzed on a Varian 3400 gas chromatograph using a HT-5 fused silica column from SGE and FID detection. The internal standard method with biphenyl as the internal standard was used for quantitation. Identification of the products was accomplished by GC mass spectrometry using a VG 70 EHF spectrometer.

The reactions containing coal and/or resid with model naphthene, aromatic or both were reacted at the same conditions as the model reactions except the reactions were conducted for 60 minutes only. Each reactant was charged at a level of one gram. After reaction the liquid and solid products were extracted with toluene to yield toluene solubles and with THF to yield THF solubles and insoluble organic matter (IOM).

Results and Discussion

Hydrogen Transfer in Thermal Coprocessing. A systematic set of experiments has been performed in our laboratory to evaluate whether hydrogen can be transferred directly from saturated naphthenes to coal and resid. The experiment performed evaluated the hydrogen transfer from naphthenic PHP to aromatics ANT or PYR. Reactions were then conducted to react PHP with Illinois No. 6 coal from the Argonne Premium Coal Bank, aromatics, ANT and PYR, with coal, and the combined system of naphthene and aromatic with coal. The same set of reactions was performed with Maya Resid: naphthene with resid, aromatics with resid, and naphthene and aromatic with resid. The final set that was performed involved naphthene, aromatic, coal and resid. Blank reactions were also performed with each individual material to evaluate the effect of the reaction conditions on the reactivity of the individual materials.

Hydrogen Transfer in the Model Reactions. The model systems that were used included the binary combinations of ANT with PHP and PYR with PHP. When reacted individually each of these reactants yielded no conversion. However, when reacted in combination the reactions involving ANT with PHP resulted in hydrogen transfer while no evidence of hydrogen transfer or any reactivity was observed with the PHP and PYR system.

The initial ANT and PHP reaction was performed with a 1 to 1 ratio of ANT to PHP. When reactivity was observed as the production of the partially saturated DHA and the formation of the unsaturated PYR, it was evident that hydrogen transfer had occurred since the only hydrogen available

was from PHP and that this reactive system should be further investigated. Three sets of experiments were performed at 60, 90 and 180 minutes with weight ratios of ANT to PHP ranging from 0.14 to ~ 10. Representative data are given in Table 1. Hydrogen transfer occurred at all of these conditions as evinced by the products formed. At 60 minute reaction time, DHA was formed at low ratios of ANT to PHP but decreased by two-thirds at an ANT/PHP weight ratio of 2 to 1. The weight ratio of DHA increased somewhat at higher ANT/PHP ratios as the production of tetrahydroanthracene (THA) began to be observed. At longer reaction times THA appeared at lower ANT to PHP weight ratios and more was formed. PYR was formed also during these reactions. The amount of PYR formed increased almost linearly with increasing ANT to PHP ratios. At the higher ANT to PHP ratios, the hydrogen donor PHP was limited while ANT was available in excess.

Given also in Table 1 are the percent hydrogenation (% HYD) and the hydrogen efficiency for these reactions. Percent HYD is defined as the moles of hydrogen needed to produce the liquid products as a percentage of those required to produce the most hydrogenated product, THA. Hydrogen efficiency is defined as the number of moles of hydrogen accepted to form a partially saturated species divided by the moles of hydrogen donated times 100%. Although some scatter appeared in these data, the % HYD appeared to the lowest and highest at low and high ratios of ANT to PHP. Hydrogen efficiency usually ranged from low to high with a minimum being present at a 2 to 1 ANT to PHP ratio. Higher hydrogen efficiencies were observed at higher ANT to PHP ratios where the stoichiometric weight ratio was approximately 6.3 to 1.

The data presented in Table 1 indicate that hydrogen transfer occurred under these conditions, albeit only a small amount of the naphthene and aromatic species reacted. These results strongly suggest that under certain reaction conditions hydrogen transfer can occur from naphthenes to aromatic species. This result may have important implications for coprocessing where a substantial portion of the resid solvent is composed of naphthenic structures and coal is composed of aromatic species.

Hydrogen Transfer in Coal and Resid Reactions. Hydrogen transfer between naphthenes and aromatics was evaluated in the presence of coal and resid individually and combinatorially. As with the model studies, all of the reactions were performed thermally in an inert atmosphere so that hydrogen transfer occurred only as a result of interactions among the reactants.

For this study, coal conversion is defined as moisture and ash free (maf) coal minus IOM divided by maf coal charged and multiplied by 100. The resid conversion or that portion of the resid remaining THF soluble is defined as the resid minus IOM divided by the resid charged and multiplied by 100. The coal and resid conversion is defined as maf coal plus resid minus IOM divided by maf coal and resid charged and multiplied by 100. The liquid to solid ratio is defined as the amount of toluene solubles divided by the amount of toluene insolubles present. Another term describing the degree of upgrading or degrading of the system in terms of the amount of toluene solubles was defined in order to provide a comparison among the different reactions with coal, resid, and coal plus resid. The degree of upgrading (TSD) is defined as the TOL solubles in the product minus the TOL solubles in the reactant divided by the upgradable materials. The upgradable materials are defined as maf coal for the coal reactions, resid for resid reactions and coal plus resid for the combined reaction. A positive number indicates that upgrading occurred while a negative number indicates retrogressive reactions.

Twelve different reaction systems were employed to evaluate hydrogen transfer between naphthenes and aromatics as shown in Tables 2 and 3. In addition, Illinois No. 6 coal and Maya resid were reacted individually to generate a baseline for their individual conversion and stability.

The binary coal systems ranked in reactivity as coal/PHP > coal/PYR > coal/ANT. The reaction of coal with PHP resulted in the highest coal conversion as compared to the coal systems with ANT and PYR. Neither ANT or PYR promoted coal conversion. In fact, ANT increased the amount of IOM present substantially, yielding very low coal conversion, less than the coal by itself, while coal/PYR system yielded a conversion that was only slightly higher than coal by itself. The substantial increase in coal conversion in the coal/PHP system resulted in part from hydrogen transfer since PYR should have a higher solvating power for coal than PHP and higher conversion was obtained with PHP than PYR. Also, some PYR was produced indicating that dehydrogenation of PHP occurred as given in Table 3. Production of DHA and THA in the coal/ANT system indicated that hydrogen was transferred from coal to ANT.

Comparison of the ternary systems showed higher coal conversion for the system of coal/PHP/PYR than for coal/PHP/ANT, although little difference was observed in their toluene soluble yields. The effect of ANT in the system may be resultant from a lower solvating power for coal than pyrene or a higher propensity for retrogressive reactions. PHP added to coal/ANT effectively blocked some of the retrogressive reactions of ANT and increased coal conversion from 13% for the binary system to 73% for the ternary system. Substantial hydrogenation of ANT occurred resulting in DHA and THA. PYR was formed from PHP.

The ternary system employing coal/PYR/PHP yielded substantial coal conversion, ~ 83%, which was quite similar to that obtained for coal/PHP of 86%. However, it is difficult to ascertain what occurred with PYR and PHP. An equal weight amount was charged and no net change in their amounts was observed. However, the error in this reaction was much higher than other ternary and binary systems indicating variability in the products produced. The chemistry of the coal/PYR/PHP system was conducive for coal conversion while the coal/PYR system was not. Hence, the presence of PHP increased coal conversion by possibly transferring hydrogen to the system.

The binary reactions of the model reactants with resid resulted in a substantial influence of the different reactants on the resid. Without added reactants, the resid underwent substantial retrogressive reactions causing 20% of the resid to become THF insoluble. The addition of PHP resulted in much more of the resid remaining THF soluble compared to the resid reacted alone. Neither the addition of ANT nor PYR blocked any of the retrogressive reactions; however, the binary system with PYR kept more of the resid THF soluble (~ 86%) than did the ANT at 79%. These binary systems yielded the same amount of THF solubles as did the resid alone. The ranking of the binary resid/model reactant systems was resid/PHP > resid/PYR > resid/ANT.

In the binary system, PHP transferred hydrogen to the resid with 7% PYR being formed. PYR showed no reactivity, but ANT underwent substantial hydrogenation, accepting hydrogen from the resid and forming both DHA and THA. The hydrogenated products showed some variability in the two different reactions, but regardless, even in the reaction with lowest reactivity, more than 13% hydrogenated products were formed.

The ternary systems involving resid had similar resid conversions of 97% for resid/PHP/PYR and 98% for resid/PHP/ANT. Likewise, 97% conversion was obtained with resid and PHP. Hence, regardless of additive the addition of PHP to resid enhanced resid upgrading and helped to inhibit retrogressive reactions. In the resid/ANT/PHP reaction more than 30% of the ANT hydrogenated yielding DHA and THA as products. More than 10% PYR was produced. The resid/PYR/PHP system, however, showed no net change in the quantity of PYR and PHP present.

The quaternary mixtures yielded similar coal conversions as the ternary system although the reaction with ANT did increase somewhat. Substantial hydrogenation of ANT occurred while 30% PYR was produced. ANT only accepted 22% of the hydrogen released thereby leaving substantial hydrogen for uptake by the coal and resid. In the quaternary systems with PYR and PHP, no net change in the weight percents of the reactants was observed; however, a large variability in the quantities was observed.

Summary and Conclusions

The effect of the different added species on the system performance can be evaluated by comparing the degree of upgrading, % TSD, occurring in each system. The highest degree of upgrading occurred in coal systems in which PHP was present. Likewise, the least amount of degrading occurred in those resid systems that contained PHP. For both coal and residuum PYR had a slightly positive effect on the system while ANT had a negative effect.

The hydrogen donor and acceptor ability of both coal and resid has been demonstrated in this study. When no other donor was present, both coal and resid transferred hydrogen to ANT, yielding partially saturated products. Reactions of PHP alone and in combination with hydrogen acceptors clearly showed that a hydrogen acceptor is required in order for PHP to act as a donor. Hydrogen transfer from PHP to aromatics, coal, and resid was obvious because of their respective conversion and the formation of PYR. The relative reactivity of ANT and PYR is of interest. ANT accepted hydrogen readily and quickly from whatever source was available while PYR was nearly unreactive. Hence, those coals and/or resids with reactive structures such as ANT can readily participate in hydrogen transfer reactions while those coal or resid materials that primarily contain nonreactive or stable species like PYR may not involve themselves as readily in hydrogen transfer reactions. Under the conditions employed in this study, hydrogen transfer was observed from the naphthene PHP to an aromatic ANT, to Illinois No. 6 coal and Maya resid.

Acknowledgement

We gratefully acknowledge the support of the Department of Energy under Contract No. DE-AC22-88PC88801.

Table 1. Products Produced from Hydrogen Transfer in Reactions of Anthracene with Perhydropyrene

Weight Ratio of ANT to PHP	Time (min)	Yield, % DHA	THA	PYR	%HYD	Hydrogen Efficiency
0.166	60	13.3	0	0.34	6.7	101
0.51	60	6.9	0	1.2	3.4	38.1
1.0	60	6.4	0	2.8	3.2	31.2
2.1	60	4.3	0	3.0	2.2	44.9
5.0	60	5.7	0	7.0	4.5	104
6.5	60	5.0	1.0	7.7	3.5	83
9.2	60	4.2	0.8	7.8	2.9	111
0.52	90	6.5	0	1.6	3.3	33.6
1.02	90	4.7	0	2.9	2.4	19.4
2.06	90	4.3	0	3.5	2.2	46.0
5.0	90	6.1	2.0	12.8	5.1	72.0
8.0	90	6.0	2.5	13.2	5.5	108
0.51	180	10.4	0	1.9	5.2	41.7
2.08	180	3.7	0	6.3	1.8	21.2
5.26	180	4.1	0	10.1	2.1	34.3
8.52	180	6.9	1.8	16.1	5.3	81.6

Table 2. Coal and Resid Reaction Products from Thermal Coprocessing Reactions

System	Toluene Solubles (%)	THF Solubles (%)	IOM (%)	Conversion (%)	TSD (%)	Liquid to Solid Ratio
Coal/PHP	75.5±2.2	17.5±0.7	7.0±1.5	85.8±3.2	24.0±3.4	3.1
Coal/ANT	50.0±3.1	14.0±1.7	36.0±1.3	13.4±7.3	-9.0±1.1	1.0
Coal/PYR	58.4±1.6	15.2±2.7	26.4±1.1	38.3±3.7	7.6±4.6	1.4
Coal/ANT/PHP	83.8±1.0	8.2±0.9	8.0±0.1	73.0±1.3	26.8±19	5.2
Coal/PYR/PHP	87.7±1.3	7.1±0.7	5.2±0.5	83.4±1.2	29.1±8.7	7.2
Resid/PHP	92.3±0.3	6.2±0	1.5±0.2	97.4±0.5	-47.6±1.9	12.0
Resid/ANT	77.8±1.0	9.4±0.2	12.8±0.8	78.7±1.7	-69.1±2.8	3.5
Resid/PYR	79.5±3.6	12.6±3.2	7.9±0.5	85.5±1.3	-55.4±4.1	4.0
Resid/ANT/PHP	96.1±0.0	3.0±0.0	0.9±0.0	97.6±0.0	-46.5±1.3	24.6
Resid/PYR/PHP	94.8±0.5	4.1±0.3	1.1±0.2	97.1±0.5	-45.1±9.7	18.4
Resid/ANT/PHP/Coal	83.1±1.2	6.9±0.9	10.0±0.4	80.6±0.1	-6.4±6.5	5.0
Resid/PYR/PHP/Coal	85.5±0.8	6.5±0.5	8.0±0.4	83.6±0.9	6.7±18	5.9
Coal	4.0±1.6	31.2±0.7	64.8±2.3	30.4±3.8	4.3±1.7	0.4
Resid	43.8	35.2	21.0	80.5	-61.8±2.4	0.8

ANT = anthracene; PHP = perhydropyrene; PYR = pyrene
Reaction Conditions: 430°C, 60 minutes, N_2 atmosphere

Table 3. Reactive Products from Model Donors and Acceptors Reactions in Thermal Coprocessing

System	ANT	DHA	THA	PHP	PYR	Hydrogen Efficiency
Coal/PHP	-	-	-	89.8±2.4	10.2±2.4	
Coal/ANT	89.6±0.1	7.3±0.1	3.1±1	-	-	
Coal/PYR	-	-	-	-	100.0±0	
Coal/ANT/PHP	56.2±1.0	19.2±2.3	24.7±1.4	84.3±0.9	15.7±0.8	49.7
Coal/PYR/PHP	-	-	-	55.4±8.0	44.6±8.0	
Resid/PHP	-	-	-	93.0±1.5	7.0±1.4	
Resid/ANT	82.8±4.2	13.4±4.4	3.8±0.2	-	-	60.6
Resid/PYR	-	-	-	-	100.0±0	
Resid/ANT/PHP	66.4±0.1	18.5±1.1	15.1±1.0	90.2±0.5	9.8±0.6	
Resid/PYR/PHP	-	-	-	47.8±5.3	52.4±5.4	
Resid/ANT/PHP/Coal	64.5±0.4	14.0±0.4	21.5±0.1	69.7±1.5	30.3±1.6	22.0
Resid/PYR/PHP/Coal	-	-	-	52.5±13.3	47.5±13.3	
Coal	-	-	-	-	-	
Resid	-	-	-	-	-	

* -: none present

CATALYTIC EFFECT ON THE GASIFICATION OF A BITUMINOUS ARGONNE PREMIUM COAL SAMPLE USING WOOD ASH OR TACONITE AS ADDITIVE

R.C. Timpe, R.W. Kulas, and W.B. Hauserman
Energy and Environmental Research Center
University of North Dakota
Box 8213, University Station
Grand Forks, ND 58202

Keywords: Gasification, Catalysis, Coal

ABSTRACT

Illinois #6 from the Argonne Premium Coal Sample Program was gasified with and without catalyst added. Catalyst loading effects and the effect of catalysis on screen fractions were studied using K_2CO_3 as the catalyst. The reactivity increased significantly with each 2.8 wt% of additional potassium as potassium carbonate until there was 11.3 wt% potassium. The reactivity increased slightly with 14 wt% potassium and again slightly with 17 wt% potassium present. The order of the reaction with respect to carbon approached zero with the higher catalyst loading. Wood ash with its high potassium (12 wt%) and calcium content (47 wt%) was shown to be as good a catalyst as the K_2CO_3. Taconite, an iron ore from northeastern Minnesota, is plentiful, relatively inexpensive, has the required characteristics for bed material, and may be a potential catalyst. In this test series, however, it exhibited only slight catalytic effects.

Beulah-Zap lignite from the Argonne Premium Sample Program was gasified with and without wood ash additive as a basis for comparison with Illinois #6 reactivities.

INTRODUCTION

Catalyzed and uncatalyzed steam gasification of low-rank coals (LRCs) to produce hydrogen-rich gas streams is a well-known process and is in commercial use today in this country (Dakota Gasification Plant, Beulah, North Dakota) and abroad. The successful process produces synthesis gas from which methane is produced to supplement clean-burning natural gas supplies. Besides augmenting transportable energy supplies, gasification provides a means of controlling undesirable emissions from coal utilization processes. Sulfur from the gasified coal is contained within the plant and is a by-product of the process. Steam gasification offers a means of utilizing high-sulfur (noncompliance) coals in such a way as to entrain and remove sulfur gasses before they are released to the atmosphere. As environmental standards become more rigid regarding sulfur emissions, gasification as a means of utilizing higher sulfur content coals may become more attractive.

Low-rank coals make good gasification feedstock due to inherent catalysts in the form of salts of alkali and alkaline earth elements and due to their reactive organic functionalities. These components give LRCs first order carbon reactivities of > 2 hr^{-1} at 750°C (1). Raw low-rank coals have consistently been shown to have higher reactivities in the gasification process than bituminous coals. Gasification of bituminous coals could become feasible if the reactivity of those coals with their greater carbon content/lb could be increased. Catalysis brought about by alkali and alkaline earth additives has been shown to increase the reactivities of these coals (2,3). Cost and availability of catalytic materials is a major concern when catalysis is required. As a result, reactivity, and supplies of inexpensive potential additives needed to increase that reactivity, becomes a primary consideration in selecting gasification feedstock. Several plentiful, naturally occurring materials (minerals) are available, including nahcolite, trona, halite, limestone, dolostone, potash, saltpeter, and

sunflower seed hulls; most of which have been investigated as catalysts (4,5). The first three mentioned minerals are rich in sodium, the next two are rich in calcium, and the last three are rich in potassium, all of which are known to be good catalysts for the coal gasification reaction. Potassium and sodium have proven to be the best catalysts of this group. The advantage of using sodium is that its mineral deposits are much more common than potassium mineral deposits, making the former less expensive. The major disadvantage of sodium is the agglomeration of particles and the ash fouling that it causes. Although it is more expensive, potassium appears to cause less operational problems. Therefore, if a source can be found that is less expensive than sources now available, and if recycling of the potassium can be made possible, potassium will become the best choice of catalyst from the alkali-alkaline earth materials mentioned above. Wood ash which typically has a high potassium content may be such a catalyst.

Transition metals have also been shown to catalyze the coal gasification reaction. Taconite, a metal ore from Minnesota, is plentiful, inexpensive, and rich in iron, making it a candidate for a gasification additive.

This paper reports the results of a bench-scale study of steam-char rate enhancement conferred to Illinois #6 from the Argonne Premium Coal Sample Program by the presence of potassium carbonate (K_2CO_3), wood ash, or taconite. An Argonne sample of Beulah-Zap lignite was gasified and reported on for comparison.

EXPERIMENTAL

The coals tested were Illinois #6 (Herrin seam) and Beulah-Zap (Beulah-Zap seam) from the Argonne Premium Coal Sample Program. They were received in 10-gram lots in sealed vials and were used directly from the vials without further preparation, other than catalyst addition. Unused sample was stored under inert gas in sealed 20-mL scintillation vials. Proximate and ash analysis are shown in Table 1.

Ten weight percent dry catalyst was admixed with each coal to be tested. Dispersal of the catalyst was accomplished by shaking the coal-additive mixture vigorously in closed vials for ca. ten minutes. The catalysts were prepared by combustion in air. Hardwood (cottonwood and aspen) ash was prepared in a small batch. The cottonwood/aspen ash was the remnants of a domestic fireplace fire. The plywood ash was provided by Northwood Panelboard Co, Solway, Minnesota.

Approximately 40 milligrams of coal or coal/catalyst material is loaded onto the pan of the DuPont 951 thermogravimetric analysis microbalance module. The quartz tube enclosing the pan and serving as the reaction chamber is secured by a knurled nut to the balance housing. The reaction chamber is purged with an ambient pressure argon flow at ca. 160 cm^3/min. The sample is heated at ~100°C/min to the target temperature at which point the $H_2O_{(g)}$ flow is introduced through the side arm of the quartz tube, and argon flow is reduced to ca. 60 cm^3/min. The reaction was carried out at 700°, 750°, and 800°C. Total gas effluent can be collected in a gas bag for analysis by GC. Weight, time, and temperature are stored by the DuPont 1090 data station for later data reduction.

RESULTS AND DISCUSSION

Illinois #6 and Beulah-Zap lignite from the Argonne Premium Coal Sample Program were gasified with and without catalyst added. As shown in Table 2, the uncatalyzed bituminous coal char had typical low reactivities with steam in the 700°-800°C temperature range when compared with those of low-rank coal. The uncatalyzed Beulah-Zap reactivities at each of the three temperatures were 40-50 times greater than those of the Illinois #6. However, in the presence of only 1-2 wt% added potassium, the difference was reduced to < ten times and with 5 wt% added potassium, .< 2 times.

Catalyst loading effects and the effect of catalysis on screen fractions of Illinois #6 were studied using K_2CO_3 as the model catalyst. The reactivity increased significantly with each 2.8 wt% of additional potassium as potassium carbonate, until there was 11.3 wt% potassium as shown in Figure 1. As potassium concentrations were increased to 14 wt% and 17 wt%, the reactivity increased only slightly. As the catalyst loading was increased, the dependence on carbon concentration decreased. The order of the reaction with respect to carbon approached zero with the higher catalyst loading, as shown in Figure 2.

Illinois #6 was sieved to get size fractions for reactivity testing. The fractions collected were +60 mesh (>0.250 mm), -60x100 mesh (0.250>p>0.149 mm), -100x140 mesh (0.149>p>0.105 mm), -140x200 mesh (0.105>p>0.074 mm), and -200x325 mesh (0.074>p>0.044 mm). Figure 3 shows the reactivity as a function of those sieve fractions.

Hardwood ash with its high potassium (12 wt%) and calcium content (47 wt%) was shown to have promise as a catalyst. Increased reactivity brought about by dry wood ash was slightly less than that of an equivalent amount of K_2CO_3, but the application of dried aqueous extract of the ash containing 39 wt% potassium did provide an equivalent increase in reactivity. Taconite, an iron ore from northeastern Minnesota, is plentiful, relatively inexpensive, and has the required characteristics for a bed material, and may be a catalyst for the coal char-steam reaction. In this test series, however, it exhibited only slight catalytic effects.

Illinois #6 agglomerated when heated to the gasification temperatures. However, addition of K_2CO_3 to the coal resulted in no observable agglomeration. A similar effect was noted on addition of the hardwood ash as a reaction catalyst, whereas addition of the ash from a plywood plant did not prevent agglomeration. Table 3 shows the elemental analyses of the ash from the coal with 10 wt% additive. The softening and collapsing of pores during agglomeration and subsequent decrease in surface area is at least partially responsible for the low reactivity of the coal. The addition of potassium carbonate and the hardwood ash resulted in decreased agglomeration as well as an increase in reactivity, whereas the ash from the plywood facility had little effect on either.

REFERENCES

1. Timpe, R.C.; Sears, R.E.; Willson, W.G.; Sondreal, E.A. "Production of Hydrogen from Low-Rank Coals - Topical Report on Char Properties and Reactivity," Topical Report to DOE-METC, DOE-FE(Number unassigned at this time), USDOE, May 1989.

2. Yuh, S.J.; Wolf, E.E. Fuel 1984, 63, 1604-1609.

3. Liu, Z.-I.; Zhu, H.-H. Fuel 1986, 65, 1334-1338.

4. Galegher, S.J.; Timpe, R.C.; Willson, W.G.; Farnum, S.A. "Kinetics of Catalyzed Steam Gasification of Low-Rank Coals to Produce Hydrogen," Final Report, DOE/FE/60181-2034(DE86012209), Office of Scientific and Technical Information, USDOE, June 1986.

5. Timpe, R.C.; Sears, R.E.; Montgomery, G.G. J. Coal Quality 1989, 8 (1), 27-31.

TABLE 1

PROXIMATE AND ASH ANALYSES OF ILLINOIS #6 BITUMINOUS AND BEULAH-ZAP LIGNITE FROM THE ARGONNE PREMIUM COAL SAMPLE PROGRAM

	Illinois #6 Raw (TGA)		Beulah-Zap Raw (TGA)	
Sample	AR	MF	AR	MF
Moisture, wt%	9.41	--	32.66	--
Volatiles, wt%	34.75	38.36	30.19	44.83
Fixed C, wt%	41.08	45.35	30.67	45.54
Ash, wt%	14.76	16.29	6.49	9.64

XRF Analysis of Coal Ash

	Ill. #6		Beulah-Zap	
Element	% of Ash	% of Coal	% of Ash	% of Ash
Silicon	20.43	3.33	8.88	0.86
Aluminum	9.68	1.58	5.35	0.52
Iron	12.59	2.05	5.88	0.57
Titanium	0.60	0.10	0.42	0.04
Phosphorous	0.09	0.01	0.31	0.03
Calcium	5.64	0.92	16.72	1.63
Magnesium	0.72	0.12	6.27	0.61
Sodium	0.00	0.00	4.01	0.39
Potassium	2.41	0.39	0.33	0.03
Sulfur	2.72	0.44	6.37	0.62

TABLE 2

REACTIVITIES OF UNCATALYZED AND CATALYZED COAL CHAR WITH STEAM*

	Illinois #6						Beulah-Zap	
Catalyst	None	K_2CO_3	A[1]	B[2]	C[3]	Tac.	None	A[1]
	k, hr^{-1}							
Temp, °C								
700	0.06	--	--	--	--	--	2.30	3.64
750	0.15	4.36	--	--	3.01	0.41	7.76	8.67
800	0.33	--	0.35	0.54	--	--	14.61	10.41
E_a, kcal/mol	5.57						38.53	

* Assumed 1st order with respect to carbon.
[1] A Provided by Northwood Panelboard Co.
[2] B Residue from combustion of cottonwood/aspen.
[3] C Aqueous extract of hardwood ash.

TABLE 3

XRF ANALYSES OF ASH FROM COAL +10WT% CATALYST, wt%

			w/Ill. #6		w/B-Zap
XRFA Results	Ill. #6	B-Zap	Ash B	Ash A	Ash A
Silicon	3.33	0.86	4.49	5.04	2.58
Aluminum	1.58	0.52	1.95	1.97	1.77
Iron	2.05	0.57	2.26	2.22	2.27
Titanium	0.10	0.04	0.14	0.12	0.11
Phosphorous	0.01	0.03	0.07	0.06	0.02
Calcium	0.92	1.63	3.88	3.39	1.26
Magnesium	0.12	0.61	0.59	0.46	0.16
Sodium	0.00	0.39	0.12	0.07	0.01
Potassium	0.39	0.03	1.12	1.07	0.50
Sulfur	0.44	0.62	0.63	0.57	0.50
Total %	8.94	5.30	15.26	14.97	9.18

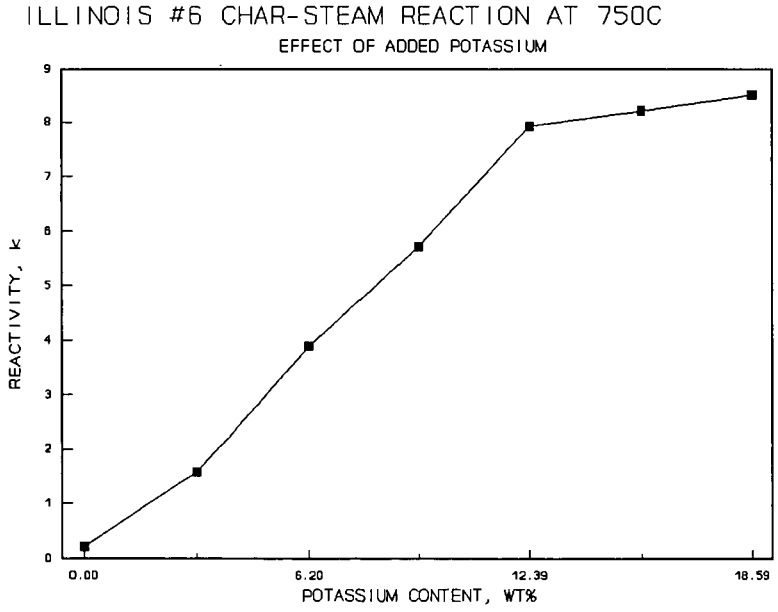

Figure 1. Effect of K_2CO_3 catalyst loading on Illinois #6 char-steam reactivity at 750°C.

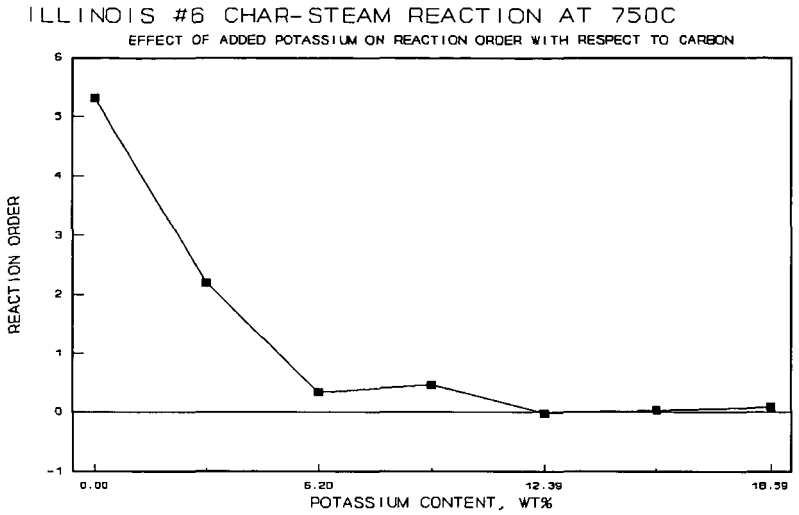

Figure 2. Effect of potassium loading on order of Illinois #6 char-steam reaction with respect to carbon.

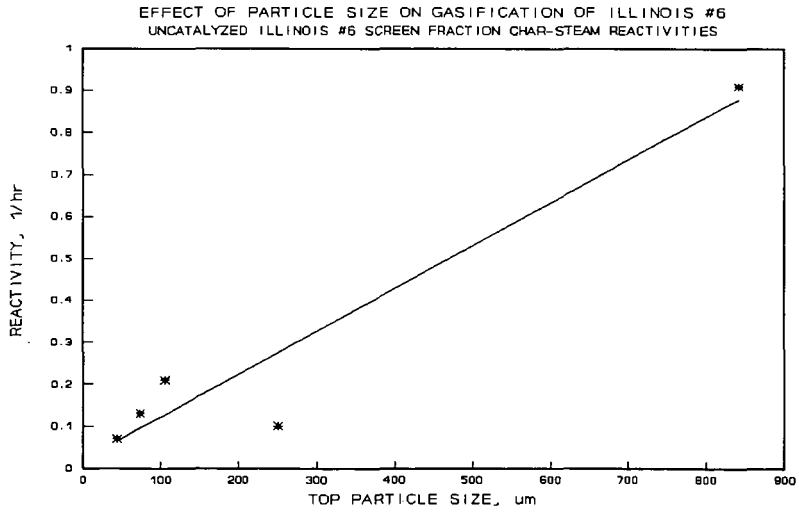

Figure 3. Effect of exclusion of particle size on Illinois #6 char-steam reactivity.

CALCULATION OF ADSORPTION ENERGIES IN SLIT-LIKE AND WEDGE SHAPED MICROPORES

J. K. Floess and Yolanda VanLishout
Department of Chemical Engineering
University of Illinois at Chicago
Chicago, Il 60680

Keywords: microporous carbons; adsorption energies; adsorption isotherms

Introduction

The analysis of the structure of microporous carbons has been undertaken using a wide range of techniques. The results of these studies suggest that microporous carbons consist of lamellae present singly or in stacks of two or three turbostratic layers[1]. The lamellae are apparently curved forming larger micropores in the shape of a triangle and small ultra-micropores between adjacent curved lamella or stacks of lamellae. The average diameter of the lamellae is a function of the heat treatment temperature and presumably also the extent of carbon conversion.

The physisorption of gases, although experimentally tedious, probably remains the most versatile method of analysis, and the results of such studies, in large part, form the basis of our understanding of the pore structure of these materials. In our work, we have undertaken to measure[2] the isosteric heats of adsorption of different gases on microporous carbons with the objective of obtaining information on pore size. As is well known, the physisorption of molecules in small pores is enhanced over that of a single surface due to the added attractive force of the second surface. This effect, though, is appreciable only in pores smaller than about 10Å. Consequently, it is possible to use heat of adsorption data to determine the size of the ultramicropores. This approach has been previously used by Everett and Powl[3], who considered adsorption in both slit-like and cylindrical pores, by Stoeckli[4], and by Chihara et al.[6] to determine pore widths in microporous carbons.

The problem with this approach, as pointed out by Wickens[6], is that it is necessary to assume a monosize pore distribution in order to obtain a pore spacing from the isosteric heat. The intention of this study was to determine the adsorption energies for a range of probable pore configurations with the objective of determining a site energy distribution for physisorption. The basic model used in the calculations assumes that the pores are formed by finite sized lamellae having 1 to 3 turbostratic layer planes per surface. Calculations were done as a function of lamellae diameter, pore spacing, the position of the adsorbate molecule, the number of turbostratic layers, and the pore angle.

Model Development

Adsorption energies were calculated by numerically summing the Lennard-Jones potential for the interaction of an adsorbate molecule with each carbon atom in a microcrystallite. The calculations assume that the total adsorption energy can be obtained from the sum of the pair-wise interaction energies between the adsorbate molecule and the individual atoms in the solid. The adsorbate molecule and each atom in the solid are assumed to act as single force centers.

The positions of the carbon atoms in the basal plane were calculated, in polar coordinates, relative to the center of a hexagonal unit in the basal plane. The size of the lamella (the basal plane) is measured by the number of hexagon rings around a central hexagon. A maximum of eight hexagon rings was considered in these calculations. This corresponds to a maximum lamellae (area equivalent) diameter of 38Å. Usually three basal planes were included in the calculation of the adsorption potential for a surface. The position of carbon atoms in the normal direction to the basal plane is not specified for crystallites in a microporous carbon since adjacent basal planes are turbostratically stacked. It was assumed in these calculations that carbon atoms in adjacent layers are stacked directly on top of each other. However, because of the large spacing between adjacent layers (3.4Å) compared to the spacing between atoms in a basal plane (1.42Å along a hexagon edge), the specific stacking arrangement has a negligible effect on the calculated adsorption energy.

Calculations were done for three positions of the adsorbate molecule: above the midpoint of a hexagon (position s); directly over a carbon atom (position c); and above a bond between 2 carbon atoms (position cb).

The Lennard-Jones potential model for the pair-wise interaction is:

$$u(r) = 4\varepsilon_{gs}[(\sigma_{gs}/r)^{12} - (\sigma_{gs}/r)^{6}] \qquad (1)$$

where r is the distance between the adsorbate molecule and a carbon atom in the solid; ε_{gs} is the depth of the potential energy minimum for the pair-wise interaction; and σ_{gs} is the distance at which the pair-wise interaction potential is zero. Values[7] of 7.98×10^{-15} ergs and 3.45 Å were used for ε_{gs} and σ_{gs} in the calculations. Here σ_{gs} is the arithmetic mean of the spacing between basal planes and the distance parameter in the Lennard-Jones potential for the adsorbate molecule (Argon) in the gas phase.

Results

Figure 1 gives the interaction energy of an adsorbate molecule with a single carbon surface of three basal planes as a function of the basal plane size (given in terms of the number of hexagon rings around the central hexagon) and for the three positions of the adsorbate molecule above the surface. For lamella as large or larger than that formed by 4 rings (~20Å in diameter), the adsorption energy is independent of lamella size. Below 20Å, however, the adsorption potential decreases significantly with lamella size. The difference in adsorption energies between the *s* and *c* or *cb* positions is less than 4%, while between the *c* and *cb* positions there is only a very

small difference in adsorption energy. As a result, energy barriers to translational motion of the adsorbate molecule across the surface are small so that physisorbed molecules exist as a mobile film on a graphite surface. Also shown in figure 1 are the interaction energies obtained by integrating the Lennard-Jones potential over a single basal plane and by summing the contribution of individual planes in the direction normal to the basal plane. Steele[7] has shown that the adsorption energy obtained by integration over a single layer plane is nearly the same as summation, provided that $\sigma_{gg}/\sigma_{ss}>1.5$. (Here σ_{ss} is the spacing between atoms in the crystal surface.) However, because of the different atomic spacings in the normal and parallel directions to the basal plane in a graphite crystal, integration in the normal direction does not give an adsorption energy that agrees with summation unless the adsorbate molecule is 1.5 times larger than basal plane spacing. Agreement between the integration and summation calculation and the discrete summation is excellent for lamella larger than ~11Å. Integration, however, does not yield information on the magnitude of energy barriers to translational motion of the adsorbate across the solid surface.

Increasing the number of layers from 1 to 2 layers increases the adsorption energy by less than 10%. Additional layers beyond 2 increase the adsorption energy by approximately 3%.

Figure 2 gives the adsorption energy as a function of pore spacing for a slit-like pore. There are two pore spacings, on each side of the maximum adsorption energy spacing, at which the adsorption energies are equal. These are referred to here as the tight and loose configurations. The maximum interaction energy is obtained at a pore spacing of 6.8Å. For pores wider than 7.7Å, the adsorption potential is a maximum in the pore at two positions, each located 3.4Å from a surface. This is shown in Figure 3, where the adsorption energy is plotted as a function of position in an 8.6Å pore. In pores smaller than 7.7Å, the equilibrium position of the adsorbate molecule will be at the center of the pore.

The adsorption energy in a 6.4Å pore, as a function of the radial position of the adsorbate (i.e. in a direction parallel to the surface) in the pore, is plotted in Figure 4. The calculations show an ~10% difference in the adsorption energies between the *s* and *c* or *cb* positions. Consequently, even in a tight pore configuration, physisorbed molecules are largely mobile. Furthermore, there is no preference for movement over the *c* or *cb* positions. At a slightly wider width of 6.8Å, the difference in adsorption energies between the *s* and *c* or *cb* configurations is 4%, so that adsorbed molecules are almost fully mobile in pores of this size or larger.

Calculations were also done for wedge shaped pores at small angles and for an angle of almost 90°. Figure 5 shows the adsorption energies in a 10° pore for a molecule equidistant from each surface as a function of the lateral position of the molecule in the pore. If the pore angle is small, the maximum interaction energy occurs at the point where the surfaces are ~6.8Å apart (the actual vertical separation between the two surfaces at the maximum interaction energy is 6.9Å). The maximum interaction energy is 2% less than in a parallel pore. The uneven variations in adsorption energy (near the maximum value) occur because the molecule position changes among the *s*, *c*, and *cb* configurations as it is moved into the wedge. The change in adsorption energy with lateral position will depend

on the angle between planes; however, there will always be a position where the interaction energy is at a maximum. This point, though, can reside in a fairly shallow energy well (if the pore angle is small) so that a molecule in a wedge shaped pore may retain a significant degree of lateral mobility. For large pore angles, the adsorbate molecule will not be as mobile; however, the adsorption energy will be less than for a small angle pore since the adsorbate will interact with the edge of least one plane. If the pore angle is formed by the edges of both surfaces, the interaction energy is approximately 25% lower than for the small angle case.

Discussion

The calculations show that the adsorption energy in a micropore depends on a range of factors: the lamella size, the pore spacing and angle, and the number of turbostratic layer planes per surface. The adsorption energies calculated by summation show that physisorbed molecules retain their mobility even in tight pores and that there is a significant degree of lateral mobility in small angle wedge shaped pores. For most other cases, however, the discrete summation method has no particular advantage over the integration method used in previous studies[3,4].

The determination of an average adsorption energy for a molecule in a microporous carbon requires both an estimate of the site energy distribution and information on the fraction of sites of a given energy that are occupied. Presumably, slit-like pores will be uniformly distributed with respect to pore spacing, so that a site energy distribution could be obtained from the data in figure 2. Such a distribution will be skewed towards the maximum adsorption energy. Similarly, small angle wedge shaped pores will also skew the distribution towards the maximum adsorption energy. A site energy distribution calculated from the data in Figure 5 is shown in Figure 6. Large angle wedge shaped pores will only contribute sites with energies some 25% lower than the adsorption energy in small angle pores.

In order to determine the fraction of sites with the same energy that are occupied, the Volmer isotherm equation[8] was evaluated at a number of different adsorption energies. (The pre-exponential factor for the equilibrium constant was obtained from the data of Floess et al.[2]). As shown by the isotherms in figure 7, adsorption in the Henry's Law regime (at 184 K) occurs predominantly on sites with energies above 3.6 kcal. (At lower temperatures, low energy sites will be occupied to a greater extent in the Henry's Law regime.) Nevertheless, since the site energy distribution is also skewed towards high energy sites, adsorption in the Henry's Law regime will occur predominantly in slit-like pores that are approximately 6.8Å wide and in small angle wedge shaped pores. The heat of adsorption in the Henry's Law regime will therefore be principally due to adsorption in these pores, and an average pore spacing calculated from heat of adsorption data will be a weighted average pore spacing for the pores that have the highest adsorption potential.

The calculations also showed that adsorbate molecules are mobile on a carbon surfaces and that they retain a high degree of lateral mobility even in a tight pore configuration. As a result, diffusion in a microporous carbon will depend on the rate of transport from one microporous slit to an adjacent one and not on the rate of

transport in a micropore itself. Therefore, if diffusion is modeled[9] as a molecule jumping from energy well to energy well over a potential barrier, the potential barrier will be that for adsorption in a micropore and the distance between energy wells will be proportional to the average lamella diameter in a microporous carbon.

References
1. McEnaney, B. *Carbon*, 1988, 26, 267.
2. Floess, J. K.; Kim, H. H.; Edens, G.; Oleksy, S. A.; Kwak, J., *Surface Area and Pore Size Measurements of Microprous Carbons*, paper presented at the AIChE National Meeting, Chicago, IL, November, 1990.
3. Everett, D. H.; Powl, J. C. *J. Chem Soc., Faraday Trans. I*, 619 (1976).
4. Stoeckli, H. F. *Helv. Chim., Acta*, 1974, 57, 2194.
5. Chihara, K.; Susuki, M.; Kawazoe, K. *J. Colloid and Interf. Sci.*, 1978, 64, 584.
6. Wickens, D. A. *Carbon*, 1990, 28, 97-101.
7. Steele, W. A., *The Interaction of Gases with Solid Surfaces*, Pergamon Press: Oxford, 1974.
8. Ross, S.; Olivier, J. P. *On Physical Adsorption*, John Wiley: New York,1964.
9. Boudart, M.; Djega-Mariadassou, G. *Kinetics of Heterogeneous Catalytic Reactions*, Princeton University Press: Princeton, NJ, 1984.

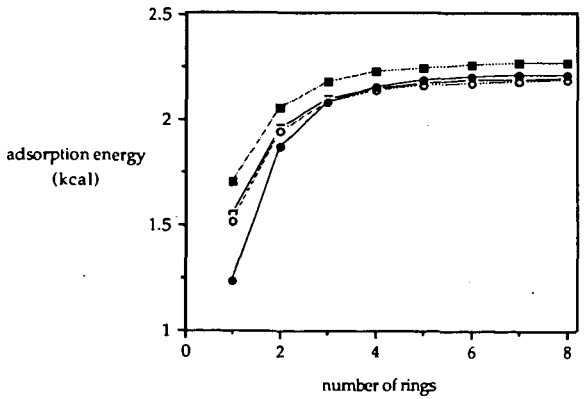

Figure 1. Adsorption energy as a function of lamella diameter: (■) s position; (○) c position; (□) cb position; (●) integral-sum calculation.

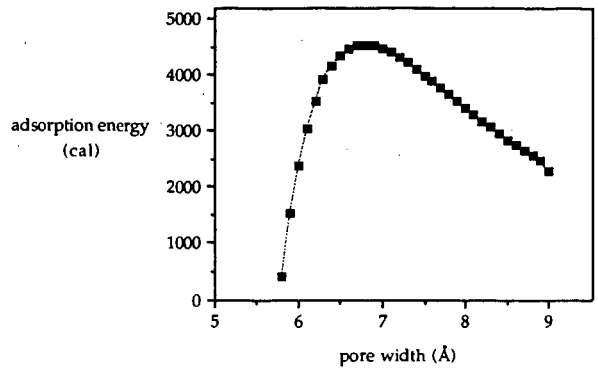

Figure 2. Adsorption energy as a function of pore width.

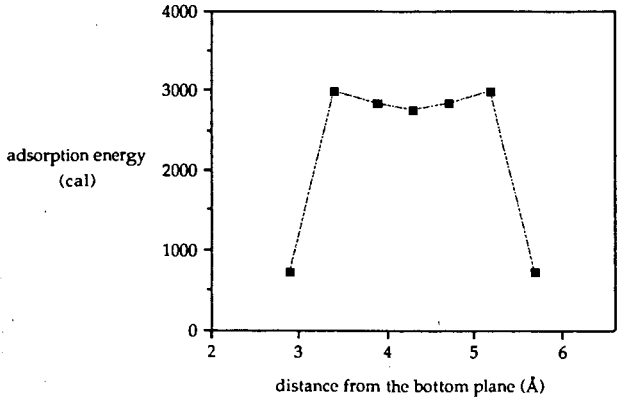

Figure 3. Adsorption energy as a function of adsorbate position in a 8.6 Å pore.

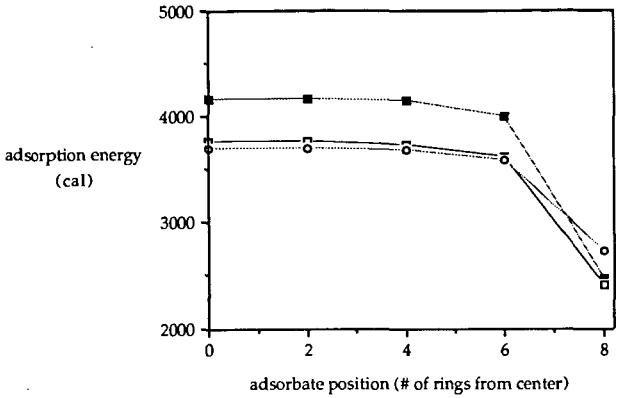

Figure 4. Adsorption energy as a function of the radial position of a molecule in a slit-like pore. Pore width: 6.4Å; (■) s position; (○) c position; (□) cb position.

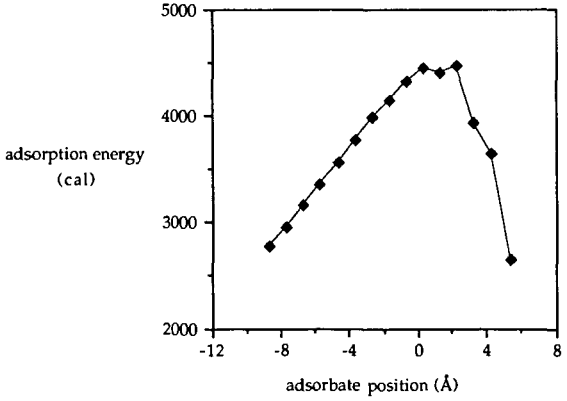

Figure 5. Adsorption energy as a function of position in a 10° pore. (0 = center of lamella; positive direction is into the angle; adsorbate equidistant from both planes.

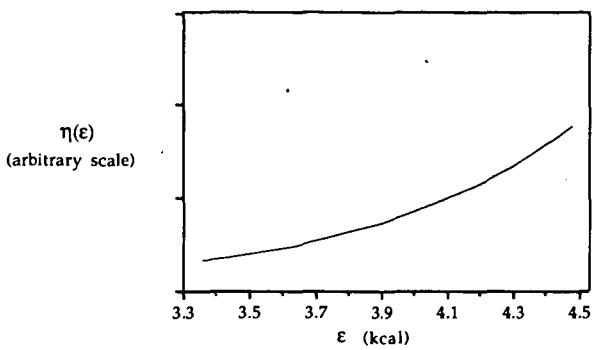

Figure 6. The density of the site energy distribution in a 10° wedge shaped pore.

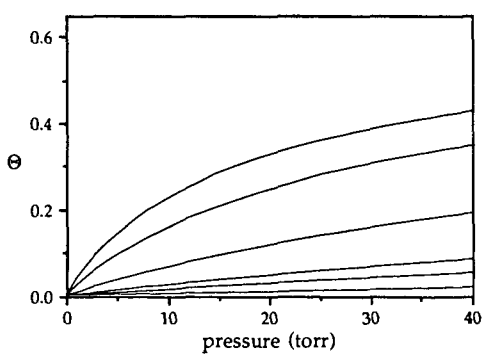

Figure 7. Volmer adsorption isotherms at 184 K for sites with adsorption energies of 4.4, 4.0, 3.6, 3.2, 3.0, and 2.6 kcal (curves from top to bottom).

A Transient Kinetic study of the Gasification of Carbon in CO_2.

F. Kapteijn, R. Meijer and J.A. Moulijn*.
Department of Chemical Engineering, University of Amsterdam
Nieuwe Achtergracht 166, 1018 WV, Amsterdam, The Netherlands.
* *at present: Department of Chemical Technology, University of Delft*

Keywords: transient kinetics, CO_2 gasification, carbon

ABSTRACT

A transient kinetic study, using labelled CO_2, has been conducted on the gasification of carbon in CO_2. Step-response (SRE) and temperature programmed desorption (TPD) experiments indicate that during steady state gasification at least two types of oxygen complexes are present at the carbon surface, both yielding CO. Upon exposure to an inert gas at gasification temperatures the decomposition of one of these complexes is fast and decays within seconds, whereas the other lasts for several minutes. However, both contribute to the overall gasification activity. Moreover, from the presence of ^{13}CO in both SRE and TPD experiments it is concluded that CO chemisorption or insertion takes place. A mechanism for the gasification reaction in CO_2 is proposed in which stable carbon-oxygen complexes can be transformed into the more reactive complexes, and in which CO insertion is included.

INTRODUCTION

The kinetics of carbon and coal gasification have been extensively studied. In most studies the rate of gasification is measured and interpreted under specified conditions. From both a practical and theoretical point of view it would be highly desirable if a method existed by which, independent of carbon type, heat treatment history or burn-off, the rate parameters which govern the gasification process could be determined.

Temperature programmed desorption (TPD) and step-response experiments (SRE), two commonly applied techniques in the field of heterogeneous catalysis, are increasingly used to determine the rate parameters and the total number and stability of active carbon-oxygen complexes present during steady state gasification of carbonaceous materials. Kapteijn and Moulijn [1] already outlined the possibilities of these transient techniques, compared to steady state measurements, in studies concerning (catalysed) carbon gasification. This experimental approach is gaining a lot of attention [2-7].

A step change in the gas phase composition at reaction temperatures, *i.e.* from a reactive to an inert gas flow and *vice versa* or from one reactive to another (labelled) reactive gas flow and analysis of the response curves of the sample under investigation, provides information on the reaction, *viz.* the amount and stability of carbon-oxygen complexes and rates of elementary processes.

An important feature of applying $^{13}CO_2$ is that it enables us to distinguish between ^{13}CO produced by gas phase oxidation of the active carbon sites and CO production originating from the carbon structure. The assumption in this two-step model (eqs.1,2) that equation (2) is the rate determining step can easily be confirmed by a gas phase step change from $^{13}CO_2$ to an inert at gasification temperature; a fast declining ^{13}CO production is accompanied by a long tailing CO production.

$$CO_2 + C_f \underset{k_{-1}}{\overset{k_1}{\rightleftharpoons}} CO + C(O) \qquad (1)$$

$$C(O) \xrightarrow{k_2} CO + C_f \qquad (2)$$

A gas phase step change from $^{13}CO_2$ to Ar will show if desorbing CO is capable of picking up a surface oxygen by reversed reaction (1) ($^{12}CO_2$ formation) and if during gasification insertion of gas phase CO has taken place, which is the case if a tailing ^{13}CO production is observed.

The most important feature of step-response experiments between $C^{18}O_2$ and CO_2 is that it provides a means to trace and quantify all reactive oxygen present on the carbon sample, while maintaining steady state gasification conditions.

The aim of this study was to obtain a more detailed description for the mechanism of the carbon gasification reaction, thus providing a sound basis for the selection of a kinetic model and its derived rate expression. In this paper results are presented of transient kinetic gasification experiments (1200–1250 K) with (labelled) CO_2, together with TPD experiments after partial gasification. These results and their implications with respect to the mechanism of the gasification reaction are discussed.

EXPERIMENTAL

Throughout this paper all labelled species are addressed with a prefix, *viz.* ^{18}O and ^{13}C, whereas in all cases C and O without prefix refer to ^{12}C and ^{16}O.

Reactants/samples

The model carbon used in this study is Norit RX1 Extra, an acid washed, steam activated peat char with a high specific surface area [6].
All gases used were of HP or UHP grade and are purified (O_2 and/or H_2O removal) before being fed to the gas mixing sections. $^{13}CO_2$ and $C^{18}O_2$ were used as received (99% pure ^{13}C and 90–91 % pure ^{18}O, MSD Isotopes) and mixed with Ar in lecture bottles. The O present in the $C^{18}O_2$ feed is present as $CO^{18}O$ (≈ 20% of the total CO_2).

Apparatus

The kinetic equipment, described in detail elsewhere [6], basically consists of three gas mixing sections. By means of a pneumatically actuated four-way valve in SRE two selected gas flow lines can be exchanged instantaneously and isobaric over the carbon sample.
The product gas is analysed by GC and by MS. Signal analysis, mass selection and sampling rate are controlled by a personal computer, equipped with Analog Devices RTI cards, through which data were collected and stored for further quantitative analysis. Up to 12 m/e values can be scanned consecutively with a minimum delay of 47 ms per m/e value. The raw MS data are corrected for background levels, fragmentation contributions (CO_2 to CO) and MS sensitivity for the different molecules. Quantitative interpretation of the step-response curves was performed by comparison with a gas phase step change performed over an inert SiC sample under exactly the same experimental conditions. These blanc runs exhibit the same response curves for CO_2 and showed that under reaction conditions the equipment had a time constant (the time to fall to 1/e of the inital step change) of less than 1 s. Thus the rate processes with larger time constants, *i.e.* with rate constants smaller than 1 s^{-1}, can be determined.

Experimental procedures

Step-response and steady state gasification experiments were performed at 1200 and 1250 K with, unless stated otherwise, a carbon sample of initially 100 mg and a flow rate of 20 $\mu mol.s^{-1}$. In order to obtain a reproducible carbon sample each sample was dried *in situ* (T = 423 K, He) and was gasified at 1200 K up to approximately 20 % burn-off.
All step-response experiments were performed several times in order to check their reproducibility. The response curves after a gas phase step change from CO_2,Ar to Ar and *vice versa* were investigated as a function of temperature (1200–1250 K), partial pressure of CO_2 (4 – 100 % CO_2) and carbon burn-off (20–50%).

In some cases at the end of the step-response or gasification experiment a temperature programmed desorption (TPD) in helium, in order to characterise the sample by its desorption products, was performed. TPD was done with a heating rate of 10 $K.min^{-1}$ up to 1273 K, followed by an isothermal period of 10 min at 1273 K. The amounts of CO released, expressed as mol CO.mol $C_a^{-1}.s^{-1}$, are plotted as a function of temperature. During TPD experiments none or a negligible amount of low temperature CO_2 desorption was observed, which, for clarity, is not shown in the figures.

RESULTS AND DISCUSSION

After a gas phase step change from 10% $^{13}CO_2$,Ar to Ar at 1200 and 1250 K, besides CO also ^{13}CO production is observed (figure 1). In both cases $^{13}CO_2$ disappears nearly instantaneously and the total CO production ($CO+^{13}CO$) immediately drops to about half the steady state value and exhibits a fast continuing decay in the first ten seconds, followed by a tailing that lasts for several minutes, which is mainly due to CO. This behaviour is observed after all gas phase step changes from a reactive to an inert gas phase at gasification temperatures.
These results indicate that ^{13}CO is inserted or chemisorbed at the carbon surface [9–11], and is released in two distinct ways. The CO production could only be described by two different parallel desorption processes. A single exponential decay or Elovich type desorption [8] were unable to do so.

In figure 2 the response curves for different gas phase step changes involving $C^{18}O_2$ at 1200 K are shown. A gas phase step change from $C^{18}O_2$ to Ar shows a tailing $C^{18}O$ production (figure 2B, insert), similar to the results of figure 1. A step change to CO_2 results in a sharp $CO^{18}O$ production peak and a decaying $C^{18}O$ production that disappears earlier (figure 2A) than upon exposure to an inert. The total $CO + C^{18}O$ production remains constant, indicating no disturbance of the steady state gasification. A blanc experiment with a SiC bed (figure 2C) shows that the sharp $CO^{18}O$ production peak in the initial seconds after the step change, when both $C^{18}O_2$ and CO_2 are present, must be ascribed to gas phase exchange through eq.(3).

$$CO_2 + C^{18}O_2 \rightleftharpoons 2\ CO^{18}O \qquad (3)$$

The longer tailing $CO^{18}O$ evolution in figure 2A compared to that in figure 2B indicates that CO, produced by CO_2 gasification, picks up ^{18}O from the carbon surface, confirming the reversibility of reaction (1). The faster disappearance of $C^{18}O$ by a step change to CO_2 instead of Ar is only partially explained by this removal, since it is also observed in the case of SRE with $^{13}CO_2$. Apparently, the presence of CO_2 speeds up the release of CO. The released amounts of CO are given in table 1 and 2.

TPD patterns obtained after steady state gasification at 1200 K in various CO_2,Ar mixtures and cooling to 673 K (figure 3), all show CO desorption above 1000 K, which can be ascribed to the decomposition of carbon–oxygen complexes from the carbon surface. In all cases the total amount of CO desorption observed during TPD upto 1273 K exceeds the amount of CO produced after a gas phase step to an inert at 1200 K (table 3).
From the CO desorption patterns after gasification in pure CO_2 at 1200 K and assuming irreversible first-order desorption, an activation energy of 213 kJ.mol^{-1} (k_0N_{CO} = 6.6 10^3 mol.mol C_a^{-1}.s^{-1}) is calculated (figure 3A), for the fractional coverage range between 0.3 to 0.9. If after TPD the carbon sample is exposed to CO at 373 K in a subsequent TPD (figure 3B) again a considerable CO desorption is observed, but with a lower activation energy (E_a = 160 kJ.mol^{-1}, k_0N_{CO} = 11.4 mol.mol C_a^{-1}.s^{-1}), indicating a weaker interaction.
It is striking that during TPD after gasification in $^{13}CO_2$ (figure 3C) above 1000 K ^{13}CO desorption is observed, indicating that during gasification in $^{13}CO_2$ insertion of ^{13}CO has taken place, confirming the SRE results. The $C^{18}O$ desorption, which is observed in TPD after gasification in $C^{18}O_2$ followed by that in CO_2 (figure 3D), indicates that not all oxygen present on the carbon surface is actively taking part in the gasification reaction. The amount of $C^{18}O$ desorption is higher after the reversed gasification order.

In summary the most important observations are *(i)* two CO desorption rates are operative, *(ii)* CO can be inserted or adsorbed on the carbon, yielding both types of desorption, *(iii)* oxygen is removed from the surface by reaction with CO, *(iv)* CO_2 enhances the CO desorption process.
This led us to the following tentative proposal for the gasification mechanism. Reaction (1) yields semiquinone structures [12,13] at the zig–zag (II) or armchair (V) edges of the graphitic carbon planes by interaction of the CO_2 with the active sites (unsaturated carbons, not terminated with hydrogen). Decomposition of this structure yields the slow desorbing CO. At the armchair edges an adjacent site can also be oxidised, yielding a diketone (IX). This is more unstable than the

semiquinone and readily breaks open resulting in two adsorbed CO molecules, carbonylic structures (X). These represent the faster CO desorption species. The release of the CO molecules is in both cases assumed to be reversible, accounting for the observed CO insertion or chemisorption. Only in the presence of CO_2 the diketone structures will be formed continuously, and part of the semiquinone structures on the armchair edges are transformed into the faster desorbing CO species. This process might explain the discrepancy that was noticed between steady state gasification rates and those calculated on the basis of rate constants and surface occupancy obtained from step response experiments [7].

The SRE results presented here agree with the TPD analysis of Magne and Duval [14], who observed four types of CO release: two easily and two less easily decomposing surface complexes, yielding CO. Apparently, our results can only discriminate between the two groups.

$$CO_2 + C_f \rightleftharpoons CO + C(O) \quad (1)$$

$$CO_2 + C_f\text{-}C(O) \rightleftharpoons CO + 2\,C\text{-}(CO) \quad (4)$$

$$C\text{-}(CO) \overset{k_a}{\rightleftharpoons} CO + C_f \quad (5)$$

$$C(O) \overset{k_b}{\rightleftharpoons} CO + 2\,C_f \quad (2)$$

II

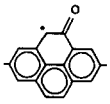

V

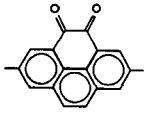

IX

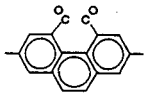

X

ACKNOWLEDGEMENT

The financial contribution of the Dutch Organization for the Advancement of Pure Research (NWO-SON), enabled the purchase of the labelled compounds.

These investigations have been executed within the framework of the Dutch National Coal research Programme (NOK), which is managed by the Project Office for energy Research (NOVEM) and financed by the Ministry of Economic Affairs.

REFERENCES

1. Kapteijn F., and Moulijn J.A., in *Carbon and Coal Gasification: Science and Technology*, eds. J.L. Figueiredo and J.A. Moulijn, NATO ASI Series E: Appl. Sci. vol. 177, Marinus Nijhoff Publ., Dordrecht, 291 (1986).
2. Huttinger K.J., *Carbon*, 28, 453 (1990).
3. Lizzio A.A., Jiang H., and Radovic L.R., *Carbon*, 28, 7 (1990).
4. Zhu Z.-B., Furusawa T., Adshiri T., and Nozaki T., *ACS Div. Fuel Chem. Prepr.*, 32, 132 (1987).
5. Huttinger K.J., and Nill J.S., *Carbon*, 28, 457 (1990).
6. Kapteijn F., Meijer R., and Moulijn J.A., in "*Fundamental Issues in Control of Carbon Gasification Reactivity*", eds. J. Lahaye and P. Ehrburger, NATO ASI Series E: Appl. Sci. vol. 192, Kluwer, 221 (1991).
7. Mc Enaney B., in "*Fundamental Issues in Control of Carbon Gasification Reactivity*", eds. J. Lahaye and P. Ehrburger, NATO ASI Series E: Appl. Sci. vol. 192, Kluwer, 1751 (1991).
8. Bonnetain L., *J. Chim. Phys.*, 34 (1961).
9. Bonner F., and Turkevich J., *J. Am. Chem. Soc.*, 73, 561 (1951).
10. Brown F., *Trans. Faraday Soc.*, 48, 1005 (1952).
11. Orning A.A., and Sterling E., *J. Phys. Chem.*, 58, 1044 (1954).
12. Marchon B., Tysoe W.T., Heinemann H. and Somorjai G.A., *J. Phys. Chem.*, 92, 5744 (1988).
13. Marchon B., Carrazza J., Heinemann H. and Somorjai G.A., *Carbon*, 26, 507 (1988).
14. Magne P. and Duval X., *Carbon*, 11, 475 (1973).

Table 1 : The total amount of CO production, relative to the amount of carbon actually present, observed after a gas phase step change from CO_2 to Ar at 1200 K as a function of carbon burn-off, together with the gasification rate, r_w, and the average rate constant for CO desorption

Burn-off (%)	N_{CO}/C_a mol.mol^{-1}	r_w mol.mol^{-1}.s^{-1} (* 10^4)	k_{mean} s^{-1}
20	0.0028	1.53	0.055
35	0.0026	1.55	0.060
45	0.0030	1.58	0.053

Table 2 : Total amounts of desorption products (μmol) observed after a gas phase step change from various CO_2,Ar mixtures to Ar at gasification conditions (sample sizes 30-80 mg carbon actually present).

gasification conditions		CO	^{13}CO	$C^{18}O$
CO_2	1200 K	20.8	-	-
$^{13}CO_2$	1200 K	17.4	4.3	-
10% $^{13}CO_2$,Ar	1250 K	4.7	1.4	-
	1200 K	2.4	0.4	-
4% $C^{18}O_2$,Ar	1200 K	-	-	6.2
$C^{18}O_2$	1200 K	-	-	11.1

Table 3 : Total amounts of desorption products, relative to the amount of carbon actually present (mol/mol), observed in TPD up to 1273 K after different treatment at 1200 K:

treatment	CO/C_a	$^{13}CO/C_a$	$C^{18}O/C_a$
SSG (CO_2)	0.0042	-	-
SSG ($^{13}CO_2$)	0.0038	0.0005	-
SSG (4% $C^{18}O_2$,Ar - 7% CO_2,Ar)	0.0010	-	0.0001
SSG (7% CO_2,Ar - 4% $C^{18}O_2$,Ar)	0.0007	-	0.0004
CO at 373 K after TPD	0.0015	-	-

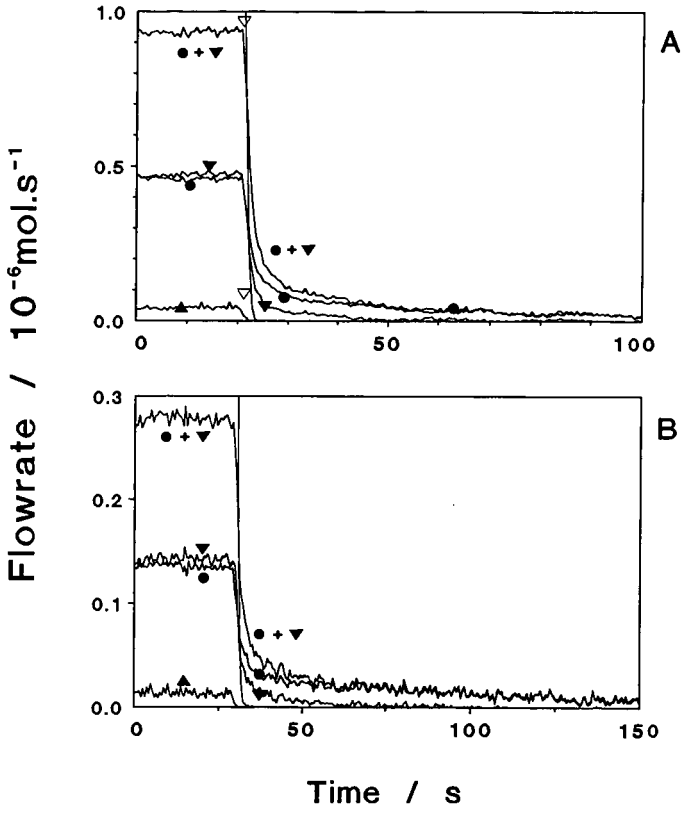

Figure 1 : Response curves after a gas phase step change from 10 % $^{13}CO_2$,Ar to Ar at different temperatures.
A. T = 1250 K; B. T = 1200 K.
Key: CO; ^{13}CO; $C^{18}O$; CO_2; $^{13}CO_2$; $CO^{18}O$; $C^{18}O_2$.

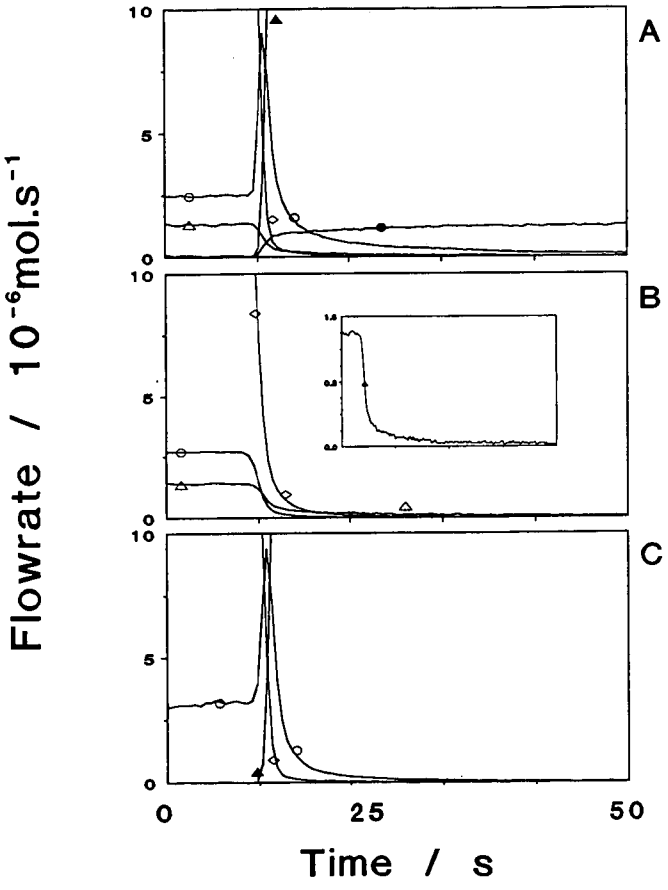

Figure 2 : Response curves after gas phase step changes at 1200 K:
A. $C^{18}O_2 \rightarrow CO_2$ (Norit)
B. $C^{18}O_2 \rightarrow Ar$ (Norit)
C. $C^{18}O_2 \rightarrow CO_2$ (SiC)
(key as in figure 1).

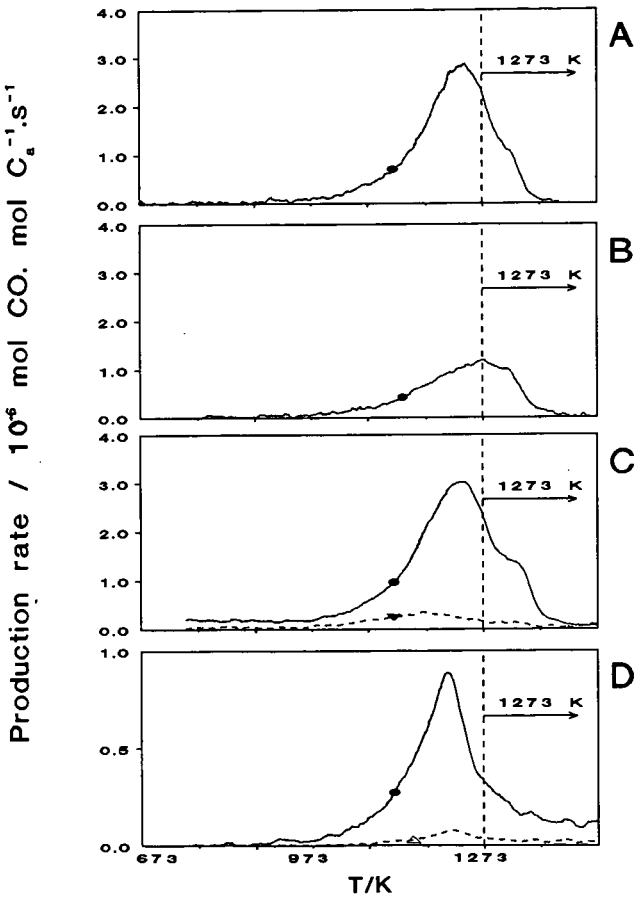

Figure 3 : TPD pattern after different treatments (key as in figure 1):
A. SSG 1200 K in CO_2;
B. TPD – CO at 373 K
C. SSG 1200 K in CO_2 followed by $^{13}CO_2$
D. SSG 1200 K in 4% $C^{18}O_2$,Ar followed by 7% CO_2,Ar.

THE ROLE OF ACTIVATED DIFFUSION IN THE GASIFICATION OF POROUS CARBONS/CHARS

J.M. Calo and M.T. Perkins
Chemical Engineering Program
Division of Engineering
Brown University
Providence, Rhode Island 02912

Keywords: Activated diffusion; mass transfer resistance; CO_2 gasification.

INTRODUCTION

The reaction rates of CO_2, steam, and hydrogen with carbonaceous solids are quite slow, such that the mass transport rate by ordinary bulk diffusion and/or Knudsen diffusion is usually more than sufficient to prevent the reaction from becoming mass transport-limited. Therefore, at first glance the issue of mass transport limitations seems to be relatively unimportant insofar as these reactions are concerned. However, the most reactive carbons are typically those with the highest internal surface areas, and thus it follows that transport in these materials must occur for the most part in pores of molecular dimensions; i.e., micropores. Transport of molecular species into or within micropores does not occur by ordinary bulk diffusion, nor even entirely by Knudsen diffusion. In this case, the energy of interaction between the solid and the gas phase species controls the process. This type of diffusion typically exhibits an Arrhenius-type temperature dependence, and in magnitude is usually slower than Knudsen diffusion. This behavior has been variously known as activated, micropore, intracrystalline, configurational, and surface diffusion [1]. Even though these terms are often used interchangeably in the literature, they may also refer to completely different mechanisms in different systems.

In the current paper we present some measurements of effective diffusion times in coal chars obtained using a transient technique, and analyze the results in terms of their potential effect on CO_2 gasification reactivity.

EXPERIMENTAL

The apparatus for measuring the effective diffusion times consists of: (1) a continuous gas flow, fixed solids, "gradientless" reactor, for carrying out the reaction under well-mixed conditions; (2) a solenoid/control valve network for generating step function changes in feed composition under conditions of constant flow rate, temperature, and pressure; (3) a supersonic molecular beam mass spectrometer system for measuring the transient response of the gas phase composition in the reactor effluent; and (4) a microcomputer for automated data logging and mass programming of the mass spectrometer [2]. In the current work, the highest operating temperature was 1273K and the highest pressure was 90 psig, although most of the data were obtained at a pressure of 30 psig. The reactor space time could be varied from about 0.01 to 2.0 min.

Sample Preparation.

Buller coal (New Zealand, medium volatile bituminous) activated char samples were supplied by Sutcliffe-Speakman Carbons Ltd. of Lancashire, England. The three other coals used in this study (PSOC-467 [Deadman #2] subbituminous, PSOC-833 [Fort Union Bed] lignite, and Wyodak subbituminous) were pyrolyzed in a tube furnace in ~50g batches at 1000°C under UHP nitrogen. Chars from the same coal produced in different batches were mixed. This large sample was divided up into reactor sample aliquots of 60-80g, and smaller characterization samples. The chars were sieved to a mean particle size of 1.6 mm. This size was selected primarily because it ensures complete retention

of the sample in the basket during operation, and yet provides minimal pressure drop through the sample bed. In addition, a mean particle size of 0.8 mm yielded results similar to those for 1.6 mm particles; i.e., ±5% for CO_2 diffusion in PSOC-467; therefore, additional particle size tests were not conducted. Once loaded in the sample basket, the chars were heated to 150°C for one hour to remove adsorbed water vapor.

Experimental Procedures.

A typical experiment was conducted as follows. The sample (60-80 cm^3) was placed in the sample basket, and positioned in the Berty reactor. A sheath-type thermocouple was inserted into the sample bed, and another was located in the free gas volume of the reactor. The reactor was then sealed and purged with argon. The reactor furnace was then turned on. After attaining operating temperature, the solenoid valve gas addition circuit was used to introduce the gas of interest as a step function change in concentration. The flow rates of the different gases were balanced such that the pressure in the reactor remained constant during the transient experiment. The reactor effluent concentration was then continuously monitored with the mass spectrometer, and the data were logged automatically. Runs typically required less than four minutes, following which the reactor was quickly refilled with argon using the gas addition flow circuit.

DATA ANALYSIS PROCEDURE

The experiment generates a time-concentration trace of the reactor effluent. A variety of analysis techniques were investigated to extract diffusion information from these data. A "difference" technique was finally selected. It is based on the "difference" variable, $\Delta C = C\text{-}C^*$, where C and C* are the time-dependent concentrations in a well-mixed reactor both without and with a porous material sink present. The corresponding differential mass balance is given by:

$$\frac{\partial \Delta C}{\partial t} = -\frac{\Delta C}{\tau} + 3\frac{D_e}{R^2}\frac{\partial C^\dagger}{\partial r}\left(\frac{V_s}{V_g}\right)(1-\varepsilon_b)(1-\varepsilon_m), \qquad [1]$$

where t is time, τ is the reactor space time at reactor conditions, R^2/D_e is the effective diffusion time within the char, $V_{s,g}$ are the solids bed and free gas volumes within the reactor, respectively, $\varepsilon_{b,m}$ are the external bed and intraparticle macropore void volumes, respectively, and $\partial C^\dagger/\partial r$ is the dimensionless concentration gradient at the surface of the microporous regions (assumed to be spherical). When ΔC is a maximum, $\partial \Delta C/\partial t = 0$, and Eq. [1] becomes:

$$\frac{\Delta C^{max}}{\tau} = 3\frac{D_e}{R^2}\frac{\partial C^\dagger}{\partial r}\left(\frac{V_s}{V_g}\right)(1-\varepsilon_b)(1-\varepsilon_m) \text{ at } t=t^{max} \qquad [2]$$

This expression requires the specification of $\partial C^\dagger/\partial r$ at the external surface of the "microparticle." This was estimated by the analytical expression for the gradient at the surface of a spherical particle driven by a "gradientless" reactor with the same space time [3]; *viz.*,

$$\frac{\partial C^{\dagger}}{\partial r}\Big|_{r=1} = e^{-t/\tau}\left(1 - \frac{R^2}{\tau D_e}\cot\left\{\frac{R^2}{\tau D_e}\right\}^{1/4}\right) - 2\left(\frac{R^2}{\tau D_e}\right)\sum_{n=1}^{\infty}(-1)^n \frac{e^{-D_e n^2\pi^2/R^2}}{\left(n^2\pi^2 - \frac{R^2}{\tau D_e}\right)} \qquad [3]$$

An iterative approach is required to solve the resultant Eq. [2] for R^2/D_e. Subsequently, the forcing function was generated from the data itself for an improved approximation.

In Figure 1 are presented some representative data for CO diffusing into PSOC-833 coal char at 285°C and 30 psig. The response of a hypothetical run at the same reactor space time with no porous char mass sink (i.e., C) is also presented, as well as the difference curve, ΔC. The maximum is located at $C/C_o = 0.25$ and t=33 s. Next, the data were fit to the expression $[1-\exp(-t/\tau_{eff})]$ to find τ_{eff}. For the data in Figure 1, the best fit is for $\tau_{eff} = 42.1$ s ($\tau = 25.9$ s). The resultant simple rising exponential expression is then used as the external forcing function to find the concentration gradient at the microparticle external surface. The best fit value of R^2/D_e is then found *via* an iterative search. For the data presented in Figure 1, the best fit value was $D_e/R^2 = 0.0134$ s^{-1}.

RESULTS AND DISCUSSION

Characteristic Diffusion Time Results.
All the results exhibited an increase in effective diffusivity with temperature. However, in general, the Arrhenius plots of the results were not very linear. Much of the data indicated a concave downward curvature which could be indicative of a change in mechanism of the transport mechanism with temperature. "Best fit" Arrhenius parameters over the entire temperature range are presented in Table I. As shown, the measured activation energies range from about 0.1 to 1.8 kcal/mole. The apparent activation energy of CO_2 was typically the largest of the gases studied in each coal char.

For a Wyodak coal char, Debelak [4] reported values for CH_4 varying from 0.9 - 3.2 kcal/mol, and values for CO_2, CO, and N_2 from 0.5-2.6 kcal/mol, over a temperature range of 50 to 250°C. A comparison of the current results for CO_2 diffusion in pre-oxidized (with air) Wyodak with the corresponding results of Debelak [4] is presented in Figure 2. Since high temperature surface cleaning, nor oxygen chemisorption in air were performed in the latter work, the actual state of the surface is uncertain. However, both sets of data still agree reasonably well. The observed differences are attributed to the different modes of burn-off (i.e., in CO_2 *vs.* O_2), which may have resulted in different porosity morphologies.

The magnitudes of the apparent activation energies from the current data are relatively low, which in some cases might be due to the influence of Knudsen diffusion. Arrhenius plots of Knudsen diffusivities ($D_K \alpha T^{1/2}$) exhibit a noticeable upward curvature, with the slope increasing with temperature. The PSOC-467 coal char had the largest mean pore radius of the coal chars examined. However, the Arrhenius plots for CO and CO_2 diffusion in PSOC-467 did not exhibit an increasing negative slope with temperature, characteristic of Knudsen diffusion. Thus, it is concluded that Knudsen diffusion was not dominant over the entire temperature range examined.

The Effect of Pressure.
Figure 3 demonstrates the effect of CO_2 pressure on the apparent diffusivity of CO_2 in PSOC-833 coal char at 285°C. As shown, there is a marked *decrease* in apparent diffusivity with increasing pressure for CO_2 pressure. In terms of classical models for activated diffusion, this is consistent with an

occluded gas model where diffusion occurs on the surface by jumping from one adsorption site to another [5]. Increasing pressure tends to populate the adsorption sites, thereby decreasing the diffusion rate.

The Effect of Burn-Off.
Samples of the Wyodak coal char were burned-off in an air fluidized bed at 300°C for intervals of about 2 hours. In between runs, the samples were weighed, and the burn-off determined. The effective surface areas for the Wyodak coal char increased with burn-off, attaining 518 m^2/g (by CO_2 BET; 450 m^2/g by N_2 BET) for the 30% burn-off sample.

As shown in Table I, E_D for the three gases generally seem to increase with burn-off, although this is not a universal trend. At the lower burn-offs in oxygen, the Wyodak coal char develops microporosity with burn-off, but the pore size distribution does not change radically [2]. However, simultaneously the remaining mineral matter is continually being concentrated at pore walls. This effect is known to enhance specific reactivity in chars with catalytic mineral matter impurities [6]. If a diffusing gas interacts strongly with the mineral matter, then this could explain the general activation energy increase with burn-off. This hypothesis is not supported by the slightly higher apparent activation energies observed for CO_2 and CH_4 in the "0% burn-off" demineralized Wyodak coal char. However, the demineralization procedure [7] is known to significantly affect the porosity, and thus a better comparison might be with a higher burn-off sample. Thus, it is noted that all three E_D values are higher for the 10.1% burn-off sample than the demineralized sample, although this result is not conclusive.

The sharp decrease in E_D for CO evident at 30% burn-off may be due to the measured shift of the pore size distribution towards larger pore radii for this char sample [2]. CO, being the smallest of the three molecules may be the most sensitive to the microporosity morphology.

Mass Transfer Limitations.
In order to explore the potential effect of mass transfer resistance on reactivity, a classical "effectiveness factor" (η) analysis was performed. CO_2 gasification reactivities were measured for the four coal chars investigated in a thermogravimetric apparatus (TGA) under 0.1 MPa of CO_2. A simple first order rate expression was assumed for the rate form. Initially, assuming no mass transport resistance (i.e., $\eta = 1$), the Thiele modulus, $\phi = [\{k_1/(D_e/R^2)\}^{1/2}]/3$ (k_1 is the first order rate constant), can be calculated from the measured reaction rate and the effective diffusion time. (For temperatures higher than those for which data were obtained, D_e/R^2 values were extrapolated using the measured apparent activation energy.) Knowing ϕ, η can be determined from the well-known analytical expression, $\eta = 1/\{1/\tanh(3\phi) - 1/(3\phi)\}$. This value can then be used to correct ϕ, and the process is iterated until η and ϕ agree.

The resultant effectiveness factors determined for the coal chars investigated, over a temperature range of 1073-1173K, are presented in Figure 4. As shown, $\eta < 1$ for all the coal chars, and $\eta \ll 1$ at 1173K, indicating almost complete mass transport control under the latter conditions. The most severely transport-limited char is the Buller (activated) coal char, while the least affected are the PSOC-833 and PSOC-467 coal chars. This is consistent with the fact that the activated Buller coal char was the most microporous, while the PSOC samples were the least microporous, since they experienced little burn-off. As might be expected, the Wyodak samples at progressive burn-offs were intermediate between these two extremes.

CONCLUSIONS

Activated transport through microporous coal chars does not appear to be generally describable by a single simple model. The behavior depends on the diffusing species and char porosity morphology and composition, as well as surface site occupancy [2]. For the results that exhibited a pressure effect, the occluded phase model appears to be more applicable. However, some of the results exhibited a decrease in apparent activation energy at high temperatures that is characteristic of two-phase model behavior. Most of the results exhibit behavior somewhere in between these two extremes. Thus, the actual mechanism is likely to be a combination of these two processes, and, possibly, others (e.g., Knudsen diffusion) as well.

The reaction of CO_2 with coal char should be mass transport-controlled in the microporosity for all the coal chars examined at temperatures greater than about 800°C, with $\eta < 0.2$ for all the samples under these conditions. In addition, the the CO_2 reactivity of Wyodak coal char would still appear to be mass transport-limited up to 30% burn-off.

Acknowledgements. This work was supported by the Department of Energy under Grant No. DE-FG22-86PC90529 from the Pittsburgh Energy Technology Center. The authors also wish to thank Sutcliffe-Speakman Carbons Ltd. of Lancashire, England for providing activated carbon samples.

REFERENCES

1. Ruthven, D.M., *Principles of Adsorption and Adsorption Processes,* Wiley, NY, 1984.
2. Calo, J.M., and M.T. Perkins, *Micropore Diffusion in Coal Chars Under Reactive Conditions,* DOE Final Tech. Report, DE-FG22-86PC90529F, May, 1990.
3. Crank, J., *The Mathematics of Diffusion,* 2nd ed., Oxford Univ. Press, 1975.
4. Debelak,K., *Influence of Changing Particle Structure on the Rate of Gas-Solid Gasification Reactions,* DOE Final Tech. Report, DE-AC21-81MC16053-F, August,1983.
5. Palekhar, M.G., and Rajadhyaksha, R.A., *J. Cat. Rev.-Sci. Eng.* **28**, 382 (1986).
6. Solomon, P.R. and J.M. Beér in *Coal Gasification: Direct Applications and Syntheses of Chemicals and Fuels,* DOE Coal Gasification Research Needs Working Group, June 1987.
7. Morgan, M.E., Jenkins, R.G., and Walker, P.L., Jr. *Fuel* **60,** 189 (1981).

Table I. Summary of parameters for $D_e/R^2 = (D_e/R^2)_o \exp(-E_D/RT)$.

Char	Species	$(D_e/R^2)_o$ (s^{-1})	E_D (kcal/mol)
Buller "B"	CO	0.022	0.32
(steam activated)	CO_2	0.029	1.2
	CH_4	0.047	1.4
PSOC-833	CO	0.012	0.57
{17.1% burn-off in 0.1MPa	CO_2	0.16	1.8
O_2 at 200°C (pre-oxidized)}	CH_4	0.028	0.42
PSOC-467	CO	0.09	0.82
{13.2% burn-off in 0.1MPa	CO_2	0.042	0.86
O_2 at 200°C (pre-oxidized)}			
Wyodak	CO	0.012	0.32
{0% burn-off;	CO_2	0.033	0.87
as pyrolyzed ("clean")}	CH_4	0.041	0.75
Wyodak	CO	0.041	1.1
{10.1% burn-off in 0.1MPa	CO_2	0.056	1.4
O_2 at 200°C (pre-oxidized)}	CH_4	0.41	1.3
Wyodak	CO	0.084	1.7
{15% burn-off in 0.1MPa	CO_2	0.045	1.3
O_2 at 200°C (pre-oxidized)}	CH_4	0.031	0.37
Wyodak	CO	0.024	0.42
{30% burn-off in 0.1MPa	CO_2	0.15	1.8
O_2 at 200°C (pre-oxidized)}	CH_4	0.095	1.1
Wyodak	CO	0.028	0.11
{0% burn-off;	CO_2	0.072	1.1
demineralized}	CH_4	0.088	0.92

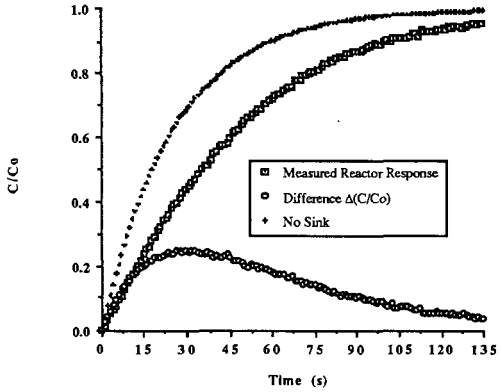

Figure 1. Data for CO diffusing into PSOC-833 coal char at T=285°C and P=30 psig, and theoretical response of a reactor with no internal porous mass sink under the same conditions.

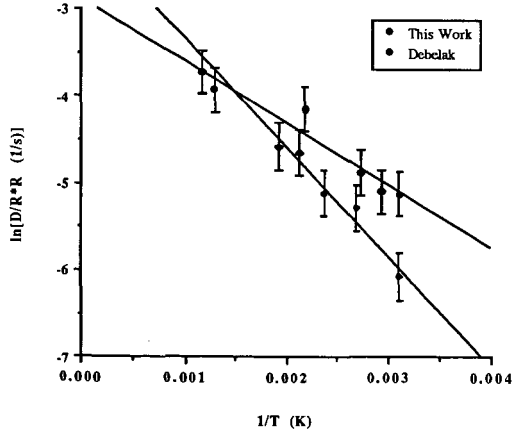

Figure 2. Comparison of activated diffusivities for CO_2 in Wyodak coal char in this work (10.1% burn-off in air) to those obtained by Debelak [4] (17.6% burn-off in CO_2).

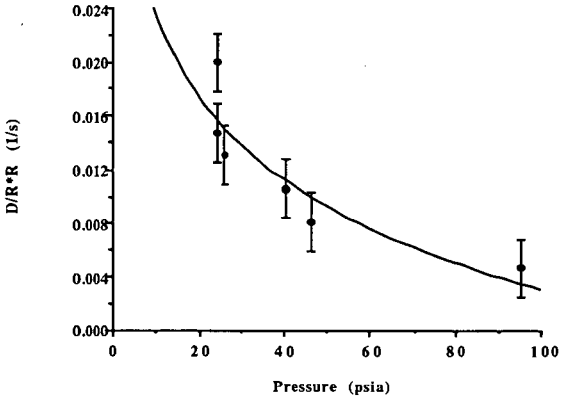

Figure 3. Effect of CO_2 pressure on effective diffusion time in PSOC-833 at 285°C.

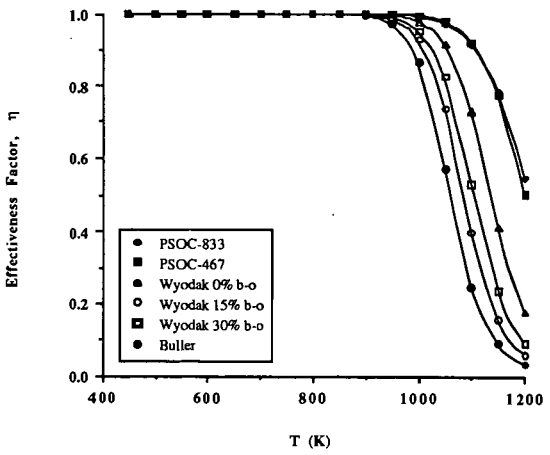

Figure 4. Calculated effectiveness factors for all the coal chars investigated.

CHEMISORPTION OF NITRIC OXIDE ON CHAR: KINETICS AND MECHANISM

Hsisheng Teng and Eric M. Suuberg

Division of Engineering
Brown University
Providence, Rhode Island 02912

Keywords : Nitric Oxide, Carbon, Chemisorption, Active Sites

INTRODUCTION

The reactions of nitric oxide with carbons have been considered as offering interesting possibilities for reduction of NO emissions from combustion systems. Some of the relevant literature on these reactions has been reviewed in a paper on the global kinetics of the gasification reaction[1]. The first step of the process, involving the chemisorption of NO on the carbon surface, has been separately considered[2]. The literature on chemisorption and/or physisorption of NO on carbons is limited[3-15]. Most of these studies acknowledge that if temperatures are kept low (i.e. well below ambient) mainly physisorption occurs,[5,8,10]. It is generally agreed that chemisorption occurs to a significant extent at temperatures above ambient. The chemisorption is generally accompanied by formation of surface oxides and release of N_2. Beyond this, the nature of the chemisorption process remains somewhat of a mystery.

One study has reported that the chemisorption of nitric oxide affects the spin-resonance absorption of charcoal in a manner similar to oxygen; there is an increase of ESR absorption linewidth with increasing extent of absorption on a cleaned carbon surface[12]. The difference is that oxygen adsorbed at room temperature can be desorbed by evacuation, whereas nitric oxide cannot. The initial absorption appears, on the basis of magnetic susceptibility, infrared, and thermal studies, to involve the addition of nitric oxide in an "N-down" configuration[5,6]. Another study cast doubt on the notion that the sites reactive towards nitric oxide addition could be spin centers[4]. It also appeared that more highly heat-treated carbons gave nitric oxide surface complexes of lower thermal stability[4]. This suggests that addition to aromatic ring structures is involved, and that the number of resonance structures affects the stability of the NO adduct. In short, it appears that the literature implies that radical addition processes occur on the surface of carbons, involving the paramagnetic nitric oxide (which is essentially free radical in nature). These addition processes appear to affect the ESR spectra, but do not destroy the measurable free radicals in carbons (which are probably of the π type). Thus the addition process does not appear to involve the "titration" of the measurable radicals in carbon by the nitric oxide. Hence the identity of the "active sites" in carbon remains unclear. The present measurements shed some new light on these issues.

EXPERIMENTAL

A standard thermogravimetric analyzer (TGA) was used for studying the kinetics of NO chemisorption on chars. Experiments were performed in a static gas environment, in He/NO mixtures at 101 kPa total pressure. The volume of the vessel was large enough to ensure that under any reaction conditions, the consumption of NO was not significant. Pulverized char samples

(50~100 mg) were held in a quartz bucket suspended in the heated zone of a quartz tube. A thermocouple placed within a few millimeters of the bucket served to indicate its temperature. The vessel could be purged following experiments, and the contents analyzed by gas chromatography.

The chars used in present study were derived from phenol-formaldehyde resins. These resins were synthesized in house in order that they contain few catalytic impurities (< 200 ppm)[16]. The resin char was prepared by pyrolysis of the phenol-formaldehyde resin in a helium environment at 1323 K for 2 hours, then ground and sieved to give the desired particle size. The surface of the char was cleaned of oxides prior to NO sorption experiments by heating the sample to 1223 K in extra high purity helium for at least 2 hours. NO sorption experiments were performed after surface cleaning by lowering the temperature of the sample from 1223 K to the desired sorption temperature, and then quickly introducing the desired NO/He mixture.

In order to clarify the mechanism of NO sorption on char, information on surface species formation during the course of sorption is required. Since N_2 and CO, both with a molecular weight of 28, are released during the thermal desorption of products from NO oxidized carbon, mass spectrometry could not be used for gas analysis. This required the use of gas chromatography (GC) as the main analytical technique. Thus temperature programmed desorption (TPD) experiments, with a linear heating rate of 22.5 K/min, were carried out in a TGA/GC system. TPD of NO treated chars were performed from 473 to 1223K. The desorbed gas products, purged from the TGA by helium, were collected in a cryogenic trap of Porapak-QS polymer kept at liquid-nitrogen temperature (77 K). This was necessary to boost product concentrations to conveniently measurable levels, as the concentrations within the TGA ambient gas were very low. The products could be desorbed from the trap by raising its temperature to ambient. Quantitative measurements of the products were performed on a Hewlett Packard GC equipped with a 2.1-m column of molecular sieve 5A. Significant amounts of NO were found to non-dissociatively adsorb on carbon surface at temperatures lower than 473K. The analysis of NO by this technique is not quantitatively reliable, but from the data on sample mass and GC analysis of other products, the quantity of NO desorbed during TPD could be evaluated from a mass balance. The surface species formed on chars were studied as a function of NO pressure, time, and temperature.

Specific surface areas of the samples were determined by the N_2 BET method at 77 K. A standard flow-type adsorption device (Quantasorb) was employed for the measurements. Prior to any such analysis, samples were outgassed in flowing N_2 at 573 K for 3 hours.

RESULTS AND DISCUSSION

The mass uptake curves obtained during chemisorption of NO on a cleaned char surface are shown in Figure 1, and as we have reported earlier, follow so-called Elovich sorption kinetics[2]:

$$r_{ad} = dq/dt = b \cdot \exp[-a \cdot q] \qquad (1)$$

where r_{ad} is the rate of sorption, a and b are fitting parameters, and q is the amount of mass uptake per unit of BET surface area. The values of a and b under different chemisorption conditions are given in Table 1. The value of a is a function of chemisorption temperature in NO sorption on char (as it is in O_2, e.g. ref 17,18). The value of a is generally a decreasing function of chemisorption temperature in the case of O_2 chemisorption. It is an increasing function of temperature in NO chemisorption. An increasing value of a with increasing chemisorption temperature can lead to a negative apparent activation energy for chemisorption , based on the following equation:

$$d\ln(r_{ad})/d(1/T) = -E_{ad}/R = d(\ln b)/d(1/T) - [da/d(1/T)]\cdot q \qquad (2)$$

where E_{ad} is the apparent activation energy for chemisorption. The first term is positive (see below) and the second term is negative, implying that E_{ad} must be negative. The increase of the value of a with increasing chemisorption temperature in the case of NO chemisorption has been attributed to the occurrence of exothermic reversible NO sorption which would result in less mass uptake at higher temperature[2]. The overall NO sorption reaction is actually a combination of reversible and irreversible process, *vide infra*, and cannot be simply represented by (1) or (2).

The physical significance of the parameter b is that it represents the initial rate of mass uptake on the clean char surface. At constant temperature, it is seen from Table 1 that the value of the parameter b increases with increasing NO pressure, as might be expected from a surface collision controlled process. This result is similar to that of O_2 chemisorption reported by other workers[18]. In the case of NO chemisorption, however, the b value decreases with increasing chemisorption temperature. This would also imply a negative activation energy for the initial chemisorption, again because of the reversible nature of NO uptake [2]. In short, Elovich-type analyses may provide satisfactory curve fitting for the NO-carbon system, but they are of no physical significance.

The existence of a certain amount of reversible sorption of NO has been earlier established[2,3]. We showed that such chemisorption data imply a heat of reversible chemisorption of -42 kJ/mol (i.e. exothermic)[2]. A heat of reversible NO adsorption on graphite of around -70 kJ/mole has been reported by others[6]. These values indicate chemisorption, since they are much higher than those for ordinary physisorption, which are usually less than 20 kJ/mol exothermic. The process can be represented in thermodynamic terms by[2]:

$$C + NO \leftrightarrow C(NO) \qquad (R\ 1)$$

This process of reversible sorption of NO is however accompanied by irreversible surface reactions involving NO. Moreover the thermodynamic representation of the reaction (R1) does not correctly portray the kinetics of this process, as discussed below.

Surface Complexes Involved in NO Chemisorption on Char

Once C(NO) is formed, it can react via thus far unestablished mechanisms to give other irreversibly bound surface species. This process can be generally represented by:

$$x_1 C(NO) + x_2 NO + \text{carbon surface} \rightarrow x_3 C(O) + x_4 C(O2) + x_5 C(N2) + x_6 N_2 + x_7 CO_2$$

The choice of the symbols on the right hand side is based on the experiments used to identify surface products.The symbol C(N2) represents the surface species that result in release of N_2 during post-chemisorption TPD. Likewise, CO is said to come from C(O), CO_2 from C(O2), and NO from C(NO). No particular structures or desorption mechanisms are implied by this nomenclature; it is selected for convenience alone. Both N_2 and CO_2 can evolve during chemisorption. The CO_2 is measured by GC, at the end of chemisorption. The N_2 is determined by mass and element balance, based upon the results of the post-chemisorption TPD analysis. The results of these analyses, following different times of sorption under 10.1 kPa of NO at 323 and 373 K, are shown in Figs. 2 and 3, in units of g/m^2. No other products are seen.

The amount of N_2 forming complexes, C(N2), remained roughly constant on the char surface

throughout chemisorption at $0.98 \cdot 10^{-4}(\pm 0.12 \cdot 10^{-4})$ and $0.76 \cdot 10^{-4}(\pm 0.10 \cdot 10^{-4})$ mmole/m^2 for 323 and 373 K, respectively. Although the sites for C(N2) have been saturated at these chemisorption conditions, the number of C(N2) complexes on the char surface under these conditions is still less than that during steady state gasification (~ $3.6 \cdot 10^{-4}$ mmole/m^2)[1]. Since in the low temperature chemisorption regime, C(N2) decreases with increasing temperature, the higher value at the higher gasification temperatures cannot be predicted by simple extrapolation of the low temperature chemisorption results. It is likely that C(N2) complexes are created by different mechanisms during gasification at higher temperatures.

We believe that C(N2) actually involves dissociated N atoms on the surface, because of the high desorption temperatures needed to release most of this product (>900K). These are relatively minor surface species, and because we observe them to form very quickly (virtually all before the first surface species measurements), they may be formed at exceptionally active surface sites on the freshly cleaned char surface. We cannot necessarily rule out the possibility that this surface species quickly builds up to a static concentration as a result of a fast dynamic equilibrium involving its formation and destruction, but this seems unlikely since the kinetics of release of N_2 during chemisorption (see Figs. 2 and 3) appear to be too slow to support such a dynamic equilibrium.

In contrast to C(N2), both C(O) and C(O2) both increase in concentration throughout chemisorption (see Figs. 2 and 3). The C(O2)/C(O) ratio on char surface is not constant during chemisorption and at 323K increases from 0.27 (molar basis) after 0.2 hour of chemisorption to 0.52 after 24 hours. For 373 K chemisorption in 10.1 kPa NO, the C(O2)/C(O) ratio increases slightly with reaction time from 0.22 after 0.2 hour to about 0.27 after 1.6 hours and remains constant afterwards. The C(O2)/C(O) ratio of 373 K sorption is less than that of 323 K sorption. The increasing C(O2)/C(O) ratio of surface species with decreasing reaction temperature is in agreement with the fact that the CO_2/CO ratio decreases with increasing steady state gasification temperatures[1]. The TPD results have revealed that the CO_2 desorption product evolves at lower temperatures than the CO desorption product. In fact, the formation of gaseous CO_2 product is significant during chemisorption at 373 K, but was too low to be accurately measured at 323 K (see Figs. 2 and 3). Considering the sum of C(O2) plus desorbed CO_2 in the case of the 373 K sorption, this value is actually seen to be quite similar to the value for C(O2) alone at 323 K, at all times. The weak temperature dependence in the kinetics of formation of the total C(O2) complexes implies that there is a process of moderately low activation energy responsible for the conversion of other surface intermediates to C(O2). The apparently strong temperature dependence of the actual C(O2) population actually reflects the temperature dependence of desorption of CO_2.

The population of C(O) on char is a weak function of sorption temperature, and is seen to slightly decrease with increase in temperature, for any time of measurement. The total yield of all irreversible C(NO) decomposition products, i.e. C(N2), C(O) and C(O2) surface complexes plus released gaseous CO_2, is relatively constant after 24 hours, for any given temperature within this range (15.4 and 14.4 mmol/m^2 for 323 and 373 K, respectively). One might expect that when CO_2 is desorbed in the 373 K case it would leave an "active site" behind that could gain further oxygen by the same mechanism as before, but this does not appear to happen. This implies that the surface appears to "heal" itself upon CO_2 desorption, and that active sites are <u>not</u> regenerated by desorption at these temperatures (This conclusion does not hold when higher temperatures are involved; TPD of this char following NO exposures up to gasification conditions shows the oxide population to be an increasing function of temperature[19]).

Since the total population of surface species changes little with time beyond about 24 hours, the behavior in NO chemisorption is quite different from that in O_2 chemisorption. In O_2, the total number of complexes quite commonly continues to increase indefinitely, until the rate of desorption begins to overtake the rate of chemisorption. In NO, it appears that there is only a particular inventory of sites that can be filled, at any temperature. What limits the inventory is unclear. The fact that the total uptake of irreversibly held species is only a weak function of temperature suggests that certain types of structures initially exist within the carbon, and that they alone are capable of participating in the formation of dissociation products.

The mass of chemisorbed oxygen atoms on the char surface can be converted to a surface area occupied by these oxygen atoms, by applying the assumption[20] that each oxygen atom occupies an area of $8.3 \cdot 10^{-20}$ m^2. The surface area occupied by oxygen atoms of any released CO_2 before its desorption from the char surface is taken into account. This surface area is obviously a weak function of chemisorption temperature and constitutes 0.094±0.003 of the total surface area (TSA = 320 m^2/g) of the sample, under the conditions at which the surface oxide inventory was measured (18% burnoff char). In the case of oxygen chemisorption on this same char, the surface area occupied by oxygen atoms is an increasing function of chemisorption temperature, accounting for 0.032 of TSA at 373 K and 0.046 at 473 K. Different numbers of "active sites" are thus apparently involved in NO and O_2 chemisorption, although this comparison is perhaps unfair in that the carbons on which oxygen ultimately resides may not be the same as the carbons involved in the initial chemisorption. It should also be mentioned that in the case of NO, there is a strong suggestion that the micropore surface area is not fully accessible[19], so the value of 0.094 may actually underestimate the fraction of accessible surface that is covered. A similar accessibility problem was not observed with O_2.

The Kinetics of Surface Complex Formation

The formation during chemisorption of each of the different types of surface complexes can be described by the Elovich equation (1) and the fitting parameters a and b for the different complexes are shown in Table 2. Again, comments similar to those related to those for total mass uptake may be made with respect to these (note trends with temperature). In this case, however, the b parameter provides some useful insights into the process. The b value is about an order of magnitude higher for the formation of C(O) than that for C(O2) at 323 K. Since b is the initial rate of complex formation, the relative magnitudes of these values apparently imply that the C(O) complexes are created earlier. This in turn suggests that some of them could serve as reactive intermediates on the char surface, and can react with NO from the gas phase or C(NO) on carbon surface, to generate the C(O2) complexes. The hypothesis that C(O2) is derived from C(O) has been advanced earlier[11].

At 323 K,the formation of reversibly adsorbed NO (i.e. C(NO)) is slightly more rapid than other surface species (see Table 2). Thus it seems to support the very plausible notion that the C(NO) surface complex may serve as an initial intermediate. Such an initial step for NO-carbon chemisorption was also proposed by previous workers[4,10]. It is unclear how the kinetics of formation of other surface species should depend on C(NO) concentration ([C(NO)]), or on the partial pressure of NO in gas phase (one or the other must be involved, based upon stoichiometric considerations). Reactions were performed at 323 K under different NO pressures to explore this

dependence. By back extrapolation of these data to zero time, the rates of complex formation on clean char surface under different NO pressures were determined.

The initial rates of C(NO) formation (r_0) on clean char surface under different NO pressures are shown in Fig. 4. It was found that the reaction of C(NO) formation on clean surface is close to second order with respect to NO pressure. Thus the reaction (R1) does not accurately portray the kinetics of this step. We hypothesize that the addition of NO occurs in a process that can be represented in two steps:

$$\text{Carbon Surface} + NO \;\text{<---> } C(NO)^* + C^* \qquad \text{(R1a)}$$
$$C(NO)^* + C^* + NO \;\text{<----> } 2\,C(NO) \qquad \text{(R1b)}$$

where C(NO)* is an unstable NO addition product, C(NO) is the stable product, and C* represents the odd electron contributed to the carbon structure by the first NO addition step. It is hypothesized that the odd electron must be paired with a second electron, in order to make two surface complexes stable. This is the origin of the second order. Note that overall, the concentration of C(NO) would still be proportional to NO partial pressure, as in (R1).

There was little C(NO) on the clean char surface initially, and it was impossible to establish the role of C(NO) in the reactions for C(O) and C(O2) formation on the clean surface by the same kind of back extrapolation to zero time. Thus the rates of C(O) and C(O2) formation were evaluated, at particular extents of total oxide surface coverage to clarify the role of C(NO) in the reaction. It was found that the rate of C(O) formation was approximately first order with respect to C(NO) and simultaneously second order with respect to gas phase NO. Thus, the process appears to be limited by the ability to form a second stable complex in the vicinity of a first stable C(NO) complex.

As for the formation of C(O2), the rate might be expected to be related to the population of C(O) on the char surface. Therefore rates of C(O2) formation were examined at constant [C(O)]. It was found that the rate was first order with respect to both C(NO) and C(O), and second order with respect to NO in the gas phase. Again, the suggestion is that the placing of a stable C(NO) complex near to existing surface complexes is a key limiting step.

CONCLUSIONS

The chemisorption of NO on char surface is not always immediately followed by the release of N_2 from the dissociation of the NO molecule. Reversibly (i.e. C(NO)) as well as irreversibly bound complexes (i.e. C(O), C(O) and C(N2)), can all exist on the char surface. The reversible sorption of C(NO) on a resin char surface is an exothermic reaction having an enthalpy of -42 kJ/mole. The rate of C(NO) formation on clean char surface is roughly second order with respect to NO pressure, but [C(NO)] is proportional to NO pressure at equilibrium. The mechanism for C(O) and C(O2) formation appears to involve both gaseous NO and C(NO) complexes. The formation of stable C(NO) surface complexes is hypothesized to involve an electron-pairing mechanism, and is important in the formation of irreversibly bound surface complexes as well.

ACKNOWLEDGEMENT

The financial support of the U. S. D.O.E. (grant DE-FG22-87PC79929) and the Exxon Education Foundation are gratefully acknowledged.

REFERENCES

1. Suuberg, E.M., Teng, H. and Calo, J.M., 23rd Symposium (Int.) on Combustion, The Combustion Institute, in press (1990-91).
2. Teng, H., Suuberg, E.M., and Calo, J.M., ACS Div. Fuel Chem Prepr., **35(3)**, 592 (1990).
3. DeGroot, W.F., Osterheld, T.H., and Richards, G.N., Carbon, **29**, 185 (1991).
4. Harker, H., Gallagher, J.T., and Parkin, A., Carbon, **4**, 401 (1966).
5. Zarifyanz, Y.A., Kiselev, V.F., Lezhnev, N., and Nikitina, O., Carbon, **5**, 127 (1967).
6. Zarifyanz, Y.A., Russian J. of Physical Chemistry, **38**, 1439 (1964).
7. Smith, R.N., Swinehart, J., and Lesnini, D., J. Phys. Chem., **63**, 544 (1959).
8. Smith, R.N., Lesnini, D., and Mooi, J., J. Phys. Chem., **60**, 1063 (1956).
9. Shah, M.S., J. Chem. Soc., 2661 (1929).
10. Brown, C.E. and Hall, P.G. , Trans. Faraday Soc. **67**, 3558 (1971).
11. Brown, C.E. and Hall, P.G. , Surface Science, **30**, 379 (1972).
12. Pastor, R., Weil, J., Brown, T., Turkevich, J., Adv. in Catalysis, **9**, 107 (1957).
13. Richter, E., Kleinschmidt, R., Pilarczyk, E., Knoblauch, K., Jüntgen, H., Thermochimica Acta, **85**, 311 (1985).
14. Richter, E., Chem.-Ing.-Tech., **55**, 986 (1983).
15. Cascarini de Torre, L.E. and Arvia, A.J., An. Quim. **64**, 349 (1968).
16. Suuberg, E.M., Wójtowicz, M., and Calo, J.M., 22nd Symposium (Int.) on Combustion, The Combustion Institute, 79 (1988).
17. Khan. M.R., Everitt, C.E., and Lui, A.P., Comb. and Flame, **80**, 83 (1990).
18. Bradbury, A.G.W. and Shafizadeh, F., Carbon, **18**, 109 (1980).
19. Manuscript in preparation.
20. Laine, N.R., Vastola, F.J. and Walker, P.L., Jr., J. Phys. Chem., **67**, 2030 (1963).

Table 1. The Elovich parameters for NO chemisorption on char- total mass uptake

Pressure (kPa)	10.1				4.04	2.02
Temperature (K)	473	423	373	323	323	323
a $[m^2/g]\cdot10^{-6}$	0.265	0.249	0.225	0.0811	0.117	0.149
b $[g/m^2hr]\cdot10^{6}$	53.5	86.1	221	337	69.8	16.0

Table 2. The Elovich parameters for formation of surface complexes.

	C(O2)	C(O)	C(NO)
T = 323 K			
$a\cdot10^{-6}$	0.213	0.248	0.147
$b\cdot10^{6}$	19.4	155	211
T = 373 K			
$a\cdot10^{-6}$	0.474	0.240	0.658†
$b\cdot10^{6}$	16.8	71.5	96.8

a is in m^2/g, and b is in $g/(hr\cdot m^2)$ † 1.6 hours of chemisorption

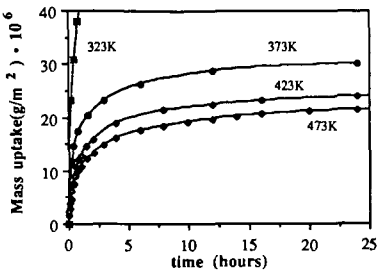

Fig. 1 Total mass uptake as a function of time in chemisorption under 10.1kPa NO pressure.

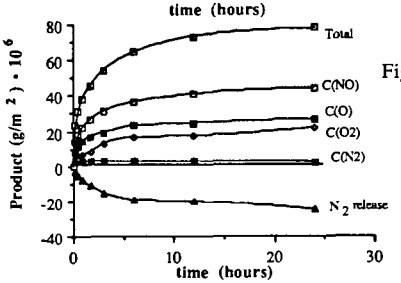

Fig. 2 Product formation during 323K chemisorption under 10.1kPa of NO (mass of carbon not included in C(NO) and C(N2) values).

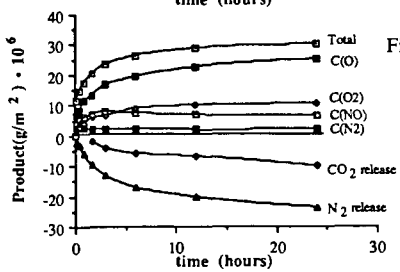

Fig. 3 Product formation during 373K chemisorption under 10.1kPa of NO (mass of carbon not included in C(NO) and C(N2) values).

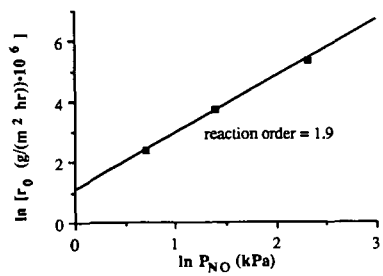

Fig. 4 Initial rate of C(NO) formation on clean char surface under different NO pressures.

MODELING OF OXYGEN CHEMISORPTION ON MICROPOROUS CARBONS

J. K. Floess
Department of Chemical Engineering
University of Illinois at Chicago
Chicago, IL

Keywords: microporous carbons; oxygen chemisorption; chemisorption kinetics

Introduction

The reaction of oxygen with carbon is believed to involve the dissociative adsorption of oxygen on the carbon to form carbon-oxygen surface complexes and the subsequent desorption of these complexes to carbon monoxide, or in a more complex sequence of steps, to carbon dioxide. The oxygen chemisorption step is effectively irreversible in that desorption to oxygen apparently does not occur; instead, desorption involves the breaking of one or more carbon-carbon bonds in the solid and the formation of carbon oxides. Because the adsorption and desorption steps involve distinct chemical pathways, however, it is necessary to investigate each of these step independently in order to determine the overall energetics of the reaction. An objective of this study was to determine activation energies for the oxygen chemisorption step by analyzing chemisorption data on a microporous char in terms of a distributed activation energy model.

This paper discusses the modeling of oxygen chemisorption kinetics with the assumption that there is a distribution of activation energies for adsorption. Two different types of heterogeneous surfaces were considered: in one case, it was assumed that the surface has an a priori distribution of activation energies for adsorption whereas in the second case, it was assumed that the activation energy increases as a consequence of oxygen chemisorption (i.e., due to induced heterogeneity). For each model, the activation energy was assumed to vary linearly with coverage. Experimental data reported by Kelemen and Freund[1] and by Floess et al.[2] show that the activation energy for chemisorption, to a first approximation at least, increases linearly with oxygen coverage. Consequently, the proposed distribution does adequately represent available experimental data. Furthermore, the use of a linear distribution function allows the model equations to be solved analytically rather than numerically. The availability of analytical equations simplifies the problem of obtaining model parameters from experimental data, and finally, an analytical solution provides insight into the behavior of the solution that is not easily discernible from numerical results.

Experimental

In this study, oxygen chemisorption data on a microporous carbon were obtained in a series of isothermal adsorption runs at temperatures between 400 and 548 K and at oxygen partial pressures up to 1atm. Experimental data were obtained using a thermogravimetric analyzer. Gas compositions in the reactor were also monitored by leaking a small amount of gas to a quadrupole mass spectrometer. A detailed description of the experimental approach is given in reference (2).

Chemisorption data were obtained with Spherocarb that had been partially reacted to 5% conversion and then outgassed. Pretreatment of the char in this manner was found to substantially increase the amount of oxygen that could be chemisorbed at low temperatures. The experimental data, which are presented later, are reported on a normalized basis with respect to the maximum amount adsorbed, which was taken to be the amount adsorbed at conditions where the rate of gasification is negligible. This oxygen uptake, however, is significantly less than the amount of oxygen typically present on a char after partial gasification. In other words, with carbon conversion, the oxygen content increases significantly above the amount present when no conversion has yet occurred. Although the choice of a normalization factor for reporting experimental data is to a degree arbitrary, its value can affect the interpretation of the model results, as will be shown later.

Chemisorption Models

The first model assumes that there exists a continuous distribution of activation energies for adsorption. Here $\eta(\varepsilon)$ is the density of the distribution function, and $\eta(\varepsilon)\Delta\varepsilon$ is the fraction of total sites with an activation energy for adsorption between ε and $\varepsilon+\Delta\varepsilon$. The rate of adsorption on sites of energy ε is:

$$\frac{d[C(O)_\varepsilon]}{dt} = k_\varepsilon C_{O_2} (1 - \theta_\varepsilon) \qquad (1)$$

where $C(O)_\varepsilon$ is the concentration of adsorbed oxygen atoms on sites of energy ε; k_ε is the adsorption rate constant; C_{O_2} is the oxygen concentration; and θ_ε the fraction of sites of energy ε that are occupied. The reverse reaction is neglected in this equation since oxygen chemisorption is assumed to be irreversible, and the analysis is limited to the case of negligible gasification. Integration of (1) yields:

$$\frac{C(O)_\varepsilon}{C_{T_\varepsilon}} = \theta_\varepsilon = [1 - \exp(-\bar{k}_\varepsilon t)] \qquad (2)$$

where $\bar{k}_\varepsilon = k_\varepsilon C_{O_2} / C_{T_\varepsilon}$.

The total amount adsorbed is obtained by integrating equation (2) over the activation energy distribution:

$$\{C(O)\}(t) = C_t \int_{\varepsilon_*}^{\varepsilon^*} [1 - \exp(-\bar{k}_\varepsilon t)]\, \eta(\varepsilon)\, d\varepsilon \qquad (3)$$

For a linear distribution function (i.e., the density of the distribution is equal to a constant), equation (3) may be integrated analytically to give:

$$\theta(t) = \frac{\{C(O)\}t}{C_t} = 1 - \eta_o RT\, [E_1(\bar{k}^* t) - E_1(\bar{k}_* t)] \qquad (4)$$

where E_1 is the exponential integral; $\eta_o = 1/(\varepsilon^* - \varepsilon_*)$; and $\bar{k}^*$ and $\bar{k}_*$ are the rate constants at ε^* and ε_*, respectively.

This equation may be differentiated to obtain the rate of oxygen chemisorption:

$$\frac{d\theta}{dt} = \eta_o \frac{RT}{t} [e^{-\bar{k}^* t} - e^{-\bar{k}_* t}] \qquad (5)$$

The rate equation for the second model, where it is assumed that surface heterogeneity is induced by oxygen chemisorption, is:

$$\frac{d[C(O)]}{dt} = k(\theta)\, C_{O_2}\, (1 - \theta) \qquad (6)$$

Here $k(\theta)$ indicates the dependence of the adsorption rate constant on oxygen coverage. This model has been used by Tokoro et al.[3] to analyze desorption data and to obtain site energy distributions from experimental data in a comparatively straightforward manner.

For the case where ε varies linearly with θ:

$$\varepsilon = a\theta + b \qquad (7)$$

equation (6) can be integrated to yield:

$$\int_0^\theta \frac{e^{a\theta/RT}}{(1 - \theta)}\, d\theta = k't \qquad (8)$$

Here $k' = A_o \exp(-b/RT)\, C_{O_2}/C_t$

This integral may be evaluated to obtain its asymptotic behavior as $\{a/RT\} \rightarrow \infty$:

$$k't = \frac{RT}{a} \frac{e^{a\theta/RT}}{(1 - \theta)} \qquad (9)$$

Equations (4) and (8) are intrinsic rate equations for oxygen chemisorption for each model. However, in applying these equations to experimental data it is necessary to correct for the effects of bulk phase mass transfer, intra-particle diffusion, and instrument response time on the observed kinetics. In this study the two principal effects were the instrument response time and and the bulk phase mass transfer resistance. (Although, as a rule of thumb, intra-particle diffusion will usually manifest itself before bulk phase diffusion, in this study this was not the case since the length scales for mass transport and intra-particle diffusion were widely different. Experimental measurements[2] confirmed that there was no effect of particle size on the chemisorption rates obtained in these experiments.)

The TGA used in the experiments had a characteristic response time of 3.4 sec. The response of the instrument to a step change in weight could be adequately fitted by a first order model (both first and second order response models were investigated).

The mass transfer coefficient was estimated from the correlations of Wigmans et al.[4] and of Treybal[5]. Both correlations yield a Sherwood number of approximately 4. over the temperature range of 300-800K and for a flowrate of 60 scc/min. However, because of the large temperature gradient in the furnace tube neither correlation is entirely valid for the actual flow conditions in the TGA. The Raleigh number for the gas flow in the furnace tube is estimated to be $3.x10^5$, and for this value, the flow in the tube is dominated by free convection[6]. In any case, the characteristic mass transfer time (at an oxygen partial pressure of 0.5 atm) is 1.0 s, so that instrument lag is the dominant resistance for the experiments reported here.

The bulk phase mass transport resistance can be incorporated in a straight forward manner into the model of Tokoro to give:

$$\frac{d\theta}{dt} = \frac{C_{o_2}^{\circ}}{\frac{1}{k_r (1 - \theta)} + \frac{1}{k_m}} \qquad (10)$$

where k_m is a mass transfer coefficient, $k_r = k(\theta)/C_t$, and $C_{o_2}^{\circ}$ is the bulk oxygen concentration. This equation can be integrated to give:

$$t = \frac{1}{k'} \int_0^{\theta} \frac{e^{a\theta/RT}}{(1 - \theta)} \, d\theta + \frac{\theta}{k_m C_{o_2}^{\circ}} \qquad (11)$$

For the distribution model no simple rate equation that includes the mass transfer resistance can be obtained.

Since the instrument response to a step disturbance is known, Duhamel's integral was evaluated to determine the actual uptake of oxygen recorded in the experiments:

$$\theta = \int_0^t \theta(s) \frac{1}{\tau} e^{-(t - s)/\tau} \, ds \qquad (12)$$

where $\theta(s)$ is the amount of oxygen adsorbed as a function of time given by equation 4, 8, or 11 and τ is the instrument time constant. The integral was evaluated analytically by locally approximating $\theta(s)$ by a straight line over a time interval Δt_i. The results of the integration are presented in Figure 1. As shown, the adsorption curves obtained when the mass transfer resistance is also included in the calculations are not appreciably different from the case where this resistance is neglected. Consequently, the mass transfer resistance is neglected in comparing the results of each model, and equations (4) or (8) are used directly in equation (12).

Discussion

Calculations were done for different ranges of activation energies, which corresponds to different slopes for the activation energy distribution shown in Figure 2. It is likely, as shown by the dashed lines in the figure, that deviations from linearity occur at both extremes of the distribution. The deviation from linearity at the low activation energy end will not appreciably affect the results since chemisorption rates here are faster than can be measured experimentally under non-vacuum conditions. At the high end, it is assumed that the fraction of sites that deviate from the linear model and also contribute appreciably to the adsorption rate is small. Calculations were also done for two different values of the normalization factor.

Predicted isothermal adsorption curves at 400, 448, 498, and 548 K for two different activation energy ranges are shown in Figures 3 and 4. Both models give adsorption curves of a similar shape, and in fact, there is no basis for distinguishing between models. As a result, the choice of a model can be largely dictated by mathematical convenience. The model of Tokoro is advantageous when corrections for bulk phase mass transport or intra-particle diffusion need to be taken into account, and this model can be used in a straightforward manner to obtain a site distribution from experimental rate data by solving a set of n linear equations in m unknowns[3]. The unknowns are the pre-exponential factor and the constants in the function assumed for $\epsilon(\theta)$. The principal disadvantage of this model is that the correct θ values for the experimental data must be known.

Changing the range of activation energies alters the rise of the individual adsorption curves and the spacing between individual curves. However, these differences in the shape of the curves are not very sensitive to a change in the activation energy range. (For the two sets of data shown, the pre-exponential factors differ by 10^6.) In general, lowering the activation energy range tends to increase the rise of the curve between the initial, approximately linear, part and the final amount adsorbed and tends to push the curves closer together and up toward $\theta=1$. This bunching effect is accentuated for data near $\theta=1$. If, however, a larger normalization factor is used in calculating θ, the isothermal adsorption curves remain approximately equally spaced and do not come together since now the curves never reach $\theta=1$. As a result, the determination of the correct activation energy range is more difficult since one can now only use the rise of the curves to discriminate between activation energy ranges.

The effect of oxygen partial pressure on the adsorption curves is shown in Figure 5. The predicted curves are in good agreement with experimental data[2] previously reported.

Experimental chemisorption data for Spherocarb are presented in Figure 6, where the data are compared to model predictions for an activation energy range of 12 to 32 kcal/mole. This range gave the best agreement with the data for the assumption of a linear variation in activation energy with oxygen coverage. Agreement between the data and the model is satisfactory, although the model predicts a more rapid initial increase in oxygen coverage than is exhibited by the data. This discrepancy may be because the linear distribution assumed in the calculations is not sufficiently accurate for representing the actual activation energy distribution with the necessary precision.

Conclusions

This paper examined kinetic models for oxygen chemisorption on two types of heterogeneous carbon surfaces. In each case, a linear variation in activation energy with oxygen coverage was assumed. The models include correction terms for the effects of bulk phase mass transport and instrument response on the observed kinetics.

It was found that the adsorption curves obtained from each model are essentially similar and that the use of one or the other can be largely dictated by computational convenience. For example, the Tokoro model can be regressed in a straightforward manner to obtain model parameters from the data and can be readily modified to include the effects of intra-particle diffusion or bulk phase mass transfer on the kinetics.

Based on an analysis of experimental chemisorption data, it is concluded that the activation energy for oxygen chemisorption on a microporous char is in the range of 12-32 kcal/mole. However, since model predictions are rather insensitive to the range of activation energies, experimental data at precise temperature intervals are needed to accurately determine the activation energy range for chemisorption kinetics.

The models can correctly account for the oxygen partial pressure dependence of the chemisorption data.

References

1. Kelemen S. R.; Freund, H. *Carbon*, 1985, 23, 723-729.
2. Floess, J. K.; Lee, K-J.; Oleksy, S. A. *Energy and Fuels*, 1991, 5, 133.
3. Tokoro, Y.; Uchijima, T.; Yoneda, Y. *J. of Catal.*, 1979, 56, 110.

3a. Tokoro, Y.; Misono, M.; Uchijima, T.; Yoneda, Y. *Bull. Chem Soc. Japan*, 1978, 51, 85.

4. Wigmans, T.; v. Cranenburgh, H.; Elfring, R.; Moulijn, J. A. *Carbon*, 1983, 21, 23.
5. Treybal, R. E. *Mass Transfer Operations*; McGraw-Hill: New York, 1980.
6. Eckert E. R.; Drake, R. M. *Analysis of Heat and Mass Transfer*; McGraw-Hill, New York, 1972.

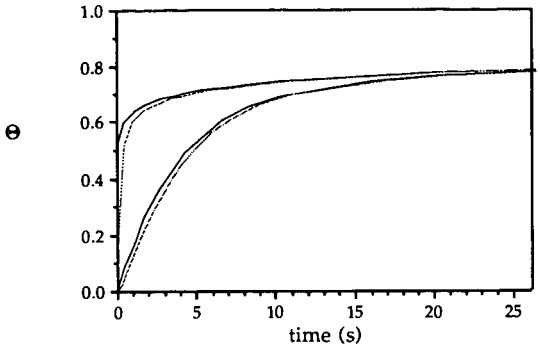

Figure 1. Effect of instrument response on chemisorption kinetics. Curves towards the left side of the graph are instrinsic kinetics; curves towards the right include instrument response; model of Tokoro: (- - -) includes mass transfer resistance; (—) no mass transfer included.

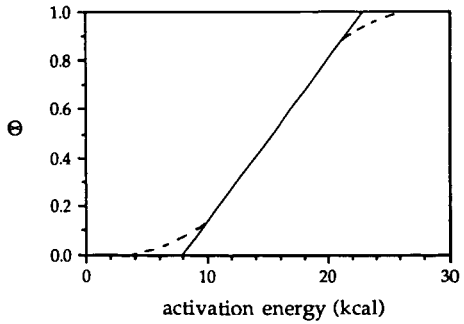

Figure 2. Activation energy distribution.

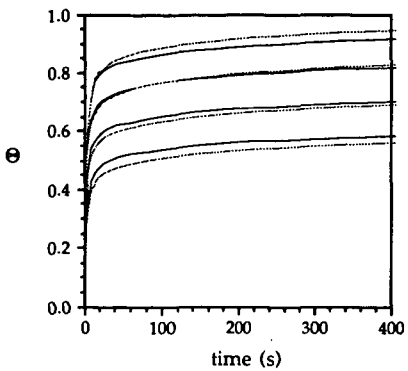

Figure 3. Predicted chemisorption curves at 400, 448, 498, 548 K, 0.5 atm oxygen partial pressure; activation energy range: 12.3 to 34.8 kcal; (---) distributed site model; (—) model of Tokoro.

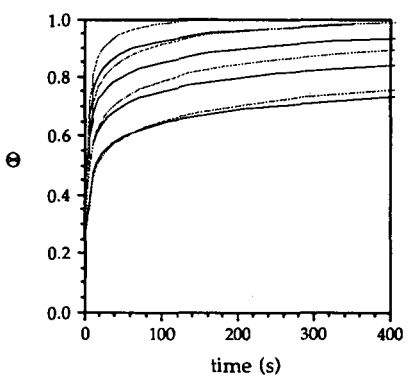

Figure 4. Predicted chemisorption curves at 400, 448, 498, 548 K, 0.5 atm oxygen partial pressure; activation energy range: 5.8 to 16.7 kcal; (---) distributed site model; (—) model of Tokoro.

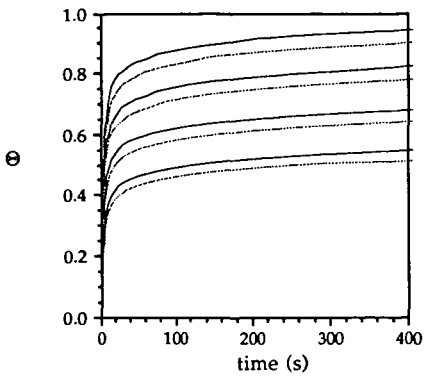

Figure 5. Model results for oxygen partial pressures of 0.5 atm (—) and 0.21 atm (---); site energy distribution model; activation energy range: 11.8 to 32.4 kcal.

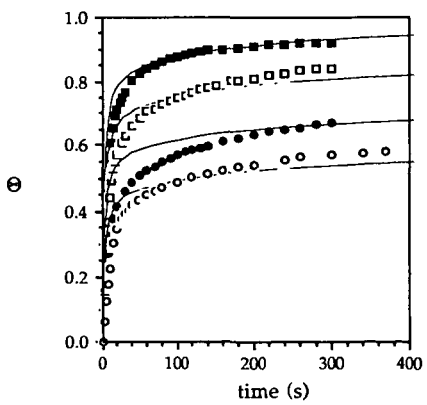

Figure 6. Comparision of chemisorption data at 400, 448, 498, and 548 K and 0.5 atm oxygen partial pressure to model results. Site energy distribution model; activation energy range: 11.8 to 32.4 kcal.

MORPHOLOGICAL CHANGES DURING OXIDATION OF A SINGLE CHAR PARTICLE

Matteo d'Amore[^], Leonardo Tognotti[*], and Adel F. Sarofim[o]

[^]University of Salerno, Chemical and Food Engineering Dept., Italy

[*]University of Pisa, Chemical Engineering Department, Italy

[o]Massachusetts Institute of Technology, Chemical Engineering Dept. Cambridge, MA 02139 (U.S.A.)

Keywords: char oxidation; morphology; electrodynamic balance.

ABSTRACT

The evolution of pore size distribution during the oxidation of single Spherocarb char particles has been measured under chemical controlled conditions. Electrodynamically levitated particles were heated to reaction temperature using a laser and the weight and size changes monitored. The laser heating was interruypted at selected conversions and the CO_2 adsorption determined at ambient conditions. As reaction proceeds, particles are found to shrink, the macropore volume decreases in proportion to the total particle volume, maintaining a constant macroporosity. The micropore volume, however, decreases with increasing conversion whereas the normalized pore size distribution remains unchanged, suggesting that the densification of the microporous volume which leads to particle shrinkage results from pore elimination. At the same time the mesopore volume increases with increasing conversion indicating that the mesopores play a dominant role in the char reaction.

1. INTRODUCTION

The reaction rate of carbon burning under chemical kinetic or internal diffusion controlled regime is strongly affected by the pore structure, which governs the extent of penetration of the reacting gases and, through the porosity evolution with conversion, the total amount of surface available for reaction (Gavalas, 1980; Mohanty et al., 1982; Reyes and Jensen, 1986).

The problem of evaluating the variation of combustion rates with conversion is usually reduced to the purely topological problem of establishing the relationship between accessible surface area and porosity as this latter changes. In the above referenced theoretical studies the assumption is made either that the reactivity is constant over the entire surface or restricted to the non microporous area (Gavalas, 1980). Accessibility to the microporous area may be restricted due to hindered diffusion in pores having dimensions approaching that of the reacting molecules and reactivities may vary due to either graphitization of surfaces or non-uniform distribution of catalysts. For this reason it is

desirable to experimentally determine the evolution of pore structure with increasing carbon conversion.

Whatever the experimental technique used, the possible occurrence of phenomena like shrinkage (Hurt et al., 1988) or fragmentation by percolation (Bar-ziv et al., 1989; Kerstein and Niksa, 1985), complicates the analysis of data to obtain basic information on porosity and surface area. Moreover, the experimental apparatuses currently used for reactivity measurements and the porosimetry techniques presently available, even when used on small amounts of samples, yield average information, since they integrate the results over the entire number of particles used. All these uncertainties result in tremendous data scattering (up to four orders of magnitude at a given temperature) when general correlations for intrinsic reactivity of coal chars are proposed (Smith, 1982).

In this study, the changes with conversion in morphology of a carbon char in the temperature range 500-1200 K are followed by using an electrodynamic balance (EDB) (Spjut et al., 1985; Dudek, 1988; Bar-ziv et al., 1989). This device allows one to measure in situ, over temperature range wider than in other apparatuses, mass, diameter, density, surface area, rate of reaction and temperature for a single, suspended submillimeter particle. By following with the EDB the changes in the char as it reacts, it is possible to study the influence of the porous texture on the reaction behavior and shed some light on the contribution by micropores to the reaction in the chemical kinetic controlled regime.

The pore sizes will be broken down into three classes: micropores (diameters between 0.8 and 3 nm), mesopores (3 <d < 20 nm), and macropores (20 nm < d). The micropores will be determined by CO_2 gas adsorption and a significant part of the results and discussions in this paper will be devoted to the interpretation of adsorption data to obtain the finer pore structure. The macropores are traditionally obtained by mercury intrusion porosimetry, although precautions must be taken to separate the contribution of interparticle voids from those of the larger macropores (Bellezza, 1985). In this study the result of Hurt et al. (1988) that the macropore volume is constant during reaction in the kinetic controlled regime will be utilized. This result was based on the observation that all macrofeatures of a particle were conserved during reaction in a chemical controlled regime and that the changes in diameters of macropores, down to the limit of resolution of 100 nm on the electromicrographs, were proportional to the change in the particle diameter. The mesopores are traditionally measured by capillary condensation with the results being somewhat dependent on the method of interpretation of the adsorption-desorption isotherms. In this study the mesopores will be determined from a volume balance utilizing the special capability of the EDB for measuring the density of a single particle.

2. EXPERIMENTAL

2.1 Apparatuses

Electrodynamic Thermogravimetric Apparatus

The electrodynamic chamber consists of three electrodes in an hyperboloidal configuration, the theory of which is described by

Wuerker et al. (1959), Davis and Ray (1980), Philip (1981) and Spjut (1985). A schematic view of the electrodynamic balance is shown in Fig. 1. The chamber creates a dynamic electric field capable of suspending a single, charged particle with a characteristic size less than 250 μm in the present configuration. The AC or ring electrode provides lateral stability to the particle through an imposed AC field oscillating sinusoidally ±2000 volts at 100 Hz. The DC top and bottom electrodes provide vertical stability by balancing the gravitational force, thus stably suspending the charged particle in the chamber. A position control system can be used which automatically adjusts the electric field to keep the particle at the chamber center. An optical microscope is used for viewing the particle and for manual control of the particle position. The microscope allows the measurement of the particle diameter to ±5 μm. A 20 W CO_2 laser is used to heat the suspended particle and a two color infrared (2 and 4 μm) pyrometry is used for temperature measurements. A gas flow system allows one to react a particle in various gaseous enviroments. Additional details on the experimental apparatus and procedure can be found in Spjut et al. (1985), Bar-ziv et al.(1989), Dudek et al. (1988).

Porosimetry

The pore size distribution of the char was measured by means of a Carlo Erba Sorptomatic 1800 static-volumetric apparatus, using N_2 at 77 K or CO_2 at 195 and 298 K as adsorption gases, and a high pressure mercury porosimeter model Carlo Erba 2000. The EDB was used as a gravimetric apparatus for CO_2 adsorption measurements on single "Spherocarb" particles at 298 K.

2.2 Char properties

The model char used in this work was "Spherocarb", a spherical microporous carbon from Analabs Inc.. The 60/80 mesh commercial fraction has been used in several previous studies (Waters et al., 1988, Dudek et al., 1988, D'Amore et al., 1988, Hurt et al., 1988) because of its high degree of uniformity and sphericity. Furthermore, the low ash content of the particles minimizes the effects of catalytic impurities, while the limited amount of volatile matter precludes the complicating effects of devolatilization on the burning behaviour. The gross physical properties and the chemical analysis of the material are reported in the following section.

Size	180-240	μm
Particle density	0.63	$g cm^{-3}$
True density	2.10	$g cm^{-3}$
BET surface area	963	$m^2 g^{-1}$
DR surface area	965	$m^2 g^{-1}$
Total surface area	1025.6	$m^2 g^{-1}$
Carbon content (weight basis, %)		96.9
Oxygen		2.4
Hydrogen		0.7

The BET area was obtained by analysing the N_2 adsorption isotherm at 77 K. Analysis of the CO_2 adsorption data at 195 and at 298 K by the Dubinin-Raduskevitch equation gave the DR area. The total surface area includes those of the micro-, meso-, and macro-pores. The good

agreement between the BET and the DR surface areas obtained in this case is somehow unexpected. Capillary condensation of the adsorption gases in the microporosity should be misinterpreted by Bet theory, which in this case would overestimate the sample surface area. On the other hand, indications have been given in the past that N_2 at 77 K hardly reaches the whole microporosity of chars. These counterbalancing effects could lead to the agreement above outlined.

Figure 2 shows the cumulative pore size distribution of the "Spherocarb" on a volume basis. The distribution has been obtained by joining distribution curves from gas adsorption together with results of high pressure mercury porosimetry (Dubinin, 1966; Spitzer et al., 1976). The method of Medek (1977) has been used to determine the size distribution of the micropores. Size distribution of mesopores has been obtained from adsorption data according to the method of Dollimore and Heal (1970). Mercury porosimetry has been used to determine the size distribution of macropores.

2.3 Experimental procedure with EDB

After capture in the EDB each particle was weighed by the technique described in detail elsewhere (D'Amore et al., 1988), and its diameter, density, porosity (D'Amore et al. 1988), surface area (Dudek et al. 1988) measured. The concentration of the gases flowing through the EDB was selected to include 5, 21 or 100% O_2 in N_2 or chromatographic-grade CO_2. The particle was heated by the $^2CO_2$ laser to the desired temperature which was measured by the two color optical pyrometry and continuously recorded. A semicontinuous reaction technique was utilized arresting the reaction by turning the laser off, and measuring at various conversions the physical parameters of the particle.

3. RESULTS

3.1 Microporosity

Theory

The adsorption data have been interpreted using the BET equation in the linear form:

$$\frac{p/p_s}{s(1-p/p_s)} = \frac{1}{s_m c} + \frac{c-1}{s_m c}\,(p/p_s) \qquad (1)$$

where s and s_m are the number of moles of gas adsorbed at relative pressure p/p_s and in a complete monolayer, per unit of sample mass, respectively.

For chars with a high fraction of microporosity, the low- and medium-pressure parts of isotherms are analysed using the Dubinin and Astakhov equation (Dubinin and Astakhov, 1971):

$$\theta = \frac{w}{w_{ts}} = \exp\,[-(A/E)]^h \qquad (2)$$

where w/w_{ts} is the ratio of the micropore volume w filled at pressure p/p_s to the total micropore volume w_{ts}, i.e. the degree of filling of micropores θ; E is the characteristic free energy of adsorption; A is the differential molar work of adsorption and is given by:

$$A = RT \ln(p_s/p) \qquad (3)$$

When w and w_{ts} are expressed in terms of moles of adsorbate s and s_{ts}, respectively, eq. (2) and (3) give:

$$\ln s - \ln s_{ts} = - (RT/E)^h [\ln (p_s/p)]^h \qquad (4)$$

For h=2 eq. (4) reduces to Dubinin-Raduskevitch equation (DR).

According to Medek's analysis (1977) the equation for the differential micropore size distribution is given by:

$$\frac{d\theta}{dr_e} = \frac{dw}{w_{ts} dr_e} = 3h\,(k/E)^h\, r_e^{-(3h+1)} \exp[-(k/E)^h\, r_e^{-3h}] \qquad (5)$$

where θ is the degree of filling of micropores, r_e the pore radius, k, evaluated according to Dubinin's affinity postulate, is equal to $7.51\ 10^{-25}$ cal m^{-3} $mole^{-1}$.

Evolution of "Spherocarb" morphology with reaction

By taking advantage of the special features of the electrodynamic balance, changes in physical characteristics of single "Sperocarb" particles with reaction have been followed.

The volume of micropores w_{ts} of single "Spherocarb" particles have been evaluated from the CO_2 adsorption isotherms at 298 K obtained in an EDB by the use of the DR equation. A complete description of the technique is given by Dudek et al. (1988). These volumes can be related to the surface areas of the micropores (Lamond and Marsh, 1964; Gan et al., 1972; Rand, 1974; Marsh et al., 1975). The char pores volumes are here reported (Figure 3) per unit mass of the particle being measured. In Figure 3, w_{ts} is reported versus fractional conversion f defined as the weight loss divided by the initial mass of carbon, for eight separate single particle "Spherocarb" oxidations. Five of the runs have been performed in oxygen, two in CO_2 and one in air. The reaction temperatures are in the range 750-830 K for reactions in oxygen and 1200-1250 K for reactions in CO_2. The initial specific volume of the micropores vary from 0.203 to 0.276 $cm^3\ g^{-1}$ with the average being 0.237 $cm^3\ g^{-1}$. These specific volumes can be compared to a value of 0.237 $cm^3\ g^{-1}$ obtained on a 0.294 g sample of "Spherocarb" (about 100,000 particles!) by Hurt et al (1988) in a conventional gravimetric apparatus. The specific volumes of the micropores for the 0.294 g sample at conversions of f=0 and f=0.65 for an oxidation run with air are also in Figure 3.

Adsorption can give, in addition to the total microporosities volumes, the pore size distribution by the use of eq. (5). Normalized distributions for fractional conversions f of 0.14, 0.23

and 0.52 for a single particle reacting in air at 770 K are compared in Figure 4 with the distributions for the unreacted char. Although the total microporous volume decreases, the fractional distribution of the residual pores is remarkably constant. This is consistent with the micropore elimination model of Hurt et al., (1988), which was presented with an alternative pore shrinkage model to explain the observation of shrinkage of particles when chemical kinetics are controlling.

3.2 Meso- and macro-porosities

The meso- and macro-porosities are obtained by volume balances on the single particle using measurements of the weight and volume of the particle to obtain total porosity.

Figure 5 shows the single particle porosity ϵ as a function of conversion for the same separate "Spherocarb" oxidations. The porosity values have been obtained from the particle densities by the relation:

$$\epsilon = (1 - \rho / \rho_t) \qquad (6)$$

where ρ is the density of a "Spherocarb" particle at a given conversion and ρ_t is the "Spherocarb" true density. Density measurements were performed discretely using the aerodynamic drag force technique (D'Amore et al., 1988). Initial porosities ranged from 0.56 to 0.68. Although conventional theory would predict particle porosity to increase linearly with conversion under kinetically controlled conditions (zone I) up to ϵ=1, the figure shows that the linearity holds up to a conversion of only 40-50%. A sort of plateau is then approached, consistent with the shrinkage-densification model proposed by Hurt et al. (1988) for chars undergoing regime I or kinetically controlled oxidation.

A particle shrinkage factor Σ has been defined as the ratio of the particle volume V to the initial volume V_0. The Σ values for the eight runs above have been reported in Fig. 6 as a function of conversion. The straight solid line in the figure represents a conventional shrinking, constant density, particle model, while the line at Σ=1 is representative of a purely internal reaction without shrinkage. The data indicates that the extent of "Spherocarb" shrinkage is not a function of temperature, or reacting gas, but only a function of conversion.

The data on total porosity and microporosity obtained in the EDB for a single particle allow one to evaluate the meso- and macropore volume of the particle at a given conversion. This can be done by a volume balance, given by the relation:

$$W = (1/\rho - 1/\rho_t - w_{ts}) (1-f) \qquad (7)$$

where W is the volume of the meso- plus macro-pores per unit initial mass. The results of such an analysis are reported in Fig. 7. In the figure, W has been normalized for each run with the initial value W_0, to account for the different characteristics of the single particles tested. In spite of the large differences in the initial porosity of the single particles (D'Amore et al., 1988), and in the

experimental conditions, clustering of the data points about one curve indicate that the particles all exhibit the same behavior: meso- plus macro-porosity increases with reaction, reaches a maximum at about f=0.3 and eventually decreases to zero at f=1, when the solid is consumed.

The meso- plus macro-pore volume fractions can be separated by utilization of the results of Hurt et al. (1988). Based on electronmicrographs studies of particles reacted to different fractional conversions, visible macropores (diameters greather than 100 nm) were found to have a constant volume fraction as particles shrank during conversion. Utilizing this information we are now in a position to show how the micro-, meso-, and macro-pore volumes change with conversion (Fig. 8), with the microporous volume fraction decreasing, the mesoporous volume fraction increasing, and the macroporous fraction remaining constant. These variations have implications on how the internal surfaces participate in the chemical reaction, which will be a subject of a subsequent paper.

4. CONCLUDING COMMENTS

Pore size distributions have been obtained for single particle using gas adsorption for micropores, the observed constancy of the macropores and a volume balance for the mesopores. The ability of the electrodynamic balance to measure densities of single macroporous particles, without need to differentiate as in conventional liquid displacement methods between macropores and interparticle interstices, provides a ready way for obtaining the mesoporous regime. The results can be depicted graphically as pie charts as shown for three conversions in Fig. 9.

The study provides support for the hypothesis of Hurt et al. (1988) that densification of the microporous regions is due to pore elimination. The interesting finding is the increase in the mesoporous region with increasing conversion, suggesting a crucial role for the mesopores in the reaction.

REFERENCES

- Bar-ziv E., Jones D. B., Spjut R. E., Dudek D. R., Sarofim, A. F. and Longwell, J.P. (1989). Comb & Flame, 75, 81, 1989
- Bellezza, C. (1985). Naples, Dept. of Chem. Eng. Dissertation.
- D'Amore M., Dudek, D.R., Sarofim, A.F., and Longwell J.P. (1988). Powder Tech., 56, 129.
- Davis E.J. and Ray, A.K.(1980). J. Colloid Interface Sci. 75, 566.
- Dollimore, D. and Heal, G.L. (1970). J. Colloid Interfaces Sci. 33, 508
- Dubinin, M.M. (1966) in Chemistry and Physics of Carbon (ed. by P. L. Walker) Vol. 2, p. 86, Marcel Drekker, New York
- Dubinin, M.M. and Astakhov, V.A. (1971). Adv. Chem. Ser. 102, 69
- Dudek, D.R. (1988). Mass. Inst, of Tech. PhD Thesis
- Dudek, E.R., Longwell, J.P. and Sarofim, A.F. (1988) Energy & Fuels, 3, 24.
- Gan, H., Nandi, S.P. and Walker, P.L., Jr. (1972). Fuel. 51, 272
- Gavalas, G.R. (1980). AIChE. 26, 577
- Hurt, R.H., Dudek, E.R., Sarofim, A.F. and Longwell, J.P. (1988). Carbon, 26, 433,
- Kerstein, A.R., and Niksa, S. (1985). Twentieth Symp. (Int.) on

Comb. The Combustion Institute, Pittsburgh, Pa. p. 941
- Lamond, T. and Marsh H. (1964). Carbon. 1, 281
- Marsh, H., Iley, M., Berger, J. and Siemieniewska (1975). Carbon, 13, 103
- Medek, J. (1977). Fuel. 56, 131
- Mohanty, K.K., Ottino, J.M. and Davis, H.T. (1982). Chem. Engng. Sci. 37, 905
- Philip, M.A. (1981). Mass.Inst. of Technology, M.S. Thesis
- Rand, B.J. (1974). J. Colloid Interface Sci. 48, 183
- Reyes, S. and Jensen, K.F. (1986). Chem. Engng. Sci. 41, 333
- Smith, I.W. (1982). Nineteenth Symp. (Int.) on Comb. The Combustion Institute, Pittsburgh, Pa. p. 1045
- Spitzer, Z., Biba, V. and Kadlec, O. (1976). 14, 151
- Spjut, R.E. (1985). Mass. Inst. of Tech. Ph.D. Thesis
- Spjut, R.E., Sarofim, A.F., and Longwell, J.P. (1985). Langmuir, 1, 355.
- Waters, B.J., Squires, R.G., and Laurendeau, N.M. (1988b). Comb. Sci and Tech. 62, 187
- Wuerker, R.F., Shelton, H., and Langmuir, R.V. (1959) J. Appl. Phys., 30, No 3, 342.

LIST OF SYMBOLS

A	differential molar work of adsorption, cal mol^{-1}
E	characteristics free energy of adsorption, cal mol^{-1}
R	gas constant, 1.987 cal mol^{-1}
T	particle temperature, K
V	particle volume, cm^3
V_0	initial particle volume, cm^3
W	single particle meso- plus macropore volume per unit initial mass, $cm^3\ g^{-1}$
W_0	single particle initial meso- plus macropore volume per unit mass, $cm^3\ g^{-1}$
c	parameter in BET equation
f	fractional conversion
h	parameter in Dubinin equation
k	interaction constant in eq.(4). For CO_2 $k=7.51\ 10^2$ cal nm^{-3} $mole^{-1}$.
p	adsorption gas pressure, atm
p_s	adsorption gas saturation pressure, atm
r_e	pore radius, nm
s	amount of gas adsorbed at relative pressure p/p_s, $mol\ g^{-1}$
s_m	amount of gas adsorbed in a complete monolayer, $mol\ g^{-1}$
s_{ts}	amount of gas adsorbed in the total micropore volume, $mol\ g^{-1}$
w	micropore volume per unit particle mass filled at pressure p/p_s, $cm^3\ g^{-1}$
w_{ts}	total micropore volume per unit particle mass, $cm^3\ g^{-1}$
ϵ	single particle porosity
θ	degree of filling of micropores
ρ	apparent particle density, $g\ cm^{-3}$
ρ_t	true particle density, g cm^{-3}
Σ	particle shrinkage factor

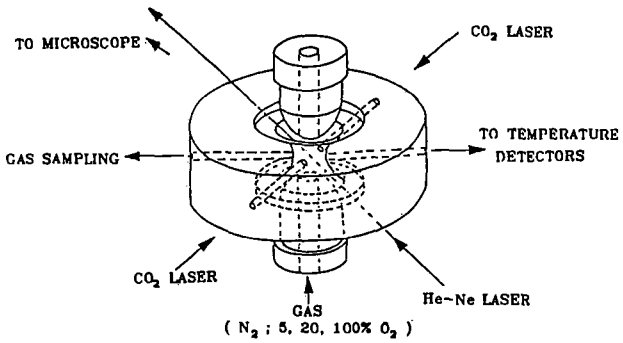

Fig. 1 - The Electrodynamic Thermogravimetric Analyser

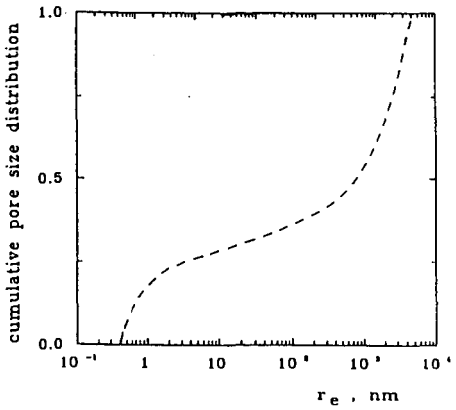

Fig. 2

Cumulative pore size distribution on volume basis

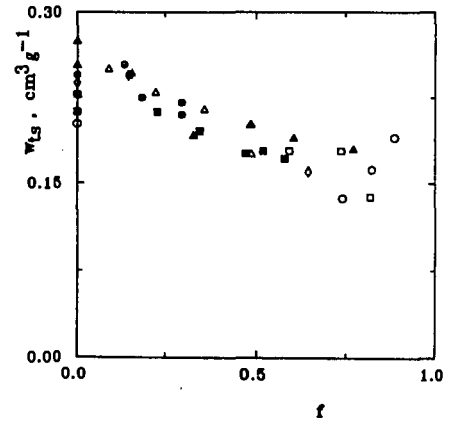

Fig. 3

Eight separate aingle particle "Spherocarb" oxidations in EDTGA.
Micropores volume per unit particle mass as a function of conversion.

◇ ▲ △ ○ □ 100% O_2
● ◒ 21% O_2
■ 100% CO_2

▨ 100,000 "Spherocarb" particles oxidation with 21% O_2 in CTGA.

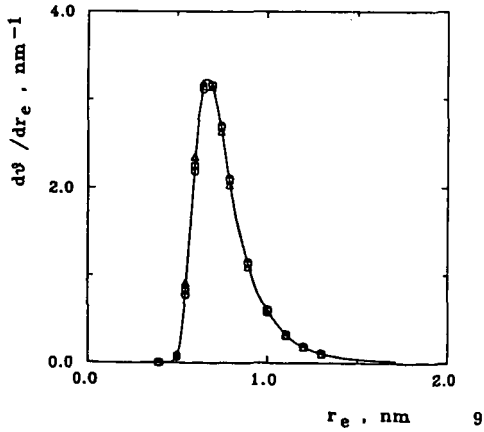

Fig. 4

Single particle "Spherocarb" oxidation with 21% O_2 in EDTGA.
Micropores size distribution at various conversions.

△ f = 0.14
□ 0.23
○ 0.52
solid line unreacted char

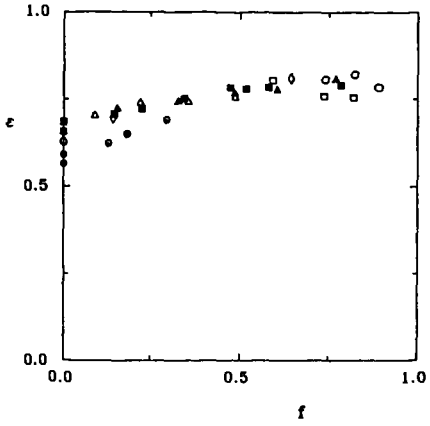

Fig. 5

Eight separate single particle "Spherocarb" oxidations in EDTGA.
Particle porosity as a function of conversion.
◇ ▲ △ ○ □ 100% O_2
● ◒ 21% O_2
■ 100% CO_2

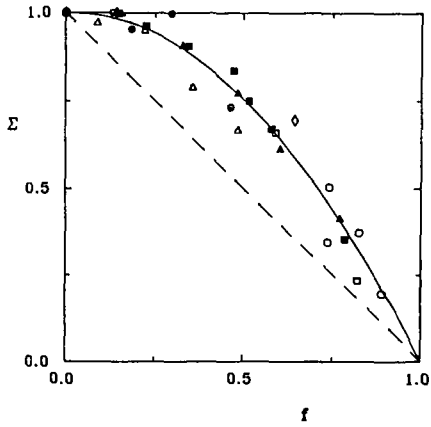

Fig. 6

Eight separate single particle "Spherocarb" oxidations in EDTGA.
Particle shrinkage factor as a function of conversion.
◇ ▲ △ ○ □ 100% O_2
● ◒ 21% O_2
■ 100% CO_2
dashed line shrinking core model
solid line best fit line

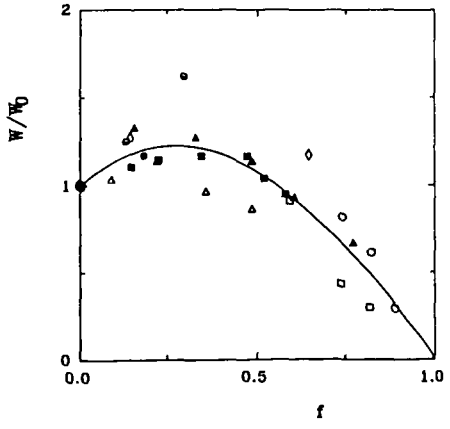

Fig. 7

Eight separate single particle "Spherocarb" oxidations in EDB.
Particle meso- plus macropore volume per unit initial mass, normalized in respect to the value at f=0, as a function of conversion.
◇ ▲ △ ○ □ 100% O_2
● ◒ 21% O_2
■ 100% CO_2
solid line best fit line

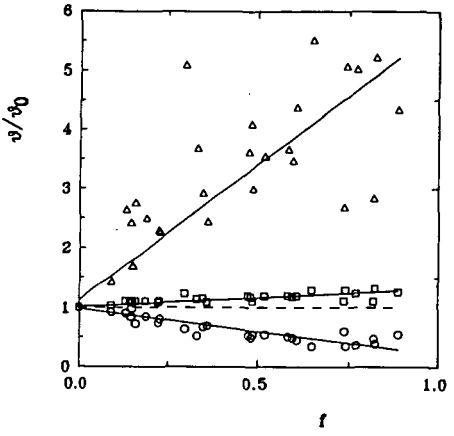

Fig. 8 - Eight separate single particle "Spherocarb" oxidations in EDB.
Pores volume fractions, normalized with respect to the value at f=0, as a function of conversion.

□ total pores volume fraction
--- macropores
△ mesopores
○ micropores

Fig. 9 - Single particle "Spherocarb" oxidation in EDB.
Volume fraction of porea and carbon at various conversions.

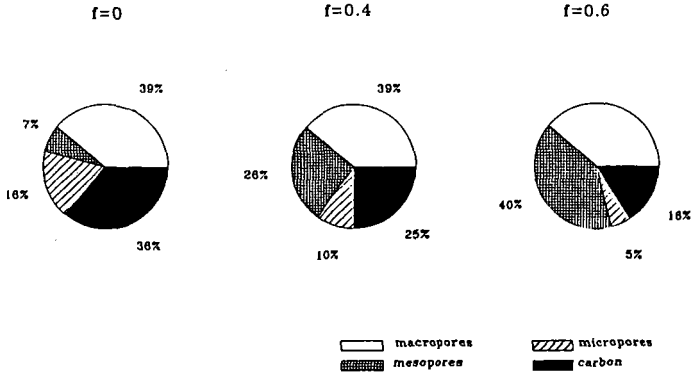

ON THE COMBUSTION KINETICS OF HETEROGENEOUS CHAR PARTICLE POPULATIONS*

R. H. Hurt and R. E. Mitchell**
Combustion Research Facility
Sandia National Laboratories, Livermore, CA 94551-0969

Keywords: coal, combustion, kinetics

An optical technique has previously been used to measure, *in situ*, the temperatures, sizes, and velocities of individual pulverized-coal char particles.[1-3] A model of mass and energy transport processes to and from the burning char particles was used to derive burning rates and kinetic parameters from the single-particle measurements. In the past, the measured joint distribution of particle temperature and size was divided into narrow size fractions, and global kinetic parameters were determined from the average temperatures and sizes in these fractions.[2,3] An effort is currently underway to extract additional information from the existing extensive data base by computing and analyzing burning rates and rate coefficients for *individual* particles derived directly from the single-particle temperature measurements. In the present article, single-particle rate coefficients are computed from optical measurements on char from Pocahontas #3 coal†, and techniques for the determination of kinetic parameters from the single-particle coefficients are investigated.

RESULTS

A laboratory-scale laminar-flow reactor was used to investigate the combustion of Pocahontas #3 low-volatile bituminous coal particles (nominal diameter range 106 -124 μm) in gas environments containing 6 or 12 mole-% oxygen over the range of gas temperatures 1500 -1700 K. An optical particle sizing/pyrometer was used to measure single-particle temperatures, sizes, and velocities during the char combustion phase (subsequent to devolatilization). Char particle sizes differ from the nominal coal particle size due to both swelling during devolatilization and surface carbon consumption. A model of mass and energy transport processes was used to extract burning rates and kinetic parameters from the single-particle optical measurements. The model treats unsteady radiative and convective heat transfer between the particle and its surroundings as well as oxygen transport to the particle surface, accounting for the effect of Stefan flow. The principle and operation of the optical particle sizing/pyrometer and the transport model are discussed in detail elsewhere.[1-3] Char oxidation kinetics are represented here by a rate law of the form:

$$q = k_s P_s^n = A\, e^{(-E/RT_p)}\, P_s^n \qquad (1)$$

where q is the burning rate per unit external particle surface area, and k_s is a global coefficient embodying the combined effects of internal surface area, pore diffusion, and intrinsic surface reactivity. The combustion behavior of a given coal char is described by the set of three global kinetic parameters, n (reaction order), E (activation energy), and A (preexponential factor).

Single-particle rate coefficients

At each measurement location in the flow reactor (i.e. at successive particle residence times), the optical technique recorded a distribution of particle sizes and temperatures. Standard deviations typically observed were 20 μm in particle diameter and 40 to 120 K.

* Work supported by the U.S. Department of Energy's Pittsburgh Energy Technology Center's Direct Utilization AR&TD Program.

** Present address: Department of Mechanical Engineering, Stanford University, Stanford, CA 94305-3032

† The Pocahontas #3 coal was obtained from the Pennsylvania State Coal Bank (designation PSOC-1508), through the Pittsburgh Energy Technology Center, and is one in a suite of ten coals under study within the Sandia Coal Combustion Science Program.

in particle temperature. In Figure 1, single-particle rate coefficients derived from the optical data on Pocahontas #3 coal, are plotted as a function of temperature, in Arrhenius form†. A characteristic feature of this and other Arrhenius plots of single-particle rate constants is the presence of distinct linear groupings of points associated with a given gas composition and a given measurement location in the reactor. These linear groupings generally exhibit slopes that are steeper than the kinetic rate expression fit to the entire data set. As a result of this feature, data taken in only a single gas environment (e.g. 12-mole% O_2) produce activation energies generally higher than those determined from a simultaneous regression of data in several gas conditions.[4]

In Figure 2, single-particle rate constants are plotted for the same data set, but for the optimum (least squares) reaction order, $n = 0.0$. By varying the reaction order, the data from Fig. 1 have been partially collapsed to a single curve. Experience with similar data for a number of coals indicates that it is often possible to find a reaction order that at least partially collapses the data from different measurement locations. For some data sets, however, no value of n collapses the data onto one curve, resulting in a kinetic expression (a set of values for n, E, and A) that does not adequately describe the entire data set. In either case, the basic trend toward collections of distinct lines with higher slopes is apparently an intrinsic property of Arrhenius plots of single particle combustion rate constants. The origin of this feature will be explained in the next section.

DISCUSSION

Characteristic curves on Arrhenius diagrams

Let us consider a simplified analysis that ignores the effect of Stefan flow (a minor correction) and assumes the particles to be in thermal equilibrium with their environment. Under these conditions, given a reaction order n, the equations governing mass and energy transport can be algebraically manipulated to arrive at the following explicit expression for the single-particle rate constant, k_s.

$$k_s = \frac{\left[\frac{Nu\lambda}{H_{rxn}\, d_p}(T_p - T_g) + \frac{\varepsilon_p \sigma}{H_{rxn}}(T_p^4 - T_w^4)\right]}{\left[P_g - \frac{d_p R(T_p + T_g)}{48 D_{ox}}\left(\frac{Nu\lambda}{H_{rxn}\, d_p}(T_p - T_g) + \frac{\varepsilon_p \sigma}{H_{rxn}}(T_p^4 - T_w^4)\right)\right]^n} \qquad (2)$$

From Eq. 2 k_S is a function of the following variables: T_p, d_p, T_g, P_g, T_w, n, D_{ox}, λ, ε_p, H_{rxn}. For a given operating condition at a given measurement height, T_p and P_g are fixed, as are T_w and the properties of the gas D_{ox} and λ, and the heat of reaction, H_{rxn}. For coal particles with an emissivity ε_p, k_s is a function only of T_p, d_p, and n. If one fixes the reaction order, n, and considers only particles of a given size, d_p, Eq. 2 reduces to a relationship between T_p (which is measured in the laboratory) and k_s, (the derived quantity of interest, the single-particle rate coefficient). In a plot of k_s as a function of $1/T_p$, Eq. 2 defines a characteristic curve representing the mass and energy balances for the reacting char particle.

An example of such a characteristic curve is the leftmost trace in Fig. 3, calculated for the specific case: $d_p = 150$ μm, $\varepsilon_p = 0.8$, $T_g = 1645$ K, and $P_g = 0.12$ atm (corresponding to the 12.7 cm measurement height in the laminar flow reactor in the 12 mole-% O_2 gas environment). It is important to note that the characteristic curves are functions of the reaction order, n, but not of the other kinetic parameters, A and E. Also in Fig. 3 are data points corresponding to the 140-160 μm size fraction (a subset of the data in Fig. 1),

† Single-particle rate coefficients can be calculated from the optical data directly if the reaction order, n, is specified. A value for the reaction order of 1/2 was chosen arbitrarily for this example. Also, the results presented in Figures 1 - 4 were generated by a simplified analysis technique which assumes that CO is the only combustion product and that the particles are in thermal equilibrium with their environment.

superimposed on the theoretically derived characteristic curves for d_p = 150 μm. This particular linear grouping from Fig. 1 is seen to lie, as it must, along a characteristic curve representing the mass and energy balance equations for reacting char particles. The characteristic curves have the following features: at low particle reactivity (low k_s) the burning rate is insufficient to generate enough heat to affect the particle temperature - the temperature in this "nonburning" regime is nearly independent of k_s (see the nearly vertical curve segments at the bottom of Fig. 3), and accurate values of k_s cannot be extracted from the measured particle temperatures. For moderate particle reactivity (moderate k_s), the surface reaction generates sufficient heat to raise the particle temperature well above the nonburning temperature. In this region particle temperature is sensitive to k_s and the burning rates and kinetic parameters can be derived from the measured particle temperatures (see the sloped portion of the curves in the center of Fig. 3). At high particle reactivity (high k_s), particles burn so rapidly that oxygen is thoroughly depleted at the particle surface and an asymptotic temperature is reached associated with diffusion-limited or zone III burning. In this region the temperature again becomes insensitive to k_s, and extraction of accurate values of k_s from measured particle temperatures is no longer possible (see the vertical curve segments at the top of Fig. 3).

The characteristic curves exhibit many of the same features as plots of k_s vs. χ used by Smith[5], where χ is the ratio of the observed burning rate to the maximum, diffusion-limited rate. Data points that lie in the nearly vertical upper or lower segments of the characteristic curves correspond to high and low values of χ respectively, For the determination of the kinetic parameters, only values within a chosen χ range (typically $0.2 < \chi > 0.85$) are used, corresponding to points that lie on the central, nearly linear segment of the curves.

Families of characteristic curves for a particle size distribution

It was shown in the previous section that rate constants, k_s, for individual burning particles of a given size, d_p, lie on characteristic curves on the Arrhenius diagram representing mass and energy balance equations for the reacting particles. In practice, even though size-graded coal is fed to the reactor, the devolatilization process broadens the particle size distribution to such an extent that the size dependence of char reactivity must be considered.

In Fig. 4 characteristic curves are presented for various particle sizes at two selected experimental conditions. Also appearing on Fig. 4 are single-particle rate constants for all particle sizes from Fig. 1, superimposed on the characteristic curves. The figure illustrates how a distribution of particle sizes at a given measurement height gives rise to a family of characteristic curves on the Arrhenius diagram. The range of particle sizes considered (100 - 200 μm) produces, for each condition, a band that contains essentially all of the measured points. There is a significant size dependence in the upper and lower extremes of the curves due to the size dependence in the convective mass and heat transfer coefficients in Eq. 2. In the central region, however, from which kinetic data are extracted, particle temperatures are only weakly size dependent and the family of curves converges to a narrow band. The measured rate constants (points) are therefore seen to lie in nearly linear groupings within the narrow bands formed by the nearly linear segments of the characteristic curve families.

It can therefore be concluded that the distinct linear groupings clearly seen in Arrhenius plots of single-particle rate constants are the outlines of the nearly linear sections of characteristic curves, with the particle size distribution causing a limited scatter about a central curve corresponding to the median particle size. These linear groupings of points, like the theoretical characteristic curves they follow, are a function of the reaction order, n, *but not the actual global kinetic activation energy E or preexponential factor, A.* The global kinetic activation energy and preexponential factor determine, rather, *where* along these curves the measured points will lie.

Implications for kinetic studies

With this background on characteristic curves, let us consider how kinetic parameters can be extracted from measurements of single-particle sizes and temperatures. A large number of single particle temperatures are measured and the model (represented here by a series of characteristic curves) is used to determine a value of k_s for each particle. As a consequence of the analysis procedure, each point on the Arrhenius diagram corresponding to a single-particle measurement from the laboratory must lie on one of the characteristic curves. This is true irrespective of the accuracy in the data - random measurement errors cause the data not to scatter *about* the characteristic curves, but to distribute *along* characteristic curves.

If kinetics are to be measured for a system in which each particle obeys a single rate law, for example the Arrhenius law, the individual data points will be the intersections of the line representing the Arrhenius rate law (Eq. 1) and the appropriate characteristic curve representing the particle mass and energy balance equations (Eq. 2). Because these curves intersect at only one point, there is only one particle temperature and one value of k_s that satisfy both the rate law and the mass and energy balances. The rate expression obtained by regression of the data will be a locus of experimental points lying on different characteristic curves.

In practice, particle-to-particle variations in properties and reactivity result in a distribution of particle temperatures at each location, producing a distribution of points along a characteristic curve, appearing as a distinctly recognizable line of slope $\beta = d(\ln k_s)/d(1/T_p)$. From the definition of the activation energy:

$$E \equiv -R \frac{d\ln k_s}{d(1/T_p)} \tag{3}$$

it is clear the the data at one experimental condition exhibit a pseudo activation energy of $-R\beta$. The slope, β, is a property of the associated characteristic curve and can be obtained by direct differentiation of Eq. 2. Examination of Eq. 2 reveals that this pseudo activation energy, $-R\beta$, associated with a given reactor height, is a function of T_p, d_p, T_g, P_g, n, T_w, D_{ox}, λ, ε_p, and H_{rxn}.

The pseudo activation energy for data from a single measurement location is therefore a function of the reaction order, properties of the gas phase, and physical properties of the char particle, *but is independent of the actual global kinetic activation energy, E*. From this we can conclude that the temperature distribution observed in a given experiment at a single measurement location contains little or no information on the activation energy.† It is primarily in the comparison of data points taken at different measurement locations that the true information on the pressure dependence (n) and the temperature dependence (E) of the char combustion rate lies.

When a single Arrhenius rate law is fit to all experimental points simultaneously, optimal (least-squares) coefficients are influenced by particle-to-particle variations in properties and reactivity, manifested in the presence of the characteristic curve segments of generally higher slope. The regression routine attempts, in effect, to fit both the true kinetics and the characteristic curve segments simultaneously. The least-squares parameters obtained will be influenced both by the kinetic parameters (A,E,n), and by the properties of the characteristic curves. In practice, the presence of the linear groupings of single-particle rate coefficients affects the data regression in the following manner: Both the characteristic curves and their derivatives are functions of n, the reaction order. A comparison of Figs. 1 and 2 illustrate that the slope, and thus the pseudo activation energy at one height, tends to decrease with increasing n. Extraction of a rate law by regression of the entire set of single-

† Limited kinetic information is contained in the observed dependence of temperature on particle size at one measurement location.

particle data often results in artificially low reaction orders, because low orders produce characteristic curves of lower slope that are more closely comparable to typically observed activation energies for oxidation of impure carbons (typically 15 - 25 kcal/mole in zone 2). A parameter set (A,E,n) with low n partially collapses the data onto nearly parallel, closely spaced characteristic curves, resulting in a lower RMS error (see Fig. 2).

The extent to which particle-to-particle variation in properties and reactivity influences the kinetic parameters can be seen by repeating the analyses for Figs. 1 and 2 with data sets formed by various temperature averaging strategies. Table 1 presents the results of applying an identical analysis technique to three different data sets derived from the original measurements of single particle temperatures, sizes, and velocities for Pocahontas #3 coal:

1. individual particle sizes and temperatures
2. average sizes and temperatures in 10 μm size bins
3. overall median particle sizes and temperatures at each experimental condition and measurement location.†

An optimal value of the reaction order was determined by minimizing the sum of the squared residuals in k_s. Table 1 shows a sharply increasing value of n with an increasing degree of temperature averaging. Averaging decreases the amount of scatter along characteristic curves and thus reduces the biasing effect on the kinetic parameters. The use of average temperatures in 10 μm size bins reduces the length of the characteristic curve segments and thus reduces the biasing effect, but does not eliminate it. Use of the overall median values, corresponding to a reaction order of 0.75, is believed to yield unbiased results for this data set.

Recommended Technique for Determination of Kinetic Parameters

The distribution of particle temperatures at one measurement location reflects the effects of particle size and of particle-to-particle variations in both physical properties and reactivity. For the Pocahontas coal char the effect of variations in particle size is quite small. To understand the origin and evolution of the observed temperature distributions, a more detailed statistical treatment is needed that explicitly considers particle-to-particle variations in both physical properties and reactivity. Gavalas and Flagan[6] have used a statistical model of char combustion to describe variability in temperature traces of individual burning coal particles.

For the more limited practical goal of predicting overall burning rates for the particle population over narrow to moderate ranges of carbon conversion, kinetic parameters describing the combustion behavior of "typical" particles in the population (those of median reactivity) is often sufficient. It has been shown here, that even this limited goal cannot be attained by direct application of nonstatistical analyses to single-particle measurements. The presence of the particle temperature distributions has been shown to introduce a systematic bias in the determination of kinetic parameters, resulting for this example, in artificially low reaction orders. In the following paragraphs, a simple analysis technique is recommended that avoids this bias and yields kinetic parameters describing the combustion of "typical" particles within a heterogeneous particle population.

In general, the joint size/temperature distribution measured by the single-particle optical technique contains valuable information on the kinetic parameters A,E, and n. There is, however, often a wide variation in temperature within a particle size fraction, which has been shown to systematically bias kinetic analyses. Classifying the single-particle data into narrow size bins preserves much of the information in the T_p-d_p relationship, but produces average temperatures for each size bin that are based on few data points. The averages therefore contain a significant fraction of the scatter present in the original temper-

† These three optimum reaction orders were determined by a kinetic analysis that assumed CO to be the only combustion product, but accounted for the influence of particle thermal inertia on the heat balance (a term arises for thermal inertia when the particles traverse regions of changing gas temperature or properties).

ature distribution, according to Eq. 4:

$$\sigma_{T_{ave}} = \sigma_T/\sqrt{N} \qquad (4)$$

where σ_T is the standard deviation in the measured temperature distribution and $\sigma_{T_{ave}}$ is the standard deviation of the averages computed from N experimental points. Wide size bins, on the other hand, produce accurate estimates of the average temperatures (reducing the bias associated with the distinct lines) but sacrifice much of the information contained in the T_p-d_p dependence. For a given experiment, there is an optimum width for the size bins that results in the most accurate determination of the kinetic parameters A,E, and n.

A simple statistical technique for determination of n^{th}-order kinetic parameters was developed and used that achieves the proper balance between temperature averaging and preservation of information contained in the joint size/temperature distribution. The single-particle data was divided into only two size categories: one containing particles between the 0^{th} - 50^{th} size percentiles (with a median at the 25^{th} percentile) and a second containing particles between the 50^{th} - 100^{th} size percentiles (with a median at the 75^{th}). Median sizes and temperatures are obtained for each of the two categories by a sorting routine and are combined with the overall median size and temperature to yield the data set for regression. Rate parameters for the Pocahontas coal determined by the technique outlined above are presented in Fig. 5. The full analysis of Mitchell[3], including the effects of thermal inertia, Stefan flow, and partial CO_2 production at the particle surface was applied. The reaction order was determined to be 0.75 by least squares regression and the CO/CO_2 ratio was adjusted to fit the measured mass-loss profiles using the correlating expression $CO/CO_2 = A_c e^{(-E_c/RT)}$. Inclusion of some CO_2 production improves the fit to the conversion profile and average values of ψ, the fractional molar conversion to CO_2, are reported in Fig. 5 for the two gas environments (6, 12 mole-% oxygen).

CONCLUSIONS

Particle-to-particle variations in properties and reactivity often give rise to a broad distribution of char particle temperatures at a given location in a combustion environment. This distribution of particle temperatures is shown to produce distinct characteristic curves or bands of points on Arrhenius plots of single-particle rate constants. These linear features exhibit pseudo activation energies that are independent of the actual global kinetic activation energy. A complete description of single-particle combustion behavior will require a detailed statistical treatment that explicitly accounts for the origin and implications of the observed temperature distributions. Accounting for particle-to-particle variations in reactivity and properties may be key to understanding reactivity at high carbon conversions. For the more limited goal of predicting overall burning rates for the entire particle population over narrow to moderate ranges of carbon conversion, kinetic parameters describing the combustion behavior of "typical" particles (those of median reactivity) is often sufficient. It has been shown here, that even this limited goal cannot be attained from single particle measurements without careful statistical considerations. The observed particle-to-particle variations in properties and reactivity are shown to dramatically bias the global kinetic parameters determined by nonstatistical analysis. A simple analytical procedure is demonstrated that extracts the true kinetic information for particles of median reactivity within a heterogeneous particle population.

LITERATURE

1. Tichenor D. A., Mitchell R. E., Hencken K. R., and Niksa S. 20^{th} *Symp. (Int.) Comb. 1213 (1984)*
2. Mitchell, R. E. and Madsen, O. H. *21^{st} Symp. (Int.) Comb.* 173 (1986)
3. Mitchell, R. M. *22^{nd} Symp. (Int.) on Comb.*, 69 (1988)
4. Mitchell, R. M., and D. R. Hardesty, in *Coal Combustion Science--Quarterly Progress Report*, Hardesty, D. R. (ed.), Sandia Report SAND89-8250 (1989).
5. Smith, I. W., *19^{th} Symp. (Int.) on Comb.* 1045 (1982)
6. Gavalas, G. R. and Flagan, R. C. "Kinetics of Coal Combustion Part III: Mechanisms and Kinetics of Char Combustion," Final Report to the Dept. of Energy, Rpt.# TRW S/N 44617

NOMENCLATURE

A	preexponential factor	R	gas constant
A_c	preexponential factor in the correlation for CO/CO_2 ratio	T_g	gas temperature
		T_p	particle temperature
d_p	particle diameter	T_w	wall temperature
D_{ox}	oxygen diffusivity	v_g	gas velocity
E	global kinetic activation energy for char oxidation	v_p	particle velocity
		Greek Symbols	
E_c	activation energy in the correlation for CO/CO_2 ratio	β	slope of characteristic curve
		ϵ_p	particle emissivity
H_{eff}	heat of combustion reaction	λ	thermal conductivity of the gas phase
k_s	rate constant	Nu	Nusselt number
n	reaction order	σ	Stefan-Boltzmann constant
P_g	partial pressure of oxygen in the bulk gas	σ_T	standard deviation of measured temperature
P_s	partial pressure of oxygen	σ_{Tave}	standard deviation of average temperature
q	burning rate per unit area of external surface	χ	ratio of observed to maximum burning

Table 1. Optimum Reaction Order for Oxidation of PSOC-1508 Char Determined From Three Different Data Sets

Data Set used in Regression	*Reaction order*
All single-particle sizes and temperatures	0.00
Average sizes and temperatures in 10 μm size bins	0.16
Overall median sizes and temperatures	0.75

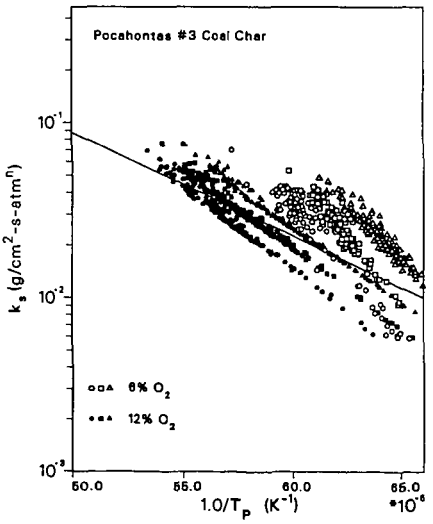

Figure 1. Rate constants for individual burning char particles from Pocahontas #3 (PSOC-1508) coal: Reaction order, n, = 1/2. Initial coal particle diameters 106 - 125 μm. Reaction product assumed to be CO. Symbols correspond to various measurement heights (particle residence times): circles: 12.7 cm; squares: 19.1 cm; triangles 25.4 cm.

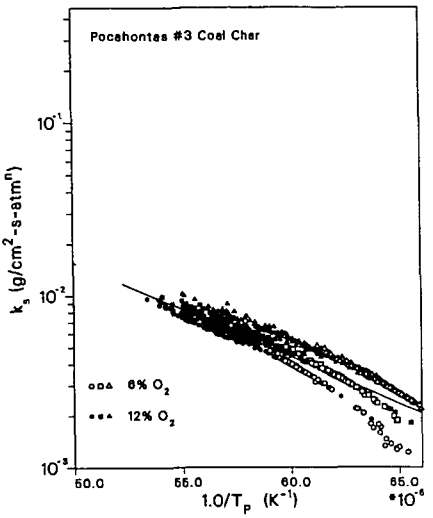

Figure 2. Rate constants for individual burning char particles from Pocahontas #3 (PSOC-1508) coal: optimum reaction order, n = 0.0. Initial coal particle diameters 106 - 125 μm. Reaction product assumed to be CO. Symbols correspond to various measurement heights (particle residence times): circles: 12.7 cm; squares: 19.1 cm; triangles 25.4 cm.

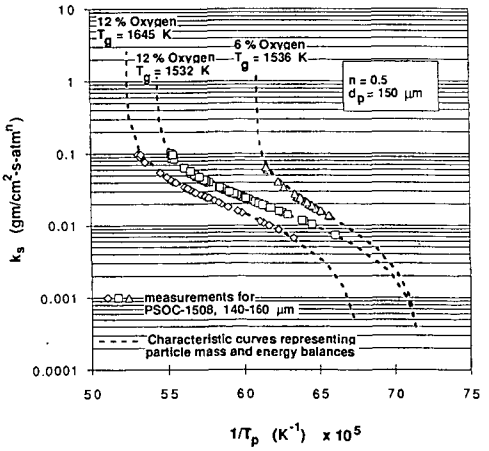

Figure 3. Characteristic curves and experimentally determined single-particle rate constants for PSOC-1508 Pocahontas #3 coal. Curves for 150 μm particles; points for particles with diameters 140 - 160 μm. Reaction order, n, ≈ 1/2.

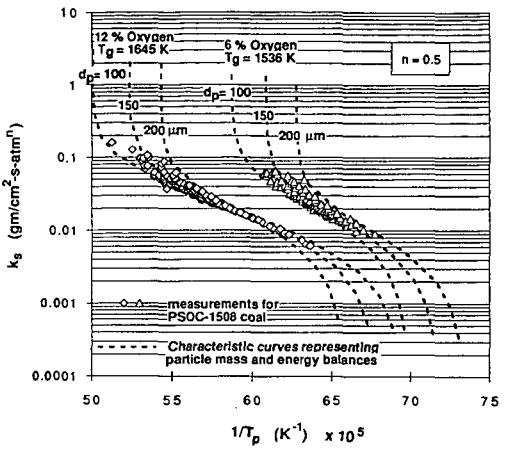

Figure 4. Families of characteristic curves for a particle size distribution and experimentally determined single-particle rate constants for PSOC-1508. Reaction order, n, = 1/2.

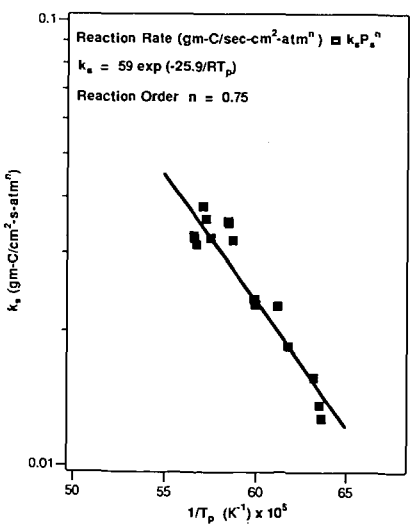

Figure 5. Global kinetic parameters for PSOC-1508 Pocahontas #3 low-volatile bituminous coal. Points represent rate coefficients calculated by the recommended simple statistical technique.

INFLUENCE OF MACERAL COMPOSITION OF RAW COAL ON POTASSIUM ACTIVITY IN STEAM GASIFICATION OF CHARS

V. Calemma, G. Del Piero and G. Passoni
Eniricerche,20097, S. Donato Milanese,
Milan, Italy

Keywords: potassium; coal gasification; steam

INTRODUCTION

The catalytic effect of potassium salts on steam gasification rate of coal chars, is one of the subjects in the field of coal gasification most widely investigated because of their potential application in commercial processes. The results of research activity,have pointed out that the catalytic activity of potassium depends upon several factors such as associated ion, mineral matter, rank of parent coal, pretratment conditions and K/C ratio[1]. As regards the latter, literature data show that gasification rates increase with potassium content until a particular value is reached after which higher values are ineffective or lead to a decrease in reactivity [2]. Moreover, it has been reported that the value of catalyst concentration at which the gasification rate saturates depends on the identity of the substrate and the procedure used to prepare the doped char[3]. The objective of the work reported here was to investigate the influence of maceral composition of the parent coal on the catalytic behavior of potassium carbonate in steam gasification of chars.

EXPERIMENTAL

Four coals were used in this study: three bituminous coals (Illinois N°6, Middelburg (S.A), Polish) and a subbituminuos Sulcis coal. Table 1 shows their maceral composition and the respective rank determined by petrographic analysis. In all cases K_2CO_3 was added to the coals by mechanical mixing before pyrolysis. A known amount of powered catalyst was added to the coal (150 - 300 μm), homogenized and then charrified at 1073 °K for 2 h under nitrogen

flow. After pyrolysis the doped chars were ground, sieved and the fraction 150-300 μm was used for this study. Potassium loading on chars was determined by AES-ICP technique on the solution obtained after an oxidizing treatment with HNO_3-H_2O_2 solution of doped samples.The kinetic experiments were carried out under a steam pressure of 3,6 MPa using a small bench-scale apparatus with a semicontinuous fixed-bed reactor consisting of 0.0127 m i.d., 0.7m long stainless steel pipe, water precision pump and steam preheater. After loading the reactor with the doped char the temperature was raised (flowing N_2) to the desired value and then the sample was reacted stopping the nitrogen flow and pumping water. The reaction temperature was 1018 °K for chars obtained from Polish coal and 973 °K for those from Illinois N°6, Sulcis, and Middleburg coals. After water removal, the product gas was sampled and analyzed by a gaschromatograph. Reactivity during gasification was determined by measuring the reaction rate (mol* h^{-1}) normalized with respect to the initial moles of carbon in the sample.

RESULTS AND DISCUSSION

The catalytic activity of K_2CO_3 towards steam gasification of the coal chars with different catalyst concentration was evaluated determining the reaction rate at 50% conversion. The relationships between reactivity and K/C ratio , shown in figure 1, point out a different trend for the chars examined. Leaving out the first part of the curves whose lower slopes are mainly due to the reaction of potassium with mineral matter[4], chars from Sulcis and Illinois N°6 coals display a linear correlation in the whole range of catalyst concentration.Differently, in the case of chars from Middleburg and Polish coals the concentration of active sites increases linearly with catalyst concentration up to a limit value after which further addition of catalyst is less effective. Studies carried out by several investigators using different substrates have yielded some conflicting results. For example Wigmans et al.[5] reported a linear increase of reactivity with catalyst loading up to 40%w. In contrast other authors [6,7] have found that gasification rates saturate at much lower K/C ratios. Generally the variation of saturation limit has been explained in terms of different preparation methods used to load the catalyst, potassium

volatilization or micropore blockage by catalyst [2,3,6,7]. In our case the preparation method was always the same and no loss of potassium was detected during gasification experiments. All this strongly suggests that besides the above mentioned factors, the value of K/C ratio at which the catalyst begins to be less effective should be also dependent on the particular features of the substrate and the interactions between catalyst and coal during the pyrolysis step. The results of petrographic analyses of the coals used in this study, listed in table 1, point out that the vitrinite content in Illinois N°6 and Sulcis coals is remarkably higher than in Polish and Middelburg coals. In this connection it is interesting to note that the decrease of catalytic activity of potassium after a given value of K/C ratio occurs only with the chars obtained from the two coals having the lowest vitrinite content. During the pyrolysis process (with or without catalyst) vitrinite undergoes to substantial changes of its chemical composition, porous structure and morphology which leads to the development of macroporosity whereas the inertinite remains almost unchanged. This situations is illustrated in figures 2, 3, 4 and 5 which show vitrinite and inertinite fragments before and after pyrolysis.It is known that upon heating the catalyst becomes extremely mobile and spreads over the accessible carbon surface through the porous system [8]. On this ground, it follows that the porosity originated during the pyrolysis step promote the contact between catalyst and the "support" and the distribution of potassium in the char matrix. An example is given in figure 6 where the oblique section of a vitrinite fragment shows how the pores can be easily penetrated by the catalyst during pyrolysis. On the contrary inertinite fragments do not develop macroporosity upon heating (fig. 7) and therefore it is reasonable to expect that higher contents of this maceral could lead to a lower ability of the coal to allow a constant dispersion of increasing quantity of catalyst. The examination of doped char samples by electron microscopy and microanalysis (SEM+EDS) confirms the hypothesis reported above.Indeed figures 8 and 9 show that the distribution of potassium on the surface of chars obtained from Polish coal is uneven and regions with higher potassium concentration are mainly those formed by pyrolysis of vitrinite. All this is particularly clear in figure 8 which shows a pyrolyzed inertinite fragment free

of potassium close to a "vitrinite" fragment with a high concentration of catalyst.

Conclusions

It has been demonstrated that regions of enhanced reaction rate are those associated with the interface between the "support" and added catalyst [9], therefore from a general point of view the existence of a linear relationship between reaction rate and K/C ratio implies a constant dispersion degree of the catalyst. In our case the porous system of the char through which the catalyst is dispersed is mainly the result of changes undergone by the vitrinite and its interaction with K_2CO_3 during the pyrolysis step. Hence the ability of a given char to allow a constant dispersion degree of increasing quantity of catalyst, besides the feature of the porous system and its evolution during gasification, will be also affected by the vitrinite content of the parent coal.

References

1. B.J. Wood and K.M. Sancier, Catal. Rev.-Sci. Eng. 26, 233 (1984)
2. D.A. Sams and F. Shadman, Fuel 62, 880, (1983)
3. C.A. Mims and J.K. Pabst, Am. Chem. Soc., Fuel Chem. Div. Prep. 25(3), 258 (1980)
4. G. Bruno, M. Buroni, L. Carvani, G. Del Piero and G. Passoni Fuel 67, 67 (1988)
5. T. Wigmans, R. Elfring and J.A. Moulijn, Carbon 21, 1 (1983)
6. D.A. Sams, T. Talverdian and F. Shadman, Fuel 64, 1208 (1985)
7. B.C. Gorrini, L.R. Radovic and A.L. Gordon, Fuel 69, 789 (1990)
8. P.R. Abel, B.J. Waters, P.C. Koenig, R.G. Squires and N.M. Laurendeau Fuel 64, 613 (1985)
9. D.J. Coates, J.W. Evans, A.L. Cabrera, G.A. Somorjai and H. Heinemann J. Catal. 80, 215 (1983)

Table 1. Maceral analyses of coals(*)

Coal	Vitrin.	Inert.	Liptin.	Reflect.%	Rank
Sulcis	93	1	6	0.49	Subbitum.
Illinois N°6	94	3	3	0.58	HVB-C
Polish	53	38	9	0.92	HVB-A
Middelburg	48	46	6	0.64	HVB-C

(*) Data are given on mineral matter free basis (% volume).
Reflectance percentages refer to vitrinite macerals
HVB: High volatile bituminous

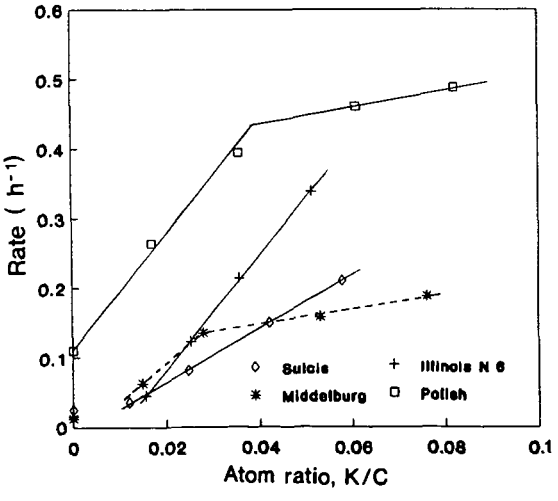

FIGURE 1. CATALYTIC EFFECT OF K_2CO_3 ON GASIFICATION RATES

FIGURE 2 FRAGMENT OF VITRINITE IN RAW COAL

FIGURE 3 FRAGMENT OF PYROLYZED VITRINITE

FIGURE 4 FRAGMENT OF FUSINITE (INERTINITE) IN RAW COAL

FIGURE 5 FRAGMENT OF PYROLYZED FUSINITE (INERTINITE)

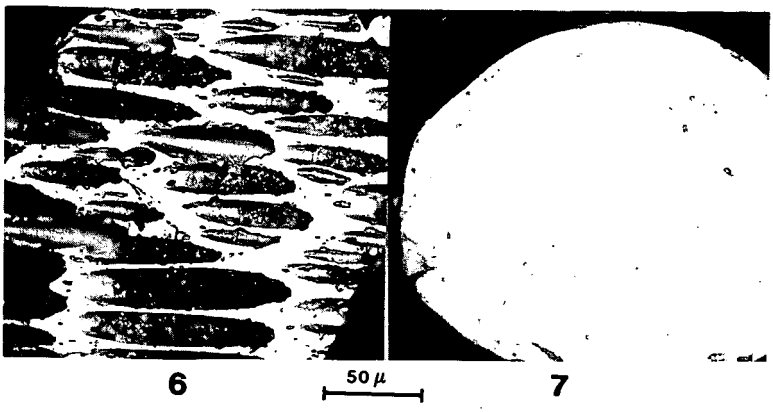

FIGURE 6 FRAGMENT OF PYROLYZED VITRINITE

FIGURE 7 FRAGMENT OF PYROLYZED MACRINITE

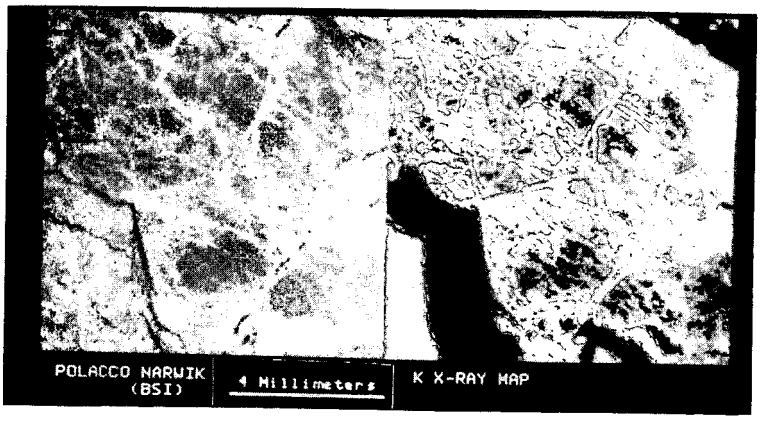

FIGURE 8. POTASSIUM DISTRIBUTION MAP OF DOPED POLISH CHAR

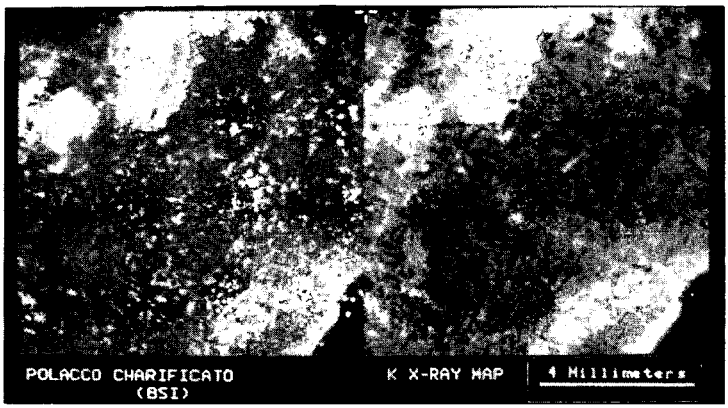

FIGURE 9. POTASSIUM DISTRIBUTION MAP OF DOPED POLISH CHAR

EFFECT OF THERMAL AND CHEMICAL PRETREATMENTS ON THE COPPER-CATALYZED GASIFICATION OF CARBON IN AIR

C.A. Leon y Leon and L.R. Radovic

Fuel Science Program, Department of Materials Science and Engineering
The Pennsylvania State University, University Park, PA 16802

Keywords: Copper Catalysts, Carbon Supports, Gasification Reactivity

INTRODUCTION

Copper is one of the most active catalysts for the gasification of carbon in oxygen [1]. Its high activity is thought to be related to the ease with which copper can undergo oxidation/reduction cycles at gasification conditions [2-6], thereby promoting the transfer of oxygen atoms to the (re)active carbon sites [2,7]. Evidently, oxygen transfer rates will be faster for smaller catalyst particles, which provide a higher degree of catalyst-carbon interface contact. (This explains the observed structure-sensitivity of the Cu- (and other metal-) catalyzed carbon gasification in air [8,9].) However, smaller particles are also more susceptible to catalyst-support interactions [10]. In this report we examine the role of carbon surface chemistry in (a) securing a high and thermally resistant Cu dispersion; and (b) affecting the kinetics of the Cu-catalyzed gasification process.

EXPERIMENTAL

For brevity this report will concentrate on the gasification of a highly pure, polymer-derived microporous carbon (Saran, Dow). Results on other (less porous or non-porous) carbons will be addressed at length elsewhere [11]. All carbons were subjected to a wide variety of thermal and/or chemical treatments aimed at modifying their surface properties (see Ref. 12). Changes in the surface chemistry and physics of the carbons were followed by techniques such as acid/base and mass titrations [12], electrophoresis [12,13], temperature-programmed desorption [14], N_2 and CO_2 adsorption [15], XPS [9], XRD [7,15] and others [11]. Selected samples were impregnated with copper acetate (Fisher) by incipient wetness or ion exchange (without filtering) to yield 5% Cu catalysts (dry carbon basis). In the latter case, the exchange on selected carbons was monitored by withdrawing small aliquots of supernatant after partial equilibration (ca. 30 min) and measuring the copper concentration remaining in solution with an ion-selective electrode (Orion). Gasification reactivities of all catalysts in 0.1 MPa air were measured on a modified TGA-7 apparatus (Perkin-Elmer) under conditions of chemical reaction control [9,14].

RESULTS AND DISCUSSION

Adding copper to Saran (and other) carbons was found to increase their maximum gasification rate in air by 2-3 orders of magnitude. (The method of Cu addition is important, since physically mixed Cu acetate was found to enhance the rate only by a factor of ca. 30.) It was also noted that both chemical and thermal treatments of the carbons alone affect their uncatalyzed reactivities, but only to well within the same order of magnitude [11]. Hence, the importance of chemical and thermal treatments lies in their effect on the distribution (dispersion) of the active catalyst phase throughout the carbon substrate [7]. In general, chemical treatments can be used to increase the dispersion of copper, and thermal treatments tend to decrease it. The contribution by these seemingly opposing effects to carbon gasification by Cu will be addressed below.

Copper Adsorption on Carbon. Anchoring metal precursors onto carbon by adsorption is thought to be neccessary in order to attain the highest possible metal dispersion [13]. Copper acetate dissociates in dilute aqueous solutions to yield mainly hydrated Cu^{+2} ions; these ions are stable below pH=6, and precipitate as hydroxide at high pH unless they are complexed by, e.g., NH_3, in which case they form a pH-dependent mixture of $[Cu(NH_3)_n(H_2O)_{6-n}]^{+2}$ ammine complexes ($1 \leq n \leq 5$) [16]. On the other hand, carbon surfaces can be pretreated to contain various kinds and amounts of surface functional groups [11-13] which differ in their chemical and thermal properties. For instance, low-temperature

oxidative treatments produce a mixture of strongly and weakly acidic oxygen complexes (discernible by neutralization with bases of increasing strength [11,14,15]) which decompose upon TPD according to their thermal strength to yield primarily CO_2 and CO (see Table 1) at relatively low and high temperatures, respectively. Increasing the pH of a carbon slurry leads to an increase in the number of dissociated, negatively charged functional groups, which can then act as anchors for metal cations [13]. Consequently, it was confirmed that the uptake of copper by carbon increases with increasing pH in the range $2.5 \leq pH \leq 11.5$ [11]. Figure 1 shows the adsorption isotherms of copper on selected pretreated carbons (see Table 1) at pH = 11.5. Relative to the untreated sample (CU), it is seen that the removal of oxygen functionalities by heat pretreatment (sample CH) lowers the copper adsorption capacity, while the introduction of functional groups by mild preoxidation (samples CA and CN) increases it.

The role of functional group dissociation in promoting metal ion sorption on carbon can be conveniently illustrated using electrophoretic mobility (EM) diagrams [13]. Figure 2 shows a typical EM diagram for a microporous, mildly oxidized carbon. It is shown that the pH of zero mobility, IEP (above which the net external surface charge of the carbon is negative), is over one pH unit lower than the point of zero net surface charge, PZC (determined by mass titration). This is taken as an indication that typical oxidative treatments or subsequent air exposure of microporous carbons leads to an inhomogeneous surface charge distribution, with the external (geometric) surface being enriched in negatively charged groups when IEP < PZC [13-15]. Hence, the observed increase in reactivity with increasing pH (Figure 2) can be attributed to an increase in the sorption of the Cu precursor leading to a higher catalyst dispersion. Figure 2 shows a maximum (and only three times higher) reactivity at pH = 8.5. Since the 5% Cu/C catalysts used to generate Figure 2 were made by ion exchange without filtering, the nonadsorbed copper probably forms larger, less active catalyst particles when the dried Cu/C samples are preheated to reaction conditions. However, the large surface area and the microporosity of these materials [12] preclude an extensive agglomeration and growth of copper particles [15], i.e., an extreme loss in reactivity. This is in agreement with XPS experiments, which indicate an external surface enrichment in Cu particles [9], particularly after heat treatment. The apparent maximum reactivity, also observed for samples prepared by incipient wetness using solutions of preadjusted pH [11], can arise from two factors. First, upon drying to remove the excess solvent, the concentration of ions (e.g., OH^-, Cu ammines) remaining occluded increases, thereby forcing further adsorption to take place in order to regain equilibrium. Since competition for sorption sites by NH_4^{+1} can be neglected, especially above pH = 9.25 [16], a maximum copper adsorption in the pH range 9-10 is to be expected [17]; above pH = 10 the contribution by hydroxides becomes measurable [16], and their precipitation facilitates Cu agglomeration upon heating. Second, the adsorption mechanisms of the predominant Cu species at different pH values may differ [18]. Attempts to desorb Cu from portions of dried (in vacuum at 313 K) batches ion exchanged at pH = 8.5, by washing with distilled water, failed. However, traces of copper could be desorbed from the samples prepared at pH = 11.5. In both cases, the strong adsorption suggests that some ligand exchange may have taken place. However, the exchange sites at both pH values differ; at pH = 11.5, more weakly acidic sites are activated for copper adsorption, but since the carbon surface becomes more negatively charged, the density of positive ions held electrostatically around these negative charges increases. (This effect is accompanied by the shrinkage of the diffuse portion of a hypothetical "double layer" surrounding the carbon surface [19].) The net result is the saturation of the carbon surface with positive charges which must repel each other and hence limit the access of the desired adsorbing cations to some negatively charged surface sites. Table 1 includes the estimated adsorption ratios of Cu to CO_2-evolving and to total acidic (NaOH-titratable) surface groups. The role of individual surface functional groups in promoting Cu dispersion and reactivity is addressed in detail in an accompanying paper [20].

Copper Dispersion on Carbon. The growth in average Cu crystallite diameter (measured by XRD) with heat pretreatment temperature is best illustrated in Figure 3. In all cases, heating the freshly prepared Cu/C catalysts in inert flowing gas (N_2) leads to Cu crystallite growth. Whereas the growth of Cu crystallites in samples CU and CH is comparable, that on sample CN is much less pronounced, despite the latter's lower surface area [12]. Since the main difference between samples CU and CH is the higher CO evolution yield of sample CU (Table 1), it follows that CO-evolving groups do not contribute directly to the adsorption or subsequent dispersion of Cu cations. (In contrast, $PtCl_6^{-2}$ [21] and $HMo_2O_7^{-1}$ [10] anion adsorption and subsequent metal dispersion were reported to be enhanced by the presence of CO-evolving groups.) On the other hand, CO_2-evolving groups appear to correlate better with copper adsorption. The amount of CO_2 evolved upon TPD is believed to be related to the

number of carboxyl-type ($-COO^{-1}$) groups present on a carbon surface, with one (plus one CO) or two CO_2 molecules being desorbed from two adjacent [21] or distant [21,22] carboxyl functionalities, respectively. Indeed, for the calcium carbon system (Ca^{+2})/CO_2 ratios of 0.5-1.25 have been taken as an indication that each cation adsorbs onto two negatively charged carboxyl groups [21]. In our case, Cu/CO_2 ratios of 0.32-0.87 (Table 1) could also be interpreted along these lines. However, since $NaHCO_3$ is believed to selectively neutralize the carboxyl groups on a 1:1 ratio [23], the poor agreement between Cu and $NaHCO_3$ uptakes (Table 1) suggests that in addition to carboxyl groups there are other (non CO-desorbable) surface groups which also participate in the copper adsorption process. Evidence in favour of the obvious choice, i.e., lactones [23], is presented in an accompanying report [20].

Gasification Reactivity of Cu/C Catalysts. Broadly speaking, the surface chemistry of carbons is related to their oxygen content [22], which can be adjusted by subjecting the carbons to selected chemical pretreatments [12]. Figure 4 shows the influence of the oxygen content of chemically pretreated Saran carbons on the gasification reactivity of the Cu/C catalysts (extrapolated when necessary to 623 K), after subjecting the catalysts to selected heat pretreatments. Following low temperature (623 K) heat pretreatments, a maximum reactivity is observed at intermediate oxygen contents. This is consistent with the observation that moderate (i.e., neither too mild nor too severe) oxidative pretreatments are most successful in producing homogeneously charged (IEP = PZC) carbon surfaces [12], because even though sample CA adsorbs less copper than, e.g., sample CN (Table 1), its adsorbed copper is more uniformly distributed (i.e., internally as well as externally) throughout each carbon particle. However, the resistance to Cu agglomeration over the surface of sample CA is inadequate and hence sample CA experiences a more severe loss of reactivity compared to all other samples (Figure 5). For all samples the normalized reactivity (at 623 K) is most severely affected by heat treatments in the range 623-923 K (Figure 5). TPD experiments indicate that the primary effect of heat pretreatments of the carbons alone in the temperature range 623-923 K is the desorption of CO_2-evolving (e.g., carboxyl and lactone) surface groups [12,22]. Hence the introduction (by chemical pretreatment) of CO_2-evolving groups prior to copper adsorption enhances not only the Cu dispersion but also the gasification reactivity of the carbon.

Figure 5 also shows that the removal of further (mainly CO-evolving) surface groups via heat pretreatments in the range 923-1223 K has less bearing on the magnitude of the loss of gasification reactivity. Nonetheless, Figure 4 suggests that the remaining (CO-evolving) groups do play a role in enhancing the magnitude of the reactivity. Since these groups are not likely to act as metal precursor adsorption sites, their role in securing a higher reactivity can be explained by recalling that the thermally stable groups remaining after each heat treatment can act as diffusion barriers to the agglomeration of Cu particles [24], in which case the higher reactivities of carbons with higher initial oxygen contents can be ascribed to their higher Cu dispersion after heat treatment.

The kinetics of the gasification process are also affected by both chemical and thermal pretreatments. Figure 6 shows that for all carbons thermal treatments of Cu/C catalysts increase the apparent activation energies (E_{ACT}) of the reaction. (An analogous behaviour is observed when using nonporous carbon black substrates [11].) The increase is more significant for the samples with the highest initial oxygen content. Samples with the lowest initial oxygen content yield E_{ACT} values approaching those of the high-temperature (1223 K) heat treated catalysts, thereby suggesting that the decrease in E_{ACT} values is related to the initial oxygen content of the carbons. Therefore, in addition to enhancing the dispersion of Cu by serving as diffusion barriers to its migration, thermally stable carbon-oxygen complexes can also be more difficult to gasify than reactive intermediates [25]. If so, oxygen-rich samples would readily yield highly dispersed catalyst particles upon thermal loss of the unstable Cu anchors, but their catalytic activity would be less temperature-sensitive than that of similar catalysts on oxygen-lean carbons, whose edges would be more susceptible to the exothermic formation of readily desorbable intermediates. This interpretation is consistent with (a) an apparent compensation effect observed for the catalysts heat treated to low temperatures [9,11], (b) the faster deactivation of (initially) oxygen-rich samples [11], and (c) a higher oxygen partial pressure dependence for the gasification of Cu/C samples with the least initial oxygen content [11].

CONCLUSIONS

Both chemical and thermal treatments play a crucial role in determining the gasification behaviour of Cu/C catalysts. Chemical pretreatments can be applied in order to enhance the concentration of CO_2-desorbable surface groups, which promote copper adsorption, catalyst dispersion, and Cu/C gasification reactivity. Thermal treatments lead to the agglomeration (and consequent reactivity loss) of the catalyst, particularly for carbons with low initial oxygen content. In both cases, the effects can be related to the influence of surface oxygen complexes on the reaction. Thermally unstable (moderately to strongly acidic, e.g., carboxyl and lactone) oxygen functional groups can favour gasification reactivity by acting as desorbable anchors for metal precursors. On the other hand, thermally stable groups appear to serve both as diffusion barriers to metal agglomeration (a desirable effect) and as stable reaction intermediates which are less readily gasified by the catalyst (an undesirable effect).

REFERENCES

1. D.W. McKee, in "Chemistry and Physics of Carbon" (Edited by P.L. Walker, Jr., and P.A. Thrower), Vol. 16, Marcel Dekker, New York (1981), p. 1.
2. D.W. McKee, *Carbon* **8**, 131 (1970).
3. J.W. Patrick and A. Walker, *Carbon* **12**, 507 (1974).
4. C. Moreno-Castilla, A. Lopez-Peinado, J. Rivera-Utrilla, I. Fernandez-Morales and F.J. Lopez-Garzon, *Fuel* **66**, 113 (1987).
5. A.J. Lopez-Peinado, J. Rivera-Utrilla, F.J. Lopez-Garzon, I. Fernandez-Morales and C. Moreno-Castilla, *Fuel* **65**, 1419 (1986).
6. T. Ganga Devi, M.P. Kannan and G.N. Richards, *Fuel* **69**, 1440 (1990).
7. L.R. Radovic, P.L. Walker, Jr. and Jenkins, *J. Catal.* **82**, 382 (1983).
8. C.A. Leon y Leon and L.R. Radovic, Proc. 20th Biennial Conf. on Carbon, Santa Barbara, CA (1991), p. 482.
9. C.A. Leon y Leon and L.R. Radovic, Proc. Int. Carbon Conf., Paris, France (1990), p. 44.
10. C.A. Leon y Leon and L.R. Radovic, Proc. 20th Biennial Conf. on Carbon, Santa Barbara, CA (1991), p. 84.
11. C.A. Leon y Leon and L.R. Radovic, in preparation.
12. C.A. Leon y Leon, J.M. Solar, V. Calemma, K. Osseo-Asare and L.R. Radovic, *Carbon*, Submitted (1991).
13. J.M. Solar, C.A. Leon y Leon, K. Osseo-Asare and L.R. Radovic, *Carbon* **28**, 369 (1990).
14. C.A. Leon y Leon, A.W. Scaroni and L.R. Radovic, *J. Colloid Interface Sci.*, Submitted (1991).
15. C.A. Leon y Leon and L.R. Radovic, Proc. 19th Biennial Conf. on Carbon, University Park, PA (1989), p. 42.
16. P. Duby, "The Thermodynamic Properties of Aqueous Inorganic Copper Systems," International Copper Research Association (1977).
17. N. Kovtyukhova and G. Karpenko, Proc. Int. Carbon Conf., Paris, France (1990), p. 680.
18. J. Wieber, F. Kulik, B.A. Pethica and P. Zuman, *Colloids Surfaces* **33**, 141 (1988).
19. J. O'M. Bockris and A.K.N. Reddy, "Modern Electrochemistry," Vol. 2, Plenum Press, New York (1977), Chapter 7.
20. C.A. Leon y Leon and L.R. Radovic, "Influence of Oxygen Functional Groups on the Performance of Carbon-Supported Catalysts," ACS Preprints, Div. Fuel Chem., New York (1991), in print.
21. A. Linares-Solano, C. Salinas-Martinez de Lecea and D. Cazorla-Amoros, *Energy & Fuels* **4**, 469 (1990).
22. B.R. Puri, in "Chemistry and Physics of Carbon" (Edited by P.L. Walker, Jr.), Vol. 6, Marcel Dekker, New York (1970), p. 191.
23. H.P. Boehm, E. Diehl, W. Heck and R. Sappok, *Angew. Chem. Internat. Edit.* **3**, 669 (1974).
24. P. Ehrburger, O.P. Majahan and P.L. Walker, Jr., *J. Catal.* **43**, 61 (1976).
25. L.R. Radovic, A.A. Lizzio and H. Jiang, in "Fundamental Issues in Control of Carbon Gasification Reactivity" (Edited by J. Lahaye and P. Ehrburger), Kluwer, The Netherlands (1991), p. 235.

Table 1. Features of Some Chemically Modified Saran Carbons Used as Cu Catalyst Supports.

Sample[a]	%O (wt.)	TPD [mmol/g][b] CO_2	CO	SN [mmol/g][b] $NaHCO_3$	NaOH	Cu ads.[c] [mmol/g]	Cu/CO_2 [mol/mol]	Cu/NaOH [mol/mol]
CH	0.8	0.09	0.30	0.01	0.09	0.03	0.36	0.37
CU	1.6	0.12	0.74	0.01	0.11	0.04	0.34	0.36
CP	5.6	0.91	1.69	0.35	2.07	---	---	---
CA	12.0	1.03	5.42	0.81	2.70	0.90	0.87	0.34
CN	20.8	4.11	4.78	0.58	2.03	1.26	0.32	0.62

[a] Pretreatments: CH, heat-treated in N_2 at 1223 K; CU, untreated; CP, oxidized in H_2O_2 at 373 K; CA, oxidized in air at 673 K (25% burnoff); CN, oxidized in HNO_3 at 363 K.

[b] TPD: Temperature Programmed Desorption; SN: Selective Neutralization (with bases).

[c] Amount of copper withdrawn from solution at pH=11.5 (adjusted using NH_4OH).

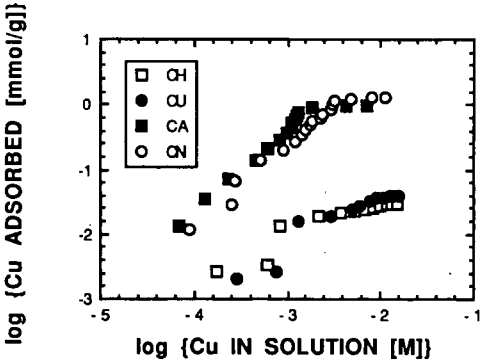

Figure 1. Influence of Chemical Pretreatment on the Adsorption of Copper by Saran Carbons (pH=11.5).

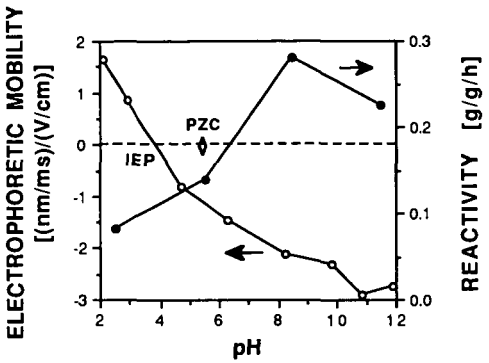

Figure 2. Relevance of Carbon Surface Charge to its Copper-Catalyzed Gasification Reactivity (at 573 K) in 0.1 MPa Air.

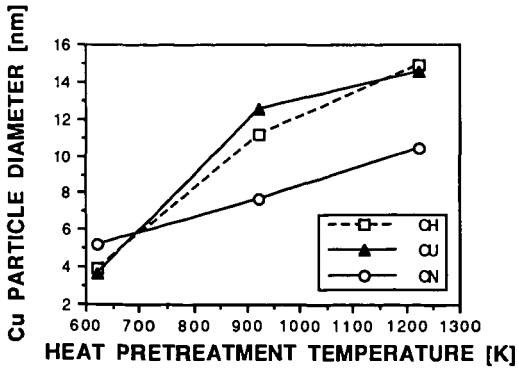

Figure 3. Variation in Average Cu Crystallite Diameter with Heat Pretreatment Temperature of Cu/Saran Catalysts.

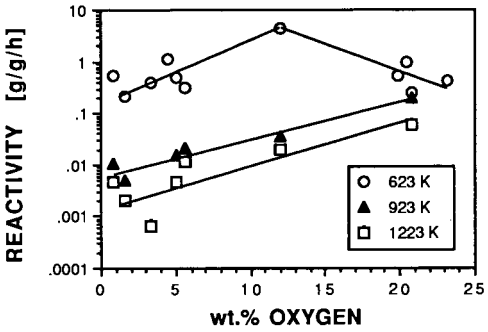

Figure 4. Effect of Carbon Surface Chemistry (% Initial Oxygen Content) on the Gasification Reactivity (at 623 K) of Cu/Saran Catalysts in 0.1 MPa Air, Following Heat Pretreatment at Different Temperatures (Indicated in the Figure).

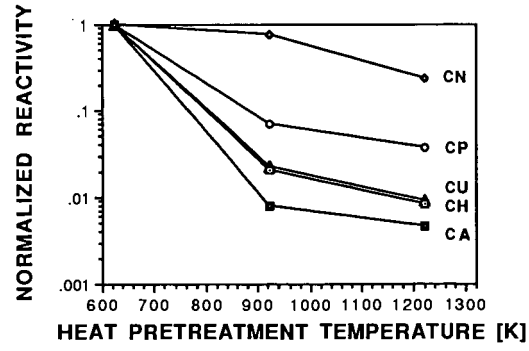

Figure 5. Normalized Loss in Gasification Reactivity (With Respect to Most Active Samples at 623 K) in 0.1 MPa Air for Cu/C Catalysts Differing in Chemical Pretreatment (see Table 1).

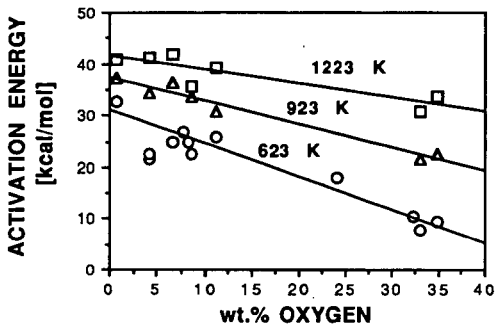

Figure 6. Effect of Carbon Surface Chemistry (% Initial Oxygen Content) on the Apparent Acivation Energy of the Gasification Reaction of Cu/Saran Catalysts in 0.1 MPa Air, Following Heat Pretreatment at Different Temperatures (Indicated in the Figure).

FURTHER EVIDENCE ON THE MECHANISM OF THE CO_2 CARBON GASIFICATION CATALYZED BY CALCIUM: TPD AFTER $^{13}CO_2$ CHEMISORPTION

Cazorla-Amorós, D., Linares-Solano, A., Salinas-Martínez de Lecea, C.
Departamento de Química Inorgánica e Ingeniería Química
Universidad de Alicante. Alicante, Spain.

Meijer, R. and Kapteijn, F.
Department of Chemical Engineering
University of Amsterdam. The Netherlands.

Keywords: Calcium catalyst, reaction mechanism

INTRODUCTION

Previous studies [1-7] have analyzed the use of the CO_2 chemisorption on the field of the carbon-gas reactions catalyzed by calcium. The results clearly show that this technique allows to understand its catalytic activity and to gain insight into the mechanism of the reaction. Important aspects of these studies are: 1) The chemisorption of CO_2 at 573 K (5-30 min) on carbons containing calcium is restricted to the surface of the CaO particles and therefore, can be used to determine the area (and dispersion) of the catalyst particles [1, 2, 3]. 2) Temperature programmed desorptions (TPD) of calcium-carbon samples after CO_2 chemisorption give information about the calcium-carbon contact, which is responsible for the catalytic activity [4, 5]. 3) Quantification of such contact provides the number of catalytic active sites (CAS) of the catalyst, which is used to normalize the CO_2 and steam reactivities of samples with different calcium loading or with different calcium sintering degrees, and to obtain kinetic parameters of interest with respect to the mechanism of the carbon-gas reaction catalyzed by calcium [6, 7].

Information about the mechanism of the reaction have been deduced from TPD of calcium-carbon samples previously contacted with CO_2 using the following reasonings: **i)** During the increase in temperature in a TPD run, a redistribution of the CO_2 is produced among the CaO particles. **ii)** The CO_2 diffuses from the external surface to the calcium-carbon contact yielding to the formation of $CaCO_3$-C species. **iii)** The decomposition of these species, which is produced at a higher temperature, takes place through the catalyst-carbon contact, by means of a two steps gasification mechanism [5,7]:

$$CaCO_3\text{-}C \rightarrow CaO\text{-}C(O) + CO \quad (1)$$
$$CaO\text{-}C(O) \longrightarrow CaO\text{-}C + CO \quad (2)$$

Accordingly to this mechanism, two types of CO should be evident; one coming from $CaCO_3$ and the other from the oxidized carbon atom. In other words, the reactive CO_2 molecule ($^*CO_2$) which proceeds from $CaCO_3$ through its contact with the carbon should give rise to two types of CO. Two types of CO have also been distinguished recently from TPD experiments in the case of potassium [8].

From the above mentioned studies -CO_2 chemisorption and TPD- it was not possible to distinguish these two types of CO because, under the experimental conditions used, they appeared very close. Changing the experimental conditions, as it has been done recently with TPD under vacuum [9], or using isotopically labelled molecules, as done in this paper and in a previous one [10], the two steps of the mechanism of the carbon gasification and the two different CO can be clearly distinguished.

The present paper deals with a series of TPD experiments performed in carbon samples with different calcium loadings and obtained after submitting these samples to a chemisorption process with $^{13}CO_2$ at different temperatures.

EXPERIMENTAL

Samples

The samples used have been extensively described elsewhere [1, 11]. In short, this study concerns with a high purity carbon, obtained from a phenol-phormaldehyde resin oxidized by HNO_3 to create oxygenated surface groups. Calcium is added by means of ionic-exchange or impregnation using a calcium acetate solution. The nomenclature of the samples is the following: A2 (corresponding to the oxidized carbon) followed by I or II, in order to distinguish between impregnation and ionic exchange, and by a number, indicating the amount of calcium loaded.

TPD after $^{13}CO_2$ interaction. Experimental procedure

The experimental procedure used to obtain the TPD spectra after interaction with $^{13}CO_2$ consists of the following steps: i) heating of the calcium-carbon sample in He up to 1223 K at 20 K/min heating rate; ii) cooling of the sample in He atmosphere to the treatment temperature (T_t) (i.e. 573 K or 773 K); iii) when the T_t is stabilized, He is switched to Ar; iv) Ar is switched to $^{13}CO_2$ and the contact with $^{13}CO_2$ is maintained for 1-1.5 minutes; v) TPD in He (20 K/min) up to 1223 K. The flow rates used were 30 ml/min (25°C, 1 atm).

All data are obtained by MS analysis and all signals are corrected for fragmentation and MS sensitivity.

RESULTS AND DISCUSSION

TPD after $^{13}CO_2$ interaction

Figure 1 presents the TPD spectra obtained after $^{13}CO_2$ chemisorption at 573 K on samples A2-II-2.9 and A2-I-1.3; Figure 2 shows the same experiment but after $^{13}CO_2$ treatment at 773 K on sample A2-I-1.3. In all the TPD runs, the evolution of ^{12}CO, ^{13}CO, $^{12}CO_2$ and $^{13}CO_2$ with temperature has been followed. The plot of the total CO and CO_2 evolution for the sample A2-II-2.9 (Figure 3) is similar to the TPD spectrum obtained from this sample after $^{12}CO_2$ chemisorption at 573 K [4], using a different coupled MS-reactor system, which shows the reproducibility of these experiments.

Figures 1 and 2 show that the TPD spectra consist on two $^{13}CO_2$ peaks and one $^{12}CO_2$ peak, together with a ^{13}CO peak and a ^{12}CO one. The baseline for the ^{12}CO does not recover the starting value and an increase in the ^{12}CO signal at temperatures higher than 1123 K is observed. This amount released at temperatures higher than 1123 K is independent of the calcium content, as can be deduced from the comparison of the TPD spectra of the samples A2-II-2.9 and A2-I-1.3 (Figure 1). In a previous publication [4] it was pointed out that the CO evolution profile observed at high temperatures corresponds to the decomposition of relatively stable oxygenated surface groups from the carbon itself, which may need temperatures higher than 1300 K for a total decomposition [12, 13]. This interpretation is confirmed by comparing Figures 1 and 2. In fact, the TPD spectrum of Figure 2 has been obtained after that of Figure 1b using the same sample, whereby, the sample has been submitted

to an additional heat treatment that produces a decrease in the number of surface C(O) complexes evolved at high temperatures.

In spite of the fact that the global TPD spectrum (Figure 3) is similar to the resulting after $^{12}CO_2$ treatment, it is obvious that the use of $^{13}CO_2$ allows us to obtain additional information about the calcium-carbon interaction. In this sense: i) three CO_2 peaks (two $^{13}CO_2$ and one $^{12}CO_2$) can be distinguished (Figures 1 and 2), whereas a two peak CO_2 profile is observed in Figure 3; ii) two CO peaks are differentiated (one ^{13}CO and one ^{12}CO). This last point constitutes the most relevant aspect of the results of these TPD experiments, because it is in agreement with the two steps mechanism previously proposed from the analysis of TPD runs. These TPD were obtained in He after contacting $^{12}CO_2$ [4] and from the same kind of experiments but performed under vacuum [9]. This mechanism consists of two steps (reactions (1) and (2)), the ^{13}CO proceeding from the decomposition of active $Ca^{13}CO_3$, that is to say, $Ca^{13}CO_3$ in the interface of contact with carbon (step (1) of the mechanism) and the ^{12}CO coming from the decomposition of the oxidized carbon sites (CaO-C(O)) of the CaO-carbon interface (step (2) of the mechanism). As this second process constitutes the determining step of the gasification mechanism, the ^{12}CO is released at higher temperatures than the ^{13}CO, as it is observed in Figures 1 and 2.

The interpretation of the different CO_2 peaks that appear in a TPD experiment, requires a more detailed analysis. It seems clear that the first $^{13}CO_2$ results from the surface or bulk calcium carbonate decomposition (inactive catalyst, which is not in contact with the carbon). This argument is in agreement with previous results [4, 5] in which was observed an increase in the amount of this first CO_2 with calcium loading. This assignment is also confirmed by the shift observed in the peak maximum to higher values with increasing the CO_2 treatment temperature (Figure 1b and 2). When T_t is higher than 573 K, the bulk calcium carbonate formation starts and hence, the CO_2 uptake increases. During a TPD experiment, this bulk $CaCO_3$ decomposes partially to the gaseous phase, increasing the CO_2 contribution of the first $^{13}CO_2$ peak, and shifting the peak temperature to higher values (Figures 1b and 2). It must be emphasized that this reasoning is in apparent contradiction with TPD experiments previously presented [4], obtained in a sample with a 3.7 Ca wt% (A2-I-3.7). In these experiments, the amount of CO_2 related to the first peak remains constant with T_t, while the total CO evolved increases with T_t, indicating that the bulk $CaCO_3$ decomposition is produced mainly through the interface. The discrepancy in the behaviour perhaps is due to the different initial dispersion of the samples studied (0.49 for the A2-I-1.3 and 0.60 for the A2-I-3.7). In any case, a more detailed study is necessary with labelled molecules to make clear this point.

In relation to the two CO_2 peaks ($^{13}CO_2$ and $^{12}CO_2$) that appear at temperatures close to the CO ones (^{13}CO and ^{12}CO respectively), the following possibility can be proposed to explain their origin:

The ^{13}CO, originated from the dissociation of the $Ca^{13}CO_3$ of the interface and the ^{12}CO, released during the decomposition of the oxidized carbon sites (CaO-C(O)), can react with oxidized carbon sites while leaving the porous network of the carbon and/or while leaving the CaO-carbon interface. Therefore, some $^{13}CO_2$ or $^{12}CO_2$ can be attributed to the following secondary reactions:

$$^{12}CO + CaO\text{-}C(O) \rightarrow CaO\text{-}C + {}^{12}CO_2 \qquad (3)$$
$$^{13}CO + CaO\text{-}C(O) \rightarrow CaO\text{-}C + {}^{13}CO_2 \qquad (4)$$

However, from the argument proposed we are unable to explain all of the experimental results. In fact: i) TPD experiments performed under high vacuum after CO_2 chemisorption at 573 K [9], show

only two CO_2 peaks whose maxima do not coincide with any of the two CO peaks observed in these experiments; this result indicates that there is some CO_2 that is not produced from secondary and/or parallel reactions. It must be pointed out that under high vacuum conditions, no secondary reactions of CO are observed. ii) The ratio CO/CO_2 calculated from TPD experiments of samples with different calcium sintering degree, decreases with increasing calcium sintering [4, 5]; in this case, should secondary reactions take place, this ratio should be constant. These two results indicate another possibility.

Some $^{13}CO_2$ of the second peak may also come from $Ca^{13}CO_3$ decomposition that is in contact with the carbon. This decomposition is produced without dissociation of the $^{13}CO_2$ molecule:

$$^{13}CaCO_3\text{-}C \rightharpoonup CaO\text{-}C + {}^{13}CO_2 \qquad (5)$$

Considering these arguments, it is possible to explain the origin of the different CO_2 peaks observed in the TPD experiments obtained after $^{13}CO_2$ treatment.

Mechanism of the reaction

From the above results it is possible to confirm the mechanism by which the CO_2 chemisorbed on the CaO reaches, during a TPD experiment, the catalyst-carbon contact and to strengthen the previously proposed mechanism for the carbon-gas reactions catalyzed by calcium [4,5].

$^{13}CO_2$ contact with the calcium-carbon samples.

a) T_t = 573 K

When the calcium-carbon sample, previously heat treated in He up to 1223 K, is contacted with $^{13}CO_2$ at T_t = 573 K, the CO_2 interaction is restricted to the CaO molecules on the surface of the particle [2,3]. At this temperature no dissociation of the $^{13}CO_2$ molecule is found as shown in Figure 4a, in which Ar flow is switched to $^{13}CO_2$ for 1.5 minutes and then to Ar. Of course when the CaO is highly dispersed, as it occurs in the sample A2-II-2.9 (in which the dispersion degree is 0.56), the catalyst should be as small particles (cluster) where the differentiation between surface and catalyst-carbon interface could not be justified. In any case, particle or cluster, the CO_2 interaction can be presented as:

$$CaO + {}^{13}CO_2 \rightharpoonup Ca^{13}CO_3 \quad \text{(surface of the particles)}$$
$$CaO\text{-}C + {}^{13}CO_2 \rightharpoonup Ca^{13}CO_3\text{-}C \quad \text{(interface of the cluster)}$$

b) 573 K < T_t < 823 K.

In this temperature range bulk carbonation occurs [3-5] and, as it is shown in Figure 4b, a small ^{13}CO peak from $Ca^{13}CO_3$ decomposition is found. Interestingly, the corresponding ^{12}CO from carbon gasification is not found, indicating the dissociation of the CaO-C(O) species does not takes place. Temperatures higher than 823 K are needed to produce the CaO-C(O) complexes evolution, as shown in the TPD experiments of Figures 1 and 2. This type of results are noteworthy because they also allow to distinguish the two types of CO above mentioned. If the dissociation of the $Ca^{13}CO_3$ takes place without evolution of ^{12}CO, it is clear that the $^{13}CO_2$ in this temperature range reaches the interface catalyst-carbon in agreement with previous findings [4,5]. The processes involved are:

$$CaO + {}^{13}CO_2 \rightleftharpoons Ca^{13}CO_3 \quad \text{(bulk and surface processes)}$$
$$CaO\text{-}C + {}^{13}CO_2 \rightleftharpoons Ca^{13}CO_3\text{-}C$$
$$Ca^{13}CO_3\text{-}C \rightleftharpoons CaO\text{-}C(O) + {}^{13}CO$$

c) T_t > 823 K.

At temperatures higher than 823 K the $^{13}CO_2$ reaches the interface and, because the temperature is high enough, in addition to its dissociation, there is also the gasification of carbon and hence the evolution of the oxygen carbon complexes (CaO-C(O)).

$$Ca^{13}CO_2\text{-}C \rightleftharpoons CaO\text{-}C(O) + {}^{13}CO$$
$$CaO\text{-}C(O) \longrightarrow CaO\text{-}C + CO$$

TPD after $^{13}CO_2$ chemisorption at 573 K.

a) During heating in He of a calcium-carbon sample which has been submitted to a chemisorption process in $^{13}CO_2$ at 573 K, the $^{13}CO_2$ previously chemisorbed on the surface of the CaO particle is being redistributed. The $^{13}CO_2$ reaches and occupies the calcium-carbon interface and part remains on the external surface.

b) As the heating proceeds, the $Ca^{13}CO_3$ on the surface of the particle (which is not in contact with the carbon), decomposes giving $^{13}CO_2$. Part of this $^{13}CO_2$ may interact with active carbon sites producing oxidized carbon atoms C(O) and ^{13}CO. It could be observed in Figures 1 and 2 that parallel to the appearance of the $^{13}CO_2$ there is also a shoulder in the ^{13}CO peak.

$$Ca^{13}CO_3 \text{ (surface)} \rightleftharpoons CaO \text{ (surface)} + {}^{13}CO_2$$
$${}^{13}CO_2 + C_f \rightleftharpoons {}^{13}CO + C(O)$$

c) At higher temperatures the active $CaCO_3$ in the catalyst-carbon contact, which could form an intermediate CaO-*CO_2-C, decomposes giving:

$$Ca^{13}CO_3\text{-}C \rightleftharpoons CaO\text{-}C(O) + {}^{13}CO$$

Most of the ^{13}CO peak of the Figures 1 and 2 comes from this reaction. Using TPD experiments in vacuum [9], it has been observed that this process is strongly affected by pressure (a shift of $\approx$ 100 K in the peak temperature is observed), indicating that this step is mainly in equilibrium. This fact is in agreement with the first step of the widely accepted mechanism of the carbon-gas reaction [14-16].

$$CO_2 + C_f \rightleftharpoons C(O) + CO$$

d) At higher temperatures (as shown in Figures 1 and 2) the decomposition of the oxidized carbon atoms in contact with the catalyst takes place, giving rise to the ^{12}CO peak.

$$CaO\text{-}{}^{12}C(O) \longrightarrow CaO\text{-}C + {}^{12}CO$$

e) Both the $^{13}CO_2$ and the $^{12}CO_2$ produced may also be ascribed to a secondary and/or parallel reactions between the large number of ^{13}CO released and oxidized carbon atoms.

$$^{13}CO_2 + CaO\text{-}C(O) \rightleftharpoons CaO\text{-}C + {}^{13}CO_2$$
$$^{12}CO_2 + CaO\text{-}C(O) \rightleftharpoons CaO\text{-}C + {}^{13}CO_2$$

f) Part of the $CaCO_3$ in contact with the carbon (maybe the perimeter of the contact zone) decomposes at slightly higher temperatures giving rise to part of the second $^{13}CO_2$ peak of Figures 1 and 2, which is superimposed with the $^{13}CO_2$ formed from the secondary and/or parallel reactions (point e). The CO_2 released as a consequence of this decomposition is clearly distinguished in the TPD experiments performed under vacuum [9].

CONCLUSIONS

TPD experiments performed in carbon samples with different calcium loadings which were previously contacted with $^{13}CO_2$ at 573 K and 773 K, have allowed to distinguish clearly two types of CO produced: ^{13}CO as a consequence of the dissociation of the CO_2 coming from active $CaCO_3$ decomposition at the catalyst-carbon contact- and ^{12}CO coming from carbon gasification -via decomposition of the oxidized carbon sites-. These two CO peaks of similar intensities confirm the following steps of the mechanism of the CO_2 gasification of carbon catalyzed by calcium:

$$Ca^{13}CO_3 \rightleftharpoons CaO\text{-}C(O) + {}^{13}CO$$
$$CaO\text{-}C(O) \longrightarrow CaO\text{-}C + {}^{12}CO$$

ACKNOWLEDGEMENTS

The authors thanks to the DIGCYT (project PB-88-0295), to the MEC for Diego Cazorla's Thesis grant and to the Department of Chemical Engineering of the University of Amsterdam.

REFERENCES

1. C. Salinas-Martínez de Lecea, M. Almela-Alarcón and A. Linares-Solano, Fuel, **69**, 21, (1990).
2. A. Linares-Solano, M. Almela-Alarcón and C. Salinas-Martínez de Lecea, J. Catal., **125**, 401, (1990).
3. D. Cazorla-Amorós, J.P. Joly, A. Linares-Solano, A. Marcilla-Gomis and C. Salinas-Martínez de Lecea, Accepted in J. Phys. Chem.
4. D. Cazorla-Amorós, A. Linares-Solano, C. Salinas-Martínez de Lecea and J.P. Joly, Carbon, **29**, 361, (1991).
5. A. Linares-Solano, C. Salinas-Martínez de Lecea, D. Cazorla-Amorós and J.P. Joly, Fundamental Issues in Control of Carbon Gasification Reactivity, (Eds. J. Lahaye and P. Ehrburger), NATO ASI Series E192, p. 409, Kluwer Academic Publishers, 1991.
6. D. Cazorla-Amorós, C. Salinas-Martínez de Lecea, A. Linares-Solano and A. Marcilla-Gomis, International Symposium on Carbon, New Processing and New Applications, Tsukuba, Tanso, Vol. 1, 4-8 Nov., p. 356, (1990).
7. D. Cazorla-Amorós, A. Linares-Solano, A.F. Marcilla-Gomis and C. Salinas-Martínez de Lecea, submitted to Energy & Fuels.
8. R. Meijer, M. Weeda, F. Kapteijn and J.A. Moulijn, Accepted in Carbon.
9. D. Cazorla-Amorós, A. Linares-Solano, C. Salinas-Martínez de Lecea, T. Kyotani, H. Yamashita and A. Tomita, in preparation.
10. F. Kaptéijn, R. Meijer, B. van Eck and J.A. Moulijn, Fundamental Issues in Control of Carbon Gasification Reactivity, (Eds. J. Lahaye and P. Ehrburger), NATO ASI Series E192, 221,

Kluwer Academic Publishers, 1991.
11. A. Linares-Solano, M. Almela-Alarcón, C. Salinas-Martínez de Lecea, Am. Chem. Soc. Division of Fuel Chemistry, **34(1)**, 136, (1989).
12. J. Wang, B. McEnaney, XIX Biennial Conference on carbon, Pennsylvania, U.S.A., p. 590, (1989).
13. B. McEnaney, Fundamental Issues in Control of Carbon Gasification Reactivity, (Eds. J. Lahaye and P. Ehrburger), NATO ASI Series E192, 175, Kluwer Academic Publishers, 1991.
14. F. Kapteijn and J.A. Moulijn, Carbon and Coal Gasification, (Eds. J.L. Figueiredo and J.A. Moulijn), NATO ASI Series E 105, 291, Martinus Nijhoff, 1986.
15. H. Freund, Fuel, **64**, 657, 1985.
16. H.J. Mühlen, K.H. van Heek and H. Jüntgen, Fuel, **64**, 994, (1985).

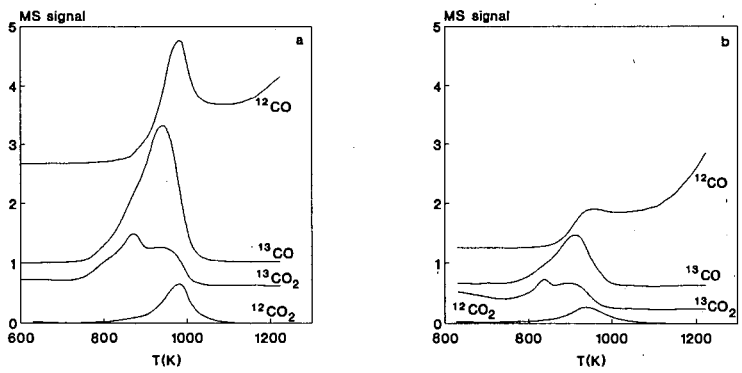

Figure 1. TPD-MS spectra obtained after $^{13}CO_2$ chemisorption at 573 K on samples: a) A2-II-2.9 and b) A2-I-1.3.

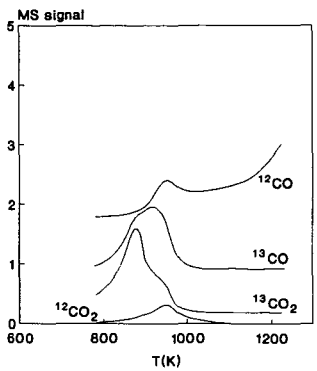

Figure 2. TPD-MS spectrum obtained after $^{13}CO_2$ treatment at 773 K on sample A2-I-1.3.

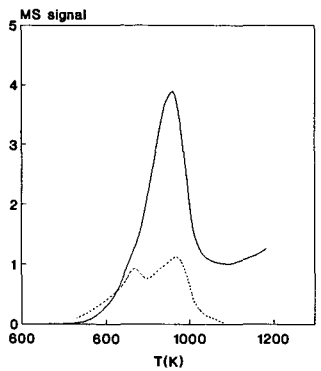

Figure 3. Total CO and CO_2 evolutions after $^{13}CO_2$ chemisorption at 573 K on sample A2-II-2.9 (—, CO; ---, CO_2).

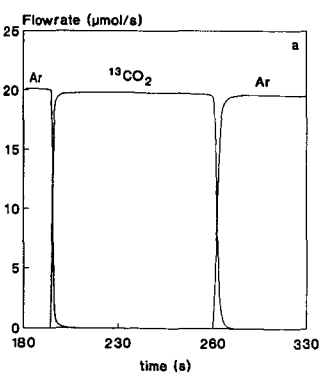

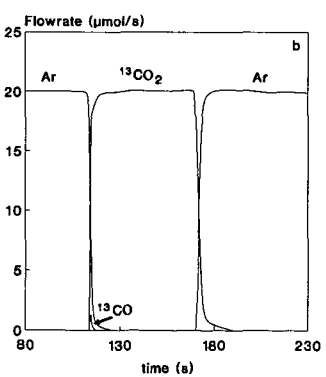

Figure 4. a) $^{13}CO_2$ chemisorption at 573 K on sample A2-II-2.9; b) $^{13}CO_2$ chemisorption at 773 K on sample A2-II-2.9.

CATALYSIS OF CHAR GASIFICATION IN O_2 BY CaO and $CaCO_3$

C.H. Bartholomew, R. Gopalakrishnan and M. Fullwood
BYU Catalysis Laboratory, Department of Chemical Engineering and
Advanced Combustion Engineering Research Center
Brigham Young University
Provo, UT 84602

Keywords: CaO catalysis; $CaCO_3$ catalysis; Coal char oxidation, catalysis of

ABSTRACT

Catalysis by CaO and $CaCO_3$ of the oxidation of a well-defined, high purity synthetic char, Spherocarb, was investigated at low reaction temperatures using thermal gravimetric analysis (TGA). Oxidation rates were likewise measured for fresh, demineralized, and Ca-impregnated samples of a high temperature char prepared in a flat-flame burner at about 1300 K from Beulah Zap coal. Spherocarb and demineralized Zap char were impregnated with Ca using aqueous impregnation and ion-exchange techniques. The resulting kinetic parameters for Spherocarb indicate significant catalytic effects--up to a 100 fold increase in reaction rate for $CaCO_3$ and 3,000 in the case of CaO. The oxidation rates of CaO-catalyzed Spherocarb and Beulah Zap char are the same within experimental error, suggesting that the high reactivity of the Zap char is due in large part to catalysis by CaO.

INTRODUCTION

Char oxidation is a complex heterogeneous process which often governs the overall rate of combustion. Oxidation rates are partially governed by surface properties of the char and reactions catalyzed by minerals within the char matrix. To date studies on catalytic effects of inorganic minerals on char oxidation have been relatively few, and many important questions regarding effects and mechanisms of mineral catalysis, and the relevance of laboratory temperature data to actual operating conditions remain unanswered.

The objectives of this ongoing study are to address some of these questions by (1) studying rates and mechanisms of CaO catalysis of the oxidation of synthetic chars and rank representative demineralized coal chars, (2) determining active sites, surface functional groups, and surface mineral phases in these chars, and (3) investigating effects of surface area and catalyst dispersion.

This paper reports TGA measurements showing the effects of CaO and $CaCO_3$ catalysis on low temperature oxidation rates of Spherocarb, a well-defined, high purity synthetic char and of a Beulah Zap char prepared in air at high temperature in a flat-flame burner.

EXPERIMENTAL

Oxidation rates of pure Spherocarb and CaO loaded Spherocarb prepared by aqueous impregnation (1.2% CaO) and ion exchange (2.8% CaO) with a solution containing an excess of calcium acetate [1] were measured using a thermogravimetric (TGA) system described elsewhere [2]. We designate the samples prepared by aqueous impregnation and ion exchange methods as 1.2% CaO(aq)/Spherocarb and 2.8% CaO(ion)/Spherocarb respectively. Spherocarb samples (Analabs, Inc.; particle diameter of 120 microns) were burned off to 50% of the initial weight at a temperature in the intrinsic rate regime of 748 K in 10% oxygen prior to preparation of the calcium-containing samples to facilitate the penetration of the Ca acetate or Ca hydroxide into the pores. Critical temperature data (temperatures for 6.5 % per minute burnoff) were initially obtained in 10% oxygen (in nitrogen) by heating 2 mg samples at 40 K/min to 1223 K. Thereafter, rates of oxidation were measured isothermally in 10%

oxygen to various stages of burnoff in the neighborhood of the critical temperature and in the region of 150-200 K below the critical temperature.

The dispersion of CaO particles on Spherocarb was measured following the procedure of Radovic et al. [3], and Solano et al. [4] using selective CO_2 chemisorption at 573 K in a TGA apparatus. Samples containing calcium were decomposed at 1173 K for 10 minutes in nitrogen flow, cooled to 573 K and after 10 minutes, exposed to flowing CO_2 in nitrogen for about 30 minutes. From the weight of CO_2 chemisorbed values of surface area (S_{CaO}), crystallite diameter (d), and percentage dispersion (D) of CaO were estimated using the equations of Radovic et al. [3].

Surface areas were determined from nitrogen adsorptions carried out at 77 K, using procedures and a flow adsorption system described previously [5]. Nitrogen adsorption isotherms were analyzed using the BET equation, and an area for the nitrogen molecule of 0.162 nm^2 was used to obtain surface areas.

High temperature Beulah-Zap (Zap) char was prepared by devolatilization in a flat flame burner of 200-230 mesh particles of the Argonne premium coal. The details of this apparatus have been described previously [6]. Feed gas consisted of 8.6% methane, 72% nitrogen, and 19.4% oxygen. The flame temperature at the collection probe was found to be 1251 K, and the residence time of the particles in the burner was 130 ms.

The Zap char was demineralized using concentrated acids (37 wt.% HCl and 49 wt.% HF). One gram of char was placed into a beaker and 200 ml of concentrated HCl was added. The beaker was heated to 333 K and stirred for two hours. Following HCl treatment, the char was washed 4 times using 1 liter of 365 K water for each wash. The HCl treatment was performed on the char 3 times, following which the same treatment was performed using HF. Following the final acid treatment the char was washed 8 times using 1 liter/wash of distilled water at 365 K and dried in a vacuum oven at 383 K overnight.

RESULTS AND DISCUSSION

Spherocarb . BET surface areas from nitrogen adsorption of untreated Spherocarb and 50% burned-off Spherocarb were determined to be 895±7 and 1039 m^2/g respectively; the value for the untreated Spherocarb compares favorably with values of 864 and 965 m^2/g reported by Waters et al. [7] and Dudek et al. [8]. In these two previous studies [7,8] surface area was observed to increase up to a conversion of 10-15% and then monotonically decrease with increasing conversion (reaching 650-660 m^2/g at 65-80% conversion); however conversion temperatures in these studies ranged from 780 to above 1300 K. In the present investigation conversion in the intrinsic rate regime at 748 K (10% oxygen) caused a 16% increase in surface area. This result suggests that densification/graphitization processes [9] are important at higher oxidation temperatures (above 750 K).

Arrhenius plots of oxidation rates for preburned (to 50%) and untreated Spherocarb are plotted in Fig. 1. The rates at any given temperature and activation energies (153 and 150 kJ/mol respectively) are the same within experimental error. Accordingly, the low temperature burnoff treatment at 748 K to open up pores for Ca impregnation does not affect the intrinsic reactivity of the Spherocarb char. The oxidation rate of Spherocarb at 667 K corrected to 21% oxygen (assuming an oxygen order of 0.6) is 2.8 μg/gs in very good agreement with a value of 2.3 μg/gs determined by Hurt et al. [10]. The activation energies from this study of 150-153 kJ/mole for oxidation of Spherocarb are in excellent agreement with the value of 153 kJ/mole determined for Spherocarb from the data of Hurt et al. [10] but somewhat lower than the value of 184 kJ/mol reported by Waters et al. [7] for Spherocarb and

very near values of 167-170 kJ/mole reported for oxidation of various synthetic mineral-free carbons [11,12]. Accordingly, the rate data and activation energies are valid for the intrinsic surface oxidation of carbon and are not influenced by pore diffusional or film mass transfer resistances.

Critical temperatures (6.5% wt. loss/min corrected for ash) for unloaded Spherocarb, 1.2% CaO(aq)/Spherocarb and 2.8% CaO(ion)/Spherocarb were found to be 968, 906 and 797 K respectively, indicating a large catalytic effect.

Rate data plotted in Arrhenius form are shown in Figure 2 for unloaded Spherocarb, 1.2% CaO(aq)/Spherocarb at 55 burnout and 2.8% CaO(ion)/Spherocarb at 50% burnout after pretreatment at 823 or 973 K. From the Arrhenius plots preexponential factors and activation energies were obtained for the unloaded Spherocarb and the two different catalytic loadings, one after pretreatment at two different temperatures (see Table 1). The activation energies for unloaded, 1.2% CaO(aq)/Spherocarb and 2.8% CaO(ion)/Spherocarb samples after pretreatment at 823 and 978 K are 150, 121, 96, and 139 kJ/mole respectively in the temperature range of 570-900 K, the magnitude of these values again indicating that the rates are probably not influenced by pore diffusional resistance in this range of conditions, since values of 125-200 are reported for mineral-catalyzed coal char combustion [13], although a value of only 64 kJ/mole was reported for Ca-impregnated char [14].

Table 1. Activation Energies and Pre-Exponential factors of oxidation of CaO-Loaded and Unloaded Synthetic and Zap Char Samples in 10% oxygen

Sample	Ea (kJ/mole)	Pre-Exponential (g/gsample s)
2.8% CaO(ion)/Spcb (823 K)	139	3.0×10^8
2.8% CaO(ion)/Spcb (973 K)	96	0.19×10^4
1.2% CaO(aq)/Spherocarb	121	3.6×10^4
Unloaded Spherocarb	150	99×10^4
Zap Char	112	1.4×10^6
1.86% CaO/Zap	117	6.9×10^6
Zap, demineralized	151	3.3×10^8

Rates calculated at 600 K from Figure 2 indicate that the 1.2% CaO(aq)/Spherocarb sample is more reactive than the unloaded sample by a factor of about 12 while 2.8% CaO(ion)/Spherocarb pretreated at 823 K is more reactive by a factor of about 100 (Table 2). This enhancement in rate is consistent with that of up to two orders of magnitude reported by Levendis et al. for CaO catalysis at low temperatures [14]; however, the 2.8% CaO(ion)-/Spherocarb pretreated at 973 K is 30 times more active than these other Ca-containing chars with a rate enhancement factor relative to the uncatalyzed sample of 2800. Apparently, the pretreatment temperature has a dramatic effect on activity. As will be shown later, the significantly higher activity after pretreatment at 973 K is due to the presence of CaO while $CaCO_3$ is present after pretreatment at the lower temperature. A smaller but still significant factor is the method of preparation; this is probably because the aqueous impregnation technique results in a dispersion that is inferior to that obtained by other techniques such as ion exchange [14].

TEM and SEM studies of unloaded and CaO loaded Spherocarb samples were also conducted to determine the distribution of CaO in the samples. The TEM results were inconclusive regarding the dispersion of CaO in the micro and mesopores of the carbon. However, the SEM pictures provided strong evidence that the aqueous impregnation deposits copious quantities of CaO on the exterior of the carbon spheres, while the ion exchange

technique provides a uniform dispersion and greater penetration of pores, especially into partially burned-out Spherocarb. Indeed, the extent of loading, dispersion, and surface area of CaO are greater for samples prepared by ion exchange than those prepared by an aqueous impregnation method (Table 3). Thus, smaller size crystallites of CaO are formed during the ion exchange process leading to better dispersion and higher surface area. Calcium loading by ion exchange probably allows calcium ions to enter into micro and mesopores of Spherocarb possibly accounting for its higher intrinsic reactivity (per surface area of CaO; see Table 2).

Table 2. Catalytic Effects of Ca in Oxidation of Spherocarb at 600 K

Sample	10^6 rate (g/gchar s)	10^4 rate (g/gCaO s)	10^6 rate (g/m^2CaO s)
2.8% CaO (ion -exch.) /Spherocarb (973 K)	237	85	
2.8% CaO (ion -exch.) /Spherocarb (823 K)	8.3	3.0	2.7
1.2% CaO (aq.-impr.) /Spherocarb	1.0	0.83	0.62
Ca-Free Spherocarb	0.085	-	-

Table 3. Effect of Method of Calcium Loading on CaO Dispersion

Sample	S_{CaO} (m^2/g CaO)	d (nm)	D (%)
1.2% CaO(aq)/Spherocarb	134	11.5	10.8
2.8% CaO(ion)/Spherocarb	180	8.5	14.5

The substantially higher reactivity of the 2.8% sample pretreated at higher temperature suggests the possible formation of a new catalytic phase. Indeed, TGA experiments of complete burning of 1.2% CaO(aq)/Spherocarb, 2.8% CaO(ion)/Spherocarb and pure calcium acetate performed in 10% O_2/90% N_2 atmosphere by ramping slowly from room temperature to 1173 K show that calcium acetate decomposes in two stages (Table 4). Comparison of weight changes observed from TGA experiments and values calculated assuming $CaCO_3$ and CaO as intermediate and final product respectively agree very well. This indicates that calcium in Spherocarb exists as $CaCO_3$ at temperatures below 823 K and CaO above this pretreatment temperature. Thus, CaO has substantially higher catalytic activity than $CaCO_3$.

Beulah Zap. BET surface areas from nitrogen adsorption of Zap char and demineralized Zap char were determined to be 322 and 348 m^2/g respectively. The value for the Zap char prepared with a residence time of 130 ms is somewhat higher than the value of 229 m^2/g reported by Hecker et al. [2] for a residence of time of 104 ms; however, this is expected since surface area of chars prepared in the flat flame burner increases very significantly with increasing residence time [2]. The larger surface area for the demineralized char is consistent with removal by acid treatment of mineral matter from micro or mesopores or pore entrances, since it is the micro and mesopores that account for most of the surface area of chars [5].

Table 4. Stoichiometry of Decomposition of Calcium Acetate by TGA

Experimental(TGA)			Calculated	
	Raw data (wt.%)	after water correction (wt.%)		(wt.%)
$Ca(Ac)_2$	100.000		$Ca(Ac)_2$	100.000
Water	5.400			
1st decomposition	60.167 (724 K)	63.601	$Ca(Ac)_2 \rightarrow CaCO_3$	63.331
2nd decomposition	33.658 (1048 K)	35.579	$Ca(Ac)_2 \rightarrow CaO$	35.476

*values in the parentheses are the temperatures of maximum decomposition rate

Arrhenius plots of rate data are shown in Fig. 3 for oxidation of Zap, 1.86% CaO/Zap (prepared by ion exchange), and demineralized Zap chars. It is evident that the reactivities of Zap and 1.86% CaO/Zap chars are very close while that of the demineralized Zap is much lower, suggesting that the high reactivity of Zap is due to the presence of Ca minerals. Activation energies for the three Zap chars are summarized in Table 1. The value of 112 kJ/mol for untreated Zap char is in excellent agreement with the value of 113 kJ/mol reported by Hecker et al. [2] for a Zap char prepared under very similar conditions in a flat-flame burner. The value of 151 kJ/mol for demineralized char is the same within experimental error as the value determined for pure Spherocarb (see Table 1), suggesting that oxidation of the demineralized char occurs by the same mechanism as the synthetic, mineral-free char.

Fig. 4 compares rate data in Arrhenius form for oxidation of catalyzed and uncatalyzed Spherocarb with those for Zap and demineralized Zap chars. The data for Zap and 2.8% CaO/Spherocarb fall nearly along the same line while rates for demineralized Zap are lower than for Zap but higher than those for uncatalyzed Spherocarb. Again, these results strongly suggest that the higher reactivity of Zap relative to demineralized Zap is due to the presence of CaO minerals in the Zap char. These results are quite consistent with data reported by Radovic et al. [15] for Zap, demineralized Zap, and CaO-catalyzed Zap pyrolysis chars prepared at a relatively high residence time (0.3 s) at 1275 K; in this latter study [15] the demineralization and CaO exchange were done on the coal. These workers likewise observed similar reactivities for Zap and CaO-catalyzed Zap chars, while that for the demineralized char was substantially lower. Apparently, significant differences in pretreatment of the coal and preparation of the chars do not affect the qualitative results, although quantitatively they are different.

CONCLUSIONS

1. The intrinsic reactivity of Spherocarb, a relatively mineral free synthetic char, is not affected by 50% oxidation at 748 K in 10% oxygen. In other words, there is no evidence of graphitization or densification under these conditions. However, there is a significant (16%) increase in BET surface area as a result of this mild oxidation treatment.

2. Kinetic parameters obtained in this study indicate a significant catalytic effect of CaO involving at least a 2800-fold increase in oxidation rate of Spherocarb compared to a 100-fold increase in rate for $CaCO_3$.

3. Ion exchange results in better dispersion and penetration of calcium into Spherocarb than other methods investigated in agreement with previous studies of synthetic chars.

4. The higher reactivity of Zap relative to demineralized Zap or uncatalyzed Spherocarb is due in large part to the presence of Ca minerals in the form of CaO.

ACKNOWLEDGEMENTS

This work was sponsored by the Advanced Combustion Engineering Research Center (ACERC). Funds for ACERC are provided by the National Science Foundation, the State of Utah, 26 industrial participants, and the U. S. Department of Energy. The authors gratefully acknowledge technical assistance by Professor W. C. Hecker, Mr. W. D. Hyde, Mr. W. E. White, Mr. K. M. McDonald, Mr. M. M. Painter, and Mr. R. F. Cope.

REFERENCES

1. Hengel, T. D., and Walker, P. L., Jr, *Fuel*, 63 (1984) 1214.

2. Hecker, W. C., McDonald, K. M., Jackson, C. D., and Cope, R. F., paper presented at the First International Conference on Combustion Technologies for a Clean Environment, Vilamoura, Portugal, Sept., 3-6, 1991.

3. Radovic, L.R., Walker, P.L.Jr, and Jenkins, R.G., *J. Catal.*, 82 (1983) 382.

4. Linares-Solano, A., Almela-Alarcon, M., and Salinas-Martinez de Lecea, C., *J. Catal.*, 125 (1990) 401.

5. White, W. E., Bartholomew, C. H., Hecker, W. C., and Smith, D. M., *Adsorption Sci. & Techn.*, in press.

6. Hyde, W. D., *Effect of Preparation Reactor and Parent Coal Rank on Coal Char Reactivity*, M. S. Thesis, Brigham Young University, 1990.

7. Waters, B. J., Squires, R. G., and Laurendeau, N. M., *Comb. Sci. & Tech.*, 62 (1988) 187.

8. Dudek, D. R., Longwell, J. P., and Sarofim, A. F., *Energy & Fuels*, 3 (1989) 24-28.

9. Hurt, R. H., Dudek, D. R. Longwell, J. P., and Sarofim, A. F., *Carbon*, 26 (1988) 433-449.

10. Hurt, R. H., Sarofim, A. F., and Longwell, J. P., "The Role of Microporous Surface Area in Gasification of Uncatalyzed Carbon," submitted, 1991.

11. Felder, W., Madronich, S., and Olson, D. B., *Energy & Fuels*, 2 (1988) 743-750.

12. Levendis, Y. A. Flagan, R. C., and Gavalas, G. R., *Combust. & Flame*, 76 (1989) 221-241.

13. Suuberg, E. M., Wojtowicz, M., and Calo, J. M., 22nd Internat. Symp. on Combustion.

14. Levendis, Y. A., Nam, S. W., Lowenberg, M., Flagan, R. C., and Gavalas, G. R., *Energy and Fuels*, 3 (1989) 28.

15. Radovic, L. R., Walker, P. L., Jr., and Jenkins, R. G., *Fuel*, 62 (1983) 209.

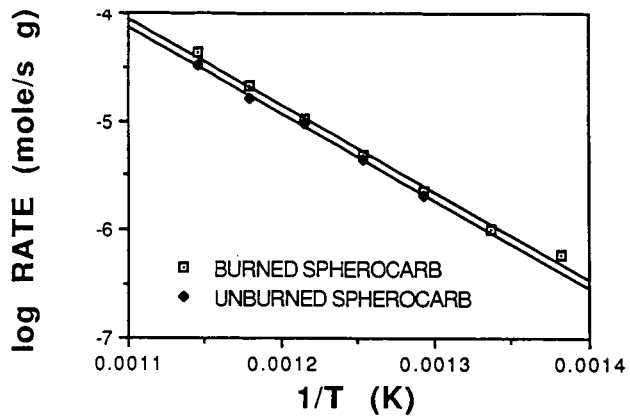

Figure 1. Arrhenius plots of oxidation rates of Spherocarb and partially oxidized Spherocarb (50% conversion at 748 K in 10% oxygen in nitrogen).

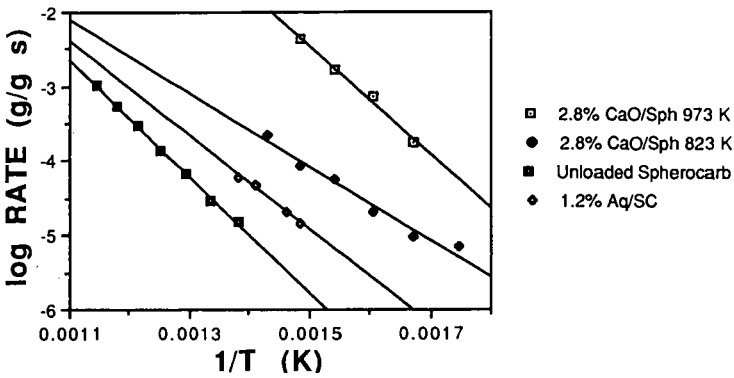

Figure 2. Arrhenius plots of oxidation rates for 2.8% CaO(ion)/Spherocarb (pretreated at 823and 973 K), 1.2% CaO(aq)/Spherocarb, and uncatalyzed Spherocarb in 10% oxygen.

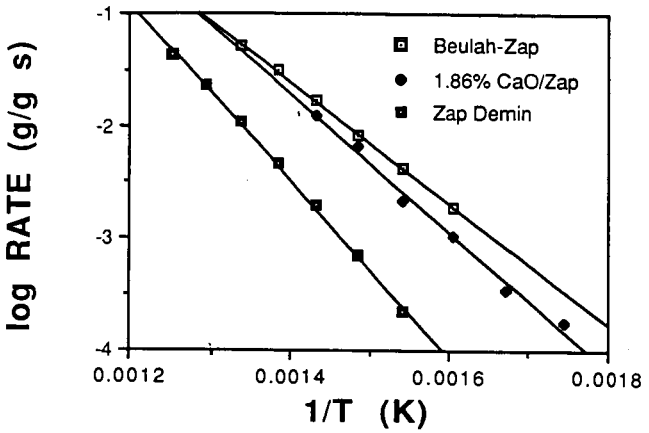

Figure 3. Arrhenius plots of oxidation rates for Zap, 1.86% CaO/Zap (prepared by ion exchange), and demineralized Zap chars in 10% oxygen.

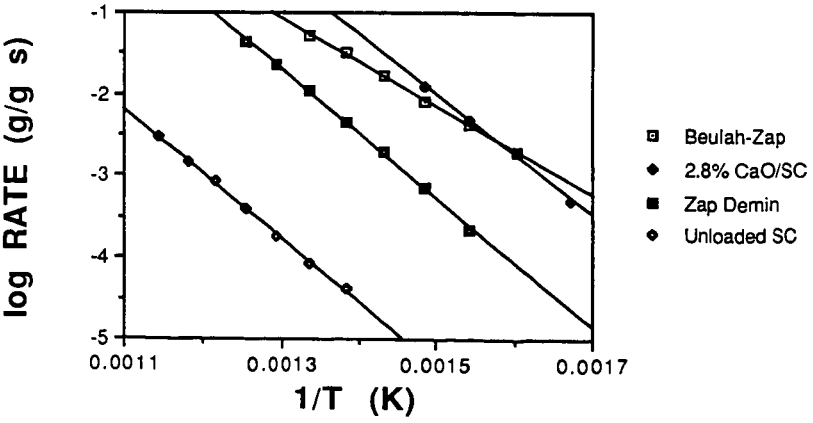

Figure 4. Arrhenius plots of oxidation rates for catalyzed and uncatalyzed Spherocarb and for Zap and demineralized Zap chars in 10% oxygen.

Potassium-Catalysed Carbon Gasification in CO_2 studied by Transient Techniques.

F. Kapteijn, R. Meijer, S.C. van Eck and J.A. Moulijn*
Department of Chemical Engineering, University of Amsterdam
Nieuwe Achtergracht 166, 1018 WV, Amsterdam, The Netherlands
* *present address: Department of Chemical Technology, University of Delft*

Keywords: transient kinetics, labelled CO_2, potassium-catalysed gasification

ABSTRACT

The K_2CO_3/carbon system has been studied under gasification conditions applying transient techniques, *i.e.* temperature programmed desorption and step-response experiments, in combination with labelled CO_2 ($^{13}CO_2$ and $C^{18}O_2$). Detailed information on the mode of catalytic action of potassium, the composition of the catalytically active alkali species and the rate of the different processes, is obtained.

Step-response experiments reveal that the potassium/carbon system is very dynamic. Upon a gas phase step change from a reactive to an inert gas phase at 1000 K the effluent gas composition is strongly affected by secondary reactions of desorbed species with the alkali catalyst on the carbon surface. The composition of the catalytically active alkali species changes with increasing gasification temperature. At 1000 K it can be represented by a cluster composed of several potassium phenolate species and contains chemisorbed CO_2 and reactive oxygen, whereas at 1200 K merely highly reactive potassium phenolate species are present. From step-response and temperature programmed desorption experiments it can be concluded that during gasification in CO_2, gas phase CO is inserted into the carbon matrix.

A model proposed for the mechanism of the potassium-catalysed gasification of carbon in CO_2 can adequately describe the observed transient and steady state behaviour taking into account that during steady state gasification in CO_2 carbon-oxygen intermediates of different stability are present which, depending on temperature, simultaneously desorb on exposure to an inert.

INTRODUCTION

Potassium-catalysed gasification is usually kinetically described by a two step model, in which the oxidation/reduction cycle (eq. 1) represents all (faster) steps preceeding gasification (eq. 2) [1].

$$CO_2 + C_f \underset{k_{-1}}{\overset{k_1}{\rightleftharpoons}} CO + C(O) \qquad (1)$$

$$C(O) \xrightarrow{k_2} CO \qquad (2)$$

Kinetic studies [1-3] have shown that addition of alkali catalysts increases the steady state concentration of carbon-oxygen intermediates and does hardly affect the equilibrium ($K_1=k_1/k_{-1}$) and intrinsic rate constant (k_2).

By applying labelled molecules [4-6] it was concluded that oxygen exchange between H_2O,H_2 and CO_2,CO is catalysed by the alkali catalyst and occurs without involvement of carbon-oxygen intermediates. The catalytically active site is envisaged as an alkali cluster M_xO_y (*), anchored to the carbon surface via plenolate groups. This cluster can contain chemisorbed CO_2 (CO_2-*), up to CO_2/M_a = 0.3 [3,4,7-9], which is present at gasification temperatures. This CO_2 is easily exchanged with gas phase CO_2 through eq. 4 [10].

A model for the potassium-catalysed gasification of carbon in CO_2 can be represented by eqs. (1,2,4-7), in which *, O-* and CO_2-* represent the different states of the catalytically active alkali cluster, and C_f and C(O) the carbon sites active for gasification.

$$^{\circ}CO_2 + CO_2\text{-}* \rightleftharpoons {}^{\circ}CO_2\text{-}* + CO_2 \qquad (4)$$

$$CO_2 + * \rightleftharpoons CO_2\text{-}* \quad (5)$$

$$CO_2\text{-}* \rightleftharpoons CO + O\text{-}* \quad (6)$$

$$O\text{-}* + C_f \rightleftharpoons * + C(O) \quad (7)$$

Temperature programmed desorption (TPD) and step-response experiments (SRE) in principle provide information on the reaction, intermediates and rates of elementary processes, especially when labelled molecules are applied [4,11-13]. Application of $^{13}CO_2$ enables us to distinguish between CO originating from gas phase reactant (^{13}CO) and CO from the carbon (CO), $C^{18}O_2$ to trace the behaviour of the oxygen in the system under study.
In this paper the results are presented of applying ^{13}C and ^{18}O labelled CO_2 in TPD and SRE experiments, that were designed to obtain detailed mechanistic information on the reactions taking place during catalysed CO_2 gasification and the role of the catalyst.

EXPERIMENTAL

Throughout this paper all labelled species are addressed with a prefix, *viz.* ^{18}O and ^{13}C, whereas in all cases C and O without prefix refer to ^{12}C and ^{16}O. Experimental details can be found elsewhere [14].
All gases used are of HP or UHP grade and are purified (O_2 and/or H_2O removal) before being fed to the gas mixing sections. $^{13}CO_2$ and $C^{18}O_2$ (MSD isotopes; 99.3 % ^{13}C and 90-91 % ^{18}O pure, respectively) were used as received. The ^{16}O in the $C^{18}O_2$ feed is present as $CO^{18}O$ (≈ 20% of the total CO_2).
The catalysed gasification in CO_2 was studied with 50-200 mg samples of K_2CO_3/Norit RX extra (K/C_i = 0.019). The alkali-metal content of fresh and used samples was determined by ICP-AES.
In step-response experiments (SRE) CO_2/Ar mixtures that flow through the sample at gasification temperatures are exchanged with an Ar flow and *vice versa* and the response of the sample on this change is followed continuously by a PC controlled MS. The raw MS data are corrected for background levels, fragmentation contributions (CO_2 to CO) and MS sensitivity for the different molecules, and converted into molar flowrates of the gaseous species leaving the reactor.
For the TPD experiments the samples were pretreated by TPD of the fresh sample (reduction) and exposed to a reactive gas mixture at different temperatures. The TPD patterns were obtained in a helium flow of 20 $\mu mol.s^{-1}$ at a heating rate of 10 $K.min^{-1}$ up to 1200 K, followed by an isothermal period of 30 minutes at 1200 K. The desorption rates of CO and CO_2 are expressed as (mol desorbed).(mol K actually present)$^{-1}.s^{-1}$. Simultaneously GC analysis was performed to quantify the (labelled) CO and CO_2 production rates monitored by the MS.

RESULTS AND DISCUSSION

Upon introduction of Ar after $^{13}CO_2$ exposure at 1000 K (figure 1A) a fast declining $^{13}CO_2$, CO_2 and ^{13}CO production, reaching the baseline within 50 seconds, and a tailing CO production, lasting up to 5 minutes, is observed. The composition of the product gas in the initial period is strongly influenced by fast CO_2 and oxygen exchange reactions, by which part of the primary desorption products ($^{13}CO_2$ and CO) are converted into CO_2 or ^{13}CO. Figure 1B shows after correction for oxygen exchange reactions the primary desorption rates of CO (amu 28+44), ^{13}CO (amu 29-44) and $^{13}CO_2$ (amu 45+44). Amounts are given in table 1.

Upon reintroduction of $^{13}CO_2$ (figure 1C) chemisorption and sample oxidation is observed. Sample oxidation can be deduced from the data in figure 1C by considering that under steady state conditions CO and ^{13}CO are produced in a 1:1 ratio (corrected for oxygen exchange with $^{13}CO_2$). Chemisorption amounts can be calculated by comparing the total carbon in the product gas molecules with that of a blanc run with an inert SiC sample (figure 1D). After approximately 50 seconds steady state gasification and oxygen exchange conditions are reached. Variation of the time span in argon at 1000 K before exposure to $^{13}CO_2$,Ar did not have any significant influence on these results.

In figure 2 the response curves for a gas phase step change from 10% $^{13}CO_2$,Ar to Ar and *vice versa* at respectively 1100 and 1200 K are shown, with an analogous data treatment.
At 1200 K all $^{13}CO_2$ is converted, resulting in equal CO and ^{13}CO production rates, whereas at 1100 K also $^{13}CO_2$ and CO_2 are present under steady state conditions. Upon a gas phase step

change to Ar no $^{13}CO_2$ or CO_2 is produced at both temperatures. However, it is striking that together with CO and in the absence of $^{13}CO_2$ a considerable amount of ^{13}CO desorption is observed. Reintroduction of $^{13}CO_2$ at 1100 K shows both a CO overshoot due to gasification and a ^{13}CO overshoot due to oxidation. At 1200 K steady state gasification conditions are directly restored without any overshoot and no $^{13}CO_2$ or CO_2 is detected in the product gas. All $^{13}CO_2$ is converted. However, a mass balance calculation shows that upon reintroduction of $^{13}CO_2$ at 1200 K a certain amount of ^{13}C is not accounted for in the product gas, suggesting an incorporation in the sample.
Similarly to the uncatalysed gasification [15] the CO release can only be well described by two parallel desorption processes. Therefore it is proposed that, apart from the catalytic clusters, two types of carbon–oxygen complexes are present, in semiquinone structures and in carbonylic structures. The former can be converted in to the more reactive latter species on armchair edges of the carbon [15]. A schematic picture is given below. Left are indicated reaction on the zig–zag edge and right on the armchair edge.

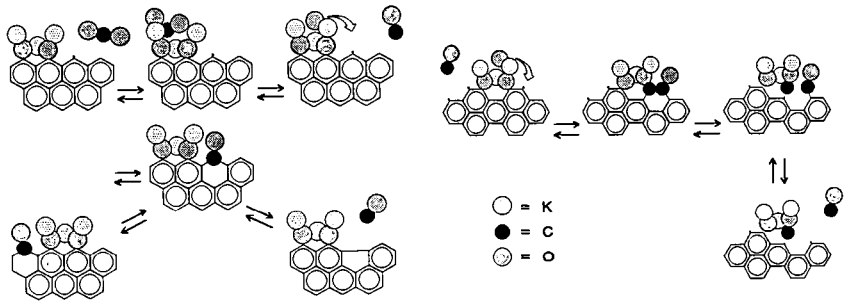

The main desorption products in a TPD after exposure to 10% $^{13}CO_2$,Ar at 673 to 1000 K are $^{13}CO_2$, released between 500 to 900 K, followed by CO above 900 K (figure 3). Additionally, between 700 and 1000 K, smaller amounts of CO_2 and ^{13}CO are observed. After exposure at 1000 K also a small amount of ^{13}CO above 1000 K is observed (figure 3C). This amount increases if the sample has been exposed to a higher partial pressure of $^{13}CO_2$.
Apparently the reduced sample is only partially reoxidised by CO_2 at 673 K, and increasingly more at higher temperatures. Therefore, the CO_2 desorption amounts decrease with exposure temperature, whereas the CO release increases. The latter is ascribed to the reduction of the potassium oxide in the cluster by the carbon or the decomposition of the phenolate groups. The small CO evolution around 950–1000 K is ascribed to decomposition of chemisorbed CO_2 into CO and O*. This is the unlabelled CO_2 since the $^{13}CO_2$ had already been replaced by fast exchange.
During TPD oxygen exchange takes place when $^{13}CO_2$ and CO are both present (around 900 K). TPD confirms the SRE experiments that some ^{13}CO is inserted in the sample, probably in the carbon, analogously to the uncatalysed case.

A TPD pattern obtained after $C^{18}O_2$ exposure at 673 K (figure 4A) shows $C^{18}O_2$ and $CO^{18}O$ desorption below 1000 K and a CO and $C^{18}O$ release spread over a wide temperature range. After $C^{18}O_2$ exposure at 1000 K (figure 4B) the CO and $C^{18}O$ desorbed is much larger and mainly takes place above 1000 K, in agreement with fig. 3. After gasification in $C^{18}O_2$ and subsequently in CO_2, the TPD pattern (figure 4C) shows low temperature CO_2 desorption and CO has become the main desorption product above 1000 K, whereas still a small amount of $C^{18}O$ desorption is observed. Compared to fig. 3C it is obvious that chemisorbed $C^{18}O_2$ must have been exchangedrapidly with CO_2, but that part of the ^{18}O in the sample is hard to exchange (fig. 4B and C).
SRE experiments with CO_2 and $C^{18}O_2$ indicate that the oxygen in the potassium cluster can be exchanged (1000 K) within 5 minutes ($^{18}O/K = 1$) by direct exchange of CO_2 with chemisorbed $C^{18}O_2$ and exchange of oxygen in the cluster with chemisorbed CO_2, yielding $C^{18}OO$.

Also in figures 4 the shoulder in the CO release, around 950–1000 K can be ascribed to decomposition of strongly chemisorbed CO_2.

In summary the step–response and temperature programmed desorption experiments, using labelled CO_2, have revealed the following principal phenomena. The active potassium oxide cluster still contains chemisorbed CO_2 at 1000 K, not above 1100 K. This chemisorbed CO_2 is easily exchanged with gas phase CO_2, and can exchange oxygen present in the cluster. It can decompose upon formation of CO and reactive oxygen in the cluster. The amount of oxygen in the cluster decreases with increasing temperature. This oxygen reacts with the carbon where it forms surface complexes, that can decompose to CO, which represents the gasification step. Two surface complexes are distinguished that decompose at different rates. The CO desorption is reversible and accounts for the incorporation of CO in the sample. All these phenomena will contribute to the gasification rate.

ACKNOWLEDGEMENT

These investigations have been executed within the framework of the Dutch National Coal Research Programme (NOK), which is managed by the Project Office for Energy Research (NOVEM) and financed by the Ministry of Economic Affairs.
The financial support of SON–NWO for purchasing the labelled CO_2 is gratefully acknowledged.

REFERENCES

1. Kapteijn F., Peer O. and Moulijn J.A., *Fuel*, 65, 1371 (1986).
2. Kelemen S.R. and Freund H., *J. Catal.*, 102, 80 (1986).
3. Koenig P.C., Squires R.G., and Laurendeau N.M., *J. Catal.*, 100, 228 (1986).
4. Cerfontain M.B., Meijer R., Kapteijn F., and Moulijn J.A., *J. Catal.*, 107, 173 (1987).
5. Saber M.S., Falconer J.L. and Brown L.F., *J. Catal.*, 90, 65 (1984).
6. Mims C.A. and Pabst J.K., *ACS Div. Fuel Chem. Prep.*, 25, 258 and 263 (1980).
7. Ratcliffe C.T., *ACS Div of Fuel Chem. Prepr.*, 30, 330 (1985).
8. Mims C.A., and Pabst J.K., *J. Catal.*, 107, 209 (1987).
9. Meijer R., Sibeijn M., van Dillen M.R.B., Kapteijn F. and Moulijn J.A., *I & E C Research* in press.
10. Cerfontain M.B., *Ph.D. Thesis Univ. of Amsterdam*, The Netherlands (1986).
11. Kapteijn F., and Moulijn J.A., in *Carbon and Coal Gasification: Science and Technology*, eds. J.L. Figueiredo and J.A. Moulijn, Nijhoff Publ., Dordrecht, 291 (1986).
12. Cerfontain M.B., Kapteijn F. and Moulijn J.A., *Carbon*, 26, 1, 41 (1988).
13. Cerfontain M.B., Agalianos D. and Moulijn J.A., *Carbon*, 25, 351 (1987).
14. Meijer R.,*Ph. D. Thesis, Univ. of Amsterdam*, The Netherlands, 1991.
15. F. Kapteijn, R. Meijer and J.A. Moulijn, ACS meeting New York, aug. 1991.

Table 1. Desorption products (μmol) after a gas phase step change from 10% $^{13}CO_2$,Ar to Ar at different temperatures. F_t = 20 μmol.s^{-1}, K_a = 115 μmol

	CO	^{13}CO	CO_2	$^{13}CO_2$
T = 1000 K	9.8	4.8	2.8	8.0
T = 1100 K	6.5	2.3	-	-
T = 1200 K	19	8.5	-	-

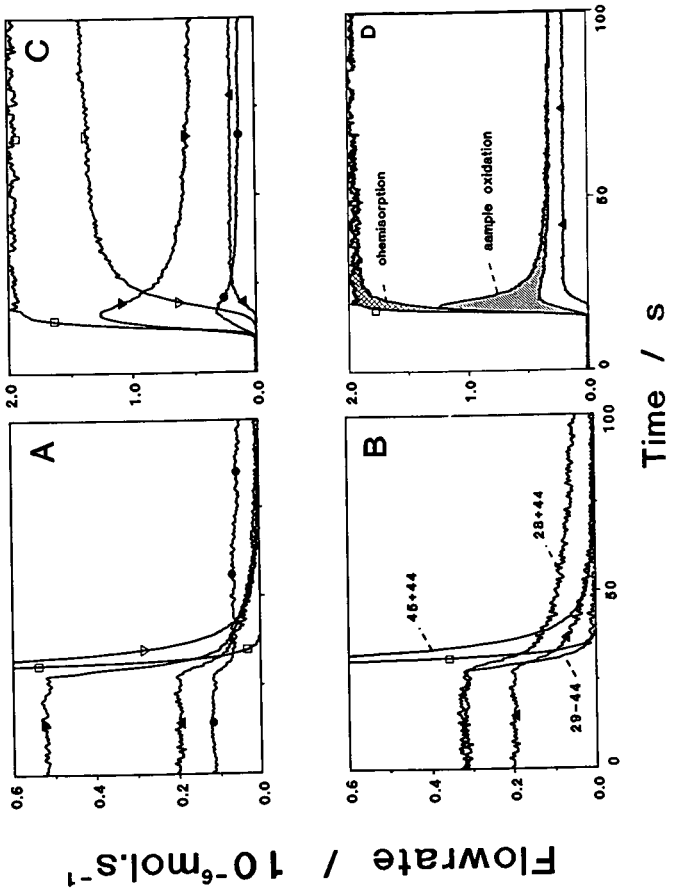

Figure 1 : Response curves for a gas phase step change from 10% $^{13}CO_2$,Ar to Ar (A,B) and *vice versa* (C,D) at 1000 K.
(A and C represent the measured signals, B and D the converted data (see data handling).

Key: CO; ^{13}CO; $C^{18}O$; CO_2; $^{13}CO_2$; $CO^{18}O$; $C^{18}O_2$, blanc run.

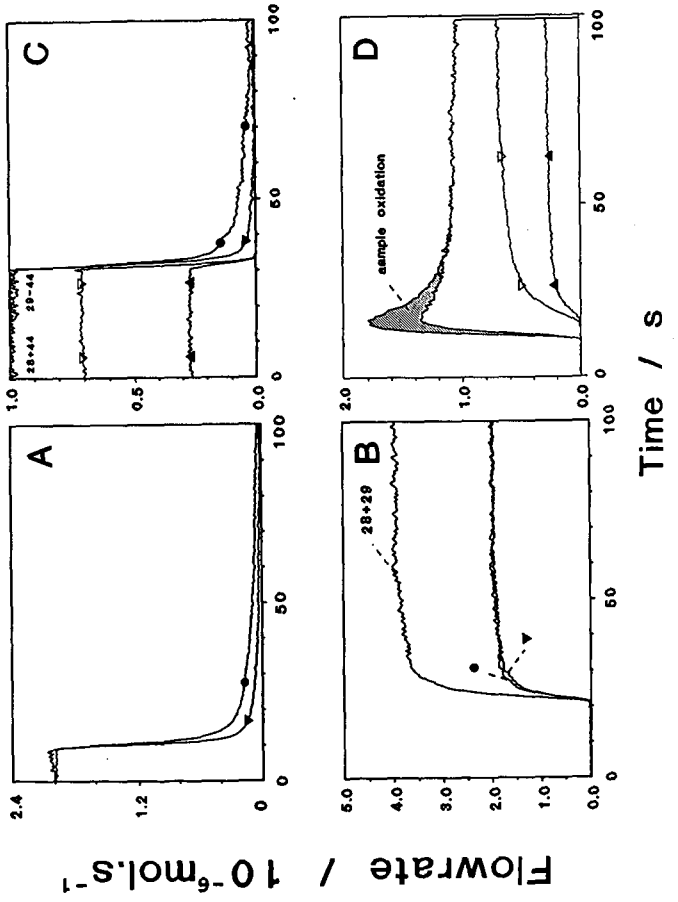

Figure 2 : Response curves for a gas phase step change from 10% $^{13}CO_2$,Ar to Ar (A,C) and *vice versa* (B,D) at different temperatures (key as in figure 1).
A,B. T = 1200 K; C,D T = 1100 K.

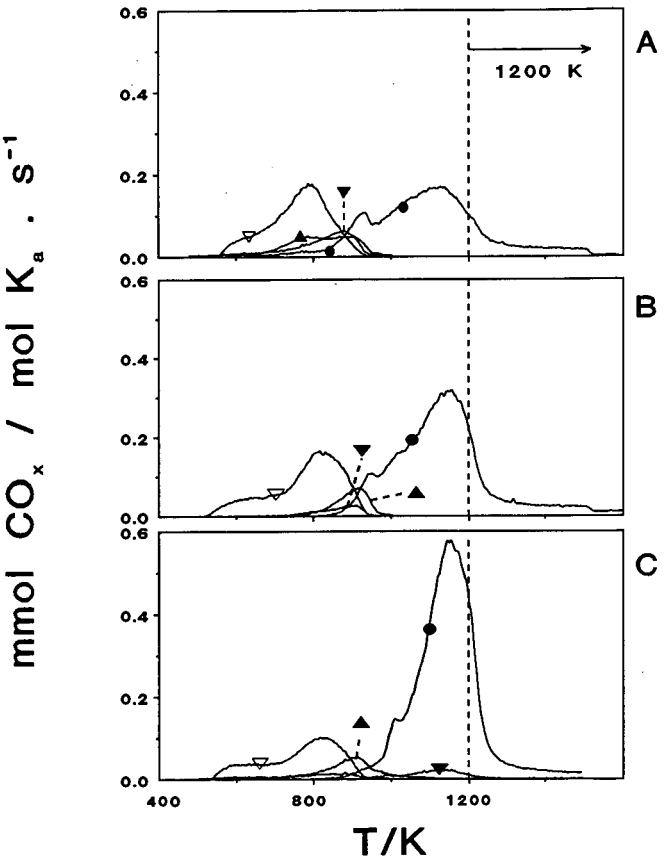

Figure 3 : TPD patterns obtained after exposure in 10% $^{13}CO_2$,Ar at: A. 673 K; B. 873 K; C. 1000 K (key as in figure 1)

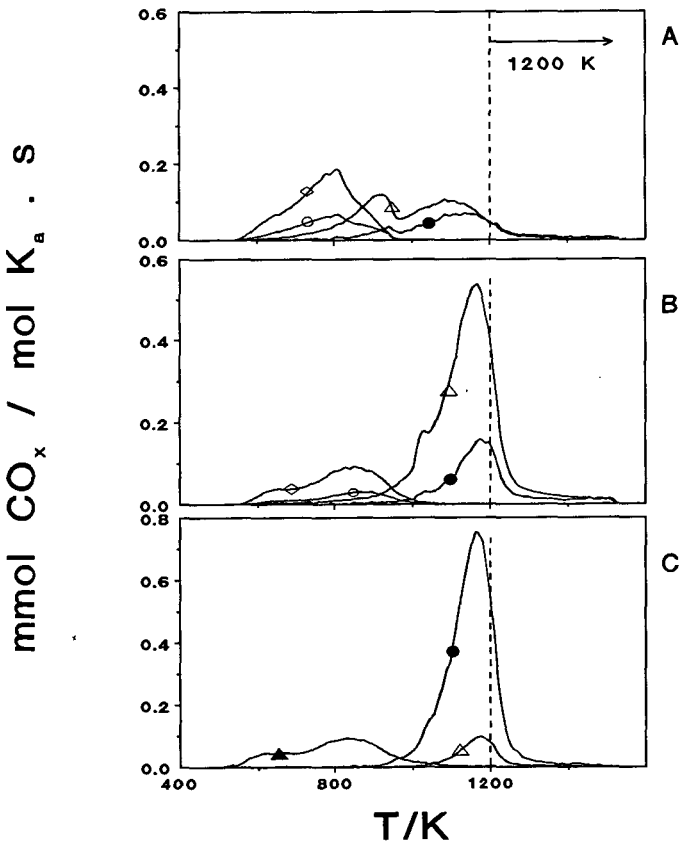

Figure 4 : TPD patterns obtained after different sample treatments:
A. $C^{18}O_2$ @ 673 K
B. $C^{18}O_2$ @ 1000 K
C. $C^{18}O_2$ @ 1000 K ⟶ CO_2 @ 1000 K (key as in figure 1)

NATURE AND STRUCTURE OF CALCIUM SPECIES DISPERSED ON CARBON: XANES AND EXAFS STUDY

Cazorla-Amorós, D., Linares-Solano, A., Salinas-Martínez de Lecea, C.
Departamento de Química Inorgánica e Ingeniería Química
Universidad de Alicante. Alicante, Spain.

Yamashita, H., Takashi, K., Tomita, A.
Institute for Chemical Reaction Science
Tohoku University. Sendai, Japan 980.

Keywords: Calcium catalyst, structure and dispersion, XANES and EXAFS.

INTRODUCTION

In a previous publication (1) the thermal behavior of calcium-carbon samples with different metal contents has been analyzed by temperature programmed desorption (TPD). The main purpose of that study was to investigate the nature and structure of calcium species dispersed on the carbon.

The most relevant aspects deduced from such study can be summarized as follow: 1) All the proton from carboxylic groups, present in the carbon surface, are ion-exchanged by Ca^{2+} ions with a 2/1 stoichiometry. 2) For calcium contents lower than the saturation of available carboxylic groups on the carbon, the ion-exchanged calcium has its coordination sphere completed with H_2O and CO_2 molecules with a coordination number of six, indicative of having an atomic distribution through the carbon matrix. 3) For high levels of calcium loading, exceeding the saturation, the ion-exchanged calcium acts as a nucleation site where crystals of calcium acetate (precursor used) grow.

TPD is not a technique which provides direct information on the structure of the analyzed species, therefore, a complementary study with an spectroscopic technique able to supply such information will be very convenient to confirm the conclusions above mentioned.

X-ray absorption fine structure spectroscopy (XAFS) has gained a great utility in the field of catalysis due to the specific information which can be obtained concerning local structure and bonds of the element examined (2-10). This technique gives information on atomic distances, coordination number and disorder degree from the interaction of the emitted electrons with the atomic environment of the absorbing atom (EXAFS) as well as information about the electronic structure and the symmetry of the atom from the multiple scattering (shape resonances) of the excited electron (XANES).

This paper presents the XANES and EXAFS results obtained with calcium-carbon samples containing different metal contents. The samples have been submitted to heat treatments at different temperatures under an inert atmosphere. The objective is to analyze the evolution of the local structure and the calcium dispersion in samples with calcium contents below and above the saturation of carboxylic groups on the carbon. The effect of pH during the ion-exchange process is also analyzed.

EXPERIMENTAL

Sample preparation was fully described in previous publications (1, 11). Briefly, a char from phenol-formaldehyde polymer resin (A) has been oxidized with HNO_3 (A2). Calcium has been introduced by

ion-exchanged with 1.5 M calcium acetate solution (the pH was not controlled) (A2-II-2.9) and at pH=10 (A2-II-4.1). Impregnation has been used to obtain other calcium contents. The impregnated samples were not washed. All calcium samples were dried at 383 K under vacuum. In the nomenclature II stands for ion-exchange and I for impregnation, and the calcium loading (wt %) is also included.

Samples have been treated in He at a flow rate of 60 ml/min at a heating rate of 20 K/min to reach different temperatures (603, 823 and 1223 K). Once the final temperature is reached, the sample is cooled down under the same atmosphere and sealed. Wafers for XAFS experiments were prepared under inert atmosphere pressing an homogeneous mixture of calcium-carbon sample and polyethylene in a ratio 2/1. Finally The samples were sealed with a polyethylene film to prevent air contact during handling.

The X-ray absorption experiments were performed at the Photon Factory in the National Laboratory for High Energy Physics (KEK-PF) Tsukuba (Japan). A Si (111) double crystal was used to monochromatize the X-ray from the 2.5-GeV electron storage ring, and the Ca K-edge absorption spectra were recorded in the transmission mode at room temperature in a range of photon energy extending from 3940 to 4720 eV. Special attention was paid to eliminate the photons from higher-order diffraction using double mirror system. Fourier Transformation was performed on k^3-weighted EXAFS oscillation, $k^3\chi(k)$, in the range of 4-10 $Å^{-1}$. The physical basis and numerous applications of XAFS spectroscopy have been discussed elsewhere (5,6,8).

RESULTS AND DISCUSSION

Reference compounds

Figure 1 presents XANES spectra and Fourier transformation of the EXAFS oscillations (FT-EXAFS) of several calcium compounds used as references. The most relevant aspects to consider are:

XANES spectra

a) Calcium oxide exhibits a pre-edge peak (I) at ≈ 4043 eV.
b) Calcium carbonate exhibits a sub-peak (II) at ≈ 4059 eV. The pre-edge peak is much less intense than in the calcium oxide.
c) Calcium acetate exhibits only one broad main peak without any sub-peak.

The pre-edge peak evolution, which is not present in the calcium acetate spectrum, is determined by the presence of different anions in the compounds: O^{2-}, CO_3^{2-}, CH_3COO^-. Differences in ionic character and symmetry originate different modification in the valence orbital of the calcium.

Fourier transform of EXAFS oscillation

A) Calcium oxide exhibits Ca-O peaks corresponding to distances ≈ 2.0 Å (uncorrected for phase shift) and Ca-Ca at ≈ 3.0 Å due to neighboring oxygen and calcium atoms respectively. Peaks appearing at higher distances correspond to Ca^{2+} and O^{2-} ions in more distant neighbor shells in the calcium oxide crystal.
B) Calcium carbonate exhibits Ca-O peaks at ≈ 1.9 Å and Ca-Ca at ≈ 3.7 Å.
C) Calcium acetate exhibits only a Ca-O peak at ≈ 2.0 Å.

Again, anions difference is the responsible of change in local atomic arrangement from one compound

to another.

Sample A2-II-2.9

Figure 2 shows the XAFS spectra (XANES and FT-EXAFS) corresponding to sample A2-II-2.9 treated at 603 K (Figure 2a, A) and 1223 K (Figure 2b, B).

According to TPD results in Figure 3 and to the interpretation given elsewhere (1), a heat treatment at 603 K does not produce carboxylic groups decomposition which occurs around 700 K. A heat treatment at 603 K only produces H_2O and CO_2 evolution. The former coming from H_2O in the carbon itself and in the coordination sphere of calcium. The second arising from CO_2 chemisorbed on calcium ion-exchanged. This interpretation is fully confirmed by XAFS results as will shall discuss now. XANES spectrum (Figure 2a) presents a broad main peak without any shoulder. FT-EXAFS oscillations exhibit only one Ca-O peak at $\approx$ 2.0 Å and no Ca-Ca peak is present. Comparing these spectra with those of reference compounds a large similarity is found with calcium acetate. This indicates that calcium is still linked to carboxylic groups at 603 K, in agreement with published results (1, 2).

The presence of a small pre-edge peak (III) in XANES spectrum (Figure 2a) indicates that coordination of oxygen atoms around calcium atom is somewhat distorted from an ideal octahedral symmetry (3, 4, 10). The evolution of H_2O and CO_2 from the coordination sphere of calcium during heat treatment at 603 K can explain this distortion.

Sample treatment at 1223 K produces important modifications in XAFS spectra. XANES spectrum (Figure 2b) shows the presence of a new pre-edge peak around 4043 eV (I) in addition to a shoulder around 4065 eV. The intensity of the pre-edge peak (III) slightly decreases in relation to that of sample treated at 603 K. FT-EXAFS spectrum (Figure 2B) presents a Ca-O peak $\approx$ 2.0 Å beside a very weak Ca-Ca peak, indicating that most of the calcium species are highly dispersed and/or forming amorphous small cluster with spectra characteristics similar to those of CaO (Figure 1 a, A) (3). These results are also in good agreement with previous results in which a high calcium dispersion was found when this sample was submitted to a similar heat treatment. Using CO_2 chemisorption the dispersion was 55 % (12).

Sample A2-II-4.1

This sample has been prepared by ion-exchange with a controlled pH of 10 unlike sample A2-II-2.9 which has been prepared by the same procedure but with the pH proper of the calcium acetate solution in contact with the carbon.

Figure 4 presents the TPD spectrum of sample A2-II-4.1. The most relevant aspect to be observed is the presence of a CO_2 peak at around 1050 K which does not appear in the TPD profile of sample A2-II-2.9 (Figure 3). This CO_2 peak presumably come from the $CaCO_3$ formed during sample preparation and not from calcium acetate, since no peak of mass 43 (characteristic of acetate) is present (1). Working at a high pH values, calcium carbonation is very probable and this will explain the above suggestion. The amount of calcium forming carbonate can be quantified from the CO_2 + 1/2 CO corresponding to this second peak. The amount obtained by this method is 0.5 wt%, therefore, the calcium ion exchanged would be 3.6 wt% which is in good agreement with the maximum calcium exchange capacity (3.5 wt%) of carbon A2 (1, 11).

XANES and FT-EXAFS spectra of sample A2-II-4.1 treated at 1223 K, appearing in Figure 5, present characteristics of CaO as in sample A2-II-2.9, but the peak intensity for the Ca-Ca peak is quite larger in the former indicating that part of the calcium is present as CaO particles with an structural order at longer range than the first coordination shell.

The disappearance of the pre-edge peak at ≈ 4040 eV indicates a smaller distortion of the calcium coordination sphere (in respect to that of sample A2-II-2.9) which again confirms the existence of a longer range order in CaO beyond the first coordination sphere. Probably, this increase in particle size from sample A2-II-2.9 to A2-II-4.1 is due to the presence of $CaCO_3$ formed during the sample preparation, as mentioned before.

Samples A2-I-6.0 and A2-I-9.4

Calcium content in these samples is larger than the maximum ion-exchange capacity of the carbon (3.5 wt%). According to the interpretation previously mentioned (1, 11), calcium in excess appears as calcium acetate crystals over the ion-exchanged one. These conclusions arise from the TPD study on these samples as well as from TG-DTA and XRD (11). TPD spectra present a peak of mass 43 at around 730 K coming from the calcium acetate decomposition and peaks of CO_2 and CO at ≈ 1030 K produced in the $CaCO_3$ decomposition (1).

To distinguish between different steps in calcium acetate decomposition, samples have been treated at different temperatures before XANES and FT-EXAFS spectra were recorded. Sample A2-I-6.0 has been treated at 823 and 1223 K, the results appear in Figure 6. Sample A2-I-9.4 has been treated at 603, 823 and 1223 K and the spectra are shown in Figure 7.

Heat treatment up to 603 K produces CO_2 and H_2O evolution from: a) the carbon (adsorbed H_2O), b) the calcium acetate (H_2O of crystallization) and c) the ion-exchanged calcium (CO_2 and H_2O coordinated). Calcium acetate remain unchanged.

From XANES and FT-EXAFS spectra similar conclusions are obtained. Figure 7 a, A shows the presence of only one broad peak in XANES spectrum and a quite intense Ca-O peak in FT-EXAFS similar to those of calcium acetate. Furthermore, the pre-edge peak (III) at ≈ 4040 eV is smaller than that for sample A2-II-2.9 treated at the same temperature (Figure 2 a, A) indicating a higher order at longer distance.

Spectra obtained after a treatment at 823 K exhibits characteristics of $CaCO_3$ in agreement with previous results (1, 11). It is interesting to observe the decrease of the pre-edge peak (at ≈4030 eV) from the spectrum of sample A2-I-6.0 to that of A2-I-9.4 which is indicative of a higher order at longer distance presents in $CaCO_3$ particle for the second sample. This observation is confirmed with the fact that Ca-Ca peak intensity is much higher for sample A2-I-9.4 than A2-I-6.0.

Finally, a heat treatment at 1223 K produces $CaCO_3$ decomposition to yield CaO (1, 11). This is also observed in Figures 6 b, B and 7 c, C. The spectra exhibit clearly the CaO characteristics. By comparison of FT-EXAFS results of samples heat treated up to 1223 K as a function of calcium content it is clear that as the calcium content increases the spectra look more similar to those of bulk calcium oxide. Therefore the CaO particle size increase in agreement with previous results (1, 11). Calcium dispersion was found to decrease from 0.55 (sample A2-II-2.9)to 0.35 (sample A2-I-9.4).

CONCLUSIONS

Sample with calcium content below the ion-exchange capacity of the carbon has, after heat treatment, most of the calcium species highly dispersed forming amorphous small cluster of CaO. Increasing pH, during ion-exchange, the calcium loading increases, however, a partial carbonation occurs leading to a particle size increase after heat treatment.

XANES and FT-EXAFS results in samples heat treated up to 1223 K clearly show that as calcium content increases the spectra look more similar to those of bulk calcium oxide indicating an increase in in CaO particle size.

XANES and FT-EXAFS study fully confirms previous conclusions obtained in the TPD study carried out in these samples.

REFERENCES

1. Linares-Solano, A., Salinas-Martínez de Lecea, C., Cazorla-Amorós, D., Joly, J. P. and Chacosset, H. Energy & Fuels **4**, 467-474 (1990).
2. Huggins, F. E.., Huffman, G. P., Lytle F. W. and Greegor, R. B. Proc. Int. Conf. Coal Science, Pittsburgh PA, USA, p.679, (1983).
3. Huggins, F. E., Huffman, G. P., Shah, N. Jenkins, R. G., Lytle, F. W. and Greegor, R. B. Fuel, **67**, 938, (1988).
4. Huggins, F. E., Shah, N., Huffman, G. P., Lytle, F. W., Greegor, R. B. and Jenkins, R. G. Fuel, **67**, 1663, (1988).
5. Sinfelt, J. H., Via, G. H. and Lytle, F. W. Catal. Rev. Sci.-Eng., **26**(1), 81, (1984).
6. Lytle, F. W., Greegor, R. B., Margnes, E. C., Biebesheimer, V. A., Sandstrom, D. R., Horsley, J. A., Via, G. H. and Sinfelt, J. H. Catalyst Characterization Science. Surface and Solid State Chemistry, Eds. M.L. Deviney y J.L. Gland, ACS, Washington, D.C., p.253, (1985).
7. Claisen, B. S., Topsøe, H., Candía, R., Villadsen, R., Lengeler, B., Als-Nielsen J. Christensen, F. J. Phys. Chem., **85**(25), 3869, (1981).
8. Chiu, N. S., Bauer S. H. and Johnson, M. F. L. J. Catal., **89**, 226, (1984).
9. Chiu, N. S., Bauer S. H. and Johnson, M. F. L. J. Catal., **98**, 32, (1986).
10. Yamashita, H. and Tomita, A. Photon Phactory Activity Report, #8, (1991).
11. Salinas-Martínez de Lecea C., Almela-Alarcón, M. and Linares-Solano, A. Fuel, **69**, 21, (1990).
12. Linares-Solano, A., Almela-Alarcón, M. and Salinas-Martínez de Lecea, C. J. Catal., **125**, 401, (1990).

ACKNOWLEDGEMENTS

The authors thank to the DGICYT (proyect PB-88-0295), to the MEC for the fellowship of D. Cazorla to travel to Tohoku University and to the Institute for Chemical Reaction Science, Tohoku University.

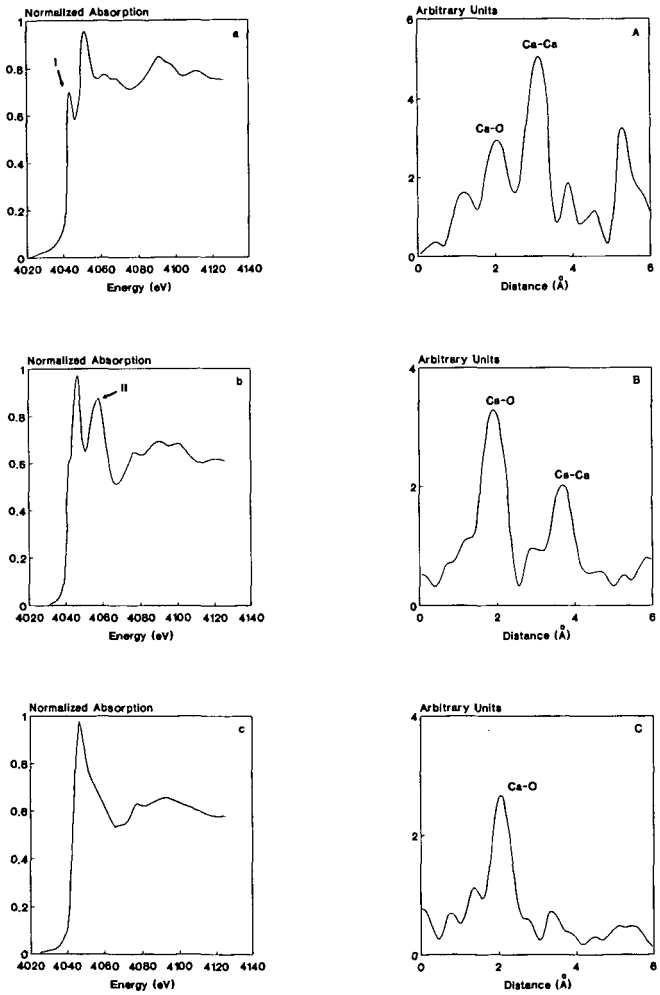

Figure 1. XANES spectra (a, b, c) and FT-EXAFS (A, B, C) of reference compounds: a, A) calcium oxide; b, B) calcium carbonate and c, C) calcium acetate.

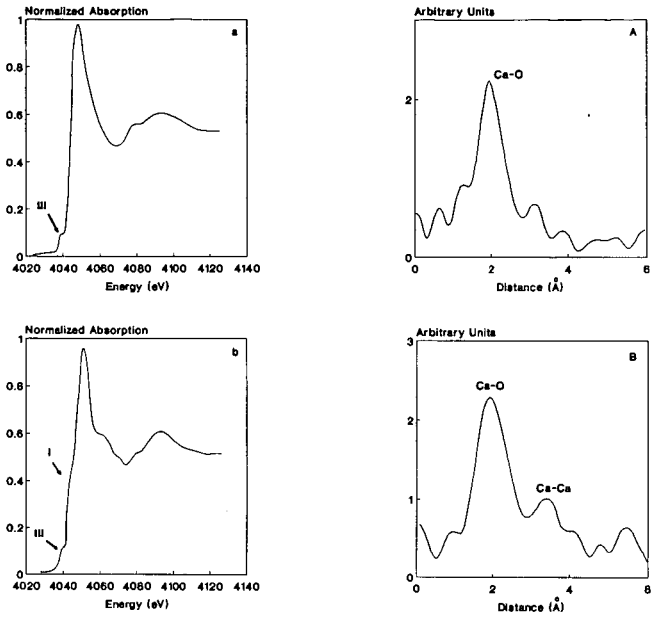

Figure 2. XANES spectra (a, b) and FT-EXAFS (A, B) of sample A2-II-2.9 after heat treatment at: a, A) 603K and b, B) 1223K.

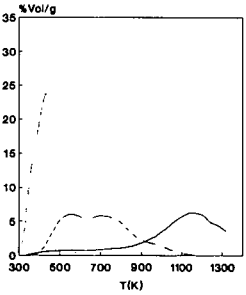

Figure 3. TPD spectrum of sample A2-II-2.9 (···, H_2O; —, CO; ---, CO_2).

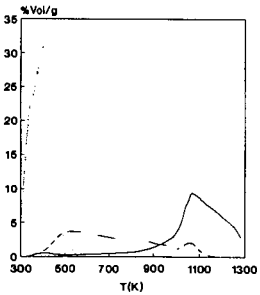

Figure 4. TPD spectrum of sample A2-II-4.1 (···, H_2O; —, CO; ---, CO_2).

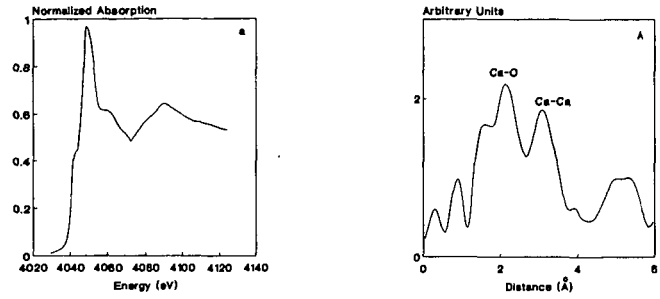

Figure 5. XANES spectra and FT-EXAFS of sample A2-II-4.1 after heat treatment at 1223 K.

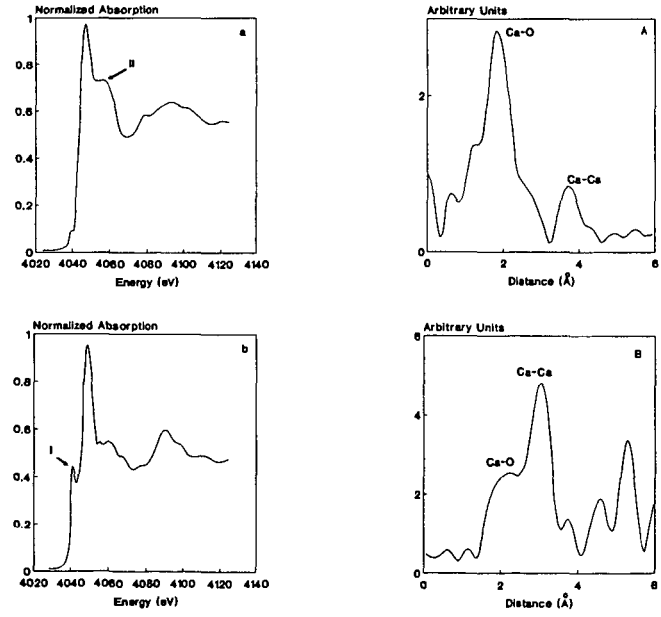

Figure 6. XANES spectra (a, b) and FT-EXAFS (A, B) of sample A2-I-6.0 after heat treatment at: a, A) 823 K and b, B) 1223 K.

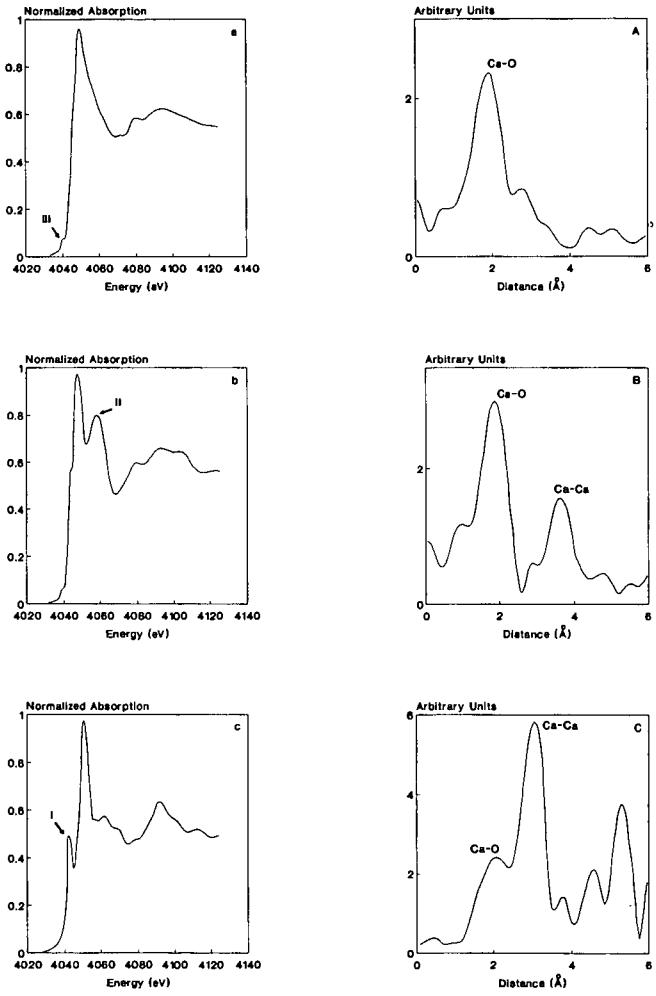

Figure 7. XANES spectra (a, b, c) and FT-EXAFS (A, B, C) of sample A2-I-9.4 after heat treatment at: a, A) 603 K; b, B) 823 K and c, C) 1223 K.

INFLUENCE OF OXYGEN FUNCTIONAL GROUPS ON THE PERFORMANCE OF CARBON-SUPPORTED CATALYSTS

C.A. Leon y Leon and L.R. Radovic

Fuel Science Program, Department of Materials Science and Engineering
The Pennsylvania State University, University Park, PA 16802

Keywords: Oxygen Functional Groups, Carbon-Supported Copper, Gasification Catalysts

INTRODUCTION

Efficient catalyst supports are materials capable of increasing the dispersion (or *percentage exposed*) of a catalyst by virtue of their physical (e.g., high surface area) and chemical (e.g., ion exchange) properties [1,2]. Numerous reports dealing with how these properties affect the performance of a variety of supported catalysts have led in many cases to improvements in their preparation [2]. The development of carbon-supported catalysts has not paralleled that of, e.g., metal oxide supports, mainly because the much richer surface chemistry of carbons complicates their characterization. Paradoxically, their rich surface chemistry makes carbons very attractive, yet poorly exploited, support materials [3]. Indeed, the open literature is very scarce in reports dealing with systematic variations of carbon properties in relation to catalyst performance [3-6]. Such variations are difficult to attain because the treatments that change the chemistry of a carbon can also change its physics, and vice versa. However, by carefully following the physical and chemical changes that accompany selected oxidative and/or thermal treatments of highly pure carbons, it has become possible to produce materials with similar oxygen content and equivalent surface areas, which nonetheless differ substantially in their specific oxygen functional group content. These supports have been loaded with a number of metals and exposed to different reaction conditions (e.g., carbon gasification in 0.1 MPa air) in order to test their performance [7]. The aim of this paper is to illustrate how the surface chemistry of carbons can be tailored to enhance the performance of carbon-supported catalysts, using the copper-catalyzed gasification of carbon as an example.

EXPERIMENTAL

Carbon Supports. For clarity, only selected results for a highly pure polymer-derived microporous carbon (Saran 928, Dow) are presented in this report; further details and results on meso- and nonporous carbons will be given elsewhere [7]. Batches of the starting material were subjected to pyrolysis (in N_2) and/or oxidation (in air, H_2O_2 or HNO_3) treatments at different conditions (i.e., different temperatures, reactant concentrations and exposure times) in order to modify their surface properties [7-9]. Changes in physical properties were followed by N_2 and CO_2 adsorption [8,9], X-ray diffraction (XRD) [8,9], and others [7], while chemical modifications were monitored via acid/base neutralizations [8-10], temperature-programmed desorption (TPD) [8,9], electrophoresis [3,8], mass titration [8] and X-ray photoelectron spectroscopy (XPS) [7,9], among others [7,11]. The three samples chosen (henceforth referred to as CA, CN and CB) were found to resemble each other the most in terms of their physical properties, while differing substantially in their surface chemistry. Samples CA, CN and CB were prepared by oxidation in boiling concentrated H_2O_2 for 15 min, oxidation in dry flowing dry air at 673 K for 3 h, and oxidation in air at 673 K for 24 h followed by pyrolysis in N_2 at 923 K for 3 h, respectively [8,11]. The active surface area, ASA (at 373 K), and the uncatalyzed gasification reactivities of each support in 0.1 MPa flowing air were measured on a modified TGA-7 apparatus (Perkin-Elmer) under diffusion-free reaction conditions [9,12].

Carbon-Supported Copper Catalysts. Samples CA, CN and CB were impregnated with aqueous (pH ca. 5.3) copper acetate (Fisher) by incipient wetness to yield 5% Cu catalysts (dry carbon basis). In addition, the adsorption capacity for Cu ammines at pH = 11.5 was determined using a Cu^{+2} ion selective electrode (Orion) coupled to a Fisher Accumet 925 pH meter [9]. The resulting catalysts were characterized by XPS, XRD and oxygen chemisorption at 373 K [12], and their gasification reactivity in 0.1 MPa air was evaluated as described above for the supports alone.

RESULTS AND DISCUSSION

Surface Chemistry and Physics of the Supports Used. Both TPD (Table 1) and ultimate analyses [7] indicated that carbons CA, CN and CB have similar oxygen contents. In all cases, the difference PZC-IEP fell within 1.6-2.3 pH units (Table 1), indicating (as discussed elsewhere [8,9]) that the external (geometric) surface of these materials is enriched in negative surface charges relative to their internal (porous) surface. However, the IEP and PZC values do not reflect the large differences in surface chemistry observed by contact angle measurements [11] or by oxygen functional group analysis (see Figure 1). Indeed, large differences in their oxygen functional group content are evidenced by their CO/CO_2 evolution ratios (mol/mol) upon TPD (Table 1). Since CO_2- and CO-evolving groups are thought to be produced primarily by the decomposition of strongly acidic (carboxyl, lactone) and weakly acidic (phenol, carbonyl) oxygen complexes [13-15], the CO/CO_2 evolution ratios can be taken as a measure of surface acidity, with lower ratios representing more strongly acidic surfaces [7,11]. Therefore, CO/CO_2 ratios have been used throughout this report as indicators of the differences in functional group quality among these samples.

Before examining Figure 1 in detail, let us consider the structural differences among samples CA, CN and CB. The corresponding changes in equivalent surface areas are shown in Figure 2. The three samples exhibited very similar N_2 isotherms at all partial pressures [7], with BET equivalent surface areas in the range 848-886 m^2/g. In a recent report dealing with Pt dispersion over an unspecified microporous carbon black and its H_2- and H_2O_2-treated derivatives, it was assumed that the observed similarity in N_2 isotherm shapes and in BET surface areas (between 895 and 956 m^2/g) indicated that differences in Pt dispersion were not related to the physical properties of the supports used, but to their oxygen functional group content [16]. Figure 2 shows that N_2 isotherms alone do not suffice to neglect any physical differences among microporous samples. Indeed, sample CA, pretreated with H_2O_2, has a significantly higher (and reproducible) Dubinin-Radushkevich (DR) surface area than that of samples CN and CB (Figure 2). Even though the actual physical meaning of equivalent surface areas of microporous materials is open to question [17,18], N_2 and CO_2 equivalent surface areas provide complementary information about the structure of a carbon [17]. Accordingly, sample CA appears to differ from samples CN and CB in that it contains a number of narrow micropores inacessible (within reasonable time) to N_2 at 77 K [17]. These narrow micropores, either generated or opened by the H_2O_2 pretreatment, are also likely to offer litlle access to hydrated metal ions in solution. Hence, for catalyst preparation purposes the accessible surface areas of samples CA, CN and CB can be taken to be of comparable magnitude [16].

In light of the above observations, it is possible to estimate the distribution of specific functional group types from the data in Figure 1 and using the following assumptions [10,13-15]:

- NaOH titrates carboxyl, lactone and phenolic groups [10];
- $NaHCO_3$ titrates carboxyl groups only [10];
- CO desorption arises from phenolic and carbonyl groups only [15]; and
- CO_2 desorption arises from carboxyl and lactone groups only [15];

The individual content of each surface group type can then be calculated from [13,15]:

- Carboxyl groups = groups titrated with $NaHCO_3$;
- Lactone groups = groups desorbed as CO_2 minus those titrated with $NaHCO_3$;
- Phenol groups = groups titrated with NaOH minus those desorbed as CO_2; and
- Carbonyl groups = groups desorbed as CO plus CO_2 minus those titrated with NaOH.

The calculated functional group contents are listed in Table 2. Because of the numerous assumptions involved in their estimates, the numbers in Table 2 must be regarded as qualitative only [13,15]. Nonetheless, Table 2 shows that the increase in surface acidity with decreasing CO/CO_2 evolution ratio is likely to be due to increases in the concentrations of both carboxyl ($pKa \approx 4.4$) and lactone ($pKa \approx 8.2$) groups [19]. The apparent absence of phenolic groups in sample CA is probably related to the diffusion-limited accessibility of NaOH to some phenol group-containing narrow micropores (Figure 2). In all cases the total oxygen coverages [20] amounted to ca. 12-17% of the N_2-BET surface areas.

Surface Chemistry vs. Uncatalyzed Carbon Gasification. Carbon supports can undergo thermal degradation when exposed to high temperatures and/or reactive environments. Because most carbons have already experienced heat treatments during their preparation, thermal degradation below, e.g., 773 K, is relatively minor in inert or reducing conditions, but can be important in oxidizing environments. Figure 3 shows the influence of oxygen functional groups on the uncatalyzed rate of gasification of the supports. The gasification reactivity of the carbon supports was found to increase with increasing surface acidity. A similar increase (ca. 20%) in active surface area, ASA [21], was also determined. (Indeed, a remarkably similar turnover frequency, or reactivity per active site, of ca. 5 s^{-1} is yielded by all supports at these conditions.) Clearly, the total surface areas (Figure 2) fail to correlate with either reactivity or ASA variations, as expected because (a) the surfaces probed by adsorbates at low temperatures ($\leq$ 298 K) are not necessarily related to the surfaces remaining at reaction conditions (i.e., after high temperature treatments), particularly if the desorbable oxygen content of the carbons is high, and (b) only a portion of the surface (the most reactive [20-23]) participates directly in the gasification process. Figure 3 suggests that the thermal treatment of surfaces rich in acidic (carboxyl, lactone) groups produces more active sites than that of surfaces rich in CO-desorbing (carbonyl, phenol) oxygen complexes. Mechanistic interpretations of Figure 3 will be addressed at length elsewhere [7].

Surface Chemistry vs. Copper Adsorption and Distribution. Metal sorption onto a support is considered necessary in order to attain a high catalyst dispersion [2,3]. Carbon materials are more flexible than most conventional (e.g., metal oxide) supports in that their surfaces can be modified to contain different kinds and amounts of surface sites [7-9], as discussed above. In an accompanying report [9] preliminary evidence suggesting the participation of lactone-type groups (in addition to carboxyl groups) to the sorption of copper by modified Saran carbons was presented. Further evidence can be gathered from Tables 1 and 2. Table 1 lists the amounts of copper taken up (primarily as Cu^{+2} ammine complexes [9]) by each support at pH = 11.5. These amounts are proportional to, but clearly exceed, the estimated carboxyl group content of each support (Table 2). Since the maximum possible stoichiometry (at equilibrium) for site-specific adsorption of divalent cations on dissociated carboxyl anions is 1:1 (i.e., $\{\text{-COO}^{-}\text{---}[Cu(NH_3)_n(H_2O)_{6-n}]^{+2}\text{---}(OH)^{-}\}$; $1 \leq n \leq 5$), carboxyl groups alone cannot accomodate all the adsorbed copper. Oxygen functional groups with intermediate (lactone-type) or lower (phenolic-type, pKa $\approx$ 10 [19]) acid strength could also serve as adsorption sites. If both lactone and carboxyl groups participated in the copper adsorption process, at equilibrium a constant Cu/CO_2 ratio could be expected, with Cu/CO_2 = 1 resulting from a either 1:1 exchange or the decomposition of adjacent carboxyl sites [9,10,24], and $Cu/CO_2 \approx 0.5$ resulting from a 1:2 exchange on adjacent sites [10]. Similar arguments can be raised about the Cu/NaOH ratio, if carboxyl, lactone and phenol groups participated simultaneously in the adsorption process. As shown in Table 1 and elsewhere [9] the Cu/CO_2 ratios for modified Saran chars fluctuate between 0.32 and 0.87, with values > 0.5 corresponding to air- (vs. liquid phase-) oxidized carbons. Cu/NaOH ratios, on the other hand, are in some instances very low (see Table 1; the exception, i.e., that of sample CA, is again related to the limited accessibility of NaOH to some of its phenol group-containing narrow micropores, as mentioned earlier). These data can be understood by postulating that copper cations interact with oxygen complexes on carbons in order of decreasing acidity, i.e., carboxyl > lactone > phenol. Once most accessible dissociated carboxyl groups are populated, additional copper cations begin to adsorb onto dissociated lactones and, subsequently, onto dissociated phenol groups. (The transition between each group range is not sharp but rather smooth, judging from the corresponding copper adsorption isotherms [7,9].) Table 1 suggests that both carboxyl and lactone groups participate in Cu^{+2} ammine adsorption at pH = 11.5, giving Cu/CO_2 ratios close to 0.5, i.e., one divalent cation for every two negatively charged groups (or $Cu/CO_2 > 0.5$ for surfaces presumably containing some isolated sites). Phenol groups appear to contribute little towards copper adsorption at these conditions. For samples CA, CN and CB, copper saturation uptakes of ca. 2.0, 1.1 and 0.3 wt.% were determined, indicating that it is not the total oxygen content of a carbon (Table 1) but its quality (Table 2) that controls the cation adsorption process.

Drying the samples containing an excess (5 wt.%) Cu leaves in all cases well dispersed metal precursors; these yield no copper XRD patterns and block a portion of the micropores, since the BET and DR surface areas decrease upon loading by ca. 60 % and 30-50 %, respectively [7]. Figure 4 shows that the XPS ratios of the dried samples approach in all cases that of the salt (acetate) used for their preparation. The most significant difference among the dried samples was an upwards shift in

binding energy with increasing support acidity (Table 1). (In agreement with this, higher Cu loadings of nonacidic carbons were found to produce XRD patterns consistent with the formation of Cu^{+1} species [25].) Unsurprisingly, sintering the catalysts (in N_2 at 623 K) reduced the Cu/C XPS ratios to values ca. 5 times higher than bulk catalyst values (Figure 4), suggesting a significant external surface enrichment by Cu in all cases. In spite of this external surface enrichment by Cu, the dispersion (or fraction exposed) of Cu on each catalyst was estimated to be relatively high, and to go through an apparent maximum for carbons of intermediate surface acidity (Figure 5). Figure 5 suggests that maximizing Cu adsorption (Table 1) does not necessarily lead to the highest Cu dispersion; indeed, as discussed below the thermal stability of the adsorbed complex must also be taken into consideration.

Influence of Surface Functional Groups on the Copper-Catalyzed Gasification of Carbon. Besides promoting a high and stable initial catalyst dispersion, oxygen functional groups can affect the sintering behaviour, the degree of reduction, the volatility, etc., of a supported metal. In the case of the catalyzed gasification of carbon, the support itself is a reactant, and the oxygen complexes are deemed to participate as reaction intermediates. Since Cu-catalyzed gasification rates exceed uncatalyzed rates by 10^2-10^3 [9], the initial surface chemistry of the support (Figure 3) has little bearing on the former other than its influence on the state of the catalyst at reaction conditions. Figure 6 shows that for low sintering temperatures the most active catalyst is the one with the highest Cu dispersion (Figure 5). In contrast, after sintering the catalysts at $\geq$ 923 K the most acidic supports provided the highest reactivity. Hence, the most adequate surface chemistry for Cu/C catalysts is seen to depend strongly on the conditions of its utilization. Sintering up to 923 K, which causes primarily the decomposition of CO_2-evolving groups [8], is accompanied by a drastic drop in reactivity, in particular for the least acidic carbons (Figure 7). Further sintering up to 1223 K, which parallels the desorption of CO-evolving groups [8], causes minor losses in reactivity, in particular for the most acidic carbons, whose small Cu particles are only then free to migrate and lose dispersion by their coalescence.

CONCLUSIONS

Oxygen functional groups influence virtually all stages of utilization of carbon-supported catalysts. The importance of the surface chemistry of carbon supports is strongly dependent on the end use of the catalyst. More than the quantity of oxygen it is the quality (type) of oxygen groups that controls the extent of metal precursor sorption, its distribution throughout the support, the resistance to active phase agglomeration upon drying/reduction, and ultimately the performance of carbon-supported catalysts.

REFERENCES

1. M. Boudart and G. Djega-Mariadassou, in "Kinetics of Heterogeneous Catalytic Reactions," Princeton University Press, Princeton (1984), Ch. 6.
2. J.R. Anderson, "Structure of Metallic Catalysts," Academic Press, New York (1975), Ch. 2.
3. J.M. Solar, C.A. Leon y Leon, K. Osseo-Asare and L.R. Radovic, *Carbon* **28**, 369 (1990).
4. A.J. Bird, in "Catalyst Supports and Supported Catalysts" (A.B. Stiles, Ed.), Butterworths, London (1987), Ch. 5.
5. H. Jungten, *Fuel* **65**, 1436 (1986).
6. P. Ehrburger, *Adv. Colloid Interface Sci.* **21**, 275 (1984).
7. C.A. Leon y Leon and L.R. Radovic, in preparation.
8. C.A. Leon y Leon, J.M. Solar, V. Calemma, K. Osseo-Asare and L.R. Radovic, *Carbon*, Submitted (1991).
9. C.A. Leon y Leon and L.R. Radovic, "Effect of Thermal and Chemical Pretreatments on the Copper-Catalyzed Gasification of Carbon in Air," ACS Preprints, Div. Fuel Chem., New York (1991), in print.
10. (a) H.P. Boehm, E. Diehl, W. Heck and R. Sappok, *Angew. Chem. Internat. Edit.* **3**, 669 (1964); (b) H.P. Boehm, *Advan. Catal.* **16**, 179 (1966).
11. C.A. Leon y Leon, V. Calemma and L.R. Radovic, "Surface Chemical Heterogeneity of Oxidized Carbon Particles," 20th Biennial Conf. on Carbon, Santa Barbara, CA, June 23-28, 1991, p. 30.
12. C.A. Leon y Leon and L.R. Radovic, Proc. Int. Carbon Conf., Paris, France (1990), p. 44.
13. K. Kinoshita, in "Carbon: Electrochemical and Physicochemical Properties," Wiley, New York (1988), Ch. 3.
14. B.R. Puri, in "Chemistry and Physics of Carbon" (P.L. Walker, Jr., Ed.), Vol. 6, Dekker, New York (1970), p. 191.
15. D. Rivin, *Rubber Chem. Technol.* **44**, 307 (1973).
16. C. Prado-Burguete, A. Linares-Solano, F. Rodriguez-Reinoso and C. Salinas-Martinez de Lecea, *J. Catal.* **115**, 98 (1989).
17. F. Rodriguez-Reinoso and A. Linares-Solano, in "Chemistry and Physics of Carbon" (Edited by P.A. Thrower), Vol. 21, Marcel Dekker, New York (1989), p. 1.
18. H. Marsh, *Carbon* **25**, 49 (1987).

19. J.S. Mattson and H.B. Mark, Jr., "Activated Carbon," Marcel Dekker, New York (1971), p. 41.
20. N.R. Laine, F.J. Vastola and P.L. Walker, Jr., *J. Phys. Chem.* **67**, 2030 (1963).
21. I.M.K. Ismail and P.L. Walker, Jr., *Carbon* **27**, 549 (1989).
22. L.R. Radovic, A.A. Lizzio and H. Jiang, in "Fundamental Issues in Control of Carbon Gasification Reactivity" (J. Lahaye and P. Ehrburger, Eds.), Kluwer, the Netherlands (1991), p. 235.
23. G.R. Hennig, in "Proceedings of the 5th Conference on Carbon," Vol. I, Pergamon Press, New York (1962), p. 143.
24. A. Linares-Solano, C. Salinas-Martinez de Lecea and D. Cazorla-Amoros, *Energy & Fuels* **4**, 469 (1990).
25. P. Ehrburger, J.M. Henlin and J. Lahaye, *J. Catal.* **100**, 429 (1986).

Table 1. Features of Modified Saran Carbons Used as Cu Catalyst Supports.

Sample	%O [wt.]	CO/CO_2[a] [mol/mol]	IEP[b]	PZC[b]	B.E.[c] [eV]	Cu ads.[d] [mmol/g]	Cu/CO_2[e] [mol/mol]	Cu/NaOH[e] [mol/mol]
CA	5.0	2.18	3.85	5.74	934.7	0.32	0.43	1.24
CN	4.5	7.29	3.65	5.23	933.7	0.17	0.58	0.14
CB	3.3	13.9	5.25	7.53	932.8	0.04	0.32	0.05

[a] CO/CO_2 evolution ratio upon TPD.
[b] IEP: isoelectric point (by electrophoresis); PZC: point of zero charge (by mass titration).
[c] B.E.: XPS copper $2p_{3/2}$ peak binding energy (freshly dried catalysts).
[d] Amount of copper withdrawn from solution at pH=11.5 (adjusted using NH_4OH).
[e] Ratio of Cu adsorbed to CO_2 evolved (TPD) and acidic groups titrated with NaOH.

Table 2. Estimated Functional Group Content of Modified Saran Carbons.

Sample	Carboxyl		Lactone		Phenol		Carbonyl	
	[mmol/g]	%	[mmol/g]	%	[mmol/g]	%	[mmol/g]	%
CA	0.23	11	0.52	24	0	0	1.37	65
CN	0.05	2	0.25	11	0.96	44	0.93	43
CB	0.01	1	0.12	7	0.69	38	0.99	54

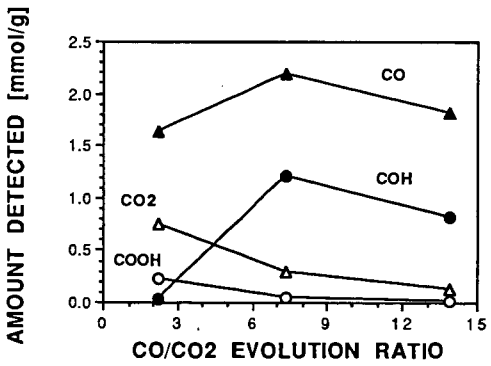

Figure 1. Variation in Oxygen Functional Group Content with CO/CO_2 Evolution Ratio (upon TPD) of Modified Saran Carbons. Triangles: amounts of CO_2 (**CO2**, or carboxyl plus lactone [15]) and of CO (**CO**, or phenol plus carbonyl) evolved upon TPD; Circles: amounts of acidic groups titrated using $NaHCO_3$ (**COOH**, or carboxyl [10]) and NaOH minus $NaHCO_3$ (**COH**, or lactone plus phenol [10]).

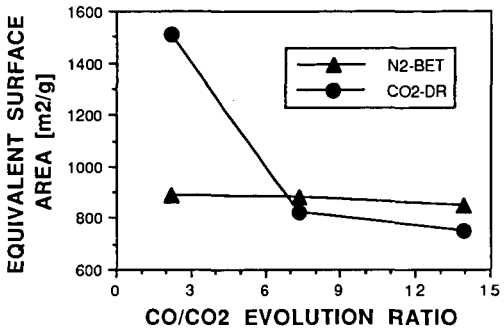

Figure 2. Equivalent Surface Areas of Modified Saran Carbons, Estimated From Volumetric N_2 (77 K) and CO_2 (298 K) Adsorption Isotherms Using the BET and Dubinin-Radushkevich (DR) Equations, respectively.

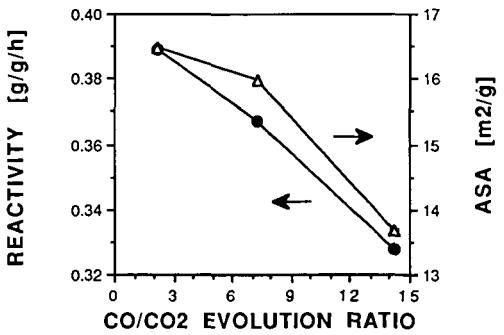

Figure 3. Influence of Oxygen Functional Groups on the Uncatalyzed Gasification Reactivity (773 K, 0.1 MPa air) and on the Active Surface Area, ASA (373 K), of Modified Saran Carbons.

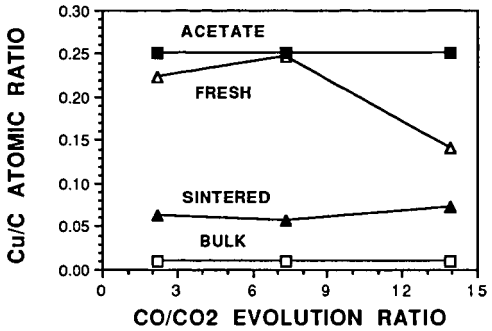

Figure 4. Comparison of Copper-to-Carbon XPS Ratios of Dried and of Sintered (in N_2 at 623 K) 5% Cu/Saran Catalysts With Those of the Precursor Salt (Acetate) and the Bulk Catalysts.

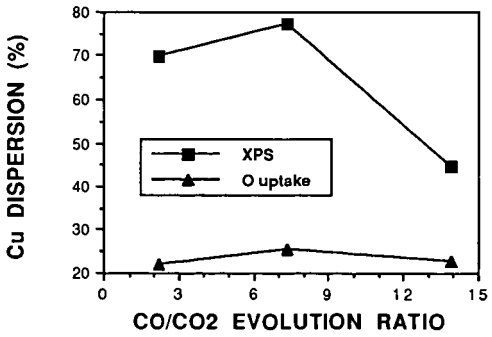

Figure 5. Copper Dispersion Over Modified Saran Carbons After Sintering 5% Cu/Support Catalysts in N_2 at 623 K, Estimated From XPS and Oxygen Chemisorption Data.

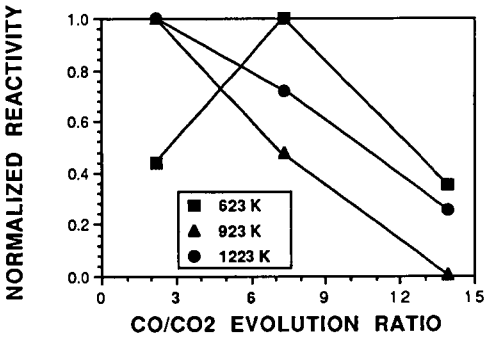

Figure 6. Influence of Carbon Surface Chemistry on the Normalized Gasification Reactivity (in 0.1 MPa air, Extrapolated to 623 K) of 5% Cu/Saran Catalysts Following Heat Pretreatments (in N_2) at Temperatures Shown.

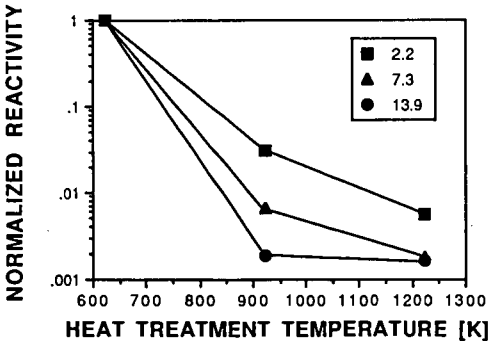

Figure 7. Effect of Heat Pretreatment on the Normalized Gasification Reactivity (in 0.1 MPa air, Extrapolated to 623 K) of 5% Cu/Saran Catalysts for Different Initial Surface Chemistry.

A POST-BUCKMINSTERFULLERENE VIEW OF CARBON CHEMISTRY

Harold Kroto
School of Chemistry and Molecular Sciences,
University of Sussex, Brighton, BN1 9QJ UK

Keywords: C_{60}, Fullerenes, carbon particles

INTRODUCTION

The discovery of C_{60} Buckminsterfullerene, Fig 1, has its origins in a research programme involving synthetic chemistry, microwave spectroscopy and radioastronomy[1]. In 1975, at Sussex (with David Walton), the long chain polyyne H-C≡C-C≡C-C≡N was synthesised and studied by microwave spectroscopy. Subsequently, with Takeshi Oka and NRC(Ottawa) astronomers, the molecule was discovered in space, Fig 2, by radioastronomy using the laboratory microwave frequencies.

This discovery led on to the detection of the even longer carbon chain molecules HC_7N, HC_9N and $HC_{11}N$ in the space between the stars[2]. Further work aimed at understanding the formation of the chains in space focussed attention on the possibility that they are produced at the same time as carbon dust in red giant stars[1,2]. During experiments at Rice University in 1985 (with James Heath, Sean O'Brien, Robert Curl and Richard Smalley), designed to simulate the conditions in these stars and explore their capacity for carbon chain formation, the exciting discovery that C_{60} was remarkably stable was made[3]. It was found that under conditions where almost all the atoms in a carbon plasma had nucleated to form microparticles the molecule C_{60} remained behind - together with some C_{70}. This result was, as is now well known, rationalised on the basis of the closed cage structure shown in Fig 1. It was proposed that the geodesic and aromatic factors inherent in such a structure could account for the stability of the molecule.

THE CIRCUMSTANTIAL EVIDENCE FOR THE EXISTENCE OF FULLERENES

Many subsequent experiments, carried out during the period 1985-90 provided compelling evidence for the exceptional stability of C_{60} whatever its structure might have been[2,4]. For instance support for the structure had been obtained by showing that the mass spectrometric magic numbers observed in cluster experiments were consistent with the formation of a whole family of closed cages, the fullerenes Fig 3[5,2]. Particularly convincing was the fact that the smallest cages, in which all the 12 pentagons needed for closure are isolated, are C_{60} and C_{70}[5].

To explain the spontaneous creation of such an unexpected species in a chaotic carbon plasma a simple refined nucleation mechanism[6,7] was developed. It was also recognised that the mechanism could not only account for C_{60} but it also[7] explained the detailed structure of carbon microparticles such as those that Iijima[8] had observed (Fig 4a). In this scheme it is proposed that when carbon nucleates, curved and closing graphitic shells form[6] (rather than flat sheets as has

traditionally been assumed) and these wrap up under epitaxial control[7]. It predicts that the embryos involved in carbon particle growth are partially closed cages which grow into quasi-icosahedral graphite particles[7]. This mechanism explains the formation of the fullerene cages, C_{60} in particular, as resulting from closure during the general carbon microparticle formation process. It is proposed that embryos that do not close grow directly into graphite microcrystals essentially consisting of imperfect, concentric quasi-icosahedral spirally interconnected shells. The mechanism is supported by simulated TEM images (Fig. 4b) derived for the structures predicted by the new scheme[9] which show excellent agreement with the elegant electron microscope images of carbon microparticles obtained by Iijima[8] in 1980, Fig 4a.

It was also recognised that there were significant similarities between the structures of the pure carbon particles and soot particles and that both could be explained by essentially the same scheme (albeit in perturbed form for soot). This proposal has been criticised on various grounds[10], however detailed analysis of soot[11] reveals that there are numerous serious gaps in our understanding of the formation process, indeed sufficient to show that the new scheme cannot be discounted readily[12]. Harris and Weiner[11] said, in 1985, that "...knowledge of the chemistry (of soot formation) has been totally absent." so there would appear to be some room for some fresh ideas on the chemistry involved. The new mechanism does appear able to explain many observations more simply than some previous models such as those involving liquid droplet formation in which it appears the substructure is thought to be held in place van der Waals forces. The mechanism predicts that C_{60} should be a by-product of the soot formation process[6]. Interestingly Gerhardt, Löffler and Homann[13] subsequently showed that C_{60}^+ is the major ion in a sooting flame. Homann has however pointed out that this observation is not necessarily to be taken as support for the new scheme.

THE PRODUCTION AND CHARACTERISATION OF BUCKMINSTERFULLERENE

In August 1990 the scepticism which surrounded the original fullerene-60 proposal was finally laid to rest by the breakthrough made by two groups, Krätschmer, Lamb, Fostiropoulos and Huffman[14] (Heidelberg/ Tucson) and Taylor et al[15] (Sussex). From the carbon deposit produced from arc processed graphite Krätschmer et al[14] obtained a crystalline material. X-ray analysis showed it to consist of arrays of sperical C_{60} molecules of exactly the expected size. Mass spectrometric and infrared data were further confirmation. From similarly processed graphite Taylor et al[15] also obtained mass spectrometric evidence for fullerene-60 and also extracted a red solution (in benzene) independently. Subsequently they chromatographically separated the material into two components C_{60} and C_{70}. The ^{13}C NMR analysis of the beautiful magenta solution of C_{60} yielded a single line resonance (Fig 5) indicating that all the C atoms in the molecule are equivalent! A result perfectly commensurate with the proposed fullerene-60 structure. Elegant support came from the spectrum of C_{70} which showed that it had five lines (Fig 5), again in perfect agreement with expectation. This result was also important as it showed that other members of the fullerene family existed.

POSTBUCKMINSTERFULLERENE CHEMISTRY

Since this breakthrough was made in September 1990 the field has exploded and all aspects of the chemical and physical properties of the fullerenes are now being investigated in minute detail. The fact that this new, third form of carbon exists, is created spontaneously and has been under our noses since time immemorial is somewhat difficult to accept. Indeed fullerenes appear to make up some 10-30% of the material produced by the carbon arc and it has now been shown to reside in soot. Howard and co-workers who have found the fullerene content of soot from a benzene flame can be as high as 7% under certain conditions.

These observations have major implications; in particular for:

1) The composition of carbon vapour,

2) The mechanism of carbon nucleation,

3) The structure of graphitisable carbons,

4) Fluid carbon phases,

5) Soot formation,

6) The structure of interstellar and circumstellar grains,

7) Structure and synthesis of new polyaromatic hydrocarbons,

8) New metal-carbon complexes and intercalation compounds

New advances are made every day as the material becomes more and more accessible and a complete review of the material published on C_{60} Buckminsterfullerene by the end of 1990 has been written[4].

ACKNOWLEDGEMENTS

The success in the most recent work at Sussex was made possible by the expertise, effort and help of: Wahab Allaf, Simon Balm, John Dennis, Laurence Dunne, Richard Hallett, Jonathan Hare, Ken McKay, A Abdul-Sada, Amit Sarkar, Roger Taylor, David Walton and Steve Wood. We also thank the SERC.

LITERATURE CITED

1. H W Kroto, Chem. Soc. Revs., 11, 435-491 (1982).

2. H W Kroto, Science, 242. 1139-1145 (1988)

3. H W Kroto, J R Heath, S C O'Brien, R F Curl and R E Smalley, Nature, 318, 162-163, (1985).

4. H W Kroto, A W Allaf and S P Balm,Chem Revs (in press)

5. H W Kroto, Nature, 329, 529-531 (1987)

6. Q L Zhang, S C O'Brien, J R Heath, Y Liu, R F Curl, H W Kroto and R E Smalley, J Phys Chem., 90, 525-528 (1986)

7. H W Kroto and K McKay, Nature, 331, 328-331 (1988)

8. S Iijma, J Cryst Growth 50 675-683 (1980)

9. K G McKay, D Wales and H W Kroto, in preparation

10. L B Ebert, R V Kastrup, J C Scanlon and R D Sherwood, 19th Biennial Conf. Carbon (Penn State) 396-397

11 S J Harris and A M Weiner, Ann. Rev. Phys. Chem., 36, 31-52 (1985)

12 H W Kroto (in preparation)

13 P H Gerhardt, S Löffler and K H Homann, Chem Phys Letts 137, 306 (1987)

14 W Krätschmer. L D Lamb, K Fostiropoulos and D Huffman, Nature 347, 354-358 (1990)

15 R Taylor, J P Hare, A K Abdul-Sada and H W Kroto, J. C. S. Chem. Comm., 1423-1425 (1990)

16 J B Howard, J T McKinnon, Y Makarovsky, A L Lafleur and M E Johnson, Nature (in press)

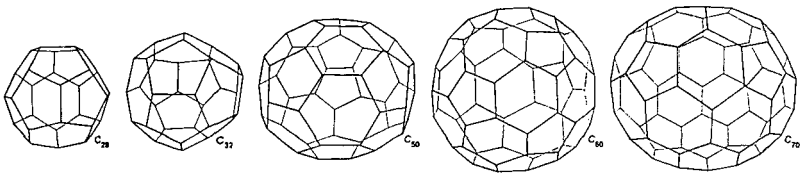

Fig 3 Family of relatively stable Fullerenes[5]

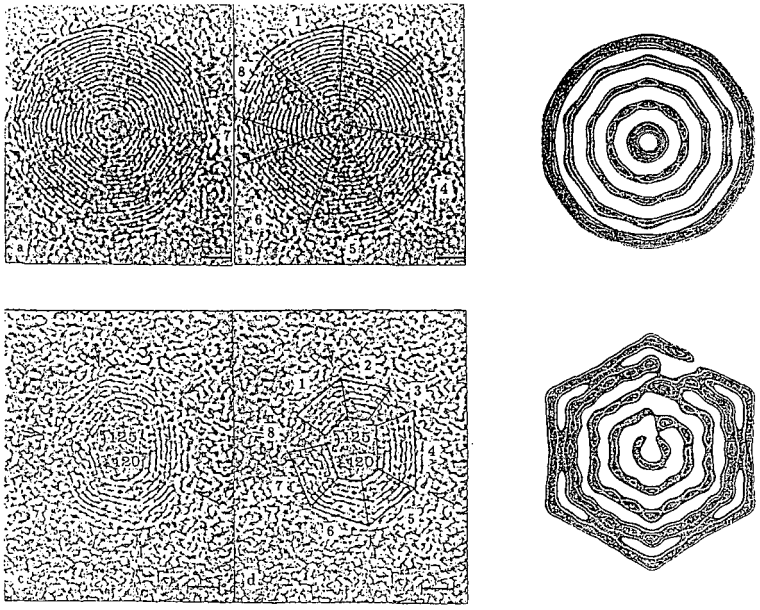

a) *b)*

Fig 4 Comparison between TEM images of polyhedral graphite microparticles observed by Iijima[8] *a) and simulated images for a hypothetical icospiral microparticle (two different angles) b)*

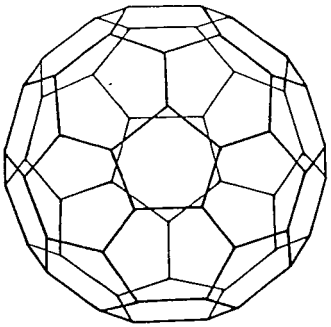

Fig. 1 C_{60} Buckminsterfullerene.

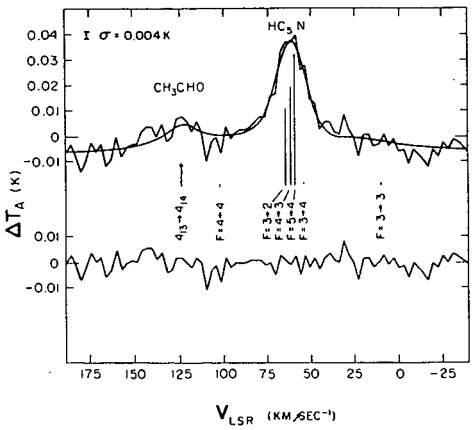

Fig. 2 Radio line of HC_5N observed in a giant molecular cloud SgrB2 near the center of the Galaxy

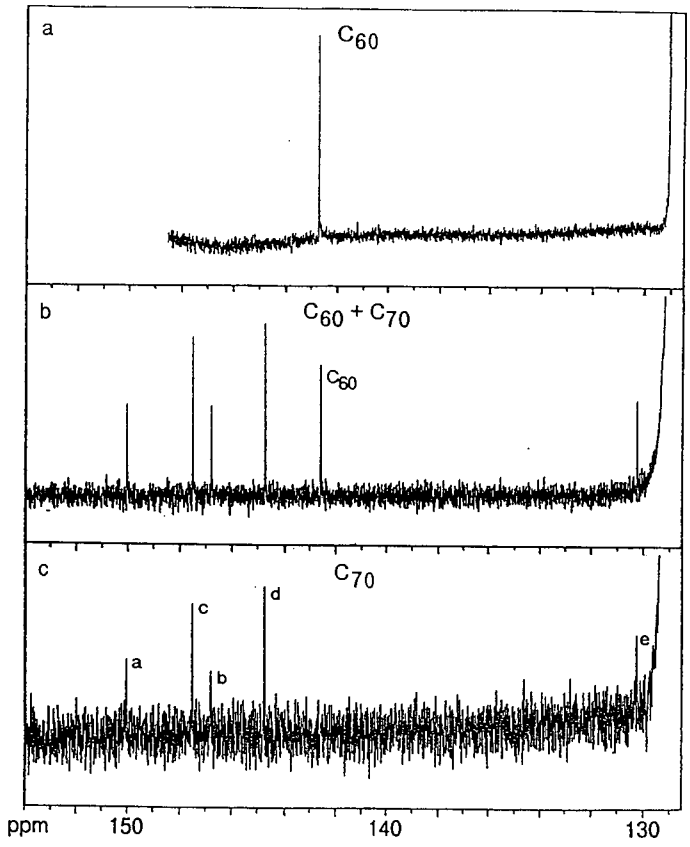

Fig 5 *^{13}C NMR spectrum of Fullerene-60*

PRODUCTION AND CHARACTERIZATION OF FULLERENES IN FLAMES

Jack B. Howard, J. Thomas McKinnon, Yakov Makarovsky,
Arthur L. Lafleur, and M. Elaine Johnson
Department of Chemical Engineering and
Center for Environmental Health Sciences
Massachusetts Institute of Technology
Cambridge, Massachusetts 02139-4307

Keywords: fullerenes, C_{60}, flames

ABSTRACT

Closed-cage all-carbon molecules referred to as fullerenes were discovered in carbon vapor from laser heating of graphite and subsequently produced in macroscopic quantities by resistive heating of carbon rods. Suggestions that fullerenes may be involved in soot formation, and the detection, in flames, of all-carbon ions having the same masses as fullerenes, have generated much interest in the possible formation of fullerenes in flames. Combustion experiments and chemical analyses will be reported which have been conducted over ranges of flame conditions to determine if fullerenes can be produced in flames and to assess the relationship between fullerenes and soot.

INTRODUCTION

Fullerenes were discovered[1] in carbon vapor produced by laser irradiation of graphite, and have recently been produced in macroscopic quantities[2,3,4] by graphite vaporization with resistive heating. Fullerene C_{60} is a closed cage carbon structure containing 20 six-membered rings and 12 five-membered rings with the appearance of a soccer ball. There has been a surge of scientific interest in these compounds because they represent a new class of carbon in addition to the two known forms, graphite and diamond. There has also been much practical interest in fullerenes. Many potential applications have been suggested, including catalysts and superconductors produced by incorporation of metal atoms with the fullerenes, and super lubricants produced by fluorination of fullerenes.

That fullerenes may be formed in sooting flames has frequently been suggested[5,6,7,8] since the early days of fullerene research. Zang et al.[5] considered the possible role of carbon shell structures in the formation and morphology of soot. They envisioned the growth of successive shells, separated by roughly the 0.33 nm intersheet distance in graphite, producing a soot nucleus consisting of concentric but slightly imperfect spheres, with the edge of the outermost shell giving a very rapid growth front. Kroto and McKay[6] described a carbon nucleation scheme involving quasi-icosahedral spiral shell carbon particles, and suggested it may apply to soot. Curl and Smalley[7] suggested carbon nets in the form of spiral structures may be important to soot formation in flames.

In spite of early predictions that fullerenes may be associated with soot formation and morphology, confirming evidence has not been produced although all-carbon ions having the same molecular weights as fullerenes have been detected in flames[9,10,11]. Also, Pope[12] (see Pope and Howard, Fuel Chemistry Div. Preprints, this Meeting) has determined that compounds in the mass range 700-750 amu in a flame behave in a manner consistent with the relatively stable fullerene C_{60} being a substantial fraction of the material in this mass range. This conclusion

resulted from a study of molecular beam mass spectrometer data obtained by Bittner[13] in a near-sooting benzene-oxygen flame. Similar flames but in the sooting regime were studied by McKinnon[14], whose data on high molecular weight soot precursors gave interesting but inconclusive evidence pertinent to the possible presence of fullerenes. The subsequent application of soot extraction techniques similar to those employed in the graphite vaporization studies revealed the presence of fullerenes in soot deposited on surfaces of the combustion chamber in McKinnon's studies (McKinnon and co-workers, submitted for publication).

EXPERIMENTAL

In order to determine if fullerenes are formed in flames, soot samples were collected from flames under ranges of conditions and analyzed using conventional techniques. Premixed laminar flames of benzene and oxygen with argon diluent were stabilized on a water-cooled burner in a low-pressure chamber equipped with windows and feed-throughs for visual observation, optical diagnostics and probes, and exhausted into a vacuum pump. The burner consists of a horizontal drilled copper plate (100 mm diameter, 12 mm thick, 1 mm diameter holes centered 2.5 mm apart in a triangular grid) in the end of a tube, upward through which the feed mixture is delivered. The flame is stabilized with a flat front uniformly displaced from a drilled copper burner plate by a short distance which depends on the velocity of the gas leaving the burner and the flame speed of the mixture. The flame is surrounded by an annular nonsooting flame which provides a thermal shield, giving an approximately one-dimensional core within which temperature and species concentrations vary only with distance, or residence time, from the burner surface. The burner was previously used in mechanistic studies of soot nucleation and growth[13], and the flames studied are of a type for which considerable data on temperature and chemical composition are available[9-18].

Flames were produced under different sets of conditions over the ranges: burner chamber pressure, 1.60-13.35 kPa; atomic C/O ratio, 0.96-1.07; mol % Ar, 0-39; gas velocity at the burner (298 K), 14-75 cm/s. Each flame was maintained for 1.6 to 2.8 hr, during which a soot sample was withdrawn from the flame at a given distance from the burner using a quartz probe connected to a room-temperature filter, vacuum pump, and gas meter. Soot was also collected from the inside surface of the burner chamber after each run. Using flame temperature and gas composition information, the soot masses and gas volumes collected with the probe in the different flames are found to correspond to soot yields in the range 0.8 to 12% of the carbon fed.

The soot samples were extracted with toluene, using an ultrasonic bath at room temperature, and filtered. The solution from one of the samples was evaporated to dryness and analyzed with a Varian-MAT model 731 mass spectrometer interfaced to a Teknivent data system using a direct injection probe heated from 373 K to 673 K and electron impact ionization. The mass spectrum has been submitted for publication.

The toluene extracts were fractionated with a high performance liquid chromatograph (HPLC) coupled to a spectrophotometric diode-array detector (DAD). A separation scheme proven effective for large polycyclic aromatic hydrocarbons (PAH)[20-22] was used. The column (4.6 mm i.d., 250 mm length) was packed with 5 μm Nucleosil octadecylsilyl-bonded silica having 300 Å pore size. A reverse-phase solvent system of methanol/dichloromethane was used. The mobile phase program consisted of a linear increase in dichloromethane concentration from 10-100% in 40 min with a 10 min hold time at 100%. The flow rate was 1.0 mL/min. In HPLC chromatograms for the toluene extracts, the broadband DAD response

is roughly proportional to mass for PAH[23].

In order to obtain broadband ultraviolet-visible (UV-Vis) spectra, solutions from HPLC fractionation of the soot extracts were concentrated by evaporation under nitrogen and the HPLC mobile phase was replaced with spectro-grade decalin. The UV-Vis spectra of the different peaks of interest were acquired over the 200-800 nm wavelength interval using a Hewlett-Packard 8450 A spectrophotometer. Mass spectra of these HPLC fractions were acquired using the equipment and technique mentioned above. The identities of the HPLC peaks suggested by UV-Vis spectra were confirmed by mass spectra. The HPLC method was then used to analyze the toluene extracts of all the soot samples.

The experimental results, which have been submitted for publication, not only show whether fullerenes are formed in flames but also reveal behavior of interest in comparison with that of the graphite vaporization technique for fullerenes production.

ACKNOWLEDGEMENTS

We thank Chenhui Zeng and Catherine Costello of the MIT Mass Spectrometry Facility (NIH Grant No. RR00317 to K. Biemann) for assistance in obtaining the mass spectra. The combustion research was supported by the Division of Chemical Sciences, Office of Basic Energy Research, Office of Energy Research, U.S. Department of Energy under Grant No. DE-FG02-84ER13282. The analytical investigation was supported in part by the National Institute of Environmental Health Sciences udner Center Grant EHS-5P30-ES02109-10 and Program Grant EHS-5P01-ESO1640-11. M.E.J. was supported by a Dow Fellowship Award from the MIT Undergraduate Research Opportunities Program.

REFERENCES

(1) Kroto, H.W.; Heath, J.R.; O'Brien, S.C.; Curl, R.F.; Smalley, R.E. Nature 1985, 318, 162-164.

(2) Krätschmer, W.; Lamb, L.D.; Fostiropoulos, K.; Huffman, D.R. Nature 1990, 347, 354-358.

(3) Ajie, H.; Alvarez, M.M.; Anz, S.J.; Beck, R.D.; Diederich, F.; Fostiropoulos, K.; Huffman, D.R.; Krätschmer, W.; Rubin, Y.; Schriver, K.E.; Sensharma, D.; Whetten, R.L. J. Phys. Chem. 1990, 94, 8630-8633.

(4) Haufler, R.E.; Conceicao, J.; Chibante, L.P.F.; Chai, Y.; Byrne, N.E.; Flanagan, S.; Haley, M.M.; O'Brien, S.C.; Pan, C.; Xiao, Z.; Billups, W.E.; Ciufolini, M.A.; Hauge, R.H.; Margrave, J.L.; Wilson, L.J.; Curl, R.F.; Smalley, R.E. J. Phys. Chem. 1990, 94, 8634-8636.

(5) Zhang, Q.L.; O'Brien, S.C.; Heath, J.F.; Liu, Y.; Curl, R.F.; Kroto, H.W.; Smalley, R.E. J. Phys. Chem. 1986, 90, 525-528.

(6) Kroto, H.W.; McKay, K. Nature 1988, 331, 328-331.

(7) Curl, R.F.; Smalley, R.E. Science 1988, 242, 1017-1022.

(8) Kroto, H. Science 1988, 242, 1139-1145.

(9) Gerhardt, Ph.; Löffler, S.; Homann, K.H. Chem. Phys. Lett. 1987, 137, 306-310.

(10) Gerhardt, Ph.; Löffler, S.; Homann, K.H. Twenty-Second Symposium (International) on Combustion, The Combustion Institute, 1989, 395-401.

(11) Löffler, S.; Homann, K.H. Twenty-Third Symposium (International) on Combustion, The Combustion Institute, Pittsburgh, in press.

(12) Pope, C.J. Fluxes and Net Reaction Rates of High Molecular Weight Material in a Near-Sooting Benzene-Oxygen Flame; M.S. thesis, M.I.T., Cambridge, Massachusetts, 1988.

(13) Bittner, J.D.; Howard, J.B. Eighteenth Symposium (International) on Combustion, The Combustion Institute, Pittsburgh, 1981, 1105-1106.

(14) McKinnon, J.T. Chemical and Physical Mechanisms of Soot Formation; Ph.D. thesis, M.I.T., Cambridge, Massachusetts, 1989.

(15) Homann, K.H.; Mochizuki, M.; Wagner, H.Gg. Z. Phys. Chem. N.F. 1963, 37, 299-313.

(16) Homann, K.H.; Morgeneyer, W.; Wagner, H.Gg. Combustion Institute European Symposium ed. F.J. Weinberg; Academic Press: London, 1973, 394-399.

(17) Olson, D.B.; Calcote, H.F. Eighteenth Symposium (International) on Combustion, The Combustion Institute, Pittsburgh, 1981, 453-462.

(18) Bockhorn, H.; Fetting, F.; Wenz, H. Ber. Bunsenges. Phys. Chem. 1983, 87, 1067-1073.

(19) Howard, J.B.; Bittner, J.D. Soot in Combustion Systems and Its Toxic Properties, eds. J. Lahaye and G. Prado; Plenum: New York, 1983, 57-91.

(20) Fetzer, J.C.; Biggs, W.R. J. Chromatogr. 1985, 322, 275-286.

(21) Fetzer, J.C.; Biggs, W.R. J. Chromatogr. 1985, 346, 81-92.

(22) Fetzer, J.C.; Biggs, W.R. J. Chromatogr. 1984, 295, 161-169.

(23) Lafleur, A.L.; Monchamp, P.A.; Plummer, E.F.; Wornat, M.J. Anal. Lett. 1987, 20, 1171, 1192.

Sublimation and Heterogenous Reactions of Fullerene (C_{60}) in Different Gases

Ismail M. K. Ismail
University of Dayton Research Institute
c/o Phillips Lab/RKFC
Edwards Air Force Base, CA 93523-5000, USA

ABSTRACT

The sublimation process and heterogeneous reactions of C_{60} Fullerene under a flow of argon, air, or hydrogen have been investigated at 25-1000 C. The results are compared against those obtained with other forms of well characterized carbons; Saran char (a highly reactive disordered carbon) and SP-1 graphite (less reactive, well ordered carbon). In Ar, 83% of the C_{60} aggregates (examined here) sublime, leaving behind a carbonaceous non-volatile residue insoluble in toluene. In air, the C_{60} first chemisorbs (reacts with) oxygen to a limit corresponding to 1.5 oxygen atoms/C_{60} molecule. The carbon then loses weight (gasifies) at a rapid rate; higher than the rate of Saran gasification. In hydrogen, while the rates of SP-1 and Saran gasification at 1000 C are insignificant, the volatile part of C_{60} aggregates completely sublimes or gasifies at 500-800 C, leaving behind the 17% residue left after the sublimation process. Some possible future applications of C_{60}, particularly in the areas of carbon composites and molecular sieve materials, are addressed.

Keywords: C_{60}, Buckyballs, Fullerene.

INTRODUCTION

Fullerene C_{60}, a newly established form of carbon, is a molecule containing 60 carbon atoms arranged in a closed hollow cage with 32 faces; 12 pentagons and 20 hexagons [1]. The molecule is a stable cluster of carbon atoms often known as "buckyball". The buckyballs are prepared by laser vaporization of graphite discs [1-3], and by carbon arc vaporization of graphite rods [4-6]. The evaporation is performed under subambient pressures (100-200 Torr) at 1000-1300 C in an inert atmosphere of helium or argon. The graphite vapor nucleates in the gas phase forming particles which are collected on a cold substrate, yielding soot and aggregates of C_{60} with a small fraction of other larger cages. To isolate the buckyballs the particles are first dispersed in a solvent; benzene [4], toluene or carbon disulfide [5,6]. The buckyballs dissolve but the other forms of carbon (soot) remain suspended. After filtration, the solvent is evaporated, leaving behind aggregates of C_{60}.

The structure of buckyballs has been supported by infrared and ultraviolet spectra [1,4], by NMR [7], and by theoretical calculations [8,9]. The literature is full of C_{60} physical properties; including electrical and magnetic properties [10,11], electron energies [12-14] and optical spectrum [14]. Scanning Tunneling Microscopy has indicated that the C_{60} molecules are arranged in hexagonal arrays with an intercluster spacing of 1.0-1.1 nm [15,16]. The spacing agrees with the sum of the theoretical molecular diameter of C_{60} (0.701 nm) plus the interlayer spacing of graphite (0.335 nm). These values are also in agreement with those calculated from X-ray and electron diffraction studies [17]. With the assumption that the C_{60} molecules are arranged in a hexagonal close-packed lattice, the estimated nearest neighbor distance is 1.002 nm, and the X-ray density is 1.678 g/cc. It is consistent with the experimental value of 1.65 ± 0.05 g/cc obtained by density gradient columns [17].

The structure of C_{60} and its different methods of preparation are well established. The buckyballs can now be prepared at a rate of 10 g/h or higher [6]. Yet, little is known about their properties and performance as a truly carbonaceous material. Because of their unique spherical structure, the C_{60} molecule does not have dangling carbon atoms or active sites as the other carbonaceous materials. The C_{60} molecules should be less reactive to air, hydrogen, or oxidizing agents than the other carbons. The treatment of soot and fullerene with perchloric acid at 100-160 C has verified this point [18]. The treatment indicated that fullerene is more oxidation resistant than soot [18]. On the other hand, C_{60} sublimes at considerably lower temperatures than the other carbons. Therefore, when exposed to air at

high temperatures, the homogeneous reaction between air and C_{60} in the gas phase (if any) could be faster than the "normal" heterogeneous reaction between air and active sites of the other carbons. Thus, it is not clear how the behavior of C_{60} in different gases compares to the other forms of carbon.

The objective of the present work is to address several subjects. First, how does C_{60} respond when heated in inert or reactive medium. Initially, we discuss the sublimation reaction of C_{60} in Ar. Then we move to the reaction between C_{60} and air or H_2. Second, a comparison is made between the reactivity of C_{60} and other forms of carbon. We finally outline some potential future applications of this form of carbon; especially in the areas of carbon composites and molecular sieve carbons.

EXPERIMENTAL

Materials

Two batches (A and B) of C_{60} crystals were graciously supplied by Professor D. R. Huffman (University of Arizona - Tucson). They were used as-received, without further purification. To understand their relative reactivity in air or H_2, two additional carbons were included in the study; a reactive Saran char and a considerably less reactive SP-1 graphite. Saran is a highly disordered non-graphitic char with a large micropore surface area of 850 m^2/g [19], an average micropore width of 1.05 nm [20], and an active surface area (ASA) of 37 m^2/g [19]. The sample has a low level of impurities [19], so we can rule out the catalytic effects which enhance the rates of C/O_2 and C/H_2 reactions. SP-1, on the other hand, is composed of well ordered natural flakes which have been purified by the manufacturer to a minimum level of impurities. It is non-porous graphite with an external surface area of 2.00 m^2/g [21] and an ASA of 0.05 m^2/g [22].

Measurements of Reaction Rates

The experiments were performed on a Cahn Thermogravimetric Analyzer (TGA), system 113, connected to a vacuum system. The samples (about 5 mg) were evacuated at room temperature until a pressure of 10^{-5} Torr was reached. The sample was flushed with ultrahigh purity Ar flowing at 50 cc/min to ambient pressure. Then, starting from room temperature, all samples were heated at a constant heating rate (HR) in, Ar, air, or H_2 flowing at 50 cc/min. The change in sample weight was monitored as a function of temperature and time every 15 sec.

RESULTS AND DISCUSSION

The Sublimation Process in Argon

Figure 1 illustrates the drop in C_{60} weight, due to sublimation, as a function of temperature (HR = 5 C/min). The sublimation in Ar begins at 550 C and ends at 900 C; the two temperature limits are dependent on HR and sample size. At higher temperatures, 900-1000 C, there was no further drop in sample weight. The apparent remaining weight of residue was 21.6 ± 0.7 % of the original sample. To get the true weight, a correction had to be made which takes into consideration the thermal and buoyancy effects imposed by reactor geometry, HR, geometry of sample container, and type of gas injected as well as its flow rate. When the TGA reactor is heated, the density of the flowing gas drops, and as a result, there is an apparent mass-gain which increases with temperature. By performing a blank run, with Ar flowing at 50 cc/min over empty sample container, the proper correction factors at different temperatures have been obtained. At 900 C, the correction factor is 4.6%. Therefore, the true weight of the C_{60} residue, left after the sublimation reaction, is 21.6-4.6 = 17.0%.

When the samples reached 1000 C in Ar, with no indication of further weight change, they were held isothermally at this limit. Air was then introduced to replace Ar at the same flow rate. The residue gasified with the liberation of only CO which is normally the main product for the carbon/O_2 reaction at 1000 C. After gasification, the apparent final weight dropped from 21.6 to 4.9%, the latter value is equivalent to the new correction factor at 1000 C, 4.9%. It means that the "non-C_{60}" residue is just

another stable form of carbon or soot. This trend has been confirmed with all batch A and B samples not only after the sublimation process, but also after the hydrogenation reaction (Section 3.4).

These results imply that the C_{60} aggregates, at least the ones examined in this study, are composed of 83% volatile C_{60} carbon contaminated with 17% of "non-C_{60}" carbon. Since the X-ray and experimental densities are very close [17], the density of both type of carbons should be essentially the same. The 83 to 17 ratio suggests that each five molecules of C_{60} are approximately associated with one particle of the "non-C_{60}" carbon. If one assumes that the particle volume is, on the average, equivalent to the size of one C_{60} molecule; 0.180 nm^3, the X-ray dimensions of the particle can be estimated. Knowing that the area of one graphitic hexagon is 0.052 nm^2, and assuming the particle has an average interlayer spacing of 0.35 nm, the number of hexagons in the particle can be estimated. If the particle has three graphitic layers, as a first reasonable guess, this number is given by: 0.180/(0.052 x 0.7) = 4.9; about 5 hexagons. A graphitic crystal with such a small size (0.57 x 0.7 nm) is hard to exist. Therefore, the "non-C_{60}" carbon component in the aggregates is probably present as larger particles of soot randomly imbeded within the C_{60} crystal.

The question is then raised regarding the residue origin. The residue could be a biproduct formed during the sublimation of C_{60}. In other words, a polymerization reaction could be taking place in Ar at elevated temperatures to form larger stable graphitic crystals. Alternatively, the residue could be composed of soot or particulates that were originally present with the buckyballs but trapped inside the aggregates. The solvent extraction process was not able to completely remove the residue because the size of these particles is very small. During the filtration process, they may have passed through the filtering device and stayed with the C_{60} extract solution. At present, the possibility of a polymerization reaction cannot be ruled out, however, the last explanation is probably more valid. It is noteworthy to add that the residue obtained after sublimation is insoluble in toluene.

Oxidation in Air

Exposure of C_{60} to air, Figure 2, is associated with two main processes; a weight increase at lower temperatures, followed by a weight decrease at higher temperatures. While the increase in weight is attributed to oxygen chemisorption or an addition reaction, the weight loss is due to carbon gasification. Unlike the sublimation process, the oxidation reaction shows some difference between batch A and B. The reason for this discrepancy may be due to the way by which the C_{60} molecules aggregate in each batch. It could also be dependent on the average particle size or distribution. Apparently either the internal structure and porosity of batch B is more open than A, or the average particle size of B is smaller than A. With either explanation, batch B chemisorbs (or reacts with) more oxygen than A as shown in Figure 2. In spite of this difference, the general trend with both C_{60} samples is essentially the same. The weight increases to reach a maximum value, then the rate gradually decreases. With batches B and A, the maximum "apparent" increase in weights at 360-380 C are 5.4 and 4.8%, respectively. After considering the proper correction factor of 2.4% at 360-380 C, the corresponding true maximum weight gains of oxygen are reduced to 5.4-2.4 = 3.0% and 4.8-2.4 = 2.4%, or 30 and 24 mg O_2/g C_{60}, respectively. The average value of the two is 27 mg O_2/g C_{60} which yields 0.73 mole O_2/mole C_{60}. This calculation assumes that the molecular weight of fullerene is 720, and that oxygen molecules are only consumed by the C_{60} component in the crystal which constitutes 83% of the total carbon.

It is interesting to note that just before the beginning of C_{60} weight loss (gasification), each molecule acquires, on the average, 0.73 x 2 = 1.46 (say 1.5) oxygen atoms. There are several possible explanations for this. First, the "attack" with oxygen starts by opening, at least, one C=C bond to form an ether-type linkage on each C_{60} molecule. Then, on every other molecule, another C=C bond opens up in the same way. Second, one C_{60} molecule forms the ether-type bond while the next molecule converts a C=C to either C-O-O-C (peroxide) or two carbonyl groups. Third, some (accessible) C_{60} molecules are attacked by more than 1.5 oxygen atoms while others (hidden inside the crystal) are not attacked at all because oxygen cannot reach them. Fourth, several complicated organic reactions between C_{60} and O_2 could be taking place. Whatever the oxidation mechanism is, it is clear

that the gasification of the C_{60} crystals starts by formation of carbon-oxygen functional groups. This is exactly the mechanism of gasifying the other forms of carbon in air. It is well known that chemisorption of oxygen on carbons is the first step of the overall gasification reaction [23,24].

Let us look at the same data in a different way. The amount of oxygen uptake can be converted to estimate the active surface areas (ASA). ASA calculations assume the area occupied by one chemisorbed oxygen atom as 0.083 nm^2/site, and that each active site chemisorbs one oxygen atom [25]. Based on the two assumptions, the ASA of batches B and A, with maximum values of 30 and 24 mg O_2/g C_{60}, are 93.8 and 75 m^2/g, respectively. If, as just mentioned, each oxygen atom is shared by two carbon atoms, the ASA values are reduced by half to yield 46.9 and 37.5 m^2/g, respectively. Compared to other forms of carbon, the C_{60} ASA values are exceptionally high. With the other carbons, typical ASA values are 0.2 - 5.3 m^2/g for graphitized carbons [25,26], 2.2 - 11.3 m^2/g for ungraphitized carbons [26], and 37 m^2/g for the highly reactive microporous Saran char [19]. In fact, the C_{60} ASA values computed here represent a low estimate. The more realistic values should be even higher because the oxygen uptake at the maxima, shown in Figure 2, represents the net of two processes. Oxygen chemisorption which increases the weight and carbon gasification which lowers the weight. If gasification were not occurring concurrently with chemisorption at the maxima , the maximum weight gain and, consequently, the ASA would have been even higher.

Now we examine how the gasification reactions of C_{60} in air compare to other forms of carbons. With the non-isothermal oxidation procedure, which has been utilized in the current investigation, the results can be presented in different ways. The most useful ones are the oxidation rate profiles (ORP) and Arrhenius plots [27]. The ORP is a relation between the rate of weight loss (gasification rate) and sample temperature. Figure 3 compares the ORP of C_{60}, Saran (a highly reactive carbon) and SP-1 Graphite (a less reactive carbon). Both rates were based on starting sample weight. Once again, there is some difference between the ORP of batches A and B. Batch A is more reactive and starts gasifying at a slightly lower temperature (360 C) than B (380 C). The maximum rate of oxidation of batch A is higher, but occurs at a lower temperature than the maximum of B (430 vs 470 C). Nevertheless, both batches oxidize at considerably lower temperatures than Saran. In fact, it was noted that most of the C_{60} completely gasified when the highly reactive Saran char was just beginning to loose some weight. The main reason for the remarkable reactivity of C_{60} in air is its highly developed ASA. It is attributed to the early attack of oxygen on C_{60} molecules. If each C_{60} molecule is, on the average, attacked by at least one oxygen atom before the start of gasification, the buckyballs begin breaking down. This process continues at a faster rate during the course of gasification. Because of the increasingly large number of nascent carbon active [25] or reactive [28] sites generated, and the small size of carbon fragments generated during oxidation, the C_{60} gasifies faster than the rest of carbons.

Behavior of C_{60} in Different Gases

A comparison is now made between the sublimation process in Ar and gasification of C_{60} in air and hydrogen. The results, illustrated in Figure 4, reveal several features. First, the oxidation reaction is the fastest, the sublimation process is the slowest, and the hydrogenation reaction is in the middle. Second, the oxidation reaction starts and ends at a region far below the sublimation temperature range. The C_{60} carbon oxidizes in the solid form before it sublimes. Third, the shape of the profiles in Ar and H_2 are essentially the same. In air, the profiles look different, indicating that the C_{60}/O_2 reaction is more complicated than the other two reactions. The profile indicates that different type of sites (or two different forms of carbon: C_{60} and soot) are gasifying at different temperature ranges. Fourth, in spite of the low temperature range at which the C_{60} gasifies, the maximum rates of oxidation are 40-50% higher than the hydrogenation or sublimation rates measured at higher temperatures. Fifth, the similarity between the profiles of the C_{60}/H_2 reaction and C_{60}/Ar sublimation process is somewhat puzzling. If the C_{60}/H_2 reaction was a typical heterogeneous reaction, the profile shown in Figure 4 should have acquired, to some extent, the shape of the C_{60}/O_2 profiles. That is, the profile in H_2 should not have been symmetrical. Since this is not the case, other possible reasons have to be considered, and this subject is addressed next.

Reduction/Gasification of C_{60} in Hydrogen

Figure 5 compares the Arrhenius plots of the C_{60} sublimation and hydrogenation reactions. The plots were computed from the corresponding ascending branches of Figure 4. The Arrhenius plots are practically linear with activation energies of 39-42 Kcal/mole for the sublimation process, and 34 (batch A) or 42 (batch B) Kcal/mole for the hydrogenation reaction. Once again, batch A is slightly more reactive to H_2 than B. Thus, the activation energy in Ar and H_2 is practically the same, suggesting that there is some similarity between the nature of the two processes. On the other hand, the activation energy for the C_{60}/H_2 reaction is in line with those values reported in the literature for other carbon/hydrogen reactions; 36 ± 6 Kcal/mole at atmospheric pressure [29], and 35.8 - 50.9 Kcal/mole at 27 atm [30]. So far, the C_{60} and the other "old" carbons appear to take the same activation energy path when exposed to H_2. However, the hydrogenation reaction of C_{60} may be different than the normal gasification reactions of other carbons which yield CH_4.

The C_{60} hydrogenation reaction takes place at a considerably lower temperature range than the rest of "older" carbons. Figure 6 illustrates this point. Under similar experimental conditions, the extent of gasifying the highly reactive Saran, and the less reactive SP-1 graphite, is small. The change in apparent sample weights between 500 and 1000 C is also small; less than 5% (no correction factor is included here). By contrast, the reaction between C_{60} and hydrogen starts at 500 C and ends at 900 C. Once again, the carbon leaves behind the "non-C_{60}" residue (soot) which has low reactivity in H_2 at 1000 C, resembling Saran and SP-1 graphite.

Although the hydrogenation reaction of C_{60} has an activation energy similar to the "old" carbon/H_2 reaction, one may conclude that fullerene is just gasifying in H_2 like a typical carbonaceous material. This may be true to some extent. Yet, at the present time, we cannot rule out other possible explanations until further conclusive experiments are performed. That is, the observed hydrogenation reaction may be taking place through an entirely different route than the "normal" C/H_2 gasification reaction. It is possible that H_2 molecules are opening the C=C bonds and saturating the surface with C-H bond, yielding $C_{60}H_{36}$ and other smaller hydrocarbons. In other words, the reaction could merely be starting with hydrogen addition rather than carbon gasification. The resulting products, with different amounts of hydrogen, could simply be a wide variety of different organic molecules that have different sizes, properties, and boiling points. If this is the major reaction, then the TGA experiments were merely measuring the weight loss due to evaporation of organic compounds with minor contribution of gasification of the carbonaceous matrix.

CONCLUSIONS

1. The C_{60} carbon crystals examined here sublime in inert atmospheres, leaving behind a non-volatile carbon residue weighing 17% of the original sample. The residue, possibly soot is another form of carbon which gasifies in air yielding CO at 1000 C and is insoluble in toluene.

2. Oxidation of C_{60} in air starts by a weight gain process during which, each C_{60} molecule acquires, on the average, 1.5 oxygen atoms. At this point, a portion of the C_{60} molecules begin opening up. With increasing temperature, the buckyballs further oxidize with a concurrent gasification reaction of the carbonaceous matrix.

3. Under otherwise similar conditions, C_{60} is considerably more reactive in air or hydrogen than the other forms of carbon. This is attributed to the fast rate of generating active sites when the C_{60} molecules start breaking.

4. The hydrogenation reaction of C_{60} may, or may not, resemble the "old" carbon/H_2 gasification reaction to yield CH_4. The current data indicate some similarity between the two carbons. However, at the present time, the possibility of other hydrogenation reactions, that may convert fullerene to other forms of hydrocarbons, cannot be ruled out.

FUTURE APPLICATIONS

There are several potential applications for this new form of carbon, especially in the areas of carbon composites and molecular sieve carbons. Carbon composites have been used extensively in several aerospace applications. When stored, especially in an environment with high humidity, the composite adsorbs (absorbs?) moisture, some of the mechanical properties may deteriorate, and the component weight increases. To avoid this, a layer (blanket) or two of C_{60} could be spread to cover the entire external surface and pore entrances of the component. The assumption is made here that C_{60} has a hydrophobic surface that does not adsorb moisture. This assumption is reasonable because the C_{60} molecule does not have functional groups which normally enhance the moisture adsorption on carbons. To "spread the blanket" on a composite, the process has to be performed in an oxygen-free atmosphere, perhaps under vacuum. While a C_{60} reservoir is heated, the composite surface is cooled. Alternatively, a very dilute solution of C_{60} in benzene or toluene can be sprayed on the substrate. The solvent is then evaporated leaving behind the C_{60} blanket. This process does not require large quantities of fullerene. Based on the 1.0 nm diameter of C_{60} molecules, the computed surface area is 675 m^2/g. This means that 6.2 g of C_{60} can make a "blanket" for a substrate whose area is equivalent to an acre!

The second potential application is the preparation of molecular sieve carbons, which are highly microporous carbons with large adsorption capacity. Yet the size of their pore entrances, the "gate", has to be tailored to the specific application. The C_{60} comes as good and bad news for preparing this class of carbons. The starting substrate for molecular sieve carbons is normally a microporous (activated) carbon with a wide micropore size distribution. If one layer of C_{60} is deposited on the micropore entrance, the "gate" is narrowed by approximately 1.0 nm. Deposition of additional layers will narrow the "gate" further by multiples of nanometers (2,3,4,5,...nm). If the average pore size is 1.3 or 2.3 nm, then deposition of one or two layers of C_{60} will reduce the "gate" (of both pores) to 0.3 nm. The product is an excellent sieve to separate argon from oxygen whose minimum dimensions are 0.38 and 0.28 nm, respectively [31]. The sieve will preferentially adsorb oxygen, leaving argon passing through the separation tower. This is the good news. Now, if the starting average pore size is 1.0 or 2.0 nm, the deposition of C_{60} will just close the pores; and with it, come the bad news.

ACKNOWLEDGEMENT: The financial support of Air Force Office of Scientific Research under contract number F04611-83-C-0046 with the Phillips Laboratory OLAC is highly appreciated. The author acknowledges Professor D. R. Huffman for providing the two C_{60} samples. Special thanks go to Dr. E. J. Wucherer, Major W. Hurley, Dr. Jeff Gilman, Dr. Pat Carrick, Dr. W. Hoffman, and Mr. M. Mahowald for the fruitful stimulating discussions.

REFERENCES

1. H. W. Koto, J. R. Heath, S. C. O'Brien, R. F. Curl and R. E. Smalley, Nature 318, 162 (1985).
2. J. R. Heath, S. C. O'Brien, Q. Zhang, Y. Liu, R. F. Curl, H. W. Kroto, F. K. Tittel and R. E. Smalley, J. Am. Chem. Soc. 107, 7779 (1985).
3. Q. L. Zhang, S. C. O'Brien, J. R. Heath, Y. Liu, R. F. Curl, H. W. Kroto, and R. E. Smalley, J. Phys. Chem. 90, 525 (1986).
4. W. Kratschmer, K. Fostiropoulos, and D. R. Huffman, Chem. Phys. Lett. 170, 167 (1990).
5. R. E. Haufler, Y. Chai, L. P. F. Chibante, J. Conceicao, Changming Jin, Lai-Sheng Wang, Shigeo Maruyama and R. E. Smalley, Mat. Res. Soc. Symp. Proc., Boston, Mass., November (1990).
6. R. E. Haufler, J. Conceicao, L. P. F. Chibante, Y. Chai, N. E. Byrne, S. Flanagan, M. M. Haley, S. C. O'Brien, C. Pan, Z. Xiao, W. E. Billups, M. A. Ciufolini, R. H. Hauge, J. L. Margrave, L. J. Wilson, R. F. Curl and R. E. Smalley, J. Phys. Chem. 94, 8634(1990).

7. C. S. Yannoni, R. D. Johnson, G. Meijer, D. S. Bethune, and J. R. Salem, J. Phys. Chem. 95, 9 (1991).
8. M. D. Newton, and R. E. Stanton, J. Am. Chem. Soc. 108, 2469 (1986).
9. H. P. Luthi and J. Almlof, Chem. Phys. Lett. 135, 357 (1987).
10. P. W. Fowler, P. Lazzeretti and R. Zanasi, Chem. Phys. Lett. 165, 79 (1990).
11. R. C. Haddon and V. Elser, Chem. Phys. Lett. 169, 362 (1990).
12. S. Satpathy, Chem. Phys. Lett. 130, 545 (1986).
13. R. C. Haddon, L. E. Brus and K. Raghavachari, Chem. Phys. Lett. 125, 459 (1986).
14. S. Larsson, A. Volosov and A. Rosen, Chem. Phys. Lett. 137, 501 (1987).
15. D. S. Bethune et.al. , Nature 348, 621 (1990).
16. J. L. Wragg et.al., Nature 348, 623 (1990).
17. W. Kratschmer, L. D. Lamb, K. Fostirpoulos, and D. R. Huffman, AZPH-Th/90-44, University of Arizona (Department of Physics) Report (1990).
18. D. Heymann, Carbon 29, 684 (1991)
19. I. M. K. Ismail and P. L. Walker, Jr., Carbon 27, 549 (1989).
20. I. M. K. Ismail, Extended Abstract, Carbone 90, Carbon Conference held in Paris, July 16-20, p.38 (1990).
21. I. M. K. Ismail, Carbon 28, 423 (1990).
22. J. M. Ranish and P. L. Walker, Jr., Carbon 28, 887 (1990).
23. P. L. Walker, Jr., M. Shelef, and R. A. Anderson, Chemistry and Physics of Carbon 4, 287 (1968).
24. P. L. Walker, Jr., Carbon 28, 261 (1990).
25. N. R. Laine, F. J. Vastola, and P. L. Walker, Jr, J. Phys. Chem. 67, 2030 (1963).
26. I. M. K. Ismail, M. M. Rose, and M. A. Mahowald, Carbon 29, 575 (1991).
27. I. M. K. Ismail, Proceedings of the 20th Biennial Conference on Carbon, University of California, Santa Barbara, June (1991).
28. A. A. Lizzio, H. Jiang, and L. R. Radovic, Carbon 28, 7 (1990).
29. E. R. Gilliland and P. Harrrriott, Ind. Eng. Chem. 46, 2195 (1954).
30. A. Tomita, O. P. Mahajan, and P. L. Walker, Jr., Fuel 56, 137 (1977).
31. S. A. Verma and P. L. Walker, Jr, Carbon 28, 175 (1990).

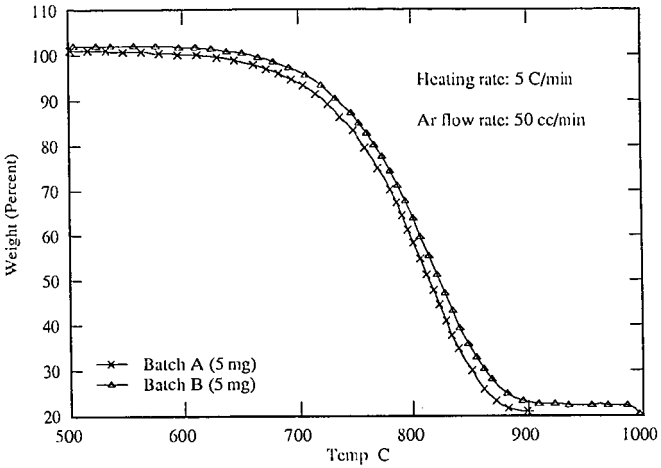

Figure 1:Sublimation of Fullerene (C60) in Argon.

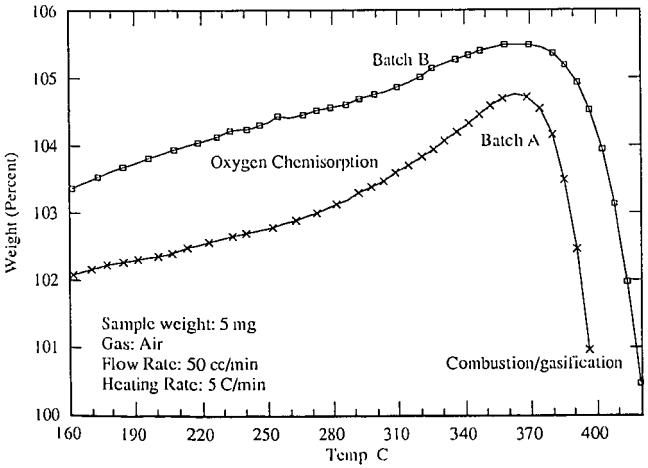

Figure 2: Reaction between Fullerene and Air at Low Temperatures.

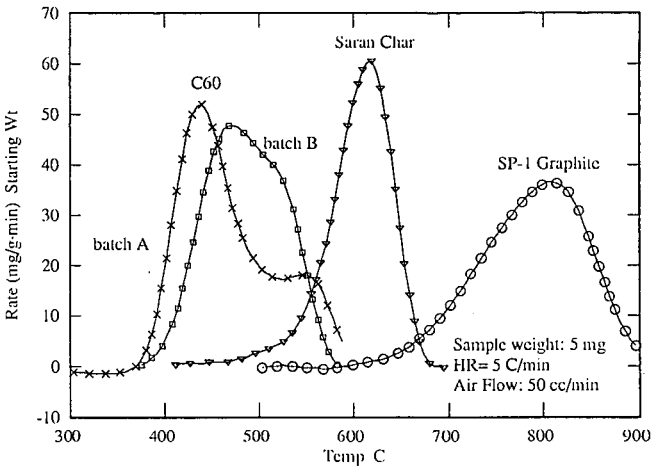

Figure 3: Comparison between Oxidation Rates of C60/ Saran/ SP-1 in air.

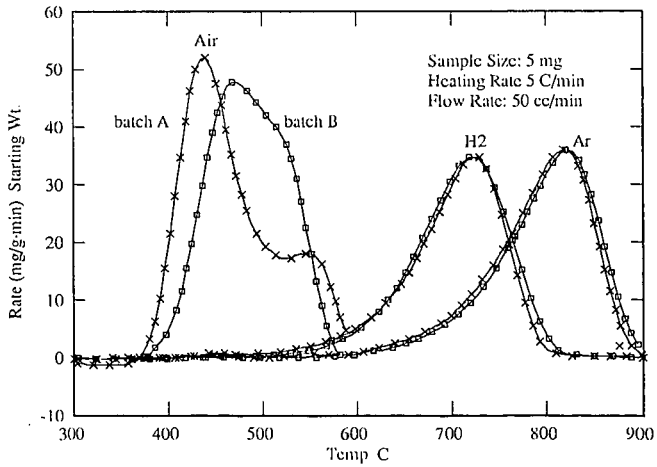

Figure 4: Reactions of Fullerene in Argon - Air and Hydrogen.

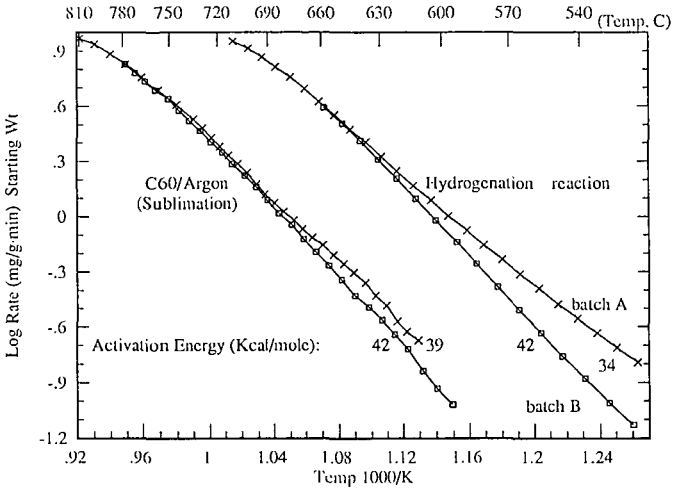

Figure 5: Arrhenius Plots for C60/Argon and C60/Hydrogen Reactions.

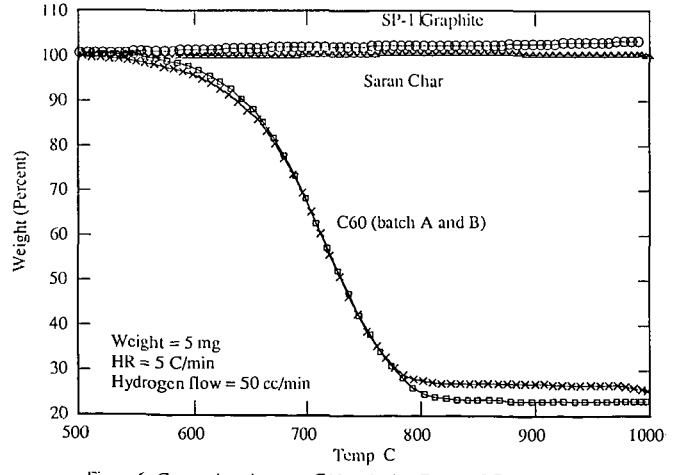

Figure 6: Comparison between C60 and other Forms of Carbon in Hydrogen.

CARBOPHANES: A NEW FAMILY OF CRYSTALLINE PHASES OF CARBON

R. H. Baughman and W. B. Hammond
Allied-Signal, Inc.
Research and Technology
Morristown, NJ 07962-1021

Keywords: Carbyne Carbon Phases, Carbophane Carbon Phases, Graphite Phase Transformation

I. Introduction:

This work is part of a continuing effort to develop structure-property predictions for new phases of carbon which are stable either at ambient or at high pressures [1]. The motivation is both to guide synthetic efforts to produce new carbon phases and to provide models for interpreting data for carbon phases of unknown structures.

Carbon crystals in which carbon exists in more than one hybridization state are the subject of the present analysis. Such materials are in sharp contrast with all available crystalline carbon phases with known structures, which contain either all sp^3 carbons (cubic diamond and Lonsdalite) or all sp^2 carbons (hexagonal graphite, rhombohedral graphite, and the newly discovered fullerenes). As is true for organic chemistry, the chemistry and physics of pure carbon is enormously expanded when one considers structures in which carbon is in more than one hybridization state. We have previously predicted structure-property relationships for a high thermal stability carbon phase which contains a mixture of sp^2 and sp carbon atoms [1]. This carbon phase, called graphyne, is presently the target of synthetic effort. Also, various high energy carbon phases have been proposed [2-7]. While carbon is known to exist in forms containing mixed states of carbon hybridization, all such well established forms are largely amorphous.

The family of carbon phases which we have constructed are called carbophanes, because of the similarities to the well known carbocyclic hydrocarbon molecules containing covalently bridged aromatic rings, which are called "phanes". These carbon phanes contain mixtures of sp^2 carbons, sp^3 carbons, and in some cases sp carbons. The structures and properties of these carbophanes will be compared with experimental results for (1) a phase or series of phases obtained by hydrostatic compression of graphite [8-14], (2) the crystalline transformation product obtained by rapid quenching of pulse-laser melted diamond [15], and (3) reported carbon phases which are often referred to in the literature as either"carbenes" or "carbynes" [16-19]. The structures are not established for any of these materials.

The high pressure transformation product of graphite which is of interest here was probably first discovered by Aust and Dickamer [8] in 1963, based on the observed increase in the resistivity of compressed graphite at about 15 GPa. However, the reported irreversibility of the phase change differs from the reversibility found in more recent work. Also, the reported x-ray data was later thought to originate from a contaminant [16]. Nevertheless, various investigators have firmly established the existence of a room temperature phase

transition for graphite which begins on increasing pressure to between 9 and 23 GPa. Upon decreasing the pressure to about 2 GPa or less, the new phase has been reported [11,12] to revert to a mixture of hexagonal and rhombohedral graphite. Electrical conductivity, optical reflectivity, and x-ray diffraction indicate that the high pressure phase is a crystalline insulator or a large bandgap semiconductor having low reflectivity between 1 and 3 eV [8-12]. This low reflectivity indicates that the interband absorption which occurs below 3 eV in graphite has been eliminated [10,13]. Also, the shear strength (determined by measuring pressure gradients and sample thickness in a diamond cell) is reported to exceed that of corundum and rhenium at 20 GPa, which is indicative of three-dimensional covalent bonding [11]. On the other hand, aromatic-like bonding is also suggested for the high pressure phase by Raman measurements at pressures between 38 and 55 GPa, which show a 100 cm^{-1} width peak centered at 1670 cm^{-1} [13]. However, other researchers report that the Raman spectrum could not be detected above 14 GPa [9]. Despite the width of this Raman line, the observation of at least three crystalline diffraction lines indicates that the transparent high pressure phase is not amorphous [11,12]. Structural models are herein proposed which provide electrical, optical and mechanical properties consistent with those observed. These carbophanes consist of covalently bonded sheets of carbon which contain aromatic rings that are isolated by sp^3 carbons. These structures are consistent with both the observed Raman line at about 1670 cm^{-1}, the low reflectivity between 1 and 3 eV, and the low conductivity. On the other hand, a high shear strength is provided by intersheet linkages via the sp^3 carbon atoms.

The experimental results reported for the carbyne phases are often contradictory and the initial structural assignment to linear chains of sp carbon atoms has added to the confusion [16-19]. There are several reasons why the above investigations are controversial. First, the reported properties of carbynes diverge from those predicted for chains of sp carbon atoms. These properties include, in specific instances, diamond-like hardness, a nonfibular morphology, colorless appearance, relatively high density, and high thermal and chemical stability. Second, atomic coordinates have not been produced which provide a satisfactory explanation for reported unit cell dimensions and diffraction intensities. This problem is understandable, since the derived unit cells are rather large and the only available diffraction data is either x-ray diffraction on polycrystalline and inhomogenous material or electron diffraction data on very small crystallites which are in a matrix of another material. Third, it is not always clearly established that the investigated crystalline phase component contains only carbon. This problem is exaggerated for synthetic routes which are claimed to produce new carbon phases from organic polymer precursors. Moreover, most of the structural characterization is by electron diffraction, which can be misleading in that highly crystalline minority phase components due to impurities can be highlighted. In fact, Smith and Buseck [20] have assigned phase components attributed by others to carbon to a variety of non-carbonaceous phases. This assignment has been contested and it is presently difficult to decide which of the results reported in the literature is an artifact and which is correctly assigned to a new phase of carbon. The reported carbyne phases of interest here are hexagonal with unit cell parameter (a) in the basal plane in the range of 4.76 - 5.45 Å (or a factor of $\sqrt{3}$ higher) and an orthogonal cell dimension of either ~7.5, ~10, ~12.5, or ~15 Å [16-19]. The reasonable consistency of the a-axis dimension, as well as the systematic

variation in the c-axis dimension, suggest polytypic structures. These facts, as well as the continuing reports from diverse laboratories over three decades, suggests that the results are not all artifacts due to impurity components.

II. Description of Carbophane Polytypes:

The basic structural motif of the carbophanes is a covalently bonded layer having the same intralayer connectivity as graphite. In other words, carbon layers in the carbophanes consist of a two-dimensional array of six membered rings. However, in contrast with graphite, these layers in the benzenoid carbophanes consist of a mixture of sp^3 carbons in rings having the hybridization of 1,4-hexadiene and sp^2 carbons which are simultaneously in both these rings with the sp^3 carbons and in benzene rings. Transformation of 1/4 of the sp^2 carbons of graphite to sp^3 carbons, so that the remaining sp^2 carbons are all in benzene rings and no sp^3 carbons are adjacent in a layer, provides the benzenoid carbophanes. Each sp^3 carbon atom is covalently bonded within the layer to an sp^2 carbon in each of three benzene rings. The remaining covalent bond to each sp^3 carbon provides a covalent interlayer bond. In the case where the covalent bonds between layers are to the same neighboring layer, a bilayer structure results in which bonding between alternating layers is non-covalent. More interesting and diversified structures result when each layer containing the hexagonal rings is covalently bonded to two neighboring layers - thereby providing three-dimensionally covalently bonded structures in which there is one interlayer covalent bond to every fourth carbon atom in the hexagonal ring layer. Examples of the hydrocarbon cyclophanes, which are structurally related to the present carbophanes, are shown in Figure 1.

The carbophane phases are categorized according to the direction of intersheet sp^3-sp^3 bonds for the fundamental structural motif, which is an aromatic ring surrounded by six sp^3 carbons (Figure 2). If a total of n sp^3 carbons bonded to a particular ring provide sp^3-sp^3 bonds to the same neighboring sheet, a total of n indices denote the configuration of sp^3-sp^3 bonds about this ring. These indices correspond to that of a ring carbon to which the associated sp^3 carbons are bonded. Correspondingly, there are seven motif isomers possible: 1,2,3,4,5,6-carbophane for n = 6; 1,2,3-carbophane, 1,3,5-carbophane, and 1,2,4-carbophane for n = 3; 1,2-carbophane, 1,3-carbophane, and 1,4-carbophane for n = 2; and 1-carbophane for n = 1. An example of a hexagonal ring sheet formed using the 1,3,5-carbophane motif is shown in Figure 2.

It is easily shown that the 1,2-, 1,4-, 1,2,3-, and 1,2,4-carbophane structures are unique. By unique we mean that there is only one way to covalently interconnect these motifs in a single motif structure. Also, the 1,3,5-carbophane has a type of uniqueness, since there is only one possible way to covalently interconnect the 1,3,5 motif, so as to provide the hexagonal ring sheet. However, these hexagonal sheets can be covalently interconnected with a neighboring sheet in two different ways, one which results in eclipsed aromatic rings, and one which results in non-eclipsed aromatic rings. These structures are named eclipsed 1,3,5-carbophane (or e-1,3,5-carbophane) and staggered 1,3,5-carbophane (or s-1,3,5-carbophane), respectively. Various mixtures of eclipsed and staggered sheets can be used to construct an infinite variety of either ordered or disordered forms of 1,3,5-carbophane which

contain basically the same structure for each hexagonal ring sheet. The structures for e-1,3,5- and s-1,3,5-carbophane viewed parallel to the molecular plane are shown in Figures 3 and 4, respectively.

In contrast with these types of uniqueness, there are an infinite number of possible ways (both periodic and non-periodic) to form covalent connections within the ring sheets using exclusively either the 1,3-carbophane or the 1-carbophane motif. Of the single motif structures, a structure with staggered (i.e. non-eclipsed) aromatic rings is possible only for 1,3,5-carbophane and 1-carbophane. Such structures are of special importance because of decreased strain energy compared with the corresponding fully eclipsed structures. As will be described elsewhere, partially staggered structures can arise for carbophanes having mixed motifs, such as an array of 1,3 and 1,3,5 motifs, where every layer can be either eclipsed on both sides or staggered on one side and eclipsed on the other. Note also that only the 1,3,5-carbophane and 1-carbophane structure could transform to diamond without the breaking of already formed covalent bonds. In such a manner, e-1,3,5-carbophane could transform to hexagonal diamond (Lonsdalite) and s-1,3,5-carbophane could transform to cubic diamond. All of the other above mentioned benzenoid carbophanes could transform to a fully sp^3 structure without bond breaking only by formation of energetically unfavorable cyclobutane rings.

There is another type of single-motif benzenoid carbophane structure which is possible, but this structure (which is analogous to the organic "superphane" shown in Figure 1) does not provide a three dimensionally covalently bonded structure. In this structure, which is denoted 1,2,3,4,5,6-carbophane, all intersheet sp^3-sp^3 bonds from one sheet are connected to the same neighboring hexagonal ring sheet. These bilayers are bound with neighboring bilayers on either side by exclusively non-covalent interactions. Correspondingly, sheets of normal graphite planes could interdisperse with the bilayers, so as to provide an infinite variety of polytypic structures. From the viewpoint of close-packing, such polytypic structures would be expected to be thermodynamically unstable with respect to phase separation of the graphite sheets to make a pure graphite phase. However, such phase separation would be extremely unfavorable, kinetically.

III. Calculation of Crystal Structures and Strain Energies:

We have used the crystal building capabilities of the software program PolyGraf [21] and a modified Dreiding force field [22] to generate energy minimized unit cell parameters and atom coordinates for the simplest members of the carbophane family of phases. The Dreiding force field was modified to reproduce the known structures for a series of organic cyclophanes [27-29] shown in Figure 1. Note that the present force field provides sp^2-sp^2 bond lengths and force constants appropriate for an isolated aromatic ring, as in a benzenoid carbophane (with a π-bonding order of 1/2 per bond). Consequently, the intralayer bond distances which are predicted for graphite are too short (the π-bond order in graphite is 1/3) and the calculated density of graphite is correspondingly too high, although the graphite interlayer distance is correctly predicted by our force field. The present calculation does not take into account changes in π-bond order in the aromatic rings due to ring distortion, which might provide contributions from quinoid-like structures.

The present crystal structure calculations for carbophane phases provide enthalpies (H_1) relative to a hypothetical reference state in which the terms in the calculation Hamiltonian are zero. The standard heat of formation of a carbophane is obtained by adding the above energy H_1 (which is largely a strain energy) to the energy of the reference state for a carbophane (relative to graphite), which is denoted H_o. H_o is calculated using experimentally derived heats of formation of model hydrocarbon molecules which contain an sp^3 carbon atom covalently bonded to three sp^2 carbon atoms in benzene rings and to an sp^3 carbon, as in carbophane. This is done by first using the molecular mechanics force field to calculate the strain energies (H_1) for the model compounds. Using this strain energy and the experimentally derived gas phase heats of formation, $H_f(g)$, for a model compound, H_o for the model compound becomes $H_o = H_f(g) - H_1 - 4RT$, where the term 4RT corrects for the enthalpy contributions due to rotational and translational motion (3RT) and the difference between constant volume and constant pressure gas phase heat capacities (RT).

Using this approach, H_o for the family of carbophanes was calculated as follows: H_o(carbophane) = 1/4 H_o(1,1,1-triphenylethane) - 1/8 H_o(ethane) - 5/8 H_o(benzene). Using gas phase formation enthalpies for these hydrocarbons reported in the literature [30,31], the resulting value of H_o for the reference state of a benzenoid carbophane is 0.85 kcal/mole carbon.

If we approximate the effective bond energy of an sp^2-sp^3 bond as the average of sp^2-sp^2 and sp^3-sp^3 bonds, a second estimate for H_o of benzenoid carbophane can be obtained from the heat of formation of diamond [32] and the gas phase heats of formation of benzene and biphenyl [31]. The equation for H_o of carbophane is then: H_o(carbophane) = 3/8 H_o(biphenyl) - 5/8 H_o(benzene) + H_o(diamond). The resulting value of H_o is -0.94 kcal/mole carbon, which is somewhat lower than the above value of +0.85 kcal/mole carbon. Which value is more reliable cannot presently be determined, since the former calculation contains an uncertainty due to the required estimation of the heat of sublimation of the triphenylethane [30], using group increments, and the latter value is uncertain because of the above bond-energy approximation. Although these values of H_o are both close to zero, the uncertainties in H_o limit our ability to calculate equilibrium transition pressures for the interconversion between graphite and the carbophanes.

IV. Properties Evaluation:

Based on experimental observations for multilayered organic benzenoid cyclophanes, the present benzenoid carbophanes are expected to be colorless. For example, Otsubo et al. [33] investigated the effect of layer number on the optical properties of [2.2]paracyclophanes having from 2 to 6 layers. The two layer form of this compound is shown in Figure 1. With increasing layer number, strong bathochromic and hyperchromic changes are observed in the ultraviolet absorption spectra. However, these effects rapidly saturate, so that little change is observed in going from a five layer to a six layer [2.2]paracyclophane, both of which form colorless crystals. Similarly, both fluorescence and phosphorescence spectra exhibit large bathochromic shifts

and the phosphorescence lifetime decreases with increasing layer number. Also, the charge-transfer complexes with acceptors, such as tetracyanoethylene or trinitrobenzene, demonstrate bathochromic shifts of the long wavelength charge-transfer band and an increased association constant for increasing numbers of layers in the paracyclophanes. These shifts in optical properties with increasing number of layers, which are close to saturation for six layer [2.2]cyclophane, largely arise from interlayer π-electron interactions between neighboring aromatic rings. Based on the similar optical properties of unsubstituted cyclophanes and cyclophanes with severe aromatic ring distortions due to eclipsed methyl substituents (as well as the absence of large shifts in the absorption curves for [m]cyclophanes having aromatic ring strain similar to the [2.2]paracyclophanes [34]), the optical property changes due to aromatic ring distortions are expected to be relatively unimportant [33].

The above observations on the multilayered organic benzenoid cyclophanes also suggest that the corresponding eclipsed benzenoid carbophanes with three-dimensional covalent bonding will display red shifts in absorption, fluorescence, and phosphorescence spectra (and a decrease in phosphorescence lifetimes) with decreasing interlayer separation, due to increased π-electron interactions in the stacks of aromatic rings. The decreased phosphorescence lifetime is expected to be a result of a lowering of the energy gap between ground and triplet states as a result of increasing interactions between benzene rings. More specifically, using observations on the stacked [2.2]paracyclophanes [33], an absorption onset at about 3.3 eV, a fluorescence maxima at about 390 nm, and a phosphorescence maxima at about 530-570 nm are expected for an eclipsed carbophane having a spacing between aromatic ring carbons of about 2.97 Å. Such spacings are in the range predicted for carbophanes. A blue shift in these spectra and an increased phosphorescence lifetime is expected for the eclipsed carbophanes in Table 1 having longer interlayer separations, while those eclipsed carbophanes having shorter interlayer separations are expected to behave in the opposite manner. Pressure will decrease the interlayer spacing and produce the corresponding effects on the electronic states.

Note that the calculated densities for the carbophanes in Table 1 range from 2.479 g/cm^3 for s-1-carbophane to 2.801 g/cm^3 for e-1,3,5-carbophane. The calculated densities of these phases are intermediate between those of hexagonal graphite (ρ(obs.)=2.267 g/cm^3) and diamond (ρ(obs.)=3.52 g/cm^3 and ρ(calc.)=3.502 g/cm^3). Excluding the highest density phases (e-1,3,5-carbophane and s-1,3,5-carbophane), the calculated strain energies of the carbophanes are represented within a maximum deviation of 0.24 kcal/mole by a linear dependence on calculated density (H_1 = -20.32 + 9.26 ρ). Staggered 1,3,5-carbophane has a 0.56 kcal/mole lower strain energy and eclipsed 1,3,5-carbophane has a 0.65 kcal/mole higher strain energy than provided by this linear correlation. Consequently, the s-1,3,5-carbophane phase is especially interesting as a phase which might be thermodynamically stable with respect to graphite at high pressure. Note that this phase shows a large density increase with respect to the density of graphite, while requiring a smaller than expected formation energy with respect to graphite at zero pressure. Although increasing the temperature will decrease the formation free energy of a carbophane relative to diamond, because of entropy contributions, diamond will

have a lower free energy than any carbophane phase at room temperature and any pressure.

Calculated bulk moduli for carbophanes and for diamond are also listed in Table 1. Using the modified Dreiding force field, a bulk modulus of 477 GPA is obtained for diamond, as compared with a measured value of 442 GPa [35]. Staggered-1,3,5-carbophane has the highest calculated bulk modulus and the highest bulk density of all the benzenoid carbophanes studied. The bulk modulus of s-1,3,5-carbophane is 240 GPa, which is 54% of the observed modulus of diamond and 7.1 times the observed [9] bulk modulus of graphite (33.8 GPa). Since 1,2,3,4,5,6-carbophane does not have three-dimensional covalent bonding, but instead consists of bilayers which are connected to neighboring bilayers by exclusively non-covalent bonding, a bulk modulus of about twice that of graphite is expected for this phase. Consistent with this view, the ratio of the calculated bulk modulus for 1,2,3,4,5,6-carbophane to the observed bulk modulus for graphite is 2.2.

V. Conclusions:

A carbophane phase provides an interesting model for the room temperature, high pressure transformation product of graphite (HP phase). A number of points provide support for such a model. First, the HP phase is reported to revert to a mixture of hexagonal and rhombohedral graphite upon a reduction in pressure at room temperature [11-12], which would appear to exclude assignment as a polytype of diamond. While the carbophanes are expected to have a considerable degree of kinetic stability at zero pressure, defects (due to imperfect phase transformation, for the ambient temperature formation process) could propagate as molecular scale cracks upon the unloading of pressure, thereby facilitating the reconversion to graphite. Second, formation of carbophanes is expected to be kinetically favorable, since no covalent bond breaking is required to transform graphite to a carbophane and a lower degree of cooperative reaction is required than to form a diamond polytype. Third, eclipsed carbophanes are predicted to be transparent up to about 3.3 eV and staggered carbophanes are probably transparent to an even higher energy. This is consistent with the reported bleaching of the interband transition of graphite below 3 eV in going to the HP phase [10,13]. Fourth, the carbophanes would provide a Raman peak (corresponding to the aromatic ring mode) close to that observed for the HP phase, since the in-plane ring stretch occurs in the 1620-1565 cm^{-1} region at atmospheric pressure for various cyclophanes [36]. Fifth, the carbophanes, such as s-1,3,5-carbophane, are calculated to have a bulk modulus which is up to 50% that of diamond, consistent with the report that the HP phase is a superhard material with a strength comparable to diamond [11].

Regarding the possibility that carbophanes might have been already observed at ambient pressure, but unrecognized as such, it is interesting to note that Weathers and Bassett [15] have reported that new crystalline carbon phases are produced as microscopic components by pulsed-laser melting of diamond at high pressures in a diamond anvil cell. As the pressure during the laser pulse is increased from 10 to 30 GPa, the long diffraction spacing observed for the transformation product decreases from 3.4 Å, as in graphite, to 2.8 Å. As shown in Table 1, this is about the range of intersheet spacings which we have

derived for three-dimensional carbophane phases (from 3.17 Å for 1,2,3-carbophane to 2.72 Å for s-1,3,5-carbophane). Additionally, it is interesting to note that the carbophanes provide the diamond-like hardness, non-fibular morphology, colorless appearance, and relatively high density that researchers have attributed to the mysterious carbyne phases [16-19]. Also, if these phases are well ordered, they could provide the high thermal and chemical stability which has been claimed for the carbynes. The directly bridged carbophanes described herein do not provide the acetylenic bond, which is the claimed component of carbynes [16-19]. The evidence for such bonds in the crystalline phase is not firmly established, because of the possibility that the spectroscopic signature for their type of bonding is from the matrix. Nevertheless, acetylene-containing polytypes can be readily constructed from the present carbophane phases by replacing sp^3-sp^3 interlayer bridges with sp^3-sp≡sp-sp^3 linkages for either a fraction or for all of the interlayer separations. We have shown that the resulting unit cell parameters reproduce reasonably well those in the literature of carbynes [16-19].

This is an interim report of continuing work on what we believe to be an important family of new carbon phases. Work in progress will extend the carbophane family of phases to mixed motif and disordered variants, refine and extend property predictions, and provide comprehensive comparisons of predicted properties with those reported in the substantial literature which claims new crystalline carbon phases. It will also be interesting to see whether or not the fundamental packing arrangements in the carbophanes provide a useful framework for structural models of "amorphous" diamond-like carbon. These materials are known to consist of mixtures of sp^3 and sp^2 hybridized carbons.

References

1. R. H. Baughman, H. Eckhardt, and M. Kertesz, J. Chem. Phys. 87, 6687 (1987).
2. M. T. Yin and M. L. Cohen, Phys. Rev. Lett. 50, 2006 (1983).
3. K. M. Merz, R. Hoffmann, and A. T. Balaban, J. Am. Chem. Soc. 109, 6742 (1987).
4. G. Laqua, H. Musso, W. Boland, and R. Aldrichs, J. Am. Chem. Soc. 112, 7391 (1990).
5. M. A. Tamor and K. C. Hass, J. Mater. Res. 5, 2273 (1990).
6. A. T. Balaban, C. C. Rentia, and E. Ciupitu, Revue Roumaine de Chimie 13, 231 (1968).
7. R. Hoffman, T. Hughbanks, M. Kertesz, and P. H. Bird, J. Am. Chem. Soc. 105, 4832 (1983).
8. R. B. Aust and H. G. Drickamer, Science 140, 817 (1963).
9. M. Hanfland, H. Beister, and K. Syassen, Phys. Rev. B 39, 12598 (1989).
10. M. Hanfland, K. Syassen, and R. Sonnenschein, Phys. Rev. B 40, 1951 (1989).
11. J. F. Shu, H. K. Mao, J. Z. Hu, Y. Wu, and R. J. Hemley, Bull. Am. Phys. Soc. 36, 479 (1991).
12. Y. X. Zhao and I. L. Spain, Phys. Rev. B 40, 993 (1989).
13. A. F. Goncharuv, I. M. Makarenko, and S. M. Stishov, High Pressure Research 4, 345 (1990).
14. A. A. Goncharuv, Zh. Eksp. Teor. Fiz. 98, 1824 (1990).

15. M. S. Weathers and W. A. Bassett, Phys. Chem. Minerals 15, 105 (1987).
16. L. I. Man, Y. A. Malinovskii, and S. A. Semiletov, Sov. Phys. Crystallogr. 35, 608 (1990).
17. A. G. Whittaker and P. L. Kintner, Science 165, 589 (1969).
18. R. B. Heimann, J. Kleiman, and N. M. Salansky, Carbon 22, 147 (1984).
19. A. M. Sladkov, Soviet Sci. Rev. Sec. 3, 75 (1981).
20. P. K. Smith and P. R. Buseck, Science 216, 986 (1982).
21. PolyGraf is an interactive molecular simulation/three-dimensional graphics program from Molecular Simulations, Inc., Sunnyvale, CA, 94086
22. The following adjustments were made in the Dreiding force field [23]. The van der Waals interactions were treated with an exponential-six potential with parameters for hydrogen (R_o=3.1665 Å, D_o=0.0200 kcal/mole, and ζ=11.2) and carbon (R_o=3.8410 Å, D_o=0.07918 kcal/mole, and ζ=13.0)[24]. A Morse potential was used for bond stretching with $B_o(sp^3\text{-}sp^3)$=1.525 Å, $B_o(sp^3\text{-}sp^2)$=1.500 Å, and $B_o(sp^2\text{-}sp^2)$=1.375 Å. A theta expansion was used for the angle bending term with $\Theta_o(sp^3\text{-}sp^3\text{-}sp^2)$=112.0°. The Dreiding force field uses a six-fold torsion term with a barrier height of 1.0 kcal/mol. and a *cis* max for rotation about an sp^3 carbon bonded to an aromatic ring. We were better able to reproduce the barriers for rotations reported by Schafer et al. for ethylbenzene [25] and isopropylbenzene [26] if this term was set equal to zero.
23. S. L. Mayo, B. D. Olafson, and W. A. Goddard, III, J. Phys. Chem. 94, 8897 (1990).
24. N. Karasawa, S. Dasgupta, and W. A. Goddard, III, J. Phys. Chem. 95, 2260 (1991).
25. T. Schaefer, G. Penner, and R. Sebastian, Can. J. Chem. 64, 873 (1986).
26. T. Schaefer, R. Sebastian, and G. Penner, Can. J. Chem. 66, 1945 (1988).
27. H. Hope, J. Bernstein, and K. N. Trueblood, Acta Cryst. B28, 1733 (1972).
28. A. W. Hanson, Cryst. Struct. Comm. 9, 1243 (1980).
29. A. W. Hanson and T. S. Cameron, J. Chem. Research (S) 336 (1980).
30. R. M. Joshi, J. Macromol. Sci.,Chem. A5, 687 (1971).
31. D. R. Stull, E. F. Westrum, Jr., and G. C. Sinke, The Chemical Thermodynamics of Organic Compounds, Sec.III, pp. 631-769 (Wiley, New York, 1969).
32. P. Hawtin, J. B. Lewis, N. Moul, and R. H. Phillips, Proc. Soc. London A 261, 67 (1966).
33. T. Otsubo, S, Mizogami, I. Otsubo, Z. Tozuka, A, Sakagami, Y. Sakata, and S. Misumi, Bull. Chem. Soc. Jap. 46, 3519 (1973).
34. N. L. Allinger, L. A. Freiberg, R. B. Hermann, and M. A. Miller, J. Am. Chem. Soc. 85, 1171 (1963).
35. M. H. Grimsditch and A. K. Ramdas, Phys. Rev. B 11, 3179 (1975).
36. P. H. Scudder, V. Boekelheide, D. Cornutt, and H. Hopf, Spectrochimica Acta 37A, 425 (1981).

Table 1. Calculated Structural Features of Carbon Phases

Carbon Phase	Space Group	Density g/cm^3	Z[a]	H_1(strain) (kcal/mol)	Interlayer Spacing,Å	Bulk Modulus (GPa)
s-1-carbophane	$P\bar{3}1m$	2.479	48	2.398	3.074	101
e-1-carbophane	$P\bar{6}2m$	2.672	48	4.345	2.926	135
	Cmcm	2.672	64	4.367	2.924	129
1,2-carbophane	Cmcm	2.547	64	3.376	3.125	109
1,3-carbophane	Cmcm	2.737	64	5.128	2.853	192
	$P\bar{6}2m$	2.733	48	5.104	2.858	191
1,4-carbophane	Immm	2.722	32	4.862	2.884	199
1,2,3-carbophane	Imma	2.514	32	3.205	3.169	106
1,2,4-carbophane	Cmca	2.707	64	4.573	2.903	195
s-1,3,5-carbophane	$R\bar{3}m$	2.840	24	5.418	2.724	240
e-1,3,5-carbophane	$P6_3/mmc$	2.801	16	6.271	2.775	238
1,2,3,4,5,6-carbophane	P6/mmm	2.636	16	4.190	2.672[b] 3.226[c]	75
graphite	$P6_3mmc$	2.405	4	-0.007	3.355	43
	$R\bar{3}m$	2.402	2	0.010	3.355	
diamond	Fd3m	3.502	8	0.992	2.059[d]	477
	$P6_3/mmc$	3.490	4	2.591	2.180[e]	473

[a] Atoms per unit cell. [b] Distance between covalently bonded layers. [c] Distance between van der Waals bonded layers. [d] (111) spacing. [e] (100) spacing.

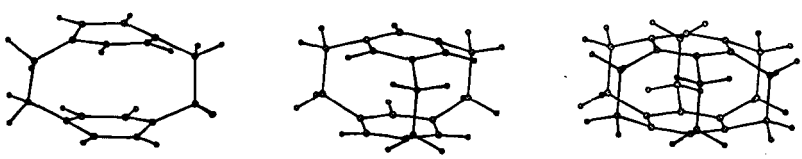

Figure 1. Organic cyclophanes which contain the intersheet bonding arrangement of 1,4-carbophane, 1,3,5-carbophane, and 1,2,3,4,5,6-carbophane.

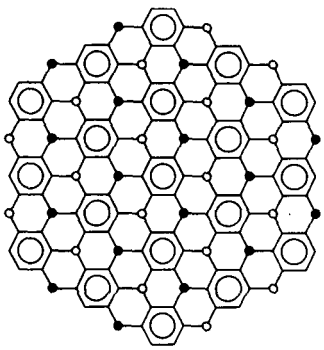

Figure 2. The bonding arrangement for e and s-1,3,5-carbophane showing the six sp^3 carbons surrounding each aromatic ring. Open and closed circles indicate sp^3 bonding below and above the layer plane, respectively.

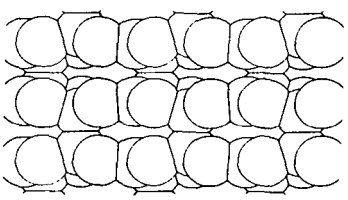

Figure 3. The crystal structure for e-1,3,5-carbophane viewed normal to the intersheet sp^3-sp^3 bond and parallel to the sheet plane.

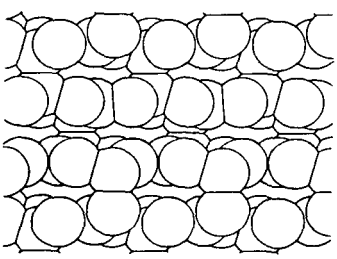

Figure 4. The crystal structure for s-1,3,5-carbophane viewed normal to the intersheet sp^3-sp^3 bond and parallel to the sheet plane.

High Temperature Raman Scattering Behaviour in Diamond

Harald Herchen and Mark A. Cappelli
High Temperature Gasdynamics Laboratory
Stanford University
Stanford, CA 94305-3032

Keywords: Diamond, First-order Raman

Introduction

The Raman spectrum of synthetic carbon films is now routinely used as an identification of the phase or measure of the quality of such films, when compared to that of natural diamond or natural and synthetic graphite.[1] Since the development of CVD diamond technology, the width and relative shift of the first-order Raman transition of polycrystalline diamond has been used to qualitatively ascribe the amount of disorder[2] (inhomogeneous strain) or homogeneous strain[3] in these new materials. In diamond, the lattice dynamics that give rise to the Raman effect are also responsible for determining the thermal properties such as specific heat and thermal conductivity. The variation with temperature of the first-order Raman mode in polycrystalline diamond in comparison to that of natural diamond can therefore be used as an additional qualitative check on the high temperature behaviour of the thermal properties of these films.

The temperature variation of the first-order Raman spectrum in natural diamond was first investigated by Nayar[4] in 1941 in an attempt to better understand the relationship between the observed shift and measured thermal expansion coefficients. A similar but more extensive study was performed by Krishnan.[5] In both cases, the highest temperature achieved (about 1100 K) was limited by diamond contamination and thermal emission, which contributed to background interference. Recently, Herchen and Cappelli[6] extended these measurements to about 1900 K, using gated photon counting and either modulated or pulsed laser excitation sources. In this paper, similar data is presented for free standing 100 μm thick diamond film. The Stokes to anti-Stokes ratio of the first-order Raman spectrum is used to infer the sample temperature. It is found that this temperature is consistent with temperatures measured by optical pyrometry, provided a diamond emissivity of close to unity is used in the analysis. These temperatures are then employed to deduce the variation in the shift and width of the Raman feature with temperature. The results are compared to similar measurements on type IIa natural diamond.

Experiment

The experimental facility is similar to that used in previous studies,[6] and is only briefly described here. The Raman spectra were obtained by exciting the free standing polycrystalline diamond samples with the 457.94 nm output from an argon-ion laser that was mechanically chopped at 2 kHz. The backscattered light from near-normal incidence was collected with f/5 optics and imaged onto the entrance slit of a 1-m scanning monochromator. The dispersed light at the exit slit was detected with a photomultiplier tube and analyzed with photon counting electronics. The spectral resolution was approximately 0.1-nm, and all spectral width measurements were corrected for instrument broadening.

The free-standing polycrystalline diamond used to obtain the results described here was provided by Crystallume Inc.[7] The thickness of the sample studied was approximately 100 μm and was grown by microwave plasma deposition. It was translucent and grey in appearance partly resulting from the scattering of light at the grain boundaries. The sample was treated for one hour by boiling in 96% sulphuric acid at atmospheric pressure prior to inserting it into a

high vacuum chamber where it was sandwiched between two electrically heated tungsten ribbons (Fig. 1). The chamber had optical access permitting laser excitation and direct measurement of the tungsten and diamond brightness temperatures.

The diamond was not expected to be in thermal equilibrium with the tungsten ribbons, and so each brightness temperature was monitored independently. A disappearing filament pyrometer with a filter centered at 655 nm was used in the measurement of the brightness temperatures. These temperatures can be corrected to the actual temperatures provided that emissivities of the two materials at 655 nm are known. The emissivity of tungsten at that wavelength is well known, however there is no available data on the emissivities of polycrystalline diamond films. Indeed, the values will be highly dependent on surface and growth conditions. Consequently, the Raman Stokes to anti-Stokes intensity ratio was used to arrive at the true diamond temperature, and this together with the measured brightness temperature provided an experimental determination of the sample emissivity.

Results and Discussion

Typical Stokes and anti-Stokes first-order Raman spectra of the free-standing polycrystalline diamond samples at approximately 1200 K brightness temperature are shown in Fig. 2. The nearby argon plasma transition from the laser discharge (Ar^+ $4s\ ^2P \rightarrow 4p\ ^2D^o$ line at 487.986 nm) appears at a shift of 1344.7 cm^{-1} and acts as an accurate calibrant for the Stokes shifted diamond component which appears here at 1309 cm^{-1}. The argon plasma spectral line at 433.12 nm is sufficiently close to the anti-Stokes component to provide a similar reference at -1251.2 cm^{-1}. It is evident that both the Stokes and anti-Stokes components are significantly broadened to about 10 cm^{-1} after correction for the instrument broadening. Their widths are nearly twice that observed for natural type IIa diamond at the same temperature.[6]

The Raman Stokes to anti-Stokes intensity ratio

$$\frac{I_{St}}{I_{a-St}} = \left(\frac{\omega_\ell - \omega_s}{\omega_\ell + \omega_s}\right)^4 e^{h\omega_s/kT}$$

can be a direct measure of the sample temperature. Here ω_s is the phonon frequency, ω_ℓ is the line center frequency of the laser excitation source, T is the sample temperature, and h and k are the Planck and Boltzmann constants, respectively. Figure 3 compares the sample temperature derived from the Stokes to anti-Stokes ratio to the tungsten ribbon temperature as measured by optical pyrometry. It is clear from this figure that the sample does not come to thermal equilibrium with the tungsten heaters and is usually 200 to 300 K cooler over the range tested. This difference can be attributed to the thermal contact resistance between the diamond sample and tungsten ribbon heaters and to significant radiative losses due to the high emissivity of this diamond sample. This result further emphasizes the need to directly measure the diamond temperatures during vapor deposition, so as to have a more accurate assessment of the deposition conditions.

The emissivity can be estimated from the temperatures derived from the Stokes to anti-Stokes ratios and the measured diamond brightness temperatures. These are given in Fig. 4. The results suggest emissivities at 655 nm of close to unity, consistent with the visual appearance of the sample. These results are intriguing in that they suggest that polycrystalline diamond coatings may be very useful as high temperature radiative surfaces in circumstances where other properties of such diamond are also advantageous.

The variation in the observed Raman shift with diamond temperature for both the Stokes and anti-Stokes components is shown in Fig. 5. The diamond temperature is found from its brightness temperature and an emissivity of unity. The error in the shift is ± 0.3 cm^{-1} which is less than the size of the symbols used to represent the data points. Also shown in the figure is

a solid line summarizing previously measured values for natural diamond.[6] The values for the polycrystalline diamond are found to be in excellent agreement with that of natural diamond over the range of temperature studied here. Furthermore, these results are in general agreement with the theoretical molecular dynamics predictions of Wang et al[8], a fit through which is shown by a dashed line in Fig. 5.

The variation in the full width at half maximum intensity (FWHM) of the Raman spectrum with temperature (again using the diamond brightness temperature and an emissivity of unity) is shown in Fig. 6. The spectra were corrected for instrument broadening. The spectral lineshapes were found to be well represented by a Voigt profile. The Lorentzian Raman profile was obtained by deconvolving the Gaussian instrument broadening from the measured profiles. The instrument contribution to the FWHM amounted to 3.7 cm^{-1} and 4.7 cm^{-1} for the Stokes and anti-Stokes components, respectively. The solid line in Fig. 6 is a fit to the results obtained for natural diamond.[6] The high temperature FWHM for the polycrystalline samples are 4 to 6 cm^{-1} greater than that for natural diamond, consistent with room temperature data. Both results however are in reasonable agreement with the predicted FWHM values of Wang et al.[8] The difference between the measured values of the FWHM for the polycrystalline and natural diamond samples can be attributed to slight disorder in the carbon-carbon bond length (inhomogeneous strain).[2] An accurate and unambiguous identification of the source of broadening in the first-order Raman spectra requires further experimental and theoretical investigation.

Summary

The data presented here suggest that one can grow polycrystalline CVD diamond that has high temperature Raman scattering characteristics comparable to that of natural diamond. The usefulness of Raman scattering as a possible unambiguous measure of the sample temperatures has been demonstrated. Furthermore, this independent temperature measurement provided the opportunity to make one of the first direct measurements of CVD diamond emissivity. Emissivities approaching unity were obtained, suggesting that CVD diamond could be quite useful as a high temperature radiative coating in chemically harsh environments.

Acknowledgements

The authors would like to thank M. Pinneo of Crystallume for providing the polycrystalline diamond sample studied here. Support for this research was provided by the Office of Naval Research.

References

1. D.S. Knight and W.B. White, J. Mater. Res. 4, 385 (1989).
2. R.G. Buckley, T.D. Moustakas, L. Ye, and J. Varon, J. Appl. Phys. 66, 3595 (1989).
3. M.A. Cappelli, T.G. Owano, C.H. Kruger, J. Mater. Res. 5, 2326 (1990).
4. R.G.N. Nayar, Proc. Indian Acad. Sci. Sect. A 13, 284 (1941).
5. R.S. Krishnan, Proc. Indian Acad. Sci. Sect. A 24, 45 (1946).
6. H. Herchen and M.A. Cappelli, Phys. Rev. B (in press).
7. Crystallume Inc., 125 Constitution Ave, Menlo Park, California, 94025.
8. C.Z. Wang, C.T. Chan and K.M. Ho, Phys. Rev. B 42, 11276 (1990).

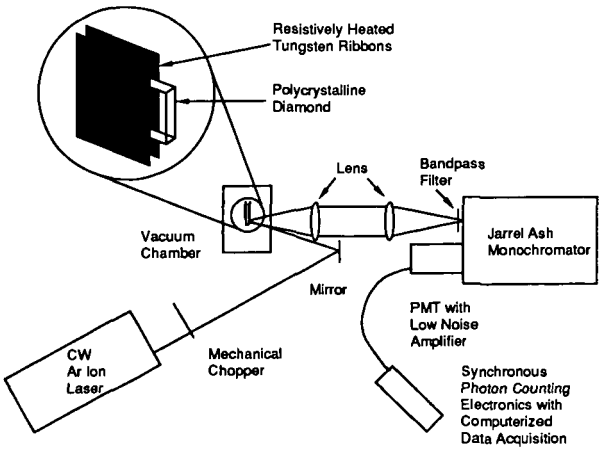

Figure 1. Schematic of the experimental setup for Raman backscattering studies of polycrystalline diamond at high temperature. The inset illustrates the mechanism used to heat and hold the sample.

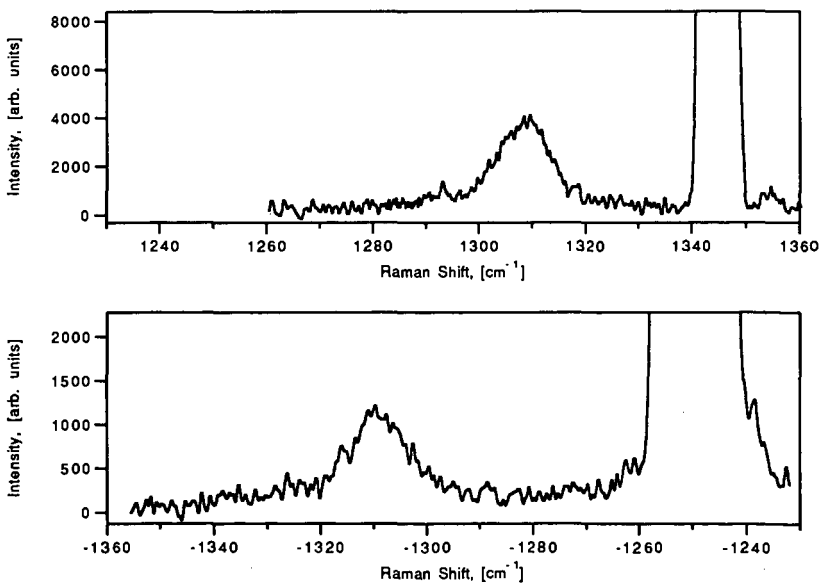

Figure 2. Stokes, top, and anti-Stokes first-order Raman spectra with argon ion emission calibration lines. The diamond temperature was 1200 K.

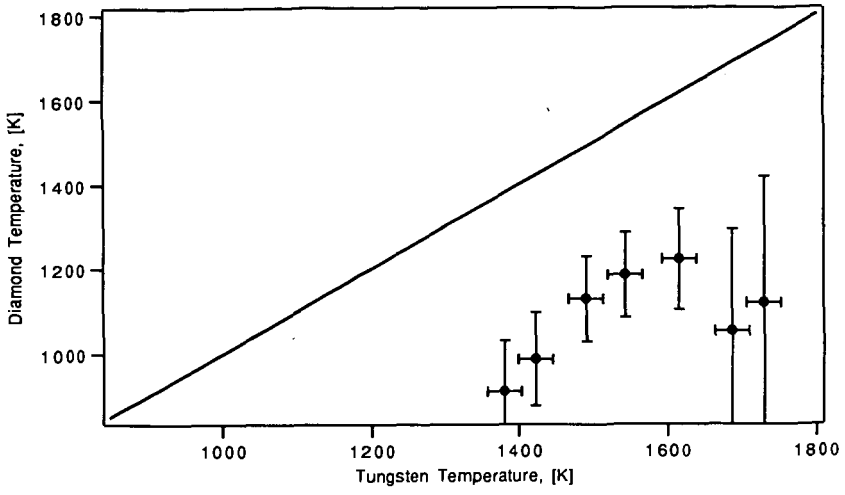

Figure 3. Polycrystalline diamond temperature based on the Stokes to anti-Stokes intensity ratio as a function of the tungsten ribbon temperature. The solid line corresponds to equal diamond and tungsten temperatures.

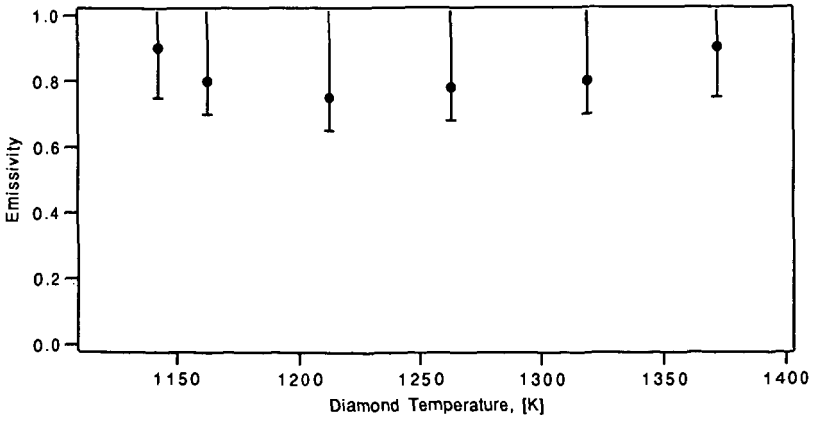

Figure 4. Polycrystalline diamond emissivity at 655 nm determined from the measured brightness temperature and the diamond temperature found from the Stokes to anti-Stokes intensity ratio.

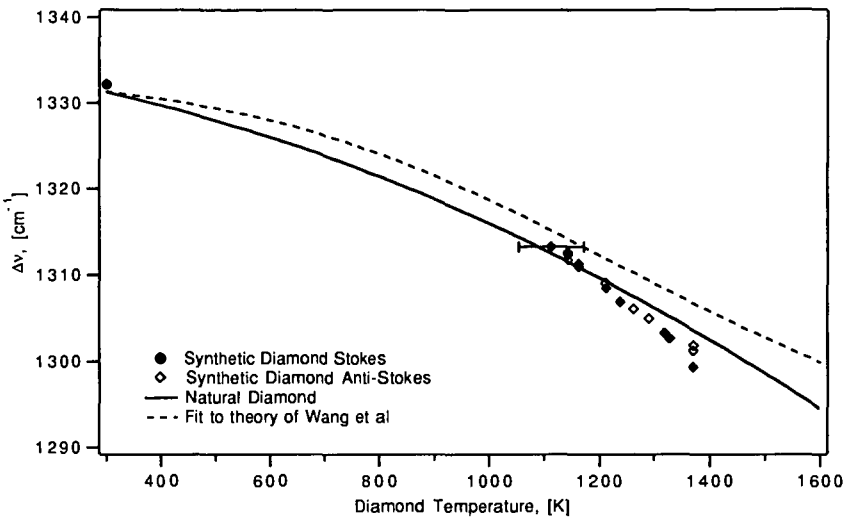

Figure 5. Variation of the first-order Raman shift in polycrystalline diamond with temperature. The diamond temperature is found using an emissivity of unity. The solid line is a fit to the first-order Raman shift for natural diamond (Ref. 6). The dashed line is a fit to the results of molecular dynamics simulation of Wang et al (Ref 8).

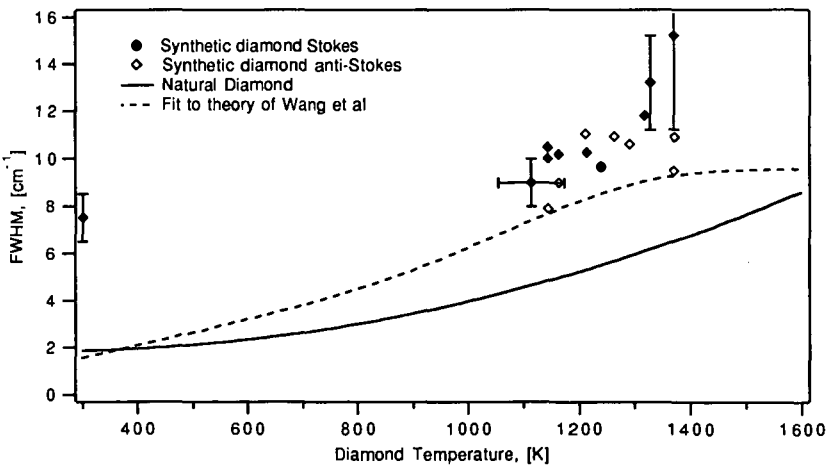

Figure 6. Variation of the full width at half maximum (FWHM) of the first-order Raman spectrum in polycrystalline diamond with temperature. The diamond temperature is found using an emissivity of unity. The solid line is a fit to the FWHM for natural diamond (Ref. 6). The dashed line is a fit to the theoretical results of Wang et al (Ref 8).

HYDROGEN BINDING AND DIFFUSION IN DIAMOND*

S. P. Mehandru and Alfred B. Anderson
Chemistry Department, Case Western Reserve University
Cleveland, OH 44106-7078

and

John C. Angus
Department of Chemical Engineering, Case Western Reserve University
Cleveland, OH 44106

Keywords: hydrogen in diamond, diffusion

INTRODUCTION

The growing interest in the surface and bulk properties of diamond, which are markedly influenced by foreign atoms, is the natural consequence of the evolving technology for low-pressure diamond film and crystal growth.[1-4] Large hydrogen concentrations are found in natural[5,6] and man-made diamond, particularly in diamond-like films.[7] Surface hydrogen is believed to be responsible for low-pressure diamond growth from C_1 and C_2 hydrocarbon fragments, whose identification is under investigation at this time.[8] During low-pressure growth, hydrogen is essentially a catalyst, maintaining tetrahedral bonding structure at the diamond surface, blocking routes to graphite formation. Bound H atoms are removed by bonding to H atoms from the gas and coming off as H_2. This process momentarily forms active dangling radical orbitals at the surface to which hydrocarbon radicals from the gas bind, in competition with H atoms, ultimately propagating diamond growth. Beyond this, the growth mechanism or mechanisms are not yet understood. We have made model atom superposition and electron delocalization molecular orbital (ASED-MO) studies of the absorption of C_1 and C_2 hydrocarbon species on the diamond (100) and (111) surfaces[9,10] and have found C_1 species may be able to diffuse on the former surface, but not the latter.

Hydrogen has been rather well studied as an interstitial impurity in silicon, but not in diamond. In silicon it is attracted to substitutional B atoms and poisons their p-dopant properties, affecting the semiconducting properties.[11] Recent theoretical works based on quantum mechanical models have shown that an isolated interstitial H atom binds in a Si-Si bond-center site and provides an attractive potential well for second interstitial H to pair with it in an interstitial antibonding site, forming H-Si-H-Si oriented in the [111] direction.[12-16] For H in diamond, theory has predicted similarly that bond-centered interstitial sites are most stable and a second H is attracted to the antibonding site.[16-19] Infra red (IR) studies of natural diamonds show well-defined stretching and bending excitations at 3107 cm^{-1} and 1405 cm^{-1}.[20-22] Recent thermal desorption studies yielded an integrated hydrogen desorption flux of about 10 monolayers of

*Supported by the U. S. National Science Foundation, Grant No. DMR-03527

hydrogen between 700 and 1100 K from a polished diamond (1x1) H-covered (100) surface.[23]

Standard free energies for alkane formation begin to favor the elements, C(di)+H_2(g), for C_6 and larger, and for all unsaturated hydrocarbon molecules the elements are favored.[24] Therefore, it might be expected that sub-surface hydrogen will be released as H_2. Single bonds between carbon atoms and H_2 single bonds are replacing CH bonds. However, the details of the subsurface H bonding are not known. Interstitial H atoms are likely to be bound weakly as is the case for Si. The release of such H as gas phase H_2 should be very stabilizing and the question of its rate is a kinetic one. If C vacancies exist and H binds to the carbon atoms surrounding these vacancies, and this would be a plausible explanation for the bending and stretching modes seen by IR, then such H would be rather strongly bound. Muon-spin-rotation (μSR) studies have shown that at temperatures greater than 800 K the +1-charged muon nuclei are in an anisotropic environment,[25] which might correspond to such a site. The loss of H, as H_2 following combination with a second vacancy-bound H, would not be stabilizing unless there is massive restructuring which forms C-C bonds and removes the vacancies, since a single H_2 bond would be replacing 2 CH bonds. Whether subsurface vacancies might have several weakly bound H atoms squeezed into them is unknown. Such H might be partially released without the need for restructuring.

With the above questions in mind, along with what is already known about H in silicon, we have undertaken an ASED-MO study of H atom interstitial and vacancy bonding and diffusion in diamond. We explain our results in terms of the orbital and electronic structures and speculate on the possible effects of p-type dopants. The atomic parameters are those used in the earlier ASED-MO diamond surface work.[9,10]

INTERSTITIAL H AND ITS MIGRATION

Our C_{46} diamond structure cluster model is terminated by 48 CH bonds to eliminate surface radical orbitals with energies in the band gap, which would interfere with our bulk property calculations. Its structure is shown in **1**, with 3 shaded atoms being those relaxed around interstitial H in bond-centered sites, which are calculated to be the most stable interstitial locations, and the hatching identifies the second shell of atoms which were also relaxed in the calculations.

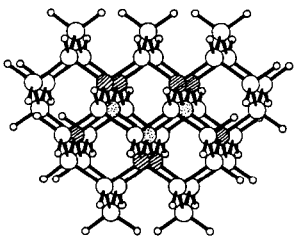

1

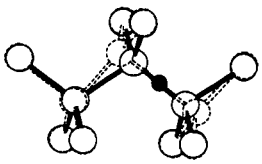

2

Rather severe distortions take place to accommodate the bond-centered interstitial H atom, shown black in **2**. The interstitial H atom is unstable relative to the free atom by 1.7 eV. The C-C stretching caused by H insertion lowers a localized σ^* orbital from the conduction band into the band-gap as shown in **3**, thus stabilizing the radical electron. The band gap orbital has a node at H and the 3-centered C-H-C σ bonding orbital is dispersed in the valence band. It may be expected that a p-type dopant atom, such as B, will stabilize the promoted electron in the band-gap orbital and then interstitial H atoms will be attracted to the vicinity of the dopant atom, as for Si.[15] This will destroy the p-dopant electrical properties of diamond. A second H binds at the antibonding site as shown in **4** 1.4 eV more strongly than the first H in the bond-centered site. The second radical electron pairs with the first in

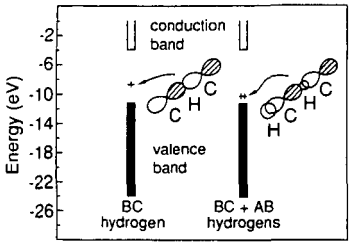

3

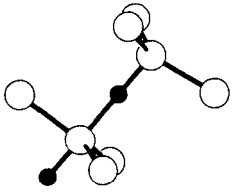

4

the band-gap orbital, which is stabilized due to overlap between it and the H 1s orbital in the antibonding site as shown in **3**. It is expected therefore that p-type dopants will attract a second, and perhaps a third, interstitial H atom.

In the presence of H in the interstitial antibonding site, the bond-centered CH vibrational excitation energy, based on the vibrational force constant in a local-mode approximation, is calculated to be ~1600 cm^{-1} greater than that calculated in the same way for a CH bond in methane. For the antibonding H it is ~1000 cm^{-1} greater. Some high-energy vibrational excitations have been observed by IR[22] but they match bending overtones and a stretch-bend combination for an isolated, perhaps vacancy, CH bond rather well. Consequently, the concentration of interstitial CH is probably relatively low. An isolated bond-centered interstitial H would, for symmetry reasons, be IR inactive.

An isolated bond-centered interstitial H will migrate to an adjacent bond-centered site by passing through a transition state with the structure shown in **5**. The calculated energy barrier is 1.9 eV. Since in the transition state two C-C bonds are stretched, two σ^* orbitals from the conduction band drop into the band gap as shown in **6** and the lower one is C-H non-bonding. This orbital, which takes the promoted electron, is 1.2 eV above the occupied band-gap orbital for the bond-centered site and contributes this much to the H migration barriers. Thus, it is expected that p-dopant atoms will decrease energy barrier for interstitial H atom migration in their vicinity.

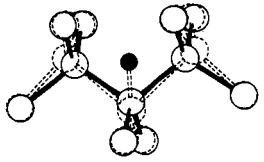

5

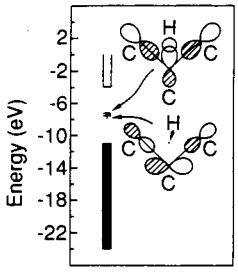

6

BINDING OF H ATOMS TO A VACANCY

A vacancy is modeled by removing the cross-hatched atom in 7 and relaxing the hatched atoms. The calculated vacancy formation energy, based on placing the removed C atom on a 3-fold (111) surface site, is calculated to be 6.0 eV. A slight tetragonal distortion, which removes the degeneracy of the doubly occupied t-symmetry set of vacancy radical orbitals, contributes 0.03 eV stability. The structures with 1-4 H atoms in the vacancy are shown in **8**. The first H atom forms a CH bond with a strength of 5.3 eV

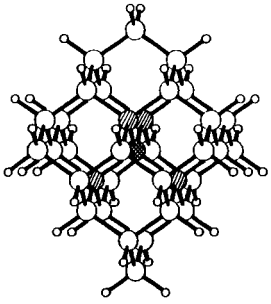

7

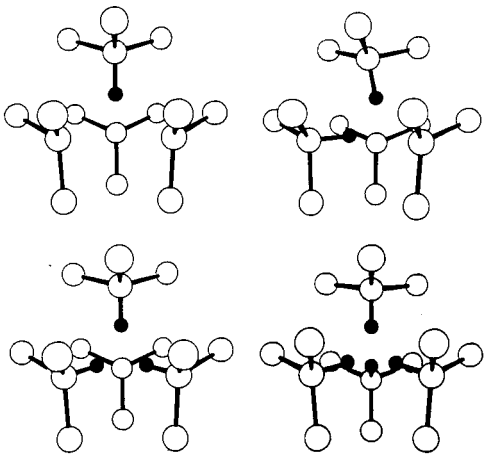

8

with respect to its removal from the lattice cluster model. Based on the tertiary C-H bond strength in t-butane, this is a bit over 1 eV too strong. Subsequent H atoms are each calculated to bind about 1 eV more weakly than the previous one. This implies a bulk vacancy could trap up to 4 interstitial H atoms. The H atoms are

crowded quite close together, 1.18 Å when four are present. If there is a substantial number of such H-filled vacancies near the surface, they could contribute to the ~10 monolayers of H_2 desorption observed by Hamza et al.[23] in the temperature-programmed thermal desorption study of the polished (100)-(1x1) surface.

In the local-mode approximation the vibrational excitation of the CH bond for a single H in the vacancy is calculated to be about 3400 cm^{-1}. This is 300 cm^{-1} higher than the CH stretch observed in natural diamond by IR.[22] Since ASED-MO calculations overestimate secondary and tertiary C-H bond strengths, they could well overestimate the CH excitation for H in a vacancy site by ~300 cm^{-1}. Thus our calculations are probably consistent with a CH bond in a vacancy site as the source of the observed 3107 cm^{-1} stretch. The calculated increases due to adding a second, third, and fourth H to the vacancy are ~400, 700 and 1400 cm^{-1}, respectively. Whether the first two of these are the cause of the observed broad IR absorption around 3700 cm^{-1} in ref. 22 cannot be established without experimental studies of H concentration dependence and more detailed theoretical analysis.

REFERENCES

1. Yarbrough, W. A.; Messier, R. Science **1990**, 247, 688.
2. Angus, J. C.; Hayman, C. C. Science **1988**, 241, 913.
3. Angus, J. C.; Buck, F. A.; Sunkara, M.; Groth, T. F.; Hayman, C. C.; Gat, R., Mater. Res. Bull. October 1988, p. 38.
4. Spear, K. E. J. Am. Ceram. Soc. **1989**, 72, 171.
5. Sellschop, J. P. F., Abstracts of the Diamond Conference, Bristol, U.K., 1987, p. 45.
6. Sellschop, J. P. F.; Madiba, C. C. P.; Annegan, H. J., Abstracts of the Diamond Conference, Cambridge, U.K., 1979, p. 43.
7. Vandentop, G. J.; Kawasaki, M.; Nix, R. M.; Brown, I. G.; Salmeron, M.; Somorjai, G. A. Phys. Rev. B **1990**, 41, 3200 and references therein.
8. a. Frenklach, M.; Wang, H. Phys. Rev. B **1991**, 43, 1520.
   b. Harris S. J.; Weiner, A. M. J. Appl. Phys., to be published.
   c. Toyoda, H.; Kojima, H.; Sugai, H. Appl. Phys. Lett. **1989**, 54, 1507.
   d. Belton, D. N.; Schmieg, S. J. J. Vac. Sci. Technol. A **1990**, 8, 2353.
9. Mehandru, S. P.; Anderson, A. B. J. Mater. Res. **1990**, 5, 2286; Carbon **1990**, 28, 797.
10. Mehandru, S. P.; Anderson, A. B. Surf. Sci., in press.
11. Pankove, J. I.; Carlson, D. E.; Berkeyheiser, J. E.; Wance, R.O. Phys. Rev. Lett. **1983**, 51, 2224.
12. Estreicher, S. Phys. Rev. B **1987**, 36, 9122.
13. Van de Walle, C. G.; Bar-Yam, Y.; Pantelides, S. T. Phys. Rev. Lett. **1988**, 60, 2761.
14. Chang, K. J.; Chadi, D. J. Phys. Rev. Lett. **1989**, 62, 937.
15. Chang, K. J.; Chadi, D. J. Phys. Rev. B **1989**, 40, 11644.
16. Chu, C. H.; Estreicher, S. Phys. Rev. B **1990**, 42, 9486.
17. Claxton, T. A.; Evans, A.; Symons, M. C. R. J. Chem. Soc. Faraday Trans. 2, **1986**, 82, 2031.

18. Estle, T.L.; Estreicher, S.; Marynick, D. S. Phys. Rev. Lett. **1987**, 58, 1547.
19. Briddon, P.; Jones, R.; Lister, G. M. S. J. Phys. C **1988**, 21, L1027.
20. Ruciman, W. A.; Carter, T. Solid St. Commun. **1971**, 9, 315.
21. Woods, G. S.; Collins, A. T. J. Phys. Chem. Solids **1983**, 44, 471.
22. Davis, G.; Collins, A. T.; Spear, P. Solid St. Commun. **1984**, 49, 433.
23. Hamza, A. V.; Kubiak, G. D.; Stulen, R. H. Surf. Sci. **1990**, 237, 35.
24. CRC Handbook of Chemistry and Physics, R. C. Weast, Editor, 67th Edition, Boca Raton, Florida, 1986.
25. Holzschuh, E.; Kündig, W.; Meier, P. F.; Patterson, B. D.; Sellschop, J. P. F.; Stemmet, M. C.; Appel, H. Phys. Rev. A **1982**, 25, 1272.

HOMOEPITAXIAL HIGH TEMPERATURE DIAMOND GROWTH FROM OXYACETYLENE FLAMES

C. M. Marks, L. M. Hanssen, J.A. Freitas*, C. L. Vold†, K.A. Snail
Optical Sciences Division, Code 6522
†Materials Science and Technology, Code 6322
Naval Research Laboratory
Washington, DC 20375-5000

*Sachs Freeman Associates
1401 McCormick Drive
Landover, MD 20785-5396

Keywords: Diamond, Flame, Acetylene.

ABSTRACT

High quality single crystal diamond is grown from natural seeds in a fuel-rich oxyacetylene torch at substrate temperatures of 1150-1350°C. The flame-grown diamonds are optically clear and have a Raman and photoluminescence spectrum comparable to natural, type IIa diamond with very low defect density. Laue X-Ray diffraction patterns indicate the growth is epitaxial. Growth rates were 100-200 μm/hr, both vertically and laterally. {100} top seeds showed macroscopic terraces on the top surface after growth. Scanning electron microscope pictures show that initially round seed crystals grew into octagons.

Introduction

Among the new materials that have appeared recently, diamond has received much interest for its superlative properties. With its high thermal conductivity, optical transmission range, index of refraction, bandgap and breakdown voltage, diamond is important for heat sink, electronic and optical applications (1). A method of producing large single crystal boules of diamond would be particularly important for use as windows in optical materials and as wafers in semiconductor applications.

Experimental

Polycrystalline diamond films have been grown in oxyacetylene torches by several groups(2-6). As in our group's previous work(7,8), a torch system was used to grow diamond homoepitaxially on seeds as shown in the apparatus diagram in figure 1. The torch was a standard #0 brazing torch with an orifice diameter of 0.89 mm. Feed gases were purified 99.6% C_2H_2 dissolved in acetone and ultra-high purity, 99.99% O_2, their flow rates controlled with mass flow controllers to a C_2H_2/O_2 ratio of 1.08. Acetone was removed from the C_2H_2 line by adsorption onto activated charcoal, while the O_2 was used without further purification. The seed was brazed with a Au-Ta braze to the face of a Mo screw, the height of which could be adjusted in a water-cooled Cu block to control the temperature. A two-color infrared pyrometer moitored the seed surface temperature, which was kept at 1250±20 °C. The flame jet impinged upon the screw, with the seed crystal remaining within the flame feather. A Mo screw with a pinhole in its top face was connected to a differentially pumped mass spectrometer. The gases in the boundary layer will be sampled and the ratio of C, H and O atoms will be correlated to the growth conditions and rates.

Results and Discussion

Figures 2a and 2b show scanning electron micrographs of the diamond seed crystal before and after a one hour-long growth. The top {100} face grew into a regular octagon. The growth rate was ~100 μm/hr. The top face of the crystal is smooth except for 10 μm wide steps and optical microscopy shows the grown diamond to be remarkably clear. The Raman spectrum of the flame-grown diamond, shown in figure 3, has the same peak position and width as natural type IIa diamond within the limits of the instrument. A very small fluorescence background can be seen, but no non-diamond carbon can be detected in the spectrum.

The Laue X-Ray diffraction photograph shown in figure 4 shows that the diamond is a single crystal and that the growth is epitaxial. This is also seen from the trapezoidal side faces in figure 2b which correspond to the {111} faces on a cubo-octahedron.

Figure 5 shows a photoluminescence spectrum of the flame-grown diamond at 6 K. It was collected at a wavelength of 488 nm and a power of 20 mW. The major features seen besides the normal diamond Raman peak at 2.375 eV (b) are at 2.155eV and 1.946 eV (d, e) and correspond to a N-vacancy complex and pair respectively, which are normally seen in flame-grown diamond (5). A small background luminescence seen across the entire spectrum is probably due to recombination of extended defects, which is seen in natural diamond as well.

Conclusions

High quality single crystal diamonds were grown in flames. The diamonds were exceptionally clear and have Raman and photoluminescene spectra showing high purity and low defect densities. Flame-grown diamonds grow at high rates and high temperatures suggesting a possible method for growing diamond boules.

References

1. E. Bruton, *Diamonds*, Chilton Book Company, Radnor, PA, 1978

2. Y. Hirose, S. Amanuma and K. Komaki, *J. Appl. Phys.* **68** 6401 (1990)

3. Y. Tzeng, C. Cutshaw, R. Phillips and S. Teradol, *Appl. Phys Lett.* **56** 134 (1990)

4. K. V. Ravi and A. Joshi, *Appl. Phys. Lett.* **58** 246 (1991)

5. L. M. Hanssen, K. A. Snail, W. A. Carrington, J. E. Butler, S. Kellogg and D. B. Oakes, *Thin Solid Films* **196** 271 (1991)

6. K. A. Snail and C. J. Craigie, *Appl. Phys. Lett.* **58** 1875 (1991)

7. K. A. Snail and L. M. Hanssen, *J. Crystal Growth* In press, 1991

8. K. A. Snail, J. A. Freitas, C. L. Vold and L. M. Hanssen, *Proc. 2nd Intl. Symp. on Diamond Matls.* The Electrochemical Society, In press, 1991

9. J. A. Freitas, J. E. Butler and U. Strom, *J Matl. Res.* **5** 2502 (1990)

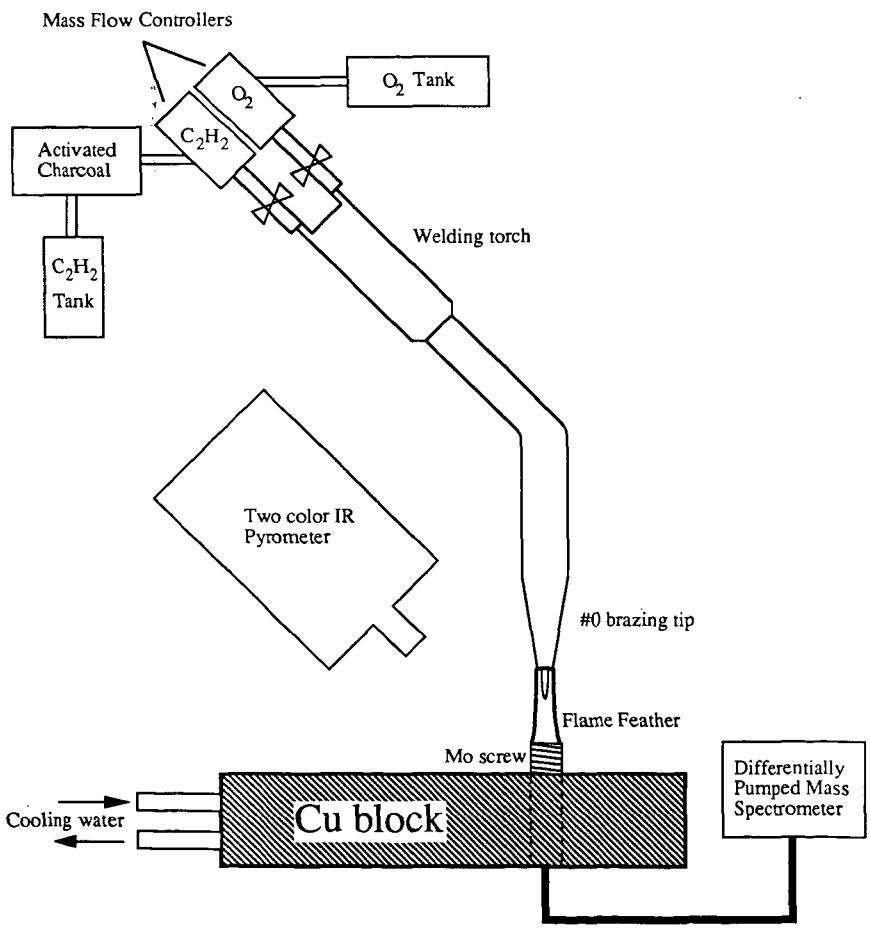

Figure 1. Oxyacetylene torch diamond growth apparatus.

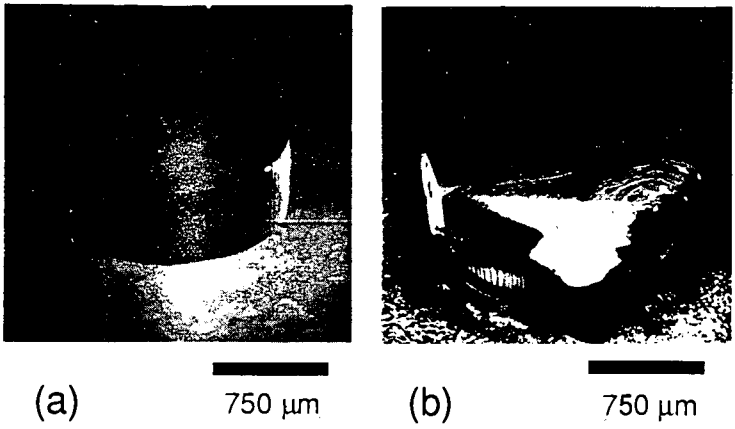

Figure 2. SEM photo of the seed diamond before (a) and after (b) growth in torch.

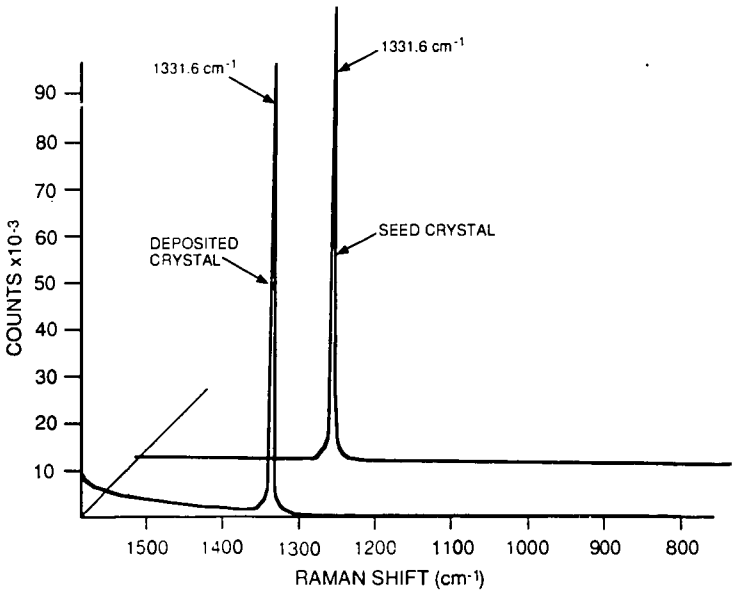

Figure 3. Raman Spectrum of the seed and flame-grown diamonds.

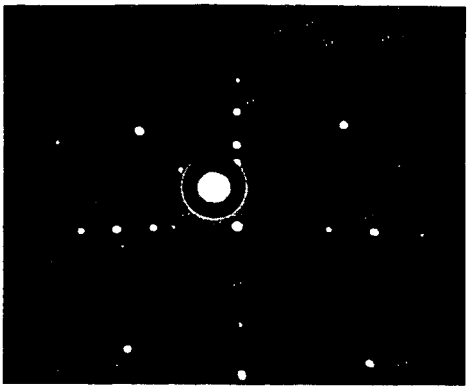

Figure 4. LaueX-Ray diffraction pattern of the flame-grown diamond.

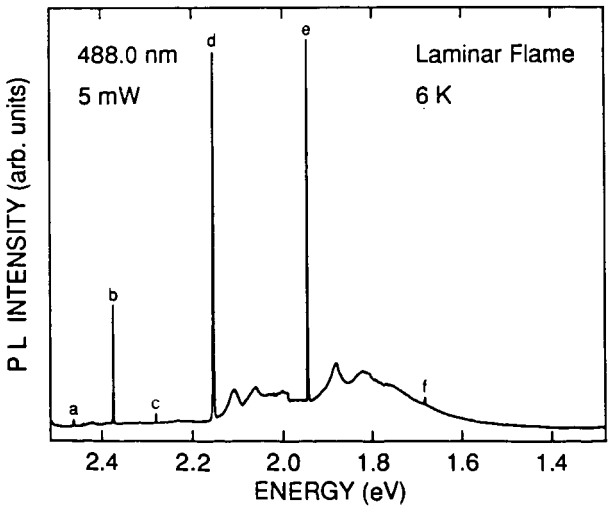

Figure 5. Photoluminescence Spectrum of the flame-grown diamond.

CARBON BLACK FROM COAL BY THE HYDROCARB PROCESS

Meyer Steinberg
Department of Applied Science
Brookhaven National Laboratory
Upton, NY 11973

INTRODUCTION

Carbon black is an ancient material and has been produced for over a century by several traditional processes.[1] The raw materials have been mainly residual oils from refineries and from natural gas. Furnace black is made by partial combustion of oil. Channel black is made by partial combustion of natural gas and the carbon is collected on iron channels. Thermal black is made from the thermal decomposition of natural gas (methane). About 2 million tons of carbon black is sold in the U.S. About 85% of the carbon black goes into the manufacture of tires for automotive purposes. It is a vulcanization and strengthening agent. The remainder goes into pigments, printing inks, and fillers. The largest part of carbon black, that which is used in tires is made from residual oil by the furnace black process. The smaller fraction is made by the thermal black process from natural gas.

There have been a number of attempts in the part to produce carbon black from coal. The recent ones deal with partial combustion in a sooty flame and collecting the fine carbon soot. However, the yields are poor and have never reached even advanced development stage. The value of searching for an alternative feedstock to oil and gas for carbon black production is important when considering the competitive use of the basic natural raw materials as energy sources, oil and gas being premium fuels. The resource of coal is an order of magnitude greater than oil and gas and as a source of carbon, coal as a feedstock is the cheapest.

Over the last six years we have conceived and are developing a process for producing carbon from coal primarily to satisfy the energy market. However, the process has implications for the carbon black commodity market.

THE HYDROCARB PROCESS

The HYDROCARB process was conceived and developed for the purpose of producing a clean carbon fuel and coproduct gaseous and liquid fuel coproducts[2,3,4] from any carbonaceous feedstock and particularly from coal.

The process basically consists of two major steps. In the first step, coal is hydrogenated to produce methane. In this step, the carbonaceous raw material is gasified with a recycled hydrogen-rich gas stream to form a light hydrocarbon, methane-rich gas, while the non-volatile ash remains behind. With the optional addition of limestone to the feed material, sulfur in the feedstock is removed as non-volatile calcium sulfide which is later oxidized to calcium sulfate for disposal. The methane-rich gas which also contains carbon monoxide and smaller amounts of water and carbon dioxide is sent to a recuperative condenser. For the production of methanol, the carbon monoxide and hydrogen in the process gas is catalytically combined to produce methanol. The deoxygenated methane-rich gas stream is then sent to a methane decomposer where the methane is cracked to pure particulate carbon and hydrogen gas. The pure carbon is removed as a clean product and most of the hydrogen-rich gas is returned to the coal hydrogenator. The two basic steps are then coal hydrogasification in a hydropyrolysis reactor (HPR) and methane decomposition in a methane pyrolysis reactor (MPR). Table 1 outlines the process chemistry and Table 2, gives a schematic broadening of the process to

any carbonaceous raw material feedstock and indicates the co-product options, which include either a hydrogen-rich gas, a methane-rich gas, and methanol. Figure 1 shows one version of a process flow sheet. The methanol co-product option appears most attractive because of its usefulness as a high value chemical commodity and an environmentally preferable liquid transportation fuel.[5]

Among the important features of the process which assures high efficiency, is the fact that the hydrogasification or hydropyrolysis step is exothermic, giving off heat and the methane pyrolysis step is endothermic absorbing heat. By transferring heat from step 1 to step 2, the process efficiency is greatly enhanced. This is accomplished by circulating solid alumina pellets as a heat transfer and transport media through the hydropyrolyzer and to the methane pyrolyzer as shown in Figure 1. The reactors can be either moving bed or fluidized bed types.

The process is based on sound thermodynamic, and process chemistry principles. Experimental data for the hydropyrolysis and methane decomposition through pilot plant scale are available. Engineering demonstration is yet to be performed.

PROPERTIES OF CARBON BLACK

Because the carbon black is ash- sulfur- and nitrogen-free it is a potentially ideal coal derived fuel which can be utilized in heat engines, i.e., diesels and turbines, as well as in power plant and industrial boilers with little modification. Its major drawback is that it has no volatility resulting in a higher ignition temperature. Radiant combustors or additives of oil or methanol can solve that problem for use in conventional systems. Because the density of carbon black is high (1.8 to 2.0 gm/cc) it can be added to hydrocarbon fuels to volumetrically energy densify those fuels. Fig. 2 shows that adding carbon to methanol will increase the heating value of hydrocarbon fuels. A 55% carbon black-45% methanol slurry has a HHV equivalent to that of gasoline.

We have produced carbon black from methane in our laboratory in a countercurrent moving alumina bed reactor at 1000°C and 800 psi which is about the design conditions for the HYDROCARB process. Photomicrographics of the carbon black are shown in Fig. 3. The figure compares the collected carbon with a commercial grade carbon designated as N-990 produced by the thermal black process from natural gas. The HYDROCARB carbon black shows similar spherical particles ranging in size from 0.3 to 1.0 micron agglomerated up to about 4.0 microns. The commerical grade ranges from 0.2 to 0.5 microns with aggregates of over 100 microns. Geometrically, the laboratory carbon black appears in the range of thermal black. We have yet to examine the surface properties or whether other particle sizes can be produced at different reactor conditions. Further characterization must be performed to determine whether commodity grade carbon black can be produced and especially its suitability for the tire market.

ECONOMIC ESTIMATES

Preliminary economic estimates of the production of carbon black in large scale coal plants using the HYDROCARB process have been made. For a 25,000 T/D high volatile bituminous coal feedstock it is estimated that the production capacity would be about 16,000 T/D maximum and taking credit for by-product hydrogen would be priced at between 3.5¢ and 5.0¢ per pound competing with $2.50 to $3.50/MMBTU or $15 to $21/Bbl of oil.[2,3] This price includes 15% return on plant equity. It is instructive to compare the economics of the manufacture of commercial carbon black from various fossil fuel resources with that projected for the HYDROCARB prices. Based on 1986 prices, Table 2 indicates that carbon black from natural gas (thermal black) and crude oil (furnace black) ranged in price from 16¢ to 35¢ per pound depending on the more than a dozen different grades produced by the industry. Recent (1990) prices run up to as high as 50¢/lb.

From the raw feedstock point of view, the cost of contained carbon from natural gas and oil ranges from about 6 to 10¢ per pound and remembering that residual oil from crude may be somewhat lower. However from coal, the contained carbon ranges from 1.1 to 1.8¢ per pound which is from 5 to 10 times lower than for oil or gas. If the HYDROCARB carbon can be found to be suitable for the tire as well as for other commodity markets, then the estimated selling price would be 3 to 10 times less than the commodity selling price of carbon black. If off-grade carbon black which is only available at times in limited quantity for as low as 10¢ per pound HYDROCARB carbon would be 2 to 3 times lower. However, one 25,000 T/D HYDROCARB plant would produce almost 3 times the entire annual capacity of commodity carbon black in the U.S. Therefore, HYDROCARB carbon black designed for supplying the fuel market could easily supply all the commodity market as a by-product.

CONCLUSION

HYDROCARB process carbon black designed primarily for the energy market can supply the commercial commodity market at much reduced prices. Much additional work is necessary to determine the characteristics of HYDROCARB carbon black for suitability for tire manufacture as well as for any other possible large scale commodity market. Process demonstration of an integrated system is necessary to prove the ability to scaleup the process to commercial size.

REFERENCES

1) J.B. Donnet and A. Voct, Carbon Black, Marcel Dekker, Inc., New York (1976).

2) E.W. Grohse and M. Steinberg, "Economical Clean Carbon and Gaseous Fuels from Coal and other Carbonaceous Raw Material," BNL 40485, Brookhaven National Laboratory, Upton, NY 11973 (November 1987).

3) M. Steinberg and E.W. Grohse, "Economical Clean Carbon Fuel and Co-product Gaseous and Liquid Fuel from Coal," BNL 42489, Brookhaven National Laboratory, Upton, NY 11973 (September 1989).

4) M. Steinberg, "Coal to Methanol to Gasoline by the HYDROCARB Process," BNL 43555, Brookhaven National Laboratory, Upton, NY 11973 (August 1989).

5) R.H. Borgwardt, M. Steinberg, E.W. Grohse, and Y. Tung, "Biomass and Fossil Fuel to Methanol and Carbon via the HYDROCARB Process," Presented at the Institute of Gas Technology Conference in Energy from Biomass XV, Washington, D.C., March 27, 1991 (to be published in Proceedings of Conference).

6) G. Wei and M. Steinberg, "Carbon Black Slurries, Preparation and Characteristics," BNL 43732, Brookhaven National Laboratory, Upton, N.Y. 11973 (November 1989).

TABLE 1
HYDROCARB PROCESS FOR
PRODUCTION OF ASH-FREE AND SULFUR-FREE
CLEAN CARBON FUEL (CARBOLINE) AND FUEL GAS FROM COAL

TWO BASIC STEPS:

I. HYDROGASIFICATION OF COAL WITH HYDROGEN TO METHANE.

BITUMINOUS COAL + HYDROGEN ⟶ METHANE + WATER + HYDROGEN + ASH

$CH_{0.8}O_{0.08}S_{0.016}N_{0.015} + 2H_2 \longrightarrow CH_4 + 0.08\,H_2O + 0.32\,H_2 + 0.008\,N_2$

+ASH + LIMESTONE ($CaCO_3$) + ASH + CaS

REACTION IS -18 KCAL/MOL EXOTHERMIC.

II. THERMAL DECOMPOSITION OF METHANE.

METHANE ⟶ CARBON BLACK + HYDROGEN.

$CH_4 \longrightarrow C + 2\,H_2$

REACTION IS +18 KCAL/MOL ENDOTHERMIC.

HYDROGEN IS RECYCLED. EXCESS HYDROGEN IS A CO-PRODUCT. CARBON BLACK IS A FUEL AND CAN BE SLURRIED WITH WATER TO PRODUCE CARBOLINE CWM PRODUCT.

OVERALL COAL CRACKING REACTION

$CH_{0.8}O_{0.08}S_{0.016}N_{0.015} \longrightarrow C + 0.32\,H_2 + 0.08\,H_2O + 0.008\,N_2$

+ ASH + $CaCO_3$ ASH + $0.016\,CaSO_4$ INERT

1067

Table 2

Comparative Economics of Carbon Black Production in the U.S.
From Various Fossil Energy Resources (1986)

Resource	Natural Gas	Crude Oil Residuals	Coal (Proposed)
Raw Material Cost			
$/MMBtu	2.00 to 3.00	2.50 to 3.50	1.00 to 0.70'
$/MSCF	2.00 to 3.00	-	-
$/Bbl	-	15.00 to 21.00	-
$/ton	-	-	25.00 to 10.00
¢/lb of contained C	6.3 to 9.5	6.2 to 8.7	1.8 to 1.1
Present Prices of Carbon Black			
Commodity Grade:			
¢/lb	16 to 35	16 to 35	Suitability for tire
$/ton	320 to 700	320 to 700	manufacture still
$/MMBtu	11.35 to 24.80	11.35 to 24.80	to be established
Offgrade (for fuel):			
¢/lb	10 (est'd)	10 (est'd)	3.5 - 5.0
$/ton	200	200	70 to 100
$/MMBtu	7.10	7.10	2.50 to 3.50
Total Present U.S. Capacity for The Production of Carbon Black			
Tons/year	0.2×10^6	2.0×10^6	5.3×10^6*
Tons/day	600	6,000	16,000
Estimated Present Availability of Fuel Grade Carbon Black			
Tons/day	200 (est'd)	2,000 (est'd)	16,000*
No. of plants	1	10	1

*Proposed HYDROCARB plant. This is the production capacity for one 25,000 T/D coal plant producing carbon black and fuel gas (corresponding to a total fuel equivalent 83,500 BPD FOE oil refinery).

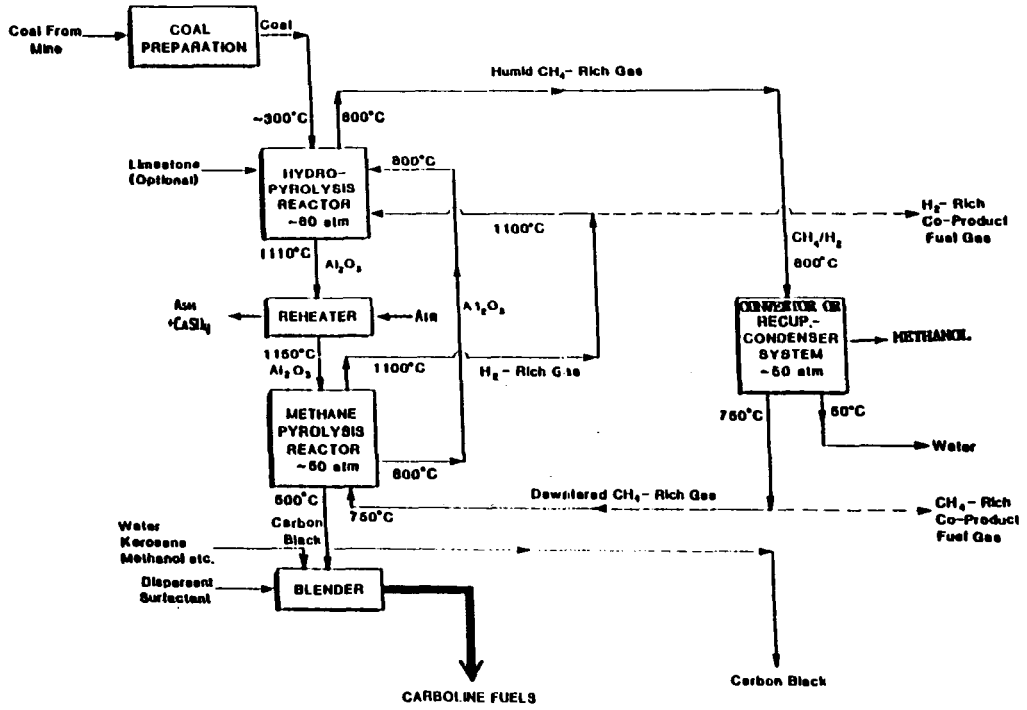

Figure 1. Clean Coal-Derived Fuels via the Hydrocarb Process

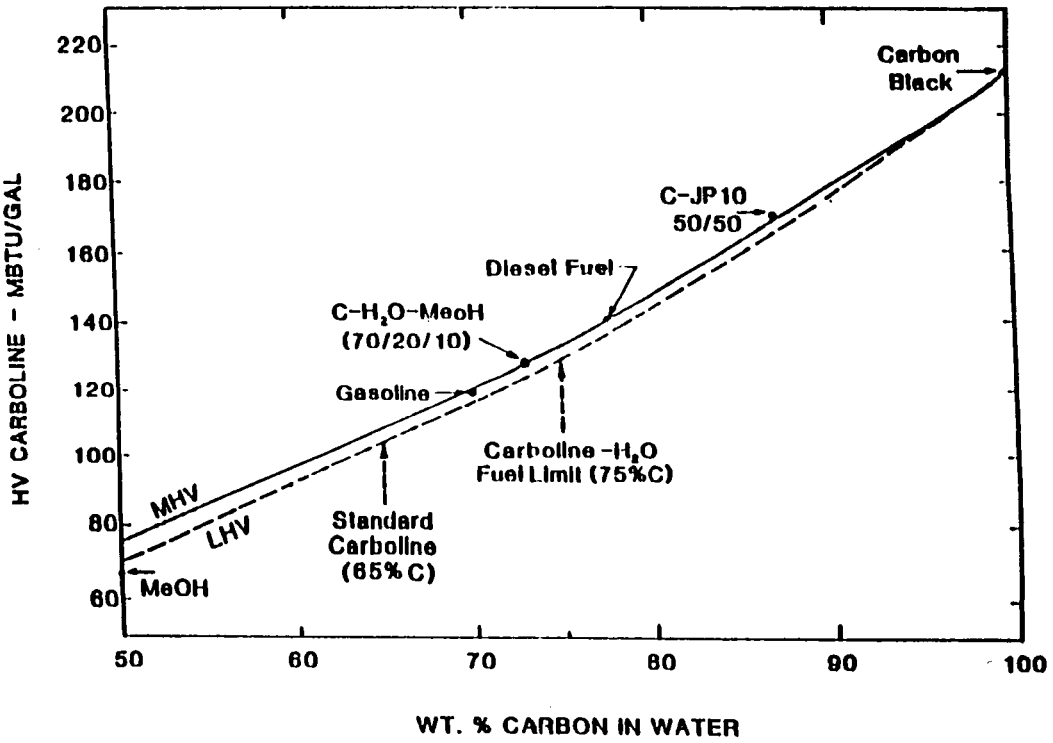

Figure 2. Heating Values of Carboline and Competitive Fuels

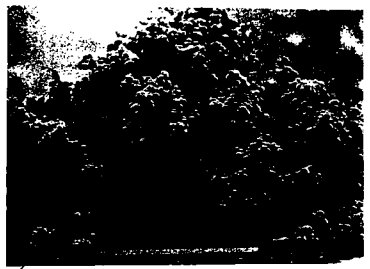

NO. 1 500 X

NO. 1 10,000 X

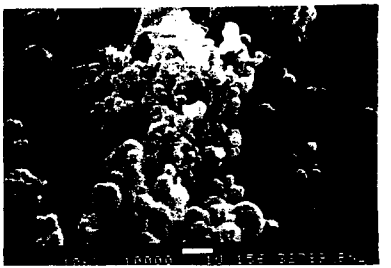

NO. 1 10,000 X

NO. 2 500 X

NO. 1 - C-BLACK FROM BNL MOVING BED REACTOR RUN NO. 1099 - PLUG IN REACTOR FORMED AT 800 PSI AND 1000°C - 0.5 TO 1μ AGGLOMERATED TO ~4μ

NO. 2 - C-BLACK FROM HUBER CO. - COMMERCIAL GRADE N-990 PARTICLE SIZE 0.2 TO 0.5μ

NO. 3 - C-BLACK FROM BNL MOVING BED REACTOR RUN NO. 1099 FILTER LOCATION FORMED AT 800 PSI AND 1000°C - 0.3 TO 2.0μ

Figure 3. Photomicrographs of Carbon Black

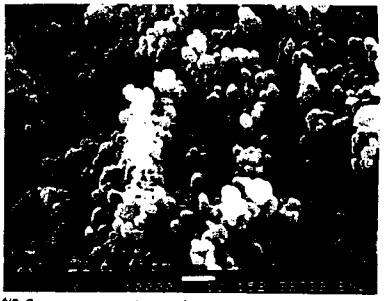

NO. 2 10,000 X

NO. 3 500 X

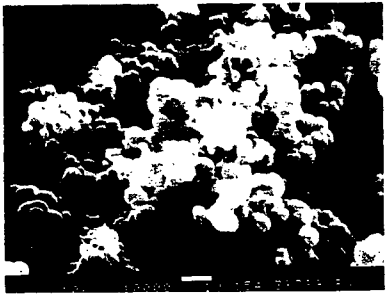

NO. 3 10,000 X

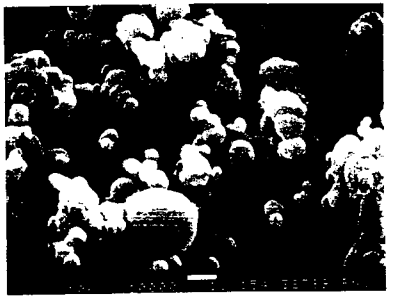

NO. 3 10,000 X

THE PRODUCTION OF ACTIVATED CARBONS FROM COALS BY CHEMICAL ACTIVATION

F J Derbyshire, M Jagtoyen, B McEnaney,
A R Sethuraman, J M Stencel, D Taulbee
and M W Thwaites

University of Kentucky Center for Applied Energy Research,
3572 Iron Works Pike, Lexington, Kentucky 40511-8433, USA.

Keywords: coal; activated carbons; chemical activation; phosphoric acid.

ABSTRACT

Activated carbons prepared from coals by chemical means using phosphoric acid as the activant have a dominantly microporous adsorptive capacity which develops up to 450 °C. Chemical activation promotes carbonization at lower temperatures than is obtained thermally and is effective in removing sulfur, mainly as hydrogen sulphide. Reducing the ash content of a bituminous coal by cleaning prior to activation has beneficial effects upon surface area development.

INTRODUCTION

Coals are widely used as feed-stocks for activated carbons produced by "thermal" methods, i.e., by carbonization followed by reaction with oxidizing gases (e.g., steam or carbon dioxide) at elevated temperatures. By contrast, the preparation of activated carbons from coals by "chemical" activation (i.e., by reaction with an ionic reagent at lower temperatures than are used for thermal activation) has been little studied. Chemically-activated carbons are commercially produced from cellulosic precursors using zinc chloride or phosphoric acid as activants (1), but here too there is little fundamental understanding of the chemistry of the conversion processes.

The objectives of the present work are to investigate the potential of coals of different rank as precursors for the production of active carbons using phosphoric acid as the activant. Specific aims are to relate the development of porosity in the carbons to the structure of the precursor and to the chemical and morphological changes. In this paper we report a study using a subbituminous coal and a bituminous coal as precursors, including some results of pre-cleaning the bituminous coal using flotation.

EXPERIMENTAL

Chemical Activation.

The sub-bituminous coal is mined from the Wyodak seam in Wyoming (designated: Wyodak coal) and the bituminous coal was selected from the Illinois Coal Basin Sample Program (designated IBC 101 coal); chemical analyses of the coals are shown in Table 1.

The ground coals (-850 μm) were reacted with 50% phosphoric acid in two temperature stages. For the Wyodak coal, the first stage involved refluxing a coal-acid mixture (4:1 ratio of acid solution to coal) for 60 min, following which the slurry was concentrated by evaporation (maximum temperature, about 130°C). In the second stage, the slurry was heat treated in a stainless steel reactor, under flowing nitrogen at atmospheric pressure and held for 60 min at a final heat treatment temperature (HTT) between 350 and 650°C.

For the IBC 101 coal, the first stage procedure was modified: a coal-acid slurry (30 ml acid:20 g of coal) was heated to 170 °C in the same reactor, and held at this temperature for about 30 minutes before heating to the final HTT. The content of H_2S released as gas was monitored with a HACH Carle gas chromatograph using standard procedures for calibration. The solid products were leached with distilled water to pH = 6 and vacuum dried at 110 °C for further analysis. For comparison, parallel series of carbonized coals were prepared by heat treatment for 1 h in flowing nitrogen (80 ml/min) at the same HTT values.

Coal cleaning.
Clean coal samples have been produced using a laboratory scale flotation unit. In a typical arrangement, fuel oil or pentane is vigorously mixed with a coal/water slurry to render the coal particles hydrophobic and to selectively agglomerate them. The agglomerated slurry is then screened; the free ash particles flow through the screen and agglomerated coal is retained.

Characterization.
Elemental analyses of the carbons were carried out using standard methods. The carbons were also examined using Fourier transform infra red spectroscopy (FTIR) and X-ray photoelectron spectroscopy (XPS). FTIR spectra were acquired using a NICOLET 20 SXC spectrometer at 4 cm^{-1} resolution. Pressed KBr pellets at a sample/KBr weight ratio of 1:200 were scanned and then normalized to 0.5 mg. Spectral subtractions were conducted on an equivalent weight basis. XPS analysis of the coal samples was carried out in a Leybold-Heraus LH-11 spectrometer equipped with a hemispherical analyzer using Mg Kα radiation (1253.6 eV) at a pass energy of 100 eV. The powdered coal samples were pressed into a thin wafer and were placed on a stainless steel sample holder using a conductive adhesive. The spectra obtained in all regions have been referenced to C1s at 284.3 eV (BE). The identification of the various chemical species has been carried out using NIST XPS Database Version 1.0 and standard compounds. Pore structure characterization was carried out using nitrogen adsorption at 77K using an Autoscan 6 automated adsorption apparatus.

RESULTS

Chemical and Structural Changes

Comparison of the thermally-treated and chemically-activated carbons, Table 1, shows that acid-treatment of both coals causes a more rapid increase in carbon content and reduction in H/C atomic ratio with increasing HTT, which are more pronounced at lower HTT. The ash contents of carbons from both precursors increase with HTT, but those for the acid-treated products are much higher, particularly at HTT > 450°C, and correlate with increases in P content. For both coals, acid-treatment up to HTT = 650 °C releases about 75% of the sulphur in the original coal, Table 1, mainly as H_2S, e.g., Figure 1. The release of sulfur as H_2S from the thermally-carbonized series shows a similar trend to that observed by Khan (2).

The FTIR spectra for the IBC 101 coal and the chemically-activated carbons are shown in Figure 2. There is a strong band at 2914 cm^{-1} in the parent coal, due to aliphatic C-H stretch, which decreases at HTT = 350°C, while the band at 3040 cm^{-1} due to aromatic C-H stretch intensifies, suggesting that aromatization may be occurring. The band appearing at 1690 cm^{-1} after HTT = 350°C is due to carbonyl (C=O) groups. It weakens in intensity at HTT = 550°C and disappears at HTT = 650°C. Carbonyl groups have also been found both in Sutcliffe Speakman 110 activated carbon (3) and in carbons produced by activation of coconut shell with phosphoric acid (4). The difference spectrum obtained by subtracting the spectrum of the thermally-treated sample from that of the acid-treated sample at HTT = 450°C (Figure 3) suggests that the coal is oxidized by chemical activation. For the chemically-activated carbons a particularly strong band appears at 1180 cm^{-1} at HTT = 450°C, 550°C and 650°C. The origin of this band is uncertain. It may be due either to additional C-O stretch, or to P=O groups attached to an aromatic structure. The source of the 1180 cm^{-1} band is being investigated.

Compilations of the C1s and P2p XPS spectra obtained from the chemically-activated carbons from IBC 101 coal after various HTT are in Figure 4; these spectra have been de-convoluted into component peaks. The C1s spectra, Fig. 4(a) to 4(e), have been fitted to four component peaks. The most intense peak, ca. 284.3 eV, is attributed to graphitic-type carbon species; the second peak at ca.285.8 eV may be due to organophosphate species; the third peak at ca. 287.9 eV coincides with that of carbonyl groups, in agreement with the FTIR results; the fourth peak at ca. 289.1 eV is due to carbonate groups. The prominent peaks at ca. 133.5 eV and ca. 135.3 eV in P2p spectra, Fig. 4(a)'-(b)', are attributed to inorganic hydrophosphate groups and to P_2O_5 respectively. When HTT increases from 350 to 450 °C, the hydrophosphate intensity decreases and there is a corresponding increase in the P_2O_5 intensity, suggesting a dehydration process. At HTT = 550 and 650 °C, the hydrophosphate and P_2O_5 peaks are

still present, but two additional peaks appear whose origins are uncertain. The peak at ca. 131.6 eV could either be due to a phosphide of a transition metal or to a phosphorous compound in association with organic sulfur species. The peak at ca. 136.1 eV may be due to a P-containing species in a high oxidation state; work on the identification of these peaks is continuing.

Pore Structure Characterization

BET surface areas, S_{BET}, were obtained from the nitrogen adsorption isotherms for the activated carbons. The isotherms were also analyzed by the α_s method (5) to yield non-microporous surface areas, S'_{BET}, and micropore volumes, V_o, Table 2. Both carbon series are dominantly microporous, although the development of microporosity is more extensive for the carbons produced from the Wyodak coal. The extents of mesoporosity in the two series (indicated by S'_{BET} values) are comparable for HTT > 450 °C. For both carbon series S_{BET} and S'_{BET} pass through maxima below HTT = 650°C, as observed by others (4). However, the effect of HTT on surface area is obscured by the substantial ash contents of the activates, Table 1. Assuming that the ash makes a negligible contribution to nitrogen adsorption, the surface areas can be recalculated on a dry, ash-free (daf) basis, Table 2. The corrected data show that, for the Wyodak coal series, the maximum in S_{BET} is shifted to a higher HTT, while, for the IBC coal series, the maximum disappears (or is possibly shifted to HTT > 650 °C). S_{BET} values for the thermally-treated coals (not shown in Table 2) increase with HTT up to 50 m^2/g for the Wyodak coal series and up to 24 m^2/g for the IBC 101 coal series. The results indicate that the thermally-treated carbons contain narrow micropores and negligible mesoporosity.

The data in Tables 1 and 2 show that coal cleaning by flotation substantially reduces the ash content of the parent IBC 101 coal by 61%; the ash content of the chemically-treated carbon produced from the cleaned coal at HTT = 550 °C is reduced by 55% when compared with that for the activate formed from the parent coal at the same HTT. Table 2 shows that coal cleaning produces a significant increases in both S_{BET} and S'_{BET}.

DISCUSSION

Chemical analyses and FTIR results show that phosphoric acid treatment of the coals promotes aromatization and carbonization at low HTT. Evidence for accelerated carbonization is also provided by reflectance measurements on the subbituminous coal (6). The processes occurring during the reaction of phosphoric acid at low temperatures are probably analogous to acid-catalyzed cracking reactions in coal liquefaction using Lewis acids. Acid catalysts can promote rupture of methylenic, etheric and thioetheric linkages between cyclic structures in coal by ionic mechanisms which involve protonation followed by bond scission (7). Proton donation from phosphoric acid to aromatic

entities, -Ar-, in the coal structure is consistent with the XPS evidence for inorganic hydrophosphates; the reactions can be represented as:

$$\cdots\text{-Ar-}\cdots + H_3PO_4 = \cdots\text{-(ArH)}^+\text{-}\cdots + H_2PO_4^-.$$

In the present case, it is likely that bond scission will be followed by rapid condensation of aromatic fragments to form a strongly cross-linked solid product at much lower temperatures than are required for thermal decomposition of the coal. The indications from FTIR and XPS for the presence of organophosphorus entities suggest that direct reactions between phosphoric acid and the coal structure also occur, particularly at high temperatures. The formation of an extensive cross-linked network at low temperatures in the chemical activation process may be linked to the early development of significant open microporosity. By contrast, the condensation processes which accompany thermal carbonization occur at much higher temperatures and lead to significant shrinkage and formation of a closed micropore network which can only be developed by subsequent thermal activation.

CONCLUSIONS

There are clear differences in porosity development between the thermally-carbonized and chemically-activated coals, which reflect differences in structural development. Acid-treatment causes the rupture of linkages in the coal structure, leading to adduction and the early development of a strongly cross-linked solid product. This process is accompanied by the development of high surface areas at moderate HTT. Work on elucidating the mechanisms of the chemical activation process is continuing.

ACKNOWLEDGEMENTS

The authors thank several colleagues at the CAER for help with this research, the Illinois Center for Research on Sulfur in Coal and the CAER for financial support, and Kerr-McGee Coal Corporation for the gift of the Wyodak coal sample.

REFERENCES

1. Smisek, M. and Cerny, S. Active Carbon Manufacture, Properties and Applications, Elsevier, Amsterdam, 1970.
2. Khan, M. R., Fuel, 1989, **68**, 1439.
3. Meldrum, B.J. and Rochester, C.H., Fuel, 1991,**70**, 57.
4. Laine, J., Calafat, A. and Labady, M., Carbon, 1989, **27**, 191.
5. Rodriguez-Reinoso, F., Martin-Martinez, J-M., Prado-Burguette, C.and McEnaney, B., J.Phys. Chem., 1987, **91**, 515.
6. Derbyshire, F. J., Jagtoyen, M., McEnaney, B., Rimmer, S. M., Stencel, J. M. and Thwaites, M. W. Proc. 20th Biennial Carbon Conference, 23-28 June, 1991, Sta. Barbara, CA., in press.
7. Derbyshire, F.J., Catalysis in Coal Liquefaction., IEA Coal Research, London, 1988, pp. 29-36.

TABLE 1. CHEMICAL ANALYSIS OF COALS AND CARBONS (wt%)

Material	HTT (°C)	C	H	N	S	P	Ash
		(daf)					(mf)
Wyodak coal							
Parent coal		74.3	5.0	1.0	1.2	0.03	8.2
Thermally	350	77.7	3.8	1.2	1.1	0.01	8.0
treated	450	82.6	2.9	1.3	0.9	0.01	9.3
carbons	550	91.6	2.0	1.5	1.2	0.01	11.9
	650	94.1	1.5	1.4	1.2	0.3	11.9
Chemically	350	87.7	2.3	1.2	0.8	1.4	9.7
treated	450	91.1	1.7	0.9	0.5	1.4	7.3
carbons	550	94.4	1.3	0.9	0.3	4.7	17.6
	650	94.6	0.4	1.1	0.3	4.4	15.9
IBC 101 coal							
Parent coal		79.8	5.2	1.4	5.2	0.0	10.5
Thermally	350	78.8	4.9	1.4	4.6	0.01	10.2
treated	450	86.5	3.1	1.7	3.7	0.01	13.6
carbons	550	91.1	2.2	1.9	4.7	0.01	15.1
Chemically	350	87.1	3.8	1.5	2.9	2.5	15.8
treated	450	86.9	2.5	1.2	1.6	5.1	26.6
carbons	550	93.4	1.4	1.4	1.2	3.9	20.8
	650	102.7	0.9	1.4	1.2	7.2	31.1
Cleaned parent		78.0	5.2	1.4	4.4	0.03	4.1
Clean carbon	550	88.9	1.9	1.1	0.9	1.5	9.2

TABLE 2. ADSORPTION PARAMETERS FOR CHEMICALLY-ACTIVATED CARBONS

Precursor	HTT (°C)	S_{BET} (m^2g^{-1})	S'_{BET} (m^2g^{-1})	V_o (cm^3g^{-1})	S_{BET} (daf)	S'_{BET} (daf)
Wyodak coal	350	416	31	0.17	461	34
	450	791	54	0.32	853	58
	550	731	47	0.30	887	57
	650	718	34	0.30	854	40
IBC 101 Coal	350	2	1	>0.01	2	1
	450	401	25	0.14	546	34
	550	575	56	0.20	726	71
	650	539	46	0.19	782	67
Cleaned coal	550	638	96	0.21	703	106

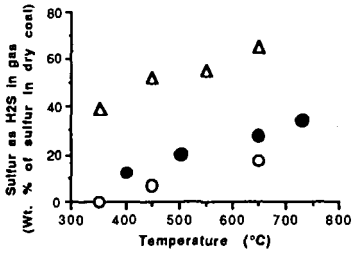

Figure 1. Liberation of sulfur as H2S

This work: △ (acid treated coal), ○ (no acid treatment)

● Khan (2), (no acid treatment)

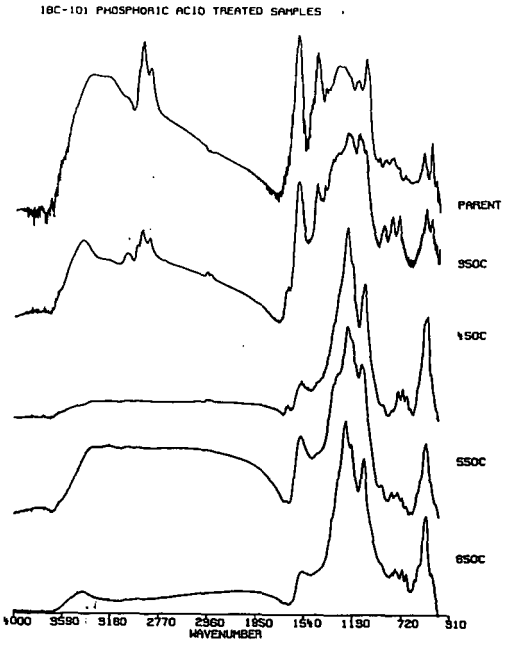

Figure 2. Infrared spectra of activated carbon prepared by chemical activation with phosphoric acid at 350, 450, 550 and 650°C along with parent coal.

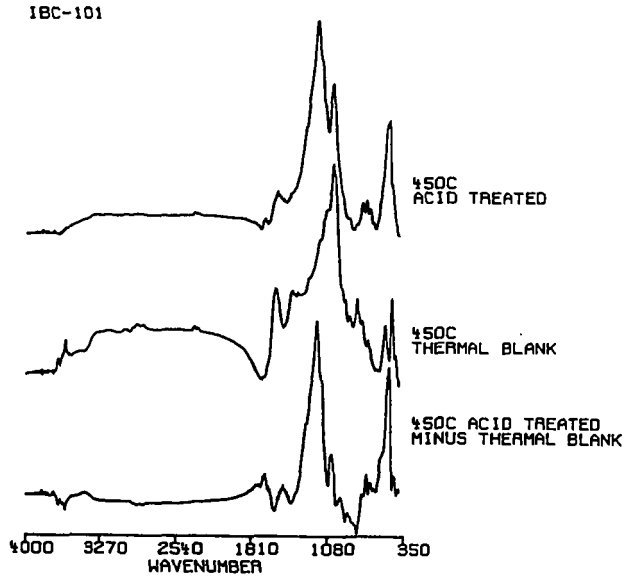

Figure 3. Infrared spectra of chemically activated carbon and thermally carbonized carbon at 450°C and a difference spectrum of chemically activated carbon minus thermal blank.

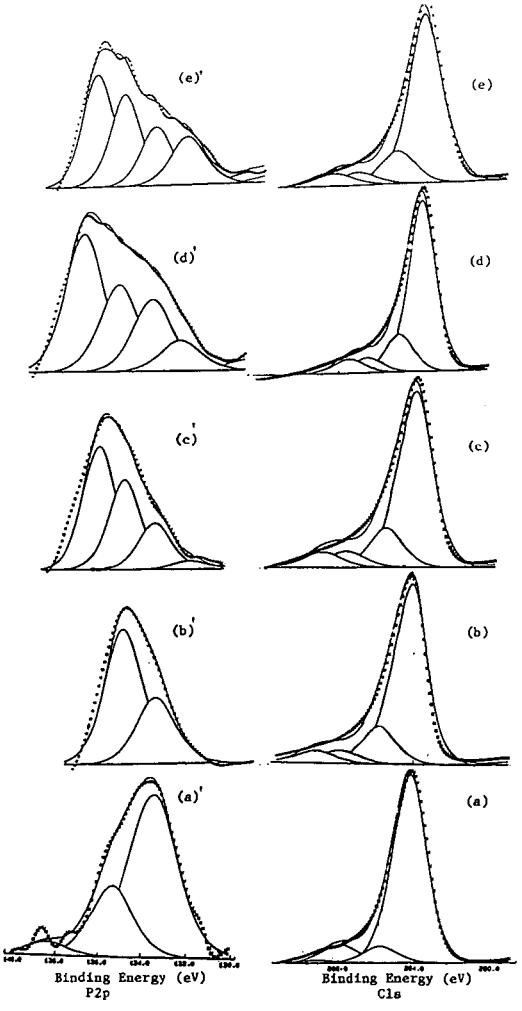

Figure 4. XPS spectra for carbons produced from IBC 101 coal. HTT(°C): 350 (a)(a'); 450 (b)(b'); 550 (c)(c'); 550 (cleaned coal) (d) (d'); 650 (e)(e').

IN SITU EVALUATION OF THE CARBONIZATION BEHAVIOR OF GRAPHITIZABLE CARBON PRECURSORS

Joaquin Rodriguez, John W. Tierney and Irving Wender
Chemical & Petroleum Engineering Department
University of Pittsburgh, Pittsburgh PA 15261

Keywords: Mesophase, Polarized light microscopy, Graphitizable carbons

ABSTRACT

Highly aromatic petroleum residues were carbonized in a high temperature high pressure cell mounted under a polarized light microscope in order to evaluate the appearance, development and type of the anisotropic mesophase. Kinetic parameters (formation and coalescence periods) were related to the nature of constitutive fractions (aromatics, resins, asphaltenes). The final type of anisotropic mesophase is determined by the nature of the starting material. However it is also sensitive to mixing and pretreatment processes such as desulfurization and thermal cracking. This technique can be used to select suitable carbon fiber feedstocks and to evaluate the effects of modifying agents, mixing and treatment processes. It has many advantages over traditional methods which measure the optical texture of polished surfaces.

INTRODUCTION

The complex nature of petroleum residues used for the production of graphitizable carbons (e.g. needle coke, mesophase pitch carbon fibers) makes it difficult to find a single chemical analysis or physical property to rank potential feedstocks in terms of final product quality. It is known, however, that high aromaticity and low Conradson Carbon values are required[1], and development of the liquid crystalline state intermediate (mesophase) is necessary[2-3]. Since the discovery of the nature of the mesophase intermediate by Brooks and Taylor[4] attempts have been made to characterize and correlate its description with the potential to produce graphitic carbons. Patrick[5] and Marsh[6] have developed two classifications in terms of the shape and size of optical texture of anisotropic cokes observed by polarized light microscopy using polished surfaces. These classifications are complemented by assignment of an arbitrary index (Optical Texture Index), related to the area of microstructural units[7]. The OTI can be implemented in point counting techniques to give an average number. Similar attempts have been made for Scanning Electron Microscope[8] and brightness histograms[9]. However, these methods require preparation of solid samples (in autoclaves) and extremely careful polishing before observations can be made. Alternatively, Perrotta[10] introduced a dynamic analysis based on in situ monitoring of mesophase development taking place in a micro-cell mounted on a hot stage polarized light microscope. It follows the actual transformation of pitch into anisotropic structures. The test can be performed in less than one hour, in comparison with several days required for previous methods.

This paper introduces a classification of mesophase structures for this dynamic test which is also applied to the evaluation of petroleum residues, constitutive HPLC (High Performance Liquid Chromatography) fractions and treated (distillation, desulfurization, thermal cracking, delayed coking) samples.

EXPERIMENTAL

A high temperature (to 500 ° C) high pressure (to 2000 psig) micro-cell (Figure 1) was designed[10-11] to fit a hot stage placed under a polarized light microscope. The cell arrangement includes a 2.9 mm o.d. by 1.25 mm cylindrical quartz pan (2 mg sample capacity) mounted on the bottom of the cell which is equipped for the flow of gases. A 5 mm o.d. by 2 mm soft copper O-ring is mounted on top of the pan and coupled with a 5 mm o.d. by 1.65 mm spinel crystal, sealed together tightly on a stainless steel cover. The cell is mounted on a Leitz 1618 hot stage incorporating a tungsten filament furnace that surrounds the bottom of the cell. The Leitz

Orthoplan microscope is equipped with interchangeable objectives (H 20X is the most convenient), a λ retarder plate and a polarizer. A color NEC camera is mounted on the microscope and connected to a PANASONIC video-recorder and a NEC Monitor to follow the carbonization reactions in situ. Temperature, pressure, time and size data are displayed on the screen. The cell is conected through 1/32" tubing to a gas system that supplies hydrogen or nitrogen at regulated pressures.

RESULTS AND DISCUSION

The development of mesophase starts with the appearance of sub-micrometer spherulites (Figure 2-a) that grow in size and occasionally also in number (Figure 2-b) and coalesce (Figure 2-c) until forming a bulk mesophase (Figure 2-d) that is characteristic of the nature (mainly the distribution of carbon atom types) of the feedstock. The time for the appearance of mesophase spherules and the coalescence period are recorded and related to the nature of the starting material and operating conditions.

A wide range of feedstocks have been evaluated in order to observe the widest range of mesophase structures to be included in the classification. This includes the case where coalescence of mesomorphic structures did not develop, leading only to isolated small spherulites, indicating no bulk formation of graphitizable carbon. Figure 3-a represents the smallest size of coalesced anisotropic structures (less than 1 μm) called fine grained mosaics, characteristic of low grade anode coke. Figure 3-b represents an improvement in the extension of aromatic layers where basic anisotropic structures can reach 50 μm, coalesced in what is named as coarse flow mosaic. Figure 3-c represents the case of extended flow domain mosaics characterized by homogeneous anisotropic structures with internal disclinations (defects caused by the folding patterns of the aromatic layers). Larger sizes (ranging from 50 to over 500 μm) correspond to higher degrees of graphitizability. This type of structure is characteristic of high quality needle coke. Finally, Figure 3-d represents the case of non-restricted flow domain mosaic: the actual size is imposed by the geometrical configuration of the micro-cell but the fluid nature of the material would make it spread over larger surfaces if available. This is characteristic of good feedstocks for carbon fiber production.

In addition to characteristic size and shape of the final mosaic, there are typical kinetic parameters (mesophase formation and coalescence period) associated with each material (Table 1): longer coalescence periods appear to be associated with granular and coarse flow mosaics, but no relation is observed with formation time.

To further explore this aspect, one of the feedstocks (FCC Decanted Oil) was fractionated (HPLC) into four constitutive fractions: saturates, aromatics, polar aromatics and asphaltenes. Each one of the fractions was evaluated under the same carbonization conditions (700 psig hydrogen, 50 ° C/min, 30-450 ° C). Figure 3 shows the differences in the final mosaic: the restricted (250 μm) flow domain mosaic of the original feedstock (Figure 3-a) is increased largely (430 μm) for the aromatic fraction (Figure 3-b), but reduced for the polar aromatic (Figure 3-c) and asphaltene (Figure 3-d) fractions, while the saturates fraction volatilizes completely and does not form mesophase. In addition, the asphaltene fraction exhibited a fast formation time similar to that of the feedstock (Table 2), while polar aromatic and aromatic fractions were characterized by longer times. The opposite tendency was observed for the coalescence period. This can be interpreted to mean that the asphaltenes fraction (even though in very small concentration), by initiating its mesophase development, provides the path for catalyzing/promoting the development of mesophase of other fractions, with a final result that is dependent upon the interactions of carbon atom types present in the reacting material.

Research was also performed to evaluate the ability to modify the carbonization process of a particular material (FCC Decanted Oil). Mixing with other feedstocks generally result in a balanced compromise: when mixed with Lube Oil Extract (Figure 4-a) that exhibits no bulk mesophase but isolated spheres, the final mosaic (Figure 4-b) was a collection of poorly coalesced and small anisotropic regions; when mixed with a conversion residue (Figure 4-c) that exhibits coarse flow, the final mosaic was an agglomerate (Figure 4-d) of several flow domain regions. Distillation (Figure 5 a-b) also alters the final mosaic: higher cut point residues tend to result in larger anisotropic strucutures. On the other hand, hydrodesulfurization (Figure 5-c) significantly reduced the size of the final mosaic. Operating the carbonization process at higher pressures (1500 psig) results in larger mosaics.

Thermal treatments (Figure 6 a-d) considerably increase the size of the final mosaic, particularly at long times and relatively low temperatures, producing a pitch that transforms into

non-restricted (fluid) flow domain (Figure 6-c), suitable for carbon fiber production; however increasing the severity of the process results in a heterogeneous and solid bulk mesophase (Figure 6-d).

CONCLUSIONS

In situ monitoring of mesophase development by hot stage polarized light microscopy has been complemented with a classification of final mosaic structures and applied to elucidate the effect of constitutive fractions, mixtures and pretreatment processes upon the carbonization behavior of petroleum residues, providing a technique for selecting graphitizable carbon (needle coke, carbon fibers) precursors.

BIBLIOGRAPHY

1. **Feintuch, H.M. et al.**, in Handbook of Petroleum Refining, pp. 3-61, McGraw-Hill (1986)
2. **Lewis, I.C. and Singer, L.S.**, in Polynuclear Aromatic Compounds, pp. 269-285, ACS (1988)
3. **Marsh, H. and Smith, J.**, in Analytical methods for coal and coal products, Vol. 2, pp.371-414, Academic Press (1978)
4. **Brooks, J.D. and Taylor, G.H.**, Carbon, 3:185-193 (1966)
5. **Patrick, J.W. et al.**, Fuel, 52(3):198-204 (1973)
6. **Marsh, H. and Menendez, R.**, in Introduction to Carbon Science, pp. 37-73, Butterworths (1989)
7. **Marsh, H. and Latham, C.S.**, in Petroleum Derived Carbons, pp 1-28, ACS (1986)
8. **Ke-shun, S.**, 19th Bien. Conf. Carbon, pp.176-177 (1989)
9. **Sunago, H. et al.**, 19th Bienn. Conf. Carbon, pp. 102-103, (1989)
10. **Perrota, A.J. et al.**, High Temp. High Pres., 13(2):159-166 (1981)
11. **McCullough, J.P.**, University of Pittsburgh, 1984

ACKNOWLEDGEMENTS

This work has been financially supported by INTEVEP S.A. (R&D Center of Petroleos de Venezuela). Special thanks are due to Carlos Mota, project leader. Also we appreciate the assitance of Michael Wen, Dave Herrick and Larry Herman.

Table 1. Classification of delayed coking feedstocks for anode and needle coke.
(Based on dynamic hot stage microscopy at 450 ° C, 50 ° C/min and 700 psig hydrogen)

Material	Aromaticity ^{13}C nmr wt%	Mesophase formation min	Coalescence period min	Optical Texture Size, μm	Uses
Lube Oil Extract	29.30	5	No	Spheres	None
Heavy Crude Oil	37.30	11	11	<1	Anode
Conversion Residue	41.43	9	13	10-50	Anode
FCC Decanted Oil	52.73	2	3	250-500	Needle
Petroleum Pitch A-240	88.61	18	-	>500	Needle,Fibers

Table 2. Mesophase development of FCC Decanted Oil HPLC fractions.
(Based on dynamic hot stage microscopy at 450 ° C, 50 ° C/min and 700 psig hydrogen)

Material	Yields wt %	Mesophase formation min	Coalescence period min	Optical Texture Size, μm
FCC Decanted Oil	-	2	3	250
HPLC Fractions				
Saturates	26.8	No	No	-
Aromatics	67.3	12	3-10	430
Polar Aromatics	4.7	9	25	50
Asphaltenes	1.2	2	>37	<1

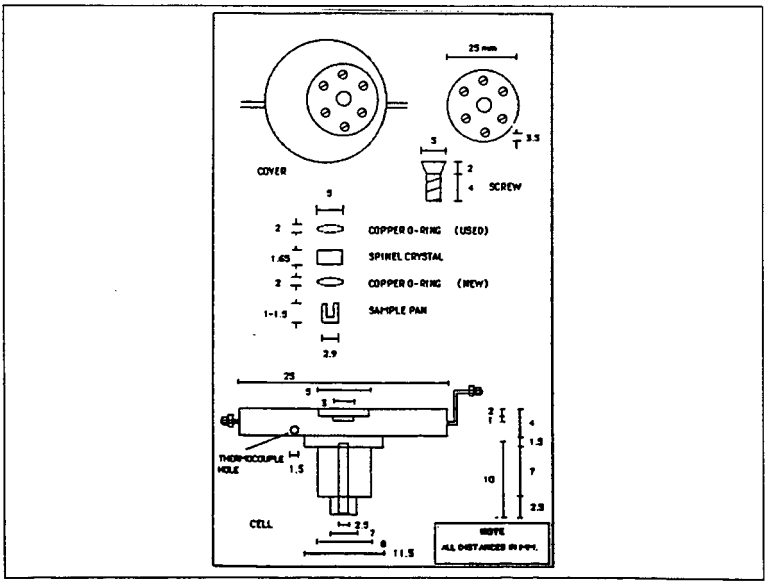

Figure 1. High Temperature High Pressure Micro-cell

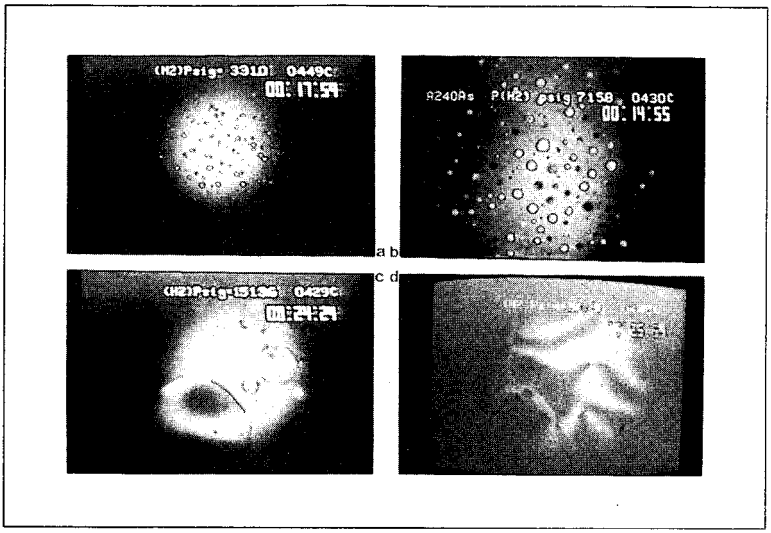

Figure 2. Evolution of mesophase development: (a) appearance, (b) growth, (c) coalescence, (d) final mosaic (screen size: 475 μm)

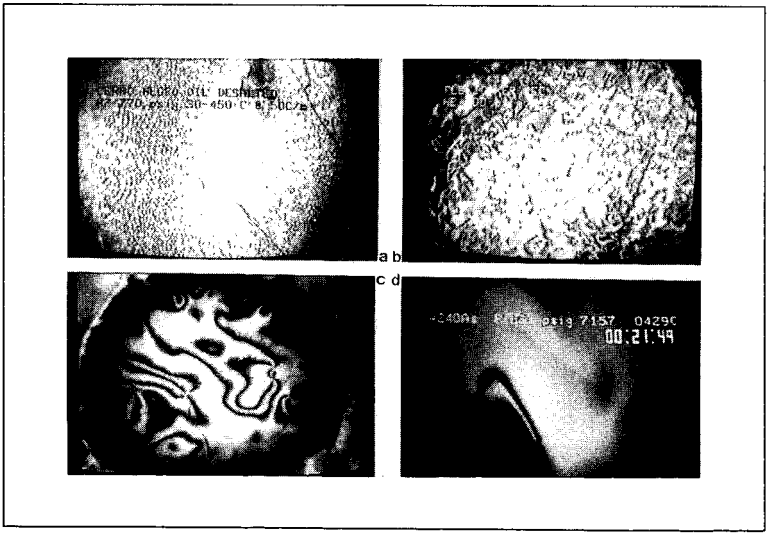

Figure 3. Clasification of final mosaic: (a) fine grain, (b) coarse flow, (c) flow domain, (d) fluid flow domain (screen size: 475 μm)

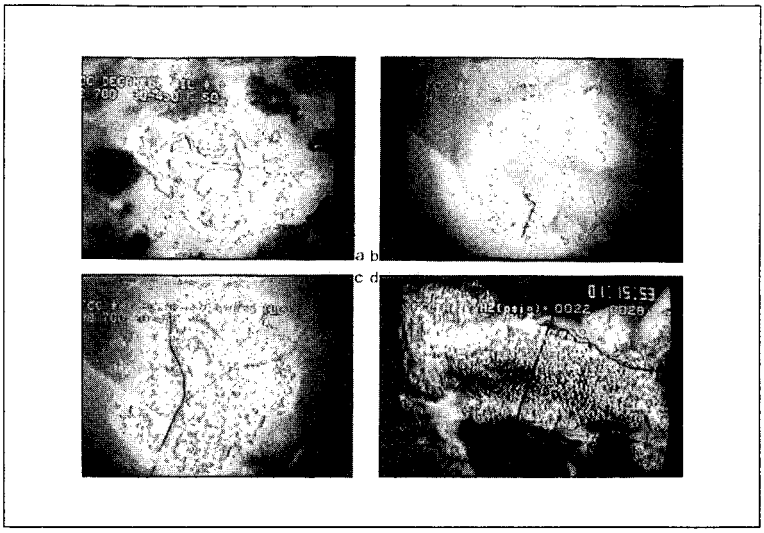

Figure 4. Final mosaics of HPLC fractions: (a) FCC Decanted Oil, (b) Aromatics, (c) Polar aromatics, (d) asphaltenes (screen size: 475 μm)

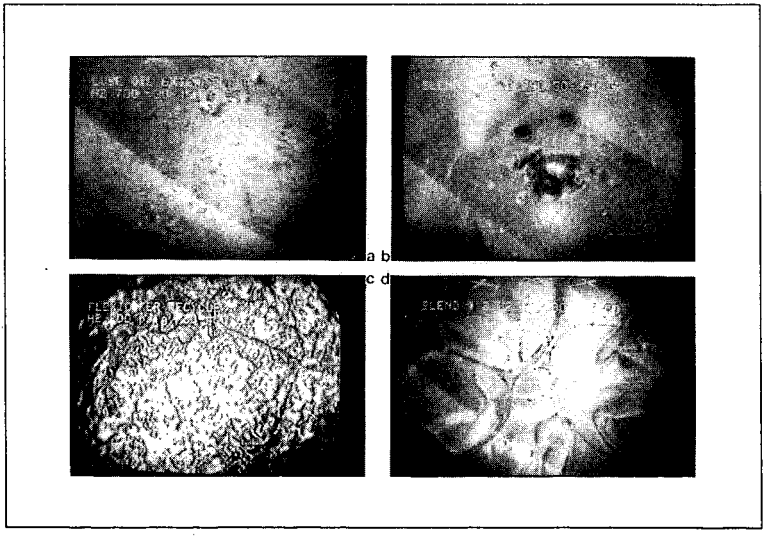

Figure 5. Final mosaics of mixtures: (a) Lube Oil Extract, (b) 70% FCCDO & 30% LOE, (c) Conversion residue, (d) 70% FCCDO & 30% CR (screen size: 475 μm)

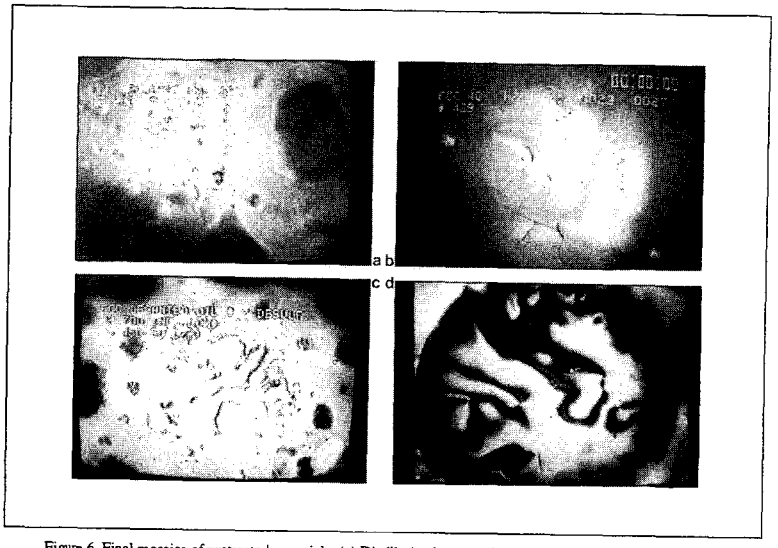

Figure 6. Final mosaics of pretreated materials: (a) Distillation bottoms 63%, (b) Distillation bottoms 40%, (c) Desulfurized, (d) High pressure carbonization (screen size: 475 μm)

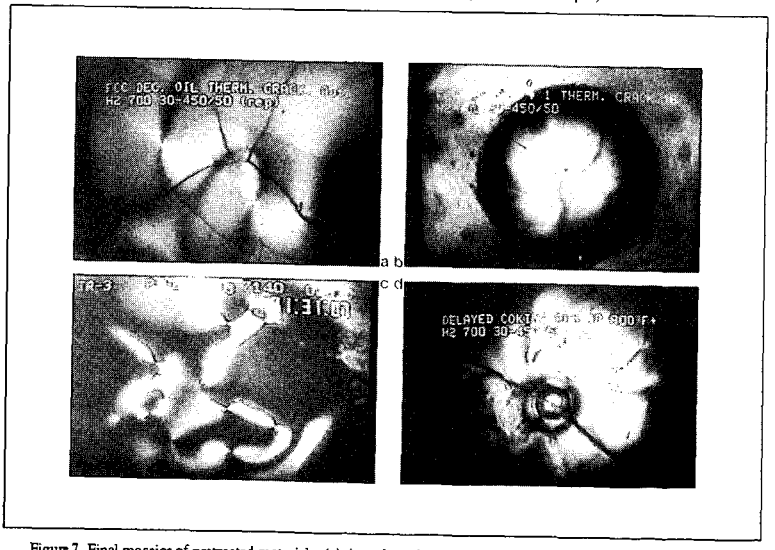

Figure 7. Final mosaics of pretreated materials: (a) Autoclave thermal cracking, (b)Pilot plant thermal cracking, (c) Severe thermal cracking (long time), (d) Delayed coking residue (screen size: (a) 190 μm, (b-d) 475 μm)

DEVELOPMENT AND TESTING OF CARBON PISTONS

J. Heuer

Research, Structural Materials
Daimler-Benz Aktiengesellschaft
7000 Stuttgart 80
Germany

INTRODUCTION

The research department of Daimler-Benz has been developing carbon pistons for combustion engines for about 3 1/2 years. In this context "carbon" means graphite without the addition of reinforcing fibres.

Although the development of the material would itself without doubt be an essential topic, this paper is restricted to the application of the material and treats the matter from the view of a mechanical engineer.

The project "Development of Carbon Pistons" is a joint project in which several partners and sub-contractors are working together and is sponsored by the German Ministry for Research and Technology.

REASONS FOR THE DEVELOPMENT OF CARBON PISTONS

Today, aluminum alloy is generally used for mass produced pistons. However, graphite has several advantages in comparison with aluminum. The most important differences are shown in Fig. 1.

The density of graphite is much lower than that of aluminum alloy. other favorable properties of graphite are the lower coefficient of thermal expansion and the higher resistance to heat. Unfavorable is that the tensile strength of graphite at room temperature is comparatively low. However, considering the tensile strength as a function of temperature, as shown in Fig. 2, you see that the strength of aluminum alloy drops at temperatures above 160 °C. In contrast to this the tensile strength of graphite even increases slightly with temperature.

On the basis of these graphite material properties the following advantages can be expected if the material is applied to pistons:

- a reduced piston weight because of the lower material density,
- a smaller piston clearance because of the low coefficient of thermal expansion.
- Furthermore, it can be expected that the carbon piston transmits less noise because of the material's damping capacity.
- Another advantage of graphite are the excellent emergency frictional properties, which make piston scuffing impossible.

These were the advantages which triggered our development of carbon pistons. As we will see later on, the carbon piston lived up to our expectations, and showed even more improvements.

DESIGN AND FABRICATION

A carbon piston was designed and built to fit into an existing production engine. As a test bed, the engine of the Mercedes-Benz model 190 E was chosen. This engine is a 4-stroke-4-cylinder-gasoline engine with a displacement of 2 litres and a bore of 89 mm.

Carbon pistons were manufactured by turning and milling from the solid with the aid of numerically controlled machines. The material for the pistons came from Poco Graphite, Inc., Decatur, Texas, which had the highest strength of all standard grades in the market.

TESTS OF FUNCTIONALITY AND DURABILITY

After the first carbon pistons were built, their functional test followed. At first, only one carbon piston was installed in the 4-cylinder engine, which was mentioned before, together with 3 standard pistons. The carbon piston was equipped with standard piston rings and a normal connecting rod but with a ceramic piston pin of silicon nitride. The engine was tested on a simple engine bench. This bench was used employing a moderate test program with alternating loads.

After 56 hours on the bench the engine was dismantled for inspection. The carbon piston and the ceramic piston pin were in an excellent condition.

At the beginning of 1989 an engine was equipped for the first time with 4 carbon pistons and 4 ceramic piston pins. The carbon pistons and the ceramic piston pins had thicker walls than the conventional metallic parts to compensate for the inferior strength. In spite of this fact the total weight of the carbon pistons and the ceramic piston pins was 20 % less than that of the corresponding metallic production parts.

This first engine, which was completely furnished with carbon pistons, was tested for 120 hours on the bench according to a rather severe test program, where almost 40 % of the running time the engine was at full load. In this program the engine was under much more load than in normal road traffic. After 120 hours the engine was disassembled and the carbon pistons and the ceramic piston pins were inspected. All components were in an excellent condition, and could be used again.

Thus the engine was reassembled and installed in a test car - a Mercedes-Benz model 190 E. In this car the engine with carbon pistons accumulated more than 15 000 miles without any trouble. The car was used by all colleagues of our department on public roads - i. e. in city - and long distance traffic. In consideration of the safety of the driver, the engine speed was restricted not to exceed

4 000 rpm. This was the only restriction.

During the road test the engine performed very well all the time. Compression graphs, which were taken before and after a distance of 15 000 miles, indicated no difference and thus a continuing good engine condition. Fig. 3 shows a carbon after 120 hours on the engine bench and 15 000 miles in the test car.

COMPARISON MEASUREMENT

After the function and a sufficient service life of the engine with carbon pistons had been established, exact measurements could be started. With the aid of these tests the expected and possible other advantages of carbon pistons in comparison to today's production pistons should be evaluated.

For the comparison measurements only one engine was used to avoid the influence by tolerances of different engines. So at first all tests were performed with carbon pistons. Then the carbon pistons and the ceramic pins were replaced by their series counterparts.

The evaluations concerned mainly the following items:

- fuel consumption
- oil consumption, and
- exhaust emissions

Fuel consumption and exhaust emissions were determined in an official test program, which is called 14-points-CVS-test. This test corresponds to city traffic.

The oil consumption was measured in a special trial run. In this test, the engine continuously ran for three hours under full load conditions at an engine speed of 4500 rpm.

The most important results of the comparison measurements are compiled in Fig. 4. All data are relative and related to the production engine with aluminum pistons. This figure indicated that the engine with carbon pistons performed better in all points than the production engine. Concerning exhaust emissions the improvements with the engine using carbon pistons were 20 % with respect to hydrocarbons (HC), 30 % concerning carbon monoxide (CO), and 3 % concerning nitrogen oxides (NO_x). A slight improvement of 3 % was also achieved with respect to fuel consumption. The largest improvement, however, was observed in oil consumption. The carbon piston engine consumed only 44 % of the lubricating oil which the standard engine needed.

CONCLUSIONS

With the use of top quality graphites, which are available on the market, it was possible to reduce the piston weight by 10 %. Another weight reduction of 10 % was realized by the application of a ceramic piston pin. Thus in a first approach the weight of the piston/piston pin assembly was already 20 % less than with the

corresponding production parts.

Function and service life could be demonstrated up to a maximum engine speed of 5 100 rpm.

Comparative tests so far revealed no disadvantages for the engine with carbon pistons. Slight improvements - in the order of 3 % - were measured with respect to power output and fuel consumption. However, one must bear in mind that all improvements were attained by a simple replacement of successful production components. Up to now, no optimization has been undertaken - neither of the carbon piston nor of the engine with respect to the special properties of graphite.

The engine with carbon pistons showed very important and clear improvements concerning exhaust gas emissions and oil consumption. Therefore, the application of carbon pistons could help to reduce environmental pollution, and to extend the useful life of the catalyst. The improvement regarding the emission of hydrocarbons is especially essential, because this constituent is difficult to diminish when the catalyst is not yet at operating temperature.

Before the carbon piston will be suitable for mass production there are at least two pre-requisites which have to be accomplished: Firstly, the tensile strength of the graphite must be improved. This is necessary to allow at the same time a further weight reduction of the piston, and to meet the requirements of full engine speed.

Secondly, economic production methods must exist which are suitable for series production.

			Aluminum alloy	Graphite
Density	ρ	g/cm^3	2.70	1.83
Coefficient of linear expension	α	1/K	$21 \cdot 10^{-6}$	$6 \cdot 10^{-6}$
Modulus of elasticity	E	GPa	80	11
Thereal conductivity	λ	W/mK	150	80
Maximum temperature	t	°C	380	460
Tensile strength	σ_B	MPa	225	70

Figure 1. Material Data of Aluminum Alloy and Graphite

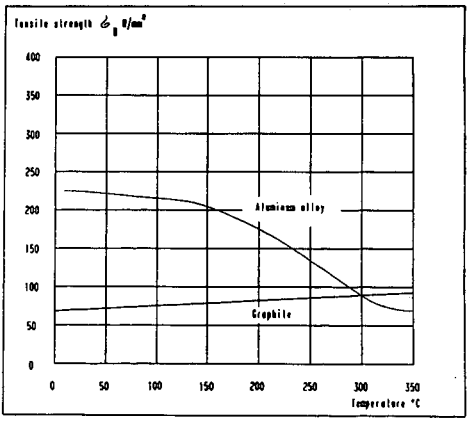

Figure 2. Tensile Strength of Aluminum Alloy and Graphite

Figure 3. Carbon Piston after 120 hours on Engine Bench and 15000 miles in Test Car.

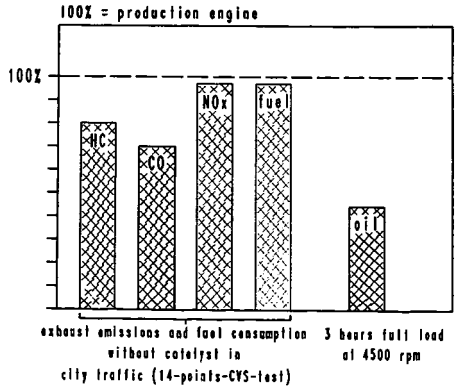

Figure 4. Engine with Carbon Pistons compared to Production Engine.

CARBON AND GRAPHITE MATRICES IN CARBON–CARBON COMPOSITES: AN OVERVIEW OF THEIR FORMATION, STRUCTURE, AND PROPERTIES

Gerald Rellick
Mechanics and Materials Technology Center, Technology Operations
The Aerospace Corporation, P.O. Box 92957, Los Angeles, CA 90009

Keywords: Carbon–carbon composites, Graphitization, Composite properties

WHY CARBON–CARBON COMPOSITES?

Carbon–carbon (C/C) composites, so-called because they combine carbon-fiber reinforcement in an all-carbon matrix, can best be viewed as part of the broader category of carbon-fiber-based composites, all of which seek to utilize the light weight and exceptional strength and stiffness of carbon fibers. However, in C/C, the structural benefits of carbon-fiber reinforcement are combined with the refractoriness of an all-carbon materials system, making C/C composites the material of choice for severe-environment applications, such as atmospheric reentry, solid rocket motor exhausts, and disc brakes in high-performance military and commercial aircraft. Their dimensional stability, laser hardness, and low outgassing also make them ideal candidates for various space structural applications.

Such mechanical and refractory properties are not met by the various bulk graphites for two reasons: (1) graphites are very flaw sensitive and, therefore, brittle; and (2) graphites are difficult to fabricate into large sizes and complex shapes. These difficulties are largely overcome by taking advantage of the "two phase principle of material structure and strength [1]."

In the classical two-phase materials system, or composite, a high-strength, high-modulus, discontinuous-reinforcement phase is carried in a low-modulus, continuous-matrix phase; e.g., graphite fibers in a thermoplastic-resin matrix. The stress in a composite structure having fiber reinforcement that is continuous in length, is carried in proportion to the moduli of the constituent phases, weighted by their respective volume fractions. Therefore, the much stiffer (higher-modulus) fibers will be the principal load bearers, and the matrix, in addition to having the task of binding together the composite, will deform under load and distribute the majority of stress to the fibers. At the same time, because the brittle carbon fibers are *isolated*, the possibility that an individual fiber failure will lead to propagation and catastrophic failure is practically eliminated.

Another major benefit of composites is that they permit the construction of complex geometries, and in such a way that different amounts of the load-carrying fibers can be oriented in specific directions to accommodate the design loads of the final structure. Closely associated with this "tailoring" feature of composites is that carbon-fiber technology enables exploitation of the exceptional basal-plane stiffness (and strength, in principle, although this is still much farther from realization) of sp^2 bonded carbon atoms—i.e., the fibers are not isotropic, but rather have their graphite basal planes oriented preferentially in the fiber axial direction.

For very-high-temperature carbon-fiber-composite applications, say, above 2000°C, even for brief periods of time, it is necessary to employ a carbon matrix; however, like the fiber, the carbon matrix is also brittle. When fiber–matrix bonding is very strong in C/C, brittle fracture is frequently observed. The explanation is that strong bonding permits the development of high crack tip stresses at the fiber–matrix interface; cracks that initiate in either fiber or matrix can then propagate through the composite. However, if the matrix or the fiber–matrix interface is very weak, or microcracked, then the primary advancing crack can be deflected at such weakened interfaces or cracks. This is the Cook–Gordon theory [2] for strengthening of brittle solids, which states, more specifically, that if the ratio of the adhesive strength of the interface to the general cohesive strength of the solid is in the right range, large increases in the strength and toughness of otherwise brittle solids may result. Therefore, good fiber strength utilization in a brittle-matrix composite like C/C depends on control of the matrix and interfacial structures.

The objective of this paper is to provide a brief overview of carbon and graphite matrices in C/C, with an emphasis on recent research on some of the more fundamental materials issues involved [3–7]. Much of what is presented is taken from our own published work, which has focused on understanding how the structure of

the carbon or graphite matrix, and fiber–matrix interphase region, is influenced by starting materials and processing methods, and, in turn, how these structures affect composite properties. For comprehensive reviews of C/C, the reader is referred to Fitzer [8,9] for an overview of the basic materials issues, and to McAllister and Lachman [10] for a thorough treatment of fabrication and processing issues. Less comprehensive but more recent reviews that build principally on those just cited but that also deal with more specialized topics, such as oxidation protection of C/C, are contained in Refs. 11–13.

FIBER ARCHITECTURE AND PREFORM DENSIFICATION

The composites designer, in addition to being able to choose from a wide variety of fiber types, also has a large number of fiber architectures available. For high-performance C/C applications, continuous (in length) fiber reinforcement is integrated to produce either a two-dimensional (2-D) or three-dimensional (3-D) fabric preform. According to Ko [14], a fabric preform is defined as "an integrated fibrous structure produced by fiber entanglement or yarn interlacing, interlooping, intertwining, or [nonwoven] multiaxial placement."

The preform may be dry, i.e., unimpregnated, as in 3-D orthogonal block structures, in which the x, y, and z yarns are "laid-in" straight to produce a structure having about 60% void volume (see Fig. 1a). The yarns may also be pultruded, i.e., impregnated with a resin binder and formed into rigid rods.

Alternatively, the fabrics may be impregnated with a thermosetting-resin binder and then the fabric plies laid up to produce the desired component (Fig. 1b). Such a structure is still termed 2-D because of the lack of through-thickness reinforcement.

To produce a C/C, the carbon–resin composite is baked, or fired, to pyrolyze the organic matrix. If the fabric is initially impregnated with a state-of-the-art phenol formaldehyde resin system, we can expect to obtain a C/C part with approximately 25% residual porosity after baking. However, experience has shown that such porosity is excessive, and that significant improvement in properties will follow if the porosity is reduced to values in the 5–15% range, depending on the particular type of structure. Therefore, not only in the dry preform, but also in the pyrolyzed "prepreg" fabric, additional volume increments of carbon matrix must be introduced into the C/C structure. The introduction can be achieved by one or a combination of three densification processes: CVI, use of coal-tar and petroleum pitches, and use of thermosetting resins. As each of these processes is discussed in turn, we will explore its characteristic structural features and densification behavior, and effects on properties. This discussion will also be used as an opportunity to introduce and discuss the various C/C characterization tools and techniques: X-ray diffraction, laser Raman microprobe spectroscopy, density measurements, and, particularly, polarized-light microscopy, and scanning and transmission electron microscopy (SEM and TEM).

CVI

The first method for C/C densification, chemical vapor infiltration (CVI) [15,16], involves the passage of a hydrocarbon gas, typically methane, through the porous preform at temperatures in the 1000–1200°C range, with resulting deposition of carbon in the open porosity. Such low-temperature CVI leads to three principal carbon microstructures as defined by polarized-light microscopy [17–19]: rough laminar (RL), smooth laminar (SL), and isotropic. Isotropic deposits are generally very low density and of little value in C/C densification. Examples of RL and SL carbons in a PAN-based carbon-fiber composite are shown in the polarized-light micrographs of Figs. 2a and b.

A characteristic feature of both the RL and SL carbons is the set of extinction crosses observed under cross-polarized light. Such crosses are a consequence of the oriented nature of the deposits; the carbon layer planes align preferentially along the fiber surface. The anisotropic structure leads to a condition of birefringence in which two of the three principal crystallographic axes of graphite oriented at 90 deg to each other have different indices of refraction. Examination of Figs. 2a and b reveals two patterns of RL and SL deposits, illustrating that not only the amount but the type of carbon deposition can vary throughout the structure, depending on local temperature and gas concentration gradients [17].

In addition to orientation, another important feature of carbon matrices is their graphitizability, which is a measure of the ease in converting the pyrolyzed carbon matrix product into crystalline graphite through high-temperature heat treatments in the ~2000–3000°C range. The state of graphitization can be assessed by a number of techniques, the most common of which is X-ray diffraction (XRD). However, in C/C it is usually very difficult to resolve the resultant composite diffraction response into the respective fiber and matrix responses, because both phases are carbon. A technique to circumvent the sample volume problem is laser Raman microprobe spectroscopy (LRMS). Although the interpretation of the Raman spectra is more ambiguous than with XRD, LRMS permits focusing of a visible-light beam, as small as 1 μm in diameter, on a region of the specimen while recording the Raman spectrum, which is active in carbon [20]. Useful structural information *on a local scale* can be obtained in principle.

One major difficulty with applying LRMS to composites is that the size of constituent phases is of the order of microns, making it necessary to prepare the specimens for examination using standard optical polishing techniques. Such polishing tends to damage the near-surface structures and leaves behind a thin layer of polishing debris. Since the probe depth of the optical beam is only about 50 nm [20], the Raman spectrum unfortunately becomes a function of the preparation technique [21–23].

A technique we have employed extensively and with good success, and which is an outgrowth of early work performed at Los Alamos Laboratories [24,25], involves SEM examination of specimens that have been polished and then cathodically etched with xenon. When the carbon structure is graphitic, and when the graphite layer planes are oriented perpendicular to the plane of section, we see, typically, a pronounced lamellar texture, as revealed for the inner- and outermost CVI layers in the C/C of Fig. 3. The lamellar texture is the result of differential etching rates of the various microstructural units, the exact nature of which is still not clear. The most likely mechanism is preferential removal at lower-density, less-ordered intercrystalline-type boundaries that separate regions of good crystalline registry; this is seen very dramatically in highly oriented pyrolytic graphites reacted in oxygen [26,27]. The technique is effective, principally, in distinguishing broadly between graphitic and nongraphitic carbon on a scale of microns.

Returning to Fig. 3, this particular specimen has the CVI deposition sequence RL/SL/RL (as determined separately from polarized-light microscopy) and has been heat-treated to 2500°C for 1 hr. The lamellar texture of the RL zones indicates their graphitized structure, whereas the absence of significant texture in the SL zone indicates that the SL structure is essentially glassy carbon. This observation was confirmed by XRD, LRMS, and by selected physical-property measurements [28]. The effect of having a graphitic *and* well-oriented matrix is illustrated by the higher thermal conductivities for heat-treated RL composites shown in Fig. 4.

Modulus enhancement is another interesting effect of a well-oriented, graphitic matrix (Fig. 5). For the particular pseudo-3-D, felt-based C/C composite of the figure, there were two CVI densifications. Following the first, the composite structure was heat-treated to 2500°C; the second CVI was left in the as-deposited state (~1000–1200°C). The relative proportions of the first and second CVI varied with each specimen, but the total CVI weights were approximately the same. The fiber volume (and weight) fraction was constant (~20%) for each composite.

The strong dependence of the modulus on the relative proportion of heat-treated CVI indicates that the carbon matrix can carry a significant fraction of the load, particularly, in this case, if the structure is heat-treated to typical graphitization temperatures. The modulus-enhancement effect by the matrix is especially striking in this composite because of the use of low-modulus fibers at fairly low volume fractions. However, as will be seen, this effect is an important materials and processing consideration in all C/C composites.

Coal-Tar and Petroleum Pitches

The second method for C/C densification is the use of coal-tar and petroleum pitches. Because they are thermoplastic, pitches are used mostly for redensification; i.e., further densifying of a C/C structure that has been "rigidized" by an earlier impregnation/densification step (e.g., a resin-impregnated fabric preform) or that has sufficient rigidity from the friction between the elements of the woven structure (e.g., 3-D braided preform).

Pitches are unique in passing through a liquid-crystalline transformation at temperatures between about 350 and 550°C [29]. In this transformation, large lamellar molecules formed by the reactions of thermal cracking and aromatic polymerization are aligned parallel to form an optically anisotropic liquid crystal known as the carbonaceous mesophase [30]. The alignment of the lamellar molecules is the basis for easy thermal graphitizability of the carbonized product. One of the features of a mesophase-based matrix is high bulk density, which is achievable because the matrix density can approach the value for single-crystal graphite, 2.26 g/cm^3.

The topic of pitch impregnation and densification of C/C introduces the subject of densification efficiency, the most meaningful measure of which is *volumetric* densification efficiency [31]. It is the ratio of the volume of carbon matrix in a process cycle to the volume of porosity available for densification.

For pitches carbonized at atmospheric pressure, coke yields are of the order of 50–60%, impregnant densities are ~1.35 g/cm^3, and, as we have noted, densities for pitch-derived matrices are ~2.2 g/cm^3. From these values we calculate volumetric densification efficiencies of only 30–40% at atmospheric pressure [31]. By resorting to so-called hot isostatic-pressure-impregnation-carbonization (HIPIC), to pressures of about 15,000 psi, carbon yields of pitches can be increased to almost 90% [10]. But even with HIPIC, volumetric filling is only 55%. Therefore, given a preform with initial porosity of 45%, typical for many 3-D woven structures, three cycles at *maximum densification efficiency* would be required to reduce the porosity to 4%. With current HIPIC procedures, however, it is found that at least five cycles at 15,000 psi are required to achieve this same level of porosity. Such reduced efficiency in real systems is the result of forced expulsion of pitch from the preform as a result of the gas-forming pyrolysis reactions accompanying carbonization.

Clearly, one way to increase efficiency, for a given weight-based carbon yield, is to select either an impregnant or an HTT that will lower the final matrix density. As will be seen in the next subsection, lower-density carbon matrices can be achieved by using resin precursors that form a glassy-carbon-type structure. But, although this approach fills more of the available space, it does so with a lower-density carbon matrix, which is different in structure from the higher-density graphitic matrix. The trade-offs in properties, particularly mechanical, are not well understood. We will touch on this topic again in the next subsection.

Approaches to improving densification efficiency of pitch-based matrices without resorting to HIPIC processing include the use of heat-treated and solvent-extracted pitches [32] and partially transformed (to mesophase) pitches [33,34]. A novel approach, developed by White and Sheaffer [35], is to oxidatively stabilize the mesophase following impregnation and transformation, an approach similar to that employed in mesophase–fiber stabilization. The result is a "hardened" mesophase that is resistant to the bloating effects of pyrolysis gases but that, upon further heat treatment, yields a dense, graphitic carbon.

The strong orienting effect of the fiber surface on the large lamellar mesophase molecules is an interesting feature of mesophase formation in C/C composites. This effect was demonstrated by the work of Zimmer and Weitz [36], who used polarized-light microscopy to show that mesophase molecules near a fiber surface in a close-packed fiber bundle always aligned parallel to the fiber surfaces, even in the presence of strong magnetic fields. Singer and Lewis demonstrated earlier that magnetic fields would orient mesophase molecules in *bulk* mesophase [37]. Zimmer and Weitz showed that mesophase would also orient in matrix-rich regions within the fiber bundles—i.e., at points far removed from fiber surfaces [36]. They calculated a magnetic coherence length of 7 μm, which corresponds roughly to the distance over which the orientation effect acts.

Such localized orientation in the liquid-crystalline state would lead one to expect the final, graphitized matrix also to be well oriented in the immediate vicinity of the fiber. First observed by Evangelides [38] using SEM in conjunction with xenon-ion-etching, such a matrix "sheath effect" is depicted in Fig. 6 in a coal-tar-pitch-densified C/C.

Modulus enhancement in pitch-based C/C has been widely reported, but whether the effect is due to the matrix or to an increase in the fiber modulus, resulting from high-temperature heat-treatment-induced structural changes in the fiber, has not been clarified [39]. The sheath effect is also pronounced in resin-based carbon matrices, but for different reasons, which we will examine in the next subsection.

Matrix microcracking is characteristic of all C/Cs, but it is particularly prevalent in graphitic matrices because of the combination of weak shear planes in polycrystalline graphite and the thermal stresses generated during heat treatment (Fig. 7) [40,41]. Microcracking also has important effects on the engineering properties of C/C materials—particularly the matrix-dominated properties in the unreinforced directions, such as the interlaminar shear strength and perpendicular-to-ply tensile strength in 2-D C/C laminates. However, as mentioned above, such microcracking appears to improve in-plane flexural and tensile strength, by way of a Cook–Gordon mechanism [42–45].

Thermosetting Resins

The third, and last, class of C/C impregnant to be discussed is thermoset resins, which are the basis for "prepreg" fabric and tapes, as noted above; resin systems can also be used for reimpregnation. In addition to their easy fabricability, thermosets have the advantage of "charring-in-place;" that is, although they soften and deform on heating, they do not fuse or liquefy, and, therefore, no special tools or techniques must be employed to retain the matrix in the composite during pyrolysis.

Thermoset resins are usually highly crosslinked, which makes them resistant to thermal graphitization *in bulk form*, even to temperatures of 3000°C [5,46]. Phenolic resins are currently most commonly used for prepreg operations, whereas furan-based resins are used more for reimpregnating. Both have char yields typically in the 50–60% range.

The development of ultra-high-char-yield resins derived from polymerization of diethynylbenzene (DEB) [47–51], usually termed polyarylacetylenes (PAA) [47], has received much focus in recent years. The structure of DEB is illustrated in Fig. 8, along with a synthesis route that involves a catalytic cyclotrimerization prepolymerization in methyl ethyl ketone solvent [48,49]. The cyclotrimerization liberates much of the exothermic heat of polymerization, thereby allowing safe, controllable curing. The principal appeal of PAAs is their extremely high char yield. From the average structure, we calculate a theoretical carbon yield of about 95%; in practice, PAAs can have carbon yields of 90% to 700°C, although more practical formulations employing monofunctional chain terminators to improve flow properties reduce this yield to about 85% [48,49].

Similar to other crosslinked thermosets, PAAs produce largely nongraphitizable carbons. To extend the range of matrix structures for this fabricable resin system, we have been exploring approaches to *in situ* matrix catalytic graphitization in C/C in our laboratory. One promising approach, by Zaldivar *et al.* [52], has been the use of boron in the form of a carborane compound. Figure 9a is a plot of room-temperature tensile strength of undoped and boron-doped unidirectional C/Cs versus HTT; the strengths are calculated relative to the fiber cross-sectional areas on the assumption that the matrix carries negligible load relative to the fibers. The strength of the fibers in the cured-resin composite is taken to be the value for full strength utilization. The plot illustrates a number of important features. First, for the undoped system, strength exhibits a large decrease as the composite proceeds from cure to carbonization, owing to conversion of the compliant polymer matrix into a well-bonded, low-strain-to-failure carbon matrix. Increasing boron levels lead to increased strength utilization for the 1100°C HTT samples: The undoped specimen behaves as a monolithic solid and fractures in a planar-catastrophic mode (Fig. 10a); the 5% B-doped samples exhibit extensive fiber pullout (Fig. 10b), which indicates a weakened interface. The reasons for the weakened interface are unclear, since X-ray diffraction revealed no significant difference in graphitization between doped and undoped specimens after this HTT.

At higher HTTs, the use of higher boron levels leads to a reduction in strength utilization (and an increase in modulus; Fig. 9b), due to catalytic graphitization of the fiber. Further HT of the undoped specimens beyond 1100°C "reclaims" much of the lost fiber strength, for the reasons discussed above. More work is needed to define the mechanisms by which catalytic graphitization of the matrix affects the properties of C/C.

We recently reported a striking modulus enhancement for the same type of 1-D composite studies (Zaldivar *et al.* [7]), using four mesophase-based fibers from DuPont and PAA resin (Fig. 11). The number in the fiber designation is the axial tensile modulus, in Mpsi. For HT to 2750°C, all the composites exhibit sharp increases in fiber moduli, to values exceeding 150 Mpsi, which is the theoretical limit of the graphite basal-plane modulus. Since the moduli are calculated relative to the original fiber cross-sectional areas, such values

indicate that the composite modulus must have significant contributions from the matrix. An example of a matrix sheath that may be contributing to the composite modulus is shown in Fig. 12.

This figure brings us to the subject of stress-induced orientation and graphitization in otherwise nongraphitizing carbon matrices in C/C. While the phenomenon of stress graphitization of hard carbons has been noted for some time [24,25,53,54], only recently have serious efforts have been made to understand the physical-mechanical mechanisms involved in matrix orientation and graphitization in C/C [5,6,55]. This topic is of more than academic interest, because the formation of a two-phase matrix of graphitic and nongraphitic, oriented and unoriented, zones can have a major influence on the mechanical properties of C/C composites.

To examine preferred orientation in thermosetting-resin-impregnated matrices, cross sections of C/C tows fabricated from Amoco T50 PAN-based fibers and a PAA resin were polished, then heat-treated to 2900°C for 1 hr and xenon-ion-etched. The polarized-light micrograph of Fig. 13a reveals that in addition to the pronounced lamellar zones, the smooth-appearing zones—which, by definition, have formed no observable texture with etching—are nevertheless oriented, as evidenced by the polarized-light extinction contours sweeping across the surface of the sample as the analyzer is rotated. We conclude that even the thickest ($> \sim 20$ μm matrix regions in this specimen are oriented. Pronounced optical anisotropy in the matrix for the same composite heat-treated to only 1200°C is revealed by Fig. 13b. As expected, etching produced no lamellar texture for this low HTT.

The highly localized nature of the combination of stress-induced orientation and graphitization is one of its more interesting features; i.e., all of the carbon matrix in the specimen of Fig. 13a is oriented to some degree, yet only certain discrete regions become lamellar graphite upon HT to 2900°C. SEMs of ion-etched specimens reveal this localized graphitization more clearly (Fig. 14); particularly striking is the shrinkage of the matrix away from the fiber, which is a result of the volume decrease accompanying graphitization.

TEM is an extremely effective technique for studying the local structure on an even finer scale. In the transverse (Fig. 15a) and longitudinal (Fig. 15b) bright-field images of thin sections of a T50 fiber/resin-derived C/C heated to 2750°C, crystallite formation and orientation are evident, particularly in the transverse section (compare with Fig. 13a). Selected area electron diffraction confirmed the highly crystalline structure of the interfilament matrix regions [56].

In the SEM of Fig. 16a, we observe an interesting effect: At the interstice of five continguous fibers there is no lamellar formation in the matrix pocket, except perhaps immediately adjacent to the filament surfaces. This effect was typically observed in close-packed groups of three to five fibers. In contrast, in more extensive matrix regions—for example, those that bound two relatively fiber-rich areas, and where the matrix boundaries are fairly straight—we observe relatively unimpeded development of lamellar structure over a distance of several microns (Fig. 16b). Such lamellar development is particularly striking at the extreme outside of the single-tow specimens where quite thick ($\sim$ 1–2 fiber diameters) lamellar zones form (Fig. 16c). In Fig. 16d, we see that an interruption in the uniformity of the interface between this outer matrix crust and the composite leads to a transition from the lamellar to nonlamellar structure.

Further microstructural features not seen in polished specimens are revealed in the SEM of a tensile-fracture surface (Fig. 17). The lamellar regions in the matrix are still evident, and the PAN-based fibers show their typical fibrillar structure. But we now observe in the matrix both lamellar and fibrillar textures, the latter resembling that seen in the T50 fibers, which are generally considered to be oriented glassy carbon [46].

Two observations suggested to us that the key factor in determining lamellar-structure formation in a C/C composite matrix is a *multiaxial* deformation of the resin during its pyrolysis to carbon. First, consider that, in normal PAN-fiber manufacture, which leads to a fibrillar structure, the filaments are subjected to a uniaxial tensile stress during oxidation stabilization. However, when carbonized without prior oxidation stabilization, *but in very thin sections*, such as between the layers of montmorillonite clay, PAN has been shown to yield a single-crystal structure following subsequent graphitization heat treatment [57]. Second, in partially oxidized (through-the-thickness) PAN fibers, the unoxidized, fusible core can form lamellar carbon [58].

In both examples, the mechanical restraints imposed on the PAN during its pyrolysis would be expected to produce multiaxial deformation. In this critical regime, a number of stresses act at the fiber–matrix interface, assuming good fiber–matrix adhesion: First, there is an axial tensile stress that acts on the matrix; it is a consequence of the large matrix pyrolysis shrinkage, and the high axial modulus and low axial thermal expansion of the fiber. This matrix shrinkage also generates two additional matrix stresses in the plane perpendicular to the axial direction—a compressive stress, which acts radially, and a tensile stress, which acts circumferentially.

We tested this hypothesis by performing a linear elastic plane-strain thermal stress analysis for three different local fiber–matrix composite configurations: a clustered arrangement of three fibers and four fibers, sketched in Figs. 18a and b, respectively, and a matrix with free boundaries. These three cases correspond closely to those seen in Figs. 16a–d. The material properties used for the PAN fiber and phenolic-resin matrix are typical values obtained from a variety of sources. The mechanical properties of the pyrolyzing matrix are those reported by Fitzer and Burger [59]. The thermal environment was a heatup from room temperature to 1000°C.

In the analysis we are concerned only with the stresses in the matrix in the plane perpendicular to the fiber axis, because the tensile stress of the matrix in the fiber direction at any point in the matrix is clearly more or less constant at a given temperature owing to the plane-strain consideration. The stresses in the radial-tangential plane may vary signficantly, depending on their relative location to the fiber. At any point in the matrix, therefore, we have a state of triaxial stress.

The development of lamellar structure in the matrix was postulated to be favored by two factors: (1) a large value of the maximum tensile stress in the plane, and (2) a small value of the ratio of minimum-to-maximum principal stress in this same plane. That is, for a given value of maximum tensile stress in the matrix, lamellar formation is favored more when the minimum-to-maximum stress ratio at any location is either small or negative (i.e., compressive). These two parameters may vary with the fiber spacing and boundary conditions, e.g., constrained or free edge.

Figure 19a, a plot of principal stress orientation and relative stress magnitudes, indicates that the maximum stress adjacent to the outside diameter of each fiber is dominated by hoop tension with a very low level of radial tensile stress; by contrast, the maximum stress in the center of the pocket is equal to about one-third that at the fiber surface, and the minimum (tensile) stress is now significant. From our hypothesis, these two factors will work in the direction of reduced lamellar formation relative to that at the fiber surface.

The effects of an increase in the a/r ratio (Fig. 18) are to decrease the maximum hoop stress at the fiber–matrix boundary and increase the stress ratio in the pocket region. In other words, when the three fibers are more closely packed, the formation of lamellar structure at the fiber surface is more favored than when they are loosely packed; however, within the pocket, it is less favored. Similar results were found for the four-fiber case.

We used the model of Fig. 18b to make the calculation for the free-boundary condition occurring along a straight, resin-rich area; the stress in the matrix along the free boundary is primarily unidirectional. Figure 19b illustrates that the relative stress magnitude and orientation correlate with the location of formation of lamellar structure depicted in Fig. 16c.

In conclusion, it is seen that the magnitude and orientation of the matrix shrinkage stresses during pyrolysis, as estimated by this analysis, are consistent with the proposed model for stress orientation and graphitization.

Much still remains to be learned about matrix stress graphitization in C/C: e.g., the effects of fiber type, fiber volume, matrix precursor, and high-temperature creep deformation. Equally intriguing is the possibility of being able to control C/C properties by controlling the matrix orientation and graphitization behavior.

SUMMARY

Carbon–carbon composites are an exceptional class of high-strength, low-weight refractory materials; however, effective utilization of the carbon fiber properties requires appropriate selection of the carbon or graphite matrix and processing conditions. The matrices may be derived from hydrocarbon gases, coal-tar and petroleum pitches, and thermosetting resins, and represent a range of structures and properties. Current research is beginning to elucidate how C/C composite properties may be controlled by controlling the structures of the matrix, both in bulk matrix regions and, more sensitively, at the crucial fiber–matrix interphase region.

ACKNOWLEDGMENTS

This paper reviews selected aspects of work funded by the Air Force Space Systems Division under Contract No. F04701-88-C-0089, and by the Aerospace Sponsored Research Program. The author wishes to thank a number of coworkers: Rafael Zaldivar, particularly, who, as an Aerospace MS and PhD Fellow, is responsible for much of the work discussed here; Dr. Dick Chang for his effective collaboration on portions of this work; and Paul Adams, Jim Noblet, Ross Kobayashi, Joe Uht, Dick Brose, and Ca Su, all of whom contributed in significant ways.

REFERENCES

1. Slayter, G., *Sci. Am.*, 124 (January 1962).
2. Cook, J., and Gordon, J. E., *Proc. R. Soc. London* **A282**, 508 (1964).
3. Jortner, J., *Effects of Weak Interfaces on Thermostructural Behavior of C–C Composites*, Office of Naval Research, Annual Report, pp. 19–31 (March 1985).
4. Peebles, L. H., Meyer, R. A., and Jortner, J., In *Interfaces in Polymer, Ceramic and Metal Matrix Composites*, H. Ishida, Ed., p. 1, Elsevier (1988).
5. Zaldivar, R. J., and Rellick, G. S., "Some Observations on Stress Graphitization in C–C Composites," *Carbon* (in press).
6. Rellick, G. S., Chang, D. J., and Zaldivar, R. J., *Ext. Abstr., 20th Carbon Conf.* (1991), p. 404.
7. Zaldivar, R. J., Rellick, G. S., and Yang, J., *Ext. Abstr., 20th Carbon Conf.* (1991), p. 400.
8. Fitzer, E., *Carbon* **25**, 163 (1987).
9. Fitzer, E., and Huttner, W., *J. Phys. D: Appl. Phys.* **14**, 347 (1981).
10. McAllister, L. E., and Lachman, W., In *Handbook of Composites*, A. Kelly and S. T. Mileiko, Eds., Vol. 4, p. 109, Elsevier (1983).
11. Hsu, S. E., and Chen, C. I., In *Superalloys, Supercomposites and Superceramics*, p. 721, Academic Press (1989).
12. Buckley, J. D., *Ceram. Bull.* **67**, 364 (1988).
13. Strife, J. R., and Sheehan, J. E., *Ceram. Bull.* **67**, 369 (1988).
14. Ko, F., *Ceram. Bull.* **68**, 401 (1989).
15. Bokros, J. C., In *Chemistry and Physics of Carbon*, P. L. Walker, Jr., Ed., Vol. 5, p. 1, Dekker, NY (1969).
16. Kotlensky, W. V., In *Chemistry and Physics of Carbon*, P. L. Walker, Jr., Ed., Vol. 9, p. 173, Dekker, NY (1973).
17. Pierson, H. O., and Lieberman, M. L., *Carbon* **13**, 159 (1975).
18. Granoff, B., *Carbon* **12**, 405 (1974).
19. Loll, P., Delhaes, P., Pacault, A., and Pierre, A., *Carbon* **15**, 383 (1977).
20. (a) Tuinstra, F., and Koenig, J., *J. Chem. Phys.* **53**, 1126 (1970); (b) *J. Compos. Mater.* **4**, 492 (1970).
21. Miller, T. G., Fischbach, D. B., and Macklin, J. M., *Ext. Abstr., 12th Carbon Conf.* (1975), p. 105.
22. Vidano, R., and Fischbach, D. B., *Ext. Abstr., 15th Carbon Conf.* (1981), p. 408.
23. Katagairi, G., Ishida, H., and Ishitani, A., *Carbon* **26**, 565 (1988).
24. Chard, W. C., Reiswig, R. D., Levinson, L. S., and Baker, T. D., *Carbon* **6**, 950 (1968).
25. Reiswig, R. D., Levinson, L. S., and O'Rourke, J. A., *Carbon* **6**, 124 (1968).
26. Rodriguez-Reinoso, F., and Thrower, P. A., *Carbon* **12**, 269 (1974).
27. Rellick, G. S., Thrower, P. A., and Walker, P. L., Jr., *Carbon* **13**, 71 (1975).
28. Rellick, G. S., *Ext. Abstr., 20th Carbon Conf.* (1991), p. 368.

29. Brooks, J. D., and Taylor, J. H., *Nature* **206**, 697 (1965).
30. White, J. L., In *Prog. Solid State Chem.*, J. O. McCauldin and G. Somarjai, Eds., Vol. 9, p. 59, Pergamon Press (1975).
31. Rellick, G. S., *Carbon* **28**, 589 (1990).
32. Zimmer, J. E., and Salvador, L. M., U.S. Patent 4,554,024 (19 November 1985).
33. Brückmann, H., Dr.-Ing Thesis, University of Karlsruhe (1979).
34. Singer, L. S., Lewis, I. C., and Bacon, R., *Proceedings of the JANNAF Rocket Nozzle Technology Subcomittee Meeting*, Naval Surface Warfare Center, Silver Spring, MD (17–19 October 1989).
35. White, J. L., and Sheaffer, P. M., *Carbon* **27**, 697 (1989).
36. Zimmer, J. E., and Weitz, R. L., *Carbon* **26**, 579 (1988).
37. Singer, L. S., and Lewis, R. T., *Ext. Abstr., 11th Carbon Conf.* (1973), p. 207.
38. Evangelides, J. S., *Ext. Abstr., 12th Carbon Conf.* (1975), p. 93.
39. Jortner, J., Appendix A in Ref. 3 above.
40. Jortner, J., In *Proc. Army Symp. on Solid Mechanics*, AMMRC MS 76-2 (1976), pp. 81–97.
41. Jortner, J., *Carbon* **24**, 603 (1986).
42. Buch, J. D., *Structure–Property Relationships in Advanced Carbon Materials*, Report No. TOR-0079(4726-04)-1, The Aerospace Corporation, El Segundo, CA (25 September 1979).
43. Manocha, L. M., and Bahl, O. P., *Carbon* **26**, 13 (1988).
44. Manocha, L. M., Yasuda, E., Tanabe, Y., and Kimura, S., *Carbon* **26**, 333 (1988).
45. Meyer, R. A., and Gyetvay, S. R., In *Petroleum Derived Carbons*, J. Bacha, J. Newman, and J. L. White, Eds., ACS Symp. Series **303**, p. 380, ACS (1986).
46. Jenkins, G., Kawamura, K., and Ban, L. L., *Proc. R. Soc. London* **A327**, 501 (1972).
47. Jabloner, H., U.S. Patent No. 4,070,333 (24 January 1978).
48. Barry, W. T., Gaulin, C., and Kobayashi, R., *Review of Polyarylacetylene Matrices for Thin-Walled Composites*, Report No. TR-0089(4935-06)-1, The Aerospace Corporation, El Segundo, CA (25 September 1989).
49. Katzman, H. A., *Polyarylacetylene Resin Composites*, TR-0090(5935-06)-1, The Aerospace Corporation, El Segundo, CA (2 April 1990).
50. Zaldivar, R. J., Rellick, G. S., and Yang, J. M., "Processing Effects on the Mechanical Behavior of Polyarylacetylene-Derived C–C," *SAMPE J.* (in press).
51. Brown, S. C., and Reese, H. F., *Proc. JANNAF RNTS Mtg.*, CPIA Publ. No. 496, Patrick AFB, FL (1986).
52. Zaldivar, R. J., Kobayashi, R., Rellick, G. S., and Yang, J. M., "Carborane-Catalyzed Graphitization in Polyarylacetylene-Derived C–C," *Carbon (in press), and Ext. Abstr., 20th Carbon Conf. (1991), p. 388.*
53. Franklin, R. E., *Proc. R. Soc. London* **A209**, 196 (1951).
54. Hishiyama, Y., Inagaki, M., Kimura, S., and Yamada, S., *Carbon* **12**, 249 (1974).
55. Kimura, S., Tanabe, Y., Takase, N., and Yasuda, E., *Jpn. J. Chem. Soc.* **9**, 1479 (1981).
56. Rellick, G. S., and Adams, P. M., Aerospace Sponsored Research Program unpublished results.
57. Kyotani, T., Sonobe, N., and Tomita, A., *Nature* **331**, 331 (1988).
58. Johnson, J. W., Rose, P. G., and Scott, G., *Third Conf. on Indust. Carbons and Graphites*, SCI, London (1971), p. 443.
59. Fitzer, E., and Burger, A., In *Carbon Fibers: Their Composites and Applications* **134**, The Plastics Inst., London (1971).

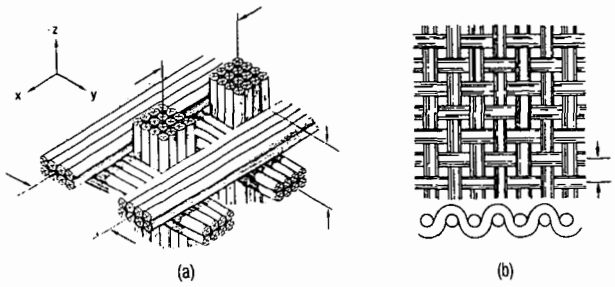

Figure 1. Schematic of (a) 3-D block construction and (b) 2-D plain-weave fabric (McAllister and Lachman [10]).

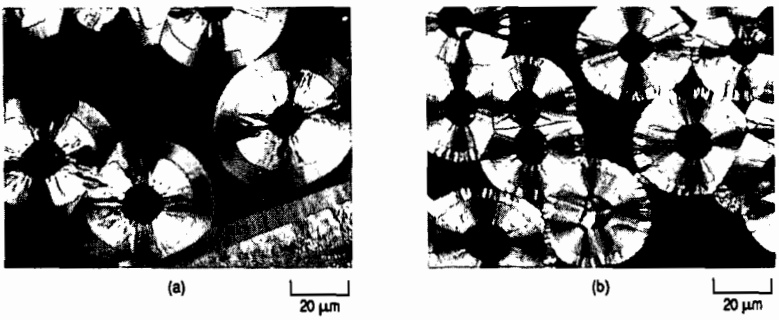

Figure 2. Polarized-light micrographs showing as-deposited CVI carbon microstructures of two specimens. Deposition sequence: (a) RL/SL; (b) SL/RL (Rellick [28]).

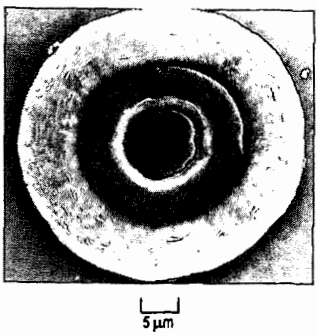

Figure 3. Scanning electron micrograph of specimen after heat treatment at 2500°C for 1 hr [28].

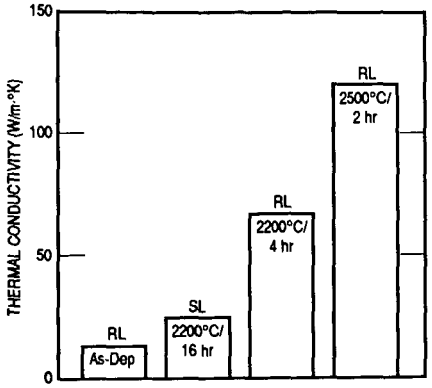

Figure 4. Through-thickness thermal conductivity (at RT) for composite specimens of different CVI structures and processing stages [28].

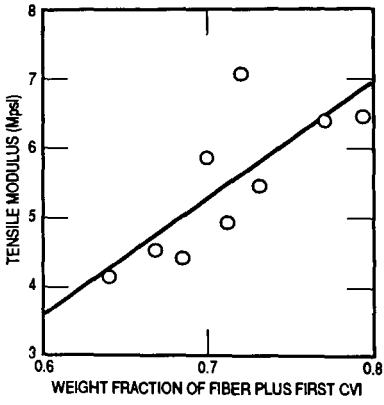

Figure 5. Composite tensile modulus versus weight fraction of fiber plus heat-treated CVI [28].

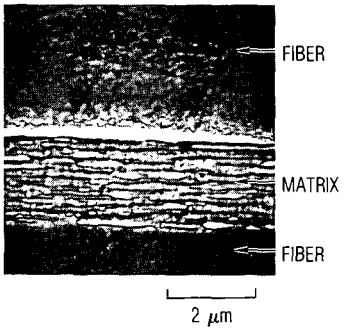

Figure 6. SEM showing highly aligned coal-tar-pitch-derived graphite matrix in the interfilament region of a C/C composite. Fibers are Amoco T50 from PAN.

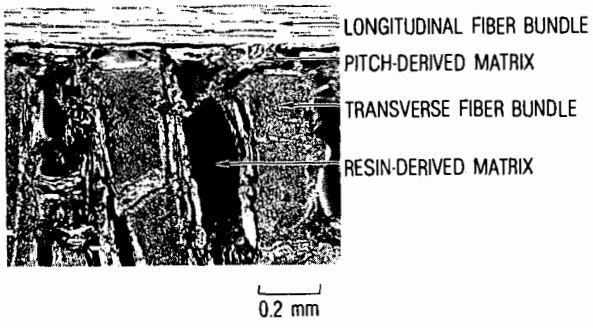

Figure 7. Optical micrograph of cross section of 3-D C/C composite densified with both pitch and resin and heat-treated to 2750°C. Note extensive matrix microcracking.

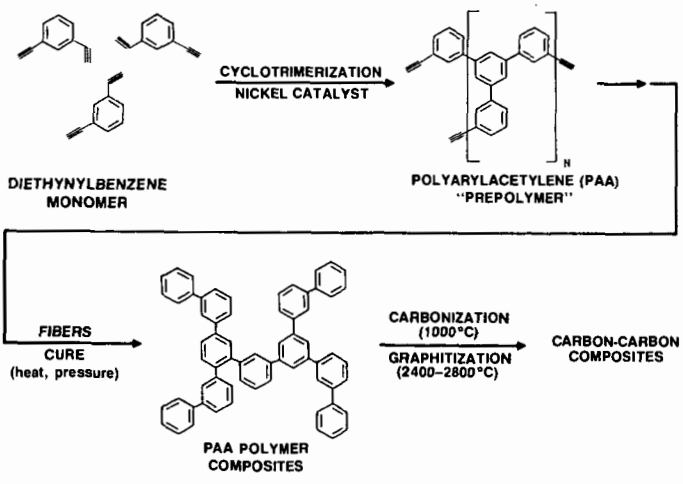

Figure 8. Chemical structure and processing of PAA-based composites (Barry *et al.* [48] and Katzman [49]).

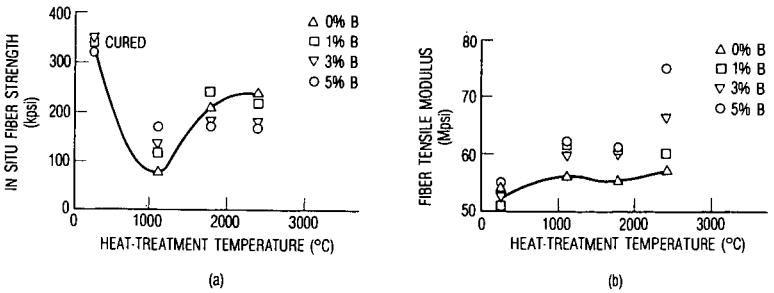

Figure 9. Plots of tensile (a) strength and (b) fiber modulus of undoped and B-doped PAA/T50 C/C composites (Zaldivar *et al.* [52]).

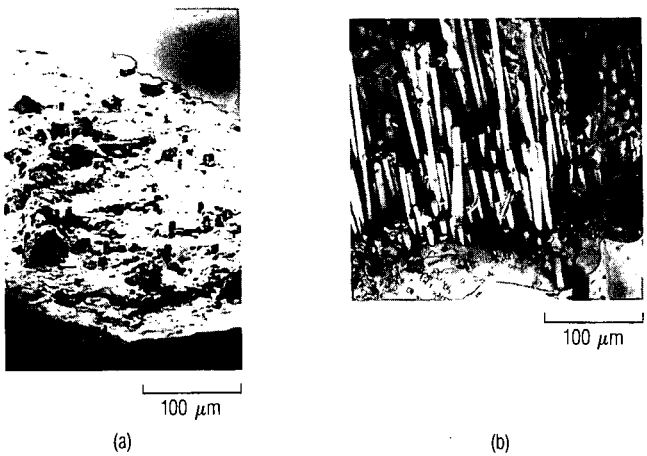

Figure 10. Micrographs of fracture surfaces of (a) undoped and (b) B-doped PAA-derived C/C composites heat-treated to 1100°C [52].

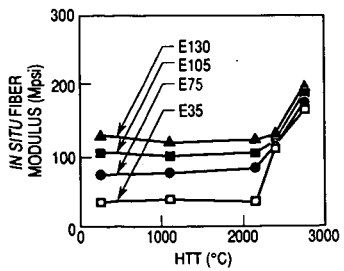

Figure 11. Moduli of composites versus HTT (Zaldivar *et al.* [7]).

Figure 12. Fracture surface of E105 composite to 2750°C HTT, showing matrix sheath tube (Zaldivar *et al.* [7]).

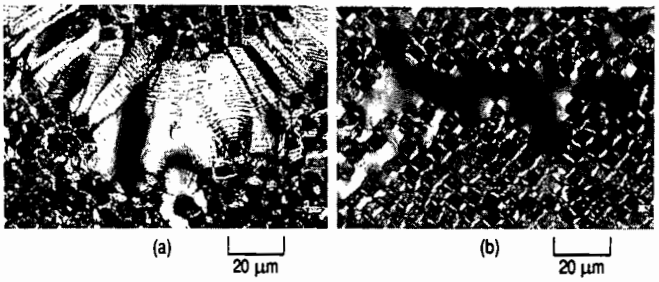

Figure 13. Polarized-light micrographs of unidirectional C/C composite heat-treated to (a) 2900°C and (b) 1100°C (Rellick *et al.* [6]).

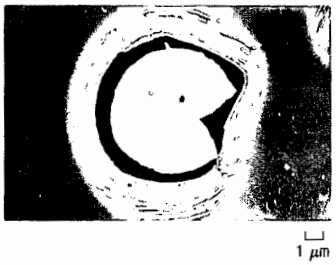

Figure 14. SEM micrograph of PX-7 filament embedded in PAA-derived carbon matrix heat-treated to 2750°C.

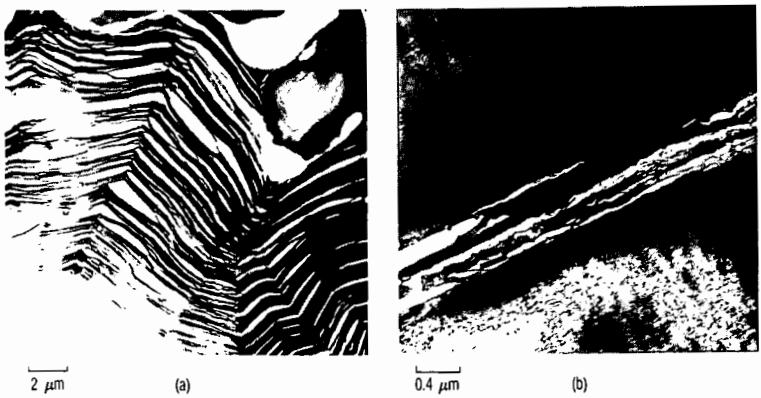

Figure 15. TEM bright-field images of C/C resin-matrix-derived unidirectional composite: (a) transverse and (b) longitudinal sections (Rellick and Adams [56]).

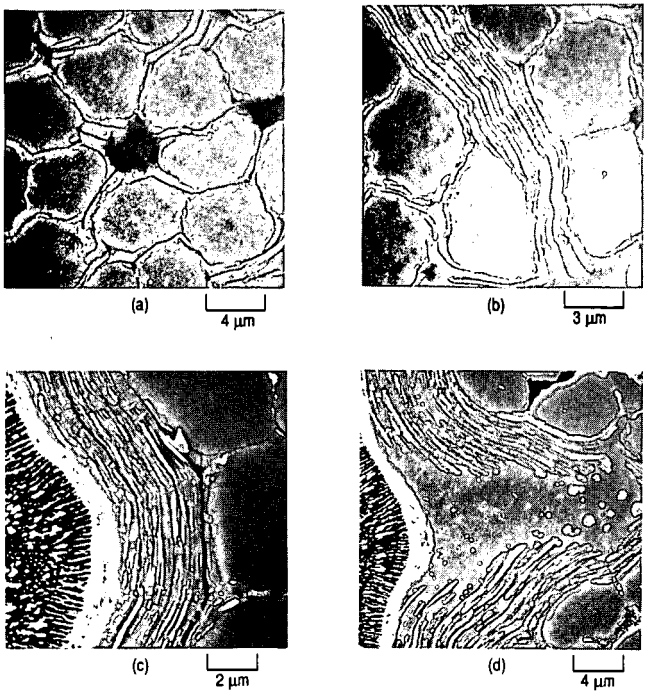

Figure 16. SEMs of ion-etched unidirectional C/Cs heat-treated to 2900°C (Rellick *et al.* [6]).

Figure 17. SEM fracture surface of T50/SC1008 heat-treated to 2900°C [6].

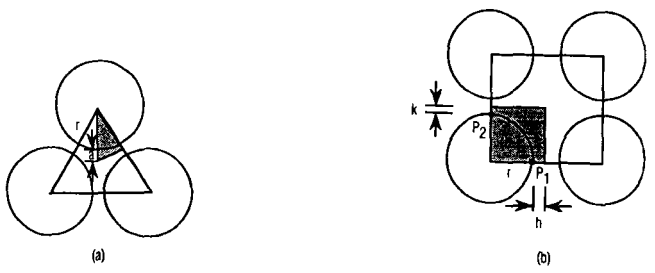

Figure 18. Schematic of the local packing arrangement of (a) three and (b) four fibers. Shaded area denotes region for which stresses are calculated [6].

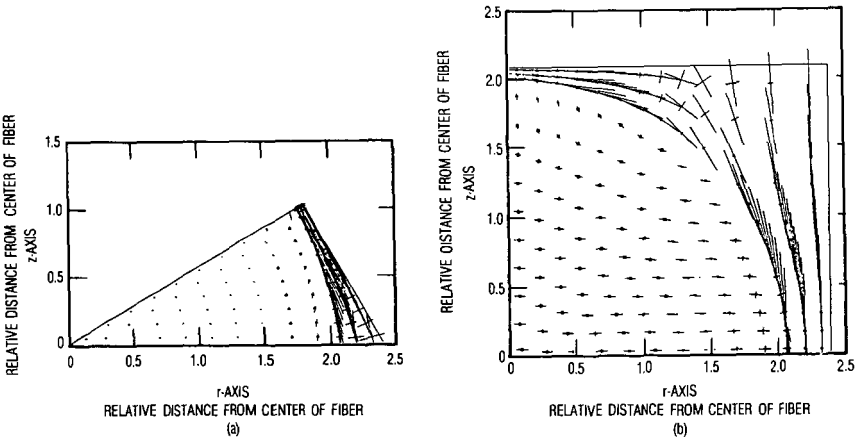

Figure 19. Computer plot of the directions and relative magnitudes of the matrix stresses in the plane of the fiber of various points, relative to Figs. 18a and b [6].

PRODUCTION OF CARBON MATERIALS FROM BIOMASS

Michael A. Serio, E. Kroo, R. Bassilakis, P. R. Solomon
Advanced Fuel Research, 87 Church Street, East Hartford, CT 06108

R. Malhotra
SRI International, 333 Ravenswood Avenue, Menlo Park, CA 94025

KEYWORDS: Biomass, Carbon, Materials

INTRODUCTION

Lignin is the most abundant renewable aromatic polymer. There is an abundance of lignin residues produced as a byproduct of pulp and papermaking which have a fuel value of between $0.00 and $0.04 per pound (1). The size of this resource can be appreciated by considering that the total amount of lignosulfonates and kraft lignin together outweigh the sum of all manmade polymers in the United States (2). Given the relatively low cost, high abundance, and renewable nature of this resource, it is not surprising that many attempts have been made to develop higher value products from lignin (1,3,4).

Carbon materials are a much higher added value product than almost any other use of the products which can be produced from lignin. This is especially true in the case of carbon fibers. Carbon fibers are becoming increasingly important as components of composite materials due to their unique chemical and physical properties (5). The finished fibers can sell for tens to hundreds of dollars per pound, so the potential exists for a large premium to be paid for a feedstock which could result in lower manufacturing costs or superior fiber properties. Consequently, the development of processes which can utilize lignins for this purpose and the production of other high value carbon materials has the potential for a high payoff. It would also result in the utilization of lignin as a raw material for a high technology, internationally competitive industry.

EXPERIMENTAL

Sample Selection - A set of eight different lignin samples was examined. The lignin samples and their sources are listed in Table 1. The first six samples were used in a previous project (6) and the last two were obtained specifically for the current project (7).

Table 1 - LIGNIN SOURCES

Lignin	Wood	Manufacturer	Pre-Treatment
Iotech	Aspen	Iotech Corp.[a]	Steam explosion
Stake (ST)	Aspen	Stake Tech. Ltd.[a]	Autohydrolysis
BEC	Aspen	Biological Energy Corp.[b]	-
Indulin I	Pine	Westvaco[c]	-
Ethanol (ET)	Aspen	d	Steam explosion
H_2SO_4	Aspen	d	Steam explosion
SE	Poplar	VPI	Steam explosion
RTI		Repap Technologies	Ethanol/water Extraction

Notes for Table 1

a. Extraction in dilute basic solution followed by precipitation with dilute acid.

b. Wood chips are cooked with an ethanol-water solution in an autoclave at 130°C for 30-90 minutes.

c. Wood is cooked with a 10% solution of 80/20 volume % sodium hydroxide/sodium sulfide. Trade name is Indulin ATR-CK1.

d. Prepared by Eitan Avni at the University of Connecticut from wood steam exploded by Iotech Corp.

The lignin samples were chosen to represent a range of wood types and preparation methods.

Experimental Approach - The production of carbon materials from lignin is made difficult by the fact that it is highly substituted with oxygen functional groups. This makes the material too reactive toward crosslinking reactions for the formation of anisotropic carbons. These groups must be removed without removing much of the aromatic material which is desirable for the production of carbon materials. The approach taken in this study was to first pyrolyze the lignins to produce a tar and then to thermally and/or catalytically treat the tars to produce a material which could be a substitute for mesophase pitch produced from petroleum. The basis for this approach was previous work done on coal tars which suggested that secondary pyrolysis of tars would reduce the amount of functional group substituents and reduce the average molecular weight (8-11). In order to implement this approach, a two-stage reactor system was developed, as described below and in Ref. 7.

Two-Stage Fixed-Bed Reactor - The lignin pyrolysis/tar cracking experiments were done in a reactor with two separate pyrolysis zones with independent temperature regulation capabilities and with the ability to monitor the product tars on-line with FT-IR spectroscopy (see details of TG-FTIR software-hardware principles discussed below) using an IBM IR-40 spectrometer. A portion of the product stream is extracted out through a filter by means of a peristaltic pump through a line which bypasses the multi-pass cell. The tar component of the products which collected on the filter (cotton wool) was washed out with acetone, dried, weighed and used for further analysis. Helium was used as the carrier gas and the best reproducibility was achieved at pumping rates which resulted in 10-30% extraction of the tar.

The typical experimental conditions were as follows: sample weight: 0.15 $\pm$ 0.05 g; He flow: 0.47 liter/min, cm^2 (inner tube I.D. is 0.7 cm). The heating rate (upper chamber) was 30°C/min. (max. temp 780°C) and the secondary pyrolysis (lower chamber) temperature was kept constant during the whole experiment at temperatures ranging from 400 to 700°C. The carbon content of the tar deposited on the wall of the inner tube or on the catalyst surface was measured by replacing the He flow with O_2. The upper and lower chamber temperatures were raised up to 700°C separately to achieve complete combustion and the CO_2 and CO measured.

This reactor was used primarily for experiments where lignin was pyrolyzed in the first stage at a constant heating rate and the tars were passed to an isothermal second stage. Experiments with both the second stage empty and filled with a catalyst bed were done.

Catalyst Selection - The catalyst examined in the second stage was Alcoa (Type F-20) chromotographic grade 80-200 mesh activated Alumina (EM Science). Glass wool was used to support the catalyst particles. Other catalysts, such as calcium oxide, were considered but good results were obtained intially with alumina and it was used for the remainder of the study. The alumina was chosen because it has a high affinity for polar materials and the goal was to selectively remove oxygen functions from lignin tar. It is also a material which can easily be regenerated once coke formation has occurred.

RESULTS

Lignin Characterization Experiments - A series of lignin screening experiments was done to see how many lignins would be suitable candidates for this approach. These experiments were done in a TG-FTIR system developed at AFR (12,13). The apparatus consists of a sample suspended from a balance in a gas stream within a furnace. As the sample is heated, the evolving volatile products are carried out of the furnace directly into a 5 cm diameter gas cell (heated to 150°C) for analysis by FT-IR. The FT-IR can obtain spectra every 0.2 s to determine quantitatively the evolution rate and composition of several hydrocarbon compounds. The system allows the sample to be heated on a pre-programmed temperature profile at rates between 3°C min^{-1} and 100°Cs^{-1} up to a temperature between 20 and 1000°C and held for a specified time. The system continuously monitors: 1) the time-dependent evolution of the gases (including specific identification of the individual species such as, CH_4, C_2H_6, C_2H_4, C_2H_2, C_3H_8, benzene, etc,; 2) the heavy liquid (tar) evolution rate and its infrared spectrum with identifiable bands from the functional groups and 3) weight of the non-volatile material (residue). An analysis of C,H,N and S in the residue at the end of the pyrolysis experiment can be obtained by introducing oxygen to burn the residue and analyzing the combustion products.

As an example of the analysis procedure, the pyrolysis of the Iotech lignin is described. Figure 1 illustrates the weight loss from this sample, the sum of the evolved products, and the temperature history. A 20 mg sample is taken on a 30°C/min temperature excursion in the helium sweep gas, first to 150°C to dry for four minutes and then to 900°C for pyrolysis. The evolutions of gases derived from the IR absorbance spectra are obtained by a quantitative analysis program that employs a database of integration regions and calibration spectra for different compounds (12,13). Figures 1b through 1f illustrate the evolution rates and integrated amounts evolved for Tar, CH_4, H_2O, CO_2 and CO, respectively. Because the data are quantitative, the sum of the evolved products matches the weight loss as determined by the TGA balance (Fig. 1a).

The results from a standard (30°C/min) TG-FTIR analysis of the eight lignin samples are summarized in Fig. 2. The tar yields from the eight samples ranged from ~10 wt. % tar for the H_2SO_4 lignin to > 50 wt. % for the Iotech lignin. A number of the lignins gave relatively high tar yields (>30 wt. %), so it appears that the generation of primary lignin tar by pyrolysis is a good starting point. An especially interesting sample was the Repap Technologies (RTI) lignin. This sample is produced in large quantities as a byproduct of a proposed organosolv pulping process.

The amount of tar formed was sensitive to the heating rate of the primary pyrolysis stage and to the bed depth (7). The results suggested that the highest yields of tar would be obtained in a dilute phase, entrained flow pyrolysis experiment. This is similar to what has been observed in the case of coal pyrolysis (14).

Experiments in Two-Stage Reactor - A series of experiments was done in the two stage reactor with an alumina catalyst with two of the lignins (SE and RTI) over a range of second stage temperatures (400-700°C). The results from the on-line absorbance measurements are shown for the RTI lignin for various cases in Figs. 3 and 4. For both lignins, a significant reduction in oxygen functions was observed in the on-line FT-IR spectra of the tar when the catalyst (alumina) is present, but not when it was absent.

The IR spectra of both the SE and RTI lignin are very similar and the oxygen containing functional groups appear at 1215, 1107 and 1060 (C-O) cm^{-1} as well as 1607 (C=O) cm^{-1}. To characterize the polar nature (oxygen content) of a tar we use the parameter

$$PI = \frac{\frac{A\ (1215)}{A\ (1508)} + \frac{A\ (1107\ or\ 1060)}{A\ (1508)}}{2}$$

where A (ν) is the peak height of the νcm^{-1} peak and PI is a polarity index. The smaller the value of PI, the less oxygen the tar contains and the better it might be as a precursor for carbon materials.

Figure 5a shows PI for the main tar evolution peaks for SE and RTI lignins. Figure 5b shows the corresponding results for the tar yield and deposit formation. These results show that relatively high yields of tar can be obtained at high oxygen removal efficiencies, with relatively low deposit formation. The optimal temperature for operation of the second bed was about 550°C.

CONCLUSIONS

The preliminary conclusions of this work are as follows:

- A set of eight lignins was characterized using the TG-FTIR programmed pyrolysis system. The amount of tar produced in a standard 30°C/min. pyrolysis of most of the lignins was about 35-50% on a dry basis. The amount of tar produced was found to be sensitive to heating rate and bed depth. Higher heating rates produced higher tar yields while larger bed depths produced lower tar yields.

- A thermal treatment of the tars in the second stage does not significantly degrade the oxygen content.

- The presence of activated alumina does significantly and selectively catalyze the decomposition of oxygen functional groups in the tar based on the on-line FT-IR analysis. The main gaseous products of the tar decomposition are CO, CO_2 and CH_4.

- The activity of the alumina appears to be a maximum for oxygen removal at ~ 550°C. The loss of tar under these conditions is about 40%.

- The net yield of modified tar from the current system appears to be ~ 15% for SE lignin and 20% for RTI lignin under the best conditions. This may be improved by an entrained bed reactor system for the primary pyrolysis stage.

ACKNOWLEDGEMENTS

This work was supported by the United States Department of Energy under Contract No. DE-FG05-90ER80880. The authors also acknowledge helpful discussions with Dr. Helena Chum of the Solar Energy Research Institute (Golden, CO) and Dr. Jairo Lora of Repap Technologies, Inc. (Valley Forge, PA).

REFERENCES

1. Glasser, W.G., "Lignin", in Fundamentals of Thermochemical Biomass Conversion, (R.P. Overend, T.A., Milne, and L.K. Mudge, Eds.), Elsevier Applied Science, 1982, pg. 61.
2. Falkehag, S.I., Appl. Polym. Symp., **28**, 247, (1975).
3. Bungay, H.R., Science, **218**(4573), 643, (1982).
4. Kringstad, K., Future Sources of Organic Raw Materials - CHEMRAWN, (L.E. St.-Pierre and G.R. Brown, Eds.), Pergamon Press, New York, 1980, pp. 627-636.
5. Hansen, C.F. and Parker, J.A., "Carbon-Fiber Technology", Presented at 16th Symposium on Polymers in the Service of Man, ACS Div. of IEC, (June 9-11, 1980).
6. Squire, K.R., Solomon, P.R., "Characterization of Biomass as a Source of Chemicals" Final Report to NSF for Contract No. CPE-8107453 (Nov. 1983).
7. Serio, M.A., Kroo, E., Bassilakis, R., Solomon, P.R., and Malhotra, R., "Innovative Methods for the Production of Polymers from Biobased Materials" Final Report to DOE for Contract No. DE-FG05-90ER80880 (May 1991).
8. Serio, M.A., "Secondary Reactions of Tar in Coal Pyrolysis", Ph.D. Thesis, Department of Chemical Engineering, Massachusetts Institute of Technology, Cambridge, MA, (1984).
9. Serio, M.A., Peters, W.A., Sawada, K., and Howard, J.G., "Secondary Reactions of Nascent Coal Pyrolysis Tars", Proceedings of the International Coal Conference on Coal Science, p. 533, Pittsburgh, PA, (1983).
10. Serio, M.A., Peters, W.A., Sawada, K., and Howard, J.G., ACS Div. of Fuel Chem. Prepr., **29**(2), 65, (1984).
11. Serio, M.A., Peters, W.A., and Howard, J.G., Ind. Eng. Chem. Res., **26**, 1831, (1987).
12. Carangelo, R.M., Solomon, P.R., and Gerson, D.J., Fuel, **66**, 960, (1987).
13. Whelan, J.K., Solomon, P.R., Deshpande, G.V., and Carangelo, R.M., Thermogravimetric Fourier Transform Infrared Spectroscopy (TG-FTIR) of Petroleum Source Rock - Initial Results, Energy and Fuel, **2**, 65, (1988).
14. Howard, J.B., Peters, W.A., and Serio, M.A., "Coal Devolatilization Information for Reactor Modeling", Report Prepared under EPRI #AP-1803/RP 986-5, (April 1981).

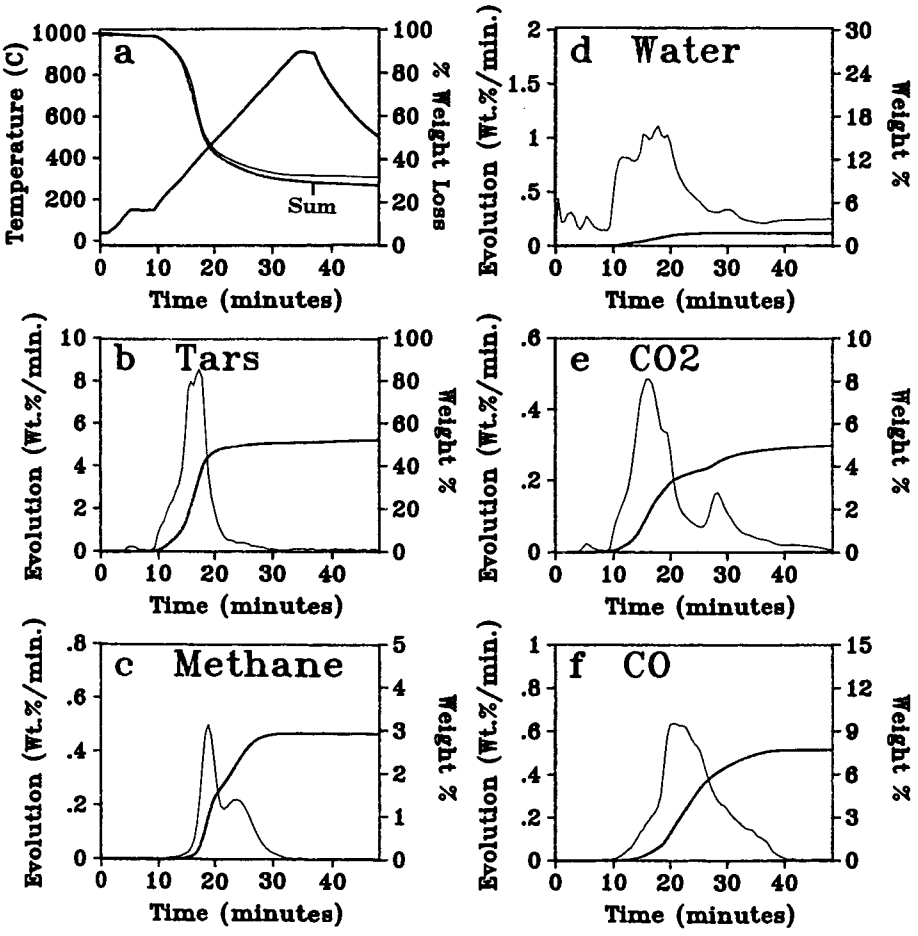

Figure 1. TG-FTIR Analysis of Iotech Lignin at 30°C/min.

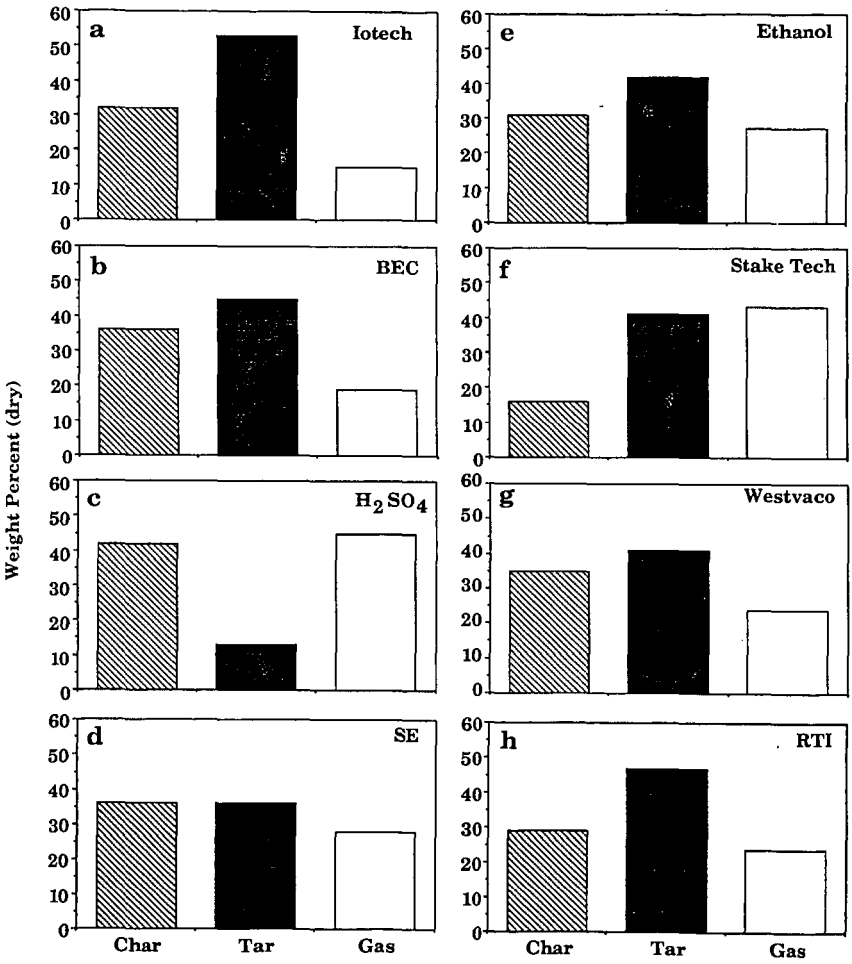

Figure 2. Comparison of Char, Tar and Gas Yields from Programmed Pyrolysis of Eight Lignins.

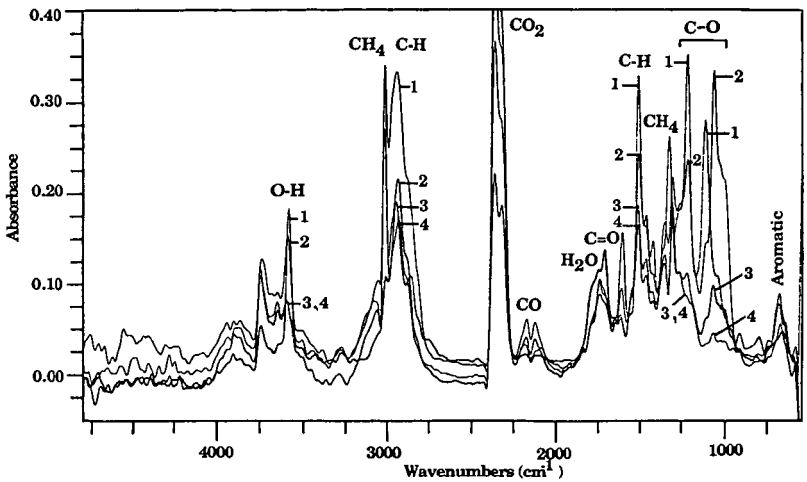

Figure 3. On-Line Tar Spectra from Experiments in the Two-Stage Fixed-Bed Reactor with RTI Lignin. Case 1 = 400°C, No Catalyst; Case 2 = 400°C, with Catalyst; Case 3 = 550°C, with Catalyst; and Case 4 = 600°C, with Catalyst.

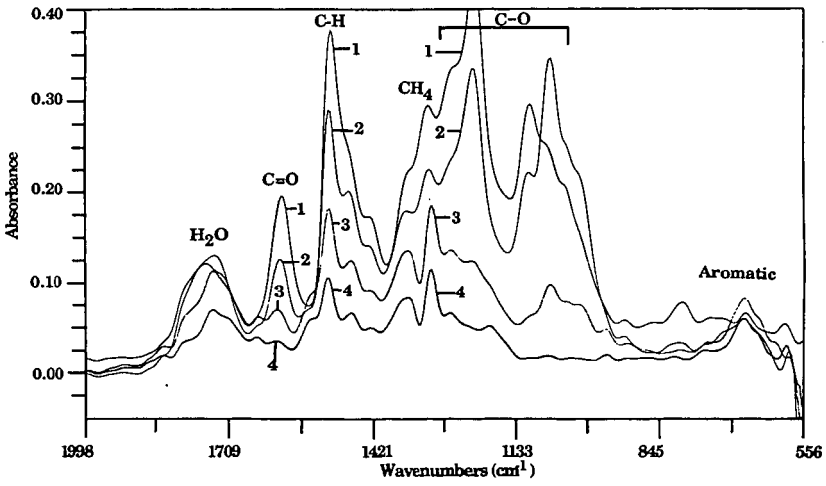

Figure 4. Expanded View of Spectra in Fig. 3.

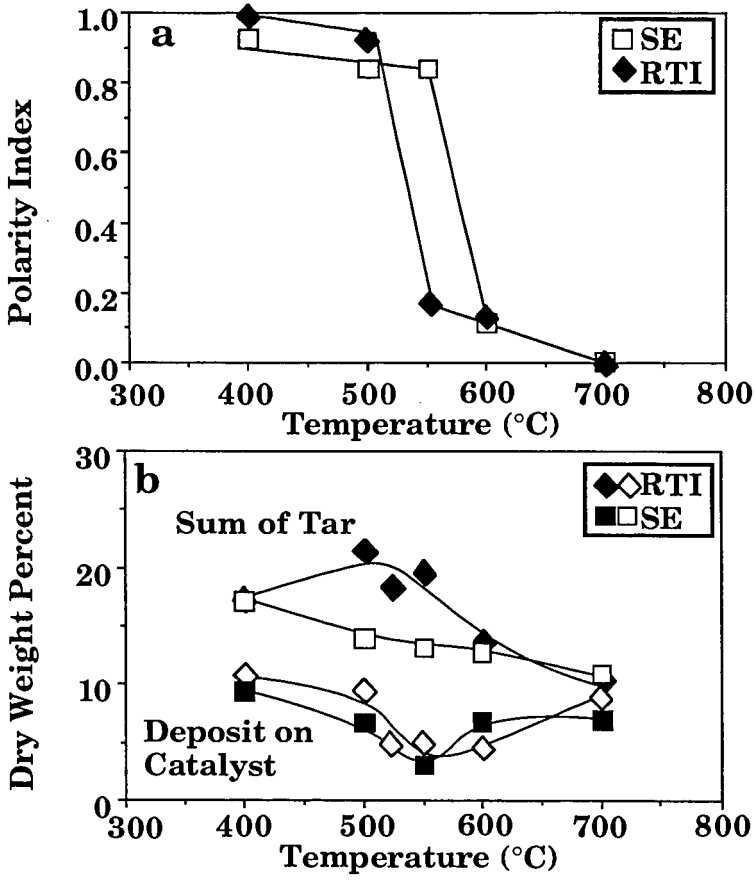

Figure 5. Effect of Lignin Type and Temperature on a) Tar Polarity Index and b) Tar Yield(◆,□), Deposit Yield (◇,■).

EFFECTS OF POLYETHYLENE TEREPHTHALATE (PET) FROM PLASTICS WASTE ON THE THERMAL PROPERTIES OF ASPHALT

RAMONA LEDESMA AND L.L. ISAACS
The City College of CUNY
Dept. of Chemical Engineering
New York, N.Y. 10031

Keywords: Thermal Characterization of asphalt/PET mixtures, waste plastic utilization, filled asphalt.

INTRODUCTION

Asphalt concretes are widely used for pavements. Asphalt itself is a bitumen and although it occurs naturally, it is mostly obtained as a byproduct of oil production. However, its thermoplastic characteristics cause difficulties with roads. It has been demonstrated that the apparent glass transition temperature of asphalt is near zero degree celsius [1,2]. Thus, asphalt concretes are susceptible to low temperature cracking that may lead to fracture. Further, in high summer temperatures asphalt undergoes flow or creep. The stability of asphalt paving surfaces requires that it does not flow or creep under heavy load. Numerous investigations are underway involving the modification of asphalt with different fillers that may improve its pavement performance. For example, the modification of asphalt with polymers leads to bituminous materials having improved properties and allows the utilization of waste products [3].

In this investigation, the effect of polyethylene terephthalate (PET) obtained from used plastic bottles on the thermal properties of asphalt, specifically its effect on the thermal expansion coefficients, glass transition temperatures, melting points, and flow properties of asphalt, PET, and asphalt/PET mixture samples, is evaluated. Polyethylenes have been confirmed as potentially useful modifiers for increasing the low temperature fracture toughness of the asphalt and may also contribute to pavement stability at elevated temperatures by minimizing distortion due to creep [4]. The abundance of used plastic bottles that contributes to the litter problem and the resultant environmental pollution caused by conventional non-degradable plastics makes PET fillers economically attractive for improving the performance of asphalt concrete paving materials.

EXPERIMENTAL TECHNIQUES

Sample Preparation

Asphalt of grade AC-20 certified to comply with the state of New York highway specifications was provided by Prima Asphalt Conc., Inc. Polyethylene terephthalate (PET) filling material was obtained from used plastic soda bottles that were first cut into

strips about 1/4 inch in thickness and then ground using a grinder with a 20 mesh sieve.

The asphalt/PET mixtures were prepared by slowly adding a weighted amount of PET to a known quantity of asphalt maintained at 120°C while the mixture was vigorously stirred. This temperature is below the melting point of PET but above that of asphalt. After several minutes of stirring, the mixtures were left to cool to room temperature, and stored until used for testing. Sample concentration ranged from 10% to 50% PET by weight.

DSC Measurements

The glass transition temperatures (Tg) and the melting points of asphalt, PET, and asphalt/PET mixtures were measured using differential scanning calorimetry (DSC). The samples were heated at a 10 °K/min rate. between 100°K and 600°K.

TMA measurements

Thermomechanical analysis (TMA) was employed to determine the expansion coefficients, glass transition temperatures (Tg), melting points, and flow properties of asphalt, PET, and asphalt/PET mixture samples. The temperature range of the measurements was between 100°K and 600°K. Cylindrical samples approximately 9.5 millimeter in diameter and between 0.3 and 3.0 millimeter in thickness were heated at a rate of 5°K/min. Expansion coefficients were calculated from the TMA expansion profiles using aluminum expansion coefficient data to determine the dynamic calibration constant. A 5 grams mass supplied the compressive force to the samples. Flow properties were measured using parallel plate rheometry. Samples were compressed by a 50 gram load.

DISCUSSION AND RESULTS

Differential Scanning Calorimetry

Based on several DSC runs, the average Tg for pure asphalt was calculated to be -41.4°C. Values for asphalt Tg's in the literature range between -0.4°C to -53°C [5,6]. In general, the change in the heat flow curve slope indicating the glass transition temperature was very small and sometimes even undetectable; consequently, it was very difficult to characterize the samples using DSC technique. However, in the cases where it was detected, the DSC results were reproducible and yield Tg values within the 5% accuracy of the instrument.

The PET/asphalt mixture DSC measurements yield Tg values in the same range as those obtained for pure asphalt. There was no

indication that the presence of PET fillers affected the Tg of asphalt. Fig. 1 is the plot of the Tg versus PET concentration.

DSC was also used to measure the melting point (Tm) of PET. For pure PET the average melting point was determined to be 235.4°C. As with the asphalt Tg, there was no indication that the melting point of PET was affected by the presence of asphalt. The average melting temperature of PET calculated using results obtained from pure PET and PET/asphalt mixtures was estimated as 234.9°C. Fig. 2 is a plot of the PET Tm values versus mixture composition. Literature gives a range for the melting point of pure PET between 250°C and 265°C. Taking into account the difference in techniques used, the accuracy of the instrumentation, and the fact that the DSC results were obtained using PET from used plastic bottles instead of pure PET, The discrepancy between the DSC findings and literature values is not unexpected.

Thermomechanical Analysis

As stated previously, the average Tg value for asphalt was estimated at -41.4°C. In general, the asphalt Tg obtained using the TMA technique is about 70 degrees higher than those obtained by the DSC technique. This discrepancy may be attributed to the fact that these techniques measure different phenomena. The Tg by DSC corresponds to a change in the ability of the sample to absorb heat, while the TMA detects the Tg as a change in the thermal expansion profile of the sample.

The average Tg for asphalt as determined by the TMA technique was estimated as 39°C; the value estimated including glass transition temperatures obtained for the PET/asphalt mixtures is 33.4°C. A plot of the average asphalt Tg values versus PET concentration is shown in Fig. 3.

The melting point of PET was also measured using the TMA technique. These measurements yield 248.3°C as an average Tm for PET, and an average Tm value of 243.8°C for the asphalt/PET mixtures. These TMA results are about 10 degrees higher compared to the DSC findings and that much closer to the literature values. In Fig 4, the average Tm values are plotted as a function of asphalt concentration.

Examination of the TMA curve shows that PET exhibits a glass transition temperature at about 81°C that was not detected when the DSC technique was used. PET TMA measurements yield an average Tg of 81.8°C with values ranging from 80.4°C to 85.8°C. The literature [7] value for PET tg is 81°C. Unlike the previous findings, the glass transition temperature of PET does seem to be affected by the presence of asphalt; so much that it was not possible to detect it with certainty from examination of the TMA curves for PET/asphalt mixtures. Furthermore, when the PET samples were subjected to a heating cycle, the Tg could not be detected.

The expansion coefficients were determined from TMA expansion/contraction profiles. An example of a TMA expansion/contraction profile for a PET sample is shown in Fig 5. Note that in this figure the slope of the TMA curve noticeably changes after the crossing of the glass transition temperature. For PET samples, two distinct regions are observed: a region that ranges from liquid nitrogen temperatures to about 81°C, the glass transition temperature of PET, and second one that extends from 81°C to the melting temperature. The average expansion coefficient for the first region is 109 μm/m/°C. The average expansion coefficient for the second region was estimated to be 955 μm/m/°C. The expansion coefficient for asphalt was found to be 290 μm/m/°C.

The addition of PET to asphalt has a more pronounced effect on the expansion coefficient. The addition of 10 wt% PET to asphalt reduces the expansion coefficient to 108 μm/m/°C. 20 wt% PET has an expansion coefficient of 89, 30 wt% PET has 85, 40% PET has 83, and a 50 wt% PET mixture has an expansion coefficient of 76 μm/m/°C, in the first region.

Additional information can be gained by studying the TMA derivative curve, using the parallel plate rheometer accessory [8]. The amplitude of the derivative curve will vary in intensity with the flow of the sample. The temperature of the peak (Ti) corresponds to the point of maximum flow rate. In general, the peak flow rate for PET/asphalt samples are very similar to those of PET. The Ti values range from 248.2°C for a 10/90 PET/asphalt sample to 252.3°C for a PET sample. This suggests that even for 10% PET concentration the overall flow of the mixture is dominated by the flow properties of PET. The PET filler acts as a binder restricting the flow of the asphalt until the filler itself starts melting. The inflection temperatures for pure asphalt range between 48.4°C to 58.6°C with an average Ti of 52.8°C. That is, the maximum flow rate for asphalt occurs at about this temperature.

Fig. 6 is a typical TMA plot for a 10/90 PET/asphalt sample featuring a derivative curve with two inflection points. The first one at 47°C corresponds to the maximum flow rate of asphalt. It is followed by a plateau due to the binding effects of the PET filler. The maximum flow rate of the mixture occurs at 252°C, the second inflection point. At this temperature, the PET filler is melting and flowing out of the rheometer plates together with the remaining asphalt.

A limited amount of viscosity information was also collected using the TMA parallel plate rheometer. The temperature dependent dimensional changes of a sample under a known load in the rheometer are converted to viscosity [9]. As expected there is a change of several orders of magnitude in the viscosity over a narrow temperature range as the sample starts to deform in the shear mode, due to thermal softening, see Figure 7. In the fluid region, the viscosity decreases with increasing temperature.

CONCLUSIONS

- Thermomechanical analysis and differential scanning calorimetry are useful techniques and yield reproducible results in obtaining melting points, glass transition temperatures, expansion coefficients, and the point of maximum flow rate (inflection temperature).

- In general, asphalt's glass transition temperature does not seem to be affected by the presence of polyethylene terephthalate fillers.

- The PET's glass transition temperature was clearly detected by the thermomechanical analysis technique even though the DSC measurements do not show a Tg for PET.

- The overall flow of the PET/asphalt mixtures is dominated by the flow properties of the PET.

ACKNOWLEDGMENTS

R. Ledesma was supported by a W.R. Grace Graduate Fellowship and by supplemental support of the Plastics Institute of America. The work presented is based on her doctoral thesis.

References

1. Kortschot, M., Woodhams, R.T., Polymer Eng. Sci., **24** (6), 252 (1984).

2. Shim Ton, J., Kennedy, K.A., Piggot, M.R., Woodhams, R.T, Rubber Chem. Technol., **53**, 88 (1980).

3. Lea,E.M., "The Chemistry of Cement and Concrete," Chemical Comp., New York, 1971.

4. Jew, P., Woodhams, R.T., Proceedings of the Association of Asphalt Paving Technologists, **55**, 541 (1987).

5. Breen, J.J., Stephens, J.E., Proceedings of the Association of Asphalt Paving Technologists, **35**, 19 (1966).

6. Schmith, R.J., Santucci, L.E., The Association of Asphalt Paving Technologists, **38**, 706 (1969).

7. Bader, A., Harvey, D., Nagarkatti, J., Aldrich Catalog Handbook, Adrich Chemical Company, Inc., (1990).

8. Fair, P.G., Gill, P.S., Leckenby, J.N., **DuPont Thermal Analysis Application Brief No. TA-90.**

9. Dienes and Kelmm, J. Appl. Phys., **17**, 458 (1946).

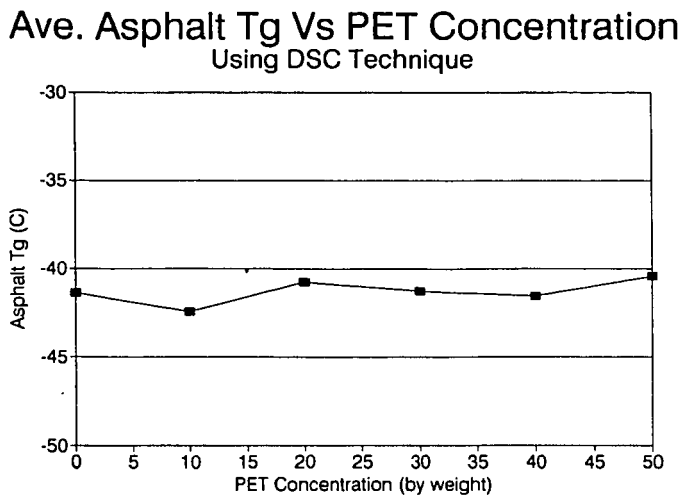

FIGURE 1.

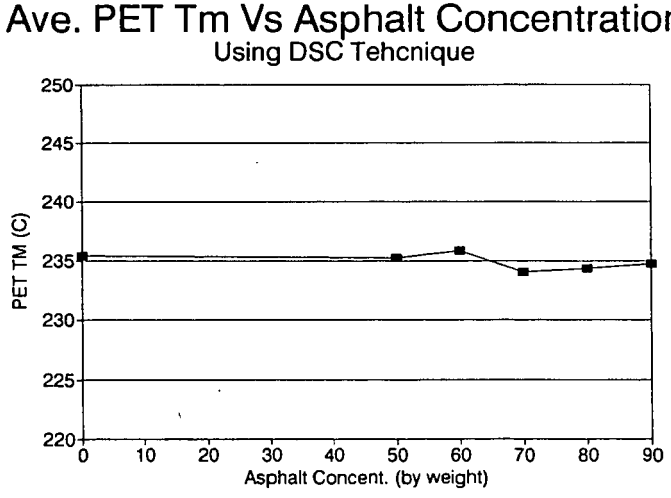

FIGURE 2.

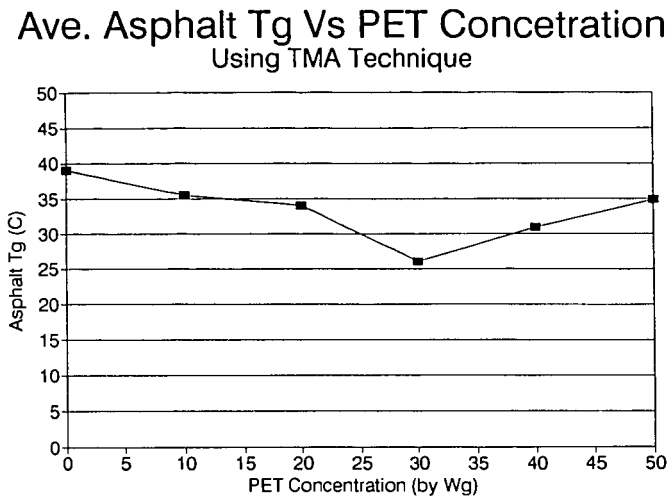

FIGURE 3.

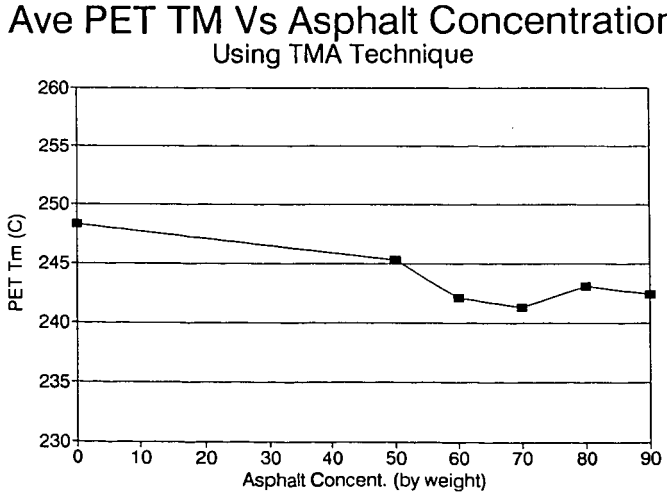

FIGURE 4.

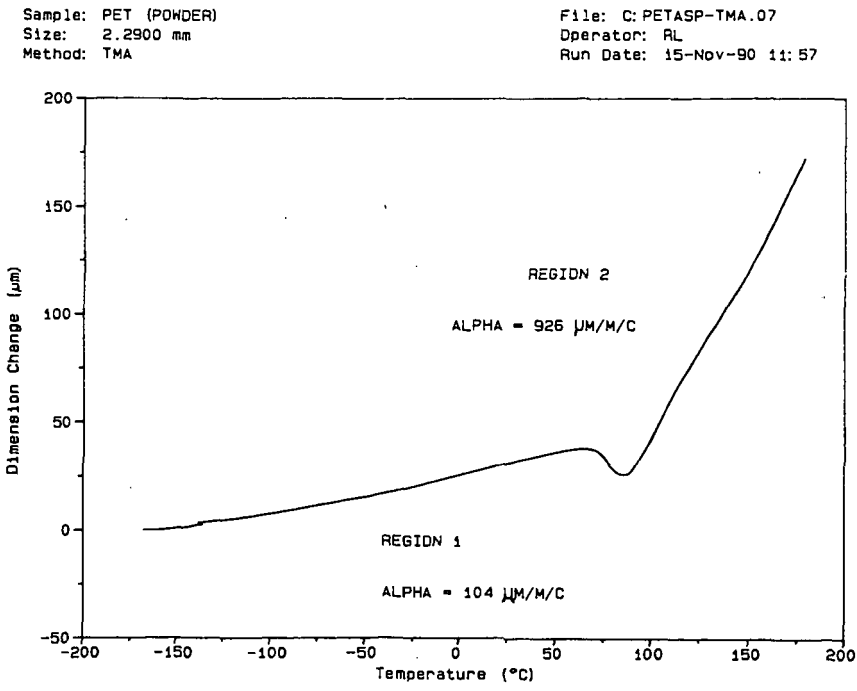
Sample: PET (POWDER)
Size: 2.2900 mm
Method: TMA
File: C:PETASP-TMA.07
Operator: RL
Run Date: 15-Nov-90 11:57
Dimension Change (µm)
Temperature (°C)
REGION 2
ALPHA = 926 µM/M/C
REGION 1
ALPHA = 104 µM/M/C
200
150
100
50
0
-50
-200
-150
-100
-50
0
50
100
150
200

FIGURE 5.

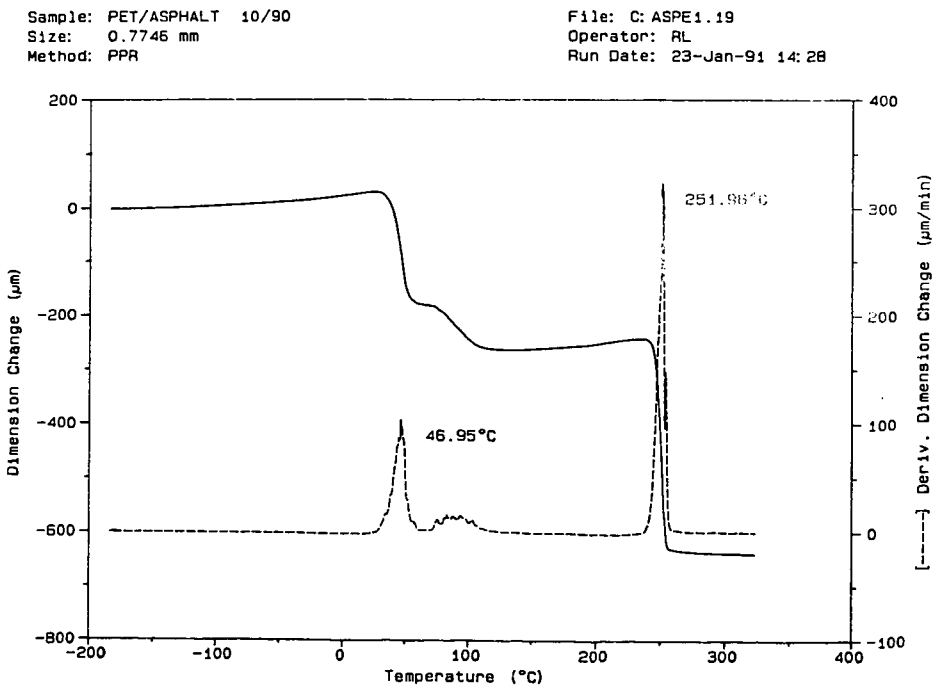
Sample: PET/ASPHALT 10/90
Size: 0.7746 mm
Method: PPR
File: C:ASPE1.19
Operator: RL
Run Date: 23-Jan-91 14:28
251.96°C
46.95°C
Dimension Change (µm)
[-----] Deriv. Dimension Change (µm/min)
Temperature (°C)
200
0
-200
-400
-600
-800
400
300
200
100
0
-100
-200
-100
0
100
200
300
400

FIGURE 6.

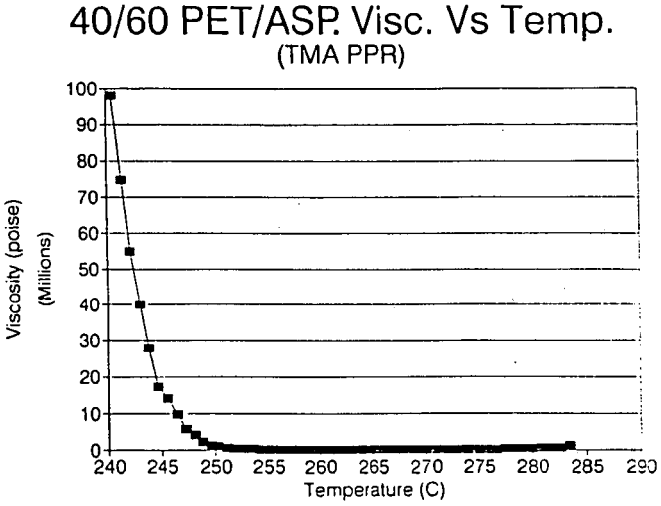
40/60 PET/ASP. Visc. Vs Temp.
(TMA PPR)
Viscosity (poise)
(Millions)
100
90
80
70
60
50
40
30
20
10
0
240
245
250
255
260
265
270
275
280
285
290
Temperature (C)

FIGURE 7.

COAL AND CARBON IN THE POST-PETROLEUM WORLD

David G. Walker of WALKER CHEMISTS INC.
904 Fleetwood Drive
Baytown, Texas 77520

Keywords: Coal, carbon, mobile motor fuel

INTRODUCTION: The petroleum age, which we now enjoy, and which makes possible the luxuries, comforts and necessities of our modern world, will not last long. As has already happened in the United States, the ability of the world to produce oil will fail to meet the market demand. The U. S. dodges this problem at present by importing nearly one-half of its oil. In the future the world has scant chance of importing oil from the moon, from Mars, or anywhere else.

The coal deposits of the world are some 100 times as big as the original oil deposits. There was a coal age which preceded the petroleum age. It was associated with the industrial revolution. Iron was made in large amounts by the use of coke from coal. Steam engines using coal drove railroad locomotives, ships and factory engines. Cities were lighted and heated with coal gas. Coal is now used only to make coke and for the generation of electricity. This last market causes air pollution or "acid rain".

Technology exists (pioneered in Germany by Bergius and Fischer-Tropsch in 1920-45) for the conversion of coal to gasoline and diesel oil. This technology was used by US industries and the government in the period 1974-82 in an attempt to make mobile motor fuel using coal as the resource base. This commercialization failed utterly. The conversion of coal to gasoline and diesel yields scarcely more than one-third of the coal's energy in useful products. In addition, the investment and operating costs of these conversion plants are some 15 times as expensive as petroleum refineries. (Gaensslen 1979)

This paper proposes that coal be used to supply mobile motor fuel by a different method. Pure carbon (Boudouard Carbon) is made as a major product from the coal. This carbon serves to replace gasoline, diesel oil and jet fuel.

Refinery Block Diagram: Post-Petroleum World (Figure 1): The future coal refinery will use coal as the raw material. Coal will also be supplemented by shale oil, tar sands and residual petroleum oil.

The coal will be coked in staged, fluidized beds with oxygen for partial combustion to supply the needed heat directly. This section, in addition to coke, will make a good grade of crude oil and sulfur as co-products. Part of the hydrogen-rich gas product is used to up-grade the volatilized hydrocarbons into a synthetic crude oil. The major product is powdered coke (Bloom 1977). The product coke, after briqueting, is transferred to the main section of the coal refinery.

Briquetted coke is gasified in a slagging-ash gas producer using air as oxidant and C02 as reductant gas (Ermankov 1957). The CO

and H2S of the producer gas are separated together from the N2, CO2 and H2 (small) by a solvent (Walker 1987) (Bartish 1983). H2S is converted into product sulfur in a Claus plant while the CO is converted into CO2 and Boudouard carbon product. (Donald 1956). The large reaction heat of the Boudouard reactor is used to make electricity as an additional product of the refinery.

Coking Section of the Coal to Carbon Refinery (Figure 2): This follows exactly the COED process which was developed by the FMC corporation and the Office of Coal Research (1960-75). (Bloom 1977). All kinds of coal can be used in this process. The temperatures of the stages of coking are somewhat different with different coals. The amount of oil produced varies from 1 to 1.5 barrels per ton depending upon the coal's volatile matter content. A minor amount of hydrogen-rich gas is available for other uses.

This coking has never been used on large scale commercially. Because the sulfur content of the coke product is just as high as that of the coal feed, the coking must be justified by the difference in price between the oil product and the coal feed. Contemporary price ratios of coal and oil are not yet different enough for this process to be economically viable as long as the coke is simply to be burned in the conventional generation of electricity. However, as is the case of this present proposal, if the coke is used to make a major high grade motor fuel, the economics will be quite different. This coking also has the desirable property of making the available hydrogen content of the coal into liquid hydrocarbons. While not of interest at the present, this can be of immense important in the future when there is no petroleum left. All of the future petrochemical industry might be supplied by this coal refinery side-product: The much larger mobile motor fuel market, at that time, would then be supplied by carbon.

Coke to Carbon Section-Coal to Carbon Refinery (Figure 3) (Hadley-Coates 1988) : Process Description: Coke is fed to a fixed bed slagging-ash gasifier fed with hot air as oxidant and hot CO2 as reductant gas(Ermankov 1957). Tar and pitch are absent from the producer gas. The sensible heat of the gas is used to generate stream. The cooled gas is dedusted and stringently dried. A separation solvent next quantitatively catches the CO and H2S content of the gas after which the residual gas is exhausted to the atmosphere (Walker 1987 and Hadley-Coates 1988). The mixed CO and H2S stream is regenerated from the solvent and then fed to an aqueous ethanolamine solvent unit to quantitatively separate the H2S from the CO. The H2S is fed to a Claus plant and converted quantitatively into product sulfur. The pure CO is converted into CO2 and product carbon in a Boudouard reactor at 500-25 C (Donald 1956). Hot CO2 is recycled to the gas producer. The temperature of the Boudouard reactor is maintained by evaporating a high temperature organic solvent within heat exchanger tubes. The gaseous organic is then fed across a turbine to generate electricity . The low pressure organic gas from the turbine is condensed in process reboilers at 150 C and recycled to the Boudouard reactor. The process reboilers are used with the separation solvents to catch CO + H2S and to separate H2S from CO.

Carbon as Motor Fuel **(Figure 4)** : Diesel engines were run for many years in Germany in a large scale development program(1910-45). This program used coal dust as the motor fuel. Many devices were developed to feed the coal dust into the engine with successful results. One such device, used by the Germans, is shown at the top of figure 4.

The coal dust engine failed to be commercially successful because of two reasons. The ash content of the coal caused unacceptable wear rates on the cylinder walls, rings and piston heads of the engine. Coal dust, as ground in practical grinders, contains too many large particles. These will not burn up completely in the short times available in a diesel engine. (Soehngen 1976)

Boudouard carbon is completely ash-free ! In addition, the intrinsic particle size of Boudouard carbon is very small (Watanabe 1929); much smaller than can be obtained than by grinding large solids into powders. (Soehngen 1976). The particle size of Boudouard carbon is small enough to burn completely in a high speed Diesel engine (Essenhigh 1979).

Otto-cycle engines compress a fuel mixture of fuel and air and then fire it by an electric spark. Some early engineers once ran a model A car successfully on flour by means of a dust carburetor! Nowadays some cars use injection methods to mix air and gasoline instead of a carburetor. Otto-cycle engines can be made to work on solid and non-volatile fuels like pure carbon.

The turbine-cycle engine is shown diagrammatically. In a turboprop airplane the propeller is tied to the power coupling. With jet planes the hot combusted pressure gas propels the plane directly. This type of engine, while not as efficient as the diesel, puts out a great deal more work per given engine weight. For airplanes this is a decisive advantage. It is also a simple engine which can run for millions of miles in its lifetime provided that the fuel used is very clean.

Boudouard carbon is fine grained and entirely free of ash, pitch or tar. (Watanabe O. 1929)

Yields and Costs of the Coke to Carbon Part of the Coal to Carbon Refinery: The overall reaction of the gasifier is approximated by:

$$1.5\ C + 1\ CO_2 + 0.5\ O_2 + 2\ N_2 = 2\ CO + 2\ N_2 + 0.5\ CO_2$$

The yields of the process (based on energy of the coke fed) are estimated to be:

Boudouard Carbon	70 %
Electricity	8 %
Useful Product Yield	78 %

Using Gaenslen's (1979) methods, it is estimated that a coal to carbon refinery will require less than one-third the investment and operating cost of present technology to convert coal to gasoline and diesel oil (Hadley-Coates 1988). It will

also make twice the yield of useful products.

Final Thoughts: A new technology is possible which uses coal to make Boudouard carbon as a major product. This product can, in the future, supply most of the mobile motor fuel requirements of the world. New directions are required in research and development in order to make this technology a practical reality. I hope that this paper will stimulate many of you to enter this vital and important field of endeavor. You can help to make both it and yourselves successful.

REFERENCES CITED

Bartish, F., et al 1983- "Carbon Monoxide" in Encyclopedia of Chemical Technology 4 3rd ed. John Wiley

Bloom, Ralph Jr.& Howard L. Malakook 1977- "COGAS Process for the Conversion of Coal to Gas and Oil Products" ENERGY TECHNOLOGY HANDBOOK D M Considine Ed. McGraw-Hill New York(I:255-61)

Donald, Jack H 1956- "An Annotated Bibliography of the Literature and Patents Relating to the Production of Carbon by the Decomposition of Carbon Monoxide" Mellon Institute of Industrial Research, Pittsburg Pa.

Ermankov, V G 1957- "Production of Technological Gases By Gasification of Lean Fuels with Removal of Liquid Slag" Khimicheskaya Pererabokta Topliva Izd AN SSSR Moscow 1957 400-7

Essenhigh H. 1979- "Coal Combustion" in COAL CONVERSION TECHNOLOGY 171-312 C Y Yen and S Lee Eds. Addison-Wesley Pub. Co,Reading, Mass.

Gaensslen, Hans 1979- "A Shortcut to Investment Costs" CHEMTECH, May 306-9

Hadley-Coates, Lyndon & D G Walker 1988- "Boudouard Carbon : An Alternate to Gasoline and Diesel Oil" INTERNATIONAL JOURNAL OF ENERGY RESEARCH 12 2443-51

Soehngen, E E 1976- "The Development of the Coal Burning Diesel in Germany" Report FE/WEPO 3387-1 Purchase Order No 3387 U S Energy Research and Development Administration

Walker, D G 1987- US Patent 4,654,202 31 March 1987 "Separation of Hydrogen Sulfide from Gases by the Use of Cuprous Aluminum Tetrachloride as a Reversible Complexing Agent"
US Patent 4,691,074 1 Sept. 1987
"Monochlorobiphenyl: Cuprous Aluminum Tetrachloride"

Watanabe, O & N. Tokunosuke 1929- "The Nature of Carbons Monoxide Produced by the Catalytic Decomposition of Carbon Monoxide" Bull. Inst. Phy. Chem Research (Tokyo) 8 288-92

FIGURE 1

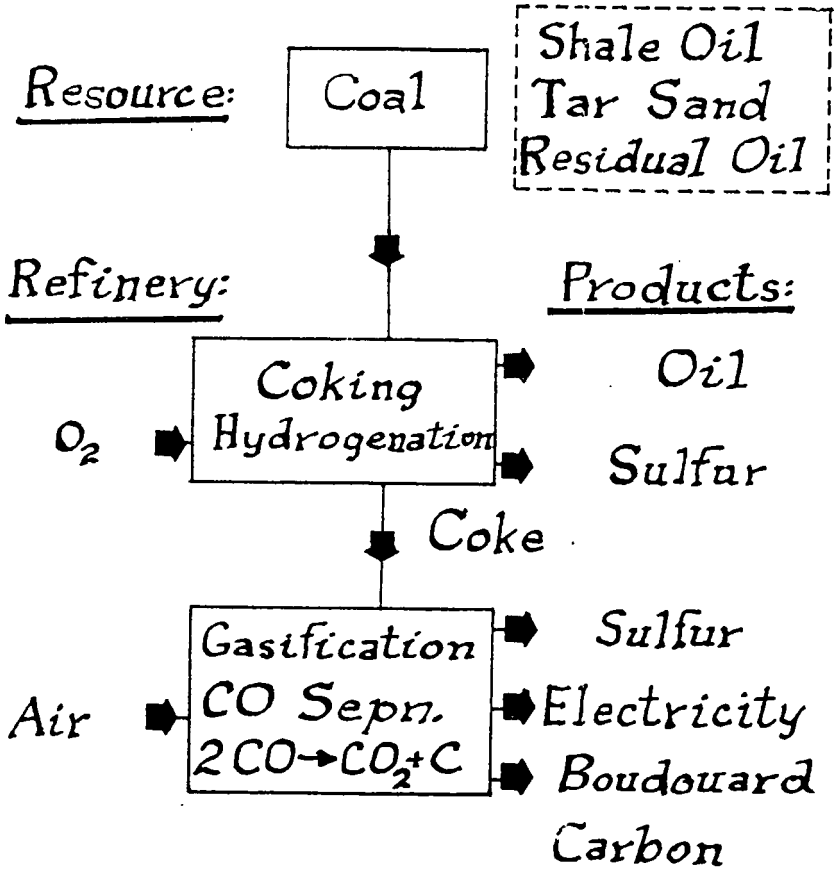

POST-PETROLEUM ECONOMY

FIGURE 2

Coal to Coke-Oil-Hydrogen: COED Process

FMC Corp. and Office of Coal Research

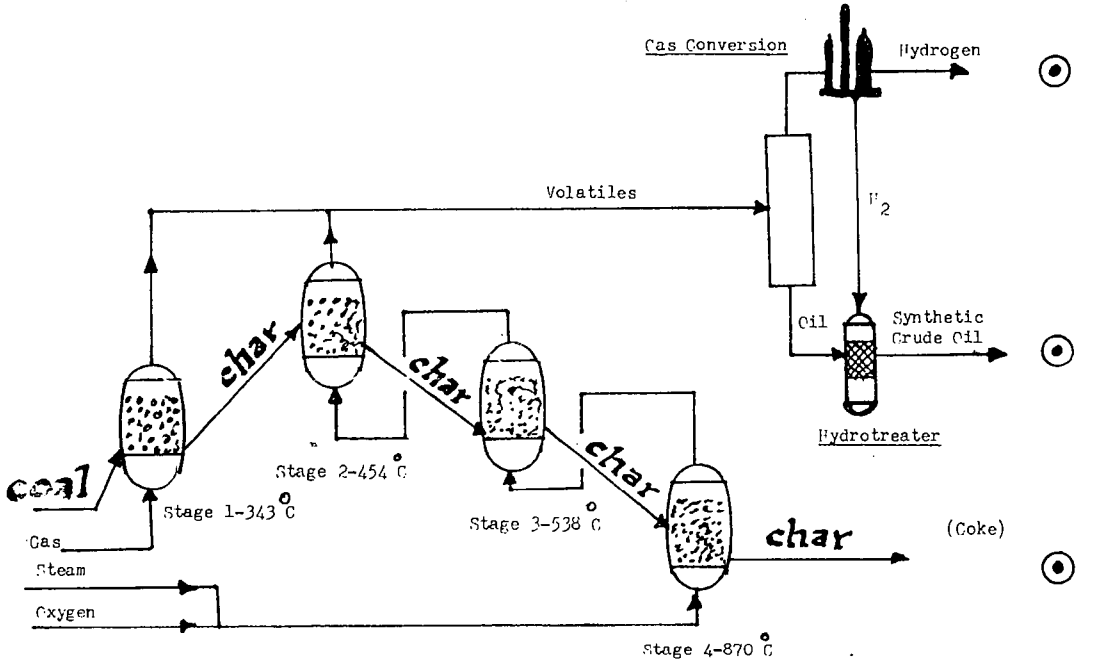

FIGURE 3

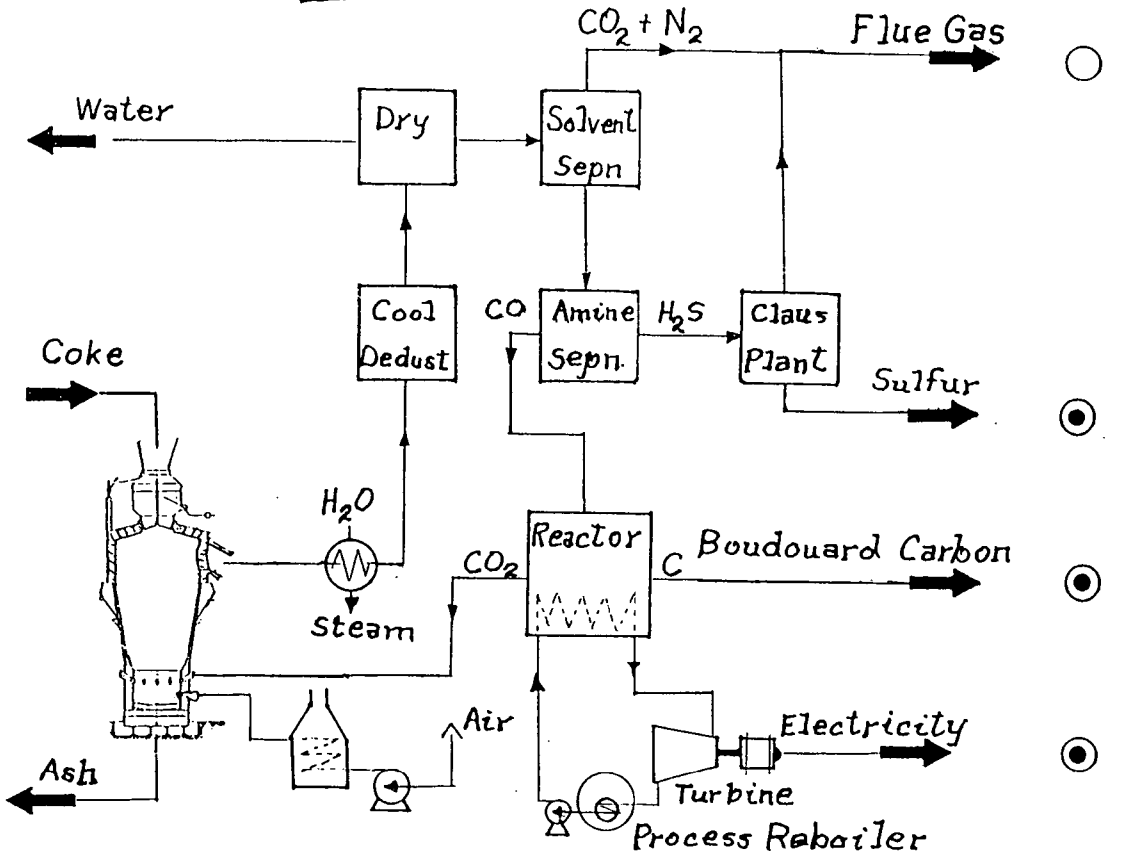

COKE TO CARBON REFINERY

Diesel Engine

Otto Cycle Engine

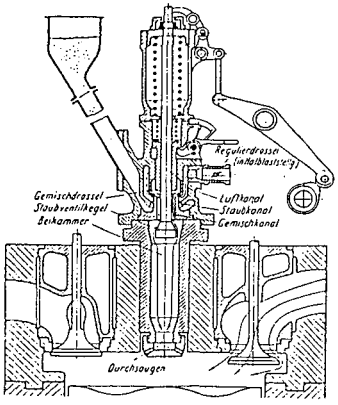

Abb. 304. Schematische Darstellung der pneumatischen Staubeinschleusung nach dem Verfahren MÄGEL-ZANDER.

Turbine Engine

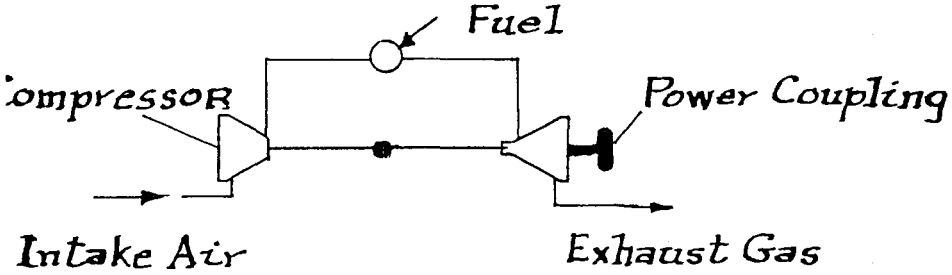

CARBON AS MOTOR FUEL

FIGURE 4

Acid Base Properties of Coals and Coal Liquids

by

Edward M. Arnett* and Tanweer Ahsan

Department of Chemistry
Duke University
Durham, North Carolina 27706

Solution calorimetry provides a straightforward method for comparing the acid-base properties of solids with homogeneous analogues. The presentation will describe the correlations (and lack of them) between heats of interactions of a series of acids and a corresponding series of bases with several such heterogeneous/homogeneous systems. For example, solutions of p-toluenesulfonic acid are compared with slurries of sulfonic acid resins in their reactions with a series of nitrogen bases. Pyridine solutions are compared with slurries of polyvinylpyridine by their reactions with a series of carboxylic and sulfonic acids. Finally, several carefully chosen coal liquids are compared with related coals of different rank and are considered in the light of the above simpler systems.

Introduction

The classification of chemicals into acids and bases is one of the broadest in Science. It is well known that coals and the liquids derived from them include a number of functionalities and structures which are acidic (e.g., phenols, carboxylic acids) or basic (e.g., a variety of amino functions, ethers, sulfides and inorganic oxides). All types of organic functionalities are potentially basic towards protons, Lewis acids and hydrogen bond donors, and most of them are also acidic, in the Brönsted sense, if they carry protons bonded to carbon or other elements. However, only a few acidic or basic functionalities are strong enough to allow study in the familiar aqueous acid-base range of the pH meter. Over the past fifty years a variety of strategies have been developed for studying even very weak bases by reaction with strong superacids, and correspondingly weak acids with superbases. Of particular importance has been the development of gas phase techniques in the past fifteen years for studying proton transfer reactions in the gas phase which provides a very broad inherent scale of acid-base strengths from which all contributions due to solvation or ion-pairing effects have been completely removed.[1-5] The impact of gas phase studies on clarifying solvent effects can hardly be exaggerated.

The acid-base properties of solids play a fundamental role across a wide panorama of materials science, including among other matters corrosion, adhesion, the behavior of solid sensors, many biochemical medical and geochemical phenomena. Of great importance to the fossil fuel industry is the use of solid acid catalysts for a wide range of processes in the petroleum and coal derivative industries.

Unhappily, the methods for establishing quantitative acid-base scales for solids stand on a much sandier foundation than those used to compare liquid acid-base systems. A solid surface may carry a variety of basic sites in the presence of Lewis acid, Brönsted acid and hydrogen-bonding donor sites of widely different strengths and accessabilities. In solution a rapid equilibration is established between different types of acid or basic sites and it is reasonable to de-

scribe a solution as representing a single acidity or basicity value within a very limited range. One would scarcely think that after mixing a solution of hydrochloric acid with sodium hydroxide that there would coexist in solution a number of strongly acid and strongly basic sites. However, due to the inflexible structure of solids a material such as a Zeolite, alumina or coal may carry on its surface both acidic and basic sites that are permanently separated and do not interact with each other directly.

The Thermochemical Approach: A number of years ago we established a very simple thermochemical method for determining the strengths of basic liquids by measuring their heats of neutralization by a common very strong acid such as sulfuric or fluorosulfuric acid.[6] Samples of the base were injected directly with a Hamilton syringe into a calorimeter vessel full of the pure strong acid. Alternatively, the base could be titrated using a motor-drived burette into a vessel containing a solution of the acid in some relatively inert solvent such as acetonitrile. Heats of ionization were determined in this manner for a 100 or so bases of widely different type and were shown to correlate very well with the best results obtained by other much more laborious methods. Heats of ionization are a direct measure of basicity.

The great advantage of the calorimetric method is that it can also be applied with facility to the study of solid acids and bases using a stirred slurry of the solid under an inert solvent instead of the homogeneous solution of the acid or base. The thermochemical titration method, therefore, provides a direct means for comparing the acidity or basicity of homogeneous solutions with solids which are presumed to carry the same acid or base structure. This article provides a current overview of our use of the thermochemical method to compare several types of solid acids and bases with their homogeneous cognates. As a simple prototype example of a Brönsted acid Dowex polysulfonic acid resin was compared with p-toluenesulfonic acid solutions. A sample of Fisher silica was examined for its hydrogen-bonding acidity compared to p-fluorophenol. Polyvinylpyridine was compared to solutions of pyridine as a standard base, and Carbopack graphitized carbon was used as a model for the dispersion force interactions which inevitably contribute to adsorption of any gas or liquid on any type of solid. Finally, several types of well-characterized coals were compared with coal liquids derived from them.

Experimental

Surface areas were obtained by nitrogen adsorption at 77K employing the BET method and using a Quantachrome Surface area analyser. The acids and bases were obtained commercially and were used as 0.25-0.5 molar solutions in carefully purified acetonitrile or neat wherever indicated. Coal samples were obtained from Argonne Coal Bank, Exxon Research and Engineering Co. and Southern Electric International, Southern Clean Fuels Division at Wilsonville, Alabama.

Titration calorimetry using the Tronac 450 calorimeter is the most desirable technique for comparing heats of interaction of strong acids or bases with solids provided that the exothermic heats of interaction are large enough and are released in a relatively short period of time (say less than two minutes). In these cases the results can be expressed in terms of kcal/mol since it is known exactly how many moles of acid are required to titrate the solid. For titration calorimetry, the apparatus is calibrated every few weeks by measuring the heat of neutralization of aqueous sodium hydroxide by titration with standard aqueous hydrochloric acid $\Delta H = -13.42 \pm 0.39$ kcal/mol.

For cases where relatively small heats of interaction must be compared, and the total heat is given out over a long period (say one hour), heats of immersion are measured with the Seteram C-80 heat flow calorimeter. This instrument measures heats of immersion by releasing the solid base into a solution of the liquid acid or a neat liquid acid. Heats of immersion may also be obtained by sealing the solid in an ampule which is equilibrated thermally with the acid

solution and then crushed in the stirred calorimeter. For immersion calorimetry in contrast to titration calorimetry it is more realistic to present results in cal g^{-1} of solid base since there is no direct means of knowing how many moles of acid or base were actually involved in the interaction. We have used heats of dissolution of KCl in water as the calibrating standard for immersion calorimetry.

Heats of adsorption on Carbopack F were determined by gas-solid chromatography by the van't Hoff method previously described in which the retention volume of the adsorbate is studied as a function of temperature.

Results and Discussion

A prototype Brönsted solid acid Dowex---polysulfonic acid resin:[7] In order to establish the feasibility of the thermochemical method for comparing solid and homogeneous acids and bases, Dowex polysulfonic acid resin was treated as a slurry in acetonitrile with a series of nitrogen bases whose strength cover a reasonably wide range. The same bases were again injected into solutions of p-toluenesulfonic acid in acetonitrile and the heats of reaction determined. Although in aqueous solution neutralization would have occurred to produce dissociated ammonium and p-toluenesulfonate ions in acetonitrile, there is every reason to expect that hydrogen-bonded ion-pairs were produced according to equation 1.

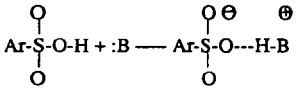

(1)

Figure 1 presents the excellent correlation between the two sets of enthalpy determinations. The quality of this correlation is of fundamental importance for our whole strategy for studying the strengths of solid acids and bases. Considering the above discussion of the real differences between the distribution of acid sites on various types of solid acids, the difference between chemisorption and physisorption, it would be possible that the difference between solid and liquid acid or base systems is inherently so great that no close correspondence between them could be found. Figure 1 emphasizes the fact that if there is ready access to surface acid sites of equivalent acidity that they respond proportionately in the same way as those same sites do if they are free molecular units in solution.

An instructive point in Figure 1 is its non-zero intercept indicating that the heats of interaction of the bases with PTSA are consistently 4-5 kcal/mol more exothermic than their interactions with Dowex resin. We have interpreted this in terms of the well-established stabilization of sulfonate anions in the presence of excess sulfonic acid according to Equation 2 which would be considerably easier in the solution phase reaction than on the solid surface where ionized sulfonate groups are separated in space from nearby unionized sulfonic acid groups. The difference of 4-5 kcal/mol is in exactly the appropriate range for the formation of such a hydrogen-bond stabilized anion.

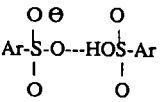

(2)

Polyvinylpyridine a prototype solid base: Following the strategy described above, a thermochemical comparison has been made between solutions of pyridine and polyvinylpyridine

in which pyridine units are attached to an extended carbon framework. Figure 2 provides exactly the same type of correlation for these liquid and solid basic systems as those presented in Figure 1 for liquid and solid acids. We believe that it is significant that in this case the intercept is within experimental error of zero which helps to support the explanation given above for the non-zero intercept in the case of the sulfonic acids. In the case of protonating the pyridines the sulfonate and carboxylate anions are left free in solution where they can be stabilized in exactly the same way (Equation 2) after reaction with free pyridine molecules or pyridine units attached to the polymeric framework.

Silica a hydrogen-bonding acid: Silica is probably one of the best characterized and best understood of solid acids.[9] Its interaction with bases, unless they are unusually strong, is usually through hydrogen-bonding from the hydroxyl groups on the silica surface. In order to probe the use of silica as a prototype hydrogen-bonding acid, a standard sample of Fisher silica was treated with a series of nitrogen and oxygen bases which are well-established as hydrogen-bond acceptors.[10] Figure 3 shows the relationship between these heats of interaction and the corresponding heats of interaction for the same series of bases with p-fluorophenol, a well-established hydrogen-bonding acid. Although the correlations are not as good as those shown in Figures 1 and 2, it is apparent that the heats of interaction of the bases with silica is indeed largely determined by hydrogen-bonding.

Since hydroxyl groups are amphiprotic, amphoteric functionalities, we tried examining silica as an acceptor base for hydrogen bonds or protons from the same series of acids used with pyridine and polyvinylpyridine.[11] To our surprise, the heats of interaction followed an entirely different pattern than would have been expected if the acids were donating protons or hydrogen bonds to silica. Instead, the simplest interpretation of the results was that the silica was actually serving as a strong hydrogen-bonding acid that it was donating hydrogen bonds to the carboxcylic and sulfonic acid functionalities instead of receiving protons from them.

Physisorption on Carbopack carbon: All matter attracts all matter through dispersion force interactions and accordingly, in the absence of all other types of interactions, gases and liquids will be adsorbed on any kind of solid. As a prototype dispersion force adsorbent we chose Carbopack F, a graphitized carbon, and determined the heats of adsorption of a variety of compounds on the surface using the van't Hoff equation and the temperature dependence of gas chromatographic retention volumes as the experimental tool.[12] It was immediately apparent from the results when compared with those presented in Figures 1 and 2 that the heats of adsorption had absolutely no relation whatsoever to the basicities or acidities of the adsorbed molecules. Instead, excellent correlations were found (Figures 4 and 5) between the simple number of main group atoms in the adsorbates and their total polarizabilities (the dipole polarizability plus the electronic polarizability).

Comparison of solid coals and coal liquids: The rest of this paper will present work mainly acquired during the summer from the heats of reaction of several well-classified coal liquids received from the Southeast Regional Laboratory at Wilsonville, Alabama and titration of slurries with the corresponding coals from which the coal liquids were derived.

References

1. Aue, D.H.; Bowers, M.T. *In Gas Phase Ion Chemistry*; Bowers, M.T.; Ed.; Academic Press: New York, 1979; Vol 2, pp 1-51 and references therein.

2. Lias, S.G.; Liebman, J.F.; Levin, R.D. *J. Phys. Chem.* Ref. data, **1984**, 13, 3, 695-808.

3. Taft, R.W. in *Progress in Physical Organic Chemistry*, John Wiley & Sons: New York, 1983, Vol 14, pp 247-350.

4. Arnett, E.M. Acc. Chem. Res. **1973**, *6*, 404.

5. Epshtein, L.M. Russ. Chem. Rev. **1979**, *48(9)*, 854.

6. a) Arnett, E.M.; Burke, J.J. *J. Am. Chem. Soc.* **1966**, *88*, 4308.
   b) Arnett, E.M.; Quirk, R.P.; Burke, J.J. *J. Am. Chem. Soc.* **1970**, *92*, 1260.
   c) Arnett, E.M.; Quirk, R.P.; Larsen, J.W. *J. Am. Chem. Soc.* **1970**, *92*, 3977.
   d) Arnett, E.M.; Mitchell, E.J.; Murty, T.S.S.R. *J. Am. Chem. Soc.* **1974**, *96*, 3875.

7. Arnett, E.M.; Haaksma, R.A.; Chawla, B.; Healy, M.H. *J. Am. Chem. Soc.* **1986**, *108*, 4888.

8. Arnett, E.M. Ahsan, T.; Amarnath, K. in press.

9. a) Iler, K.R. *The Chemistry of Silica*, John Wiley and Sons, 1979.
   b) Legrand, A.P.; et al., *Adv. in Coll. & Interf. Sci.* **1990**, *33*, pp 91-330.
   c) Morrow, B.A.; McFarlan, A.J. *J. Non-Cryst. Solids* **1990**, *120*, 61.
   d) Nawrocki, J. *Chromatographia* **1991**, *31(3-4)*, 177.
   e) Nawrocki, J. *Chromatographia* **1991**, *31(3-4)*, 193.

10. Arnett, E.M.; Cassidy, K.F. *Rev. Chem. Intermed.* **1988**, *9*, 27.

11. Arnett, E.M.; Ahsan, T. in press.

12. Arnett, E.M.; Hutchinson, B.J.; Healy, M.H. *J. Am. Chem. Soc.* **1988**, *110*, 5255.

Figure 1

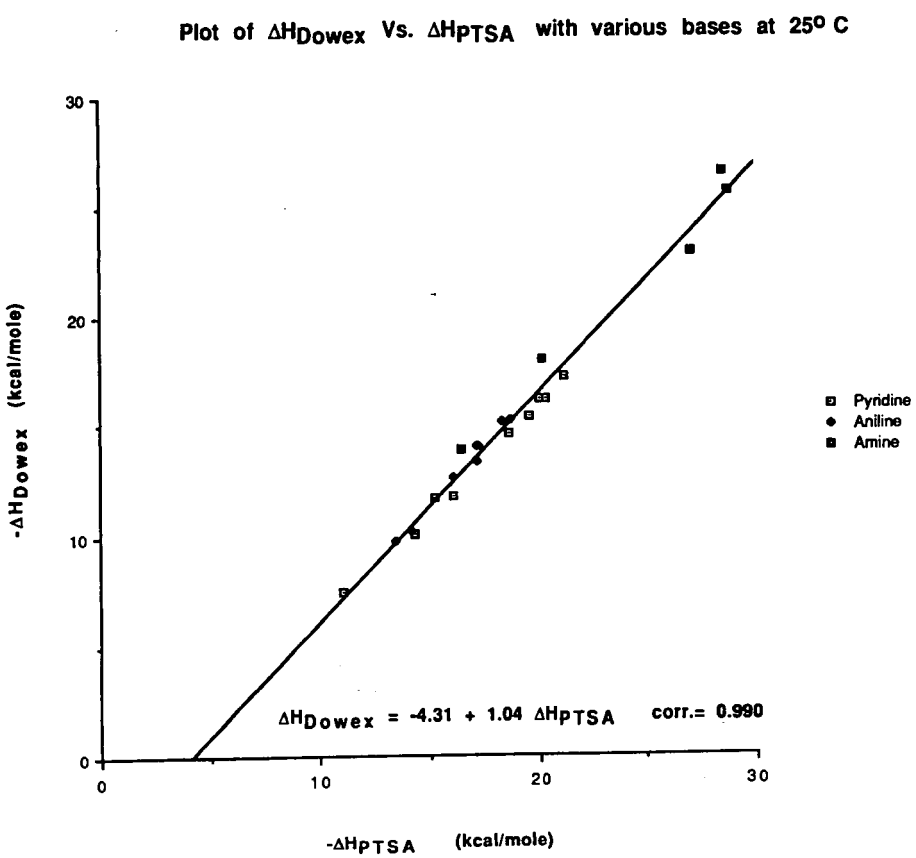
Plot of ΔHDowex Vs. ΔHPTSA with various bases at 25° C
-ΔHDowex (kcal/mole)
-ΔHPTSA (kcal/mole)
ΔHDowex = -4.31 + 1.04 ΔHPTSA
corr.= 0.990
Pyridine
Aniline
Amine
0
10
20
30

Figure 2

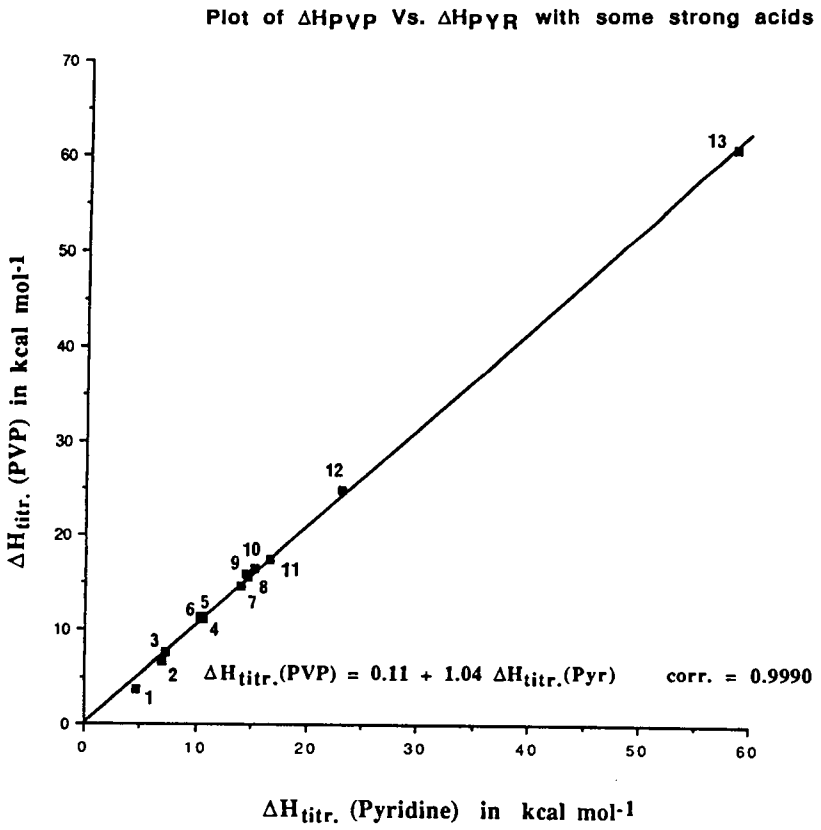
Plot of ΔHpVP Vs. ΔHpYR with some strong acids
ΔHtitr. (PVP) in kcal mol-1
ΔHtitr. (Pyridine) in kcal mol-1
ΔHtitr.(PVP) = 0.11 + 1.04 ΔHtitr.(Pyr)
corr. = 0.9990
0
10
20
30
40
50
60
70
1
2
3
4
5
6
7
8
9
10
11
12
13

Figure 3

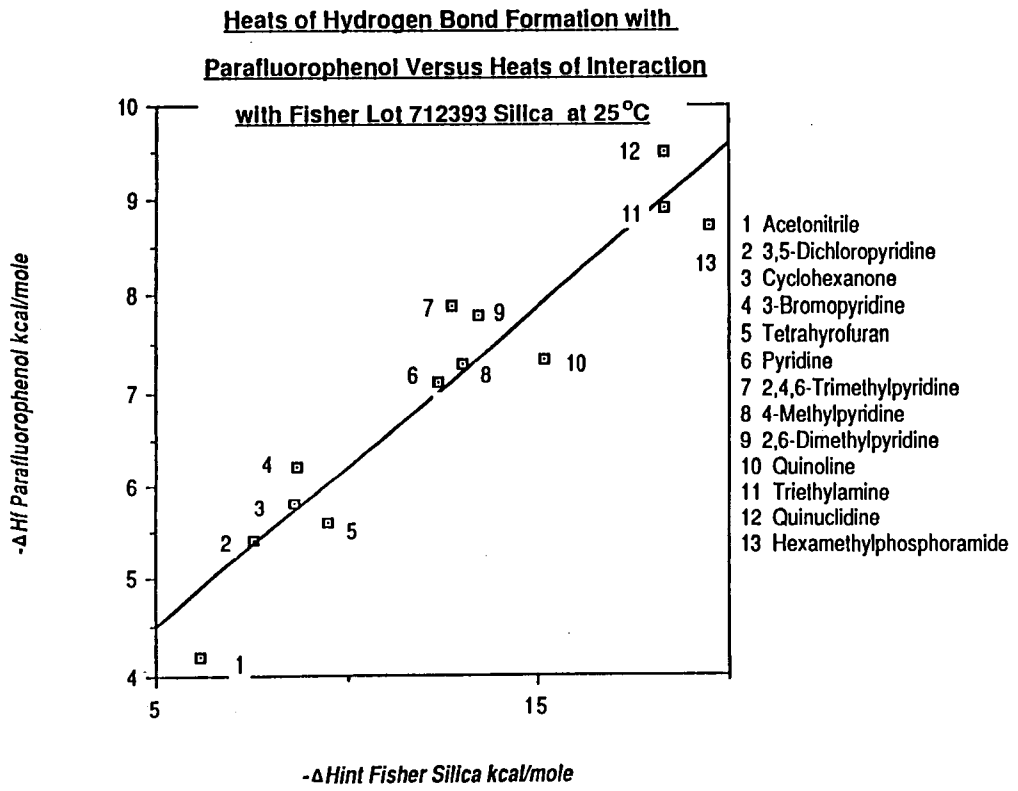
Heats of Hydrogen Bond Formation with
Parafluorophenol Versus Heats of Interaction
with Fisher Lot 712393 Silica at 25°C
-ΔHf Parafluorophenol kcal/mole
-ΔHint Fisher Silica kcal/mole
10
9
8
7
6
5
4
5
15
1 Acetonitrile
2 3,5-Dichloropyridine
3 Cyclohexanone
4 3-Bromopyridine
5 Tetrahyrofuran
6 Pyridine
7 2,4,6-Trimethylpyridine
8 4-Methylpyridine
9 2,6-Dimethylpyridine
10 Quinoline
11 Triethylamine
12 Quinuclidine
13 Hexamethylphosphoramide

Figure 4

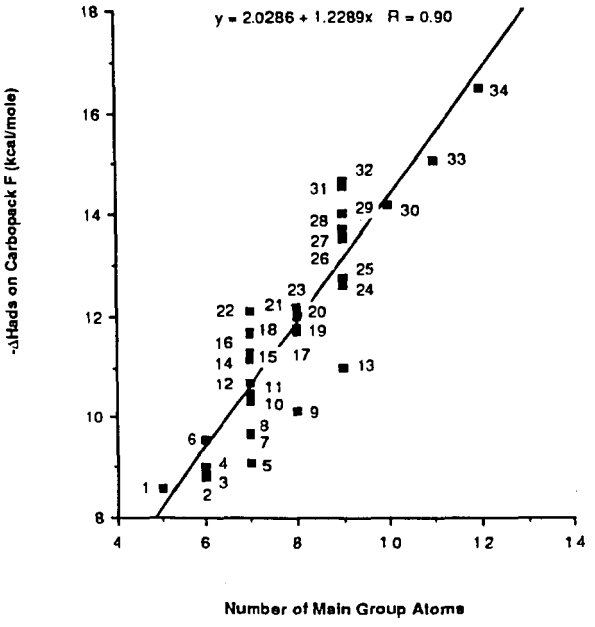

1. *n*-Butylamine
2. *n*-Pentanol
3. Pyridine
4. Benzene
5. Cyclohexanol
6. Hexane
7. Cyclohexanone
8. Cyclohexylamine
9. Methyl valerate
10. *n*-Hexanol
11. Toluene
12. 2-Methylpyridine
13. Methyl caproate
14. 3-Methylpyridine
15. 4-Methylpyridine
16. *n*-Hexylamine
17. *m*-Cresol
18. Bromobenzene
19. Benzonitrile
20. Octane
21. 2,6-Lutidine
22. 1-Bromohexane
23. Anisole
24. *n*-Octanol
25. Nitrobenzene
26. 2,4,6-Collidine
27. Nonane
28. Octylamine
29. 1-Chlorooctane
30. *n*-Butylbenzene
31. *o*-Bromoanisole
32. *p*-Bromoanisole
33. Undecane
34. Dodecane

Heats of Adsorption of a Variety of Adsorbates on Carbopack F *versus* the Number of Main Group Atoms.

Figure 5

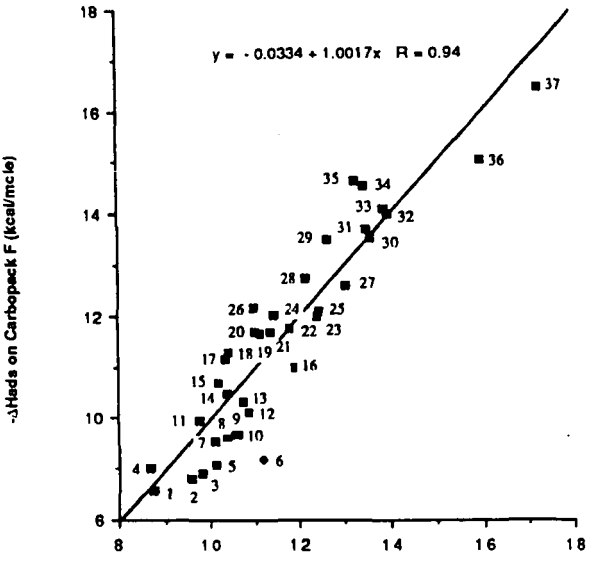

-ΔHcalc = 0.646(electronic polarizability) + 0.015 (orientation polarizability) + 2.410

1. *n*-Butylamine
2. *n*-Pentanol
3. Pyridine
4. Benzene
5. Cyclohexanol
6. Triethylamine
7. Hexane
8. Cyclohexanone
9. Dimethyl sulfoxide
10. Cyclohexylamine
11. Propylene carbonate
12. Methyl valerate
13. *n*-Hexanol
14. Toluene
15. 2-Methylpyridine
16. Methyl caproate
17. 3-Methylpyridine
18. 4-Methylpyridine
19. *n*-Hexylamine
20. *m*-Cresol
21. Bromobenzene
22. Benzonitrile
23. Octane
24. 2,6-Lutidine
25. 1-Bromohexane
26. Anisole
27. *n*-Octanol
28. Nitrobenzene
29. 2,4,6-Collidine
30. Nonane
31. Octylamine
32. 1-Chlorooctane
33. *n*-Butylbenzene
34. *o*-Bromoanisole
35. *p*-Bromoanisole
36. Undecane
37. Dodecane

Heats of Adsorption on Carbopack F *versus* Electronic plus Orientation Polarizability.

SHORT RANGE RING STRUCTURING IN A META-ANTHRACITE COAL

David L. Wertz
Department of Chemistry & Biochemistry
University of Southern Mississippi
Hattiesburg, MS 39406-5043

Key Phrases: Molecular scattering, graphitic layers, cluster size

INTRODUCTION

X-ray characterizations of coals and coal products have occurred for many years.[1-9] Hirsch and Cartz[1], several years ago, measured the diffraction from several coals over the reciprocal space region from X = 0.02 $Å^{-1}$ to 1.2 $Å^{-1}$ (X = [2/λ]·sinθ). In these studies, a 9 cm powder camera was used to study the high angle region, and a transmission type focussing camera equipped with a LiF monochromator was used for the low angle measurements. They reported that the height of the [002] peak (at ca. 3.5 Å) measured for each coal is proportional to the % carbon in several coals. Hirsch[2] also suggests that the Pontyberem anthracite (94.1% carbon, 3.0% hydrogen, and 5.3% volatile matter with a specific gravity of 1.46) has a layer diameter of ca. 16 Å corresponding to an aromatic lamellae of ca. C_{87}. For coals with lower carbon content, Hirsch proposes much smaller lamellae; C_{19} for a coal with 80% carbon, and C_{24} for a coal with 89% carbon.

Because of the importance placed by coal scientists on correctly characterizing the nature of the cluster(s) in coals and because of improvements in both x-ray experimentation capabilities and computing power, we have measured the x-ray diffraction and scattering produced from irradiation of a meta-anthracite coal[10] with hard xrays.[11] The objective of our study is to determine the intra-planar, and where possible inter-planar, structural details of coals and to determine the extent to which layering in coals mimics that of crystalline graphite and/or synthetic polymers. To accomplish the former we have utilized the methods normally used for the molecular analysis of non-crystalline condensed phases such as liquids, solutions, and amorphous solids.[12-23]

The coal, a meta-anthracite which was derived from the Portsmouth, RI mine (southeastern Narragansett Basin), was supplied to us by Professor James W. Skehan, S. J. of the Department of Geology and Geophysics at Boston College.

Reported herein are the results obtained from the hard x-ray analysis of this coal.

EXPERIMENTAL

META-ANTHRACITE COAL. From a 10 gram sample of the coal, a 3 gram aliquot was ground into a fine powder using our SPEX ball mill. The resulting powdered coal was passed through a -100 mesh filter.

A 0.4869 g sample of the finely ground powder was mounted onto a PVC sampleholder and mounted into the x-ray diffractometer.

X-RAY EXPERIMENTS. Mo xrays were used as the exciting radiation. The diffractometer was equipped with a θ-compensating slit, a sample spinner, and a LiF crystal in the secondary x-ray beam.[11] A diffraction pattern of the powdered coal mounted onto the PVC substrate was obtained by collecting intensities for five second intervals at $d2\theta = 0.01^\circ$ over the range from $2\theta = 8.00^\circ$ to $2\theta = 120.00^\circ$. The diffraction pattern from the PVC sampleholder was obtained using exactly the same protocol.

A diffraction pattern of a 0.3878 g sample of reagent grade graphite (Alfa Products) was obtained using the same sampleholder and methodology.

RESULTS AND DISCUSSION

Shown in Figure 1 is the diffractogram of the meta-anthracite sample as well as the diffractogram of the graphite sample.

THE 3.4 Å DIFFRACTION PEAK. The location of this large peak in the meta-anthracite diffractogram corresponds to the [002] diffraction peak which dominates the diffraction pattern of graphite (d = 3.37 Å). Hirsch[1,2] and Franklin[3] report this peak at 3.5 Å in previous studies. Ebert, Scanlon, and Clausen[12] find a similar large first peak in the diffractogram of a combustion tube soot. Comparison of the diffractograms indicates that while the first peaks occur at ca. 3.4 Å, the details of these peaks are quite dissimilar, suggesting that the regularity of the inter-planar spacings, reported to be the cause of the 3.4 Å peak, is considerably less in this meta-anthracite than in graphite.

AMORPHOUS SCATTERING DUE TO THE CARBONACEOUS CONTENT OF THE META-ANTHRACITE. Shown in Figure 2 is the separation of the diffraction peaks (2A) from the molecular scattering (2B) for the meta-anthracite. The molecular scattering curve, $I_A(2\theta)$, is similar in shape to the scattering curve obtained previously for an amorphous carbon black,[6] and also to the scattering curves measured for liquids, solutions, and other amorphous solids.[12-23]

The molecular scattering was fitted to the independent scattering curve[24-26] to obtain the reciprocal space interference curve i(s) where $s = (4\pi/\lambda)\sin\theta$. The latter is a description of the average 1-dimensional structural features of the meta-anthracite.

Using conventional methods the atom-pair radial-distribution function was calculated for the meta-anthracite from its

interference function via Fourier transform. The APRDF (Figure 4) provides a measure of the atom-pair distances and their relative importance in the non-crystalline material. The APRDF contains major peaks centered at 1.40 Å, 2.42 Å, 2.85 Å, 3.6 Å, 4.8 Å, 6.0 Å and to r → 15 Å.

P_1 (centered at 1.40 Å) is due to the bonded C-C distance, i.e. C_r-C_1 in Figure 3. The 2.42 Å peak (P_2) is due to the nearest non-bonded C··C atom-pairs. From P_1 and P_2, the average C-C-C bond angle was calculated to be 120° (±4°). P_3 (centered at 2.84 Å) is also attributed to non-bonded C··C atom-pairs. The relative P_1, P_2, and P_3 distance and magnitudes as well as the C-C-C bond angle indicate that the average PAH ring is quite similar to those found in anthracene, napthalene, and pyrene.[27-32] The remaining several peaks in the RDF are due to inter-ring C··C atom-pairs and are being used to estimate the planarity and size of the average PAH cluster in the meta-anthracite. Our results will be compared to those presented by other investigators.[33-39]

REFERENCES

1. Cartz, L. and Hirsch, P. B., 1960 (252) 68.
2. Hirsch, P. B., 1954 (226) 143.
3. Franklin, R. E., Acta Crystallogr., 1950 (3) 10.
4. Kwan, J. T. and Chen, T. F., Proc. Div. Fuel Sci., 1976 (21) 67.
5. Diamond, R., Act Crystallogr., 1958 (11) 129.
6. Wertz, D. L., Powder Diff., 1988 (3) 153.
7. Wertz, D. L., Smithhart, C. B., and Wertz, S. L., Adv. X-Ray Anal., 1990 (33) 475.
8. Davis, B. L., Powder Diffr.,.1986 (1) 244.
9. McCarthy, G. J., Powder Diffr., 1986 (1) 50.
10. Skehan, J. W., Rast, N., and Mosher, S., "Paleonenvironmental and Tectonic Controls of Sedimentation in Coal-Forming Basins of Southeastern New England", Geological Society of America, Special Paper 210, 1986; Skehan, J. W. and Rast, N., Pre-Mesozoic Evolution of Avalon Terranes of Southern New England. Geological Society of America, Special Paper 245, 1990.
11. Wertz, D. L., Powder Diffr., 1990 (5) 44.
12. Mitchell, G. R. and Windle, A. H., J. Appl. Crystallogr., 1980 (13) 135.
13. Wertz, D. L. and Kruh, R. F., J. Chem. Phys., 1967 (47) 388.
14. Levy, H. A., Danford, M. D., and Narten, A. H., ORNL Report No. 3960, 1966.
15. Harris, R. W. and Clayton, G. T., J. Chem. Phys., 1966 (45) 2681.
16. Ohtaki, H. and Wada, H., J. Solution Chem., 1985 (14) 3.
17. Lovell, R., Mitchell, G. R., and Windle, A. H., Acta Crystallogr., 1979 (A35) 598.
18. Johansson, G. and Wakita, H., Inorg. Chem., 1985 (24) 3047.
19. Yamaguchi, T. S., Hayashi, T., and Ohtaki, H. Inorg. Chem., 1989 (28) 2434.
20. Bell, J. R., Tyvoll, J. L., and Wertz, J. Am. Chem. Soc., 1973 (95) 1456.
21. Wertz, D. L. and Hicks, G. T., J. Phys. Chem., 1980 (84) 521.
22. Wertz, D. L. and Holder, A. J., J. Phys. Chem., 1987 (91) 3479.
23. Wertz, D. L. and Cook, G. A., J. Solution Chem., 1985 (14) 41.
24. Hajdu, F., Acta Crystallogr., 1971 (A27) 73; 1972 (A28) 250; Palinkos, G., private communications, 1980.
25. Kruh, R. F., Chem. Rev., 1962 (62) 319.
26. Konnert, J. H. and Karle, J., Acta Crystallogr., 1973 (A29).
27. Cruickshank, D. W. J., Acta Crystallogr., 1959 (12) 208.
28. Abrahams, S. C., Robertson, J. M., and White, J. G., Acta Crystallogr., 1949 (2) 233.
29. Cruickshank, D. W. J., Acta Crystallogr., 1957 (10) 504.
30. Ahmed, F. R. and Cruickshank, D. W. J., Acta Crystallogr., 1952 (5) 852.
31. Cruickshank, D. W. J., 1956 (9) 915.
32. Robertson, J. M. and White, J. G., J. Chem. Soc., 1947 358.
33. Solum, M. S., Pugmire, R. J., and Grant, D. M., Energy Fuels, 1989 (3) 187.
34. Sethi, N. K., Pugmire, R. J., Facelli, J. C., and Grant, D. M., Anal. Chem., 1988 (60) 1574.
35. Murphey, P. D., Cassady, J. J., and Gerstein, B. C., Fuel, 1981 (61) 1233.
36. Miller, D. J., Hawthorne, S. B., and Timpe, R. C., Div. Fuel Chem. Am. Chem. Soc., 1988 (33) 455.
37. Wornat, M. J., Sarofim, A. F., and Longwell, J. P., Energy Fuels, 1987 (1) 431.
38. Aigbehinmua, H. B., Darwent, J. R., Gaines, A. F., Energy Fuels, 1987 (1) 386.
39. Wertz, D. L., Bissell, M., and Vorres, K. S., unpublished results, 1991.

FIGURE ONE. DIFFRACTOGRAMS

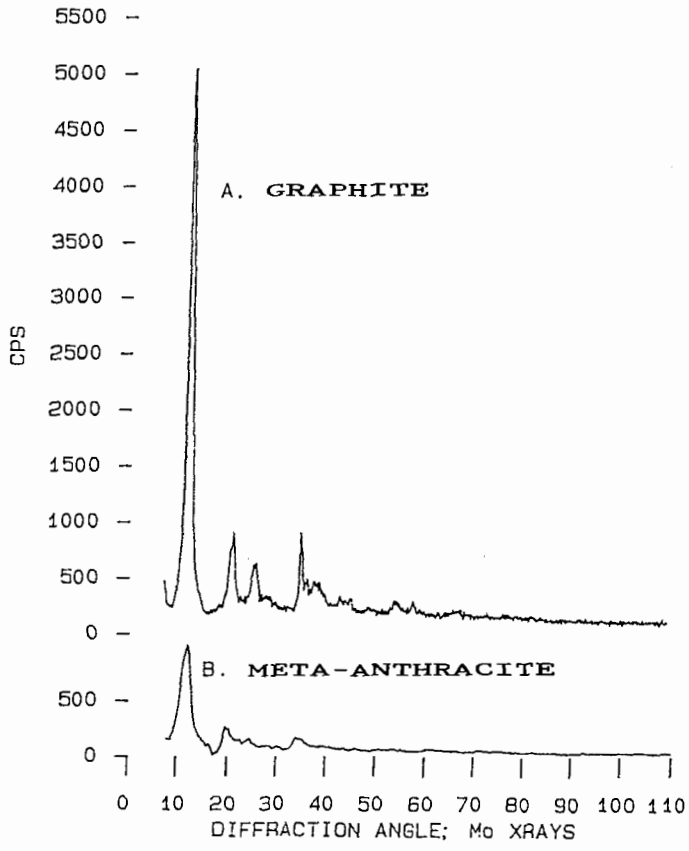

FIGURE TWO. SEPARATION OF DIFFRACTOGRAM INTO COMPONENTS

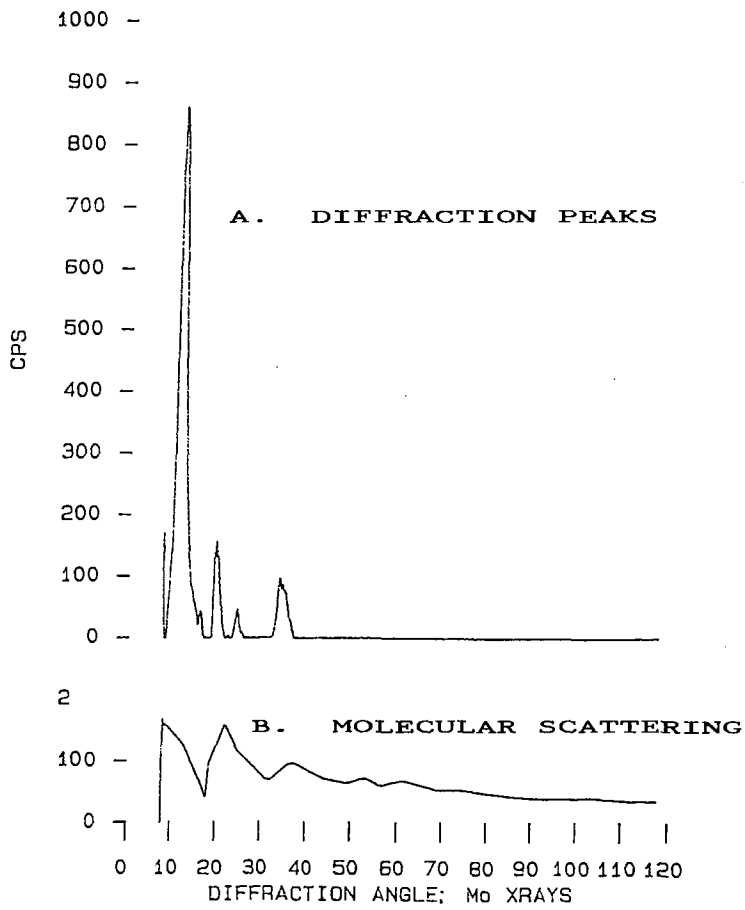

FIGURE THREE. RECIPROCAL SPACE FUNCTIONS

3A. Molecular Scattering Curve (dots)
3B. Calculated Independent Atom Scattering Curve
3C. Interference Curve

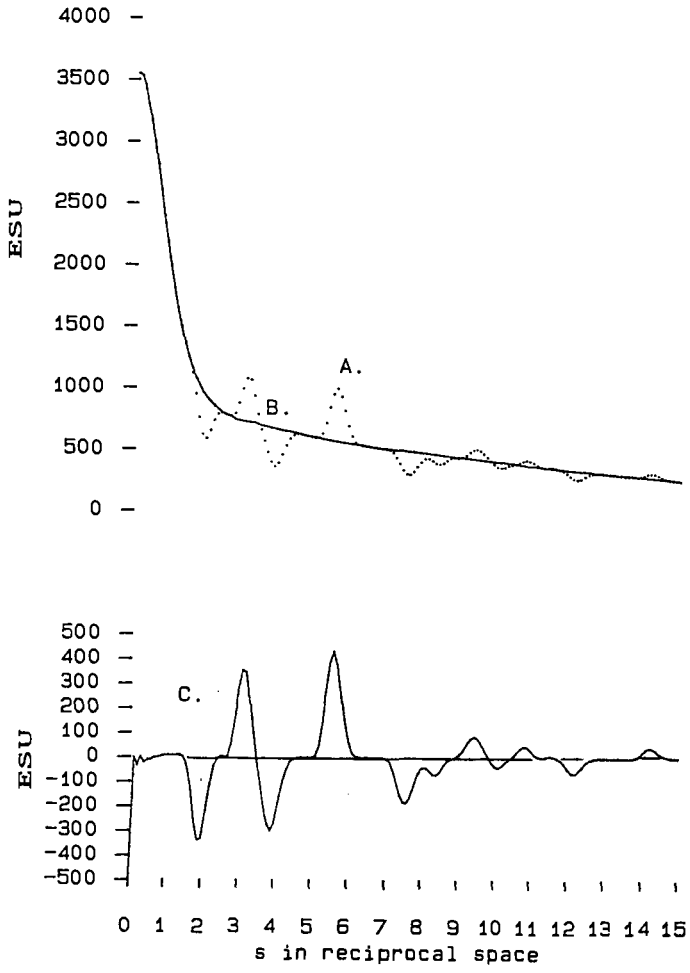

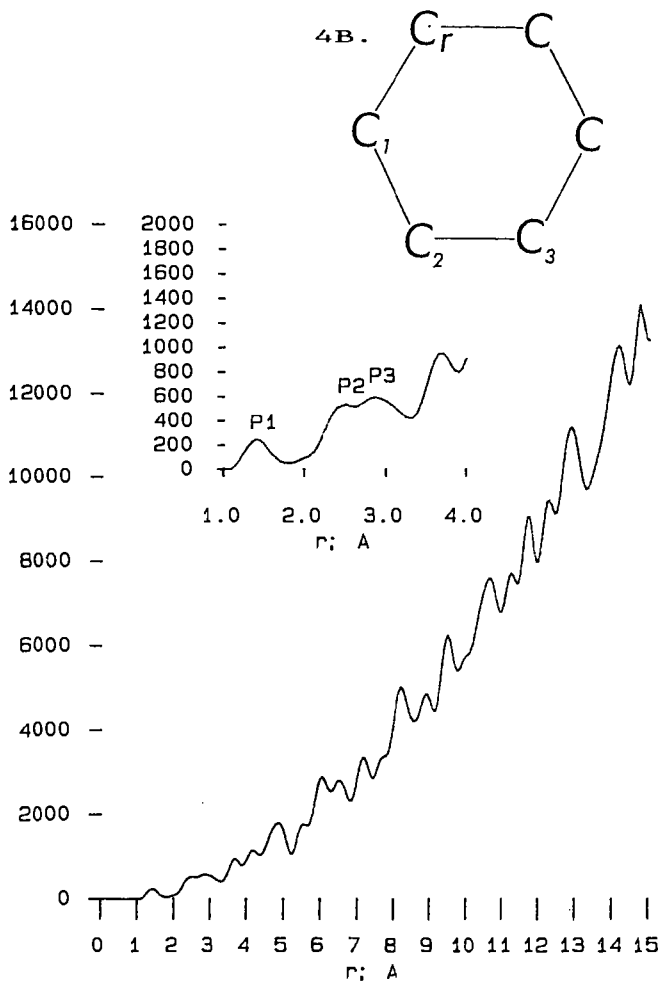

FIGURE FOUR. THE APRDF AND AN AROMATIC RING (4B)

Development of Computer-Controlled Scanning Electron Microscopy (CCSEM) Techniques for Determining Mineral-Maceral Association

G. P. Huffman, N. Shah, and F. E. Huggins, 233 Mining & Mineral Res. Bldg., University of Kentucky, Lexington, KY 40506-0107
and
G. S. Cassucio and W. J. Mershon, RJ Lee Group, Inc., 350 Hochberg Rd., Monroeville, PA 15146

I. INTRODUCTION

The solutions to several important problems in coal science depend critically on being able to determine mineral-maceral association. Perhaps the most obvious of these is physical coal cleaning. Liberated or nearly liberated mineral matter will normally be most easily removed in advanced physical cleaning processes, such as froth or microbubble flotation or oil agglomeration. Although the oxidation state of the coal and mineral particle surfaces also plays an important role,[1] it is generally felt that liberation is the primary factor in determining coal cleanability by physical methods.

A second topic that is receiving increasing attention is the effect of mineral-maceral association on ash slagging and fouling behavior during coal combustion.[2] Slagging behavior is usually more severe under reducing combustion conditions than under oxidizing conditions. This is primarily because ferrous iron derived from pyrite reacts more readily with clay minerals and quartz to form molten slag than does ferric iron.[3] Thus, quantitative determinations of the amounts and types of mineral matter and carbonaceous material associated together in coal particles may be useful in predicting slagging distributions on a particle by particle basis.

Recently, Straszheim, Markuszewski and coworkers[4] have succeeded in making the first quantitative measurements of the association of mineral matter with the organic coal matrix using CCSEM. By mounting the crushed coal in carnauba wax, which has an average atomic number that is somewhat lower than coal, they were able to clearly distinguish between the mounting medium and the coal in the backscatter electron imaging (BEI) mode. A CCSEM automatic image analysis (AIA) procedure was used to determine the amounts of different minerals and the amount of organic matter ("coal") associated with each particle on a particle by particle basis. This allowed them to determine the amounts of each major mineral (pyrite, kaolinite, illite, etc.) associated with various amounts of coal (0 - 20%, 20 -40%, etc.).

In the current research, we have investigated mineral-maceral (the term "maceral" is used here in the generic sense) association using a somewhat different approach. Specifically, we are attempting to combine the use of a digital imaging technique called "microimaging"[5,6] with ternary and quaternary representations[7,8] of particle chemistry determined from energy dispersive x-ray (EDX) spectra obtained using a light element detector. The results indicate that this approach is rather promising.

II. EXPERIMENTAL PROCEDURE

Ternary diagram representation of CCSEM EDX data has proven to be very useful in allowing graphic interpretation of trends that develop in particle chemistry as a result of various types of processing or reaction. Previously, we have used this method for investigating reactions that occur between different minerals during coal combustion[7,8] and carbonization[9]. Briefly,

three elements are selected and one or more thresholds are set as a basis for admitting a given particle into the data set. For example, in the current investigation, mineral-maceral association is of primary interest, so we have examined C - S - Fe diagrams, which are representative of pyrite - coal maceral association. The approximate chemical compositions of the particles are calculated from the raw EDX spectra using the background-subtracted peak areas. Several variations on this basic presentation proved to be very useful. For example, the sum of two or more elements can be used as a vertex and the diagram C - (Fe + S) - (Al + Si) is effectively a coal - pyrite - clay/quartz diagram. Additionally, the number or percentage of particles in a given compositional increment can be displayed in a four dimensional graph, which provides a much more vivid representation of the particle-by-particle compositional trends. Such frequency-composition dependence may also be presented in binary form across any linear strip of the ternary diagram. Finally, particle size histograms for any user-selected composition range are readily generated in a cursor-window mode.

The coals investigated in this study were Illinois #6 samples obtained from the Argonne Premium Coal Sample Bank (APCSB)[10] and from the University of Kentucky Center for Applied Energy Research (CAER).[11] The APCSB coal was hand ground to 100% -200 mesh (<75 microns) before investigation; a simple laboratory cleaning process was used for this sample, which consisted of floating the coal in carbon tetrachloride and centrifuging. The CAER sample was micronized to <10 - 20 microns and cleaned using a column flotation process discussed in detail elsewhere.[12]

One method of sample preparation used was essentially identical to that developed by Straszheim et al.;[4] that is, the coal powder was mixed with molten carnauba wax, pressed into a pellet in a hydrostatic press, and polished using petrographic methods with diamond paste (< 1 micron) finish. The second method consisted of dispersing the particles directly onto a beryllium (Be) substrate.

The basic CCSEM analysis is conducted in the usual manner,[13,14] by moving the electron beam over the sample in discrete increments, measuring the backscattering electron intensity (BEI) at each stopping point, and collecting an energy dispersive x-ray spectrum (EDX). In the current work, the discrimination level discerning particles from background was set low enough to allow coal maceral material to be detected, as opposed to the usual CCSEM mode for coal[13,14], in which only minerals are detected. The EDX spectra were then collected over a period of 15 seconds while the electron beam was rastered over the whole coal particle. Since a light element detector was used, the resulting EDX spectra were characteristic of whole coal particles, including both mineral and maceral material. An additional novel feature of the current work was the simultaneous acquisition and storage on disks of digital images of all particles, a procedure called microimaging,[5,6] which will be addressed in a future paper.

III. RESULTS AND DISCUSSION

The principal results are best summarized by perspectively plotted phase diagrams in which number percentage is shown as a fourth, vertical dimension. The C-S-Fe diagrams in figures 1 and 2 illustrate the degree of liberation of pyrite in the -200 mesh Illinois No. 6 coal and the extent of its removal in a simple laboratory cleaning operation, centrifugation in carbon tetrachloride. These diagrams have been drawn using a rather low threshold value of C + S + Fe > 15%; therefore most of the coal particles examined are represented in the diagrams. It is seen by comparison of Figures 1 and 2 that the two sample preparation methods gave results that are qualitatively similar. Presumably, the samples prepared by dispersal of the coal particles onto beryllium give EDX spectra that are more characteristic of the coal particle surfaces than the polished carnauba wax samples, since the electron beam penetrates only a few

microns into the coal and the particles in the polished specimens are cross-sectioned, on average. This suggests that the distribution of pyrite on the surfaces of the crushed coal particles is not markedly different from its bulk distribution for this particular coal.

It is evident that most particles containing < 30 - 40% C on the basis of the EDX spectra have been removed in the cleaning operation. It must be noted, however, that the compositions shown in these diagrams have not been corrected for preferential absorption of the low energy carbon X-rays (277 eV) relative to the absorption of the higher energy sulfur (2308 eV) and iron (6404 eV) X-rays, which occurs primarily in the thin window of the light element detector. Such corrections are important if we wish to use such diagrams as quantitative composition guides. For example, the particles having compositions along the C-S border represent coal particles that contain primarily organic sulfur. With appropriate calibration of the relative strengths of the C and S X-rays, such data could be used to make direct measurement of the organic sulfur content on a particle by particle basis.

An alternative way of presenting the data is shown in Figures 3 to 5. Here, the corners of the diagram are C, (Fe + S), and (Al + Si), and the threshold is taken as 80%. As seen from the number of particles plotted, this encompasses nearly the whole data set. With this representation, the vertexes for these diagrams are effectively coal (that is, mineral free coal particles), pyrite, and clay plus quartz (Figures 3 - 5). This representation has the advantage of illustrating the efficiency of a given cleaning process for removing all of the major minerals in coal, not just pyrite. It is seen from the perspectively plotted ternary diagrams (Figures 3 - 5) that the two methods of sample preparation give results that are significantly different for the clay/quartz abundance in the as-crushed coal. Presumably, this indicates that this coal fractures most easily along clay-coal interfaces. This would cause the sample prepared by dispersion of the coal particles onto beryllium to exhibit a higher percentage of clay/quartz rich particles than the polished carnauba wax-mounted specimen, since the EDX spectra are derived primarily from the top 1 - 2 microns of the coal. The results for the cleaned coals are again qualitatively similar for the two sample preparations, with most of both the pyrite and clay/quartz having been removed.

A sample of Illinois No. 6 coal was also examined before and after a column froth floatation cleaning process described in more detail elsewhere.[12] Only the sample preparation method of dispersing coal particles onto a beryllium disk was used for these samples. Results for the feed coal, which is micronized to < 10 to 20 microns, are shown in the top half of Figure 11. It is seen that these coal particles exhibit a heavy preponderance of clay minerals, again indicating a tendency of the coal to fracture at coal-clay interfaces. In the column floatation process, both the ash and pyritic sulfur are dramatically reduced, as shown by the perspective ternary diagram in the bottom half of Figure 5.

Such CCSEM diagrams could be very useful in predicting cleaning behavior of individual mineral species. One can easily envision cases where it is easier to remove pyrite than clays and quartz and vice-versa. Certain types of cleaning operations could then substantially change the slagging and fouling behavior of a coal.

IV. SUMMARY AND CONCLUSIONS

In this research, the feasibility of determining mineral-maceral ("maceral" is used in the generic sense) association using four-dimensional ternary composition - number percentage diagrams generated from CCSEM data has been investigated. The results indicate that this approach is promising. The degree of liberation of pyrite and its removal during physical cleaning is perhaps most clearly illustrated by perspectively plotted C - S - Fe diagrams with number percentage shown as a fourth vertical ordinate (Figures 1 and 2). Alternatively, a C -

(Fe + S) - (Al + Si) ternary diagram is effectively a coal - pyrite - clay/quartz ternary. Four dimensional frequency of occurrence - coal - pyrite - clay/quartz diagrams (Figures 3 - 5) illustrate the degree of liberation and removal during cleaning of most of the principal minerals in coal. They also indicate a marked tendency of Illinois #6 coal to fracture at coal - clay interfaces.

Future papers will discuss other aspects of this work, including particle size distributions, direct measurement of organic sulfur content and variation, and analysis of stored digital particle images.

ACKNOWLEDGEMENT

The authors would like to acknowledge the support of the U.S. Department of Energy under DOE Contract No. DE-FG02-90ER8079.

REFERENCES

1. Attia, Y.A.; Elzeky, M.; and Ismail, M.; Processing and Utilization of High-Sulfur Coals III, Eds., R. Markuszewski and T.D. Wheelock, 1990, Elsevier, 187 - 196.
2. Helble, J.J.; Srinivasachar, S.; and Boni, A.A.; Idealized Combustion Determination of Ash Particle Formation and Surface Stickiness; Task 8 - Model Development and Integration, Phase I Final Report, U.S. DOE Contract No. DE-AC22-86PC90751, March, 1990, pp.8-1 to 8-195.
3. Huffman, G. P.; Huggins, F. E.; and Dunmyer, G. R.; Fuel, 60 585-597 (1981).
4. Straszheim, W.E.; and Markuzewski, R.; Energy & Fuels 1990, 4, 748-754.
5. Schwoeble, A. J.; Dalley, A. M.; Henderson, B. C.; and Casuccio, G. S.; Journal of Metals, August 1988, pp. 11-14.
6. Casuccio, G. S.; Schwoeble, A. J.; Henderson, B. C.; Lee, R. J.; Hopke, P. K.; Sverdrup, G. M. "The Use of CCSEM and MicroImaging to Study Source/Receptor Relationships." Receptor Models in Air Resources Management, Air Pollution Control Association, Pittsburgh, PA, 1989.
7. Huffman, G.P.; Huggins, F.E.; Shah, N.; and Shah, A.; Prog. in Energy & Combustion Sci., 1990, 16(4), 243-252.
8. Shah, N.; Huffman, G.P.; Huggins, F.E.; Shah, A; Mershon, W.J.; and Casuccio, G. "Graphical Representation of CCSEM Data for Coal Minerals and Ash Particles." To be published in ACS Div. of Fuel Chem. Preprints, Atlanta Meeting, April, 1991.
9. Huffman, G. P.; Huggins, F. E.; Shoenberger, R. A.; Walker, J. S.; Greegor, R. B. and Lytle, F. W.; Fuel 65, 621-632 (1986).
10. Vorres, K.S. Users Handbook for the Argonne Premium Coal Sample Program, Oct. 1, 1989.
11. Samples provided by B.K. Parekh of the University of Kentucky Center for Applied Energy Research.
12. Parekh, B.K.; Groppo, J.G.; Stotts, W.F.; and Bland, A.E.; Column Floatation 88, Chapt. 24, 227-233.
13. Huggins, F. E.; Kosmack, D. A.; Huffman, G. P.; and Lee, R. J.; Scanning Electron Microscopy/1980/I, 531-540, SEM Inc., AMF O'Hare, Chicago, IL 60666, USA.
14. Huggins, F. E.; Huffman, G. P.; and R. J. Lee, ACS Symposium Series No. 205, pp. 239-258, Coal and Coal Products: Analytical Characterization Techniques, Ed., E. L. Fuller, Jr., American Chemical Society, 1982.

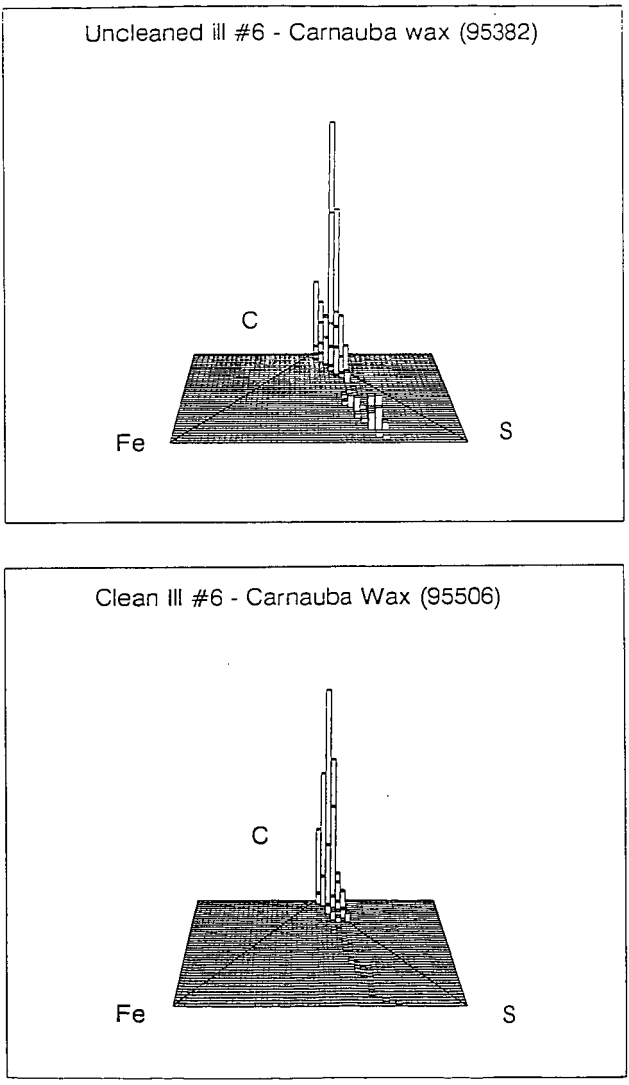

Figure 1. CCSEM number percentage (vertical ordinate) versus composition in a ternary C-Fe-S diagram for raw (top) and cleaned (bottom) Illinois #6 coal mounted in carnauba wax.

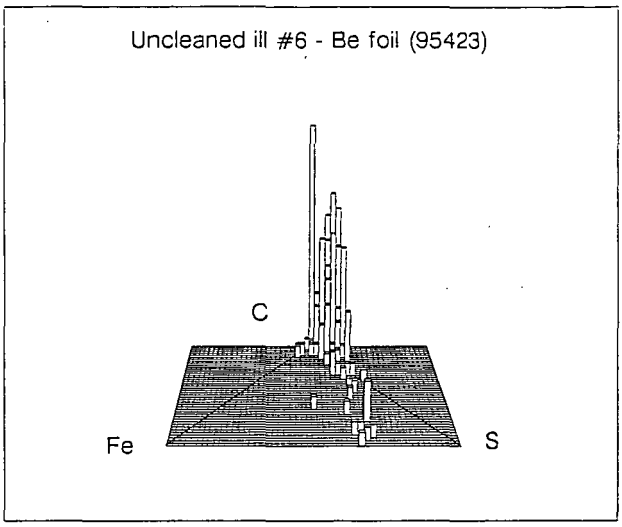

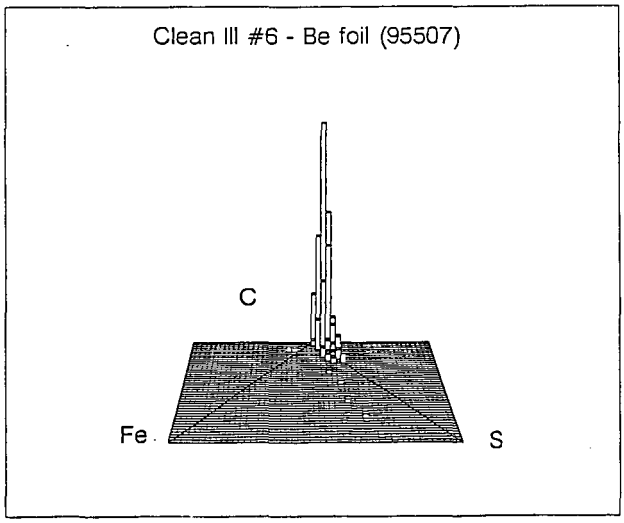

Figure 2. CCSEM number percentage - composition data for raw and cleaned Illinois #6 coal dispersed on beryllium.

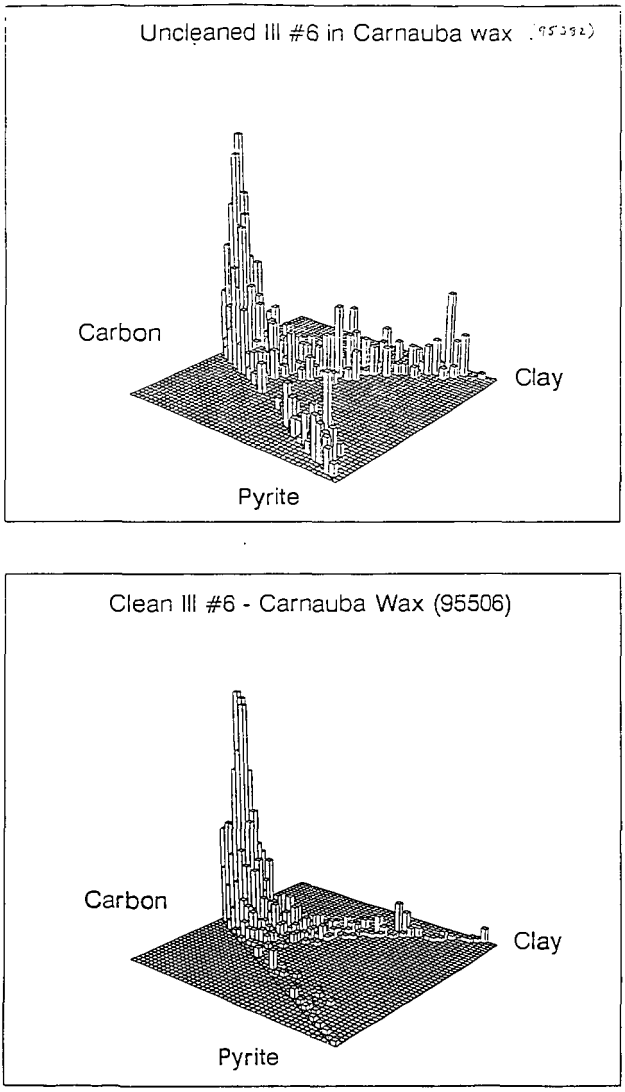

Figure 3. CCSEM number percentage vs. composition in a coal (C) - pyrite (Fe + S) - clay/quartz (Al + Si) diagram for raw (top) and cleaned (bottom) Illinois #6 coal mounted in carnauba wax.

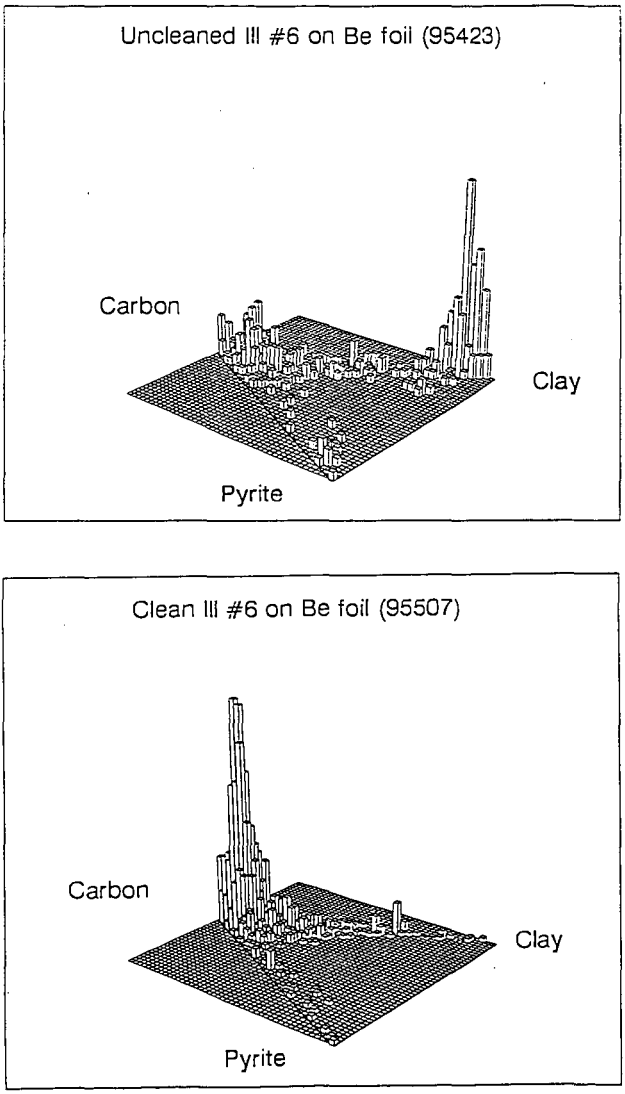

Figure 4. CCSEM number percentage vs. "composition" in a coal-pyrite-quartz/clay diagram for raw (top) and cleaned (bottom) Illinois #6 dispersed on beryllium.

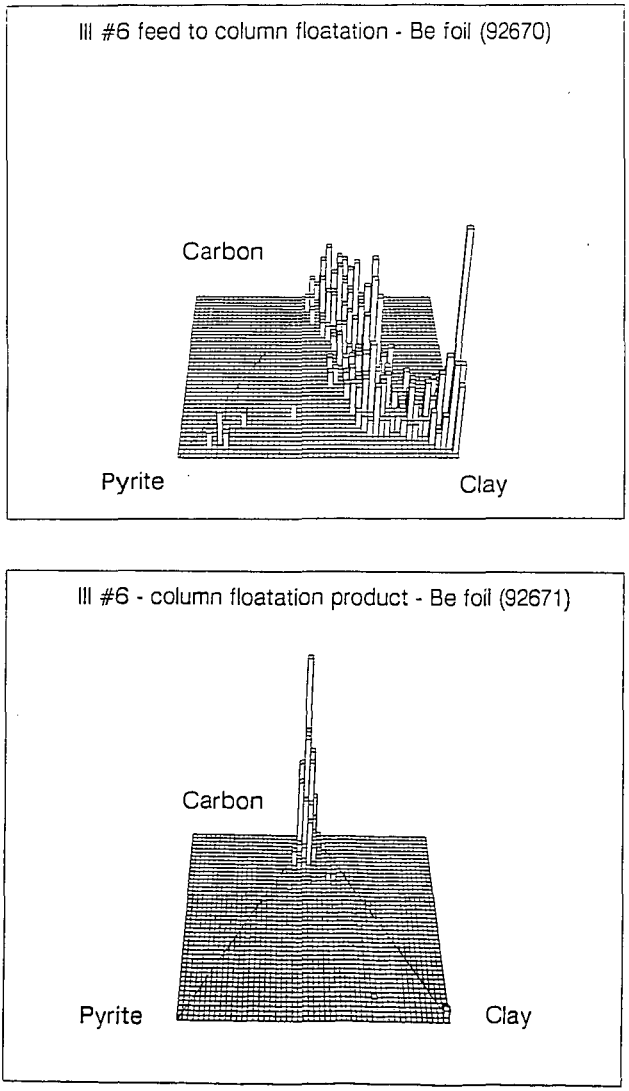

Figure 5. CCSEM number percentage vs. coal-pyrite-clay/quartz composition for Illinois #6 coal before and after column floatation cleaning.

Application of Fluorescence Microscopy to Coal-Derived Resid Characterization

R.F. Rathbone, J.C. Hower and F.J. Derbyshire
Center For Applied Energy Research, Lexington, Kentucky 40511-8433
Keywords: Microscopy, Fluorescence, Resid

INTRODUCTION

This study evaluates the usefulness of a fluorescence microscopy methodology to analyze coal-derived resids and interpret the data in the light of liquefaction processing conditions, process response, the inferred resid reactivity, and in relation to results of other analytical data. The fluorescence technique utilized has been widely applied to coal and kerogen characterization, albeit with some modifications, but is novel in its application to the characterization of coal liquids.

Fluorescence is the emission of light energy which occurs when electrons, having been excited to a higher energy orbital, return to their lower energy ground state. The majority of organic molecules that fluoresce are those with conjugated double bonds (chromophores), such as aromatics, characterised by pi-electrons less strongly bound within the molecule than sigma electrons, that can be excited to anti-bonding pi-orbitals (1,2,3). Increasing the extent of pi-bond conjugation (i.e. larger molecular size) generally imparts a shift in absorption and emission spectra to longer wavelengths. Resid fluorescence largely depends on the concentration and degree of conjugation of aromatic chromophores in the high molecular weight liquids, possibly with ancillary effects from oxygen functionalities. In this context, fluorescence analysis of liquefaction resids can potentially evaluate process performance, since direct liquefaction processes endeavor to break down the macromolecular structure of coal, and reduce the molecular weight of polycondensed aromatics through hydrogenation, the opening of ring structures, and heteroatom removal.

EXPERIMENTAL

Composited Wilsonville CC-ITSL resid samples (combined samples from an entire liquefaction run) received from Consolidation Coal Co., Pittsburgh, PA, consisted of eight non-distillable (at 850°F* or 454°C*) coal liquids (resid) from runs 251-II, 259, 250, and 257. In addition, four pressure filter liquids (PFL) were supplied from the HRI ITSL bench unit, Run I-27 (Table 1). The Wilsonville resids are designated as "interstage" (sampled between the first and second reactor stages) and "recycle" (sampled after the second reactor stage). Samples from HRI Run I-27 are designated with a number representing the sampling day (e.g. PFL P2 = run day 2). Each resid sample was added to several drops of cold setting epoxy resin (with hardener), placed into an epoxy pellet cavity, and allowed to harden. After setting, the sample surface was ground and polished by hand on a rotating lap using a series of grinding papers and alumina polishing compounds.

Fluorescence emission from the resids' polished surface was measured with a Leitz MPV Compact microscope photometer, equipped with a diffraction grating monochromator, a photomultiplier tube, and a 100 W mercury arc lamp (as an excitation source). A Leitz Ploemopak vertical illuminator, housed the necessary filters for ultraviolet-violet (355 to 425nm) illumination, and supported a 50X air immersion objective in the light path. The microscope photometer was interfaced with a computer for data acquisition. Fluorescence spectra were acquired, in argon gas to inhibit photo-oxidation during the analyses, by recording fluorescence intensities every 2.5nm (nominal resolution of 5nm) from 470nm to 700nm. The fluorescence emission from a selected area of resid was scanned 20 times and averaged to get one spectrum per resid particle. Raw spectral data were normalized, a correction factor applied, and then re-normalized so the maximum intensity equaled 100%. The

uncorrected spectra were used to assess fluorescence intensity differences between samples by calculation of the area beneath the spectra. Unlike other chemical analysis methods employed to characterize the liquefaction resids (e.g. refs. 4 & 5), the precision was difficult to evaluate due to inherent variabilities within the Wilsonville resid samples. However, results from replicate fluorescence analyses on the optically homogeneous pressure filter liquids from HRI Run I-27 indicated that fluorescence spectra are repeatable within 3 to 4 nm.

The random reflectance at 546nm off a polished resid surface was obtained utilizing the same microscope photometer employed for fluorescence analysis. A 100 W tungsten-halogen lamp was the illuminant, and isotropic glass standards were used for system calibration. Reflectance analyses were conducted in air immersion because of observed interactions between the resids and microscope immersion oil.

III. Results and Discussion

A. Interstage vs. Recycle Resids

Run 251-II (Wyodak coal, T/C) Fluorescence spectra from the Run 251-II interstage and recycle resid samples are shown in figure 1a, and reveal a shift of the recycle resid fluorescence spectra to shorter wavelengths (spectral "blue shift") compared to the interstage resid. A small, discrete portion of the recycle resid, not shown, displayed a relatively intense yellow fluorescence with an wavelength of maximum intensity (Lmax) of 578 nm. It is possible that it represents one of the three pasting solvent components from the V131B solvent surge tank that was incompatible with the other two components. The mean random reflectance of resids from Run 251-II decreased slightly from the interstage to recycle sample, and, analagous to vitrinite reflectance (6), is considered to represent a decrease in the degree of aromatization and condensation of the recycle resid.

Run 250 (Illinois #6 coal, T/C) A fluorescence spectral "blue shift" and fluorescence intensity increase was recorded for the Run 250 recycle resid compared to its interstage equivalent (Figure 1c). Mean reflectances of the resids decreased by 0.54% from the interstage to recycle sample (Table 1). The difference is significant, as it is greater than 3 standard deviations from the mean values of each sample.

Run 257 (Illinois #6 coal, C/C) Qualitative observations of resid fluorescence revealed substantial variations in these samples, represented quantitatively in figure 1d as two general fluorescence "populations". The origin of this fluorescence variability is not yet known. However, figure 1d does show that, like the Run 251-II and Run 250 resids, the recycle resid fluorescence spectra are at shorter wavelengths than the interstage spectra. The mean resid reflectances from Run 257 decreased by 0.34% from interstage to recycle.

Accompanying the fluorescence "blue shift" of the recycle resids compared to their interstage equivalents, is a decrease in the percentage of aromatic protons, an increase in beta+gamma (≈ aliphatic) protons, and a shift of the phenol peak location to higher wavenumbers (smaller aromatic ring size) in the recycle sample (Table 1). The fluorescence and chemical data from the Run 251-II and 250 resids suggest that the catalytic second stage provided considerable upgrading of resid produced in the thermal liquefaction unit (TLU). This is not unexpected since it is generally considered that the primary role of the first stage TLU is to dissolve the coal (and recycled resid), whereas the second stage upgrades the first stage products (7). Resid from the first stage is derived from the recycle solvent and coal that has been processed for the first time, whereas resid sampled after the second stage catalytic reactor is mainly derived from coal liquids and a much smaller proportion of unreacted coal. It is therefore plausible that the catalytically hydrogenated recycle resid sample displayed a more intense fluorescence, at shorter wavelengths than the interstage sample, indicating the presence of less condensed, lower molecular weight aromatic structures. A similar interpretation is suggested for the Run 257

(catalytic/catalytic) resids: the catalytic second stage has upgraded the products from the catalytic first stage, consistent with the suggestion that some aromatics from the first stage reactor resid product were hydrogenated to less condensed structures.

The selective rejection of preasphaltenes in the critical solvent deasher (CSD) might also have effected the observed fluorescence properties of the Wilsonville resids. A preferential removal of condensed, high molecular weight aromatics can occur in this processing stage, and would contribute to a fluorescence intensity increase and spectral blue shift of the recycle resid.

Run 259 (Pittsburgh coal, C/C) Similarities in the average fluorescence spectra (Figure 1b) and intensities of the interstage and recycle samples suggest that the second catalytic stage in Run 259 did not substantially alter the overall molecular size or concentration of aromatics after the resid had been through a catalytic first stage. The recycle resid exhibited a reflectance slightly lower than that of the interstage sample, although the reflectance values were nearly within one standard deviation of each sample. The minor changes in fluorescence and reflectance properties between the interstage and recycle samples correspond to other chemical properties. The data revealed only a slight decrease of aromatic protons in the recycle sample, and a small increase in beta+gamma proton content.

B. Comparisons Between Wilsonville Runs

The comparisons of the interstage and recycle resid fluorescence properties suggest the spectral distribution and intensity are potential indicators of liquefaction process performance. Strongly bonded high molecular weight condensed aromatic structures, that are likely to be more refractory to upgrading than lower molecular weight less condensed aromatic compounds, would exhibit fluorescence with a low intensity, at comparatively long wavelengths. Conversely, intensely fluorescing resids with spectral distributions at shorter wavelengths are inferred to be relatively reactive to further upgrading.

Interstage Resids The fluorescence spectra of the interstage resids (Figure 2a) suggest the products from Run 259 (Pittsburgh coal, C/C) and Run 251-II (Wyodak coal, T/C) are the least reactive, with relatively low fluorescence intensities, and fluorescence peaks at 700nm or greater. The Run 259 resid is assumed to be comprised of larger, more condensed aromatic structural units than the resid produced in Run 251-II, as indicated by a low fluorescence emission in the 470nm to approximately 600nm region. Proton NMR data indicate the interstage resid from Run 259 has approximately the same percentage of total aromatics as the Run 251-II counterpart, although the latter has relatively more uncondensed aromatics than Run 259 resid. This is not unexpected considering the differences between the two feedstocks: product derived from the subbituminous Wyodak coal is expected to contain smaller, less condensed aromatic structural units than the bituminous-rank Pittsburgh coal. The Run 250 (Illinois #6 coal, T/C) interstage resid has a fluorescence spectrum that is shifted to shorter wavelengths than that of the Run 251-II (Wyodak coal, T/C) or Run 259 (Pittsburgh coal C/C), with an average intensity that is slightly greater than or equal to Run 251-II, but significantly lower than the Run 259 resid. Relative to Run 259, interstage resid from Run 250 was slightly more aromatic (from NMR data in Table 1), contributing to a fluorescence intensity reduction. However, it contains relatively fewer condensed aromatics and more uncondensed aromatics than the interstage resid from Run 259 (hvAb feedstock), probably causing the observed spectral "blue-shift" of the Run 250 resid.

Despite the variability in fluorescence properties of the Run 257 (Illinois #6 coal, C/C) interstage resid (Figure 2a), it is evident that the fluorescence emission of this product is substantially shifted to shorter wavelengths

relative to the other Wilsonville interstage samples investigated. In addition, the total interstage resid composite was substantially less aromatic than the other Wilsonville interstage resids (>10% difference in aromatic protons), with evidence of overall smaller aromatics (phenol peak shifted to higher wavenumbers). The reflectance percent was also significantly lower than the other Wilsonville resids (Table 1), probably due to the lower aromatic content and reduced condensation of the aromatic molecules.

Recycle Resids Between the runs, similar relationships hold for the fluorescence properties of the recycle resids as for their interstage equivalents, figure 2b. As shown in the figure, the average fluorescence spectrum from the Run 251-II (Wyodak coal, T/C) recycle resid was somewhat similar to that from Run 250 (Illinois #6 coal, T/C). Compared to the other Wilsonville resids studied, the Run 257 recycle resid contained the lowest concentration of aromatic protons, while it also had the highest percentage of beta+gamma protons and the phenol peak at a higher wavenumber (3302 cm^{-1}) (Table 1).

C. HRI Run I-27 Resids

The wavelength of maximum intensity (Lmax) of the Run I-27 resids was substantially shifted to longer wavelengths from sample PFL P2 to PFL P18 (Figure 3a), along with a monotonic reduction in relative intensity at the shorter wavelengths, indicating aromatic ring condensation increased as the run progressed. Figure 3b indicates that sample PFL P2 had the greatest average fluorescence intensity, whereas sample PFL P25 had the lowest intensity, suggesting an increased concentration of aromatic chromophores (causing an increase in energy delocalisation) occurred over the course of the run. There was also a progressive increase of resid reflectance from sample PFL P2 to P25. The trends exhibited by the fluorescence and reflectance properties are accompanied by systematic chemical changes. From sample PFL P2 to P25, there is a monotonic increase in percent aromatics, a decrease in beta+gamma proton concentrations, and a shift in phenol peak frequency from 3305 to 3296 cm^{-1} (Table 1), indicative of increasing ring condensation.

The fluorescence "red-shift", intensity decrease, and increase in resid reflectance percent over the course of Run I-27 suggest that, with an increase in age, the catalyst became less effective in upgrading the non-distillable fraction of coal liquids to low molecular weight, less aromatic products as aromatic ring hydrogenation became less pronounced during the run. A possible cause of these deleterious changes in resid properties over the course of the run is the partial deactivation of catalyst from deposition of carbonaceous materials onto the catalyst surface, which is believed to occur most rapidly in the early stages of the liquefaction run (8). Other process variables that may have influenced resid fluorescence and chemical properties include increased reactor temperatures, a solvent/coal ratio reduction, and an increase in the solvent cut-point (9).

VI. Summary and Conclusions

Quantitative fluorescence microscopy is potentially a rapid, inexpensive technique which can provide new insight into the structure and composition of coal-derived resid, and could lead to more effective process control. Perhaps the greatest strength of quantitative fluorescence microscopy is its ability to resolve inhomogeneities within coal-derived resid samples, including, but not limited to, minerals, unreacted macerals, and multiple resid phases. This capability is not possible with most other analytical techniques which typically require resid dissolution in a solvent prior to analysis. Whereas these analytical techniques provide chemical and structural information on a homogenized resid sample, and only on the soluble portion, inherent variability within the coal liquids can be identified and measured with fluorescence microscopical methods.

Acknowledgements

This work was supported by subcontract from Consolidation Coal Co. under U.S. Department of Energy Contract No. DE-AC22-89PC89883.

VII. References

(1) Bridges, J.W., In Luminescence in Chemistry (Ed. E.J. Bowen), D. Van Nostrand Co., 1968, pp. 77-115.
(2) Wehry, E.L., In Fluorescence: Theory, Instrumentation and Practice (Ed. G.G.Guilbault), Marcel Dekker, 1967, pp. 37-132.
(3) George, G., In Luminescence Techniques in Solid State Polymer Research (Ed. L. Zlatkevich), Marcel Dekker, 1989, 318 pp.
(4) Robbins, G.A., Winschel, R.A. and Burke, F.P., Am. Chem. Soc. Div. Fuel Chem.Prepr., 1985, 30(4), pp. 155-163.
(5) Winschel, R.A., Robbins, G.A. and Burke, F.P., Fuel, 1986, 65, pp. 526-532.
(6) McCartney J.T. and Teichmuller, M., Fuel, 1972, 51, pp. 64-68.
(7) Derbyshire, F.J., Varghese, P. and Whitehurst, D.D., Fuel, 1983, 62, pp. 491-497.
(8) Derbyshire, F.J., Catalysis in Coal Liquefaction: New Directions for Research, IEA Coal Research, 1988, 69 pp.
(9) Consolidation Coal Co., personal communication to authors.

Table 1

Run No.	Coal	Sample[1] Type	Proton NMR Data[2] Arom. (%)	Bet+Gam (%)	Peak[3] (cm^{-1})	Reflectance[4] (%)	s.d.
251-II	Wyodak	T/C, Int	33.2	37.6	3294	7.80	0.22
251-II	Wyodak	T/C, Rec	26.8	44.8	3298	7.66	0.25
259	Pittsburgh	C/C, Int	33.3	35.6	-	7.82	0.11
259	Pittsburgh	C/C, Rec	31.5	40.2	-	7.70	0.26
250	Illinois #6	T/C, Int	34.5	35.3	3292	7.84	0.13
250	Illinois #6	T/C, Rec	26.1	45.2	3299	7.30	0.15
257	Illinois #6	C/C, Int	21.8	49.5	3300	6.82	0.20
257	Illinois #6	C/C, Rec	19.9	52.0	3302	6.48	0.19
I-27	Illinois #6	C/C, Day 2	14.5	57.3	3305	6.21	0.12
I-27	Illinois #6	C/C, Day 8	20.7	51.0	3301	6.80	0.07
I-27	Illinois #6	C/C, Day 18	29.2	40.5	3297	7.57	0.14
I-27	Illinois #6	C/C, Day 25	38.3	32.8	3296	8.06	0.08

1. T/C = thermal/catalytic, C/C = catalytic/catalytic, Int = interstage resid, Rec = recycle resid
2. Arom. = aromatic protons, Bet+Gam = beta and gamma protons (ref. 5)
3. Peak = FTIR phenol peak location (see ref. 4)
4. (%) = mean reflectance %, s.d. = standard deviation

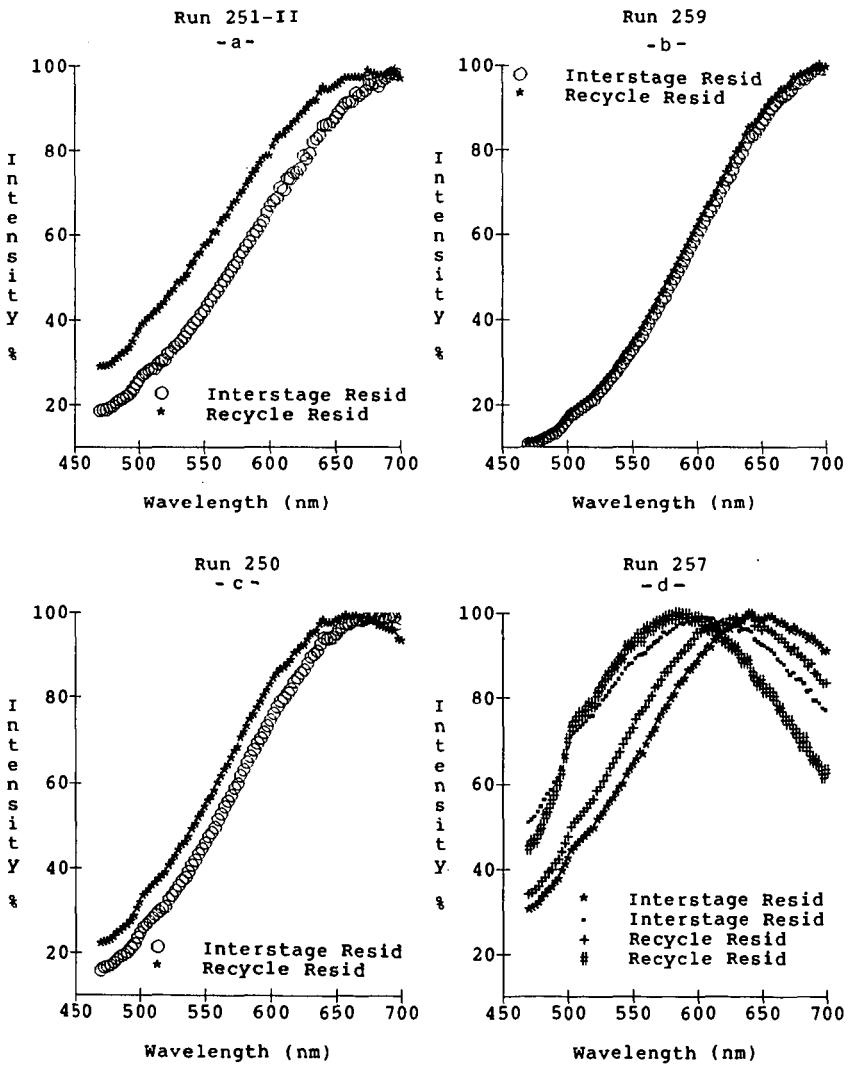

Figure 1. Corrected fluorescence spectra of resids from Run 251-II (a), Run 259 (b), Run 250 (c), and Run 257 (d). Data for each resid sample represent the average of five spectra.

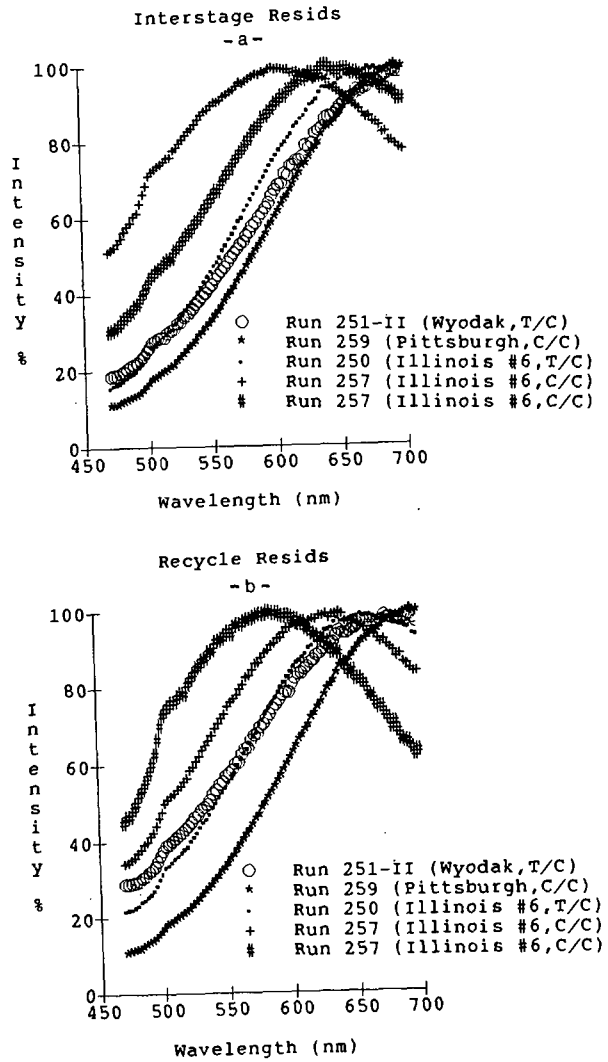

Figure 2. Corrected fluorescence spectra for the Wilsonville interstage (a) and recycle (b) resids. Data for each resid sample represent the average of five spectra.

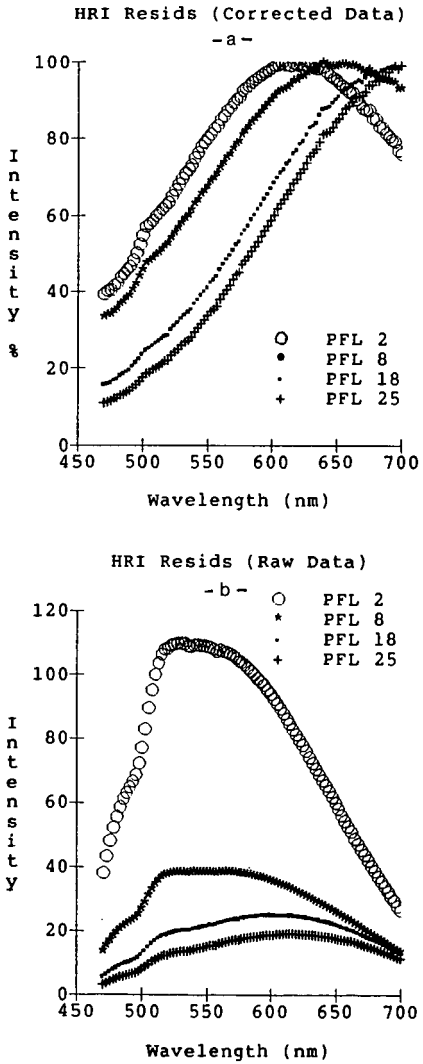

Figure 3. Corrected (a) and uncorrected (b) fluorescence spectra for HRI Run I-27 PFL resids. Data for each resid sample represent the average of five spectra.

THE APPLICATION OF ADVANCED ANALYTICAL TECHNIQUES TO DIRECT COAL LIQUEFACTION

Susan D. Brandes, Richard A. Winschel, Francis P. Burke
CONSOLIDATION COAL COMPANY
Research & Development
4000 Brownsville Road
Library, PA 15129

Keywords: Liquefaction, Analytical Techniques

INTRODUCTION

Direct coal liquefaction is a complicated and ill-defined chemical process. In order to promote coal liquefaction as a feasible alternative-energy technology, fundamental chemical understanding of the direct liquefaction process must be obtained. There exists, however, a gap between the advanced, modern techniques of the analytical chemist and the application of those techniques by the direct coal liquefaction process developer. There are two major reasons for the existence of this gap: 1) Much research in advanced analytical chemistry concentrates on instrument development and not method application, and 2) appropriate direct coal liquefaction samples for method applications are frequently difficult to obtain.

Consol is coordinating a program designed to bridge the gap, and thus to advance our knowledge of the process chemistry of direct coal liquefaction. The program is designed to provide well-documented samples to researchers who are utilizing techniques potentially useful for the analysis of coal derived samples. The choice of samples and techniques was based on an extensive survey (1) made by Consol of the present status of analytical methodology associated with direct coal liquefaction technology. Sources of information included process developers and analytical chemists.

Identified in the survey are a number of broadly characterizable needs. These categories include a need for:

- a better understanding of the nature of the high molecular weight, non-distillable residual materials (both soluble and insoluble) in the process streams.
- improved techniques for molecular characterization, heteroatom and hydrogen speciation and a knowledge of the hydrocarbon structural changes across coal liquefaction systems.
- better methods for sample separation.
- application of advanced data analysis methods.
- the use of more advanced predictive models.
- on-line analytical techniques.
- better methods for catalyst monitoring.

Various analytical techniques currently in routine use provide a valuable, but incomplete, understanding of direct coal liquefaction process chemistry, and thus cannot fully address these needs. In this program, specific methodologies (or

techniques) potentially relevant to addressing some of these needs have been identified (Table 1). Many of these methods are new only in that they have not been fully demonstrated for their applicability to coal liquids. Other techniques are "cutting edge" and are currently under development for a number of applications, including natural product analyses. Organizations or research groups that are involved in the program are identified, in Table 1, with the method that they are employing.

Methods under consideration in this program are directed towards the characterization of the non-distillable resid portion of liquefaction oils because of the importance of this material to the liquefaction process. In current direct liquefaction technology, the heaviest soluble materials produced from the coal are recycled to near extinction. These heavy soluble materials (850°F+) typically account for 50% of the recycle stream fed to the first reactor stage in current U.S. two-stage liquefaction technology. At a 2:1 recycle stream to coal feed ratio to the first stage, the principal reactor feedstock is recycled resid, not coal. The analysis of this heaviest portion of the direct liquefaction product stream (the resid) is a much more challenging problem than analysis of the lighter materials produced by coal liquefaction. It is believed that by understanding the composition and behavior of this heavy material an improved understanding of the direct coal liquefaction process will be achieved.

PROGRAM STRUCTURE

In order to bridge the gap between the process developer and the analytical chemist and improve our fundamental understanding of the chemistry of coal conversion to liquid products, a program was organized by Consol to coordinate the distribution of well-documented direct coal liquefaction samples to evaluate potentially useful analytical techniques. The results are being evaluated in regard to the usefulness of the analytical information in adding to the chemical knowledge of the direct liquefaction process. The program is structured into two phases. In Phase I, a number of organizations were chosen to participate in the program (Table 1). Eighteen different analytical methods were incorporated into the program for Phase I. These methods are, for the most part, well established analytical techniques which are uncommon in their application to coal-derived materials. Each researcher is responsible for the interpretation of the results of the tests in light of the processing information provided by Consol with each sample. In order to provide the maximum information on any one sample, Phase I of the program was structured to use techniques which both complement and supplement each other. Phase II of the program may include expansion of Phase I tests with methods that appear to be promising, the addition of methods and techniques not considered in Phase I, and a concerted effort to tie together the methods which were chosen in Phase I. Phase II also will be the appropriate point in the program to evaluate the reliability of the analytical information from promising techniques. This may be accomplished, when practical, by round robin tests.

SAMPLES

A key to the success of the program is the proper selection of samples. Evaluation of the analytical methodologies will be based in part on the utility of the method for identifying differences in the samples which can be attributed to differences in the conditions under which the samples were produced. This may include such diverse variables as feed coal rank, reactor temperature, catalyst type, age, or use in one or both reactors (in a two-stage system), sampling point in the direct coal liquefaction plant, and whether or not the feed coal was in some way treated before liquefaction. It is necessary to provide a diverse set of samples to the analytical researcher for testing. In Phase I of the program, sample sets for each method were

chosen with large differences in production variables (Table 2). Analytical methods that cannot only distinguish among the samples, but can provide information useful for predictive purposes will be considered successful techniques.

All samples in the program come from the Consol sample bank, which includes materials from the Wilsonville, Lummus, HRI, H-Coal Pilot Plant, and UOP liquefaction and coprocessing programs. In addition, Consol continues to obtain and analyze samples from active DOE-sponsored process development programs. All samples distributed in the program were analyzed by Consol. Such analyses include (when appropriate): elemental analysis, ash content, ash elemental analysis, solubility fractionation, phenolic -OH concentration, calorific value, and hydrogen classes by ^{1}H-NMR. In addition, Consol has documented the full history of the samples (plant, process conditions, age, storage conditions, hydrogen consumption, and yield data for the associated run). Kinetic parameters were calculated for a number of the coal liquefaction runs from which samples were selected for the program. All information was supplied to the program participants to aid in the evaluation of the analytical methods.

The sample sets for the entire program were integrated so that the maximum information content can be obtained not only by judicious choice of samples for analysis by any one method, but by the application of as many of the methods as possible to a single sample. A total of eighteen different methods will be utilized in Phase I of the program. Some of these methods, for example Field Ionization Mass Spectrometry and Field Desorption Mass Spectrometry, will be used for identical samples and will yield similar information. In other cases, different analyses will provide a better understanding of the sample, for example: the use of carbonization tests to determine the propensity of the process oil to undergo retrogressive reactions will be supplemented with information on the chemical content of that oil obtained by separation technologies, such as supercritical fluid chromatography. Numerous other examples of integration of the methods exist in the program. These become apparent by examination of Table 1.

ANALYTICAL METHODOLOGIES

The analytical methodologies employed in the program are most easily discussed by categorizing them with the needs that they address. The research groups or organizations that are investigating the use of these techniques are identified in the following text; more detail can be found in Table 1.

Resid Analysis

Resids will be inspected by microscopic techniques. The Pennsylvania State University will study samples with reflectance techniques, the University of Kentucky Center for Applied Energy Research will use fluorescence techniques. Changes in reflectance of certain macerals can indicate if the material has undergone forward reaction (hydrogenation) or retrogressive reaction (condensation). Chemical analysis of resids will include various separation techniques, specifically liquid chromatography (LC), supercritical fluid chromatography (SFC), and solubility fractionation. Supercritical fluid chromatography will be employed by Virginia Polytechnic Institute to study higher molecular weight materials with limited volatility. Coupled with mass spectrometry, SFC is a powerful technique for the examination of materials with molecular weights in excess of 600 Daltons. The National Institute for Petroleum and Energy Research will use a methodology for the separation of resids into more tractable fractions for further analysis by separation based on solubility fractionation, acid/base/neutral separations, and separations based on functionality. Analysis of the resulting fractions will simplify the correlation of the behavior of the material to the process conditions.

Two potential spectroscopic techniques for resid analysis are infrared or Fourier transform infrared (FTIR) spectroscopy and mass spectrometry (both field ionization mass spectrometry (FIMS) and field desorption mass spectrometry (FDMS)). The combination of FTIR with thermogravimetric analyses (TG-FTIR), which will be done by Advanced Fuel Research, allows for the rapid spectral identification of the components of the thermally evolved material. The char remaining in the TG is subsequently burned in oxygen and CO_2, H_2O, and SO_2 are measured. Battelle PNL will employ field desorption mass spectrometry (FDMS) as another technique suitable for the direct analysis of resids. Using ionization modes such as field desorption (FD), high molecular weight samples can be ionized directly from the condensed phase without the need for vaporization by heating. SRI international will utilize FIMS (field ionization mass spectrometry) which has an advantage over other methods of ionization in that it produces molecular ions in high abundance with fragmentation occurring only rarely; thus a molecular weight profile of the material is obtained with reasonable clarity and accuracy.

Heteroatom Speciation

One of the most important problems associated with the analytical work on coal liquids is that of being able to follow and identify the heteroatom species through the process, from the feed coal to the various product streams. Determination of the functional groups important for retrograde reactions and resid reactivity is considered of paramount importance. The most difficult to detect and measure directly are the oxygenated species. A method which will be used by SRI International to attempt to track some of the oxygenated species is trimethyliodosilane derivatization. The method is a wet chemical technique for partial analysis of the oxygen functional groups in coal-derived resids. It involves the reaction of $(CH_3)_3SiI$ with alkyl carbon-oxygen bonds (ROR', ROAr, RCOOR', RCOR', RCOH, and ROH) to produce alkyl carbon-iodine bonds. Sulfoxides also react, though this is not an expected group in coal liquids. Alkyl carbon-oxygen bonds are quantified by measuring reacted iodine. A more direct technique which will be employed by Advanced Fuel Research to determine the concentration of hydroxyl groups is quantitative Fourier transform infrared spectroscopy (FTIR). In addition, qualitative analysis of the resid material by FTIR may yield information on the types of ether linkages present (oxygen linked to aliphatic or aromatic carbon).

Hydrogen Speciation and Hydrocarbon Structure

Tracking of the hydrogen in the coal liquefaction system is a formidable task. One technique which will be examined by Western Research Institute for estimation of the hydrogen consumed in hydrogenation and bond cleavage reactions, and heteroatom removal, is based on both ^1H and ^{13}C solid-state NMR. Solid-state NMR measurements can be made on whole coals, resids, and insoluble fractions obtained at different stages in the liquefaction process, and from different liquefaction processes. Two-dimensional NMR will also be applied to coal samples by Battelle PNL. A second technique which will be applied to both resids and distillates by Advanced Fuel Research is FTIR. Determination can be made of the distribution of aromatic hydrogen (whether 1, 2 or more adjacent hydrogens are on a ring), and the forms of aliphatic hydrogen (methyl, or methylene).

On-line Analyses

Methodologies for on-line analysis of liquefaction process streams are difficult to formulate. Techniques which rely on optical throughput or scattering often are not amenable to materials which are opaque or contain particulate matter. One method with some potential is FTIR. This technique has not yet been applied to coal liquefaction process streams, although it has proven useful for on-line stability measurements of jet fuels. Preliminary scoping studies by Advanced Fuel Research will show if the method is feasible.

Application of Standard Petroleum Feed Tests to Coal Liquefaction Products

A definite analytical need of the processor of coal liquefaction products is to know the refining requirements of the raw liquid products. A correlation drawn between operating variables of the finishing process and net product characteristics (in regard to specification requirements) will be extremely useful. In addition, this knowledge will provide more accurate estimations of upgrading costs to specification fuels. Although it is acknowledged that the standard petroleum feedstock tests are not tailored for the analysis of coal liquids, it is believed that they are at least a starting point for this analysis. Therefore, in a directed attempt to meet this particular analytical need, standard petroleum refinery feed analyses were performed by Conoco, Petroleum Products Research Division, on products of the Wilsonville plant.

CONCLUSION

The goal of this work is to bridge the gap between the analytical chemist and the direct coal liquefaction process developer by identifying, demonstrating, and verifying the usefulness of novel analytical techniques for the analysis of direct coal liquefaction derived materials. As described above, this program successfully matches these analytical needs and the novel analytical technologies.

ACKNOWLEDGEMENTS

This work is funded by the U.S. Dept. of Energy under contract No.DE-AC22-89PC89883

REFERENCES

1. Brandes, S.D.; Robbins, G.A.; Winschel, R.A.; Burke, F.P. "Coal Liquefaction Process Streams Characterization and Evaluation - Analytical Needs Assessment, Topical Report"; DOE Contract No. DE-AC22-89PC89883, March 1991.

TABLE 1

ANALYTICAL METHODOLOGIES

Organization Analytical Method	Samples	Variables
SRI International		
Field Ionization Mass Spectrometry (FIMS)	Distillation Resids (850°F⁺)	Coal Rank Reactor Configiguration Sampling Point
Oxygen Speciation by Derivatization	Whole Process Oils	Coal Rank Thermal Pretreatment
Battelle PNL		
2-D NMR spectroscopy	Distillation Resids (850°F⁺) Feed Coals	Coal Rank Sampling Point
Field Desorption Mass Spectrometry (FDMS)	Distillation Resids (850°F⁺)	Coal Rank Reactor Configuration Sampling Point
Supercritical Fluid Chromatography (SFC)	THF-Soluble Portion of Distillate Resids	Coal Rank Reactor Configuration Sampling Point
The Pennsylvania State University		
Gold Tube Carbonization	Distillation Resids (850°F⁺)	Coal Rank Reactor Configuration Sampling Point Thermal Pretreatment
Reflectance Microscopy	THF-Insoluble Resids	Coal Rank Reactor Configuration
Advanced Fuel Research		
FTIR	Distillation Resids (850°F⁺) THF-Soluble Portion of Distillate Resids	Coal Rank Sampling Point Catalyst Age
TG-FTIR	Distillation Resids (850°F⁺) THF-Soluble Portion of Distillate Resids	Coal Rank Sampling Point

TABLE 1 (Cont'd)

ANALYTICAL METHODOLOGIES

Organization Analytical Method	Samples	Variables
University of Kentucky/Center for Applied Energy Research		
Fluorescence Microscopy	Distillation Resids (850°F⁺) THF-Soluble Portion of Distillate Resids	Coal Rank Sampling Point Catalyst Age
Virginia Polytechnic Institute		
LC-FTIR • Sampling Point	THF-Soluble Portion of Distillate Resids	Coal Rank Reactor Configuration Ashy/Deashed Streams
SFE-SFC • Sampling Point	THF-Soluble Portion of Distillate Resids	Coal Rank Reactor Configuration Ashy/Deashed Streams
Western Research Institute		
Solid State $^{1}H/^{13}C$ NMR	Distillation Resids (850°F⁺)	Coal Rank Sampling Point
^{13}C NMR	Process Oils	Coal Rank Sampling Point
National Institute for Petroleum and Energy Research		
Acid/Base/Neutral Separation	Distillation Resids (850°F⁺)	Coal Rank Sampling Point
High-Performance Liquid Chromatography (HPLC)	Filter Liquids Process Oils	Pretreatment Coal Cleaning
2-D NMR	Distillation Resids (850°F⁺) Process Oils	Coal Rank Sampling Point
Conoco Inc., Petroleum Products Research Division		
ASTM Crude Oil Analyses	Net Product Oil	Coal Rank

TABLE 2

PROGRAM SAMPLE SET

Wilsonville Pilot Plant Samples

850°F+ Distillation Resid Samples
Runs: 250, 251, 257, 259, 255, 256, 257
Sample Streams: Recycle, Interstage, Second Stage Product

Tetrahydrofuran Insoluble of 850°F+ Distillation Resids
Runs: 250, 251, 257, 259
Sample Streams: Recycle, Interstage

Tetrahydrofuran Soluble Portion of 850°F+ Distillation Resids
Runs: 250, 251, 256, 257, 259, 260
Sample Streams: Recycle, Interstage, Second Stage Product

Whole Oil Samples
Runs: 251, 255, 257, 259
Sample Streams: Recycle, Interstage, Second Stage Product, Net Overhead Products

THF Soluble Portion of Whole Oil Samples
Run: 259
Sample Stream: Recycle

HRI Bench Unit Samples

850°F+ Distillation Resid Samples
Runs: I-27, CC-2, CC-5
Sample Streams: Pressure Filter Liquid, First Stage Process Oil
Tetrahydrofuran Portion of 850°F+ Distillation Resids
Runs: CC-2, CC-5
Sample Streams: Pressure Filter Liquid, First Stage Process Oil
Whole Oil Samples
Runs: CC-1, CC-2, CC-5
Sample Streams: Pressure Filter Liquid, First Stage Process Oil, Separator Process Overhead Distillate

Lummus Process Development Unit

850°F+ Oistillation Resid Samples
Run: 3LCF10
Sample Stream: Feed to LC-Finer

Tetrahydrofuran Soluble Portion of 850°F+ Distillation Resids
Run: 3LCF10
Sample Stream: Feed to LC-Finer

DETERMINATION OF ORGANIC/INORGANIC ASSOCIATIONS OF TRACE ELEMENTS IN AN OIL SHALE KEROGEN

Gregory E. Mercer, Scot Fitzgerald, Jeffrey Day and Royston H. Filby
Department of Chemistry
Washington State University
Pullman, WA 99164-4630

INTRODUCTION

The distributions of trace element in crude oils have been used to classify crude oils into families (1-4). Relatively little work, however, has been performed using trace element abundances for oil-source rock correlations. One reason for the paucity of oil-source rock correlations using trace elements is the difficulty in obtaining accurate trace element data for the organic matter (bitumen and kerogen) found in source rocks. The most difficult problem is the determination of trace element abundances in kerogens which are the precursors to crude oils. The chemical species of metals present in kerogens must be known to provide the relationship between such species and the metal complexes in crude oils. Difficulties in kerogen analysis arise primarily from the method of isolation, i.e., dissolution of the mineral matrix of the rock. In the conventional method of isolation the mineral matrix is dissolved in HCl/HF. This leaves a kerogen containing HCl/HF resistant minerals and neoformed fluorides. Several methods to remove or account for these inorganic contributions to the kerogen composition have been proposed, and include low temperature ashing (LTA) (5), density separations (6) and chemical removal of residual mineral matter (7-9). Although most of these methods improve trace element data, they have drawbacks; for example, density separations are usually incomplete (7) and chemical removal techniques do not dissolve the major resistant minerals without seriously altering the organic matter. The LTA method which is based on low temperature oxidation of organic matter to CO_2 + H_2O and conversion of organically combined metals to acid-soluble oxides is affected by the presence of neoformed fluorides and by partial oxidation of pyrite/marcasite (11).

This paper compares two methods of determining inorganic/organic trace element abundances in kerogen with the LTA method developed previously (11). A combination of INAA with X-ray diffraction analysis and analysis of mineral grains by electron microprobe (EMP-XRF) was used to analyze density fractions of the New Albany Shale kerogen and a mineral-rich fraction of the kerogen. The New Albany kerogen was chosen because of the large Ni and V concentrations and because of the high metalloporphyrin concentrations in the shale (12).

EXPERIMENTAL

1. Kerogen Isolation. Mississippian New Albany shale (Henryville Bed Clark County, IN) was ground to ~200 mesh in a ring mill, washed with distilled water and vacuum dried at 65°C. Resultant shale samples were extracted with toluene-methanol (7:3) to remove bitumen and demineralized as indicated in Figure 1. Detailed geological information on New Albany shale may be found elsewhere (10).

2. Density Separations. A kerogen sample isolated using the scheme shown in Figure 1 were subjected to a density fractionation using chloroform. In this separation the kerogen was sonicated in chloroform at 40°C for an hour and centrifuged. Roughly 80% of the kerogen was recovered in a float fraction, 15% as a sink fraction and ca. 1% as a mineral residue which was approximately 85% pyrite and marcasite. A portion of the mineral residue was treated with 3M nitric acid at 45°C for one hour to remove the pyrite and marcasite from minor mineral components, (e.g., rutile, chalcopyrite, anatase, etc.).

3. Instrumental Neutron Activation Analysis (INAA). All samples were analyzed for trace element contents by INAA using a method similar to that of Jacobs and Filby (13).

4. X-ray Diffraction (XRD). the major mineral composition of the samples was determined by XRD using a Siemens x-ray diffractometer. Appropriate portions of each powdered sample were smeared on a glass slide and diffraction patterns measured using the Cu-K_α line.

5. Electron Microprobe X-ray Fluorescence (EMP-XRF). Trace element associations with individual mineral grains within the kerogen were determined by EMP-XRF. Electron dot maps of several elements in ashed kerogen were made using a Cameca electron microprobe. The microprobe was also used in the SEM mode to obtain electron micrographs of the mapped mineral grins. For both electron dot maps and micrographs an electron accelerating voltage of 20keV was used. Concentrations of several elements in individual mineral grains were also determined.

6. Low Temperature Ashing (LTA). Kerogen samples were ashed using a LFE Model LTA-302 low temperature asher operated at 50 RF watts and an O_2 flow rate of 2 mL/min. Ashed samples were treated with 2M HCl and heated to 40°C with constant stirring for one hour to remove metal oxides formed in the ashing process. The acid-leached ash was isolated by centrifugation.

RESULTS AND DISCUSSION

1. X-ray Diffraction Results

The major minerals identified by XRD in New Albany kerogen were pyrite and marcasite. Additional minor mineral components were identified by ashing the kerogen followed by removal of the pyrite and marcasite from the mineral residue with 3M HNO_3. In the ashed kerogen ralstonite ($NaMgAl(F,OH)_6.nH_2O$) was identified. This mineral is an artifact of the kerogen isolation procedure as discussed elsewhere (5,11). Leaching of the ash with 3M HNO_3 removed ralstonite, pyrite and marcasite and XRD identified anatase, rutile and chalcopyrite ($CuFeS_2$). With these inorganic contributions revealed, correction methods were focused on the minerals identified above.

2. Fractionation of Kerogen by Density: Determination of Concentrations in Inorganic and Organic Components.

The concentrations of trace elements determined by INAA for the kerogen and its density fractions are listed in Table 1. A number

of general conclusions concerning the inorganic/organic nature of trace elements in the kerogen may be drawn from the data. Elements which tend to concentrate in the float fraction (Ni, V, Mo, Sb) probably have high organic associations. Similarly, elements concentrating in the most dense fraction, the mineral residue (As, Cr, Fe, Hf, Mn, Ti, Zr) most likely are present predominantly in mineral form. The elements which concentrate in the intermediate density sink fraction (Al, Mg, Na, Cs, Rb, Sc) appear to be associated with neoformed fluorides, such as ralstonite. However, some elements show no appreciable concentration in any fraction (Co, Se) and possibly exist in both inorganic and organic forms in the kerogen.

A method to determine the concentrations of the elements in the "organic" and "inorganic" compounds was formulated based upon the weight fractions of the organic and inorganic components. In this method the following assumptions are made:

1) The mineral matter and organic matter are similar in the float and sink fractions. The fractions differ only in the relative amounts of organic and mineral matter.

2) The concentration of V in organic combination is very large relative to the V in inorganic combination.

3) The concentration of Fe in inorganic combination is very large relative to the Fe in organic combination.

Using these assumptions, the inorganic and organic weight fractions for the sink and float kerogen samples were determined as shown in Figure 2. Once the weight fractions (f_{1O}, f_{1m}; f_{2O}, f_{2m}) are known, the concentration of any element may be determined for both the organic and inorganic components of kerogen by solving the two simultaneous equations shown at the bottom of Figure 2. The trace element concentrations in the "organic" and "inorganic" components of the original kerogen, as determined by this method, are listed in Table 2.

3. Determination of Organic and Inorganic Associations by Analysis of the Mineral Residue.

Pyrite and marcasite were the only minerals identifiable by XRD in the mineral residue. After removal of pyrite and marcasite with HNO_3, however, the XRD pattern confirmed the presence of chalcopyrite, rutile and anatase as minor mineral components in the kerogen. The trace element concentrations in the mineral residue before and after the HNO_3 treatment are shown in Table 3 and confirm the XRD data. A number of elements (e.g., As, Co, Fe, Mn, Mo, Ni, S, and Sb) are 90-100% leached by $3MHNO_3$. These elements are thus associated with pyrite, marcasite or other minerals which are soluble in dilute HNO_3 (but not in HCl/HF). As a result, the inorganic associations for these elements in the kerogen may be accounted for based upon their dissolution in the HNO_3 relative to the dissolution of Fe. The assumptions made in this method for estimating mineral associations are as follows:

1) The mineral residue is representative of the inorganic component of the original kerogen. This will not be true for neoformed fluorides (e.g., ralstonite).

2) The fraction of Fe in organic form in the kerogen is small.

3) The amount of an element dissolved is proportional to the amount of Fe dissolved. This will not be the case for elements associated with ralstonite (Na, Mg, Al, etc.).

This technique is limited to elements which form sulfides but may be more reliable for most of these elements than the density fractions method as a result of the basic assumptions behind each method. A correction for Se, however, cannot be made due to the formation of elemental S (and hence elemental Se) during the pyrite dissolution. The data for Cu in Table 3 indicate that roughly 4% of the sulfur in the HNO_3-treated mineral residue sample is in the form of chalcopyrite leaving ~20% of the sample as elemental S. Thus, the true inorganic Se content would be underestimated in this "pyrite dissolution method" because of the chemical similarities between S and Se, i.e., oxidation of H_2Se to Se^o by HNO_3 would occur. The inorganic contributions to the original kerogen trace element content, as determined by this method, are listed for several elements in Table 4 (see also Table 2).

4. EMP-XRF Analysis. Electron micrographs and elemental distributions of the ashed kerogen indicate that both framboidal and massive type pyrite/marcasite are present in the kerogen. Analysis of mineral grains shows that Ni is present in both forms of pyrite/marcasite and in the chalcopyrite but not in rutile. The Ni X-ray data also indicates that Ni is present at higher concentrations in the framboidal pyrite than in the massive pyrite. Semiquantitative EMP-XRF data gave Ni concentrations of approximately 0.04 ± 0.02 percent and 0.01 ± 0.01 percent for framboidal and massive type pyrites, respectively. Correction for the Ni content of the kerogen in pyritic form thus cannot be made from the analysis of individual massive pyrite grains.

4. Determination of Inorganic/Organic Associations by the LTA Method.

Previously in this laboratory, the inorganic associations of the elements in kerogens were based upon the LTA of the kerogen (11). In this method the organic matter was oxidized using LTA and the ash was treated with dilute HCl to remove oxides formed in the ashing process. The remaining mineral matter was then considered to be representative of the inorganic fraction of kerogen. In this study a similar procedure was followed for both float and sink kerogen fractions. The ash and HCl-treated ash samples were analyzed by XRD and INAA. The results of these analyses are shown in Table 5. The XRD patterns of both the float and sink ashes revealed the presence of the neoformed fluoride ralstonite. The XRD patterns of the HCl-treated ashes and the trace element data in Table 5 indicate that the ralstonite is soluble in dilute HCl after ashing. Hence, as suggested by Van Berkel and Filby (11) the LTA method cannot be used to determine the organic association of fluorides that precipitate as ralstonite (Na, Mg, Al, etc.) or which coprecipitate with ralstonite.

A major problem with the LTA technique is the partial oxidation of sulfide minerals (pyrite or marcasite) during the ashing procedure. The float ash consistently had a rust color on its surface after a few hours in the asher. This color is a result of the oxidation of pyrite (to Fe_2O_3) as confirmed by the deep yellow color of the HCl wash of the ash and the analytical data in Table 5. Thus, the Fe and other metals leached from oxidized sulfide minerals are not the result of oxidized organic complexes. Because pyrite contains Ni and other transition metal complexes, correction for the contribution of each element in the oxidized pyrite would have to be made. Because the forms of pyrite may have different composition, the correction cannot be based on the composition of the residual pyrite.

CONCLUSIONS

New Albany kerogen concentrates isolated by the scheme shown in Figure 1 were found to contain several residual minerals identified by XRD. Several elements (As, Co, Mo, Mn, Ni, Sb, Se, Zn) appeared to have some association with the major residual mineral, FeS_2, or with other less abundant inorganic forms which were soluble in 3M HNO_3. Of these elements only Mn was found to have no significant contribution to the organic fraction of the kerogen. The remaining elements, along with V, were shown to have substantial organic associations and may be useful in future work on oil-source rock correlations using trace elements.

The results of the two techniques used to quantify the inorganic fraction of the kerogen are compared in Table 6 for the elements mentioned above. The data for the organic compound shows good agreement between the two techniques. For the mineral component agreement for most elements between the two methods is good, except for Mo, Sb, and Se.

It is evident that although the methods allow calculation of organic/inorganic associations of elements in the kerogen isolated from the shale, the "true" concentrations of these elements in the kerogen in the shale cannot be determined. Undoubtably the isolation procedure removes labile elements from the kerogen and adds artifact minerals (ralstonite).

REFERENCES

1. Abu-Elgheit, M., Khalil, S.O., and Barakat, A.O., Prepr. Div. Petrol. Chem. ACS 24, 793-97 (1979).

2. Ellrich, J., Hirner, A., and Stark, H., Chemical Geology 48, 313-23 (1985).

3. Hitchon, B. and Filby, R.H., Bull. Am. Assoc. Petrol. Geol. 68, 838-49 (1984).

4. Curiale, J.A., in "Metal Complexes in Fossil Fuels," R.H. Filby, and J.F. Branthaver, Editors, ACS Symposium Series No. 344, American Chemical Society, Washington, DC, 1987.

5. Van Berkel, G.J., Ph.D. Thesis, Department of Chemistry, Washington State University (1987).

6. Odermatt, J.R., Curiale, J.A., Hirner, H.V., Mercer, G.E. and Filby, R.H., "Determination of Metals in Kerogens: A Comparative Study". Abstract, 197th ACS meeting, Dallas, TX, April 1989.

7. Durand, B. and Nicaise, G., in "Kerogen: Insoluble Organic Matter from Sedimentary Rocks," B. Durand, Editor, Editions Technip, Paris, 1980.

8. Saxby, J.D., in "Oil Shale," T.F. Yen and G.V. Chilingarian, Editors, Elsevier, Amsterdam, 1976.

9. Robinson, W.E., in "Organic Geochemistry", G. Englinton and M.T.J. Murphy, Editors, Springer Verlag, Berlin, 1969.

10. Hasenmueller, N.R., Woodward, G.S. "Studies of the New Albany Shale (Devonian and Mississippian) and equivalent strata in Indiana"; Indiana Geological Survey Contract Report to U.S. Department of Energy, Contract DE-AC-21-76MC05204, 1981; 100 p.

11. Van Berkel, G.J. and Filby, R.H. in "Geochemical Biomarkers", T.F. Yen and J.M. Moldowan, Editors. Horwood Academic Publishers, London, 1988.

12. Van Berkel, G.J., Filby, R.H. and Quirke, J.M.E., Org. Geochem. 14, 119 (1989).

13. Jacobs, F.S., and Filby, R.H. Anal. Chem. 55, 74-7 (1982).

Table 1. Trace element data for New Albany kerogen and density fractions.

Element (µg/g)	Original Kerogen	Float Fraction (d<1.48)	Sink Fraction (d>1.48)	Mineral Residue
Al	4120	3920	11400	2400
As	114	62.7	308	810
Co	130	120	166	187
Cr	41.2	40.1	86	192
Cs	8.16	7.35	21.4	0.838
Fe	48800	17200	177000	376000
Hf	3.09	0.566	10.4	61.0
La	32.6	25.5	79.0	78.8
Mg	2690	<3000	4020	<1500
Mn	47.0	11.5	173	417
Mo	2190	2380	2190	1290
Na	1900	1600	4940	500
Ni	2000	2090	1430	947
Rb	129	135	369	<40
Sb	62.3	70.8	53.7	60.2
Sc	2.90	2.35	7.58	4.56
Se	181	178	202	186
Sm	3.37	3.04	7.01	12.0
Ta	1.93	1.97	2.45	3.33
Ti	2270	730	9540	19000
V	980	1070	541	140
Zn	82.8	78.0	135	258
Zr	154	84.2	442	1960
Mass Used/ Recovered	10.0g	7.9g	1.5g	0.086g

Table 2. Trace element concentrations in mineral and organic components of kerogen calculated from density fractions.

Element (Mg/g)	Concentration in kerogen	Concentration in organic fraction	Concentration in mineral fraction
Al	4120	3117	8991
As	114	36.4	557
Co	130	115	213
Cr	41.2	35.2	133
Cs	8.16	5.84	35.7
Fe	48800	0	340000
Hf	3.09	0	20.4
La	32.6	19.8	133
Mg	2690	--	--
Mn	47.0	0	337
Mo	2190	2400	1997
Na	900	1240	8330
Ni	2000	2160	760
Rb	129	110	606
Sb	62.3	72.6	36.3
Se	2.90	1.79	7.88
Sc	181	175	226
Sm	3.37	2.61	11.0
Ta	1.93	1.92	2.94
Ti	2270	0	18500
V	980	1130	0
Zn	82.8	71.9	193
Zr	154	45.8	805
Float f_{10} = 0.9494		f_{1m} = 0.0506	
Sink f_{20} = 0.4782		f_{2m} = 0.5218	

Table 3. Trace element concentrations in mineral residue sample before and after 3M HNO_3 treatment.

Element (µg/g	Mineral Residue (100%)	HNO_3-Treated Mineral Residue (16%)	Percent Mass Lost
Al	2240	8150	41.8
As	626	38.1	99.0
Co	224	27.1	98.1
Cr	137	829	3.2
Cu	4800	31600	0.0
Cs	1.20	<0.58	--
Fe	390000	32100	98.7
Hf	31.1	182	6.4
La	97.7	12.3	98.0
Mg	1140	1460	79.5
Mn	408	32.1	98.7
Mo	1250	520	93.3
Na	448	814	70.9
Ni	905	1510	73.3
Rb	29.0	<17	--
S	452000	240000	91.5
Sb	40.8	28.3	88.9
Sc	3.37	18.7	11.2
Se	247	649	58.0
Sm	13.8	11.7	86.4
Ta	2.62	16.6	0.0
Ti	8760	66800	0.0
V	98.4	580	5.7
Zn	330	726	64.8
Zr	997	5610	10.0

Table 4. Trace element contents of organic and mineral components for elements showing solubility in dilute HNO_3.

Element (µg/g)	Original Kerogen	Percent Organic	Concentration in Organic Fraction*	Concentration in Inorganic Fraction
As	114	31.1	41.2	540
Co	130	78.5	119	192
Fe	48800	0	0	336000
La	32.6	62.8	23.9	82.5
Mn	47.0	0	0	323
Mo	2190	93.2	2390	1010
Ni	2000	95.8	2240	578
Sb	62.3	71.3	52.0	123
Se	181	90.0	191	124
Zn	82.8	67.2	65.1	187

*Using f_{10} = 0.8546 for kerogen.

Table 5. Trace element data for low temperature ash and HCl-leached ash from kerogen density fractions.

Element (µg/g)	Kerogen* Float 100%	Float Ash 14%	Float Ash-HCl 4.2%	Kerogen Sink 100%	Sink Ash 55%	Sink Ash-HCl 33%
Al	8530	54200	4540	30300	49900	7630
As	64.6	444	340	265	492	564
Co	138	947	590	195	358	228
Cr	31.3	227	240	69.8	125	152
Cs	12.3	88.7	5.87	42.3	74.0	9.19
Fe (%)	1.46	10.5	21.7	13.1	26.2	40.1
Hf	0.299	2.29	7.13	6.53	13.7	19.9
La	36.2	254	33.5	158	274	60.8
Mg	4100	26500	1380	12300	22500	1390
Mn	9.11	61.6	172	166	270	418
Mo	2390	16700	1590	2080	3810	216
Na	2880	20500	1100	10300	18000	2060
Ni	2260	16200	2020	1710	3080	810
Rb	194	1520	197	733	1250	309
Sb	77.7	536	26.9	57.8	102	24.1
Sc	3.69	27.0	2.82	12.6	21.7	5.34
Se	145	576	201	270	396	178
Sm	3.01	22.3	3.85	11.4	20.7	8.46
Ti	<960	<2300	3940	4060	7530	9820
V	911	6480	358	491	950	66.8
Zn	86.1	587	207	145	293	292
Zr	102	602	268	291	542	481

*Percentages refer to mass of original unashed and untreated sample. HCl refers to ash leached with 2M HCl.

Table 6. Comparison of trace element concentrations calculated by the pyrite dissolution method (PDM) to the density fraction method (DFM).

Element (µg/g)	Organic Fraction PDM	Organic Fraction DFM	Inorganic Fraction PDM	Inorganic Fraction DFM
As	41.2	36.4	540	557
Co	119	115	192	213
Fe	0	0	336000	340000
La	23.9	19.8	83.9	133
Mn	0	0	323	337
Mo	2390	2400	1010	2000
Ni	2240	2160	578	760
Sb	52.0	72.6	123	36.3
Se	191	175	124	226
V	1150	1130	0	0
Zn	65.1	11.9	187	193

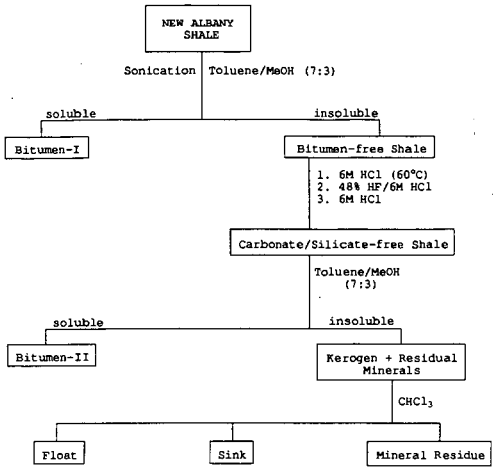

Figure 1: Kerogen Isolation Scheme

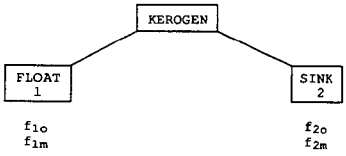

Vanadium concentration organic = V_o
Vanadium concentration mineral = V_m

$$V1 = (f_{1o})(V_o) + (f_{1m})(V_m) \qquad V_2 = (f_{2o})(V_o) + (f_{2m})(V_m)$$

Assume $V_m << V_o$, Hence

$$\frac{V_1}{V_2} = \frac{f_{1o}}{f_{2o}}$$

For iron, assume $Fe_m >> Fe_o$

$$\frac{Fe_1}{Fe_2} = \frac{f_{1m}}{f_{2m}}$$

Thus, for each element X

$$X_1 = (f_{1o})(X_o) + (f_{1m})(X_m)$$
$$X_2 = (f_{2o})(X_o) + (f_{2m})(X_m)$$

f_{1o}, f_{2o} = weight fraction organic in float and sink

f_{1m}, f_{2m} = weight fraction inorganic in float and sink

Figure 2: Calculation of organic/inorganic associations from density fractions

HIGH PRESSURE TPR APPARATUS TO INVESTIGATE ORGANIC SULPHUR FORMS IN COALS.

C.J. Lafferty, C.E. Snape, R. Garcia*, S.R. Moinelo*.
University of Strathclyde
Dept. of Pure and Applied Chemistry
Glasgow G1 1XL
Scotland, United Kingdom.
*Instituto Nacional del Carbon y Sus Derivados
33080 Oviedo
Spain.

ABSTRACT

Temperature programmed reduction (TPR) has been used to investigate the distribution of organic sulphur forms in coals. However, the method used thus far suffers from a number of inherent drawbacks including the low proportion of thiophenic sulphur observed directly and the likelihood of secondary reactions converting sulphides into thiophenes. These drawbacks have largely been overcome using a well swept fixed-bed reactor at relatively high hydrogen pressures (~ 150 bar) with an effective dispersed hydrodesulphurisation catalyst, such as sulphided molybdenum. For three high sulphur coals (a Spanish and a Turkish lignite and a US hvc bituminous coal), levels of desulphurisation were in excess of 90% for the organic sulphur. The first results from the high pressure TPR apparatus with a quadrupole mass spectrometer for on-line analysis of hydrogen sulphide is presented.

1.0 INTRODUCTION

The identification and quantification of the various organic sulphur species in coals is of great importance due to their effects, both beneficial and detrimental, on the subsequent devolatilisation and liquefaction of coal and coal-derived products. At present no established method exists for the direct determination of the distribution of organic sulphur in coal and coal-related products. Several novel techniques have been proposed.

Flash pyrolysis studies on the thermal decomposition of sulphur groups in coal showed that aliphatic sulphur containing groups decompose at much lower temperatures than aromatic groups. However resolution between different aliphatic and aromatic groups was poor[1].

X-ray studies, both surface (XPS)[2,3] and bulk (XANES)[4] characterisation techniques, have shown that it is possible to distinguish between thiophenic and non-thiophenic sulphur groups, however the narrow absorption energy range observed for sulphur containing model compounds coupled with the known number of forms of organic sulphur present in coals results in poor resolution between groups. A larger range is observed for oxidised sulphur

groups[2], it is therefore possible that selective oxidation before x-ray analysis may offer improved resolution.

Another method which has been investigated involves the oxidative pyrolysis of the coal which converts the sulphur into SO_x for subsequent on-line gas analysis, however the resulting resolution between functional groups is generally not as good as that achieved with TPR[5,6] (see following).

In recent years several researchers have been investigating the use of Temperature Programmed Reduction (TPR) for the identification of organic sulphur forms in coal and related products[7,8,9,10]. TPR is based on the principle that each form of organic sulphur exhibits a characteristic reduction temperature, which in a hydrogen rich environment, results in the formation of hydrogen sulphide. The ease of reduction of the various sulphur forms have been found to be in the order thiols > aliphatic sulphides > aromatic sulphides > thiophenes[9]. The current TPR methods generate the hydrogen rich atmosphere by refluxing the coal in a mixture of hydrogen donor solvents[9]. The evolved hydrogen sulphide is swept from the reaction pot by a stream of inert carrier gas at atmospheric pressure. The original method used lead acetate impregnated paper as the H_2S detector[7,9], later workers have used a potentiometric system to measure the evolved H_2S as the sulphide ion, giving a greater degree of quantitation[9]. Sulphur sensitive Flame Photometric Detection (FPD) has also been used however flame stability was found to influence overall sensitivity to a large extent [10].

The TPR method has been the most widely used technique, however at present it contains several limitations which reduce its effectiveness as an analytical technique. The solvent mixture used to generate the hydrogen atmosphere has a relatively low boiling point (< 400°C), consequently complex thiophenes are not detected and must be estimated by difference[10]. Overall sulphur balances are poor, with sulphur of all functionalities remaining in the char after analysis, possibly due to mass transfer limitations inherent to the reaction pot, which could result in retrogressive reactions including transformation of aliphatic sulphides to thiophenes[11,12]. Finally, the overall contribution of pyrite to the evolved H_2S signal, particularly the transformation of pyrite to pyrrhotite and to iron with the subsequent evolution of H_2S appears to have been overlooked or considered negligible by previous researchers.

This paper presents results obtained for three high sulphur coals from a high pressure fixed bed hydropyrolysis reactor which is relatively unaffected by any mass transfer effects and any associated retrogressive reactions resulting in effective desulphurisation, including the removal of complex thiophenes. This reactor has been modified through the fitting of a suitable gas analysis system to form a TPR reactor.

2.0 EXPERIMENTAL

Table 1 lists the ultimate analyses and sulphur distributions of the coal samples studied.

The hydropyrolysis reactor has been described previously[13]. The desulphurisation experiments were conducted on a 5g scale at 520°C using a gas velocity of ~ 0.2 m s^{-1} to virtually overcome mass transfer limitations to volatile release. For each coal (75-200um), three tests were conducted using a pressure of (i) 150 bar nitrogen and (ii) 150 bar hydrogen with and without a sulphided molybdenum (Mo) catalyst (1% loading prepared from ammonium dioxydithiomolybdate[13]). In addition, the thermal desulphurisation of the three coals was also investigated in the temperature range 250-500°C using the BS volatile matter test (BS1016).

For the TPR runs, a smaller but otherwise identical reactor system was used. 2g of coal was heated from ambient to 570°C at 2°Cmin^{-1}. The hydrogen pressure was again 150 bar and the gas velocity ~ 0.2 m s^{-1}. On line analysis of the gas stream for H_2S and other gaseous products is performed using a quadrupole mass spectrometer in multiple ion monitoring mode. The atmospheric pressure side of the exit stream from the reactor was connected to the mass spectrometer by a 1.8 m length of heated capillary tubing sampling at a rate of 25 ml min^{-1}. The reactor thermocouple signal is also fed to the mass spectrometer allowing direct plots of evolved gas concentration against bed temperature to be generated.

Concentrations of pyritic and pyrrhotitic sulphur in the chars were determined. FTIR was used to compare the relative amounts of sulphatic sulphur in the chars and corresponding low temperature ash samples, sulphate absorbances occurring in the range 1110-1150 cm^{-1}. Gas chromatography (GC) with mass spectrometric (MS) and flame photometric detection (FPD) were carried out to compare the distribution of thiophenic compounds in the tars.

3.0 RESULTS AND DISCUSSION

3.1 DESULPHURISATION

Table 1 lists the distribution of sulphur forms in the original coals and Table 2 summarises the char and tar yields for the desulphurisation tests as well as the sulphur distributions in the pyrolysis products. The two lignites gave broadly comparable tar yields and total conversions in corresponding tests, but these were slightly higher than those obtained for Bevier-Wheeler coal. As anticipated, the total conversions increased in going from pyrolysis to high pressure hydropyrolysis and catalytic hydropyrolysis (Table 2). The extent of desulphurisation (sulphur in gas plus tar as a percentage of that in the original coal) increased with increasing conversion (Table 2) but a number of marked differences were found for the coals investigated.

In Table 2 it has been assumed that sulphatic sulphur remains in the chars and is unaffected by pyrolysis. Indeed, only small differences were found in the absorbances of the characteristic IR sulphatic bands at 1110-1150 cm^{-1} between the chars and the corresponding low temperature ashes when the spectra were normalised to 1mg cm^{-2} of mineral matter. For all three coals, significantly more pyrite is reduced during high pressure hydropyrolysis than in pyrolysis (Table 2). The ease of pyrite reduction to pyrrhotite and iron is greatest for Bevier-Wheeler coal and optical microscopy has shown that it would appear to correlate with the size of pyrite particles in the coal. For the lignites, much of the pyrite occurs as fine grains dispersed in both the organic and mineral matter. In Bevier-Wheeler coal, the pyrite is mainly present as relatively large particles which are presumed to be more accessible to hydrogen than fine grains.

The three coals display completely different trends for the removal of organic sulphur (Table 2). For Cayirhan lignite, nearly all of the organic sulphur is eliminated as tar and gas in pyrolysis compared with ~75% for Mequinenza lignite.The implication is clearly that little of the organic sulphur exists in condensed thiophenic structures for Cayirhan lignite. Indeed, nearly all the organic sulphur is also removed in the standard volatile matter test at 500°C with ~ 20% being eliminated below 250°C (Figure 1). The fact that much more of the sulphur is released from the Cayirhan lignite below 250°C (Figure 1) implies that this lignite contains a greater proportion of aliphatic sulphides/thiols than Mequinenza lignite. However there is the strong possibility that some thiophenic sulphur results from cyclisation and aromatisation of non-thiophenic forms during pyrolysis[11,12]. As anticipated, the extent of organic sulphur removal is low for Bevier-Wheeler coal with only ~ 20% being eliminated in pyrolysis and also at 500°C in the volatile matter test (Table 2 and Figure 1). However, in catalytic hydropyrolysis the proportion eliminated is ~ 90%.

For Mequinenza lignite, GC has shown that thiophenes are the dominant species over benzo- and dibenzothiophenes in the pyrolysis tar. However, in the high pressure hydropyrolysis tars, thiophenes are present in trace amounts which is consistent with the greater ease of hydrodesulphurisation of single ring thiophenes. For Cayirhan lignite, benzothiophenes are the major thiophene class present in the pyrolysis tar but in going to catalytic hydropyrolysis, dibenzothiophenes and other high molecular weight thiophenes become the dominant species.

3.2 HIGH PRESSURE TEMPERATURE PROGRAMMED REDUCTION

Figure 2 shows the H_2S evolution trace for Mequinenza lignite (A) untreated and (B) impregnated with the molybdenum catalyst. The higher resolution trace obtained without catalyst shows seven distinct peaks which can be assigned to various functional groups based on characteristic reduction temperatures identified in earlier studies [9]. At present, studies are under way to confirm

the reduction temperatures of various model compounds in the swept bed TPR reactor.

The trace for the catalyst impregnated sample shows a loss of fine resolution, but more thiophenic sulphur is detected around 300-400°C, and over a smaller temperature range than for the untreated sample. The loss of resolution may be as a result of a continual adsorption/desorption of H_2S on the hot catalyst surface. Different catalyst compositions and loadings will be investigated in order to improve the resolution observed for catalyst impregnated coals.

4.0 CONCLUSIONS

The use of a fixed bed pyrolysis reactor swept with high velocity hydrogen has been shown to effectively desulphurise high sulphur coals. The reactor is relatively unaffected by any mass transport limitations and as a result, retrogressive sulphur transformations are avoided. The reactor system has been adapted to enable the characterisation of organic sulphur species within the coals via high pressure temperature programmed reduction and initial results have shown a high degree of resolution between functional groups.

5.0 ACKNOWLEDGEMENTS

The authors acknowledge funding provided by the Science and Engineering Research Council (Project No. GR/G/26600) and by DGICYT (Project No.PB87-0417).

6.0 REFERENCES

1. Calkins W.H., 1985, Am. Chem. Soc. Div. Fuel Chem., prepr., 30(4), 450.
2. Jones R.B., McCourt C.B. and Swift P., Proc. 1981 Int. Conf. on Coal Science (IEA). 657.
3. Keleman S.R., George G.N. and Gorbaty M.L., 1990, Fuel, 69, 939.
4. Gorbaty M.L., George G.N. and Keleman S.R., 1990, Fuel, 69, 945.
5. Boudou J.P., Boulegue J., Malechaux L., Nip M., de Leeuw J.W. and Boon J.J., 1987, Fuel, 66, 1558.
6. La Count R.B., Anderson R.R., Friedman S. and Blaustein B.D., 1987, Fuel, 66, 909.
7. Attar A., 1983, DOE/PC/30145TI Technical Report.
8 Attar A., in C. Karr (Ed), Analytical Methods for Coal and Coal Products, Vol III, Academic Press, 1979. Ch. 56.
9. Majchrowicz B.B., Franco D.V., Yperman J., Reggers G., Gelan J., Martens H., Mullens J. and van Poucke L.C., 1991, Fuel, 70, 434.
10. Dunstan B.T. and Walker L.V., 1988, Final Report to Australian National Energy Research Development and Demonstration Council.
11. Keleman S.R., George G.N., Gorbaty M.L., Kwiatek, P.J. and Sansone, M., 1991, Fuel, 70, 396.

12. Cleyle P.T., Caby W.F., Stewart, I. and Whiteway S.G., 1984, Fuel, 63, 1579.
13. Snape C.E. and Lafferty C.J., 1990, Am. Chem. Soc. Div. Fuel Chem., prepr., 35(1), 1.

Table 1. Ultimate and Sulphur Analyses of Coal Samples

		Lignites		hvc Bituminous PSOC 1409
		Mequinenza (Spain)	Cayirhan (Turkey)	Bevier-Wheeler (Nth America)
(% daf)	C	66.4	64.3	76.9
	H	5.8	5.1	5.5
	N	1.6	2.3	1.8
Sulphur (% db)	Total	9.0	4.8	6.8
	Pyritic	0.5	1.0	4.0
	Sulphate	0.5	0.9	0.3
	Organic	8.0	2.9	2.5

Table 2. Distribution of Sulphur in Pyrolysis Products (% Original Sulphur in Coal)

	% Yield		Char					Tar	Gas*	%DS
	Char	Tar	S_T	S_p	$S^=$	S_{SO4}	S_o*			
Mequinenza			100	6	<1	6	88			
Py	53	33	38	4	1	6	27	25	37	62
Hypy	27	50	13	1	2	6	4	18	69	87
C.Hypy	13	63	10	1	2	6	1	23	67	90
Cayirhan			100	21	<2	19	54			
Py	49	39	45	16	5	19	<1	20	35	55
Hypy	25	57	27	1	6	19	<1	11	62	73
C.Hypy	16	63	22	1	1	19	<1	12	66	78
Bevier Wheeler			100	59	<1	5	36			
Py	63	25	61	10	16	5	30	7	32	39
Hypy	39	48	27	2	9	5	11	9	64	73
C.Hypy	30	56	20	1	11	5	3	6	74	80

* := by difference
S_T := Total sulphur
S_p := Pyritic sulphur
%DS := % Desulphurisation
$S^=$:= Pyrrhotitic sulphur
S_{SO4} := Sulphatic sulphur
S_o := Organic sulphur

SULPHUR REMOVAL IN VOLATILE MATTER TESTS

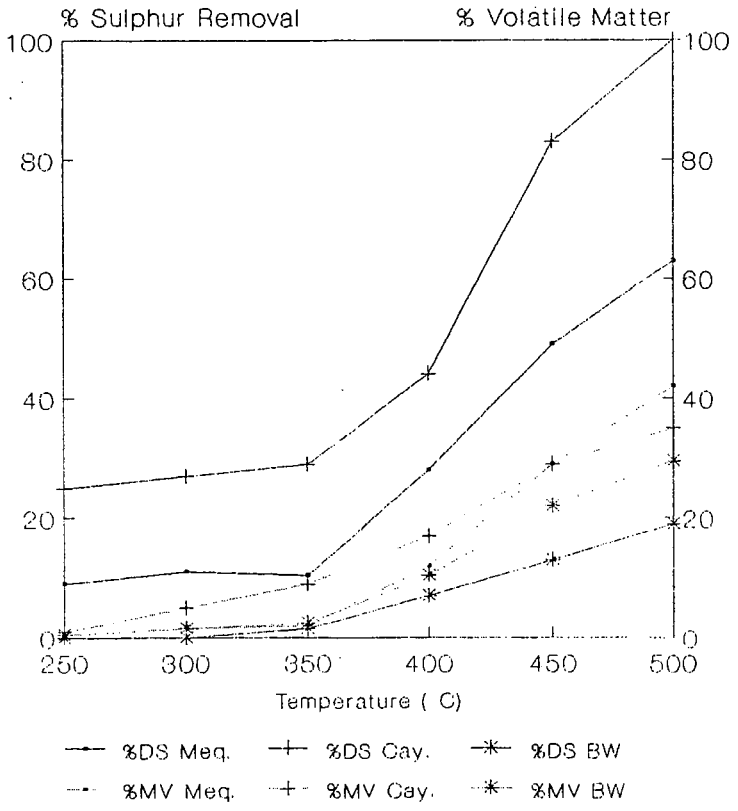

Fig.1. Desulphurisation and Volatile Matter Yields.

(A) Mequinenza No Catalyst

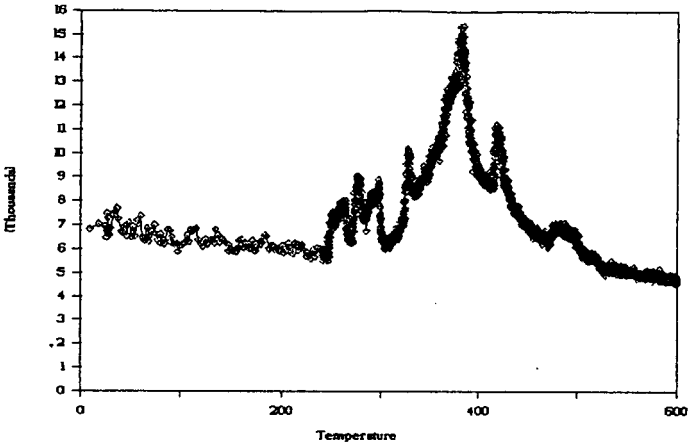

(B) Mequinenza 1% Mo Catalyst

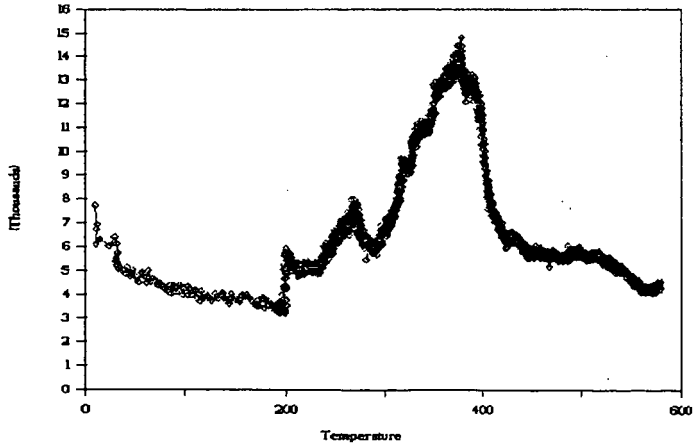

Fig. 2. TPR Traces for Mequinenza Lignite

A STANDARD ADDITIONS METHOD FOR THE MEASUREMENT OF SULFATE PRODUCED DURING THE DETERMINATION OF SULFUR FORMS IN COAL USING PERCHLORIC ACID

K. Shawn Ailey-Trent, Chris W. McGowan,
Department of Chemistry, Tennessee Technological University
Cookeville, Tennessee 38505

Elwira Lachowicz and Richard Markuszewski
Ames Laboratory, Iowa State University, Ames, Iowa 50011

Keywords: sulfur forms in coal, oxidative degradation, perchloric acid

INTRODUCTION

A reaction scheme has been developed and tested at the Ames National Laboratory for the direct determination of the sulfur forms in coal (1). The variable oxidizing power of perchloric acid was used to selectively dissolve the various sulfur-containing components and convert them to sulfate for turbidimetric measurement. Sulfate was extracted with a perchloric acid solution boiling at 120°C. Pyrite was then determined by reacting the residue from the previous step with a perchloric acid solution boiling at 155°C. From the second residue, organic sulfur was oxidized with a 9:1 solution of concentrated perchloric acid and concentrated phosphoric acid boiling at 205°C. The phosphoric acid was used to prevent foaming of the mixture during the heating process. In all three steps, sulfur-containing gases were trapped in 15 percent hydrogen peroxide. Sulfate was then determined in the trap and in the aqueous solution by precipitation as barium sulfate followed by turbidimetric measurement. For some coals, the total sulfur recovered was slightly less than the total sulfur in the coal as determined by the ASTM procedure. Generally, the recoveries were on the order of 0.2 to 0.4 percent low out of a total sulfur content of about five percent. Possible explanations included: 1) the incomplete absorption of sulfur-containing gases by the neutral peroxide trap, 2) the dissolution of some organosulfur compounds at 155°C without being converted to the measurable sulfate form, and 3) the incomplete precipitation of barium sulfate during turbidimetric analysis due to the high acidity of the solutions.

It is possible that acidic gases, such as hydrogen sulfide or sulfur dioxide, might not be completely trapped by neutral hydrogen peroxide. Therefore, in order to test the first hypothesis, the oxidations were run using a peroxide trap made basic with ammonium hydroxide. Sulfate was then determined as before. The filtrate solution from the 155°C reaction was yellow-brown due to the dissolution of some organic material. Upon standing, a brown precipitate formed in these solutions. Dilution which occurred during filtration caused the perchloric acid to become more aqueous resulting in the precipitation of some organic material. To test the second hypothesis, the

precipitate was filtered and oxidized with perchloric acid boiling at 203°C in the Bethge apparatus with a peroxide trap. Sulfate was then measured by the turbidimetric method as above. Also, 5 mL aliquots from the 155°C filtrate were oxidized with hydrogen peroxide and again sulfate was measured turbidimetrically. To test the third hypothesis, sulfate was measured using a standard additions technique in which aliquots of a standard sodium sulfate solution were added to the test samples and sulfate was measured turbidimetrically.

EXPERIMENTAL

The coal used in this study was obtained from the Kentucky #9 seam and was ground to minus 100 mesh. A modified Bethge apparatus was used to maintain a constant boiling mixture. The Bethge apparatus has been described previously by McGowan and Markuszewski (2). The system was fitted with a gas trap, containing 15 percent hydrogen peroxide to collect sulfur-containing gases and convert them to sulfate, and with a nitrogen purge line.

A Note on Safety. The use of perchloric acid alone as an oxidizing agent for organic materials always poses a hazard. In this study, all reactions were performed in a hood and behind an explosion shield. In order to minimize the possibility of a fire or explosion, the authors urge that extreme caution be used anytime perchloric acid alone is used as an oxidizing agent. The authors recommend that reactions be performed at low temperatures first and that small amounts of organic material be employed.

Reaction Procedure. For each oxidation experiment, perchloric acid was added to the Bethge apparatus and the boiling point was adjusted to the desired temperature. By varying the initial amount of perchloric acid added, a final volume of approximately 50 mL was obtained. The boiling point could be increased by removing reflux condensate from the condenser. The boiling point could be decreased by adding water through the top of the apparatus. The 15 percent hydrogen peroxide trap was attached to the apparatus for each oxidation. Nitrogen was used as a purge gas. A weighed 1-g sample of coal was added to the flask. The sample was reacted with perchloric acid boiling at 120°C (actual reaction temperatures were noted in each step) for 45 min. The reaction mixture was filtered. The residue from the previous step was reacted with a perchloric acid solution boiling at 155°C for 1.5 hrs. The reaction mixture was filtered. The residue from above was reacted for 1 hr. with a 9:1 solution of concentrated perchloric acid and concentrated phosphoric acid boiling at 205°C. The phosphoric acid was added to inhibit foaming during the reaction. The reaction mixture was filtered and any residue was discarded. The filtrate from each of the three reactions was diluted to 250 mL. Each of the peroxide trap solutions was boiled to insure oxidation of the sulfur to sulfate and to reduce the volume to about 25 mL. The trap samples were then diluted to 50 mL. In each fraction, sulfate was determined by precipitation with barium and the turbidity of the resultant

barium sulfate suspension was measured spectrophotometrically using a calibration curve. For the solutions that were colored, the absorbance of the sample without the added barium was measured and subtracted from the absorbance of the test solutions. Sulfate in the coal sample was determined as sulfate in the filtrate, and sulfide in the coal was determined from the sulfate accumulated in the peroxide trap after the 120°C reaction. Pyritic sulfur was determined from the sulfate in the filtrate and peroxide trap after the reaction at 155°C. Organic sulfur was determined in the filtrate and in the peroxide trap after the reaction at 205°C. Total sulfur in the coal was determined by reacting 0.1-g samples of the coal with the perchloric acid and phosphoric acid mixture.

To test the first hypothesis, the above reaction scheme was performed using a 15 percent hydrogen peroxide trap which was made basic by the addition of 15 mL of concentrated ammonium hydroxide. To test the second hypothesis, the precipitate from the 155°C reaction was filtered and reacted with boiling concentrated perchloric acid. Sulfate was measured in the trap and in the reaction solution. Also, sulfate was measured using a 5.0 mL aliquot of the supernatant solution from the 155°C reaction. Another 5.0 mL aliquot from the same solution was then oxidized with 30 percent hydrogen peroxide, followed by the measurement of sulfate. To test the third hypothesis, a standard additions method was applied to the turbidimetric method used to measure sulfate. Amounts of 0.0, 0.1, 0.2 and 0.3 mL of a standard sodium sulfate solution which contained 0.62 g of sulfur/L were added to the appropriate volume of each solution, and the turbidity of each solution was measured as before.

RESULTS

The sulfate results from the oxidations run with the neutral trap on the Kentucky #9 coal appear in Table 1. The total sulfur, determined using the ASTM procedure, for this sample also appears in Table 1. The results with the basic trap, using a different split of this same sample of coal, appear in Table 2. The total sulfur for this sample was determined using the perchloric acid method (1). The sulfur recoveries, although still slightly low when using the basic hydrogen peroxide trap, were comparable to previous results, indicating that the neutral trap does an adequate job of absorbing the sulfur-containing gases. The results for the oxidations of the precipitate formed in the solutions from the 155°C reactions are presented in Table 3. No additional sulfur was recovered from these precipitates. The results for sulfur found in the solutions from the 155°C reactions, before and after oxidation with hydrogen peroxide, are presented in Table 4. Some additional sulfur (<0.1%) was recovered, although not enough to account for the low sulfur recoveries. Based on previous work (1-3), it was suspected that some sulfur might be lost in this step but that it would be small. It was interesting that additional sulfur was recovered from the aqueous solution and not from the precipitate formed from that solution. This would indicate that the dissolved

organosulfur compounds remained soluble while other organic compounds precipitated under the more aqueous conditions. Possibly the organosulfur compounds formed under these mildly oxidizing conditions were sulfonic acids and thus more soluble.

The sulfur recovery results using the standard additions technique on the Kentucky #9 coal appear in Table 5. The sulfur recoveries for this experiment were very close to the total sulfur in the coal. When these results were compared to the corresponding results for the same coal in Table 2, a slight increase was observed for each sulfur form (except sulfide). This indicated that there could be a systematic error in the turbidimetric technique used to measure sulfate. This error apparently involved the inability to match the conditions of the calibration curve to the matrix effects of the samples.

CONCLUSIONS

The neutral hydrogen peroxide trap is sufficient to trap sulfur-containing gases. Only a small amount of sulfur is converted to a soluble organosulfur compound at 155°C and is not measured as sulfate by the turbidimetric technique. Sulfur recoveries using the standard additions method are comparable to the total sulfur measured in the coal.

ACKNOWLEDGEMENTS

Ames Laboratory is operated for the Department of Energy by Iowa State University under Contract No. W-7405-Eng-82. This work was supported by the Assistant Secretary for Fossil Energy, through the Pittsburgh Energy Technology Center.

LITERATURE CITED

1. McGowan, C.W. and R. Markuszewski, "Direct Determination of Sulphate, Sulphide, Pyritic and Organic Sulphur in Coal by Selective, Step-wise Oxidation with Perchloric Acid," Fuel, 67, 1091 (1988).

2. McGowan, C.W. and R. Markuszewski, "Fate of Sulfur Compounds in Coal during Oxidative Dissolution in Perchloric Acid," Fuel Process. Technol., 17, 29 (1987).

3. McGowan, C.W., K.Q. Cates and R. Markuszewski, "The Conversion of Organic Sulfur in Coal to Sulfate Using Perchloric Acid," Am. Chem. Soc. Div. Fuel Chem. Preprints, 33, 225 (1988).

TABLES

TABLE 1. Sulfur forms (in percent) determined for the Kentucky #9 coal using the perchloric acid procedure and a neutral trap

SULFUR FORM	1	2	3	4	AVG.
SULFATE	0.30	0.31	0.30	0.34	0.31
SULFIDE	0.02	0.03	0.01	0.00	0.02
PYRITE	2.81	2.70	2.80	2.83	2.79
ORGANIC	1.36	1.41	1.24	1.47	1.37
RECOVERY	4.49	4.45	4.35	4.64	4.48
TOTAL SULFUR (by the ASTM procedure)					4.86

TABLE 2. Sulfur forms (in percent) determined for the Kentucky #9 coal using the perchloric acid procedure and an ammoniacal trap

SULFUR FORM	1	2	3	4	AVG.
SULFATE	0.38	0.40	0.37	0.42	0.39
SULFIDE	0.14	0.01	0.03	-	0.06
PYRITE	2.69	2.91	2.91	2.46	2.74
ORGANIC	1.32	1.31	1.56	1.48	1.42
RECOVERY	4.53	4.63	4.87	4.36	4.60
TOTAL SULFUR (by the perchloric/phosphoric acid procedure)					4.96

Table 3. Sulfur (in percent) in precipitates from the solutions after the 155°C reactions

FRACTION FROM	1	2	3
FILTRATE	0.00	0.00	0.00
TRAP	0.00	0.00	0.00

TABLE 4. Sulfur (in percent) recovered from solutions after the 155°C reactions

SOLUTION	1	2	3
BEFORE H_2O_2 OXIDATION	0.37	0.62	0.53
AFTER H_2O_2 OXIDATION	0.46	0.67	0.61
ADDITIONAL SULFUR	0.09	0.05	0.08

TABLE 5. Sulfur forms (in percent) determined for the Kentucky #9 coal when sulfate was measured using standard additions

SULFUR FORM	1	2	AVG.
SULFATE	0.69	0.39	0.54
SULFIDE	0.01	0.01	0.01
PYRITE	2.81	2.91	2.86
ORGANIC	1.52	1.56	1.54
RECOVERY	5.03	4.87	4.95
TOTAL SULFUR (by the perchloric/phosphoric acid procedure)			4.96

QUANTITATIVE ANALYSIS OF SULFUR FUNCTIONAL FORMS AND REACTIONS BY XAFS SPECTROSCOPY

G. P. Huffman, N. Shah, M. M. Taghiei,
Fulong Lu, and F. E. Huggins

Consortium for Fossil Fuel Liquefaction Science
233 Mining and Mineral Resources Building
University of Kentucky
Lexington, KY 40506-00107.

INTRODUCTION

Recently, significant progress has been made in quantifying the measurement of different functional forms of sulfur in coal using X-ray absorption fine structure (XAFS) spectroscopy. As discussed in detail elsewhere, three methods of analyzing the X-ray absorption near edge structure (XANES) have been proposed.[1-6] In the current paper, we will briefly review the method developed by our group, which consists of direct least squares analysis of the XANES and conversion of the photoelectron s $\Rightarrow$ p transition peak areas into sulfur percentages using empirically determined calibration constants.[3] A number of applications of this method will be briefly summarized, including investigation of sulfur forms as a function of rank,[3] in situ studies of sulfur transformations during pyrolysis and oxidation,[7-9] and chemical and biological reactions of sulfur in coal.[10]

EXPERIMENTAL PROCEDURES

Experimental details are discussed elsewhere.[1-3,7-10] All XAFS experiments were conducted in the x-ray fluorescent mode[11] at beamline X-19A at the National Synchrotron Light Source (NSLS) at Brookhaven National Laboratory. The in situ experiments were carried using an XAFS compatible high temperature cell with the sample under flowing helium, hydrogen, or helium-5% oxygen at temperatures ranging from 200 to 600°C.[7-9] An XAFS spectrum was acquired at each temperature, making the pyrolysis and oxidation treatments fairly slow.

The suite of coals examined have included the Argonne Premium Coal Sample Bank (APCSB) coals, numerous additional whole coals, a suite of maceral separates, and a variety of chemically and biologically treated samples.

RESULTS AND DISCUSSION

Typical least squares analyzed XANES spectra are shown in Figure 1. The lower spectra in Figure 1 are room temperature spectra of an APSCB Illinois No. 6 coal and a low-rank Victorian brown coal (Glencoe). The upper half of Figure 1 shows high temperature spectra obtained in situ during oxidation of the Glencoe coal at 450°C and pyrolysis of the APCSB Illinois No. 6 coal at 600°C. As discussed elsewhere,[3] the least squares analysis method fits the XANES spectra to a series of photoelectron s $\Rightarrow$ p transition peaks using 50:50 Lorentzian:Gaussian peak shapes, and to one or two arctangent step functions representing the photoelectron transition to the continuum. Because the major sulfur forms in coal and coal derivatives have characteristic s $\Rightarrow$ p transition energies, the s $\Rightarrow$ p peak associated with each sulfur form can be identified. It is found that the s $\Rightarrow$ p transition energy increases with valence, as follows: pyrrhotite, -1.5 eV; pyrite, -0.5 eV; elemental sulfur, 0.0 eV; organic disulfide, 0.2ev;

organic sulfide, 0.7 eV; thiophenic sulfur, 1.3 - 1.8 eV; sulfoxide, 3.4 eV; sulfone, 7.5 eV; and sulfate, 9.9 - 10.1 eV.[1] Once the s ⇒ p peak areas have been determined from the least squares fit, empirically determined calibration constants are used to convert them to sulfur percentages.[3]

The results for the APCSB coals and a number of additional whole coals are summarized in Table 1. A number of points are worth noting. First, the only APCSB coal that exhibits significant sulfur oxidation is the Beulah (ND) lignite, which contains a sulfate component believed to be gypsum. Second, the pyritic sulfur percentages derived from XANES agree reasonably well with those derived from Mössbauer spectroscopy.[11,12] Third, the percentage of organic sulfur that is sulfidic increases with decreasing rank as shown in Figure 2, although thiophenic sulfur was the dominant organic sulfur form for all coals examined. The thiophenic and sulfidic percentages determined for the APCSB coals agree fairly well with those determined by Gorbaty et al.[5] using a third derivative method of analyzing the XANES spectra.

We have also completed XANES analysis of a suite of maceral separates, and find that the sulfidic content of exinite is consistently higher than that of vitrinite or inertinite.[3] Additionally, it is found that the inertinite separates frequently contain fairly high percentages of pyrite, indicating that coal particles containing fine included pyrite are often incorporated into the specific gravity range corresponding to inertinite during density gradient centrifugation.

Several coals have been investigated by high temperature in situ XAFS spectroscopy conducted during pyrolysis and oxidation. The results, which are discussed in more detail elsewhere,[7-9] are summarized in Figure 3. Briefly, the organic sulfide component decreases above approximately 300°C, under both pyrolysis and oxidation conditions, with the sulfide percentage falling to about half of its initial value on reaching 500 to 600°C. The disulfide percentage for the Australian brown coal begins to decrease between 200 and 300°C, reaching approximately one fourth of it original value at 500 to 600°C. The Illinois #6 data shows that pyrite transforms to pyrrhotite during pyrolysis and to pyrrhotite and sulfate during oxidation, above approximately 400°C. During oxidation of the Glencoe coal, a sulfate phase is also formed, but it is unlikely to be an iron sulfate since the coal contains no pyrite and very little iron. Either an organic sulfate or calcium sulfate are possibilities. During pyrolysis of the Glencoe coal, a negative valence (~-2) sulfur species is observed to form and increase to approximately 40% of the total sulfur at 500°C. A double-bonded C-S compound, such as a thioketone, or calcium sulfide, are possible candidates.

There is considerable interest in the effects of various chemical and biological reactions on sulfur in coal. We have examined the effects of several such treatments on a number of coals using XANES spectroscopy. A more detailed summary of the results is available in a forthcoming paper [10]. For the current article we will summarize some recent data obtained on the use of perchloroethylene (PCE) for removal of sulfur from coal. In this treatment,[13] coal is treated with a five-fold excess of PCE at close to its boiling point (125°C) for no more than 30 minutes, in which time a significant reduction (up to 50%) in the organic sulfur is claimed to occur. The exact mechanism has not yet been clarified, but the observation has been made[13] that the sulfur removed from the coal by PCE can be readily extracted in the form of elemental sulfur. However, this focus on elemental sulfur has lead others[14,15] to criticize this method by claiming the PCE is only removing the elemental sulfur already present in the coal. As

[1]The energy of the elemental sulfur s ⇒ p transition, which is actually approximately 2472 eV, is chosen to be 0, and all other energies are measured relative to that standard.

oxidation of pyrite is the principal and possibly only method by which elemental sulfur can come to be present in the coal,[14,16,17] it has been postulated that the PCE method will only be effective with oxidized coals.

A number of samples before and after treatment with PCE have now been examined with both XAFS and Mössbauer spectroscopies. The Mössbauer results[10] show that the amounts of pyrite in these samples are basically unaltered by the PCE treatment. Hence, the pyritic sulfur in these coals is *not* affected by the PCE treatment.

The sulfur K-edge XANES data for the Upper Freeport coal before and after PCE treatment are shown in Figure 4 and the results on the sulfur forms derived from the least-squares fitting are summarized in Table 2. The XANES results for Freeport coal clearly show a major reduction in at least one form of sulfur. Based on the peak position (0.3 eV) of the peak that disappears, it is difficult to reconcile it with an organic sulfide, the peaks of which occur typically at around 0.7 eV. After the PCE treatment, there is a peak located at 0.7 eV, which is approximately 30% of the intensity of the peak present before PCE treatment. This peak position is compatible with an organic sulfide. Hence we interpret the large peak present in the XANES spectrum of the sample before PCE treatment as a composite peak consisting of contributions from both elemental sulfur and organic sulfide. This would also account for its position intermediate between that for sulfide (0.7 eV) and elemental sulfur (0.0 eV). Such an interpretation strongly suggests that the peak removed is due primarily to elemental sulfur, and based on the XANES analysis, we estimate that about 0.6 - 0.7 wt% sulfur is removed in this form. The value was later confirmed independently by D. Buchanan (E. Illinois University).

It should also be noted that there appears also to be some decrease in the amount of thiophenic sulfur (≈0.15 wt%) based on the total sulfur value estimated for the coal (3.2 wt%) after elemental sulfur removal. However, this amount is within the experimental uncertainty of the technique and may not be significant.

A sample of Indiana #5 coal also exhibited distinct changes with the 30-minute boiling PCE treatment. The organic sulfur forms, calculated from the peak areas in the XANES spectrum and identified on the basis of their peak position, are summarized in Table 2. It would appear that the sulfur species in the Indiana #5 that are reduced by the PCE treatment are elemental sulfur and, to a lesser extent, possibly also the organic sulfide species. However, such a small change is within the estimated experimental errors of the XANES measurement.

A number of other coals subjected to treatment with boiling PCE exhibit essentially the same spectrum after treatment as before and therefore do not show any significant preferential removal of different sulfur forms. Such coals investigated to date include an Ohio #5/#6 coal, an unoxidized Illinois #6 coal from the Argonne Premium sample bank, an oxidized Illinois coal obtained from Prof. D. Buchanan (E. Illinois University), and high sulfur (5.7 wt%) Australian brown coal (Glencoe) that contained a large organic sulfide content and virtually no pyritic sulfur (<0.2 wt.%).

SUMMARY AND CONCLUSIONS

Least squares analysis of sulfur K-edge XANES spectra is a powerful method for quantitative analysis of the functional forms of sulfur in coal and related materials. Thiophenic sulfur is the dominant organic sulfur form observed in all of the coals we have examined, but sulfidic sulfur increases significantly with decreasing rank. Sulfidic sulfur is higher in exinite

maceral separates than in vitrinite or inertinite. Pyritic sulfur measured by XANES agrees with that determined by Mössbauer spectroscopy.

The reactions of different sulfur forms during chemical, biological, or thermal treatment can be quantitatively followed using XANES spectroscopy. Quantitative in situ XANES measurements during coal pyrolysis and oxidation have been carried out at temperatures up to 600°C.

ACKNOWLEDGEMENT

We gratefully acknowledge the support of the Electric Power Research Institute under EPRI contract no. RP-8003.

REFERENCES

1. Huffman, G.P.; Huggins, F.E.; Mitra, S.; Shah, N.; Pugmire, R.J.; Davis, B.; Lytle, F.W. and Greegor, R.B.; *Energy & Fuels,* **1989**, *3*, 47-50.
2. Huffman, G.P.; Huggins, F.E.; Francis, H.E.; Mitra, S.; and Shah, N.; *Processing and Utilization of High Sulfur Coals III*, Eds., R. Markuszewski and T. D. Wheelock, Elsevier, **1990**, 21-32.
3. Huffman, G.P.; Mitra, S.; Huggins, F.E.; Shah, N.; Vaidya, S.; Lu, F.; "quantitative Analysis of All Major Forms of Sulfur in Coal by XAFS Spectroscopy," *Energy & Fuels*, in press.
4. George, G.N.; Gorbaty, M.L.; *J. Amer. Chem. Soc.*, **1989**, *111*, 3182.
5. George, G.N.; Gorbaty, M.L.; Kelemen, S.R.; Sansone, M.; *Energy & Fuels*, **1991**, *5*, 93-97.
6. Waldo, G.S.; Carlson, R.M.K.; Modowan, J.M.; Peters, K.E.; and Penner-Hahn, J.E. *Geochimica et Cosmochimica Acta*, in press.
7. Taghiei, M.M.; Huggins, F.E.; Shah, N.; Huffman, G.P. Amer. Chem. Soc., Div. Fuel Chem. **1991**, *36(2)*, 757-764.
8. Huffman, G.P.; Shah, N.; Taghiei, M.M.; Huggins, F.E.; and Mitra S., to be published in the Proceedings of the International Conference on Coal Science, Newcastle, England, 1991.
9. Taghiei, M.M.; Shah, N.; Huggins, F.E.; Lu, F.; Huffman, G.P.; 1991, submitted for publication in *Energy & Fuels.*
10. Huggins, F.E.; Mitra, S.; Vaidya, S.; Taghiei, M.M.; Lu F.; Shah, N.; Huffman, G.P.; to be published in the Proceedings of the Fourth International Conference on Processing and Utilization of High Sulfur Coals, Idaho Falls, ID, 1991.
11. Huffman, G.P. and Huggins, F.E.; *Fuel*, 1978, *57*, 592.
12. Shah, N.; Keogh, R.A.; Huggins, F.E.; Huffman, G. P.; Shah A.; Ganguly, B.; and Mitra, S., *Prepr. pap. -- Amer. Chemc. Soc., Div. of Fuel Chem.*, 1990, *35(3)*, 784-792.
13. Lee, S.; Kesavan, S.K.; Lee, B.G.; and Ghosh, A.; Proceedings: Thirteenth Annual EPRI Conference on Fuel Science and Conversion, Electric Power Research Institute Report, GS-6219, 1989, pp. 1-1 to 1-21.
14. Buchanan, D.H., Coombs, K.J.; Chaven, C.; Kruse, C.W.; and Hackley, K.C., in: R. Markuszewski and T.D. Wheelock (Eds.) Processing and Utilization of High-Sulfur Coals III, Coal Science and Technology 16, Elsevier, Amsterdam, 1990, pp. 79-87.
15. Buchanan, D.H. and Warfel, L.C. Preprints, ACS Div. Fuel Chem., 35(2) (1990) 516-522.
16. Duran, J.E.; Mahahsay, S.R.; and Stock, L.M., *Fuel*, 65 (1986) 1167-1168.
17. Huggins, F.E. and Huffman, G.P.; in: C.R. Nelson (Ed.), Chemistry of Coal Weathering, Coal Science Technology 14, Elsevier, Amsterdam, 1989, pp. 33-60.

TABLE 1: Derived percentages for forms of sulfur in Argonne Premium coals and several additional coals.

Argonne Premium Coal Sample	Wt% Total Sulfur	Sulfur Forms, %					
		Pyrite	Sulfide	Thioph.	Sulfox.	Sulfone	Sulfate
Pocahontas #3, VA	0.66	24	0	75	0	1	0
Upp. Freeport, PA	2.32	62	6	33	0	1	0
Pittsburgh #8, PA	2.19	52	13	35	0	1	0
Lewis.-Stock., WV	0.71	26	16	56	1	1	0
Blind Canyon, UT	0.62	40	15	46	0	0	0
Illinois #6, IL	4.83	48	19	33	0	0	0
Wyodak-Anders., WY	0.63	24	29	46	0	0	0
Beulah, ND (fresh)	0.80	29	28	30	2	0	12
Beulah, ND (2nd.)	0.80	37	24	30	2	0	7
Additional Coals							
Illinois #6, IBC-101	3.08	34	21	38	3	4	1
Wyodak (micronized)	n.r.	27	25	45	0	0	3
Texas Lignite	n.r.	49	18	30	0	1	2
Glencoe brown coal	5.73	0	44*	55	0	0	1

*Sulfide contribution is 27%; disulfide (± polysulfide) contribution is 17%.

TABLE 2: Derived percentages for forms of sulfur in coals treated with PCE.

Coal Sample treated with PCE	Wt% Total Sulfur	Sulfur Forms, %					
		Pyrite	Sulfur	Sulfide	Thioph.	Sulfone	Sulfate
Freeport, before	3.75	1.8	0.65	0.25	0.85	0.0	0.2
Freeport, after	3.10*	1.9	0.0	0.25	0.7	0.0	0.25
Indiana #5, before	2.50	0.85	0.35	0.4	0.4	0.05	0.45
Indiana #5, in situ	(2.25)	(0.85)	0.2	0.3	0.4	0.05	0.45
Indiana #5, after	1.90	0.85	0.0	0.25	0.4	0.05	0.35

Pyritic sulfur values from Mössbauer spectroscopy.
*Total sulfur estimated as (Total sulfur of coal before - sulfur removed)
Values in () are estimated values, assuming no change in pyritic sulfur.

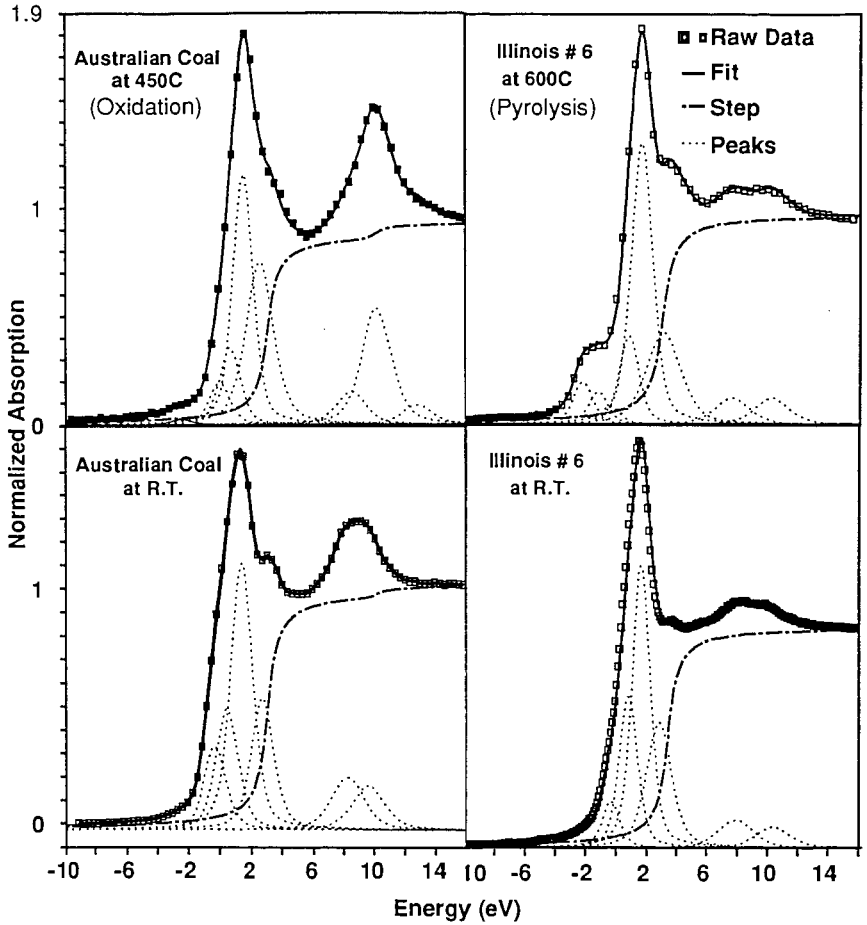

Figure 1. (Right) Fitted XANES spectra of the Illinois # 6 coal obtained at room temperature and at 600C in helium. (Left) Fitted XANES of Australian brown coal at room temperature and at 450C in a helium-oxygen mixture.

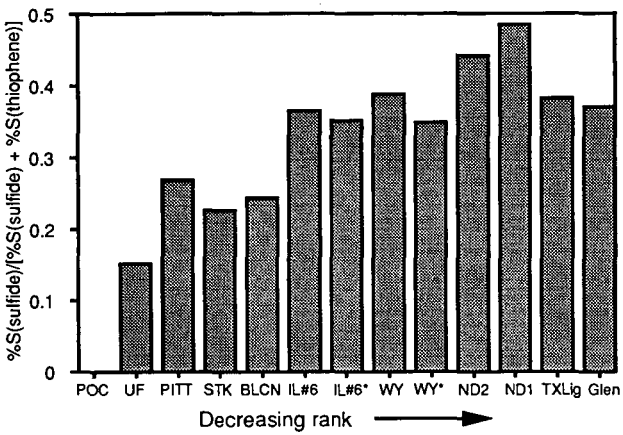

Figure 2: %S(sulfide)/[%S(sulfide)+%S(thiophene)] ratio plotted as a function of rank for the Argonne Premium Coal samples and a number of additional coals. The samples marked with a * are float samples of Illinois #6 and Wyodak coal obtained from Southern Illinois University. Results for two samples of APCSB Beulah-Zap, ND1 and ND2, are also shown.

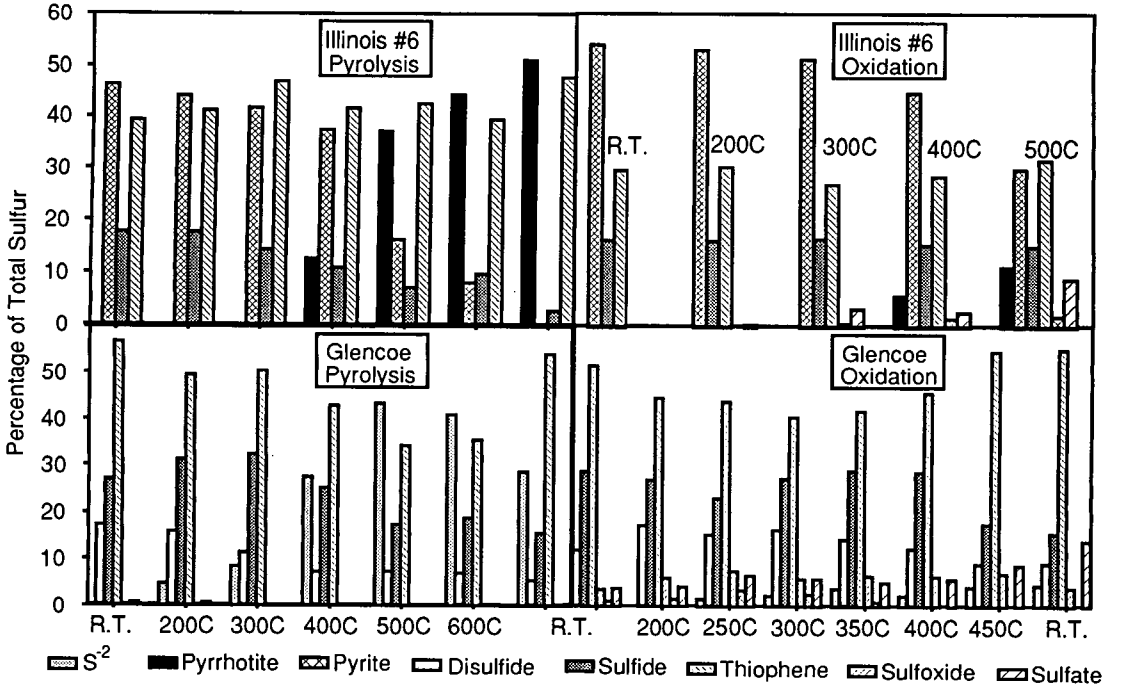

Figure 3. Percentage of sulfur in various functional forms determined by in situ XAFS spectroscopy as a function of temperature for: Illinois # 6-Pyrolysis (upper left); Illinois # 6-oxidation (upper right); Glencoe-Pyrolysis (lower left); Glencoe-oxidation (lower right).

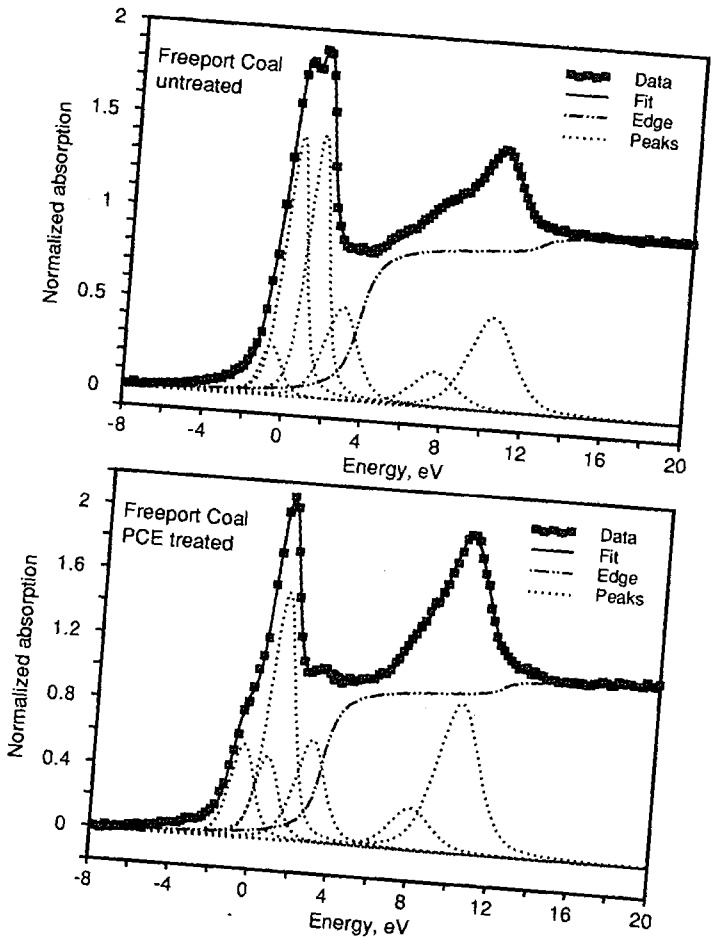

Figure 4: Least-squares fitted sulfur K-edge XANES spectra of Freeport coal before and after treatment with perchloroethylene (PCE).

REACTIVITY OF OXIDIZED ORGANIC SULFUR FORMS IN COAL

S. R. Kelemen, M. L. Gorbaty, G. N. George and P. J. Kwiatek

Exxon Research and Engineering Company
Route 22 East; Clinton Township
Annandale, N.J. 08801-0998, USA.

1. INTRODUCTION

Recent work has shown that it is possible to distinguish and quantify the different organic sulfur types in coal using X-Ray Photoelectron Spectroscopy (XPS) [1-3] and X-Ray Absorption Near Edge Structure Spectroscopy XANES [3-6]. These methods have been employed in the study of fresh coals of different rank and to follow the transformation of organic sulfur under mild pyrolysis conditions (T = 400°C) [7]. The characterization of oxidized organic sulfur forms resulting from mild coal oxidation [2, 8-11] and the subsequent thermal reactivity of these oxidized sulfur forms have not been as extensively explored. The nature of oxidized organic sulfur forms can yield insight into the forms initially present [12]. Initial work with Rasa coal showed that sulfide sulfur forms are converted to oxidized forms while thiophenic forms were mostly unreacted [2]. This paper extends that work to other coals and explores the subsequent thermal reactivity of the oxidized organic sulfur forms.

2. EXPERIMENTAL

The procedures for obtaining XPS and XANES spectra have been discussed elsewhere [1,3]. Pyrolysis with GC gas product analysis were done in a quartz reactor contained within a furnace. The details of these experimental arrangements have been previously described [7,13]. Heating rates were on the order of 0.5°C/min up to 400°C. The temperature and heating conditions were chosen because little of the ultimate amount of hydrocarbons in the volatile matter is released, while much of the H_2S and SO_2 evolve from low rank coals. Spanish lignite (Mequinenza), New Zealand (Charming Creek) and Rasa coal were chosen for study because of the unusually high amounts of organically bound sulfur and unusually low levels of pyritic sulfur [14-16] present. Oxidation was done in the dark, in air (ambient relative humidity 60%) and in an oven kept at 125°C for 5 days.

3. RESULTS and DISCUSSION

The oxidation conditions were chosen because it was found in other coal oxidation studies that the relative rate of total organic oxidation corresponded closely with that of oxidized organic sulfur during the first 5 days at 125°C [10]. Also, the oxidation rates at 125°C can be related kinetically to those that occur near ambient conditions [10,11]. There is roughly two orders of magnitude acceleration of time at 125°C relative to room temperature. Table I shows the XPS quantitative speciation of sulfur forms in the fresh and oxidized coals. Note that sulfides, mercaptans and disulfides are included as "sulfide" in Table I. These results show that a large fraction of the sulfides initially present in the fresh coals is converted to oxidized forms, while thiophenic forms are relatively stable under these mild conditions. For Rasa coal, the dominant oxidation product was identified to be sulfonic acid. For the other

coals, sulfones and sulfoxides are the major oxidation products. Pure compound work has shown that sulfonic acids can arise from the oxidation of disulfides or mercapatans, while sulfoxides and sulfones result from oxidation of sulfides [17,18]. It is apparent from the data above for the Spanish and New Zealand coals that sulfides are converted to sulfoxides and sulfones. For Rasa coal, the evidence supports the speculation that disulfides are the precursors of sulfonic acids. In support of this, the "sulfidic" value for the fresh Spanish coal contains a 15% contribution from an XPS feature associated with mercaptans [7]. This feature does not decrease upon oxidation, nor is sulfonic acid a major product of oxidation. Mercaptans were not identified in fresh Rasa and New Zealand coals. Thus disulfides appear to be the most likely precursors of sulfonic acids in oxidized Rasa coal.

It has been shown that aliphatic sulfur forms decompose to H_2S with some conversion to aromatic forms upon mild pyrolysis [7]. Table II shows the amount of H_2S and SO_2 generated upon pyrolysis for 5 minutes at 400°C, expressed on an atomic S/C basis. Data in Table II show that for fresh Rasa coal sulfide sulfur preferentially decomposes to H_2S, while H_2S formation and conversion to aromatic forms takes place with New Zealand and Spanish coal. The thermal reactivity of the oxidized coal samples shows considerably less H_2S product than the fresh coals. The relative loss in H_2S production roughly tracks the relative loss of sulfide forms in each coal. This supports the view that sulfide sulfur forms are preferentially converted upon oxidation. Data in Table II show that the oxidized organic sulfur forms are lost as SO_2 upon mild pyrolysis. Rasa coal is the most reactive with the appearance of 43% of the oxidized forms as SO_2. For the New Zealand and Spanish coals 7% and 18% respectively of bound oxidized sulfur appeared as SO_2 by this analysis.

These results together with XPS and XANES analysis of the low temperature chars indicate that most of the sulfur present as sulfoxides and sulfones formed during low temperature oxidation is retained in the coal after low temperature pyrolysis. As found for these initial coals [7,14] little sulfide sulfur remains after pyrolysis. While previous work demonstrated that the relative level of aliphatic or "sulfide" sulfur decreases with increasing coal rank [3,7] the present work shows that there can be significant differences in the nature of the components that comprise "sulfide" sulfur. Distinctions can be made on the basis of products following mild oxidation and subsequent thermal reactivity of the oxidized coals.

4. CONCLUSIONS

Sulfide sulfur forms are converted to oxidized forms during mild coal oxidation. Thiophenic forms are largely unreactive. The oxidation products of Spanish lignite and New Zealand coal were mostly sulfones and sulfoxides while Rasa coal gave sulfonic acids. TPD and reactor studies show that the conversion of organic sulfides to oxidized products causes a large decrease in H_2S production upon pyrolysis. A portion of the oxidized organic sulfur forms are lost during low temperature pyrolysis as SO_2. Rasa coal is the most reactive and the amount of SO_2 produced corresponds to 43% of the oxidized species originally present. XPS analysis of oxidized Rasa coal after pyrolysis shows sulfonic acids represent most of the loss. A much smaller fraction of the oxidized sulfur forms initially present in the other coals yield SO_2 upon low temperature pyrolysis. TPD, XPS and XANES results indicate that most of the sulfur initially present as sulfoxides and sulfones is retained in the coal after low temperature pyrolysis.

Acknowledgement: The authors wish to thank P. J. Kwiatek for technical help with the XPS and reaction studies.

5. REFERENCES

1 Kelemen, S. R.; George, G. N.; Gorbaty, M. L. Fuel, 1990, 69, 939.

2 Gorbaty, M. L.; George, G. N.; Kelemen, S. R. Fuel, 1990, 69, 1065.

3 George, G. N.; Gorbaty, M. L.; Kelemen, S. R.; Sansone, M. Energy Fuels, 1991, 5, 93.

4 George, G. N.; Gorbaty, M. L., J. Am. CHem. soc. 1989, 111, 3182.

5 Gorbaty, M. L.; George, G. N.; Kelemen, S. R. Fuel, 1990, 69, 945.

6 Shah, N.; Keogh, R. A.; Huggins, F. E.; Huffman, G. P.; Shah, A.; Ganguly, B.; Mitra, S. ACS Fuel Chem. Div. Preprints, 1990, 35(3), 784.

7 Kelemen, S. R.; Gorbaty, M. L.; George, G. N. Fuel, 1991, 70, 396.

8 Wu, M. M.; Robbins, G. A.; Winschel, R. A.; Burk, F. P. Energy and Fuels 1988, 2, 150.

9 Wu, M. M.; Baltrus, J. P.; Winschel, R. A. Coal Sci. Technol. 1990, 16, 745.

10 Kelemen, S. R.; Freund, H. Energy Fuels 1989, 3, 498

11 Kelemen, S. R.; Freunt, H. Energy Fuels 1990, 4, 165.

12 Wallace, S.; Bartle, K. D.; Baxby, M.; Taylor, N.; Majchrowicz, B. B.; Yperman, J.; Martens, J. J.; Gelan, J. ACS Fuel Chem. Div. Preprints, 1989 34, 721.

13 Freund, H.; Kelemen, S. R. Am. Ass. Pet Geo. Bull. 1989, 3, 42.

14 Torres-Ordonez R. J.; Calkins, W. H.; Klein, M. T., ACS Symposium Series #429, American chemical Society, Washington, D.C., pp. 287-295.

15 Given, P. H. Prog. Energy Combust. Sci. 1984, 10, 149.

16 Ignasiak, B. S.; Fryer, J. F.; Jadernik, P. Fuel 1978, 57, 578.

17 Suter, C. M. in "Organic Chemistry of Sulfur", John Wiley and Sons, London, UK, 1944.

18 Reid, E. E., "Chemistry of Divalent Sulfur", Chemical Publishing Co., New York, USA, 1960.

Table I XPS analysis of sulphur before and after oxidation at 125°C

Mole per cent

Sample	Sulfide	Thiophene	Sulfoxide	Sulfone	Sulfonic Acid
Rasa Initial	26	70	1	1	2
Rasa Oxidized	7	69	4	8	12
Spanish Initial	66	34	0	0	0
Spanish Oxidized	38	42	5	8	4
N.Z. Initial	38	62	0	0	0
N.Z. Oxidized	13	67	8	8	4

Table II Amount of oxide and sulfidic components and the subsequent amount of H_2S and SO_2 produced upon pyrolysis

Atom Ratio S/C (x100)

Sample	XPS Sufide	H_2S Pyrolysis	XPS Oxides	SO_2 Pyrolysis
Rasa Initial	1.83	1.53	0.24	0
Rasa Oxidized	0.42	0.18	1.43	0.61
Spanish Initial	4.25	1.49	0	0
Spanish Oxidized	2.64	0.89	1.18	0.21
N.Z. Initial	1.06	0.17	0	0
N.Z. Oxidized	0.35	0.08	0.56	0.04

ADVANCES IN COAL CHARACTERIZATION BY PROGRAMMED-TEMPERATURE OXIDATION

R. B. LaCount, D. G. Kern, W. P. King, R. B. LaCount, Jr., D. J. Miltz, Jr., A. L. Stewart, T. K. Trulli, D. K. Walker*, and R. K. Wicker**

ViRoLac Industries, Waynesburg, PA 15370
and
Dept. of Chem., Waynesburg College, Waynesburg, PA 15370.
* Dept. of Computer Science, Marshall University, Huntington, WV 25755
** Dept. of Chem., Washington and Jefferson College, Washington, PA 15301

Keywords: coal analysis, sulfur, oxidation

ABSTRACT

This paper describes the current status for the characterization of coal by controlled-atmosphere programmed-temperature oxidation (CAPTO). Distinctive gas evolution patterns are observed among coals of different rank and between raw and treated coals. In addition to two resolved SO_2 peaks, assignable to the oxidation of pyrite and the decomposition of sulfate, two others, assignable to organic structures in the coals, are observed.

INTRODUCTION

Interest continues to be strong in methods to reduce the levels of SO_x and NO_x in the atmosphere as a control strategy for acid deposition. Retrofit technologies (pre- and post-combustion and combustion modification) used singularly or in combination offer the coal-fired utilities a potential route to meet state and federal regulations while limiting capital expenditures in comparison to repowering technologies. Conventional physical cleaning methods result in some inorganic sulfur (pyritic and sulfatic) reductions from coal while the advanced physical coal cleaning procedures under development offer the potential for significant pyrite reduction[1]. Physical cleaning along with coal switching and post-combustion scrubbing techniques are the primary routes currently in use by the utilities in an attempt to meet air emission regulations.

Numerous precombustion chemical beneficiation procedures were developed in the 1970's that removed most of the inorganic sulfur (pyritic and sulfatic) and some of the organic sulfur from coal. Morrison[2] provides an excellent review of these technologies. Bioprocessing as a route for sulfur removal from coal is now under intensive study[3]. Continued development of advanced coal cleaning technologies generates a need for suitable analytical techniques to monitor progress of the work.

The ASTM organic sulfur determination for coal is based upon the difference between the total sulfur analysis and the sulfatic and pyritic sulfur analyses of coal (Method D2492). The method works well for most untreated coals. However, the presence or formation of certain inorganic sulfur species in coals, particularly treated coals[4], that are partially insoluble in hydrochloric or nitric acid, results in a higher reported value for organic sulfur. This limitation presents a serious problem to all laboratories involved in coal desulfurization and other clean coal research. A number of routes to characterize the sulfur distribution in coals have been, and continue to be, studied. Friedman[5] recently presented a critical review of sulfur analyses of coal and Stock et al.[6] reviewed methods to determine sulfur distribution in American bituminous coals. A generally accepted, routine method to distinguish between the organic-sulfur functional groups or to classify the organic sulfur present in treated and untreated coals is vital to those involved in clean coal research.

Reductive and oxidative techniques have been developed as potential routes to classify the sulfur types present in raw and treated coals. Yergy et al.[7],

using a reductive approach, monitored the hydrogen sulfide evolved from a linear increase in temperature and noted five different types of hydrogen-induced sulfur release. Additionally, Attar[9] described a non-isothermal kinetic method for estimation of the organic sulfur functional groups in coal. Majchrowicz et al.[8] recently described an automated approach to the temperature programmed reduction route. However, these reductive approaches do not respond to much of the organic sulfur in coal and cannot be utilized to give any reliable quantitative information for the inorganic, organic, and total sulfur in coal.

Numerous groups have also investigated oxidation as a route to identify sulfur species. Chantret[10], monitored airflow through a differential thermal analysis chamber for SO_2 and CO_2. Temperature rise in an absorbent, lead dioxide for SO_2 and Ascarite for CO_2, was used to detect the presence of the gases. LaCount et al.[11] using a thermal oxidative technique coupled with evolved gas analysis, described a route to qualitatively and quantitatively[12,13] characterize the sulfur, carbon, and hydrogen in coals and treated coals. A coal sample thoroughly dispersed in an inert diluent used to control the exothermic oxidation reactions was exposed simultaneously to a linear increase in temperature and an oxygen/argon flow. Continuous measurement of the concentration of gases evolved from the sample provided a concentration/time or temperature profile for each evolved gas. By use of model compounds and polymeric substances, each SO_2 evolution maxima produced from coal was eventually related to the probable structural type causing the maxima. Integration of the profiles provided an estimate of the sulfur forms and the total sulfur in the coal sample. Total sulfur values were in good agreement with those obtained from ASTM analyses. However, significant overlap of the SO_2 evolution maxima resulting from pyrite and organic sulfur prohibited quantitative estimation of the sulfur forms in raw coals.

Boudou et al.[14] briefly reviewed work in programmed pyrolysis, reduction, and oxidation. Using procedures similar to Chantret's and several other methods, they studied the sulfur species in several high organic sulfur coals.

Calkins[15] described pyrolysis experiments directed toward the determination of organic-sulfur-containing structures in coal and briefly reviewed work in this area. Fixari et al.[16] studied oxidative pyroanalysis as a route to the elemental analysis for the volatile and nonvolatile fractions of coals.

Other routes for a direct determination of organic sulfur in coal have been investigated. Some of these involve the electron microprobe[17,18], the scanning electron microscope[19], or the transmission electron microscope[20]. The equipment involved is costly and variations in the organic sulfur content in coal requires averaging over a number of sites in each sample. Huffman et al.[21] investigated the molecular structure of organic sulfur in coal macerals by X-ray absorption fine structure (XAFS) spectroscopy. However, additional work is required on model systems to clarify ambiguities in the interpretation of the XAFS data.

A step-wise procedure using perchloric acid for determination of sulfate, sulfide, pyrite, and organic sulfur in a single coal sample has been reported[22]. However, the procedure is tedious and probably not suitable for routine analyses.

DISCUSSION

This paper describes recent improvements in oxidation conditions and in the detection system of the controlled-atmosphere, programmed-temperature oxidation (CAPTO) apparatus previously described[13]. The effort is directed toward development of methodology to obtain well resolved evolution profiles that will enhance our understanding of the nature of sulfur present in coal. This knowledge is basic to the development of improved technology for sulfur removal from coals and for selecting those coals which have the greatest

beneficiation potential. The unit also offers potential as a one-step direct analysis route for the inorganic, organic, and total sulfur present in untreated and treated coals.

Several current applications utilizing a partially modified instrument are discussed. A complete description of the totally redesigned CAPTO instrument/method (patent pending) will be presented elsewhere.

INSTRUMENT MODIFICATIONS AND METHOD

Portions of the system shown in ***Figure 1*** have been previously described[13]. An FTIR spectrometer is used as a detector for analysis of the SO_2, CO_2, H_2O, and NO_2 formed instead of the nondispersive infrared analyzers formerly used.

The CAPTO technique is used to analyze coals, treated coals and other high molecular weight substances reduced to a particle top eize of -60 mesh, or smaller. The sample is thoroughly dispersed in a diluent (to reduce exotherms that occur during oxidation) and exposed simultaneously to a linear increase in temperature and to an oxygen/argon flow. The oxidized gases are monitored continuously and intermittent evolution maxima are observed for SO_2, CO_2, H_2O, and NO_2 as the oxidation proceeds. If the SO_2 evolution maxima are well resolved, a quantitative estimation of the sulfur types present in the sample can be obtained. However, the oxidation conditions used in previous work (diluent, 10% O_2 in argon, and a temperature ramp of 2 - 5°C/min.) resulted in overlap between the evolution maxima detected from pyritic sulfur and that from the second major occurrence of organic sulfur in coal.

In order to improve the oxidative technique, experiments were completed with the reaction parameters (temperature ramp, oxidant flow, and oxygen concentration) varied systematically. Optimum temperature ramp and flow were established. Using these conditions the programmed temperature oxidation of coal samples was studied as a function of oxygen concentration.

A series of CAPTO experiments were performed with ROM Illinois No. 6 coal. A different oxygen concentration was used in each experiment. The oxygen concentration in argon was varied from 4% to 16% in 2% increments. No improvement in resolution of the SO_2 evolution profile was noted. In fact, the pyritic and second organic SO_2 evolution maxima showed a decrease in resolution with increasing oxygen concentration. Careful measurement of the pyritic SO_2 evolution maxima revealed a slight shift to higher temperatures with increasing oxygen concentration (e.g. 4% - 430°C; 10% - 435°C). A CAPTO experiment using 20% oxygen resulted in one SO_2 evolution maxima at 445°C for the pyritic and aromatic sulfur.

Although loss of oxidative selectivity between the two major occurrences of CO_2 and SO_2 derived from organic structures in the coal was a concern, CAPTO experiments were completed using pure oxygen. The results (***Figure 2***) show that the oxidative selectivity between the first (290°C) and second (420°C) major evolutions of SO_2 from organic structures is retained and, importantly, the pyritic sulfur is oxidized at a higher temperature (478°C) than the organic sulfur. ***Figure 2*** also shows SO_2 evolution due to decomposition of iron sulfate at 585°C.

Previously, ^{13}C CP-MAS n.m.r. work[13] was completed on coal samples both before and after a CAPTO experiment that was terminated at 400°C. The n.m.r spectrum prior to the experiment clearly indicated the presence of aromatic structures and nonaromatic structures (f_a = 0.69). After the sample was exposed to CAPTO conditions up to 400°C, the spectrum revealed an essentially unchanged aromatic region; however, the nonaromatic region had been almost totally eliminated (f_a = 0.87). Thus, the lower temperature CO_2 and SO_2 evolutions resulting from organic structures were attributed to carbon and sulfur lost primarily from oxidation of nonaromatic coal structures, and the CO_2 and SO_2

evolutions from organic structures above 400°C were attributed primarily to carbon and sulfur lost during oxidation of the aromatic coal matrix. We still believe this to be a generally valid premise. However, as noted in our earlier work[13], stable aryl sulfides and sulfones oxidize above 400°C and would be included in addition to thiophenic structures in what we term "aromatic".

APPLICATION OF CAPTO TO MICROBIAL TREATED COAL

An example in which both CO_2 and SO_2 evolution profiles are important in characterizing a coal/treated coal is shown below. A -200 mesh Illinois No. 6 ROM coal was treated with a mixed consortium of Thiobacillus ferrooxidans for 15 days at 30 - 35°C (CO_2 purge). The CAPTO results from the untreated and treated coal are shown in ***Figures 3*** and ***4***. The SO_2 evolution profile for the untreated coal shows the presence of temperature maxima for nonaromatic sulfur (290°C), aromatic sulfur (410°C), pyritic sulfur (478°C), and sulfate (590°C). This sulfur profile is consistent with other Illinois No. 6 raw coal samples tested in our laboratory. The SO_2 evolution profile from the treated coal shows that (1) the nonaromatic SO_2 evolution temperature is unchanged and (2) the pyritic sulfur and sulfate have been removed. However, a portion of the aromatic sulfur has been oxidized at 385°C, 25°C below the oxidation temperature of aromatic sulfur in the untreated coal.

The CO_2 evolution profile for the untreated coal (***Figure 4***) shows temperature maxima for nonaromatic carbon oxidation at 290°C and aromatic carbon oxidation at 420°C. The CO_2 evolution profile for the treated coal shows the oxidation temperature of the nonaromatic carbon to be unchanged, but a portion of the aromatic carbon is oxidized at 390°C, 30°C below that of the untreated coal.

The CAPTO technique is sensitive to changes in coal structure and sulfur content resulting from the bioprocessing of coal.

APPLICATION OF CAPTO TO MOLTEN CAUSTIC LEACHING

A Pittsburgh Seam (ROM) coal (Ohio No. 8) from Belmont County, Ohio was thoroughly mixed with an inorganic diluent, and simultaneously subjected to an oxygen flow and a programmed linear increase in temperature. Pyrite oxidation occurs after the organic sulfur has been oxidized as shown in ***Figure 5***. This sample of Pittsburgh Seam coal was taken from a feed coal used in a molten caustic leaching treatment. The CO_2 and H_2O evolutions are also shown in ***Figure 5***.

The products resulting from two different molten caustic treatments were also examined oxidatively under the same CAPTO conditions as the feed coal. The results are shown in ***Figures 6*** and ***7***. The molten caustic leached product used to produce the CAPTO results of ***Figure 6*** had been treated with 1:1 KOH/NaOH, 2:1 caustic/coal at approximately 438°C (kiln outside wall temperature). Essentially all of the pyrite and iron sulfate have been removed by the caustic treatment. A small broad SO_2 evolution peak centered at 330°C is present indicating that the nonaromatic/aromatic sulfur content has been significantly reduced compared to that of the feed coal shown in ***Figure 5***.

The molten caustic leached product used to obtain the CAPTO results shown in ***Figure 7*** had been treated with NaOH at a caustic to coal ratio of 2:1 at approximately 415°C (kiln outside wall temperature). Sulfur dioxide from pyrite and iron sulfate do not appear in the profile. The aromatic sulfur has been markedly reduced in this sample; however, a small residual aromatic sulfur evolution centered at 415°C is noted. The nonaromatic sulfur hae been removed to a lesser degree and a small SO_2 evolution peak centered at 290°C is noted. These results confirm our earlier findings[13] that the molten caustic treatment in this temperature range removes more aromatic sulfur than nonaromatic sulfur.

The CO_2 and H_2O evolution profiles have also been recorded and plotted in ***Figures 6*** and ***7***. This information is routinely obtained from the oxidative degradations and provides a route to continuously measure the C/H ratio as oxidation proceeds. Thus, it is of value beyond the C/H ratio obtained simply from total carbon and hydrogen analyses. Note the differences between the CO_2 evolution profiles in ***Figures 6*** and ***7***. A shoulder denoting oxidation of nonaromatic carbon at 310°C is present in ***Figure 7***. ***Figure 6*** (results of treatment at 438°C) shows less nonaromatic carbon compared to the coal treated at 415°C (***Figure 7***). ***Figure 7*** also shows considerably more water resulting from oxidation of nonaromatic hydrogen than ***Figure 6***. The molten caustic product (***Figure 6***) formed at 438°C appears to be much more "charlike" than the product (***Figure 7***) formed at 415°C. One would expect the product formed at 415°C to have better combustion properties than the product formed at 438°C.

Measurement of CO_2 evolved as the oxidative degradation proceeds also helps to better define the point at which the SO_2 produced must be derived from a noncarbon source. The CAPTO technique is sensitive to changes in coal structure and sulfur content resulting from changes in molten caustic leaching conditions.

CAPTO MODEL SYSTEMS

The redesigned CAPTO apparatus utilizes a high oxygen concentration flow. A change in concentration from 10% oxygen in argon to 100% oxygen is associated with an increase in the pyrite oxidation temperature from 430°C to 478°C. While the oxidative selectivity between the two major occurrences of CO_2 and SO_2 from organic carbon and sulfur has been retained, the oxidation temperatures have decreased. Additionally, one must expect that the oxidation temperatures of standards and model systems originally used to establish a correlation between their oxidation temperatures and the oxidation profile of coals will change. Accordingly, the key standards and model systems are being oxidized under the new conditions. The oxidation results obtained to date are compared in ***Table 1***. The SO_2 evolution temperatures of the model systems under the new conditions are consistent with the coal assignments.

CONCLUSIONS

Using high oxygen concentrations, the CAPTO SO_2 evolution peaks due to the oxidation of the aromatic and pyritic sulfur are sufficiently resolved so that small differences in the amounts of nonaromatic, aromatic, and inorganic sulfur may be detected. This is important for use of CAPTO in selecting those coals which have the greatest upgrade potential when subjected to new or existing sulfur removal technologies.

The improved resolution may also be sufficient for CAPTO to be used as a one step direct determination of organic, inorganic and total sulfur. We are presently completing extensive quantitative studies to assess the feasibility of this determination.

ACKNOWLEDGEMENTS

This work has been supported in part by Department of Energy SBIR Phase II Grant No. DE-FG01-90ER81055 and in part by the Ben Franklin Technology Center of Western Pennsylvania through Pennsylvania's Ben Franklin Partnership Program. The authors wish to thank the Pittsburgh Energy Technology Center (PETC) and specifically Sidney Friedman, Robert Warzinski, and Bernard Blaustein for their interest and support in the early phases of the work. The authors also thank Waynesburg College for its cooperation and support. Special thanks go to David J. Boron of PETC for his ongoing helpful discussions and for the coal samples used in this study.

REFERENCES

1. Markuszewski,R., Wheelock, T.D., Editors. Processing and Utilization of High-Sulfur Coals III. Elsevier Science Publishers, Amsterdam, 1990.
2. Morrison,G.F., "Chemical Desulphurization of Coal" Report Number ICTIS/TR15, IEA Coal Research London, November, 1982.
3. Proceedings: 1990 First International Symposium on the Biological Processing of Coal. Orlando, Florida: Electric Power Research Institute GS-6970, May, 1990.
4. Warzinski, R. P., Friedman, S., Ruether, J. A., and LaCount, R. B., "Air/Water Oxydesulfurization of Coal - Laboratory Investigation", DOE/PETC/TR-80/6, August, 1980, 113 pages.
5. Friedman, S., "Sulfur Analyses of Coal - A Critical Evaluation." In Proceedings: 1990 First International Symposium on the Biological Processing of Coal. Orlando, Florida: Electric Power Research Institute GS-6970, May, 1990, p. 1-3.
6. Stock, L. M., Wolny, R., Bal, B., "Sulfur Distribution in American Bituminous Coals", Energy & Fuels, 1989, 3(6), 651-661.
7. Yergy, A. L., Lampe, F. W., Vestal, M. L., Day, A. G., Fergusson, G. L., Johnston, W. H., Snyderman, J. S., Essenhigh, R. H., Hudson, J. E., "Nonisothermal Kinetics Studies of the Hydrodesulfurization of Coal", IEC Proc.Res. Dev. 1974, 13, 233-240.
8. Attar, A., "Sulfur Groups in Coal and Their Determinations", Analytical Methods for Coal and Coal Products, Vol. 3, Acad. Press, New York, 1979, 585-625.
9. Majchrowicz, B. B., Yperman, J., Mullens, J., Van Poucke, L. C., "Automated Potentiometric Determination of Sulfur Functional Groups in Fossil Fuels." Anal. Chem, 1991, 63, 760-763.
10. Chantret, F., "Identification of Pyrites and Organic Material by Differential Thermal Analysis in Conjunction with Continuous Gas Analysis." C. R. Acad. Sci., Paris, 1967, 264, 1825.
11. LaCount, R. B., Gapen, D. K., Dell, David A., Simpson, F. W., Helms, Charles A., "Thermal Oxidative Degradation of Coal as a Route to Sulfur Functionality: An Initial Study", in New Approaches in Coal Chemistry, A.C.S. Symposium Series, 169, 415 (1981).
12. LaCount, R. B., Anderson, R. R., Helms, C. A., Friedman, S., Romine, W. B., "Construction and Operation of A Controlled-Atmosphere Programmed-Temperature Reaction Apparatus", DOE/PETC/TR-8315, Apr., 1983.
13. LaCount, R. B., Anderson, R. R., Friedman, S., Blaustein, B. D., "Sulfur in Coal by Programmed - Temperature Oxidation", Fuel 1987, 66(7), 909.
14. Boudou, J. P., Boulegue, J., Malechaux, L., Nip, M., deLeeuw, J. W., Boon, J. J., "Identification of Some Sulphur Species in a High Organic Sulphur Coal." Fuel 1987, 66(11), 1558.
15. Calkins, W. H., "Investigation of Organic Sulfur-Containing Structures in Coal by Flash Pyrolysis Experiments", Energy & Fuels 1987, 1(1), 59-64.
16. Fixari, B., LePerchec, P., Bigois, M., "Oxidative Pyroanalysis: Elemental Analysis in Volatile and Non-Volatile Fractions of Coals and Related Materials." Fuel 1990, 69(7), 851.
17. Karner, F. R., Hoff, J. L., Huber, T. P., Schobert, H. H., "Electron Microprobe Techniques for Quantitative Analysis of Coal and Coal Macerals", Prepr. Pap. - Am. Chem. Soc., Div. Fuel Chem. 1986, 31(1), 29.
18. Raymond, R. Jr., and Gooley, R., "A Review of Organic Sulfur Analysis in Coal and A New Procedure", Scanning Electron Microscopy/1978/I, 93 (1978)
19. Straszheim, W. E., Greer, R. T., Markuszewski, R., "Direct Determination of Organic Sulfur in Raw and Chemically Desulfurized Coals", Fuel 1983, 62(9), 1070-75.
20. Wert, C. A., Hsieh, K. C., Tseng, B. H., Ge, Y. P., "Applications of Transmission Electron Microscopy to Coal Chemistry", Fuel 1987, 66(7), 915
21. Huffman, G. P., Huggins, F. E., Mitra, S., Shah, N., Pugmire, R. J., Davis, B., Lytle, F. W., Greegor, R. B., "Investigation of the Molecular Structure of Organic Sulfur in Coal by XAFS Spectroscopy", Energy & Fuels 1989, 3(2), 200-205.
22. McGowan, C. W., Markuszewski, R., "Direct Determination of Sulphate, Sulphide, Pyritic, and Organic Sulphur in a Single Sample of Coal by Selective, Step-Wise Oxidation with Perchloric Acid", Fuel 1988, 67(8), 1091-1095.

Table 1

SULFUR DIOXIDE EVOLUTION TEMPERATURES
OF COALS AND MODEL SYSTEMS

Coal/Model System	Temperature, Degrees C	
	10% O_2	100% O_2
Illinois No. 6 (ROM)		
Nonaromatic	330	295
Aromatic	470	420
Pyritic	430	478
Sulfate	-	585
Pittsburgh Seam (Ohio No. 8, ROM)		
Nonaromatic	320	300
Aromatic	475	428
Pyritic	430	482
Sulfate	-	592
Pyrite (Deister Table concentrate)		
Pyritic	430	485
Sulfate	620	560, 595
Ferrous Sulfate	620	595
Ferric Sulfate	620	595
Polydibenzothiophene	540	450
Poly(thiophene-tetrahydrothiophene)		
Nonaromatic	300	290
Aromatic	475	410

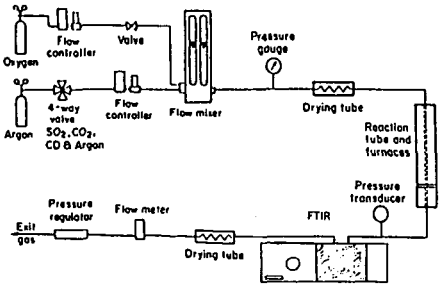

Figure 1. Controlled-atmosphere, programmed-temperature (CAPTO) instrument flow system.

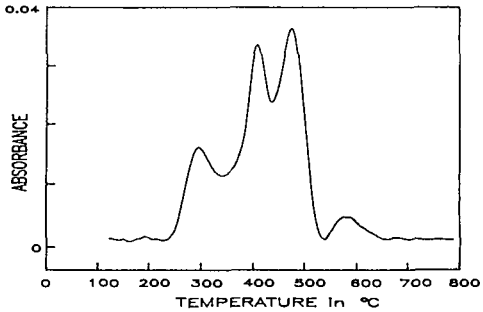

Figure 2. CAPTO evolution profile for sulfur dioxide from Illinois No. 6 ROM coal.

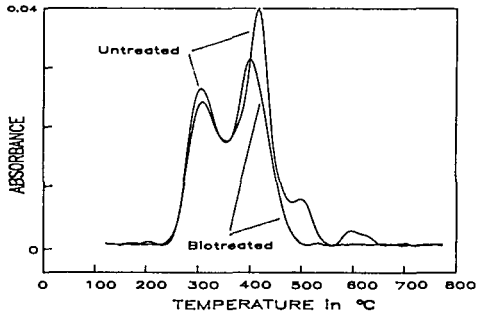

Figure 3. CAPTO evolution profiles for sulfur dioxide from 80 mg of Illinois No. 6 ROM coal (biotreated and untreated).

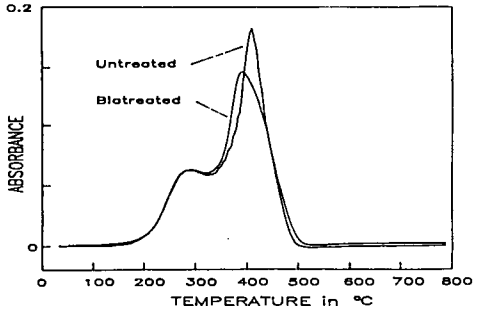

Figure 4. CAPTO evolution profiles for carbon dioxide from 80 mg of Illinois No. 6 ROM coal (biotreated and untreated).

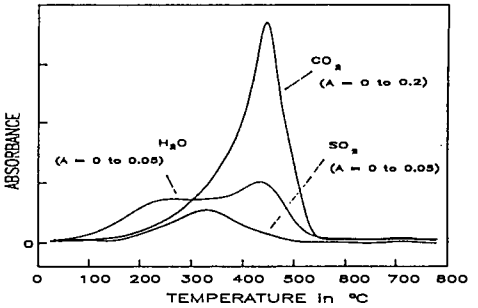

Figure 6. CAPTO evolution profiles from molten caustic treated (438°C) Pittsburgh No. 8 coal.

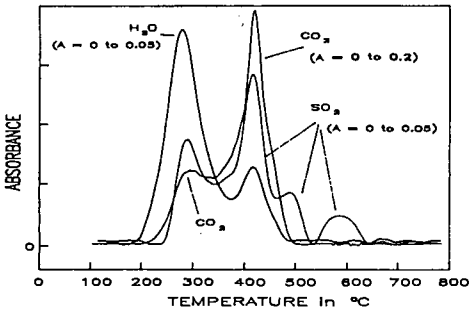

Figure 5. CAPTO evolution profiles from Pittsburgh No. 8 ROM coal (Belmont County, Ohio).

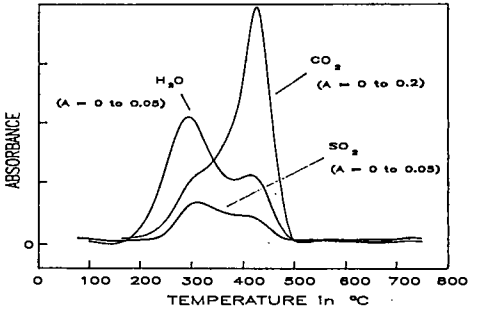

Figure 7. CAPTO evolution profiles from molten caustic treated (415°C) Pittsburgh No. 8 coal.

Transformation Kinetics of Organic Sulfur Forms in Argonne Premium Coals During Pyrolysis

S. R. Kelemen, M. L. Gorbaty, S. N. Vaughn and G. George

Exxon Research and Engineering Company
Corporate Research Laboratories
Route 22 East
Annandale, NJ 08801

The evolution of H_2S during pyrolysis of Argonne premium coal has been monitored with a mass spectrometer in Temperature Programmed Decomposition (TPD) experiments. X-ray Absorption Near Edge Structure Spectroscopy (XANES) and X-ray Photoelectron Spectroscopy (XPS) have been used to follow the changes that occur in the distribution of organic sulfur forms after pyrolysis of these coals to 400°C. The low temperature (T<400°C) elimination of aliphatic sulfur as H_2S is accompanied, in some cases, by the conversion of aliphatic sulfides to aromatic sulfur forms. This work explores the kinetics of H_2S formation. The method of heating rate variation was used in the TPD experiments to derive kinetic parameters for H_2S production during pyrolysis. The results indicate that the decomposition reaction of organic sulfides to form H_2S proceeds prior to most of the conversion of organic hydrocarbons to volatile matter during pyrolysis. This trend is consistent with XANES and XPS findings that there is very little sulfidic sulfur remaining after low temperature pyrolysis of different rank coals.

I. Introduction

Recent advances in the ability to directly quantify sulfur forms in coal by XANES and XPS [1-5] and gaseous sulfur pyrolysis products in a controlled environment [6-8] provides an opportunity to examine the detailed kinetics of the sulfur related chemistry that occurs during laboratory pyrolysis. The monotonic decrease in aliphatic sulfur forms with increasing coal rank has been established by direct measurement [4]. Another XANES and XPS study of several low rank coals has provided evidence that most of conversion of aliphatic sulfides to aromatic forms occurs under milder pyrolysis conditions than those required for the production of almost all of the organic volatile matter of coal [8]. In addition some of the aliphatic sulfur forms are eliminated as H_2S. Pyrolysis studies of model compounds show that organic sulfides are reactive at low temperature (T<750°C) while heterocyclic sulfur structures are not [6,7,9].

The current accuracy of XANES and XPS probes for quantitative determination of organic sulfur forms does not easily allow a detailed kinetic study of the transformation of aliphatic sulfur to aromatic forms during laboratory pyrolysis. While a direct relationship between the initial amount of aliphatic sulfur present in coal and H_2S formed during pyrolysis cannot be made it is certain that the reactions signified by H_2S evolution during pyrolysis of low rank coal are partially responsible for the relatively high levels of aromatic sulfur following mild (T < 400°C) pyrolysis [8]. A comparison of the TPD pattern of H_2S evolution for high rank coal with those of very low temperature chars made from low rank coals show that they are remarkably

similar [8]. The present work focuses on the thermal chemistry and the kinetics of the reaction of aliphatic sulfur forms in coals from the Argonne Premium sample program.

II. Experimental

The procedures for obtaining XPS and XANES spectra have been discussed elsewhere [1-4]. XANES experiments were conducted at the National Synchrotron Light Source at Brookhaven National Laboratory on line X-10C. Sulfur speciation was accomplished by spectra reconstruction based on third derivatives of the absorption spectra of model compounds. XPS spectra were obtained on a stand alone laboratory Vacuum Generators (VG) ESCA lab system using 5 channel detection. MgKa non-monochromatic radiation was used. Sulfur speciation was based on a self-consistent curve resolution methodology using experimental instrumental response functions and energy positions from pure model compounds. This methodology has been extensively described [2,4].

The TPD unit is comprised of an ultra high vacuum (UHV) compatible reaction vessel differentially pumped and attached to a UHV main chamber. H_2S detection was accomplished with a mass spectrometer located in the main chamber. The pressure rose to a maximum of 1×10^{-5} torr in the section where the reaction vessel was located and resulted in a maximum pressure rise of 5×10^{-7} torr in the main chamber. A typical coal sample size ranged from 0.5 to 5 mg, loaded into a 3mm x 15mm ceramic vessel. A fine chromel-alumel thermocouple was inserted into the center of the sample bed and the top of the vessel was packed with quartz wool. The vessel was indirectly heated by surrounding tantalum resistive heating elements. Linear heating rates of from 0.05 to 5.0°C/sec were used. Further details of this experimental arrangement appear elsewhere [8,10].

The method of heating rate variation was used to analyze the TPD data [11-13]. A plot of ln B/Tp2 (vs) 1/Tp where B equals the experimental heating rate and Tp equals the temperature of the peak maximum, produces a line with slope equal to -(Ea/R) [11,12]. These Arrhenius parameters provide input for a more detailed discrete distribution of activation energy kinetic model.

The model is based on parallel first order reactions to describe the pyrolysis kinetics of H_2S evolution. The preexponential factor was determined from the experimentally derived activation energy and peak maximum. In order to describe the potential contribution from multiple kinetic processes to the TPD spectrum, a series of kinetic expressions was calculated at 2 kcal/mole increments about the experimentally derived energy value for the peak maximum while the preexponential factor was assumed to remain constant. The temperature of the peak maximum for each process is fixed by these constraints for a given heating rate. The level of contribution from each assumed first order reaction, calculated at 2 kcal/mole increments, is determined by a least squares fit of the calculated sum to the experimental data. Least squares calculations were done using a Cray X-MP/14se computer.

III. Results and Discussion

XANES and XPS were used to characterize the level of aliphatic sulfur initially present in fresh Argonne premium coal samples and following brief pyrolysis of coal at 400°C. Table I shows the results. The change in the relative aliphatic content is most pronounced for lower rank that have high initial aliphatic sulfur

contents. Most of the aliphatic sulfur is converted to aromatic sulfur forms or eliminated as H_2S during this mild pyrolysis. The XANES data for Illinois #6 char produced at 700°C show that there is little further decline in the aliphatic content.

The evolution of H_2S measured by TPD from Argonne Premium coals at a fixed heating rate of 0.23°C/sec is shown in Figure 1. The position of the peak maximum occurs at a lower temperature as the coal rank decreases. The very sharp H_2S evolution spike seen at high temperature in all cases is associated with pyrite decomposition. This sharp spike is not apparent in coals with high organic sulfur and very low inorganic sulfur. As an example of this, the sharp spike is not observed with samples of depyritized Illinois #6 coal nor with samples of extracts of Illinois #6 coal since neither contains pyrite. Lower rank coals such as Wyodak and Illinois #6 show a distinct peak near 400°C in the TPD H_2S trace. For higher rank coals such as Pocahontas the onset of evolution occurs at much higher temperature and appears almost as a shoulder on the sharp pyrite related spike. Coals such as Wyodak and Illinois #6 provide the opportunity for more accurate and detailed analysis.

Ion peaks of evolved gases during TPD experiments at varying heating rates were measured for Illinois #6 and Wyodak coal. The kinetic behavior of gases other than H_2S have been extensively studied [14-16] and their kinetic behavior is important to tie the present work to other kinetic studies. The resultant Arrhenius plot for H_2S, CH_4 and light hydrocarbons (m/e = 41; C_3-C_8) determined in this work are shown in Figure 2. The different products show distinct kinetic patterns that will be discussed below. The resultant activation energies derived from the slopes of the lines in Figure 2 appear in Table II along with the calculated preexponential factor. The activation energy is based on least squares analysis. The comparable data for Wyodak coal is also found in Table II.

The position of the m/e = 41 peak is closely related to the position of the peak maximum for tar production as measured by infrared at the same heating rate for the Argonne Premium coals [17]. The activation energy and preexponential factor for hydrocarbons from Illinois #6 coal are in good agreement with those of previous studies [15,16]. The kinetic parameters for hydrocarbons from Wyodak coal also agree with previous findings [15] except in one where roughly a 10 kcal/mole higher activation energy was found [16]. The rate constants, however are similar. The present findings appear more reliable since only 3 different heating rates were used in reference [16]. while the results of the present work are based on a larger number of experiments.

The kinetic parameters for H_2S evolution from Argonne Premium coals have not been previously examined. Table II shows those for H_2S are significantly different that those for hydrocarbons. The reactions responsible for the elimination of H_2S from Illinois #6 and Wyodak coals happens faster than those that produce most of the volatile hydrocarbons during thermolysis. It is recognized that a single first-order reaction does not provide a good description of the complex hydrocarbon pyrolysis processes of coal [16]. While a single first-order expression is inadequate for a complete description of the H_2S TPD data, most of the H_2S evolution at different heating rates can be accounted for using a small number of Arrhenius for each coal. The TPD data for H_2S were analyzed in the context of the discrete distribution of activation energy kinetic model described in the Experimental section. Table III shows the results of the analysis. Figure 3 shows the TPD spectrum

of H_2S from Wyodak coal at a heating rate of 0.2 deg/sec and the simulated TPD spectrum based on the results of the discrete distribution of activation energy kinetic model. Contributions related to the pyrite H_2S spike are not considered. Table III shows that processes with activation energy lower than the value of the main peak contribute more in the case of Wyodak, a lower rank coal relative to Illinois #6.

It is interesting to note that the present kinetic results can be examined in the context of the early stages of coal metamorphism. Extrapolation of the results for H_2S derived here for Wyodak and Illinois #6 coal, to geological temperatures and times (several million years below 100°C) would predict that much of the H_2S would have been eliminated prior to the loss of much of the other hydrocarbon matter. The relative hydrocarbon kinetic reference is taken as that of the m/e = 41 peak. The H2S is predicted to be progressively eliminated over extremely long times at low temperature as coal rank increases. The present kinetic data for H2S along with XANES and XPS data on the depletion in the relative level of aliphatic sulfides still leaves open the possibility that the organic reactions specific to sulfur that occur during laboratory pyrolysis may be related to those that occur during the early stages of coal metamorphism.

IV References

1) George, G. N.; Gorbaty, M. L. J. Amer. Chem. Soc., 1989, 111, 3182.

2) Kelemen, S. R.; George, G. N.; Gorbaty, M. L. Fuel 1990, 69, 939.

3) Gorbaty, M. L.; George. G. N.; Kelemen, S. R. Fuel 1990,69, 945.

4) Gorbaty, M. L.; George, G. N.; Kelemen, S. R. Energy and Fuels 1991, 5, 93.

5) Shah, N; Keogh, R. N.; Huggins, F. E.; Huffman, G. P.; Shah, A.; Ganguly, B.; Mitra, S. ACS Fuel Chem. Div. Prep., 1990, 35, 785.

6) Torres-Ordonez, R. J.; Calkins, W. H.; Klein, M. T. ACS Symposium Series #429; Washington DC; pp. 287-295.

7) Boudou, J. ACS Symposium Series #429; Washington DC; pp. 345-364.

8) Kelemen, S. R.; Gorbaty, M. L.; George, G. N.; Kwiatek, P. J.; Sansone, M. Fuel 1990, 70, 396.

9) Calkins, W. H. Energy Fuels, 1987, 1, 59.

10) Freund, H.; Kelemen, S. R. Am. Ass. Pet. Geo. Bull., 1989, 73, 1011.

11) Readhead, P. A. Vacuum, 1962, 12, 203.

12) Falconer, J. L.; Schwarz, J. A. Cat. Rev. Sci. Eng., 1983, 25, 141.

13) Burnham, A. K.; Braun, R. L.; Gregg, H. R.; Samoun, A. Energy Fuels, 1987, 1, 452.

14) Serio, M. A.; Solomom P. R.; Carangelo, R. M. ACS Fuel Chem. Div. Prepr. 1988, 33, 295.

15) Solomon, P. R.; Serio, M. A.; Carangelo, R. M.; Bassilakis, R.; Gravel, D; Baillargeon, M.; Baudais, F; Vail, G. Energy Fuels, 1990, 4, 319.

16) Burnham, A. K.; Oh, M. S.; Crawford, R. W. Energy Fuels, 1989, 3, 42.

17) Kelemen, S. R.; Vaughn, S. N.; Gorbaty, M. L. Energy Fuels, Submitted.

Table I

Mole percent aromatic Sulfur by XPS and XANES for Argonne Premium Coal Samples Before and After 400°C Pyrolysis

Coal	% Carbon (dmmf basis)	XANES		XPS	
		Fresh	Char	Fresh	Char
Beulah-Zap	74.05	63	94	55	-
Wyodak-Anderson	76.04	67	89	63	84
Illinois #6	80.73	67	95	69	87
Blind Canyon	81.32	76	95	65	-
Pittsburgh #8	84.95	78	95	75	-
Lewiston	85.47	80	91	86	-
Upper Freeport	88.08	87	96	81	-
Pocohontas	91.81	87	94	100	-

Table II

Kinetic Parameters for Pyrolysis Products Determined by the Method of Heating Rate Variation

Coal	Product	Preexponential Log A	Activation Energy kcal/mole	Number of Experimental Observations
Wyodak	H_2S	11.8	44.7 (+1.1)	6
Illinois #6	H_2S	11.9	45.0 (+2.3)	7
Wyodak	C_3-C_8	13.0	50.8 (+1.2)	17
Illinois #6	C_3-C_8	12.9	50.6 (+1.0)	11
Wyodak	CH_4	11.8	50.0 (+2.0)	14
Illinois #6	CH_4	11.8	50.4 (+2.1)	10

Table III

Distribution of Activation Energies Found to Simulate H_2S Evolution. The Contribution of Each Kinetic Process is Calculated Using a 2 kcal/mole Energy Increment. The Amount Due to Processes >+4 and those <-4 kcal/mole Have Been Combined in the Table. All Values Are Listed as the Percentage of the Total.

Coal	<-4	-2	Main Peak	+2	>+4
Wyodak	16	20	26	16	22
Illinois #6	3	13	41	11	32

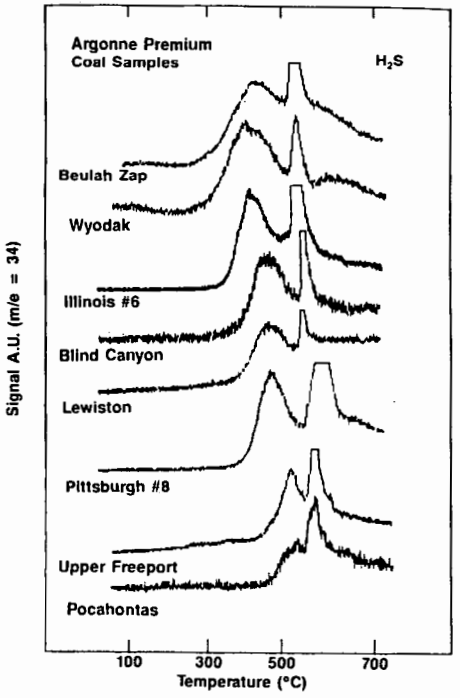

Figure 1

The H2S TPD Spectra of Argonne Premium Coals.
The Heating Rate Was 0.23 deg/sec.

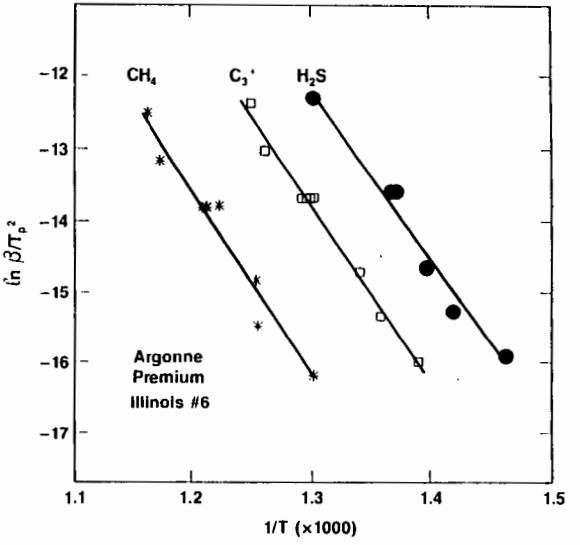

Figure 2

Arrehenius Plot Derived From the Method of Heating
Rate Variation For Argonne Premium Illinois #6 Coal.

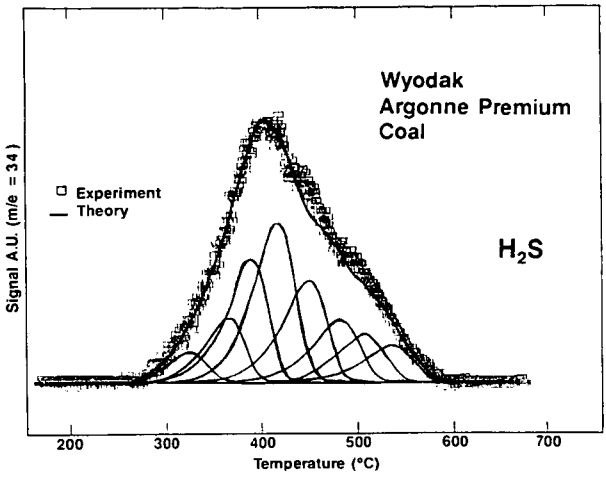

Figure 3

An Example of the H2S TPD Spectrum of Argonne Premium Wyodak and the Simulated Spectrum Based on the Discrete Distribution of Activation Energy Kinetic Model. The Heating Rate Was 0.23 deg/sec. The Sharp Pyrite Related H2S Spike Is Not Considered.

DIFFERENTIATION OF PRIMARY, SECONDARY, AND TERTIARY AROMATIC AMINES IN FOSSIL FUELS USING TRIFLUOROACYLATION
I. ANALYTICAL METHODOLOGY

By

J. S. Thomson, J. B. Green, S. K.-T. Yu, and R. P. Vrana

Department of Fuels Research

IIT Research Institute

National Institute for Petroleum and Energy Research

P. O. Box 2128

Bartlesville, OK 74005

918-336-2400

INTRODUCTION

Aromatic amines are of interest to the refiner because they are produced during the conversion of the heavy ends of petroleum to distillate fuels (1,2). Synthetic crudes from coal and shale oil also contain aromatic amines. In coal liquids, primary polyaromatic amines have been implicated as the most mutagenic compound class present (3).

Until recently, aromatic amines were difficult to differentiate in fuels using GC/MS because of the similarity of electron impact fragmentation patterns of underivatized primary, secondary, and tertiary amines. During the late 1960's, an improved analysis of these compounds as trifluoroacetamide derivatives was reported by Saxby et al. (4-6). Since then, several researchers have reported using acetylation and trifluoroacetylation to distinguish between primary and tertiary aromatic amines in gasoline (7), creosote oil (8) and coal liquids (9-12). Later et al. used an analogous derivatization with pentafluoropropionic anhydride to detect primary aromatic amines in an SRC II coal liquid (13,14), and Bartle et al. adducted anilines with hexafluoroacetone for analysis via ^{19}F nuclear magnetic resonance spectroscopy (15).

In these acetylations, one acetyl or trifluoroacetyl group was substituted onto both primary and secondary amines, such as anilines or partially hydrogenated azaarenes. Tertiary aromatic amines, i.e., azaarenes such as naphthenopyridines or quinolines, did not react. The increased mass and easily distinguished fragment ions of the derivatized compounds, as well as shifts in their GC retention times, were used to aid in their identification using GC/MS.

However, monotrifluoroacetylation does not distinguish between primary and secondary amines which are isomass. For example, aminoindans, which are primary amines, will have the same mass (229) as methyl indoline and 1,2,3,4- tetrahydroquinoline after derivatization. The differentiation of primary and secondary amines is important when developing improved processes for the upgrading of heavy ends of petroleum. Research on the hydrodenitrogenation (HDN) of heavy crude feedstocks would benefit from improved analytical techniques which would allow better monitoring of the concentration of aromatic amine intermediates (16).

For these reasons, an analytical method which distinguishes between primary, secondary, and tertiary aromatic amines has been developed. Rigorous reaction conditions are used to form di- and mono-trifluoroacetylated derivatives of primary and secondary amines, respectively. GC/MS is then used to analyze the derivatized base concentrate. The method has been applied to the analysis of a mildly upgraded SRC II coal liquid and preliminary results are reported here.

EXPERIMENTAL

Fuel Fractionation

The history of the raw and hydroprocessed SRC II coal liquid is described elsewhere (17). The feed (HT-9) and a mildly upgraded product (HT-8) were distilled into 200-325° C distillates, acid-base-neutral separations were performed (18), and bases were subfractionated into 7 fractions (19). The whole base fraction accounted for 7.9 percent of feed and 14.1 percent of the hydrotreated (980 SCF/bbl H_2 consumption, 325° C, NiMo catalyst, 1.0 LHSV) 200-325° C distillate (2).

Chemical Derivatization

Standard blends of 6-8 pure compounds, retention index markers (4-fluorophenol, 1-naphthol, and 9-phenanthrol), and an internal standard (4-fluoroaniline) were prepared in dichloromethane (5 mg/mL/component). Concentrations of 50 mg/ml for base fractions, with 5 mg/mL internal standard and retention index markers, were typical. Aliquots (0.2 µl) of the above mixtures were combined with 0.5 mL catalyst (0.8 M 4-dimethylaminopyridine (DMAP) or 4-pyrrolidinopyridine (PPY) in dichloromethane) and 0.4 mL trifluoroacetic anhydride in a 5 mL heavy wall glass reaction vial (Supelco, Bellefonte, PA, cat. 3-3299) fitted with a Teflon cap (ibid., cat. 3-3303). Samples were held at 60° C for 10 minutes, and rapidly cooled. Hexane (2.0 mL) was added, samples were shaken well, and chilled at 0° C to facilitate precipitation of the catalyst as its trifluoroacetate salt. The supernatant was analyzed within 5 hours.

GC/MS

A Kratos (Ramsey, NJ) MS-80 GC/MS system consisting of a Carlo Erba model 4162 temperature programmed GC, modified in-house with a Hewlett-Packard cool-on-column inlet, capillary direct interface, EI source, MS-80 magnetic scan mass spectrometer and Data General Nova 4-based DS-55 data system was used for all analyses. Samples (0.2 to 0.4µl) were injected, and the column (Restek Corp., Bellefonte, PA, RTX-1 fused silica, 105 m, 0.25 mm I. D., 0.5 µm film) was held 2 minutes at 30° C, programmed at 20° C/min to 70° C, then 2° C/min to 320° C, and held 10 minutes.

Other instrumental conditions were : GC/MS interface 310° C, He column flow 1 mL/min, column head pressure 3.0 Kg/cm^2; mass spectral conditions - 70 eV ionizing voltage, 1,000 resolution, 0.5 sec/decade scan rate, source pressure 10^{-5} torr, and source temperature 300° C.

Retention Indices

The retention indices were calculated using acetylated 4-fluorophenol, 1-naphthol, and 9-phenanthrol as reference compounds as shown in Eq. 1, below:

$$\text{Eq. 1} \qquad I_x = 100\left[I_N + \frac{t_{(x)} - t_{(N)}}{t_{(N+1)} - t_{(N)}}\right]$$

I_x is the retention index and $t_{(x)}$ is the retention time of each acetylated amine derivative, and $t_{(N)}$ and $t_{(N+1)}$ are the retention times of the acetylated reference compounds whose elution times bracket each amine. I_N for 1-fluorophenol is 1, 1-naphthol is 2, and 9-phenanthrol is 3, with N representing the number of aromatic rings present in each reference compound.

Although it is customary to use retention index reference compounds with the same functionality as the compounds examined, phenols were used here for two reasons. First, these same reference compounds were used to calculated a large body of retention indices reported earlier for trifluoroacetylated hydroxyaromatics (20). Use of the same reference compounds will allow a common basis of comparison of trifluoroacetylated fuel components. Secondly, 2- and 3-ring trifluoroacetylated hydroxyaromatics are stable at GC temperatures which cause breakdown of the equivalent 2- and 3-ring diamides. If desired, the $I_{(x)}$ values reported here can be converted to values based on aromatic amines as reference compounds.

Relative Response Factors

Relative response factors (RRF) were calculated according to Eq. 2, below:

$$\text{Eq. 2} \qquad RRF = (A_x/A_S)(W_s/W_x)$$

where A = area percent, based on the GC/MS total ion current, and W = weight, x = derivatized aromatic amine, and s = derivatized standard (4-fluoroaniline).

RESULTS AND DISCUSSION

Derivatization Reactions

Table I lists the compounds derivatized to form amides along with their retention indices (I_x) and their total ion current responses relative to that of 4-fluoroaniline (RRF). The compounds are listed in their underivatized form, grouped into primary, secondary, and tertiary amines.

In general, primary aromatic amines such as anilines and aminoindans are reacted twice to form di-trifluoroacetamides (diamides), secondary amines such as N-alkylanilines, 1,2,3,4-tetrahydroquinolines, indolines, and carbazoles, react once to form monotrifluoroacetamides (mono-amides), and tertiary amines such as quinolines and 2,3-cyclohexenopyridines (5,6,7,8-tetrahydroquinolines) do not react.

A catalyst is necessary during the reaction (21, 22). Initially, DMAP was used as a catalyst, but PPY was found to provide more complete trifluoroacetylation of some compounds. Reaction conditions were optimized using 2,6-diethylaniline, which is a sterically hindered primary amine, and N,N-diethylaniline, which is a tertiary amine that undergoes ring acetylation at the ortho and para positions. Catalyst and reagent concentrations and reaction time (10 minutes) were held constant and the reaction temperature was varied. At room temperature, 58 percent of the 2,6-diethylaniline was converted to the diamide derivative, with the balance in the monoamide form. At both 50 and 60° C, it was 100 percent converted to the diamide form.

It was initially hoped to avoid ring acetylation of N,N-dialkylanilines using mild reaction conditions, but, at room temperature, N,N-diethylaniline was completely converted to the mono-ring-acylated form, with 92 percent addition at the para- and 8 percent at the ortho-position. No evidence for the addition of more than one trifluoroacetyl group to the ring was found at either 50 or 60° C when the supernatant was analyzed within 4 hours storage at 0° C. The appearance of

"over-reaction" peaks was noted after 6 hours storage, however, so subsequent samples were analyzed within 5 hours of derivatization and storage.

One other tertiary amine, 2,3-cyclopentenopyridine, underwent ring-acetylation, forming a derivative with mass 311, indicating addition of 2 trifluoroacetyl groups to the saturated ring. The percentage of the derivative formed was quite reproducible, however, as shown by a RRF standard deviation of 6 percent. 2,3-cyclohexenopyridine (5,6,7,8-tetrahydroquinoline) and its alkyl-substituted homologs did not form derivatives.

The percentage of each aromatic amine which reacted to form the expected derivative is shown in Table 1, column 3. Twenty five of the 31 primary aromatic amines formed only diamides. Those cases of incomplete conversion were generally of two types. The first includes compounds such as methylbenzylamines, where the relatively low acidity of the amine hydrogens makes their displacement difficult. The second type involves higher boiling aromatic diamides, which appear to thermally decompose above a column elution temperature of about 200° C.

Derivatization Reproducibility

Each blend of aromatic amines and internal standards was derivatized 3 times, and each reaction mixture was analyzed twice, with no more than 5 hours between GC/MS injections. As shown in Table 1, replicate response factors from the 6 runs on each blend typically varied less than ±10 percent. Since this variation included contributions from both GC injections and mass spectral measurements, the reproducibility of replicate reactions was undoubtedly higher than 90 percent in most cases.

The few examples where RRF standard deviations varied more than ±10 percent were caused either by derivative decomposition on-column or by the tailing of underivatized tertiary amines such as quinoline (±24.7 percent) or N,N-dimethylbenzylamine (±27.7 percent) on the capillary column.

Mass Spectral Fragmentation Patterns

Trifluoroacetyl derivatives of primary aromatic amines typically show strong molecular ions and distinctive mass fragmentation patterns. Characteristic $[M-69]^+$ and $[M-97]^+$ ions are present in mass spectra of almost all aromatic amine derivatives, but the $[M-97]^+$ ion is usually more prominent for amide derivatives, and $[M-69]^+$ more intense for carbon-acylated compounds. Spectra of 2-n-alkylanilines usually show a fragment at $[M-18]^+$, corresponding to loss of H_2O. The major fragment in 4-n-alkylaniline derivatives corresponds to benzylic cleavage of the n-alkyl group. Addition of the trifluoroacetyl group(s) often markedly changes the fragmentation pathway of the derivative compared to the parent compound (21).

Figure 1 shows the spectra of 4 underivatized isomeric aromatic amine compounds of interest in HDN studies; 2,3-cyclohexenopyridine (a), 1,2,3,4-tetrahydroquinoline (b), 1,2,3,4-tetrahydroisoquinoline (c) and 5-aminoindan (d). Three of the spectra (a, b, and d) are virtually indistinguishable, and the fourth (c) differs only by the presence of a prominent m/z 104 fragment. Derivatization, however, enables differentiation of all four compounds, since, as shown in Figure 2, (a) remains unchanged, while (b) and (c) form mono- and (d) diamides. The two monoamides can be easily differentiated by a fragment at $[M-15]^+$, present in the spectrum of (c), but absent in (b). The spectrum of the diamide (d) now shows a molecular ion at m/z 325, 96 mass units higher than that of (b) and (c), and 192 units higher than (a). These spectra illustrate the marked improvement in ease of compound identification after trifluoroacetylation.

SRC II Coal Liquid

SRC II Coal Liquid

The main aromatic amine compound types identified so far in SRC II 200-325° C base fractions are shown in Figure 3. For the hydrotreated fractions, these include: Fraction 4- anilines and 1,2,3,4-tetrahydroquinolines; Fraction 5 - the bulk of the anilines, from C1 through C6, and 4-aminoindan and its alkyl homologs; Fraction 6 - homologues of quinoline and 2,3-cyclohexenopyridines, 5-aminoindan, indoline, an unidentified naphthenoquinoline type, and small amounts of alkylanilines, and Fraction 7 - *t*-decahydroquinoline and its alkylhomologues.

Fraction 6 from the feed material (about 70 percent of the total basic nitrogen in the distillate, by weight) consists primarily of azaarenes, with large amounts of quinolines, and some partially hydrogenated nitrogen compounds also present.

The following tenative conclusions may be drawn from data collected so far: First, more decahydroquinolines than 1,2,3,4-tetrahydroquinolines (by weight) are present in the hydrotreated material, as predicted by Steele, et al. (16). Secondly, there are more 2-substituted anilines, particularly 2-ethyl and 2-propyl-, than other isomers, an indication of their production from ring-opening of larger compounds. In general, hydrogenation of the nitrogen-containing aromatic rings in azaarenes occurs preferentially over that of other rings. Compounds such as aminoindans may be derived from partially hydrotreated azaarenes, such as 1,2,3,4-tetrahydroquinolines, via rearrangement, or via some other source.

CONCLUSIONS

Most primary, secondary, and tertiary aromatic amines in fuels boiling below 350° C may be differentiated by the formation of trifluoroacetyl derivatives, which are eluted and identified using GC/MS. Replicate response factors of the derivatives, based on the GC/MS total ion current, typically vary less than ±10 percent.

ACKNOWLEDGMENT

Financial support by the U. S. Department of Energy under Cooperative Agreement DE-FC22-83FE60149 is gratefully acknowledged.

LITERATURE CITED

1. Dorbon, M., and Bernasconi, C., Fuel 68, 1067-1074 (1989).
2. Green, J. B., Grizzle, P. L., Thomson, J. S., Hoff, R. J., and Green, J. A., Fuel 64, 1581-1590 (1985).
3. Wilson, B. W. , Willey, C. , Later, D. W. , and Lee, M. L. , Fuel 61, 473-447 (1982).
4. Saxby, M. J., and Irvine, W. J., J. Chromatogr. 43, 129-131 (1969).
5. Saxby, M. J., Org. Mass Spectrom. 2, 835-842 (1969).
6. Chaytor, J. P., Crathorne, B., and Saxby, M. J., J. Chromatogr. 70, 141-145 (1972).
7. DiSanzo, F. P., J. High Resolut. Chromatogr. 4, 649-651 (1981).
8. Del Bianco, A., Zaninelli, M. and Girardi, E., Fuel 66, 55-57 (1987).
9. Wood, K. V., Schmidt, C. E., Cooks, R. G., and Batts, B. D., Anal. Chem. 56, 1335-1338 (1984).
10. Tomkins, B. A. , and Feldman, C., Anal Chim. Acta. 119, 283-290 (1980).
11. Burchill, P., Herod, A. A., and Mitchell, C. A., Chromatographia 21 , 67-76 (1986).
12. Burchill, P., Herod, A. A., and Pritchard, E., J. Chromatogr. 246, 271-295 (1982).
13. Later, D. W., Lee, M. L., and Wilson, B. W., Anal. Chem. 54, 117-123 (1982).
14. Later, D. W., Lee, M. L., and Wilson, B. W., Anal. Chem. 55, 2126-2132 (1983).
15. Bartle, K. D., Matthews, R. S., and Stadelhofer, J. W., Fuel 60, 1172-4 (1981).

16. Steele, W. V. and Chirico, R. D., "Thermodynamics of the Hydrodenitrogenation of Quinoline". Topical Report NIPER-468, 1990 (NTIS Report No. DE900000245).
17. Sutterfield, D., Lanning, W. C., and Royer, R. E. in Upgrading Coal Liquids, (Ed. R. F. Sullivan), Am. Chem. Soc., Washington, DC (1981), Chapter 5.
18. Green, J. B. and Hoff, R. J., J. Chromatogr. 209, 231-250 (1981).
19. Green, J. A., Green, J. B., Grigsby, R. D., Pearson, C. D., Reynolds, J. W., Shay, J. Y., Sturm, Jr., G. P., Thomson, J. S., Vogh, J. W., Vrana, R. P., Yu, S. K.-T., Diehl, B. H., Grizzle, P. L., Hirsch, D. E., Hornung, K. W., Tang, S.-Y., Carbognani, L., Hazos, M., and Sanchez, V. Analysis of Heavy Oils; Method Development and Application to Cerro Negro Heavy Petroleum. Topical Report NIPER-452, v. 1 and v. 2, 1989 (NTIS Report Nos. DE90000200 and DE 90000201.)
20. Yu, S. K.-T., Vrana, R. P., and Green, J. B. "Retention Indices, Relative Response Factors, and Mass Spectra of Trifluoroacetate Esters of Phenolic compounds Determined By Capillary GC/MS." Topical Report NIPER-396 (1989).
21. Schriven, E. F. V., Chem. Soc. Rev. 12, 129-161 (1983).
22. Hofle, G., Steglich, W., and Vorbruggen, H., Angew. Chem. Int. Engl. Ed. 17, 569-583 (1978).

TABLE 1

GC Retention Indices and MS Response Factors of Trifluoroacetylated Amine Compounds

CHEMICAL NAME	% Reacted	I_x	Response RRF	Response %σ
PRIMARY AROMATIC AMINES[1]				
4-fluoroaniline	100	125.65	1.00	-
aniline	100	130.16	1.29	5.2
2-methylaniline	100	142.16	1.16	9.5
3-methylaniline	100	146.64	1.15	9.0
4-methylaniline	100	150.59	1.05	6.8
2,6-dimethylaniline	100	156.32	1.10	4.9
2-ethylaniline	100	158.18	1.03	4.8
2,5-dimethylaniline	100	158.46	1.03	5.2
3,5-dimethylaniline	100	162.66	1.04	5.1
2,4-dimethylaniline	100	162.78	1.14	4.5
2-isopropylaniline	100	165.44	1.01	2.1
2,3-dimethylaniline	100	165.51	1.06	4.6
4-ethylaniline	100	168.24	1.05	3.7
3,4-dimethylaniline	100	172.33	1.00	4.8
2-propylaniline	100	173.48	0.92	5.2
2,4,6-trimethylaniline	100	176.29	1.07	5.8
2,4,5-trimethylaniline	100	183.29	1.01	2.6
4-propylaniline	100	185.61	1.08	2.7
2,6-diisopropylaniline	100	201.02	0.98	7.0
4-n-butylaniline	100	204.48	0.83	5.3
4-nonylaniline, monoamide	92	317.08	1.19	12.9
4-nonylaniline[5]	8	290.53	0.10	76.0
4-decylaniline	31	305.75	0.47	62.7
benzylamine	100	152.73	0.99	6.3
4-methylbenzylamine	92	172.84	0.99	5.8
2-methylbenzylamine	95	173.09	1.12	6.9
(2-aminoethyl)benzene	93	173.26	1.15	3.6
5-aminoindan	100	202.02	0.89	5.1
1-amino-5,6,7,8-tetrahydronaphtha	100	213.38	0.95	2.2
2-aminonaphthalene, monoamide[4]	42	258.22	0.49	20.2
2-aminonaphthalene	36	225.83	-	-
9-aminophenanthrene, monoamide	100	340.21	1.22	27.0
2-aminobiphenyl	100	233.33	1.03	10.9

CHEMICAL NAME	% Reacted	I_x	Response RRF	Response %σ
SECONDARY AROMATIC AMINES[2]				
t-decahydroquinoline	100	214.42	1.15	5.2
N-ethylaniline	100	171.90	0.96	4.4
N-butylaniline	100	207.53	1.03	5.9
1,2,3,4-tetrahydroquinoline	100	219.70	0.97	8.2
1,2,3,4-tetrahydroisoquinoline	100	227.96	0.93	2.5
indoline	100	210.31	0.80	8.8
diphenylamine	100	254.43	1.01	5.1
N-phenyl-1-naphthylamine[4]	60	329.78	0.64	5.5
TERTIARY AROMATIC AMINES[3]				
N,N-dimethylaniline, para derivitive	90	229.71	0.80	4.8
N,N-diethylaniline, para derivitive	96	255.67	1.01	9.1
N,N-dimethylbenzylamine	0	147.77	0.59	27.7
2,3-cyclohexenopyridine	0	178.42	0.53	4.4
quinoline	0	180.89	0.73	24.7
2,3-cyclopentenopyridine	100	212.67	0.81	6.5

[1] di-(trifluoroacetamides), except as noted

[2] mono-(trifluoroacetamides), except as noted

[3] derivitized compounds are all ring-acylated

[4] RRF average of 4 determinations

[5] RRF average of 5 determinations

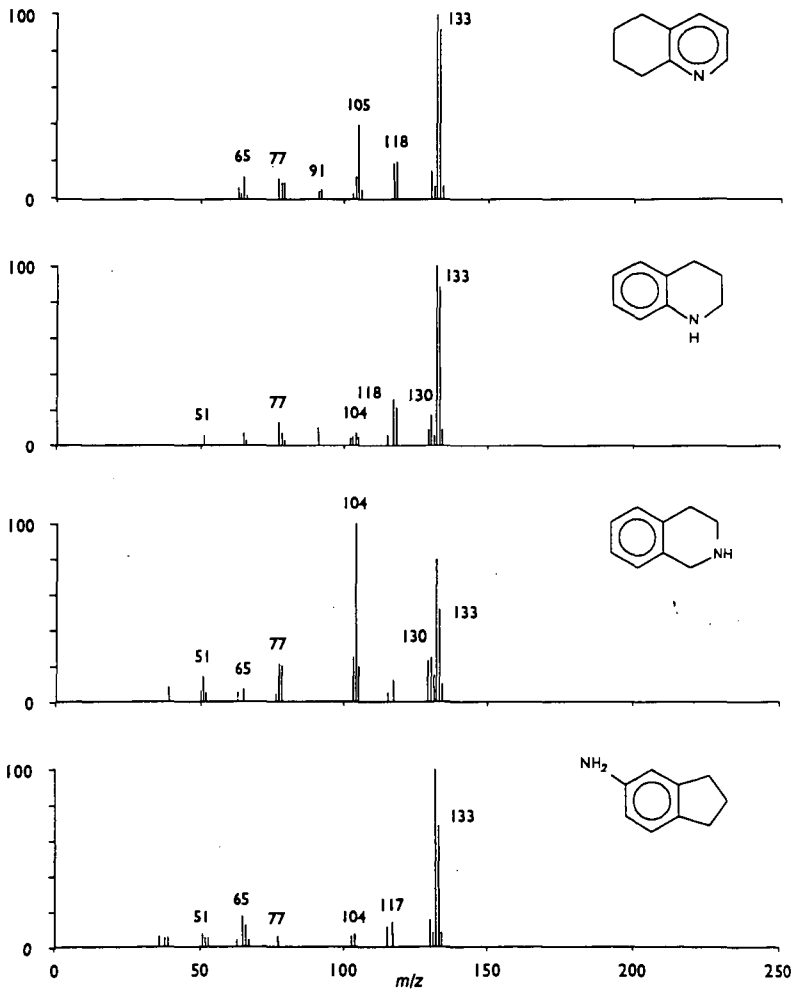

Figure 1. Mass Spectra of Hydrodenitrogenation Intermediates.
(Twenty Most Prominent Ions)

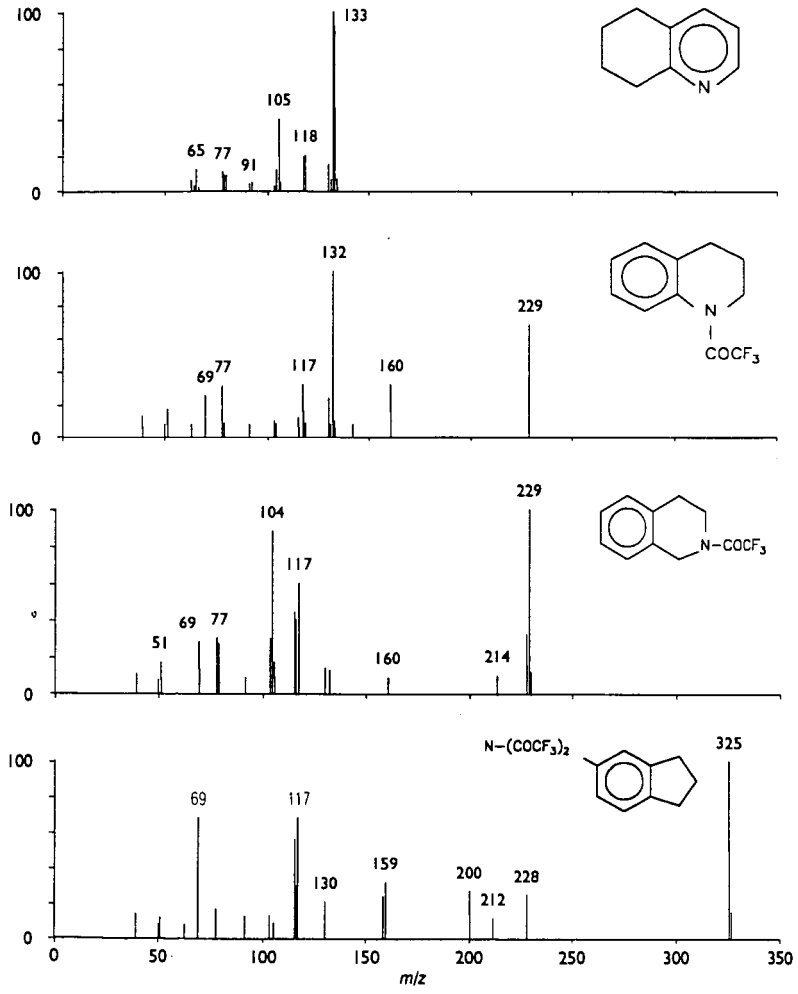

Figure 2. Mass Spectra of Hydrodenitrogenation Intermediates Derivatized to form Mono- or Di-trifluoroacetamides.
(Twenty Most Prominent Ions)

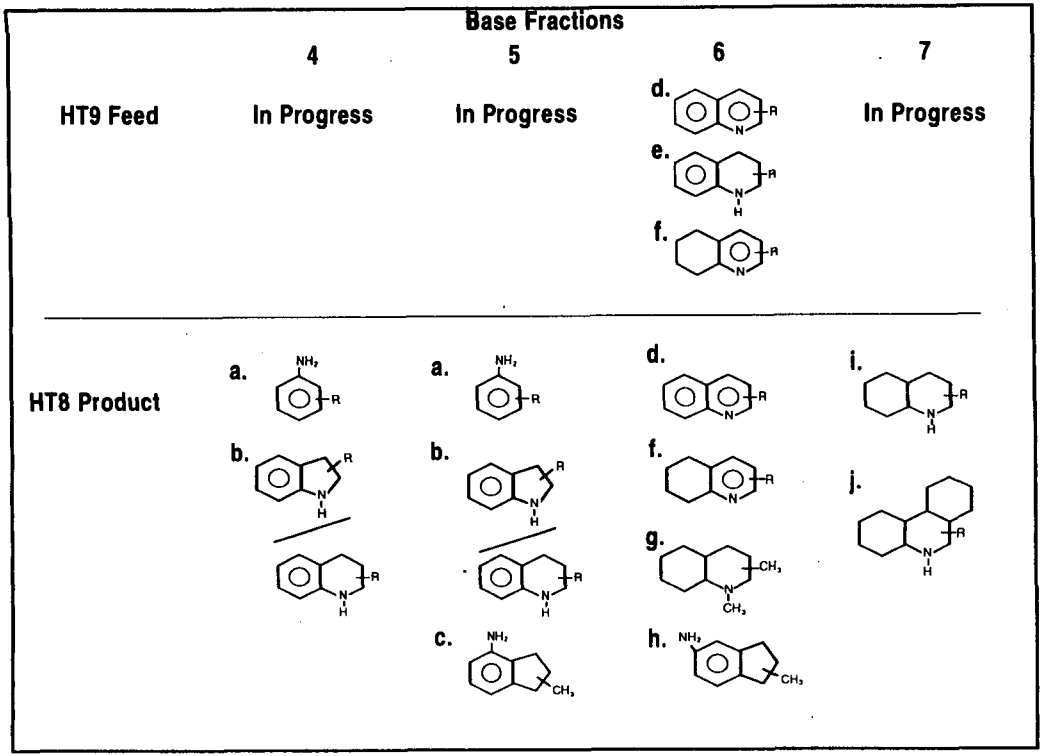

Figure 3. Aromatic Amine Compound Types in an SRC II 200-325° C Coal Liquid Feed (HT9) and Lightly Hydrotreated Product (HT8): a. anilines, b. indolines/1,2,3,4-tetrahydroquinolines, c. 4-aminoindans, d. quinolines, e. 1,2,3,4-tetrahydroquinolines, f. 2,3-cyclohexenopyridines, g. N-alkyldecahydroquinoline, h. 5-aminoindans, i. decahydroquinolines, and j. tetradecahydrophenanthridines.

PYROLYSIS-FOURIER TRANSFORM INFRARED SPECTROMETRY AS A TECHNIQUE FOR ANALYZING FUNCTIONAL GROUPS WITH OXYGEN IN COAL

C. V. Philip, S. Vadakumcherry, J. A. Bullin and R. G. Anthony
Department of Chemical Engineering, Texas A & M University,
College Station, Texas 77843

INTRODUCTION

Pyrolysis, flash pyrolysis and thermogravimetric analysis (TGA) were used to characterize coals based on thermolysis products [1-7]. The coals are known to release volatiles such as CO_2 and methane even at sample storage and handling conditions used for Premium Coal samples at Argonne National Laboratory[9,10]. Coal conversion process produces these volatiles in larger quantities. The maximum amount of small species including CO_2 and CO are produced under pyrolytic and gasification conditions. There are reports on the temperature dependance of the thermolysis of functional groups in coal[2,4,5]. The volatiles were quite often identified by using techniques such as GC, MS, GC-MS and FT-IR. Long hydrocarbon chains in Texas lignites and other coals were analyzed by Pyrolysis -GC[1]. Flash pyrolysis using GC-MS was used for determining organic sulfur structures in coal[3]. The use of TGA-FT-IR for coal analysis based on devolatilization products has been reported[6].

Quantification of oxygen in coal is often accomplished by indirect methods. Since the estimation of organic oxygen is interfered by the moisture content and the oxygen in the mineral matter, oxygen content of coal is reported in more than one format[9]. Pyrolysis can convert organic oxygen to oxides of carbon which can be estimated using a gas chronographic detector. A gas chromatograph with detector for organic oxygen is now available from Carlo Erba for estimating oxygenated organic species. The GC effluents are pyrolyzed at 1400°C . The oxides of carbon are converted to methane with hydrogen in the presence of a Ni catalyst, and the methane is then estimated by flame ionization detector. This technique however cannot distinguish CO_2, CO or CH_4, but the concept that pyrolysis converts organic oxygen to oxides of carbon is established.

Using a continuous-mode pyrolyzing inlet for GC, available commercially[8], we have conducted experiments to develop a new technique for analyzing coal, particularly the organic oxygen. The samples are pyrolyzed in a pyrolyzer which is fitted to the injection port of capillary gas chromatograph on-line with FT-IR spectrometer with GC-FT-IR interface. The system allows both qualitative and quantitative analyses. The IR peaks of volatiles are at least a hundred fold larger than what is observed by TGA-FT-IR experiments[6]. Small species such as CO, H_2O and CH_4 often missed by GC-MS are easily identified and even estimated by GC-FT-IR. The results of our preliminary experiments using pyrolysis-GC-FT-IR indicate that useful data on organic oxygen as well as its distribution in various functional groups can be obtained.

EXPERIMENTAL

The pyrolysis experiments were conducted using a number of simple organic compounds which were obtained from commercial sources and contained one or more functional groups with oxygen. Eight Premium Coal samples from Argonne National Laboratory were the coal samples. Table 1 lists some of the reported analysis data of the Premium coal samples[9]. The Texas lignite sample was obtained from a local mine at Carlos about twenty miles away from the campus and was analyzed in the Chemistry Department.

The Instrumental setup consisted of a Pyrojector[8] (Scientific Glass Engineering, SGE, Austin Texas), Fourier Transform infra red (FT-IR) spectrometer (Nicolet 60SXR) with gas chromatographic interface and a capillary gas chromatograph (Hewlett Packard , HP5890) with on-column injection port. The Pyrojector was installed on the on-column injection port using an adaptor made in the machine shop of the Chemical Engineering Department .

Septum injection technique was used. Helium was used as the carrier gas.There were purges at the septum of the pyrojector as well as at the on-column injector. The carrier gas flow through the capillary column was derived from the gas flow through the Pyrojector as well as the carrier gas flow of the gas chromatograph through the injection port. The sample size as well as these flow rates were optimized for quantitative results. The furnace temperature of the pyrojector was varied from 300°C to 1000°C. The GC oven temperature of the gas chromatorgraph was maintained at 50°C. The FT-IR was used as the detection technique. The gas chromatograph was equipped with a 25 meter 0.32 mm id capillary column with 1 um BP-5 (5%phenyl 95% methyl silicon bonded phase, SGE). In this study only smaller species which were volatile in oven at 50°C were detected by FT-IR. A mercury cadmium telluride (MCT-A, Nicolet) detector was used on the gas chromatographic port of the system. The IR spectra were scanned at 4 cm^{-1} resolution. Either 8 or 32 scans were collected per file. The data collection was initiated 1.5 minutes after sample injection and discontinued after 6 minutes. The spectra were collected in this time frame in several files. The spectrum collected just before the appearance of the products was used as background which was subtracted from each sample spectrum.

The instrument was calibrated by injecting 0.25 ml standard gas mixture (2% methane, 20% carbon monoxide, 50% carbon dioxide and 28% nitrogen) using a pressure tight gas syringe. Areas under major IR peaks were used for response factor calculations. Liquid samples were injected using a 10 ul syringe. The initial Prolysis experiments were conducted on acetic acid , ethylacetate, tetrahydrofuran, hydroxybenzoic acid and several other compounds. These compounds represent organic molecules having functional groups with oxygen. Samples were pyrolyzed at temperatures ranging from 400°C to 1000°C in order to determine the optimum temperature for removal of oxygen from these molecules as oxides of carbon. The solid samples were introduced into the Pyrojector either as a pellet (which was prepared using a pelletizer from SGE) or as pressed powder using a solid injector. The sample sizes were 1 mg for pure organic compounds. About 2 mg samples were used for coals. The sample size was not very precise as the powder was packed into the barrel of the solid injector (mostly same volume of powder) and pushed into the inlet of the Pyrojector.

Experiments were also conducted using cryofocussing technique. During the first five minutes after sample injection the volatiles were trapped by cooling a small segment of the capillary column in liquid nitrogen. After five minutes the column was removed from liquid nitrogen and allowed to warm up while scanning the IR spectrum.

RESULTS AND DISCUSSIONS

Making the pyrolysis experiments reproducible was very challenging. Several initial experiments were irreproducible due to leaks and noncompatible flow conditions. The pyrojector was composed of quartz pyrolyzing tube which was heated in a furnace with free standing control module. The samples were injected from the top of the tube through the septum and the pyrolyzed products were immediately swept into the capillary column and to the light pipe of the GC-FT-IR interface. The carrier gas He entered from the top of the pyrojector as well as through the inlet of GC. The gas head pressures at these points were optimized for better detection. This was achieved by varying the head pressures while injecting acetic acid samples. 10 psi He pressure at the Pyrojector head was found suitable while the pressure at the column inlet was kept slightly lower. Both the septum purge of the Pyrojector and GC inlet purge were kept at a level of less than 1 ml per minute. Higher purge flows caused the escape of products.The experiments to calibrate the instrument using standard gas mixture revealed that the gas sample was spread over a 3 minute peak width due to the spreading of the sample in the quartz liner in the Pyrojector. The relative IR response of CH_4 : CO_2 : CO was observed as 4 : 5: 1.

The reports on pyrolysis-FT-IR are limited. In a number of reported studies on the use of TGA-FT-IR, the volatile from the thermographic balance was allowed to pass through a gas cell while scanning FT-IR spectrum. The FT-IR signal intensity was very weak. We are able to obtain very strong signals due to the use of the light pipe in the GC-FT-IR interface instead of a gas cell. The pyrolysis products appear 2 minutes after the injection of the sample and product peaks maximized in 2.5 minutes and was spreading another 2 or 3 minutes. The reason for such tailing was the larger diameter of quartz tubing (volume = 0.5 ml) compare to the capillary column. The experiments using cryofocussing showed the elution of pyrolysis products in narrow bands comparable to capillary GC peaks. When cryofocussing was used, the products had undergone gas chromatographic separations. Both CO and methane appeared first, and CO_2 eluted later. For the comparative study of coals the spectrum collected at 2.5 minutes without the aid of cryofocussing was used as it included all the light products.

The thermal decomposition of simple organic compounds depends on the nature of functional group as well as on the pyrolytic temperature. The effect of pyrolysis temperature on acetic acid is shown in Figure 1. At temperatures below 650°C acetic acid pyrolyzed to produce small amounts of CO_2. Methane and CO were produced at 750°C and above. At 750°C tetrahydrofuran (THF, Figure 2) did not produce any oxides of carbon. However at 800°C it pyrolyzed to produce CO and hydrocarbons including methane. No CO_2 was produced from THF indicating that the oxygen from ether link can only be extracted as CO but requires higher temperatures. The amount of CO produced from THF did not increase at higher temperatures. If all the ethers behave like THF the oxygen from ethers can be extracted as CO at 800°C. Ethylacetate (Figure

3) produced CO_2 and relatively higher levels of CO compared to acetic acid. The CO production peaked at 800°C for both acetic acid and ethyl acetate and levels went down at higher temperatures. At 950°C methane and other hydrocarbons were produced the most. Methanol thermolyzed to CO, CO_2 and H_2O below 800°C and CO was the predominant species above 950°C. Ethanol produced only CO at 800°C and above.

Hydroxy benzoic acid has two functional groups -- hydroxy group and carboxylic group. Based on the results from the experiments with alcohols such as methanol and ethanol the hydroxyl group was expected to produce CO at temperatures above 800°C. Figure 4 shows that both CO_2 and H_2O were produced at lower temperatures. The oxygen in hydroxyl groups can be extracted either as water or as CO. At temperatures below 800°C only H_2O was formed. CO was formed most at 950°C.

The FT-IR spectra of volatiles from Texas lignite pyrolyzed at different temperatures is shown in Figure 5. The CO_2 and CO obtained at 700°C was from the carboxylic groups. Since the amount of CO does not increase from 700 to 800°C the ether bond represents only a small fraction of organic oxygen in lignite. The amount of CO produced at 1000°C is 50% higher than at 800°C, about 1/3 of all the CO was from hydroxyl groups. Of the oxygen extracted as oxides of carbon by pyrolysis at 1000°C, about 90% of the Oxygen was in the carboxylic groups and 10% was from the hydroxyl groups and less than 1% could be from ether groups

Premium Coal samples were also subjected to pyrolysis at temperatures from 400°C to 1000°C. Injection of packed powdered sample was easy at 700°C and above. Lower temperatures produced mostly CO2. Experiments conducted at 750°C produced CO_2, CO and CH_4 and is used for illustration. Table 1 lists all the coals and its oxygen content on an ash free basis and the products evolved. The FT-IR spectrum of the thermolysis products are shown in Figure 6. There is direct relationship between the oxygen content and CO_2 and CO produced. Higher temperatures produced slightly more oxides of carbon but did not observe any enhancement of CO.

CONCLUSIONS

Preliminary studies on Pyrolysis -GC-FT-IR of pure organic coals indicates that the analytical techniques can be developed for identifying and estimating oxygenated functional groups in organic species. The order at which functional groups thermolyzed is follows:- Carboxylic groups at 700- 800°C, ether groups at 800-900°C and hydroxy groups 900-1000°C or higher temperatures. The preliminary test results strongly supports the viability of the technique.

ACKNOWLEDGEMENTS

The financial support of the Texas A&M University Center for Energy and Mineral Resources is very much appreciated. Discussions with Karl Vorres of Argonne National Laboratory were very helpful. Ms Bamini Vittal had helped to conduct experiments

REFERENCES

1 Giam, C. S., Goodwin, T. E., Giam, P. Y. Rion, K. F. and Smith, S. G. "Characterization of lignite by pyrolysis-gas chromatography" *Anal. Chem. 1977, 49, 1540.*

2. Suuberg, E. M., Peters, W. A.,and Howard, J. B. "Product composition and kinetics of lignite pyrolysis" *ACS Fuel Division Preprint,1977*22, 122

3. Philip, C. V., Bullin, J. A. and Anthony, R. G. "Analysis of lignite-derived gases by automated gas chromatography" *J. Chromatogr. Sci. 1979,17,*523.

4. Calkins, W. R. "Determination of Organic Sulfur-containing structures in Coal by Flash Pyrolysis experiments" *ACS Fuel Division Preprint,1985,* **30, #4,** 450.

5. Attar, A. and Dupuis, F. "On the Distribution of Organic Sulfur Functional groups in Coal" *ACS Fuel Division Preprint,1978*23, #2, 44.

6. Carangelo, R. W., Solomon, P. R. and Gerson, D. J. "Application of TG-FT-i.r. to study hydrocarbon structure and kinetics" *Fuel1987,* **66,**960

7. Eglinton, T. I., Damste, J. S. S. Kohnen, E. L. and Leeuw, J. W. de "Rapid estimation of the organic sulfur content of kerogens, coals and asphaltenes by pyrolysis-gas chromatography" *Fuel 1990,* **69,** 1394

8. Wright, D. and Dawes, P. "Applications of a continuous-mode pyrolyzing inlet for GC" *American Laboratory 1986, Nov.*

9. Vorres, K. S,, 'Users Hand book for the Argonne Premium Coal Sample Program' 1989, Oct. 1

10. Vorres, K. S,, Private communications and "Gas content in sealed Argonne Premium Coal samples" International Conference on Coal Science, Sponsoerd by Member Countries of the International Energy Agency, October 23-27, 1989, Tokyo, Japan.

Table 1 Analysis[9] and pyrolysis data of the coal samples

	Ash	Volatile	Oxygen	CO2	CO
Texas Lignite	23.6	39.5	26	0.33	0.12
Wyodak Subbitumino	6.3	32.2	18	0.15	0.05
ND Beulah-Zap	6.6	30.5	20.3	0.14	0.04
Illinois #6	14.3	36.86	13.5	0.09	0.06
Blind Canyon Seam	4.5	43.7	11.6	0.05	0.03
Pittsburgh #8	9.1	37.2	8.8	0.03	0.02
Penn Upper Free Port	13	27.1	7.5	0.02	0.04
Stockton Seam	19.4	29.4	9.8	0.02	0.01
Pocahontas #3	4.7	18.5	2.5	0.01	0.01

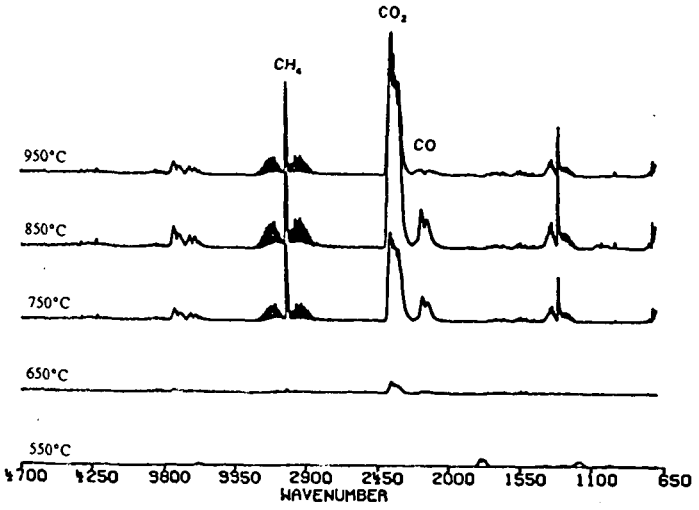

Figure 1. FT-IR spectra of decomposition products of acetic acid as a function of Pyrojector temperature.

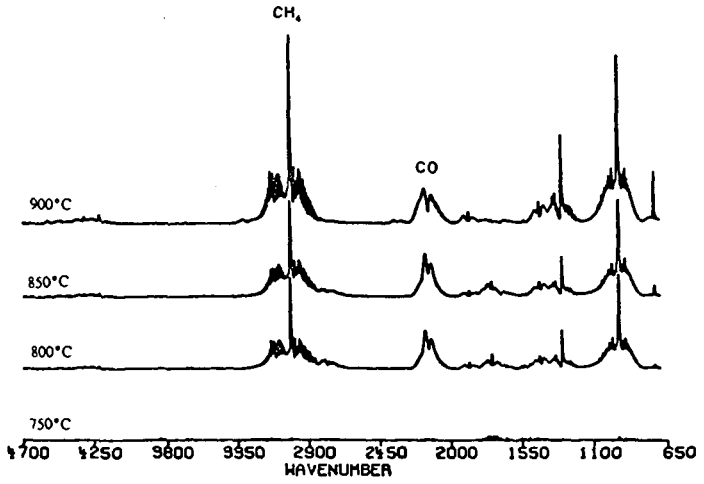

Figure 2. FT-IR spectra of decomposition products of tetrahydrofuran(THF) as a function of Pyrojector temperature.

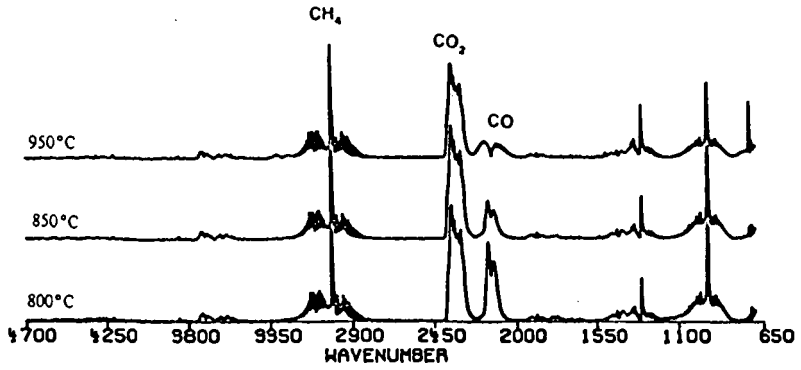

Figure 3. FT-IR spectra of decomposition products of ethyl acetate as a function of Pyrojector temperature.

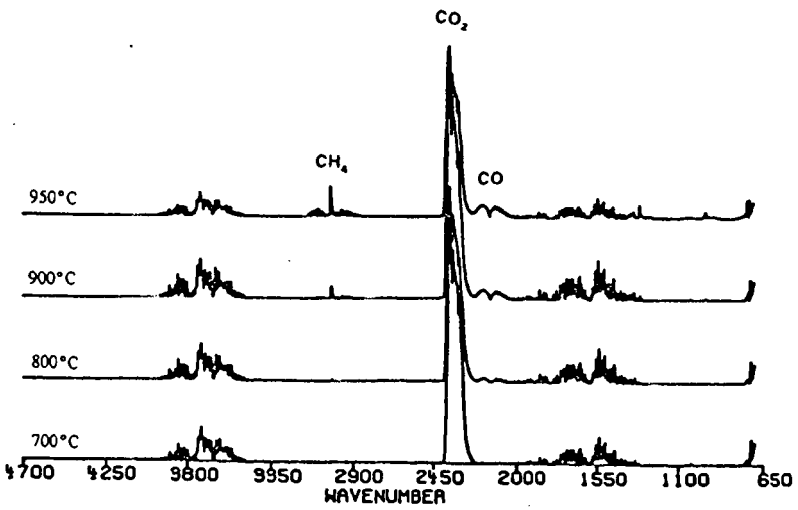

Figure 4. FT-IR spectra of decomposition products of hydroxy benzoic acid as a function of Pyrojector temperature.

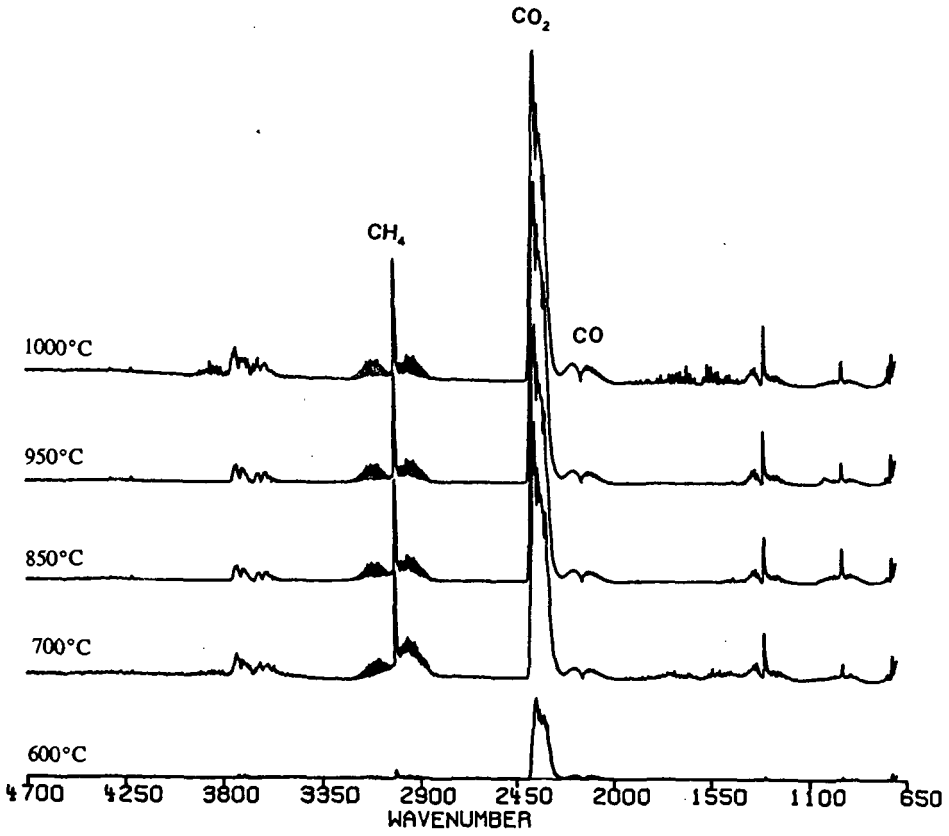

Figure 5. FT-IR spectra of decomposition products of Texas lignite as a function of Pyrojector temperature.

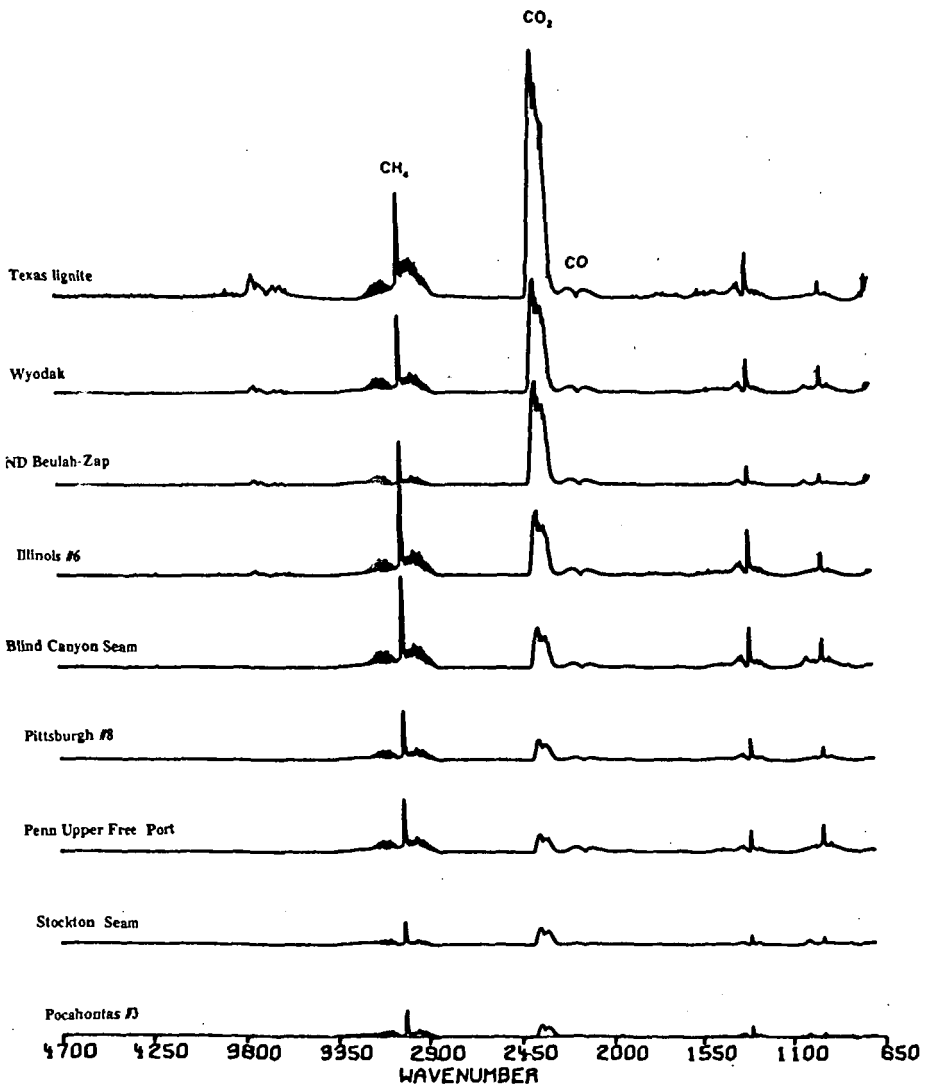

Figure 6 FT-IR spectra of pyrolysis products obtained from Texas lignite and Premium Coals. Pyrolysis temperature, 750°C

CHARACTERIZATION OF THE ARGONNE PREMIUM COAL SAMPLES BY FIELD IONIZATION MASS SPECTROMETRY

Ripudaman Malhotra, Donald F. McMillen, and David L. Huestis
Chemistry and Molecular Physics Laboratories, SRI International, Menlo Park, CA 94025-3493

Keywords: FIMS, Argonne Premium Coals, Pyrolysis

INTRODUCTION

The technique of field ionization mass spectrometry (FIMS) has proven to be quite useful for analyzing complex mixtures, particularly fossil fuels.(1) The technique of field ionization (FI) consists of ionizing molecules by the application of an intense electric field and results in the formation of only the molecular ions for most organic compounds.(2) Thus, complications arising from fragmentation during ionization are minimized in this method. Another advantage of field ionization is that the relative field ionization efficiencies of various hydrocarbon types are within a factor of two of alkyl aromatics except for saturated acyclic hydrocarbons, which ionize about a third as efficiently. For many other ionization techniques such as field desorption or low-voltage electron impact, the relative ionization efficiencies can differ by as much as two orders of magnitude. Thus, even without any corrections for sensitivity, the FI mass spectra represent the true molecular weight profile fairly accurately.

In this paper we present the results obtained by pyrolyzing the eight coal samples from the Argonne Premium Coal Sample Program (APCSP) in the inlet of the mass spectrometer and analyzing the volatiles by FIMS. From these data we can deduce relative amounts of several structural types. We also identify salient rank-dependent trends. Some of these trends are known from other studies,(3-6) but FIMS provides an easy means for quantifying them and developing indices that could be used in modeling.

EXPERIMENTAL

The FIMS system used in this study has been described elsewhere.(7) It consists of an activated tantalum foil field ionizer interfaced with a 60° magnetic sector mass analyzer and a PDP 11/23 computer for data acquisition and processing. In a recent study of various configurations for mass spectrometric analysis of coals, Muezelaar and coworkers reported that a combination of direct insertion pyrolysis followed by FI and magnetic sector mass analysis provides the most detailed and accurate mass spectra.(4) We find this result gratifying because it basically vindicates our approach. Approximately 1-2 mg of the sample is introduced via a heatable direct insertion probe. Mass spectral data of the evolving tars are collected by repeatedly scanning the magnet over a preset range (50 to 1400 Da) while the sample is gradually heated at a fixed rate of 5°C/min from the ambient temperature to approximately 700°C. At the end of the run, the sample holder is retrieved and weighed to determine the fraction that was devolatilized during the analysis. For a given sample, many spectra are collected, each representing a certain range of temperature. The individual spectra are added and normalized to obtain a spectrum of the evolved tars. These spectra are also used produce a thermal evolution profiles of the total tars or of selected mass peaks.

RESULTS AND DISCUSSION

Mass Spectral Profiles

The spectra for the total tars evolved during temperature-programmed pyrolysis for the Argonne coals are shown in Figures 1 and 2 in the order of increasing rank. Several features are immediately apparent and noteworthy. In general, the spectra appear to be composed of two groups of peaks: (a) there is a cluster of peaks consisting of various homologous series in the low molecular weight range (100-200 Da) and (b) a broad, roughly gaussian, distribution of peaks spanning the mass range of 150 to 1000 Da. The low molecular weight cluster is particularly dominant in the Beulah Zap lignite and the Wyodak subbituminous coal. With increasing rank, the prominence of this cluster decreases relative to the broad gaussian

envelope, whose mean appears to shift to higher masses with increasing rank. In the higher rank coals there is also a second cluster of homologous peaks in the 200 to 400 Da range riding on the broad profile. A few peaks in the 300 to 350 Da range that are substantially more intense than the general profile can be seen in the spectrum of the the Utah coal. These peaks are most likely due to biomarkers. The most intense among these is at 324 Da, which corresponds to a tetracyclic monoaromatic alkane ($C_{34}H_{36}$). There is also a peak at 320 Da, which would correspond to the diaromatic analogue. Interestingly, these peaks have also been observed in the terpenoid resins associated with other coals from Utah.(8)

Chemical Characterization

The most prominent peaks in the low molecular weight range are at m/z 84, 108, 110, 122, 124. These peaks correspond to homologous series of phenols and dihydric phenols. Although assigning structures on the basis of nominal masses only is generally risky, in this case there can be little doubt about the assignment because very few reasonable structures can be written for these masses. Besides, there is corroborating evidence for these structures from studies using high resolution mass spectrometry.(9) The ratio of monohydric to dihydric phenols generally increases with the rank. This trend is illustrated in Figure 3, which shows that the peak at m/z 108 (C_1-phenol) is only about 80% of that at m/z 110 (catechol) for the Beulah Zap lignite, but reaches about 5 times the peak due to catechol for the Upper Freeport and Pocahontas coals. In absolute terms, the intensity of the C_1-phenol peak has only declined by a factor of about 20, while that of the catechol peak has declined by a factor of about 100.

The FIMS data are typically organized in a table with fourteen columns. This arrangement places intensities of ions of a given homologous series in the same column. Thus the intensities of benzene, toluene, C_2-benzenes and so on, all fall in the same column one below the other. An abrupt change in intensity of ions belonging to the same column (apparent degree of unsaturation or $\dot{z}$) is often an indication of the start of another homologous series. For example, acyclic alkanes and alkylnaphthalenes share the same nominal masses (i.e., have the same $\dot{z}$ value), and it would not be possible to determine their relative amounts using low resolution FIMS data. However, an examination of the intensities for the homologous series corresponding to acyclic alkanes and alkylnaphthalene (58, 72, 86, 100, 114, 128, 142, and so on) shows an abrupt increase (about 3 fold) in going from 114 to 128 reflecting the fact that most of the intensity is due to naphthalenes. In general the peak at m/z 156 (C_2-naphthalenes) is the most prominent in that series. Therefore, we have used that peak as a representative of the hydrocarbon (non-oxygenated) structure and compared its intensity with that at m/z 108 (C_1-phenol). Figure 4 shows that the ratio of the intensity at 108 (C_1-phenol) to that at 156 (C_2-naphthalene) decreases with coal rank (primarily due to a decrease in the intensity of m/z 108). The Pittsburgh coal is somewhat at variance with the trend, due to a jump in the cresol evolution.

A examination of the column corresponding to $\dot{z} = -8$, (pentacyclic alkanes or tetralins) often shows a jump in ion intensities at m/z 202, and indicates the start of the pyrene (or fluoranthene) homologous series. This discontinuity is apparent in the high rank coals but not in the low rank coals, and is consistent with increasing importance of polycyclic aromatic structures in the higher rank coals. The Pocahontas and Upper Freeport coals best illustrate the growth of multi-ring systems. Figures 5 shows the intensities of the ions in that column ($\dot{z} = -8$) for the Pocahontas coal. As expected, the intensity of this series begins increasing at m/z 202, due to the prominence of pyrene (and fluoranthene), and reaches a maximum at m/z 244, representing C_3-pyrenes. Less obvious in origin is the periodicity in the intensity of the $\dot{z} = -8$ series. The maxima in this series are nine nominal CH_2 units apart. However, it makes little sense that alkylpyrenes would show maxima at C_3, C_{12}, C_{21}, etc. Much more likely is that the 126 Da difference arises from successive naphthylation of the pyrene nucleus rather than from addition nine methylenes.

Inspection of the spectra for Pocahontas and Upper Freeport coals also reveals the growth of PCAH structures through peri- and cata-condensation. In other words, for a given intense peak there is often another intense peak 50 Da higher, which corresponds to peri-condensation as in the naphthalene to phenanthrene transformation. Often there is an intense peak at 24 Da higher, which corresponds to cata-condensation, for example phenanthrene to pyrene transformation. Two successive peri-condensations followed by a cata-condensation result in a net addition of 224 Da. Interestingly, because 224 is an integral multiple of 14 (16 times), this peak has the same $\dot{z}$ value, and can obscure the naphthylation sequence discussed above. The progressive growth of PCAH structures is not apparent in the lower rank coals, although the start of phenanthrene and pyrene series is clearly indicated even in the Illinois No. 6 coal.

Rather than manually inspect and uncover the prominent repeat units (Δ), we attempted to determine them through Fast Fourier Transform (FFT) procedures. However, chemically significant Δ's, such as 14, 50, and 126 do not persist for sufficient number of cycles to be easily identified, before they are blurred by other variations. For example, varying degrees of hydrogenation and oxygenation coupled with simple homologation with methylenes cause 2-mass unit shifts, and thus obscure the importance of a given Δ by making $\Delta \pm 2$ also important. Consequently, we have not been able to uncover anything meaningful from FFT analysis.

Liquefaction of low rank coals is known to be more difficult than that of medium and higher rank coals, and requires better liquefaction solvents to achieve reasonable conversion to liquids. One possible reason for this required solvent quality is that the low rank coals are deficient in indigenous "donors" and therefore need them in the solvent. However, if we examine the ratio of the peaks at m/z 132 and 128 (representing tetralin and naphthalene respectively), we find that the ratio actually decreases with increasing rank. Thus, the lack of indigenous donors is not an appropriate explanation for the difficulty of liquefying low rank coals, and the propensity for the structures in low rank coals to undergo crosslinking reactions (and/or the crosslinked nature of the starting structures themselves) is a more likely explanation.

Thermal Evolution Behavior

As mentioned above, FIMS data are collected over the temperature range as many individual spectra. From these spectra, we can construct the evolution profiles of either total tars or of selected ions. In order to compare the absolute amounts of these ions from different coals it is necessary to correct for the total weight of tars evolved. However, the total weight loss obtained at the end of FIMS analysis also includes light gases, such as CO, CO_2, water, and methane, which are generally excluded from FIMS analysis primarily for two reasons. First, they do not field ionize efficiently, and second, scanning the magnet down to these low mass range requires an inordinately longer time that could compromise the data of the bulk of the materials. These gases are more readily analyzed by TG-FTIR, and in that regard FIMS complements this technique. For inter-sample comparisons we corrected the normalized FIMS intensities for the tar yields reported by Solomon and coworkers for pyrolysis of these coals at a comparably slow heating rate. We examined the thermal evolution profile of several compound types. The principal finding is that while the amounts of these compound types changed substantially with rank, the evolution profile of most compound types, except phenolics, showed only a slight shift to higher temperatures with increasing rank. This result is consistent with the essence of the FG-DVC model of of Solomon and coworkers.(6)

Table 1

Coal	Weight Loss During FIMS (%)	Number Average Molecular Weight	Weight Average Molecular Weight
Beulah Zap	42	239	370
Wyodak	39	274	404
Illinois No. 6	42	402	441
Utah Blind Canyon	45	444	568
Lewiston-Stockton	31	436	521
Pittsburgh	39	379	459
Upper Freeport	27	422	496
Pocahontas	16	455	501

ACKNOWLEDGEMENT

We gratefully acknowledge the support of the Morgantown Energy Technology Center of the U.S. DOE for financial support through Contract No. DE-AC21-87MC23286. Some of the coals discussed in this

paper were analyzed for Advanced Fuel Research and we are thankful to Drs. Peter R. Solomon and Michael A. Serio for permitting us to use the results.

REFERENCES

1. Sullivan, R. F.; Boduszynski, M. M.; Fetzer, J. C., *Energy Fuels* **1989**, *3*, 603.

2. Beckey, H. D., *Field Ionization Mass Spectrometry*, Pergammon Press, Elmsford, NY, 1971.

3. Freihaut, J. D.; Proscia, W. M.; Seery, D. J, *Energy Fuels* **1989**, *3*, 692.

4. Huai, H.; Lo, R.; Yun, Y.; Muezelaar, H.L.C., *Am. Chem. Soc, Div. Fuel Chem., Preprints* **1990**, *35(3)*, 816.

5. Schulten, H.-R.; Marzec, A.; Dyla, P.; Simmleit, N.; Müller, R., *Energy Fuels* **1989**, *3*, 41.

6. Solomon, P. R.; Serio, M. A.; Carangelo, R. M.; Bassilakis, R.; Gravel, D.; Baillargeon, M.; Baudais, F.; Vail, G, *Energy Fuels* **1990**, *4*, 319.

7. St.John, G. A.; Buttrill; S. E., Jr.; Anbar, M., in *Organic Chemistry in Coal*, J. Larsen, Ed.; ACS Symposium Series 71, Washington, DC, 1978, p. 223.

8. Malhotra, R.; Anderson, L. L., unpublished results.

9. Winans, R. E.; McBeth, R. L.; Neill, P. H., *Am. Chem. Soc, Div. Fuel Chem., Preprints* **1988**, *33(3)*, 85.

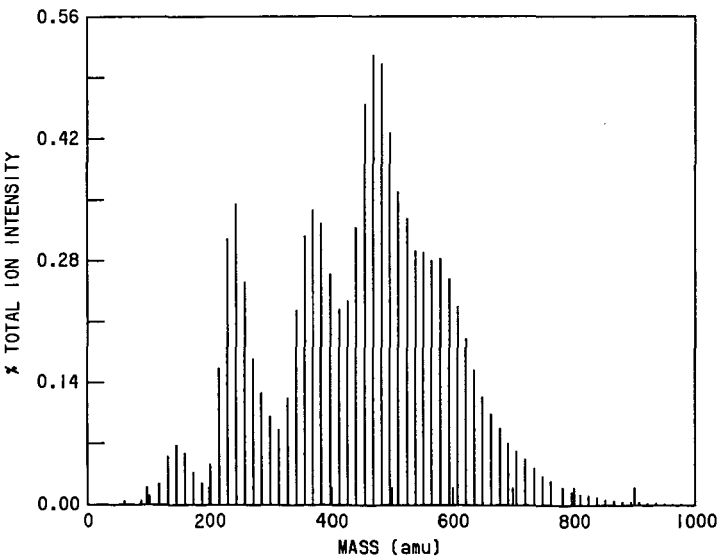

Figure 5. Intensities of ions belonging to the $\dot{z} = -8$ series for the Pocahontas coal.

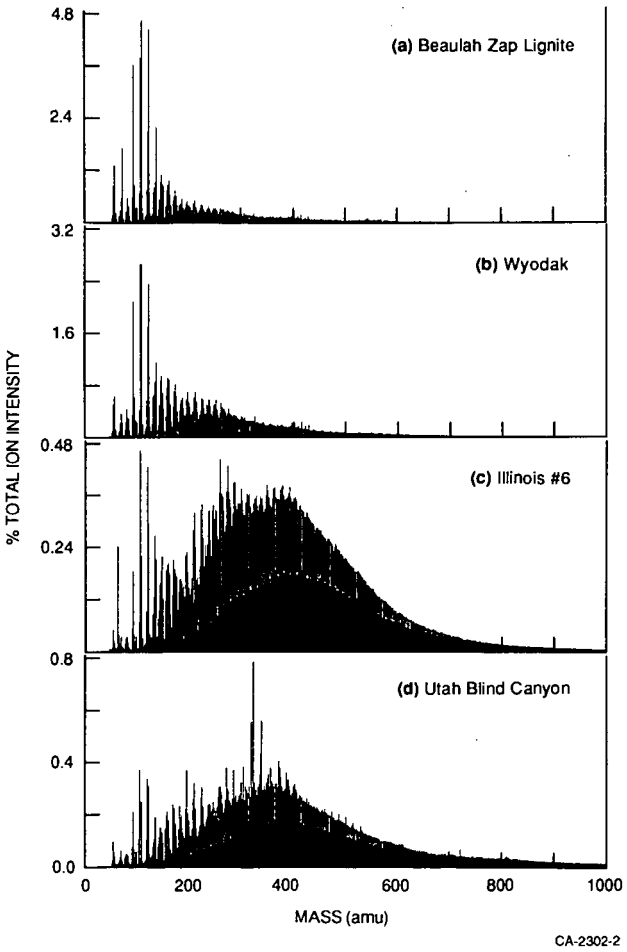

Figure 1. FI-Mass spectra of the four lower rank coals from the Argonne Premium Coal Sample Program.

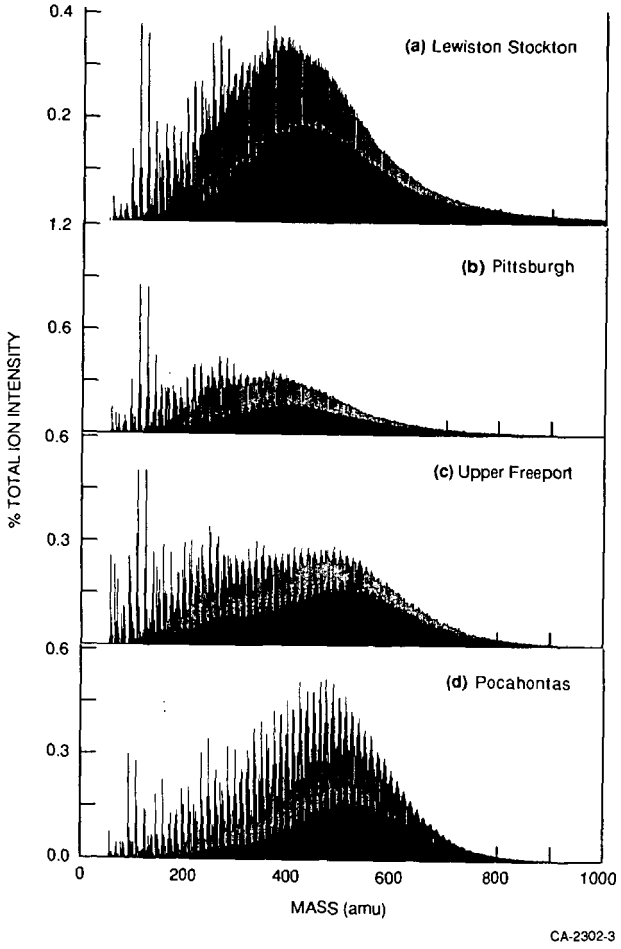

Figure 2. FI-Mass spectra of the four higher rank coals from the Argonne Premium Coal Sample Program.

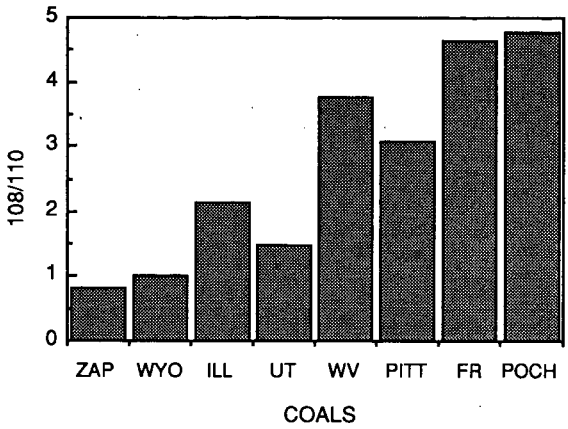

Figure 3. Variation of the relative amounts of representative monohydric and dihydric phenols with coal rank.

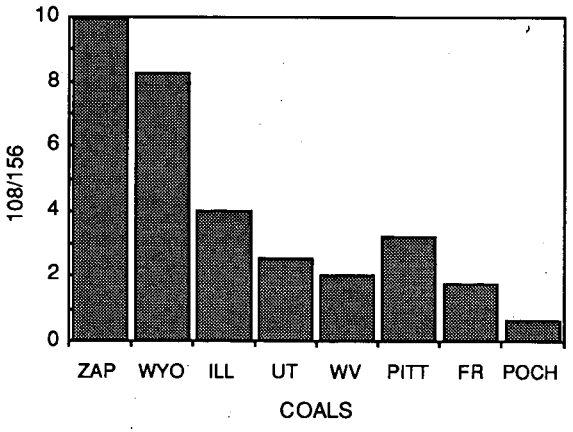

Figure 4. Variation of the relative amounts of representative phenols and hydrocarbons with coal rank.

HYDROGEN TRANSFER DURING COAL LIQUEFACTION DETERMINED BY $^2H/^1H$ MEASUREMENT

Tohru Kamo, James G. Steer, and Karlis Muehlenbachs
Department of Geology
University of Alberta
Edmonton, Alberta, Canada, T6G-2E3

Keywords: liquefaction, hydrogen transfer, isotope

ABSTRACT

Liquefaction of Highvale coal was carried out with tetralin under 6.9 MPa H_2 gas pressure at 400°C and 450°C. The natural ^2H contents of the gas, tetralin, and coal differed substantially and were utilized as tracers of hydrogen transfer. The effect of Fe_2O_3 catalyst, reaction time, and temperature on hydrogen transfer were studied. Products from autoclave tests were separated into light oil, oil, pentane soluble, pentane insoluble - benzene soluble, benzene insoluble - THF soluble, and THF insoluble fractions. At the initial stage of coal liquefaction, hydrogen transfer or exchange between feed gas and coal derived products predominated. But, hydrogen transferred from tetralin was dominant in the more advanced stages of coal liquefaction. Fe_2O_3 catalyst accelerated the interaction between hydrogen gas feed and the coal derived products.

INTRODUCTION

The role of hydrogen is important during coal liquefaction and the control of hydrogen transfer is central to optimizing product distribution. Thus, many attempts have been made to elucidate the mechanisms of hydrogen transfer by deuterium tracer [1] [2], NMR [3] [4] and radioisotope tracer method [5] [6]. Recently, stable isotope methods were used to study coprocessing reactions [7]. In this study, the stable isotope technique was used to identify two separate hydrogen transfer mechanisms during coal liquefaction.

The natural isotopic ratio ($^2H/^1H$) in hydrogen gas, coal and tetralin differ substantially. Products derived from coal have $^2H/^1H$ ratios that may approach either that of tetralin or feed gas identifying the source of the hydrogen. The size of the shifts reflect the relative proportions of hydrogen transfer into coal from gas or tetralin.

EXPERIMENTAL METHODS

Materials. Highvale coal (analysis: C, 71.6; H, 4.4; O, 23.0; N, 0.7; S, 0.3; ash 13.7 wt%, dry basis) was ground to <100 mesh and dried at 110°C for 3 days under vacuum condition. Tetralin, H_2, catalyst (Fe_2O_3) and sulfur were obtained from commercial sources.

Liquefaction procedure. All reactions were done in a 150 ml stirred autoclave. The coal (12g), tetralin (36g), iron oxide (Fe_2O_3, 1.2g), sulfur (0.18g), and H_2 were charged into the autoclave at an initial pressure of 6.9 MPa. The autoclave was heated at 15°C/min and maintained at 400°C and 450°C for 0 min, 60 min and 120 min. For

comparison, tetralin alone, was treated with H_2 and catalyst. After reaction, the autoclave was cooled by blowing air. The volume of gas products was measured and collected in Teflon bags for analysis.

Light oil and oil were obtained by vacuum distillation after filtration of the reaction products. The vacuum residue was extracted to four parts PS (pentane soluble), PI-BS (pentane insoluble - benzene soluble), BI-THFS (benzene insoluble - THFS soluble), and THFI (THF insoluble). A 30 m OV-101 capillary column was used to characterize the liquid products.

Analytical procedure. The feeds and products were analyzed for $^2H/^1H$ by conventional methods of stable isotope geochemistry described previously [7]. The isotopic ratios are determined by isotope ratio mass spectrometry, and the data are reported in the conventional delta notation, relative to the international standard, SMOW.

$$\delta D = ([^2H/^1H] - [^2H/^1H]_{SMOW})/[^2H/^1H]_{SMOW} \times 1000$$

$$[^1H/^2H]_{SMOW} = 1.558 \times 10^{-6}$$

The δD of the coal was -174 ppt, that of tetralin, -105ppt, H_2, -480ppt. The error on replicate analyses was ±3 ppt.

RESULTS AND DISCUSSION

Liquefaction of Highvale coal was carried out in tetralin and H_2. Fig. 1(a) and Fig. 1(b) show the effect of reaction time and the action of Fe_2O_3 catalyst on product distribution at 400°C. THFI decreased with reaction time. Conversion of THFI was a little higher with catalyst than without catalyst. BI-THFS, PI-BS, light oil and gas increased gradually with time. The yield of PS and oil increased slightly with reaction time. These observations indicate that cracking of coal to products lighter than PS was difficult at 400°C. Less light oil and gas were produced when Fe_2O_3 catalyst was added.

The distribution of products from the 450°C runs are shown in Fig. 2(a) and Fig. 2(b). The initial rate of cracking coal was very rapid, nearly 65 % of coal was already converted at 0 min, or when the reactor reached operating temperature. BI-THFS decreased slightly with reaction time without catalyst. With catalyst, BI-THFS gave a low yield already at 0 min. The yield of PI-BS increased at first, but then decreased after 60 min of reaction time. PS, light oil and crack gas increased gradually. The early yield of PI-BS at 450°C was higher than that at 400°C. These trends show that the conversion of coal to PI-BS was rapid and PI-BS was decomposed gradually to PS.

When tetralin was treated without coal but with catalyst at 450°C, naphthalene, 1-methylindan and butylbenzene were produced in small amounts (2.0 wt%, 2.8 wt%, and 1.4 wt%). Therefore, under the experimental conditions, dehydrogenation and decomposition of tetralin was less than 6 wt% in presence of catalyst, and 5 wt% in

absence of catalyst at 450°C. Mainly naphthalene was produced from tetralin during coal liquefaction. 1-Methylindan and butylbenzene were identified in the product. The yield of these compounds in the oil was 1.5 wt% and 4.3 wt% at 400°C and 450°C from the 60 min runs. The δD of tetralin before and after reaction with catalyst at 450°C and 400°C in absence of coal was -105 ppt, -114 ppt and -115 ppt. These small shifts in deuterium content implied no more than 1.5% of hydrogen of the tetralin exchanged with feed gas.

Fig. 3 shows the amount of naphthalene produced in oil at 400°C during coal liquefaction. Naphthalene increased linearly with THFI conversion without catalyst. But, with catalyst, naphthalene increased only gradually. Under this reaction condition, where hydrogenation of naphthalene is very slow [8], the Fe_2O_3 catalyst accelerates hydrogenation of naphthalene back to tetralin. In the tests without catalyst, the amount of naphthalene corresponds to hydrogen transferred from tetralin to coal. Fig. 4 shows hydrogen transfer from tetralin at 450°C. Hydrogen was donated from tetralin to coal when high conversion of coal was achieved.

Fig. 5 shows the δD of the products obtained without catalyst. The δD of products decreased at 400°C with THFI conversion. These products approached the isotopic composition of the feed gas (-480ppt). In contrast, at 450°C, δD of the coal derived products, excluding oil and light oil, increased with THFI conversion. The increase in δD of the higher temperature products reflects hydrogen donation from the tetralin solvent (δD=-105). Fig. 6 shows the isotope ratio of all the product fractions at 0 min of reaction time. The δD of PS, PI-BS, BI-THFS, and THFI were from -190 ppt to -230 ppt. These negative shifts from original δD of Highvale coal (δD =-174 ppt) show that H_2 was more reactive towards coal than was tetralin. More extensive hydrogen exchange was observed in the presence of catalyst.

The δD of products at 60 min are shown in Fig. 7. The δD of fractions from 450°C were higher than that of products at 400 °C. This suggests that at 450°C, hydrogen transfer from tetralin is dominant. The larger shifts of δD with catalyst show that the Fe_2O_3 catalyst accelerated the interaction of H_2 gas and coal. Inspection of the δD values shows that hydrogen from tetralin preferentially reacts with heavier molecular weight fractions THFI and BI-THFS. In contrast, hydrogen in PS and PI-BS reflects more exchange with feed.

These observations show that hydrogen transfer during coal liquefaction proceeds by at least two different pathways. Initially, hydrogen transfer to coal is dominated by absorption of feed hydrogen gas. But, as reactions proceed, hydrogen transfer and exchange between tetralin and coal derived products become increasingly more important. The decrease of δD of the light oils reflect the incorporation of low-^2H feed gas showing

that the light oil was produced by cracking of coal directly followed by hydrogenation with feed gas.

CONCLUSION

1. Two separate mechanism of hydrogen transfer to coal products were identified. Hydrogen transfer from feed gas occurs at the earliest stages of liquefaction whereas hydrogen transfer from tetralin dominates the more extensive, later stages.

2. Fe_2O_3 catalyst accelerated the interaction between hydrogen feed gas and the coal derived products.

3. Hydrogen from tetralin preferentially goes into heavier fraction such as THFI and BI-THFS. Hydrogen in PS and PI-BS is more exchangeable with feed gas.

4. The efficiency of producing products lighter than PS from coal at 400°C was low. When Fe_2O_3 catalyst was added, light oil and gas production was even less. The cracking rate of coal to PI-BS was fast but this fraction gradually decomposed to PS at 450°C.

ACKNOWLEDGEMENTS

We thank Dr. M. R. Gray, Department of Chemical Engineering, University of Alberta, for use of the autoclave and GC and Dr. Y. Sato at National Research Institute Pollution and Resources in Japan for elemental analysis. This work was funded by grants from OCRT of Alberta and the NSERC of Canada.

REFERENCES

1. D. C. Cronauer, R. I. McNei, D. C. Young, and R. G. Ruberto, Fuel, 61, 610 (1982).

2. J. Pajak, Fuel Process. Technol. 23, 39 (1989).

3. M. A. Wilson, P. J. Collin, P. F. Barron, and A. M. Vassallo, Fuel Process. Technol., 5, 281 (1982).

4. R. P. Skowronski, J. J. Ratto, I. B. Goldberg, and L. A. Heredy, Fuel, 63, 440 (1984).

5. T. Kabe, K. Yamamoto, K. Ueda, and T. Horimatsu, Fuel Process. Technol., 25, 45 (1990).

6. T. Kabe, K. Kimura, H. Kameyama, A. Ishihara, and K. Yamamoto, Energy & Fuel, 4, 201 (1990).

7. J. G. Steer, T. Ohuch, K. Muehlenbachs, Fuel Process. Technol.,15, 429 (1987).

8. T. Kabe, O. Nitoh, E. Funastu, K. Yamamoto, Fuel Process. Technil., 14, 91 (1986).

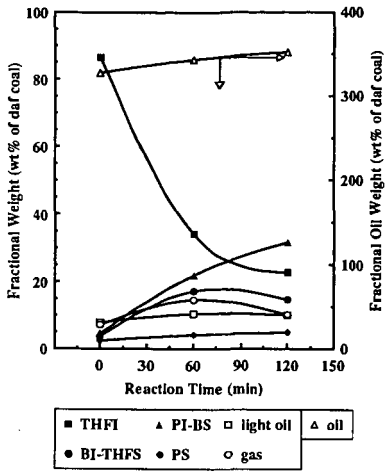

Fig.1(a) Product distribution with catalyst at 400℃.

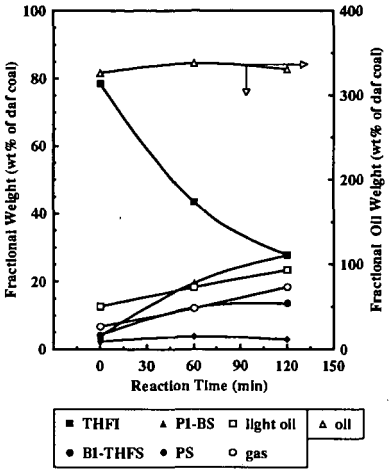

Fig.1(b) Product distribution without catalyst at 400℃.

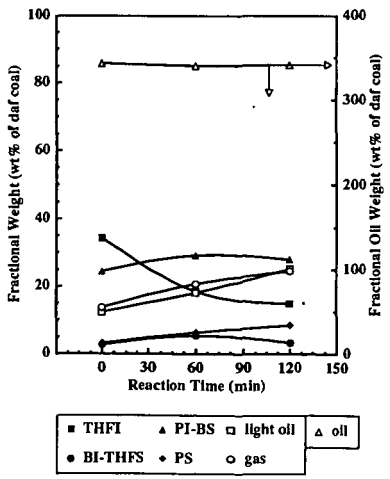

Fig.2(a) Product distribution with catalyst at 450℃.

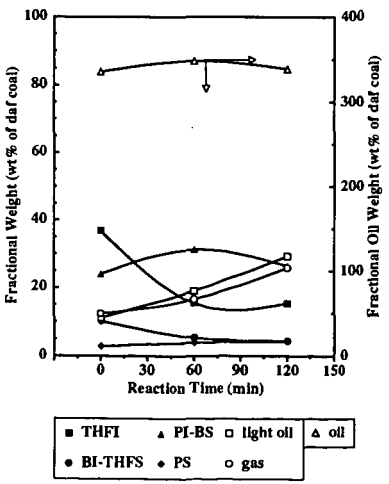

Fig.2(b) Product distribution without catalyst at 450℃.

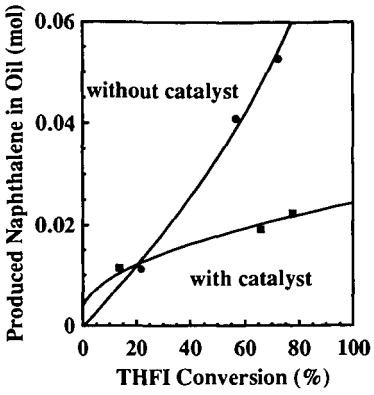

Fig.3 Amount of naphthalene produced in oil at 400°C.

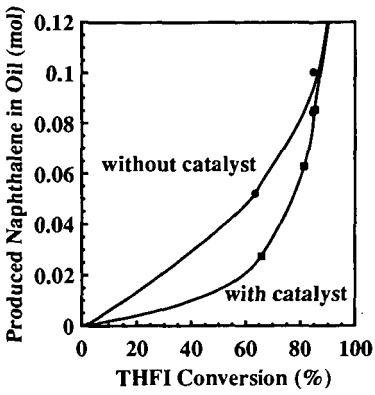

Fig.4 Amount of naphthalene produced in oil at 450°C.

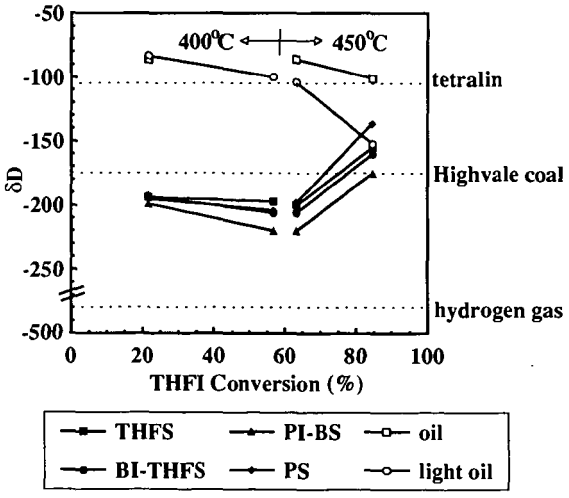

Fig.5 Shifts in $^{2}H/^{1}H$ of products as a function of THFI conversion without catalyst.

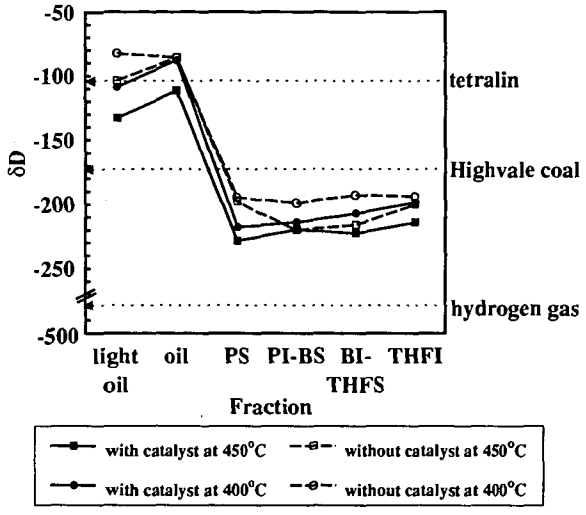

Fig.6 Isotope distribution in products at 0 min

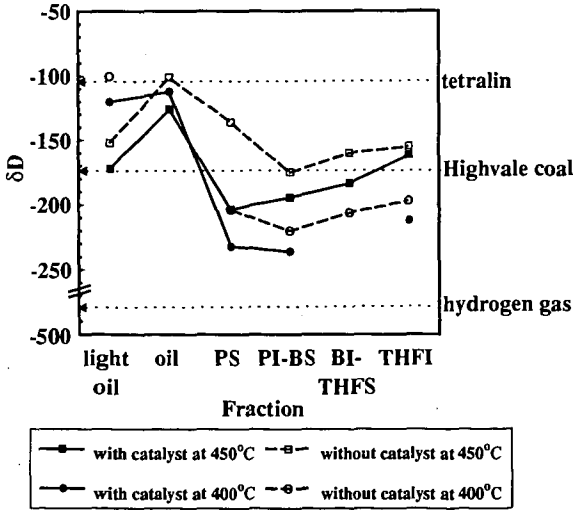

Fig.7 Isotope distribution in products at 60 min

STABLE CARBON ISOTOPE ANALYSIS OF COPROCESSING MATERIALS

Michael S. Lancet, Richard A. Winschel, Francis P. Burke
CONSOLIDATION COAL COMPANY
Research & Development
4000 Brownsville Road
Library, PA 15129

Keywords: Coprocessing, Carbon Isotopes

INTRODUCTION

The purpose of obtaining stable carbon isotope analyses of coprocessing products is to determine the amount of coal (or petroleum) carbon that is present in any reaction product. This *carbon-sourcing* of distillate fractions, soluble resid, and insoluble organic matter, etc. is useful in modeling reactions, and evaluating synergistic effects if they exist. A complete description of the method outlined in this paper, including all experimental details and calculation methods can be found in Reference 1.

Basic Method of Application

In general, the ratio of the two stable isotopes (carbon-12 and carbon-13) differs by small but measurable amounts for different natural hydrocarbons like coal and petroleum. The isotope ratio is reported in units of parts-per-thousand (per mil) difference from a standard. For example, Pittsburgh seam coal has a carbon isotope ratio of about -24 per mil. Cold Lake bitumen has a carbon isotope ratio of about -30 per mil. If we analyze a physical mixture of the two and it has a carbon isotope ratio of, say, -26 per mil, we can use a simple mixing equation to calculate that (-24 - (-26))/(-24 - (-30)) x 100 = 33.3% of the carbon in the mixture is petroleum carbon or, alternatively, that 66.7% is coal carbon. The precision and accuracy of the method are adequate for mixtures of practical interest (2).

Selective Isotopic Fractionation

Actual coprocessing, however, involves considerable bond breaking. Because ^{12}C - ^{12}C bonds are slightly weaker than ^{13}C - ^{12}C bonds, the lighter products, particularly the C_1 x C_4 gases, are slightly enriched in ^{12}C relative to the feed. The heavier products are slightly enriched in ^{13}C. At high conversion conditions (1), this selective isotopic fractionation becomes significant and must be accounted for. The simple physical mixing equation tends to under-account for the isotopically heavier component (usually the coal) in the lighter product fractions, and to over-account for it in the heavier fractions.

PROCEDURES

Sampling and Analysis Procedures

Practical application of stable carbon isotope analysis requires that the coal and petroleum have sufficiently different carbon isotope ratios. In general, a difference of at least 2 per mil is necessary, but a difference of 4 per mil is preferable, particularly if selective isotopic fractionation is expected. With careful attention to sampling and analysis procedures, it is possible to achieve analytical reproducibility (difference between repeat analyses) of about 0.2 per mil routinely. Therefore, the inherent accuracy of the method is about 5% (relative). Without

adequate attention to sampling and analysis procedures it is possible to encounter reproducibility errors of 1 per mil or more, rendering the application essentially useless. The biggest problem appears to be homogeneity for residual samples (i.e., nondistillate oils), although gas samples also are a problem. For viscous liquids and tar samples, the best approach is to homogenize the residual samples by melting, mixing, freezing (in liquid nitrogen), grinding, and remixing, then supplying a small (~1g) aliquot of the sample to the analyst. All isotope analyses were performed at least in duplicate, and an additional replicate analysis was obtained when those results differed by more than 0.2 per mil. Secondary standards similar to the analyzed material should be analyzed routinely to assure accuracy. The standard NBS 22 was analyzed 79 times during this work, giving a standard deviation of 0.04 per mil.

Correcting for Selective Isotopic Fractionation

Selective isotopic fractionation is the most significant problem in applying carbon isotope analysis to carbon-sourcing of coprocessing products. Attempts have been made to account for isotopic fractionation by doing "blank" runs in which the petroleum is processed alone (3). However, it is impossible to do a coal-only run at coprocessing conditions, without the use of a vehicle solvent, and this would require further correction. Ignoring the isotopic fractionation of the coal is convenient; however, we found (1) that higher-rank coals, in particular, undergo significant isotopic fractionation. It is also impractical to do a petroleum-only run and a coal-only run for each coprocessing run. Therefore, we sought a correction method that could be applied for the most common cases in which correction factors from blank runs are unavailable.

The correction method (4,5) is based on the fact that isotopic fractionation will make the hydrocarbon gases isotopically lighter than the respective feed, often by a substantial amount (4-10 per mil relative to the feed). However, because the gas usually represents only a small portion of the carbon (5-10%), the non-gaseous products will differ from the feed by only 0.1 to 1.0 per mil. Therefore, the yield, isotope ratio and carbon content of the gas can be used to calculate the carbon isotope ratios of those portions of the feed coal and feed petroleum that report to the non-gaseous products.

It is not possible to determine from isotope analysis how the coal and petroleum individually fractionate. Overcoming this requires two assumptions. First, we assume that the gaseous carbon is produced from coal and petroleum carbon in equal proportion to their concentrations in the feed. Second, we assume that the degree of fractionation is the same for both feeds. That is, if the isotope balance requires that the gas is 4 per mil lighter than the total feed carbon, we assume that both the coal and petroleum each produce gas that is 4 per mil isotopically lighter than the respective feed carbon. The results of a sensitivity analysis (6) show that, for reasonable relaxations of these assumptions, relative errors are 5-10% if the feedstock pair has a sufficiently large difference in isotope ratio (>4 per mil). A third assumption is that the non-gaseous products from a particular feed all have the same isotope ratio. That is, that the coal-derived carbon in the naphtha has the same isotope ratio as the coal-derived carbon in the resid. In fact, there probably is some heterogeneity in the isotope ratios of the non-gaseous products, with the heavier products being isotopically heavier. This error is minimized by choosing feedstock pairs with large isotopic differences.

It is difficult to obtain valid data on gas samples. However, the carbon content and isotope ratio of the gas can be forced based on the feed analyses and analyses of the non-gas products. If valid gas data are available, they can be used.

EXAMPLE OF APPLICATION TO CONTINUOUS COPROCESSING SAMPLES

This section provides an example of the computations necessary to employ the standard method of correction. The data from five product samples and two feedstock samples from period 11 of Hydrocarbon Research Inc. (HRI) coprocessing Bench Run 238-1, also known as Bench Run No. 2, are used in this example. The feedstocks to this run were Westerholt coal (German bituminous) and Cold Lake vacuum still bottoms (VSB). The large difference, 5.5 per mil, between the isotope ratios of the two feedstocks make the Westerholt coal/Cold Lake VSB pair a good candidate for carbon sourcing via the stable carbon isotope method. The products obtained included initial boiling point (IBP) x 350°F, 350 x 650°F and 650 x 975°F distillates, 975°F$^+$ pressure filter liquid (PFL) and tetrahydorfuran (THF) washed pressure filter cake (PFC). Operating conditions, conversions, and yields (7) from Run 238-1 are given below. A 1:1 MF coal/petroleum ratio was used.

OPERATING CONDITIONS AND PROCESS PERFORMANCE
HRI Coprocessing Bench Run 238-1, Period 11

Conditions	
Feedstock Ratio (dry coal/petroleum):	1
Nominal Pressure, psig:	2500
Temperature, °F (both stages):	810
Relative Space Velocity:	1.0
Process Performance	
Coal Conversion (% MAF):	90
975 °F+ Resid Conversion (% MAF):	82

The input data required for the carbon sourcing calculation are the feed compositions, carbon and carbon isotope analyses of the feed components, and yields, carbon contents, and carbon isotope ratios of the product fractions. These are shown below. As noted above, we found it convenient to calculate the carbon content and isotope ratio of the carbonaceous gas because of problems with sample acquisition and analytical reliability. However, measured values may be used if available. In this example, the gas analyses are calculated by forcing the carbon and isotope analyses. The input data for the example case are given below:

Feed Composition	wt % Feed	wt % Carbon	lb Carbon/ 100 lb feed	$\delta^{13}C$, per mil
Coal (MF)	50.0	77.9	38.9	-24.30
Petroleum	50.0	84.0	42.0	-29.84
Total Feed	100	80.9	80.9	(a)

Feed Composition	wt % Feed	wt % Carbon	lb Carbon/ 100 lb feed	$\delta^{13}C$, per mil
C_1 x C_4, CO_x	12.4	(a)	(a)	(a)
IBP x 350°F	16.1	86.2	13.9	-27.39
350 x 650°F	32.1	87.0	27.9	-27.18
650 x 975°F	19.5	89.2	17.4	-26.12
975°F+ liquid	11.9	91.2	10.9	-25.61
PFC, THF-washed	8.0	66.1	5.3	-23.99
H_2 Consumption	-4.5	-	-	-

(a) Not analyzed.

Based on the feed composition and coal and petroleum analyses, the isotope ratio of the total feed can be calculated as:

$$\delta^{13}C_{feed} = \frac{(-24.30)(38.90) + (-29.84)(42.00)}{80.9} = -27.18 \text{ per mil} \qquad (1)$$

The carbon yield in the product gas is the difference between the feed carbon (80.9 lb) and the sum of the carbon in the other products (13.9+27.9+17.4+10.8+5.3), or 5.6 lb carbon, giving a gas carbon content of 5.6/12.4 x 100 or 45.1%. By forced isotope balance, the isotope ratio of the carbon in the carbonaceous gas is given by:

$$\delta^{13}C_{gas} = \frac{(80.9)(-27.18)-[(13.9)(-27.39)+(27.9)(-27.18)+(17.4)(-26.12)+(10.8)(-25.61)+(5.3)(-23.99)]}{5.6} = -36.0 \text{ per mil} \qquad (2)$$

This illustrates the commonly observed effect of selective isotopic fractionation: the gas (-36.0 per mil) is isotopically lighter (more negative) than either of the feed components.

Based on the calculated carbon isotope ratio of the gas, the isotope ratio of the total non-gaseous product (distillates + resid + PFC) is calculated as:

$$\delta^{13}C_{non\text{-}gas} = \frac{(80.9)(-27.18)-(5.6)(-36.0)}{(13.9 + 27.9 + 17.4 + 10.8 + 5.3)} = -26.52 \text{ per mil} \qquad (3)$$

We assume that the carbon in the product gas is produced from each feedstock in proportion to its carbon in the feed, or 2.7 and 2.9 lb carbon from the coal and petroleum, respectively. We also assume that the difference (X) between the isotope ratio of the coal and petroleum carbon and the gases they produce is the same. X, for each feed, is equal to the difference in the isotope ratio calculated for the product gas and that of the total feed:

$$X = -27.18 - (-36.0) = 8.82 \text{ per mil} \qquad (4)$$

Then the carbon isotope ratios of the non-gas coal and petroleum carbons are calculated as:

$$\delta^{13}C_{coal'} = \frac{(38.9)(-24.3)-(2.7)(-24.30-8.82)}{(38.9 - 2.7)} = -23.64 \text{ per mil} \qquad (5)$$

$$\delta^{13}C_{petr'} = \frac{(42.0)(-29.84)-(2.9)(-29.84-8.82)}{(42.0 - 2.9)} = -29.19 \text{ per mil} \qquad (6)$$

Actually, it was not necessary to calculate the isotope ratio of the gas. The correction to be applied to each of the non-gaseous feedstocks is the difference between the isotope ratio of the total feed (-27.18 from Equation 1) and the total non-gaseous product (-26.52 from Equation 3). These values differ from those of the original feedstocks by 0.66 per mil. Compared to the difference of 5.5 per mil in the coal and petroleum isotope ratios, this represents a relatively small correction. We have documented cases in which isotopic fractionation is more severe, and if feedstock pairs have closer isotope ratios, failure to correct for isotopic fractionation can lead to unacceptably large errors.

To complete the calculation, these corrected values are used in lieu of the original feedstock isotope ratios, to calculate the coal carbon contents of the non-gaseous products. For example, the coal carbon content of the IBP X 350 °F distillate (-27.39 per mil) is given by:

$$\% \text{ Coal Carbon} = \frac{-29.19 - (-27.39)}{-29.19 - (-23.64)} \times 100 = 32.4\% \qquad (7)$$

The remainder of the product compositions are calculated in a similar manner. The results are shown below.

Product Fraction	% Coal Carbon	% Petroleum Carbon
$C_1 \times C_4$, CO_x	48.1	51.9
IBP x 350°F	32.4	67.6
350 x 650°F	36.2	63.8
650 x 975°F	55.4	44.6
975°F+ liquid	64.6	35.4
PFC, THF-washed	93.8	6.2

Conversions

Knowing the relative proportions of coal and petroleum carbon in the product fractions, it is possible to calculate the conversion of either feedstock to that fraction. This could be useful information in reaction modeling, or for investigating the possibility of feedstock synergisms. The conversions from this example are given below:

	Conversion	
Product Fraction	% Coal Carbon	% Petroleum Carbon
$C_1 \times C_4$, CO_x	6.9	6.9
IBP x 350°F	11.6	22.3
350 x 650°F	26.0	42.4
650 x 975°F	24.7	18.5
975°F+ liquid	18.0	9.1
IOM	12.7	0.8
Total	99.9	100.0

Selectivity

The coal-conversion selectivity is simply the ratio of the percent coal carbon in a given product fraction to that in the feed (in this case 48.1%). A value greater than unity indicates that the coal carbon is preferentially converted to (or retained in) that product fraction. Selectivities for this example are given below.

Product Fraction	Coal Carbon Selectivity
IBP x 350°F	0.7
350 x 650°F	0.8
650 x 975°F	1.2
975°F+ liquid	1.3
PFC, THF-washed	2.0

These results indicate that the lower boiling distillates were preferentially produced from the petroleum, while the higher boiling distillates, resid and IOM were preferentially produced from the coal. Note that there is no information on

the gas. We assumed in correcting for selective isotopic fractionation that it was produced with equal selectivity from the coal and petroleum.

SUMMARY

It was demonstrated that, under appropriate circumstances, stable carbon isotope analysis can be an excellent method to determine the contributions of the individual feedstock to coal/petroleum coprocessing products and to follow the reaction pathways of the individual feedstocks. There are two primary considerations in applying this method: 1) the difference in the stable carbon isotopic compositions of the two feedstocks ($\delta^{13}C$), and 2) selective isotopic fractionation errors. An adequate difference in the isotope ratios of the coal and petroleum can be assured by selecting the appropriate coprocessing feedstocks. Selective isotopic fractionation is a consequence of the coprocessing process. It is affected by processing severity, and most coprocessing operations are at high enough severity to induce significant isotopic fractionation. Nevertheless, errors introduced by isotopic fractionation can be corrected, at least in some circumstances.

Even in those cases where the feedstocks are isotopically similar and where isotopic fractionation effects are significant but not corrected (worst case), the method provides data that are useful for discerning trends. However, for use of the method as a quantitative tool, it is important to maximize the difference in the isotope ratios of the coprocessing feedstocks and to follow good, careful sampling and analytical practices. This method allows one to examine the fate of the individual feedstocks through the coprocessing process.

ACKNOWLEDGMENTS

The authors gratefully acknowledge J. E. Duddy and S. V. Panvelker of HRI for supplying the samples and yield data. This work was funded by the U.S. Department of Energy under contract No. DE-AC22-88PC88800.

REFERENCES

1. Winschel, R. A.; Lancet, M. S.; Burke F. P. "Stable Carbon Isotope Analysis of Coprocessing Materials - Final Report" DOE Contract No. DE-AC22-88PC88800, Report No. DOE/PC 88800-43, April 1991.

2. Winschel, R. A.; Lancet, M. S.; Burke F. P. "Stable Carbon Isotope Analysis of Coprocessing Materials - Quarterly Technical Progress Report, July 1 - September 30, 1989". DOE Contract No. DE-AC22-88PC88800, Report No. DOE/PC 88800-26, July 1990.

3. Steer, J. G.; Ohuchi, T.; Muehlenbachs, K.; *Fuel Process. Technol.* 1987, *15*, 429-438.

4. Winschel, R. A.; Burke, F. P.; Lancet, M. S. "Application of Stable Carbon Isotope Analysis to Continuous Coal/Oil Coprocessing", Preprints, Fuel Chemistry Division, American Chemical Society vol. 35, No.4, p 1032, 1990.

5. Burke, F. P.; Winschel, R. A.; Lancet, M. S. "Stable Carbon Isotope Analysis of Coprocessing Materials - Quarterly Technical Progress Report, April 1 - June 30, 1989". DOE Contract DE-AC22-88PC8800, Report No. DOE/PC 88800-25, May 1990.

6. Lancet, M. S.; Winschel, R. A.; Burke, F. P. "Stable Carbon Isotope Analysis of Coprocessing Materials - Quarterly Technical Progress Report, January 1 -

6. Lancet, M. S.; Winschel, R. A.; Burke, F. P. "Stable Carbon Isotope Analysis of Coprocessing Materials - Quarterly Technical Progress Report, January 1 - March 31, 1990". DOE Contract DE-AC22-88PC8800, Report No. DOE/PC 88800-34, December 1990.

7. Duddy, J. E., personal communication to R. A. Winschel, May 9, 1988.

ADVANCED ELECTRON PARAMAGNETIC RESONANCE (EPR) TECHNIQUES FOR THE STUDY OF COAL STRUCTURE

B.G. Silbernagel, M. Bernardo, L.A. Gebhard and H. Thomann
Corporate Research—Exxon Research & Engineering Co
Route 22 East, Annandale, NJ 08801

Keywords: Coal, Electron Paramagnetic Resonance, Double Resonance

INTRODUCTION

Electron Paramagnetic Resonance (EPR) has been extensively applied to the study of coal [1]. In conventional EPR relatively featureless microwave absorptions are observed, from which one extracts the width and position (g–value) of the microwave absorption as well as the density of carbon radicals in the sample. For example, in a conventional EPR study of isolated coal macerals [2], these properties vary with increasing coal rank: g–values fall from values expected for oxidized aromatics to those of aromatic radicals, while radical densities and linewidths generally increase. Microwave saturation techniques (i.e. measuring the intensity of the absorption as a function of applied microwave field) show that high rank coals are much less easily saturated. The relation to the relaxation properties of the carbon radicals is less obvious, since saturation depends on the product of two relaxation parameters of the carbon radicals.

The conventional EPR absorption width results largely from interactions of the unpaired electron spin on the carbon radical with protons in its vicinity, either as a result of direct wave function overlaps (contact interactions) or dipole interactions. Distributions in g–values and dipolar interactions among the carbon radicals themselves will also contribute to the observed width. Identifying and separating these contributions can not be done by conventional EPR alone. The present paper describes two classes of pulsed EPR experiments, analogous to widely–used pulsed NMR techniques: Electron Spin Echo (ESE) determinations of spin–lattice (T_1) and spin–spin (T_2 or T_{m1}) relaxation and double resonance techniques like pulsed ENDOR (Electron Nuclear Double Resonance) [3]. While such techniques can be applied with great effect to relatively homogeneous systems, such as individual compounds or the active sites in enzymes, it is not obvious, *a priori*, that such elaborate schemes will yield useful information in a material as heterogeneous as coal. The present paper will demonstrate the nature of the information that can be obtained and assess its usefulness.

EXPERIMENTAL

The experiments described here have been performed on two series of samples: the isolated coal macerals [2] and a series of "as received" samples of Argonne Premium Coal samples [4]. While there is some concern about the quantitative nature of the data from the "as received" Argonne Premium Coal samples—due to the presence of significant levels of paramagnetic species, the qualitative features are still illustrative. The pulsed EPR experiments were run at microwave frequencies from 9.1–9.4 GHz. The relaxation measurements were performed at room temperature, while the double resonance measurements were done at ~100K. For the double resonance experiments, the rf frequency used to excite the protons was swept from 1–30 MHz.

RELAXATION RESULTS

The relaxation properties of the isolated vitrinite macerals as a function of coal rank probe the interactions of radicals in the coal [5]. Instantaneous diffusion contributes to phase memory loss in higher rank coals and can be separated from the asymptotic phase coherence decay rate, T_{m1}^{-1}, which is the EPR analog of T_2. Values of T_{m1}^{-1} and T_{1e}^{-1} for vitrinites varying in rank from subbituminous C to low volatile bituminous are shown in Fig 1. The T_{1e}^{-1} values are more than an order of magnitude smaller than T_{m1}^{-1} in all cases: spin lattice relaxation is much slower than phase memory loss. The contribution of the dipole coupling to the width of the conventional EPR line can be estimated from the magnitudes of T_{m1}^{-1}, and is much smaller the contributions from hyperfine interactions.

Both T_{1e}^{-1} and T_{m1}^{-1} values are relatively small for low rank coals, with T_{m1}^{-1} beginning to

increase in the vicinity of 78 wt. % carbon, and T_{1e}^{-1} showing a sharp increase near 82 wt. % carbon. The T_{ml}^{-1} values vary nearly linearly with carbon radical density indicating that they result from dipole interactions among the radicals. By contrast, the sharp change in T_{1e}^{-1} does not track radical density and appears related to changes in the local order of the aromatic molecules with increasing coalification.

DOUBLE RESONANCE EXPERIMENTS

Double resonance experiments require that the carbon radicals and the protons be simultaneously excited by microwave and rf pulses. Two of the double resonance schemes, for pulsed ENDOR and EPR detected sublevel coherence, are shown in Fig 2. In each experiment, the electron spin population of the radicals is prepared by the applying microwave pulses and then rf pulses are applied to the protons. At an appropriate time the electron and nuclear spin systems are allowed to mix and the results are detected in the electron spin system. The cavities required to allow simultaneous microwave and rf operations are a challenge to design and construct and remain at the frontiers of the technique development.

Fig 3 shows pulsed ENDOR data on a sample of Pocahontas coal [3]. In one case the ENDOR experiment was performed with the microwave frequency at the absorption center ($g = 2.0026$) and also with the frequency positioned on the low field (i.e. high g–value ≈ 2.0091) portion of the absorption. In each instance, a sharp signal centered at the proton Larmor frequency is seen from "matrix" protons—i.e. those not directly coupled to the radical but interacting with it via dipole interactions. The broader spectrum, which extends at least 15 MHz on either side of the center, comes from "local" protons—i.e. those interacting directly with the moments via some form of wave function overlap. The shape of the local ENDOR signal is nearly identical for all of the high volatile bituminous coal samples observed and has the same shape at 298K and 85K. The ratio of the matrix to local ENDOR signals does vary with rank and temperature, the matrix signals being relatively stronger in the lower rank coals. There is no evidence for major structure in the local ENDOR for any of the samples examined. Fig 3 also shows that the shape of the local ENDOR signal does vary for different positions of the microwave frequency. We suggest that this reflects the different chemical forms of the radical–bearing molecules lying at different places in the resonance line—particularly for the heterocyclic molecules which lie at high g–values.

EPR detected sublevel coherence measures proton dynamics on the carbon radicals, an exciting prospect since magnetic broadening usually renders these protons unobservable by NMR techniques. The protons contributing to the matrix ENDOR have faster T_2 relaxation than those in the local ENDOR component of the signal—presumably a result of field inhomogenieties associated with protons close to the radical.

CONCLUSIONS

Advanced EPR techniques provide new, quantitative information about coal chemistry and its variation with rank. The greater information obtained about interactions on the radical itself should further progress in the understanding of coal microscopics.

REFERENCES

1 Retcofsky, H.L. Coal Science and Technology, Academic, New York, 1982.

2 Silbernagel, B.G., Gebhard, L.A., Dyrkacz, G.R. and Bloomquist, C.A.A. ESR of Isolated Coal Macerals, Fuel, 1986, 65, 558–565.

3 Keijzers, C.P., Reijerse, E.J., and Schmidt J. Pulsed EPR: A New Field of Applications, North Holland, Amsterdam, 1989.

4 Vorres, K.S. The Argonne Premium Coal Sample Program, Energy & Fuels, 1990, 4, 420–426.

5 Thomann, H. Silbernagel, B.G. Jin, H. Gebhard, L.A., Tindall, P. and Dyrkacz,

G.R. Carbon Radical Spin Dynamics in Isolated Vitrinite Radicals, Energy & Fuels, 1988, 2, 333–339.

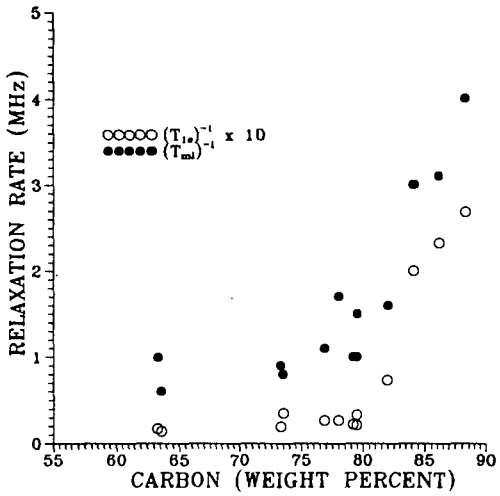

Fig 1 *Relaxation rate measurements on isolated vitrinite macerals [5] show significant increases in both T_{ml}^{-1} and T_{1e}^{-1} with increasing coal rank.*

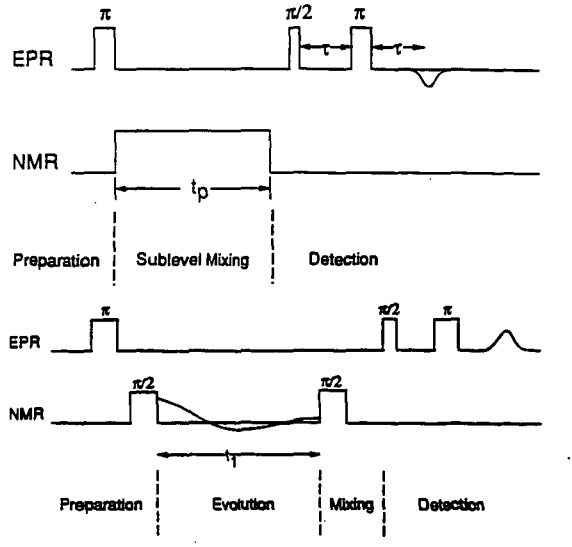

Fig 2 *Double resonance schemes for doing pulsed ENDOR (top) and EPR detected sublevel coherence (bottom) experiments.*

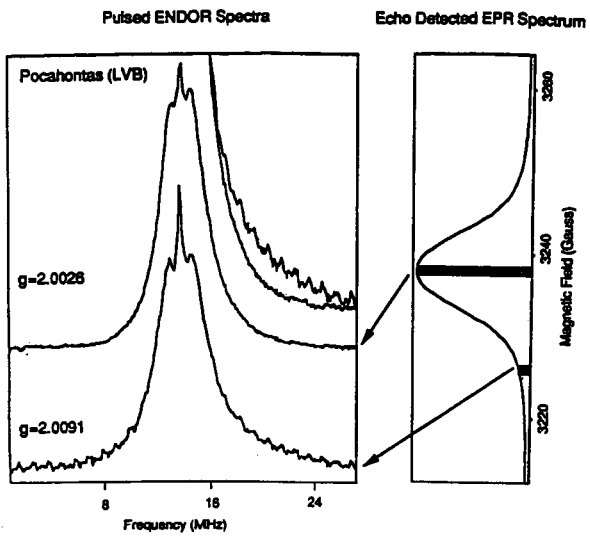

Fig 3 *The ENDOR spectra from the center of the resonance (g = 2.0026) and the low field end (g = 2.0091). Both matrix and local ENDOR signals are observed. The shape of the local ENDOR spectrum is significantly different at high g−value.*

AN INVESTIGATION OF THE CHEMISTRY OF THE PORE STRUCTURE OF COAL IN THE PRESENCE OF A SWELLING SOLVENT USING A NOVEL EPR TECHNIQUE

Dennis R. Spears, Wojciech Sady and Lowell D. Kispert

Box 870336, Chemistry Department
The University of Alabama, Tuscaloosa, AL 35487-0336

KEYWORD: Porosity, coal swelling, EPR, nitroxyl spin probe

ABSTRACT

To study the hydrogen bonding ability of functional groups in pores of Argonne Premium Coal Samples (APCS) exposed during swelling, small nitroxide spin probes with reactive R groups differing in polarity were diffused into APCS coals during swelling and the concentration of the trapped probes measured by an EPR method. As the hydrogen bonding ability of R increases, the degree of probe retention increases; however, probe retention decreases with rank. Polar solvents like pyridine interact specifically with polar functional groups on the micropore wall and prevent binding with polar guest molecules.

INTRODUCTION

The pore structure of coal plays an important role in the behavior of coal during mining, benefaction, and utilization. The pore structure of coal has three components, macropores (>300 Å diameter), mesopores (300 - 12 Å diameter) and micropores (< 12 Å diameter). The micropores make up as much as 88% of the total pore volume of low rank coals and up to 12% of the total pore volume of anthracites (1). Since most of the surface area of coals is located in the micropores (2), rates of reaction are limited by rates of diffusion through the micropore structure.

The micropore structure has been studied by several methods. Helium adsorption is the oldest method(3,4). More recently, small angle x-ray scattering (SAXS) (5,6) and small angle neutron scattering (SANS) (7,8), have been used to examine the micropore structure of coal. The micropore system undergoes changes in the presence of swelling solvents. Gethner showed that weakly swelling solvents such as cyclohexane do not change the micropore structure significantly from the dry state (9). Gethner (8), Winans and Thiyagarajan (7) showed that in the presence of benzene, micropores were spherical in shape. In the presence of pyridine, pores become elongated and cylindrical.

B. G. Silbernagel et. al. (10) first expanded EPR to examine guest molecules incorporated into coal. Silbernagel (10) wanted to study guest molecule inclusion into coals. He used 2,2,6,6-tetramethylpiperidine-1-oxyl, TEMPOL (Figure 1), as a probe. TEMPOL is a stable free radical and gives a highly articulated EPR spectrum. In the presence of coal, the center peak is overlapped by the carbon radical peak. Over several hours, the TEMPOL signal broadens and diminishes. However, the total spin density remains constant during this time, implying that TEMPOL is not being destroyed. The broadening occurs when the rate of motion of TEMPOL molecules drops below the value need for motional narrowing (10^8 sec^{-1}). The restriction of motion implies that, since the TEMPOL is not being destroyed, it must be included in the coal matrix (10).

To study the dynamics of the inclusion process, Silbernagel et al. (10), measured the derivative height of the TEMPOL spectrum as a function of time for Illinois No. 6 hvb coal swelled with benzene. A rapid reduction of the derivative intensity was observed after the first few minutes, indicating that adsorption had taken place. After the first few minutes, the reduction of derivative intensity became slower. A plot of the product of derivative intensity and $t^{1/2}$ versus time indicated that TEMPOL was indeed diffusing into the coal. With these experiments, Silbernagel et al. had developed a unique method for investigating the microporosity of coal (10).

Kispert and coworkers expanded on this technique to study the effect of low temperature swelling on the micropore system of coal. Wu and Kispert (11) showed that a wide variety of spin probes could

be incorporated into coal to study the micropore structure of coal. Cooray (12) studied the mechanism of probe interaction with coal by measuring $2A_{zz}$ as a function of temperature. Cooray concluded that at temperature above 220 K the spin probes exhibited no significant interaction with coal (12). Goslar and Kispert (13) conducted electron double resonance spectroscopy (ENDOR) on coals doped with nitroxyls and confirmed the absence of significant coal-spin probe interaction, at least through the N-O bond.

The effect of low temperature swelling conditions on pore size and shape has been extensively studied by Spears et al. (14,15). Coals contain spherical pores when swelled at low temperature and with a mild swelling solvent. Upon swelling with hydrogen bonding solvents such as nitrobenzene or pyridine, pores become elongated and cylindrical. The degree of elongation is dependent on both the polarity of the swelling solvent and the swelling temperature. To determine the number of spherical probes present TEMPOL was used as a spin probe. TEMPOL, although spherically shaped, has an -OH group which could potentially interact with the coal. Gethner has recently shown that pore walls in coal are covered with oxygen functionalities. (16) Although it was known that nitroxyls did not interact significantly at 300 K with coal through the N-O bond, it was thought that the polar R group of TEMPOL might.

To understand the chemistry of the micropore walls, a series of similarly sized nitroxyls were incorporated into the micropore structure of Argonne Premium Coal Sample (APCS) coals. The effects of rank, swelling solvent polarity, swelling temperature, and drying of the coal were investigated.

EXPERIMENTAL

The experimental procedure has been described elsewhere in detail (11-15). Spin probes were imbibed into the pore structure of coal in the presence of a swelling solvent. The solvent was removed, causing the pore structure to collapse about the incorporated nitroxyls. The coal was then washed with cyclohexane. If the spin probe was unable to penetrate a pore because it had not swelled open sufficiently, it was removed in the cyclohexane wash. If the probe molecule was trapped in a pore much larger in size, it was also removed in the cyclohexane wash. Thus, after the cyclohexane wash, all probes retained were trapped in pores similar in size and shape to the nitroxyl molecule.

The general structural shape of the spin probes used in this study are shown in Figure 1 where R represents the substitutent for each spin probe. The specific spin probes are numbered in the same manner as defined previously (12). Spin probe VIII, 2,2,6,6-tetramethylpiperidine-1-oxyl, is the basic structural unit for all nitroxyl spin probes studied. Spin probes VIII, I, VI, and VII are similar in size (molecular volume approximately 140 $Å^3$) and are spherically shaped. Spin probe X is larger (molecular volume 310 $Å^3$) and cylindrically shaped. All eight APCS coals were studied (Table 1). Coals were swelled in either toluene or pyridine at 333 K for 18 hours. Spin probe concentration was determined by EPR and normalized to 1 g of coal.

DISCUSSION

The number of spherically shaped micropores was determined by imbibing spin probe VIII into coal. Spin probe VIII should exhibit no significant interaction with coal. The results of swelling coal at 333 K with solutions of spin probe VIII are shown in Figure 2 as a function of rank and swelling solvent. Carbon content was used as convenient rank indicator throughout this study. For coals swelled in toluene, the number of small, spherically shaped pores is small such as for Beulah-Zap lignite and Wyodak subbituminous coals (74 and 76% carbon, dmmf, respectively), and quickly fall to zero as rank increases. In pyridine at 333 K, none of the APCS coals retained spin probe VIII. This indicated that all of the small, spherically shaped micropores had vanished.

Comparing the results with spin probe X, a spin probe larger than spin probe VIII and cylindrical in shape, shows that the micropores are enlarged and elongated. Figure 3 shows the change in spin probe X and VIII concentration with carbon content for coals swelled in either toluene at 333 K. The coals retained larger concentrations of spin probe X than spin probe VIII. This showed that the micropores were indeed becoming elongated.

Pore elongation in swelled coals meant that coals should not retain significant amounts of small, spherically shaped pores. However, previous data showed that coals swelled in toluene retained significant amounts of spin probe I and 333 K, especially compared to spin probe VIII. The main

difference between spin probe VIII and spin probe I was the polar R group. Thus the retention in coal was due to association of the -OH group with the pore walls.

Micropore walls, especially in swollen coals, are covered with polar functionalities. Gethner showed that micropore walls in low rank coals were linked with carboxylic acid groups (16). Coals contain significant amounts of hydrogen bonding. Hydrogen bonding in coal has been attributed to oxygen-containing functional groups. The swelling of coal in polar solvents has been ascribed to the disruption of these bonds by solvent molecule interaction. As polar functionalities are exposed by the swelling solvent, spin probes with polar R groups should be retained. The degree of retention should be directly related to the hydrogen-bonding ability of the R group. As the hydrogen-bonding ability of the R group increased, the strength of the spin probe-coal interaction should increase.

To test this hypothesis, APCS coals were imbibed with 4 spin probes differing in the polarity of the R group in toluene at 333 K. The R groups were -H, -OH, $-CO_2H$, and $-NH_4$ (spin probes VIII, I, VI, and VII respectively). The results are shown in Figure 4. As the relative R group polarity increased, the degree of retention increased, especially for low rank coals. Although the micropore system was enlarged by toluene swelling at 333 K, polar spin probes were still retained. This indicated that spin probes with polar R groups were retained in macropores larger than the size of probe molecule itself. Retention was apparently due to interaction of the polar R group with the coal surface. This mechanism of retention was considerably different from the simple physical entrapment for other spin probes studied (11-15).

The polarity of the functional groups in the micropore walls is apparently low. Highly polar functionalities should show little specificity of retention between the spin probes studied. A knowledge of the dissociation constants or the electron donor numbers of the spin probes should give more specific details as to the polarity of coal function groups.

Low rank coals contain larger quantities of oxygen functionalities and so should retain more of polar spin probes. The degree of retention decreased with rank, and the influence of R group polarity decreased with rank, but even at the highest ranked APCS coals, the effect of R group polarity was still significant. These results showed that polar functionalities were still present even at high rank coals. These functionalities are likely responsible for the hydrogen bonding which earlier spin probe studies had indicated that existed in coal of all ranks (15).

If hydrogen bonding was indeed a factor in the coal tertiary structure, then swelling coal in pyridine at 333 K would disrupt the hydrogen bonding network considerably. Previously results showed that swelling coal in pyridine at 333 K caused considerable opening of the micropore structure (15). This could only be the result of disruption of the hydrogen bonding network. Such disruption, followed by solvent removal, could lead to the exposure of polar functionalities within the coal, and result in greater retention of polar spin probes.

To test this hypothesis, APCS coals were imbibed with 4 spin probes differing in the polarity of the R group in pyridine . The R groups were -H, -OH, $-CO_2H$, and $-NH_2$ (spin probes VIII, I, VI, and VII respectively). The results are shown in Figure 5. As for coals swelled in toluene, an increase in the relative R group polarity resulted in increased retention although the difference between spin probe VI and spin probe VII is negligible. However, a comparison of Figure 4 with Figure 5 shows that, for a given spin probe, coals swelled in pyridine retained fewer spin probes than coals swelled in toluene, contrary to expectations.

Green showed that molecules capable of hydrogen bonding interact with specific sites in coal. (17) Pyridine interacts strongly with coal, and is not entirely removed even under the most severe vacuum drying. It is possible that unremoved solvent molecules tied up existing hydrogen bonding sites, reducing the number of sites available for spin probe-coal interactions. If many of the reactive sites in coal are tied up, then the polar spin probes would be trapped in enlarged micropores with fewer sites available for specific interaction. This would result in removal during the cyclohexane wash. To examine the swelling characteristics of the APCS coals after drying, APCS coals are now being subjected to vacuum drying at either room temperature or at 100°C. Results of these studies will be presented.

CONCLUSION

In conclusion, micropore enlargement occurs as the degree of swelling increases. The micropore structure is held together by hydrogen bonding, which can be disrupted by swelling with polar solvents. The micropore walls contain polar functional groups. The number of these functional groups decreases with rank. Polar solvents like pyridine interact specifically with these sites and prevent them from bonding with polar guest molecules. Thus, using a strongly polar solvent to swell coal in conversion processes might actually defeat the purpose by tying up reactive sites.

REFERENCES

1. Gan, H.; Nandi, S. P.; Walker, P. L., Jr. *Fuel* **1972**, *51*, 272.
2. Mahajan, O. P.; Walker, P. L., Jr.; in *Analytical Methods for Coal and Coal Products*, C. Karr, ed., Academic, New York, **1978**, 162.
3. Nelson, J. R., Ph. D. Dissertation, Pennsylvania State University, State College, **1979**.
4. Fuji, S.; Tsuboi, H. *Fuel* **1967**, *46*, 361.
5. Spitzer, Z.; Ulicky, L. *Fuel* **1976**, *50*, 21.
6. Lin, J. S.; Hendricks, R. W.; Harris, L. A.; Yust, C. S. *J. Appl. Crystallogr.*, **1978**, *11*, 621.
7. Winans, R. E.; Thiyagarajan, P. *Am. Chem. Soc. Div. Fuel Chem. Prepr.* **1987**, *32*, 227.
8. Gethner, J. S. *J. Appl. Phys.* **1986**, *59*, 1068.
9. Gethner, J. S. *Am. Chem. Soc. Div. Fuel Chem. Prepr.* **1987**, *32*, 239.
10. Silbernagel, B. G.; Ebert, L. B.; Schlosberg, R. H.; Long, R. B. *Adv. Chem. Ser.* **1979**, *192*, 23.
11. Wuu, S. K.; Kispert, L. D. *Fuel* **1985**, *64*, 1681.
12. Cooray, L. S.; Kispert, L. D.; Wuu, S. K. *Am. Chem. Soc., Div. Fuel Chem. Prepr.*, **1988**, *33*, 32; Cooray, M. L. S., M.Sc. Thesis, University of Alabama, Tuscaloosa, 1988.
13. Goslar, J.; Kispert, L. D. *Fuel*, **1990**, *69*, 564.
14. Spears, R.; Goslar, J.; Kispert, L. D. in *Techniques in Magnetic Resonance for Carbonaceous Solids*, Botto, R., and Sanada, Y., eds., ACS Symposium Series No. 229, In Press.
15. Spears, R.; Kispert, L. D.; Piekara-Sady, L. *ACS Div. Fuel Chem. Prepr.* **1991**, *36*, 29.
16. Gethner, J. S. *Am. Chem. Soc. Div. Fuel Chem. Prepr.* **1987**, *32*, 239.
17. Green, T. K.; West, T. A. *Fuel* **1986**, *65*, 298.

Table 1. Major element composition of Argonne Premium Coal Samples, dmmf basis.

Coal	% C	% H	% N	% S	% O
Upper Freeport	88.08	4.84	1.60	0.76	4.72
Wyodak-Anderson	76.04	5.42	1.13	0.48	16.90
Illinois No. 6	80.73	5.20	1.43	2.47	10.11
Pittsburgh No. 8	84.95	5.43	1.68	0.91	6.90
Pocahontas	91.81	4.48	1.34	0.51	1.66
Blind Canyon	81.32	6.81	1.59	0.37	10.88
Lewis-Stockton	85.47	5.44	1.61	0.67	6.68
Beulah-Zap	74.05	4.90	1.17	0.71	19.13

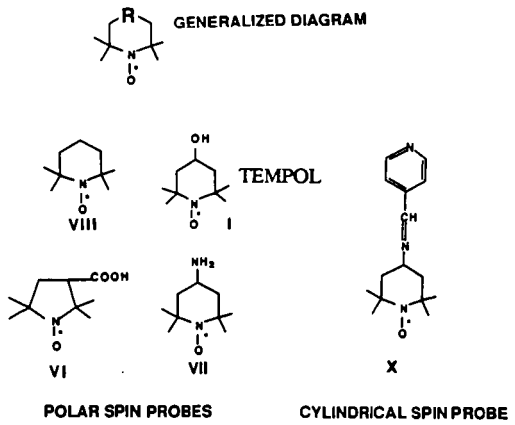

Figure 1. Nitroxyls used as spin probes in this study: A generalized diagram of a nitroxyl molecule is listed as well as; VIII, 2,2,6,6-tetramethylpiperidine-1-oxyl, R = -H; I, 4-hydroxy-2,2,6,6-tetramethylpiperidine-1-oxyl, R = -OH; VI, 3-carboxy-2,2,5,5-tetramethyl- pyrrolidine-1-oxyl, R = $-CO_2H$; and VII, 4-amino-2,2,6,6-tetramethylpiperidine-1-oxyl, R = $-NH_2$; X, Cylindrical nonpolar spin probe, amino-2,2,6,6-tetramethylpiperidine-1-oxyl 4-pyridine carboxaldimine.

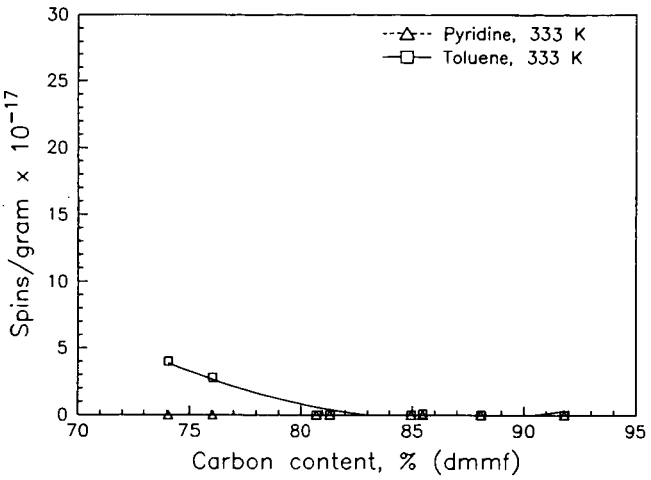

Figure 2. Effect of solvent on the quantity of spherically shaped micropores in coal. Spin probe VIII concentration (spins/g x 10^{17} in coals swelled at 333 K in either toluene (□) or pyridine (△) versus rank as % carbon on a dry, mineral matter-free (dmmf) basis.

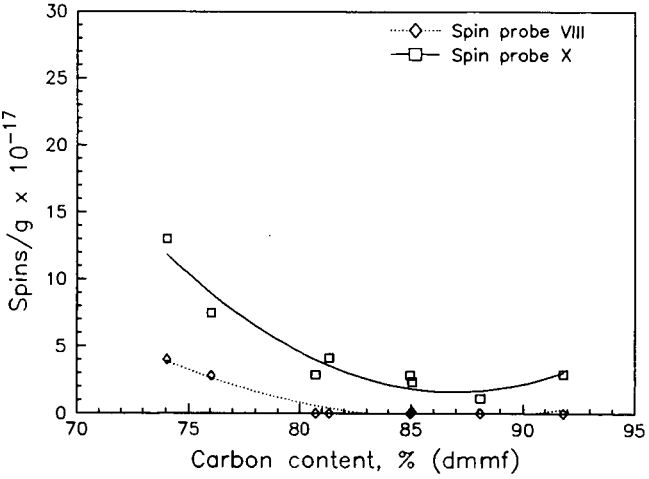

Figure 3. Effect of solvent swelling on micropore shape/size. Spin probe X (□) and spin probe VIII (◇) concentration (spins/g x 10^{17}) in coals swelled in toluene at 333 K, vs. carbon content (%, dmmf).

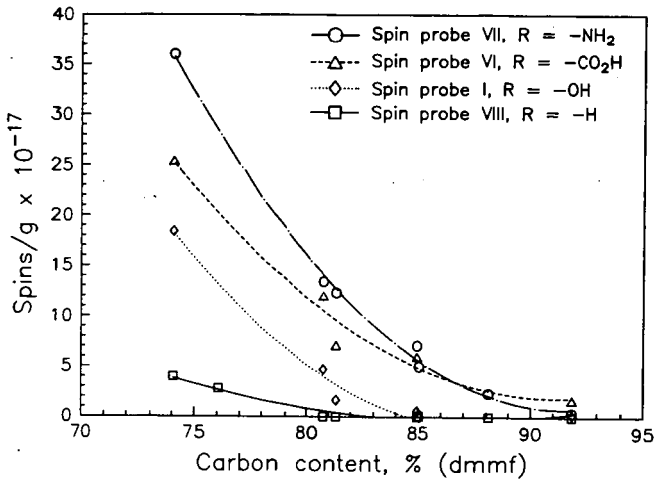

Figure 4. Effect of spin probe R group on spin probe retention in coal for coals swelled in toluene at 333 K. Spin probe VIII, R = -H, (□); spin probe I, R = -OH, (∧); spin probe VI, R = $-CO_2H$, (Δ); and spin probe VII (O)R = $-NH_2$; concentration (spins/g x 10^{-17}) vs. carbon content (%, dmmf).

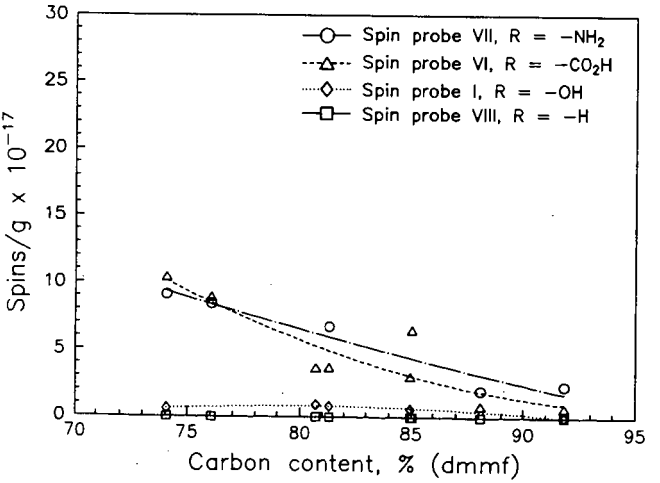

Figure 5. Effect of spin probe R group on spin probe retention in coal for coals swelled in pyridine at 333 K. Spin probe VIII, R = -H, □; spin probe I, R = -OH, (◊); spin probe VI, R = $-CO_2H$, (Δ); and spin probe VII(O)R = $-NH_2$; concentration (spins/g x 10^{-17}) vs. carbon content (%, dmmf).

VERY HIGH FREQUENCY EPR SPECTROSCOPY AND NMR IMAGING OF COAL

R. B. Clarkson, K. Motsegood, W. Wang, A. G. Webb, and R. L. Belford
Illinois EPR Research Center, University of Illinois, Urbana, IL 61801

Keywords: EPR, MRI, organic sulfur, solvent swelling

INTRODUCTION

Last year we began a program to develop and apply Very High Frequency Electron Paramagnetic Resonance (VHF EPR) to non-destructively analyze for organic sulfur molecular forms in coal and separated macerals. The starting point of our work was a preliminary observation that when EPR spectra of coal were taken on our newly constructed VHF spectrometer [1], signals related to organic sulfur were observable. These spectral features could only be resolved at high magnetic fields, and hence had gone undetected in all previous EPR studies of coal, although their presence had been inferred from indirect evidence [2]. Figure 1 clearly shows the resolution of sulfur-related features in an Illinois #6 whole coal at 96 GHz. We also began to develop magnetic resonance imaging techniques to non-destructively assess the effects of various solvents on coal, including the measurement of solvent swelling and solvent penetration. In this report we will discuss recent progress made in both of these areas.

VHF EPR ANALYSIS

What makes the discovery of sulfur-related peaks in the VHF EPR spectra of coal useful as well as interesting is the fact that spectra like that shown in Fig. 1 have the potential to be understood theoretically, thus allowing for the development of a technique which can be analytical for organic sulfur in coal. Furthermore, information from organic sulfur model compounds like dibenzothiophene and benzonaphthothiophene, shown in Figure 2, allow theory to be tested on ideal molecular systems with properties thought to be very similar to those of whole coal. We have developed chemical techniques to synthesize stable cation radical forms of such coal model sulfur compounds, utilizing either (i) boric acid glass matrix isolation followed by UV irradiation, or (ii) formation by electron transfer on catalytically active silica-alumina surfaces [3]. Spectra from compounds such as these form the basis of our interpretation of the more complex spectra obtained from coal.

Three examples will be given to illustrate some of the potential in the VHF EPR method, and the rationale of our approach. The first, shown in Figure 3, compares the VHF EPR spectra of vitrinite and sporinite macerals separated from an Illinois #6. Careful destructive chemical analysis suggests that the vitrinite contains 2.9% organic sulfur, while the sporinite contains 4.3%. Analysis of the VHF EPR spectra of these two samples on the basis of a two-species model, involving the summation of spectra from sulfur and non-sulfur containing species indicates almost identical sulfur levels as obtained by chemical analysis [4]. While the two-species model seems crude, it has proven to be quite useful in analyzing VHF EPR coal spectra, and may represent a reasonable generalization regarding the classes of organic molecular forms contributing to the spectral lineshape. We suggest that at 96 GHz, spin-orbit coupling between unpaired electrons and aromatic sulfur produces the downfield shifts which we resolve in spectra from high-sulfur coal; similar SO coupling effects from oxygen species produce shifts too small to be resolved at this frequency. In collaboration with Prof. Jack Freed (Cornell University), we have examined samples at 250 GHz, and there see lineshapes which may allow a more detailed analysis of

heteratom (S,O) effects.

Figure 4 compares two "before and after" samples in order to study the effects of two desulfurization methods on an Illinois #6. In Figure 4(a), the coal was subjected to extraction with perchloroethylene (PCE) at 120°C for 3.5 hours. As can be seen by inspection, very little changed in the VHF EPR spectra as a result of this treatment, suggesting that little organic sulfur (of the aromatic variety to which our method is believed to be sensitive) was removed, in agreement with D. H. Buchanan and co-workers, from whom the samples were obtained [5]. Figure 4(b) shows spectra of the Illinois #6 before and after low temperature (285°C) pyrolysis for two hours under vacuum conditions ($P < 10^{-5}$ Torr). The greatly reduced low-field peak ($g = 2.00434$) in the pyrolyzed coal suggests that this treatment significantly altered and removed aromatic organic sulfur, as has been reported by Kruse and Shimp [6]. We currently are employing VHF EPR to study the effects of low-temperature pyrolysis on coal structure, and have observed complex spectral changes which need to be understood before a complete interpretation of these effects can be made.

Figure 5. shows VHF EPR spectra of the two model compounds in Figure 2. One primary difference between DBT and BNT is that DBT contains 12 aromatic carbons, while BNT contains 16. As the figure illustrates, this difference of four atoms has a large effect on the spectral lineshape. One component of this sensitivity of lineshape to aromatic ring size is that the g-anisotropy brought about by spin-orbit interactions ($\lambda\ \mathbf{L} \cdot \mathbf{S}$) depends strongly on the unpaired electron spin density on sulfur. As aromatic ring size increases and the unpaired electron delocalizes over a larger carbon skeleton, density on sulfur decreases, resulting in diminished anisotropy, which agrees with the changes seen in the spectra of Fig. 5. We currently are studying a series of thiophenic compounds with varying aromatic ring sizes, in order to develop this theory further.

NMR IMAGING OF SOLVENTS IN COAL

Nuclear magnetic resonance imaging (MRI) can be used in a completely non-invasive way to visualize and measure the changes in pore size as coal is swollen with organic solvents. Preliminary experiments have been carried out using two separate radiofrequency and gradient coil configurations in order to determine the feasibility of studying solvent diffusion into coal samples. The imaging system used is the SISCO 200/330 imaging spectrometer system, located in the Biomedical Magnetic Resonance Laboratory at the University of Illinois/Urbana. This instrument operates at a field strength of 4.7T (ν(proton) = 200 MHz). The first approach used the system's 8 cm. inner diameter double saddle radiofrequency probe as the transmit and receive coil, with the system's magnetic field gradients being driven by Oxford gradient amplifiers to give a maximum gradient strength of 2 G/cm. Additional work now is being carried out using an imaging probe from Doty Scientific, consisting of a solenoidal radiofrequency probe of inner diameter 1.5 cm., and maximum gradient strength of 15 G/cm., when driven by three Techron power supplies.

Samples were obtained from the Illinois State Geological Survey. First, the coal sample was immersed in water, doped with manganese chloride, in order to reduce solvent proton T_1 to 400 msec, and allowed to soak for a week. MRI images then were taken. The water then was removed, and the sample was placed in acetone, doped with 10 mM chromium acetoacetonate (AcAc) in order to reduce solvent proton T_1 to 400 msec. After 48 hours of immersion, the sample was again imaged. Lastly, the acetone was removed, and the sample was immersed in DMSO, again doped with chromium AcAc. After another 48 hours of soaking, a third set of images were obtained.

Figure 6. shows a series of five images from a multislice data set obtained on a sample of Illinois #5 coal (Galatin County, IL), with dimensions of 19 x 19 x 38 mm. Since coal is not swollen by the water, these images define the outer surface of the pre-swollen coal, providing a

reference for subsequent swelling experiments. Each image represents a slice through the coal sample with an in-plane thickness of 1 mm. In plane spatial resolution is 500 microns.

Figure 7. shows the same coal sample after immersion in doped acetone. Some swelling and permeation of the solvent into the coal sample is clearly seen, although the covalent cross-linking in the coal is not yet being substantially broken. Figure 8. follows the same sample after 48 hours of immersion in doped DMSO. The images clearly show significant pore enlargement and swelling of the coal. It should be remembered that these images are internal views of the solid sample, permitting non-destructive analysis, and hence sequential solvent studies on the same piece of coal.

MRI results agree qualitatively with those obtained using methods where no spatial localization or visualization was possible. Estimates of the swelling ratio, Q, for our coal sample in DMSO and acetone, made from the images in Figs. 7 and 8, yield a value of 1.9. Szeliga and Marzec obtained a value of Q = 1.6 for these solvents in a similar coal [7]. These authors have shown that swelling and solvent electron-donor number (defined as the negative of the enthalpy change for the interaction of the solvent with $SbCl_5$ in a dilute solution of dichloroethane) show a reasonably strong correlation, and they discuss the solvents used in our MRI work. Brenner has shown that initial swelling is rapid, although weeks or even months may be necessary to reach equilibrium swelling [8]. He concluded that access of solvent to the sites where swelling is induced is highly variable: some pathways are accessible to the solvent molecules in seconds, others may take days. In the future, we hope to further develop MRI methods to follow these processes in greater detail.

ACKNOWLEDGEMENTS

Partial support for this work was provided by the U.S. Department of Energy (University Coal Research Program, DE-FG22-88PC88921), the Illinois Department of Energy and Natural Resources (Center for Research on Sulfur in Coal, SENR CRG91 CLARKSON), and the National Institutes of Health (RR 01811).

REFERENCES

1. R. B. Clarkson, W. Wang, M. J. Nilges, and R. L. Belford, in *Processing and Utilization of High-Sulfur Coals III*, R. Markuszewski and T. D. Wheelock, eds, Elsevier, Amsterdam, 1990, pp. 67 - 78.

2. H. L. Retcofsky, M. R. Hough, M. M. Maguire, and R. B. Clarkson, in *Coal Structure*, M. L. Gorbaty and K. Ouchi, eds., ACS Advances in Chemistry No. 192, 1981, 37 - 58.

3. R. B. Clarkson, R. L. Belford, K. S. Rothenberger, and H. C. Crookham, *J. Catalysis*, 1987, ***106***, 500.

4. R. B. Clarkson, W. Wang, D. R. Brown, H. C. Crookham, and R. L. Belford, *FUEL*, 1990, ***69***, 1405.

5. D. H. Buchanan, K. J. Coombs, C. Chaven, C. W. Kruse, and K. C. Hackley, in *Processing and Utilization of High-Sulfur Coals III*, R. Markuszewski and T. D. Wheelock, eds., Elsevier, Amsterdam, 1990, pp. 79 - 87.

6. C. W. Kruse and N. E. Shimp, in *Coal Processing Technology, v. VII*, AIChE., 1981, 124.

7. J. Szeliga and A. Marzec, *FUEL*, 1983, ***62***, 1229.

8. D. Brenner, Am. Chem. Soc. Div. Fuel Chem. Preprints, 1982, ***27***, 244.

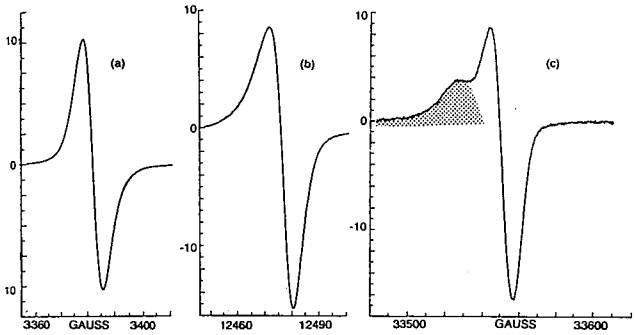

Figure 1. First evidence that VHF EPR can resolve sulfur-related spectral features in coal. (a) 9.5 GHz, (b) 35 GHz, (c) 96 GHz. Shaded area is the sulfur-related region.

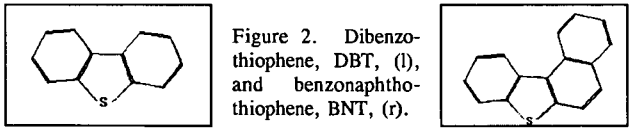

Figure 2. Dibenzothiophene, DBT, (l), and benzonaphthothiophene, BNT, (r).

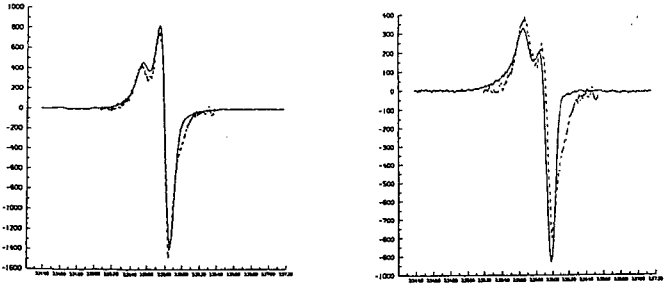

Figure 3. (a) Vitrinite, 2.9% organic S; (b) Sporinite, 4.3% organic S.

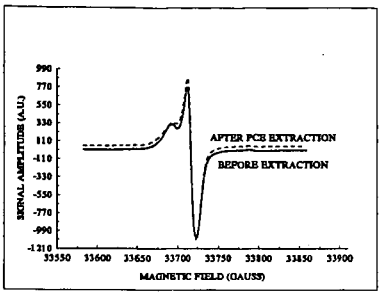

Figure 4(a). VHF EPR spectra of an Illinois #6 before (___) and after (---) PCE extraction.

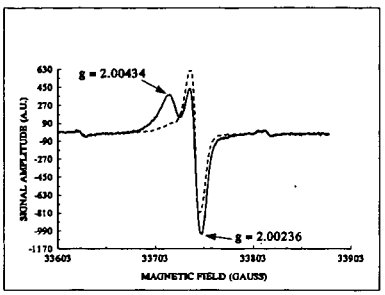

Figure 4(b). Illinois #6 coal before (___) and after (---) low temperature pyrolysis.

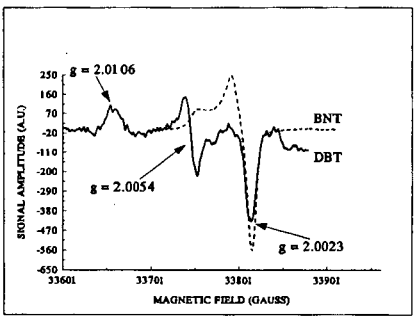

Figure 5. VHF EPR (ca. 96 GHz) spectra of DBT+ and BNT+ in boric acid glass.

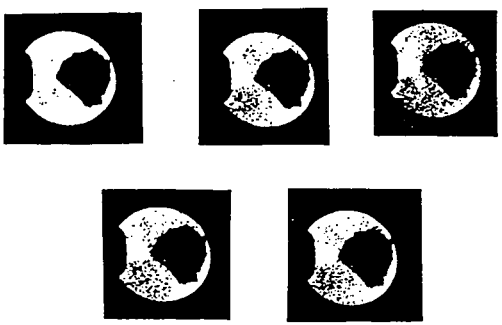

Figure 6. MRI images corresponding to five 1 mm. thick slices through an Illinois #5. Since water does not swell coal, this experiment defines the outer surface of the coal sample.

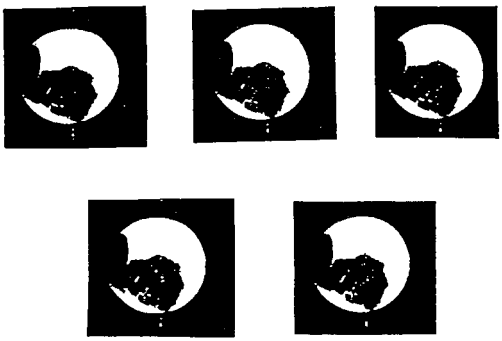

Figure 7. Same sample as in Fig. 6, but with acetone now as the solvent. A small degree of diffusion and swelling is observed.

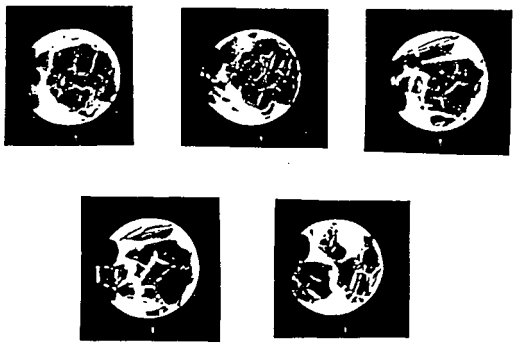

Figure 8. Same sample, now with DMSO as the solvent. Pore enlargement and swelling are now clearly visible.

NMR IMAGING: A 'CHEMICAL' MICROSCOPE FOR COAL ANALYSIS

D. C. French, S. L. Dieckmant, N. Gopalsamit, and R. E. Botto
Chemistry Division and †Materials and Components Technology Division
Argonne National Laboratory
9700 So. Cass Avenue
Argonne, IL 60439

Keywords: NMR, Imaging, Coal

ABSTRACT

This paper presents a new three-dimensional (3-D) nuclear magnetic resonance (NMR) imaging technique for spatially mapping proton distributions in whole coals and solvent-swollen coal samples. The technique is based on a 3-D back-projection protocol for data acquisition, and a reconstruction technique based on 3-D Radon transform inversion. In principle, the 3-D methodology provides higher spatial resolution of solid materials than is possible with conventional slice-selection protocols. The applicability of 3-D NMR imaging has been demonstrated by mapping the maceral phases in Utah Blind Canyon (APCS #6) coal and the distribution of mobile phases in Utah coal swollen with deuterated and protic pyridine.

INTRODUCTION

Coals are comprised of microscopically discernible regions (termed macerals) corresponding to different plant materials that have been geologically altered over time.[1] These discrete regions are known to exhibit widely different chemical behavior, thereby complicating coal processing technologies for the production of usable, high quality fuels and chemicals.

NMR imaging is sensitive to local chemical environments in complex molecular solids. Moreover, the technique has the unique capability of spatially mapping a sample's chemical or physical properties independently. Two-dimensional NMR imaging has proven to be a promising tool for the characterization of macerals in a dried specimen of Utah Blind Canyon coal.[2] However, a major difficulty in obtaining adequate spatial resolution in the third dimension rests with the intrinsic NMR properties, i.e., broad line widths, that are characteristic of many solids.

In this paper, we describe a 3-D NMR method that is based on a back-projection protocol in combination with image reconstruction techniques based on 3-D Radon transform inversion. Similar techniques have been described previously for imaging of liquid samples.[3,4] The method incorporates the experimental flexibility to overcome the difficulties which are presented by broad-line materials.

EXPERIMENTAL METHODS

The NMR imaging system used in this study consisted of a Bruker CXP-100 NMR spectrometer fitted with a home-built imaging accessory which is described in detail elsewhere.[5] The accessory, designed specifically for examining solid materials, consists of a versatile home-built IBM-PC based pulse programmer, three (X,Y,Z) Techron audio range 1-kW gradient amplifiers, a RF shaping unit, and a home-built, singly-tuned imaging probe capable of operating at 1-kW RF levels. The probe also contains forced-air-cooled gradient coils capable of operating with duty cycles in excess of 20% while producing a higher linear magnetic field gradient of 58 G/cm over a spherical space of 30 mm in diameter.

In a conventional 2-D NMR back-projection tomographic experiment, one applies a linear magnetic field gradient in a plane at numerous projection angles. For each angle, the Fourier transform of the data represents a planar integral of the proton density normal to the gradient vector. Similarly, in the 3-D back-projection experiment, by varying the gradient vector in order to sample the entire 3-D space, one obtains a 3-D Radon transform of the proton density. Let Rf(P) be the Radon transform of the object function f(M), where P and M are discrete points in the Radon and object space, respectively (Fig. 1).

$$Rf(P) = \int_{(OP.OM)=0} f(M)dM \qquad (1)$$

The inversion of this transform can be obtained by double differentiation and back projection. Marr et al.[6] have shown that the fastest way to invert the Radon transform is to use two sets of back projections, one along the meridian planes and the other along planes of constant latitude. The inversion can then be written as (Fig. 2):

$$f(M) = \frac{1}{4\pi}\int_{\theta=0}^{\theta=\pi}\int_{\phi=0}^{\phi=\pi}\frac{\partial^2 Rf}{\partial\rho^2}(\rho(M,\theta,\phi),\theta,\phi)sin\theta d\theta d\phi \qquad (2)$$

where ρ, θ, ϕ are the classical parameters of spherical coordinates, and $\rho(M,\theta,\phi) = OM \cdot n$, where O is the origin and n is the unit vector in the direction (θ,ϕ). The reconstruction algorithm of the 3-D Radon transform inversion was implemented as proposed by Grangeat and coworkers.[7]

Three-dimensional NMR imaging data were acquired on specimens using 128 complex data points, and a total of 3600 projections (30 θ angles over $\pi/2$ radians x 120 ϕ angles over 2π radians). A gradient strength of 25 G/cm and a sweep width of 200 kHz were used. A total of 64 averages were acquired by using an approximate 90° pulse and a recycle delay time of 0.25 s. A spectroscopic resolution of 80_x x 80_y x 80_z μm^3 was achieved. A total of 9 hours was required for data acquisition using these parameters.

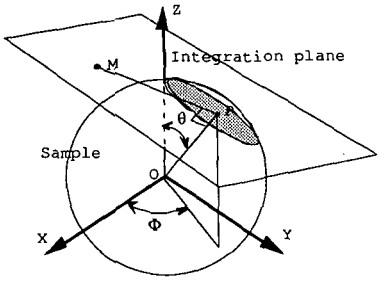

Fig. 1. Definition of 3-D Radon transform. Value of 3-D Radon transform in P is the integral of points M in plane defined by OP⊥MP.

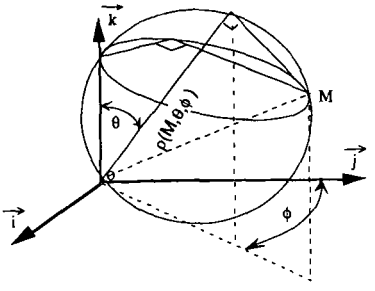

Fig. 2. Decomposition of integral over a sphere in two series of back-projections.

RESULTS AND DISCUSSION

In an earlier study, we had demonstrated the use of multi-pulse proton decoupling and back-projection reconstruction imaging methods to spatially resolve macroscopic resinite and vitrinite regions within a dried sample of Utah Blind Canyon coal.[2] Image contrast between the maceral phases was achieved on the basis of differences in proton density or spin-lattice relaxation (T_1). In the present study, we focus on the effects of solvent penetration to the swelling behavior of Utah coal.

The proton NMR spectrum of a specimen of Utah Blind Canyon coal swollen with "100%" deuterated pyridine is shown in Fig. 3. The spectrum displays three distinct proton resonances: there is a broad resonance (ca. 27 kHz) that corresponds to rigid protons in the sample, and there are two relatively narrow resonances (see expanded region at upper right) that correspond to aromatic and aliphatic protons in mobile environments. Line simulation subspectra were calculated from the experimental data by using a Pascal line simulation program on the Aspect 3000 computer as shown in Fig. 3. Analysis of the broad and narrow components indicates that approximately 14% of the protons are in the mobile phase. The fraction aromaticity (f_a^H) of protons in this mobile phase is calculated from line simulation as 0.45, compared with a value of 0.24 obtained from proton CRAMPS analysis of the dried coal. Because residual protons of the deuterated pyridine are expected to contribute less than 0.1% of the total proton signal, one can conclude that pyridine mobilizes highly aromatic regions within Utah coal preferentially.

A 3-D surface-rendered NMR image of the Utah coal specimen swollen with deuterated pyridine is shown in Fig. 4. The image was recorded with a short recycle-delay time in order to suppress signal from the broad "solid" component having a longer T_1. Thus, the image displays the proton distribution of mobile phases within the coal specimen preferentially. Surface rendering is performed by applying a user-adjusted threshold intensity to define a minimum intensity that is used to calculate the contiguous surface. The particular threshold employed was chosen to give the most accurate representation of the sample topology while suppressing low signal-to-noise structures near the sample surface. The image displayed is a good representation of the topology of the coal specimen; however,

it should be realized that surface features seen in the image represent areas with more or less density of mobile protons. For example, the feature seen at the front left of the object (indicated by arrow) is a crack in the specimen resulting from swelling with pyridine. Other features on the surface may be due to regions where there is a higher density of solid phase.

An 80-micron thin section (slice) of the 3-D NMR reconstructed image taken as a horizontal plane near the center of the specimen is shown in Fig. 5. Areas of bright intensity represent highly mobile regions within the specimen. Low intensity regions indicate solid phases or voids within the coal. The crack is clearly visible at the lower right portion of the image (indicated by arrow).

SUMMARY

We have demonstrated the feasibility of performing microtomographic NMR imaging on solid materials in three spatial dimensions. Methods were developed which combined 3-D back-projection protocol with image reconstruction using a Radon transform inversion technique. Using this methodology, we were able to spatially map maceral phases within a solid Utah coal specimen and monitor the distribution of mobile phases created upon swelling the specimen with pyridine.

ACKNOWLEDGMENTS

This work was performed under the auspices of the Office of Basic Energy Sciences, Division of Chemical Sciences, U.S. Department of Energy, under contract number W-31-109-ENG-38, and by the U.S. Department of Energy, Assistant Secretary for Conservation and Renewable Energy, Office of Transportation Systems, as part of the Ceramic Technology for Advanced Heat Engines Project of the Advanced Materials Development Program, contract number ACK-85234.

REFERENCES

1. *Chemistry and Characterization of Coal Macerals*; Winans, R.E. and Crelling, J.C., Eds.; ACS Symposium Series 252, American Chemical Society: Washington, D.C., 1984.
2. Dieckman, S.L.; Gopalsami, N; Botto, R.E. *Energy and Fuels* **1990**, *4*, 417.
3. Lauterbur, P.C.; Lai, C.-M. *IEEE Trans.* **1980**, *27*, 1227.
4. Lai, C.-M.; Lauterbur, P.C. *J. Phys. E.* **1980**, *13*, 747.
5. Gopalsami, N.; Foster, G.A.; Dieckman, S.L.; Ellingson, W.A.; Botto, R.E. *Development of NMR Imaging Probes for Advanced Ceramics*, Rev. Prog. in QNDE, Thompson, D.O. and Climenti, D.E., Eds.; Plenum Press, 1990.
6. Marr, R.B.; Chen. C.; Lauterbur, P.C. In *Aspects of Computerized Tomography*; Herman, G.T. and Natterer, F., Eds.; Springer-Verlag, 1980.
7. Grangeat, P.; Hatchadourian, G.; Le Masson, P.; Sire, P. *Logiciel Radon, Notice Descriptive Des Algorithmes Et Des Programmes*; Version 2.1 du 13-04-1990, LETI/DSYS/SETI/90-180 PS, Grenoble, 1990.

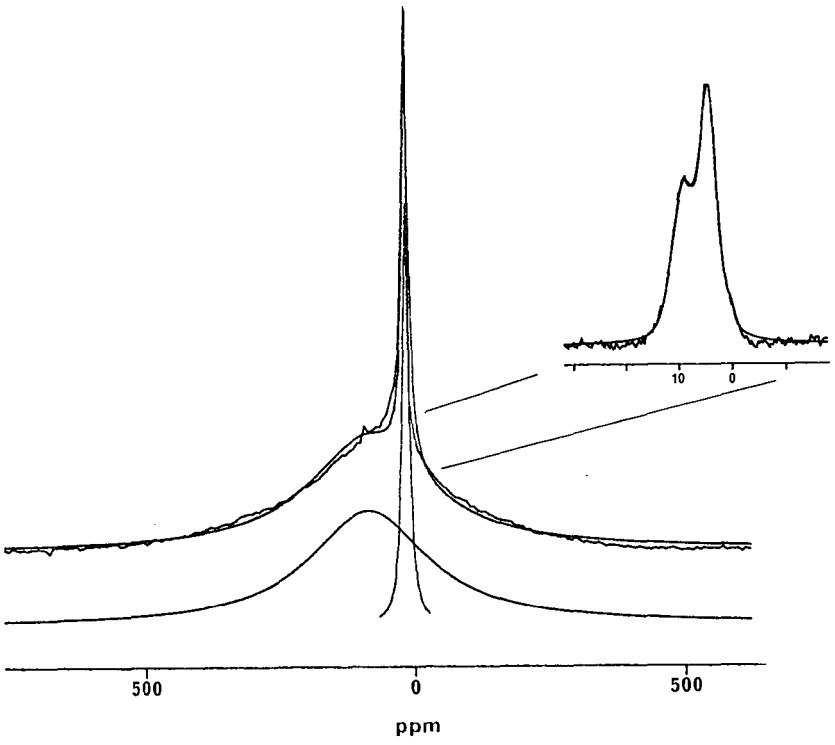

Fig. 3. Proton NMR spectrum of Utah Blind Canyon (APCS #6) coal specimen swollen with "100%" deuterated pyridine. Expanded plot at upper right displays narrow resonances with baseline correction applied.

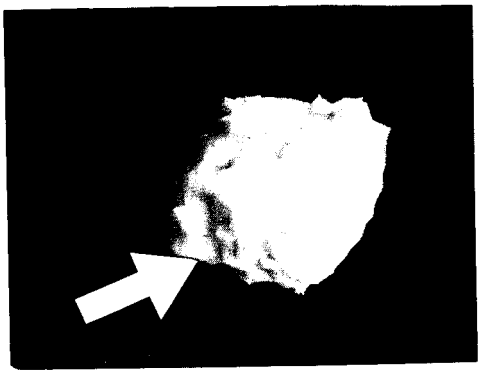

Fig. 4. Surface reconstructed 3-D NMR image of Utah Blind Canyon (APCS #6) coal specimen swollen with deuterated pyridine.

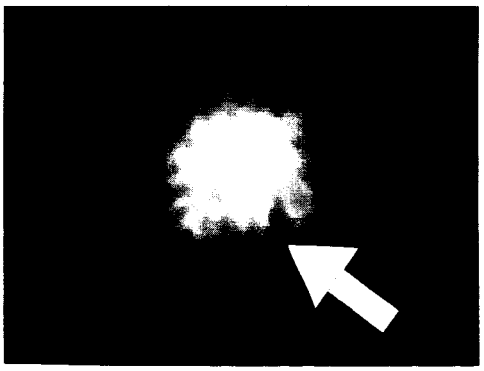

Fig. 5. Internal 2-D thin section of 3-D NMR reconstructed image of Utah coal specimen as shown in Fig. 4.

CHARACTERIZATION OF DELAYED COKING FEEDSTOCKS AND PRODUCTS BY ^{1}H AND ^{13}C NMR

Joaquin Rodriguez, John W. Tierney and Irving Wender
Chemical & Petroleum Engineering Department
University of Pittsburgh, Pittsburgh PA 15261

Keywords: Delayed coking, NMR spectroscopy, petroleum residues

ABSTRACT

^{1}H and ^{13}C nuclear magnetic resonance spectroscopy has been systematically applied to the characterization of delayed coking feedstocks (petroleum residues) as well as liquid products (naphtha, distillate, oils) and solid products (coke) to evaluate the type and extent of the cracking, polymerization and condensation reactions taking place. NMR results, combined with gas chromatography, elemental analysis and pilot plant data, yield mass balances at the atom-type level. A substantial increase in aromatic type carbons (40 wt%) occurs (for a particular feedstock), primarily at the expense of naphthenic type carbons (35 wt%), and is accompanied by a significant reduction in the number of protons attached to aromatic carbons (80 wt%). This methodology can be used to measure the severity of delayed coking and to estimate product yields and compositions.

INTRODUCTION

Delayed coking is the most widely used process for the conversion of petroleum residues[1]. Residues are pumped through a coker heater, where the temperature is raised to 450-500 ° C in a short period of time, and then fed into one of two coke drums (adiabatic reactors). Cracking, polymerization and condensation reactions, initiated in the heater, proceed forming vapors (gases, naphtha, oils) that leave the reactor and are sent to a fractionation tower. A highly viscous carbonaceous material remains in the drum and finally is transformed into a solid product (coke) which can be used (depending upon specifications) as fuel or as filler for the production of carbon anodes (aluminum industry) or arc-electric furnace electrodes (steel industry)[1,2].

Delayed coking feedstocks (vacuum and conversion petroleum residues) contain mainly aromatic hydrocarbons with aliphatic substituents, paraffins, naphthenic compounds and heteroatoms (mostly in heterocyclic compounds). The aromatic components are the network members of the final coke structure: higher aromatic contents give more extended aromatic arrangements and consequently better coke quality due to more ordered domains of oriented molecules[3]. On the other hand, reactivity of these feedstocks is related to the number of substituents attached to the aromatic compounds: high aromaticity with only a few substitutents (coal tar pitches) corresponds to low reactivity and moderate aromaticity with many substituents (vacuum residues) to high reactivity. A balance is desired for optimum carbonization[4].

Nuclear magnetic resonance (^{1}H and ^{13}C NMR) is a powerful technique to evaluate delayed coking feedstocks and the corresponding carbonization process, due to its ability to elucidate basic constituents present in these materials. ^{13}C NMR provides direct measurement of the types of carbon atoms which determine the pyrolysis chemistry[5]. Quantitative information is obtained by integrating line intensities. These are proportional to the number of carbon atoms of each type[6]. With additional information from ^{1}H

NMR, average molecular parameters can be derived, and even structural configurations can be drawn (only useful as illustrative tools because these materials embrace a large range of organic molecules as indicated by the broad molecular weight spectra). This constitutes a sound basis for understanding carbonization mechanisms and for comparing different delayed coking feedstocks.

EXPERIMENTAL

Delayed coking products were obtained in a thermal conversion pilot plant with a 4 lt. reactor capacity operating in continuous up-flow mode at 1500-2000 g/h, 60-140 psig and internal temperature profiles between 400-500 ° C. Gas product was monitored by gas chromatography every 20 minutes and the weighted average reported. Liquid product collected during operation was characterized and later distilled in consecutive ASTM D-86 and D-1160 assays to yield four fractions: naphtha (IBP-400 F), distillate (400-650 F), light oil (650-800 F) and heavy oil (800 F+). Coke was recovered after cooling the reactor.

NMR spectra were collected in a Bruker 300 MSL spectrometer. Liquid ^{13}C NMR spectra were obtained at 75.468 MHz in a 10 mm probe, using a gated program with decoupler on during acquisition and off during the rest of the experiment to suppress the Nuclear Overhauser Effect. Relaxation times of 5 to 10 seconds were used, 45 pulse angle (corresponding to 5 μs pulse time) and 31 μs for dead time delay. Resolutions of about 1.3 Hz were achieved with receiver gains of 10-30. Liquid ^{1}H NMR spectra were obtained at 300 MHz in a 5 mm probe with repeated pulses of 6.1 μs. Band assignments for integrating atomic groups were selected from the extended consensus in the field (reference to TMS standard)[5,7-8]:

	^{13}C NMR		^{1}H NMR	
Aromatics	110-160 ppm	Aromatics	6.5 -9.0	ppm
-protonated	110-130 ppm	-single ring	6.5 -7.25	ppm
-quaternary	130-160 ppm	-multi. ring	7.25-9.0	ppm
Aliphatics	5- 60 ppm	Aliphatics	0.5 -4.0	ppm
-paraffinics	5- 25 ppm +	-terminal CH_3	0.5 -1.0	ppm
	25- 60 ppm peaks	-internal	1.0 -1.8	ppm
-naphthenic	25- 60 ppm envelope	-α aromatic C	1.8 -3.8	ppm
Olefinic	80-100 ppm	Olefinic	4.5 -6.3	ppm

Gas chromatography data were converted to a similar atom type distribution. Solid state MAS $^{13}C/^{1}H$ cross-polarization spectra (for cokes)[9-10] were obtained at 75.473 MHz and 3500-4000 rpm spinning rates with a proton enhanced pulse program (PENMR).

RESULTS AND DISCUSION

Pilot plant data include the distribution of product yields and basic characteristics of feedstocks and products (Table 1). ^{1}H and ^{13}C NMR spectra for feedstocks and liquid products are presented in Figures 1-6.

A solid state NMR spectrum for coke is presented in Figure 7. It shows an aromatic carbons peak at the center (100-150 ppm) and two pairs of side-bands. This indicates that only quaternary aromatic carbons and protonated aromatic carbons (that have been calculated to match C/H ratios) are present.

NMR data have been integrated into a weighted distribution (Table 2) and is

compared with the feedstock analysis (Table 3) to determine the differences and to calculate changes (defined by Difference*100/Feedstock).

It is observed that a significant increase in aromatic carbons (39.4 wt%) occurs, mainly at the expense of a reduction in the naphthenic carbons (-35.0 wt%) with small changes in protonated aromatic carbons (8.5 wt%) and paraffinic carbons (-3.8 wt%). This can be interpreted to mean that the main polymerization/condensation mechanism involves aromatization of naphthenic rings attached to aromatic rings (in this case probably in a 1/1 ratio).

Also, the substantial reduction in protons attached to aromatic carbons (mainly in multiple ring systems) suggests that the carbonization reactions in the liquid phase (leading to coke formation) proceed through benzyl type radicals, while in the vapor phase, cracking reactions substantially reduce the size of the molecules, bringing complex high boiling compounds (present in the feedstock) down to lighter molecules (gas, naphtha, oils).

CONCLUSIONS

A systematic application of ^{13}C and ^{1}H NMR analysis to delayed coking feedstocks and products results in a quantitative evaluation of the polymerization/condensation reactions and can be used as a measurement of the severity of the process and to estimate product composition.

BIBLIOGRAPHY

1. **Feintuch, H.M. et al.**, in Handbook of petroleum refining, R.A. Meyer (ed), pp. 3-61 (1986).
2. **De Biase, R. et al.**, in Petroelum Derived Carbons, ACS, pp. 155-171 (1986).
3. **Winter, L.L.**, Kirk-Othmer Enc. Chem. Tech., pp.570-576 (1978).
4. **Mochida, I. et al.**, Oil Gas J. 86(18):73-77 (1988).
5. **Seshadri, K.S. et al**, Fuel, 61(4):336-340 (1982).
6. **Gillet, S. et al.**, Fuel, 60(3):221-225 (1981).
7. **Cookson, D.J. and Smith, B.E.**, in Coal Science and Chemistry, A. Volborth (ed), pp. 31-60 (1987).
8. **Yamashita, G.T. et al.**, Preprints ACS Div. Petroleum Chem., 34, (2) 301-305 (1989).
9. **Nakamizo, M. and Adacchi, Y.**, 19th Bienn. Conf. Carbon, pp. 148-149 (1989).
10. **Hinckley, C.C. et al.**, SIU Carbondale, Sixth Ann. Conf. Mater. Techn. Center, pp. 14-31 (1990).

ACKNOWLEDGEMENTS

This work has been financially supported by INTEVEP S.A. (R&D Center of Petroleos de Venezuela). Special thanks are due to Mr. Carlos Mota, project leader. Also we appreciate the assistance of Dr. Lurie Galya and Dr. George Marcelin in the operation of the NMR instrument.

Table 1. Delayed coking pilot plant data

Material	Yield wt%	Boiling range, ° F	API gravity	Impurities wt%
Feedstock	-	350-600	14.6	3.03
Gases	10.31	-	-	0.22
Naphtha	24.66	IBP-400	57.9	0.25
Distillate	26.57	400-650	30.2	1.88
Light Oil	12.33	650-800	15.3	3.24
Heavy Oil	7.84	800+	4.6	3.88
Coke	18.28	-	-	4.47

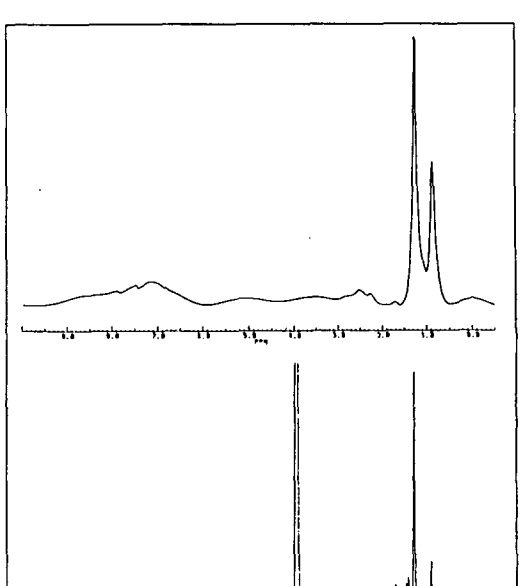

Figure 1. ^{1}H and ^{13}C NMR spectra of a delayed coking feedstock

Table 2. Distribution of proton and carbon atoms in delayed coking products

Atom type wt%	Gas wt%	Naphtha wt%	Distillate wt%	Light Oil wt%	Heavy Oil wt%	Coke
CARBON	8.12	21.54	23.01	10.67	6.80	17.28
Aromatic	0.00	4.27	6.14	4.18	3.26	17.28
-protonated	0.00	2.13	2.95	2.10	1.73	2.16
-quaternary	0.00	2.14	3.20	2.07	1.53	15.12
Aliphatic	7.64	17.28	16.87	6.50	3.55	0.00
-paraffinic	7.64	13.83	10.14	4.03	2.36	0.00
-naphthenic	0.00	3.45	6.72	2.47	1.19	0.00
Olefinic	0.48	0.00	0.00	0.00	0.00	0.00
PROTON	1.98	3.06	3.06	1.26	0.74	0.18
Aromatic	0.00	0.12	0.17	0.19	0.13	0.18
-single	0.00	0.07	0.11	0.06	0.03	0.00
-multiple	0.00	0.05	0.07	0.13	0.10	0.18
Aliphatic	1.88	2.83	2.83	1.04	0.59	0.00
-terminal	1.58	1.15	0.84	0.24	0.12	0.00
-internal	0.31	1.47	1.57	0.58	0.34	0.00
-α arom. C	0.00	0.20	0.41	0.22	0.13	0.00
Olefinic	0.06	0.11	0.06	0.03	0.01	0.00

Table 3. Atom type balances in delayed coking reactions

Atom type	Feed wt%	Products wt%	Difference wt%	Change %
CARBON	85.99	87.43	+ 1.44	+ 1.68
Aromatic	25.19	35.13	+ 9.93	+39.42
-protonated	10.20	11.07	+ 0.87	+ 8.53
-quaternary	15.00	24.06	+ 9.06	+60.40
Aliphatic	60.79	51.82	- 8.97	-14.76
-paraffinic	39.50	37.99	- 1.51	- 3.82
-naphthenic	21.29	13.83	- 7.46	-35.04
Olefinic	0.00	0.48	+ 0.48	+
PROTON	10.98	10.26	- 0.72	- 6.56
Aromatic	3.89	0.80	- 3.09	-79.52
-single	1.11	0.27	- 0.84	-75.85
-multiple	2.78	0.53	- 2.25	-80.98
Aliphatic	7.09	9.17	+ 2.07	+29.21
-terminal	2.14	3.93	+ 1.79	+83.52
-internal	4.37	4.27	- 0.10	- 2.22
-α arom. C	0.58	0.96	+ 0.38	+65.37
Olefinic	0.00	0.27	+ 0.27	+
H2	-	0.03	+ 0.03	+

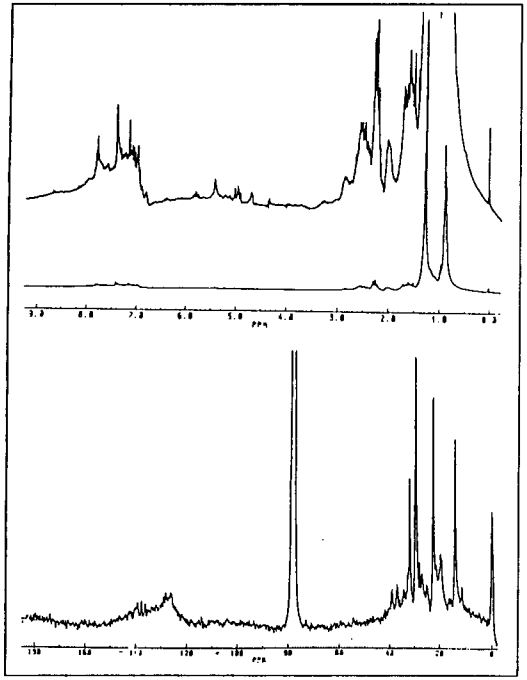

Figure 2. ^{1}H and ^{13}C NMR spectra of a delayed coking liquid product

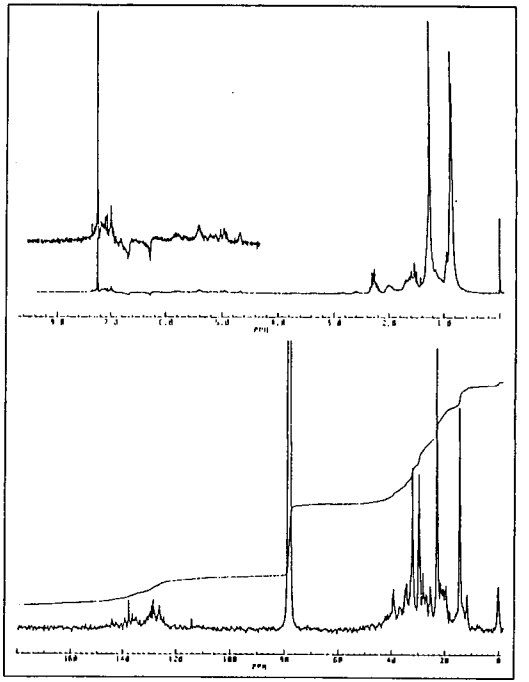

Figure 3. ^{1}H and ^{13}C NMR spectra of a delayed coking naphtha

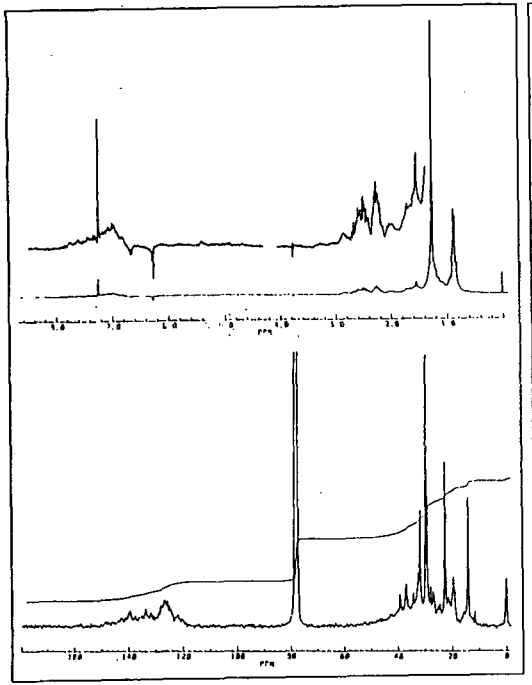

Figure 4. ^{1}H and ^{13}C NMR spectra of a delayed coking distillate

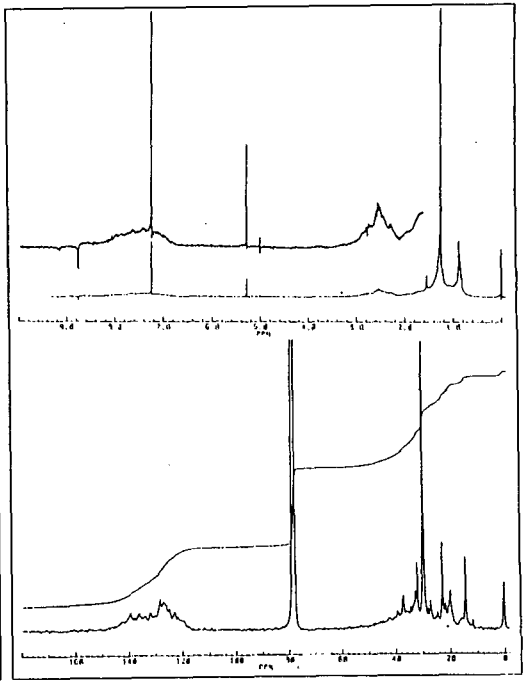

Figure 5. ^{1}H and ^{13}C NMR spectra of a delayed coking light oil

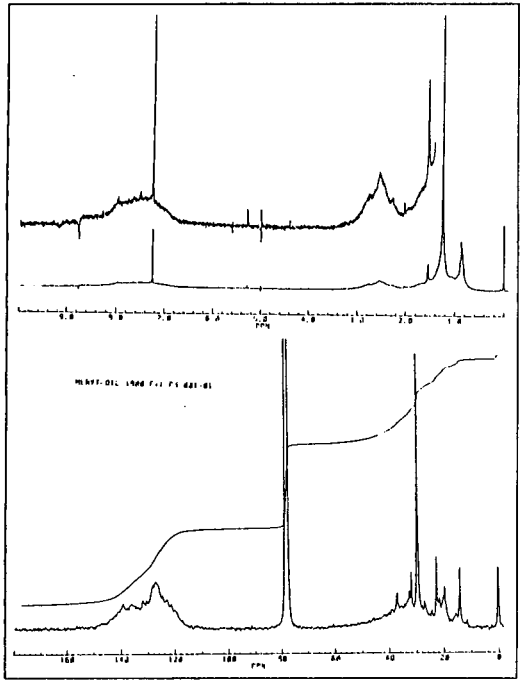

Figure 6. ^{1}H and ^{13}C NMR spectra of a delayed coking heavy oil

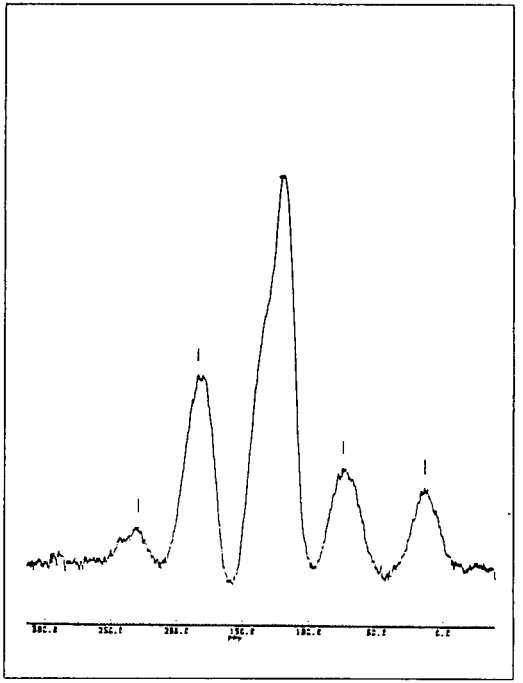

Figure 7. $^{13}C/^{1}H$ crosspolarized MAS solid NMR spectrum of a petroleum coke

THE DETERMINATION OF LOCAL STRUCTURE IN ORGANOFLUORIDES USING FLUORINE-19 CARBON-13 DIPOLAR COUPLING

Edward W. Hagaman
Chemistry Division, Oak Ridge National Laboratory
Oak Ridge, Tennessee 37831

Keywords: Solid State NMR, ^{19}F-^{13}C Dipolar Coupling, Fluorinated Coal

INTRODUCTION

A facet of our research has been directed toward the elucidation of "reactive sites" in the organic milieu of coals. The conceptual framework for these experiments is the chemical introduction of a unique, NMR active nucleus at or adjacent to a reactive site in the coal network and the subsequent utilization of this nucleus to extract site specific structural information by solid state ^{13}C NMR spectroscopy. Fluorine-19 and phosphorus-31 nuclei are good NMR choices, having large magnetic moments, 100 % natural abundance, and spin 1/2. The absence of a quadrupole moment translates into narrow, well-resolved spectral resonances. Both are suitable in applications to coal derivatization, having small natural concentrations in the organic matrix of most coals.[1] Fluorine is attractive from the standpoint of chemical manipulation of coals in that a large and increasing number of fluorinating reagents are available to specifically incorporate fluorine into organic substances. It should be possible to label diverse sites in the coal by a judicious choice of fluorinating reagent and reaction conditions.

The use of an introduced magnetic nucleus in an organic environment as a probe of local structure utilizes in some fashion the dipolar interaction between the probe nucleus and proximate ^{13}C nuclei to selectively observe the interactive carbons. Since ^{13}C is dilute by virtue of low natural abundance, these dipolar couplings are often isolated spin pair interactions. Two experiments that selectively detect carbons dipolar coupled to a probe nucleus are cross polarization between the nuclear pair, and dephasing of ^{13}C magnetization by interference with rotational echo formation. The first class of experiments are known as double cross polarization (DCP) NMR[2,3]; the second as rotational-echo double resonance (REDOR) NMR[4]. This paper reports experiments that demonstrate the REDOR experiment is ineffective when applied to the ^{19}F-^{13}C nuclear pair in models of molecular weight < 300. A new experiment that uses the cause for the REDOR failure, ^{19}F spin diffusion, is used to regain site specific structural information encoded by the ^{19}F-^{13}C dipolar coupling.

RESULTS AND DISCUSSION

We have examined the perturbation of the conventional CP/MAS ^{13}C NMR spectrum of organic substances due to the incorporation of a of a single ^{19}F atom in the structure. In molecules in which the

fluorine atom undergoes little motion in the solid, e.g., as in 16α-fluoroestrone-3-methyl ether, (1), the carbon directly bonded to fluorine has a resonance so broad (> 2500 Hz) that it is not observed in the spectrum. In molecules that exhibit motion in the crystal that modulates the ^{19}F-^{13}C dipolar interaction, as in ortho-fluorophenylglycine, the ^{19}F-^{13}C dipolar coupling is partially averaged by the motion and the directly fluorinated carbon is observed. In this case the resonance is narrowed enough that the J-coupling (250 Hz) between the directly bonded pair is apparent in the conventional spectrum. Longer range ^{19}F-^{13}C dipolar interactions result in a graded, r^{-3} internuclear distance dependent broadening of near neighbor carbon resonances in the spectrum. Simultaneous ^{1}H and ^{19}F high power decoupling applied during the free induction decay acquisition time efficiently eliminates heteronuclear dipolar coupling from the spectrum. This triple resonance capability is required to obtain high quality CP/MAS ^{13}C NMR spectra on organofluorides obtained at routine (< 5 kHz) MAS speeds.

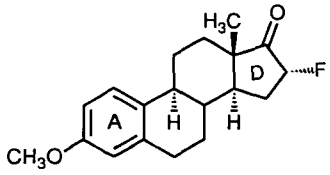

1

The spectral response described above may not be anticipated on first glance since the dipolar interaction between two spin 1/2 nuclei has the form $(r^{-3})(3\cos^2\theta-1)$ and should be averaged to zero by MAS. However, MAS is successful only when the rotation rate is large in comparison to the dipolar interaction linewidth. The maximum dipolar linewidth, $2D_{CF}$, for a directly bonded pair is about 26 kHz, the consequence of the large magnetic moment of F19 and short C-F bond distance ($r \approx 0.13$ nm). In this instance the actual 4.2 kHz spinning used in these experiments is ineffective. This MAS speed is just comparable to typical ^{19}F-^{13}C dipolar linewidths for atoms separated by two bonds ($r \approx 0.23$ nm, $D_{CF} \approx 4.5$ kHz). In the absence of ^{19}F dipolar decoupling, these resonances have a ca. 50 Hz residual linewidth contribution due to incomplete averaging of the dipolar interaction by MAS.

The REDOR experiment requires that the dipolar coupled spin pair (^{19}F-^{13}C in the present case) in a system be isolated. If so, the time average of the resonance frequencies over one MAS rotor period is zero, i.e., full recovery of signal intensity occurs after each rotor cycle, producing a train of rotational echoes. REDOR uses π pulses applied to the probe nucleus (^{19}F) to intentionally cause echo destruction of those ^{13}C resonances dipolar coupled to ^{19}F. These are detected in a difference experiment. In 1, for example,

the anticipated REDOR difference spectrum would contain only ring D carbon resonances with intensities that reflect an r^{-3} distance dependence. The placement of π pulses and signal acquisition are timed to rotor position; REDOR signals can be accrued over even, integral multiples of the rotor cycle.[5]

Attempts to perform REDOR on **1** and smaller molecules has met with marginal success in our laboratory. Initial REDOR difference signal intensities in 3-fluoro-4-methoxybenzoic acid (evolution for two rotor cycles) do not exhibit the expected intensity ratios based on ^{19}F-^{13}C internuclear distance. The resonances of C(2) and C(4) have greater integrated areas than the fluorinated carbon resonance, C(3). Continued evolution (4-20 rotor cycles) yields a strong selective attenuation of the REDOR signal set. We have shown in separate ^{13}C T_2 experiments, with and without ^{19}F decoupling, that the signal decay is governed by the ^{19}F T_2. In effect, ^{19}F intermolecular spin diffusion provides a dephasing mechanism for coupled ^{13}C nuclei that competes with the experimentally imposed π pulses of REDOR, violating the isolated pair precondition in this experiment. This failure mode has been observed in ^{15}N-^{13}C REDOR experiments in which spin diffusion among ^{13}C nuclei defeat the REDOR difference signal.[6]

For isolated spin pairs, REDOR accesses the dipolar interaction between the pairs, and, hence, is a direct method to obtain structural information. This experiment will work for the ^{19}F-^{13}C pair in high molecular weight molecules where ^{19}F spin diffusion is suppressed by large internuclear distances. The applicability of this experiment in coal structure analysis is great for chemical derivatizations that introduce low concentrations of fluorine into the material. For more highly fluorinated coals, an new experiment has been created that uses the dipolar interaction to provide site selective structural information. The experiment accrues the difference signal between spectra that measure C13 T_2 over even integral multiples of the rotor period (to allow refocussing of ^{13}C chemical shift anisotropy), with alternate scans employing ^{19}F heteronuclear decoupling during the rotor evolution period. Signals arise from those carbons that show differences in T_2 arising from ^{19}F-^{13}C dipolar dephasing mediated by the ^{19}F spin diffusion. Carbon signal intensities in this T_2 difference map do not provide a direct measure of ^{19}F-^{13}C dipolar coupling. The structural information that can be gleaned from this and related experiments is under current investigation. Further studies are planned to delineate ^{19}F internuclear distance boundaries that are appropriate for these experiments.

ACKNOWLEDGEMENTS

This research was sponsored by the Division of Chemical Sciences, Office of Basic Energy Sciences, U. S. Department of Energy under contract DE-AC05-840R21400 with Martin Marietta Energy Systems, Inc.

REFERENCES
1. Hagaman, E. W. Energy & Fuels **1988**, 2, 861-862.

2. For C13-N15 cross polarization: (a) Schaefer, J.; McKay, R. A.; Stejskal, E. O. J. Magn. Reson. **1979**, 34, 443-447.
(b) Stejskal, E. O.; Schaefer, J.; KcKay, R. A. J. Magn. Reson. **1984**, 57, 471-485. (c) Schaefer, J.; Stejskal, E. O.; Garbow, J. R.; McKay, R. A. J. Magn. Reson. **1984**, 59, 150-156.

3. For C13-P31 cross polarization: (a) Hagaman, E. W.; Ho, P. C.; Brown, L. L.; Schell, F. M.; Woody, M. C. J. Am. Chem Soc. **1990**, 112, 7445-7450. (b) Hagaman, E. W. Energy & Fuels **1988**, 2, 861-862.

4. Gullion, T.; Schaefer, J. J. Magn. Reson. **1989**, 81, 196-200. Marshall, G. R.; Beusen, D. D.; Kociolek, K.; Redlinski, A. S.; Leplawy, M. T.; Pan, Y.; Schaefer, J. J. Am. Chem.Soc. **1990**, 112, 963-966.

5. Gullion, T.; Poliks, M. D.; Schaefer, J. J. Magn. Reson. **1988**, 80, 553-558.

6. Christensen, A. M.; Schaefer, J., private communication.

The Application of Microdilatometry to Solvent Swelling of Coals

George D. Cody, Alan Davis, Semih Eser, and Patrick G. Hatcher

Energy and Fuels Research Center and the Fuel Science Program
The Pennsylvania State University, University Park, PA 16802

Introduction

Since Sanada and Honda's initial application of polymer solution theory to solvent swelling to coals (1), many researchers have used solvent swelling as a useful means of obtaining at least qualitative information on the nature of coal's macromolecular network. Solvent swelling analysis exploits the thermodynamic relationship between solvent-coal mixing and elasticity of coal's macromolecular network. As was shown by Flory and Rehner (2), at equilibrium a polymer immersed in an excess of solvent will contain a specific volume of solvent, the total amount of solvent constitutes a thermodynamic balance between the reduction the free energy due to mixing and the increase in elastic free energy of the network resulting from dilation.

To date, a variety of analytical techniques have been used to measure the equilibrium volume of solvent in coal. No one technique is free of difficulties. Moreover, the specifics of a given research problem may dictate which technique is chosen. In this paper a new means of measuring equlibrium swelled volumes is introduced and compared to values obtained using a more traditional method.

Sanada and Honda's measurements employed a temperature controlled gravimetric device. The equilibrium volume of a solvent (they used pyridine) was determined from the weight gain of approximately 0.1 g of coal measured from the extension of a quartz spring. They report a high degree of precision such that + or - 0.8 mg weight change is detectable. Since their study many other researchers have employed gravimetric methods to determine the equilibrium swelled volume of solvents in coal. Obvious advantages to the gravimetric technique are 1) the high degree of sensitivity and 2) solvent swelling measurements at solvent activities less than 1.0 can be readily obtained. A disadvantage of this technique is that significant condensation of solvent can occur within coal's pore structure. This potential error is delt with by correcting the gravimetric data assuming that capillary condensation has occurred in pores. Thus prior to swelling the extent of porosity in coals must be known. One problem with this correction, however, is that it has been shown that upon swelling of coal in pyridine significant changes in coal's pore structure take place (3), therefore, a correction based on "dry" pore volume may not be sufficient.

Liotta et. al (4) published a simple technique for measuring the equilibrium volume of solvent in coal by simply measuring the volume expansion of the coal. Green et al.(5) confirmed the accuracy of this technique by comparing results so obtained to those gathered using gravimetric techniques. The advantages of the volumetric technique is that it is rapid, exhibits good

reproducibility, and requires no special equipment. A potential error is that interparticle volume contributes to the total volume of the sample. This potential source for error is typically addressed by using very fine mesh coal particles and assuming that the change in interparticle void volume upon swelling is exactly proportional to the increase in coal's volume upon swelling. The volumetric method enjoys much use by many coal researchers today because of its convenience and high degree of reproducibility.

In addition to these methods there are a variety of other techniques which although fundamentally related to one or the other of the above techniques use significantly different means by which a measurement is obtained. Aida and Squires (6), for example measured the volume expansion of particulate coal using an apparatus similar in concept to a vapor pressure osmometer. They reported that their apparatus gave results which compared well to established techniques and afforded a greater facility in measuring the kinetics of swelling. Cody et. al. (7) used solvent swelling of coal thin sections using the preparation method designed by Brenner (8) and recorded the equilibrium solvent uptake via changes in linear dimension measured parallel and perpendicular to the bedding plane. This method also yielded values comparable to bulk values and was especially well suited for studying effects of residual network strain and subsequent strain relaxation upon the swelling behavior of un-extracted coals.

This paper will focus on the application of a high sensitivity micodilatometer for the purpose of measuring linear expansion of coal slabs following immersion in a solvent.

Experimental:

The microdilatometer employed in this study was originally used to study the expansion of particulate coals under gasification conditions (9). Figure 1 is a schematic diagram of the dilatometer. The microdilatometer measures the change in position of a linear variable differential transformer (LVDT) core composed of soft iron. The LVDT is attached directly to a glass probe which rests on top of the sample. The position of the LVDT between two electric coils within the dilatometer is sensitively detected using the principles of mutual inductance. At its most sensitive setting extremely small vibrations in the lab are readily detectable by the dilatometer. Thus, the practical lower limit in measurement without resorting to a vibration dampening table is on the order of 1 μm. As will be discussed shortly, in the current experiments expansions of coal due to solvent swelling are on the order of hundreds of microns using millimeter scale samples.

Two important modifications to the dilatometer have enabled its use in precisely measuring solvent swelling. First, the dilatometer probe is modified as follows. In place of the solid pyrex probe, a hollow probe with vents at the probe tip has been manufactured. Higher up on the probe lies an access port for a syringe for the purpose of injecting solvent. Second, the entire probe/LVDT assembly weighs approximately 20 g. Using a counter balance it is possible to reduce the effective weight of the probe/LVDT assembly to approximately 100 mg. This weight is just

enough to exceed frictional forces within the system. The error that this force adds to the final expansion value is evaluated as follows. The elastic modulus of coal will be the least at the most swollen state. For solvent swollen coal the elastic modulus (on compression) was measured by Doug Brenner and is in the range of 500 psi (10). The typical compressive stress on the samples in this study are in the range of 5×10^{-2} psi. Using a standard equation for strain for uniaxial compression of a polymeric material (equation 1)(11) we calculate a deviation of the true expanded dimension to be less than one tenth of 1 percent.

$$P = E/3(\lambda - \lambda^{-2}) \qquad (1)$$

In equation 1, P = pressure, E = the elastic modulus, and λ is the compression ratio.

The second important aspect of this experiment involves preparation of the samples. Table 1 lists the samples and other pertinent information. Three of the coal samples are vitrains from large coal blocks, the other two are coalified logs. For the purpose of comparing the volume expansion values measured using the microdilatometer with values obtained using a bulk volumetric analysis pyridine extracted (exhaustively) samples were required.

The following sample preparation protocol was applied for solvent swelling using a microdilatometer. Vitrain bands were selected from large particle samples of each coal (in the case of the coalified woods all of the matter is vitrain). Small slabs were cut from each sample using a fixed SiC disc grinding wheel. The initial size of the sample is typically on the order of 1 x 1 x 1.5 mm. To avoid forming microcracks during extraction each slab was first equilibrated with pyridine vapor, typically 1 -2 days of equilibration. Following this the samples were immersed in a large excess of pyridine liquid (approximately 10 ml) and gently heated at a temperature of about 40 ·C. After no less than 4 days of immersion, the samples were de-swelled by sequential series of dilutions with chlorobenzene, each dilution was 9:1 chlorobenzene to solution by volume. Finally the samples were placed "wet" in a desiccator with a tray of chlorobenzene and allowed to come into equlibrium with chlorobenzene vapor. . The "dry" samples were then transferred to a vacuum oven and dried for approximately 1 day. This protocol generally resulted in samples free of microcracks.

Prior to swelling each sample was carefully inspected under the microscope for the presence of microcracks. Only Pittsburgh No. 8 presented major difficulties. Regardless of the amount of time allowed for each step of the preparation protocol, samples of Pittsburgh No. 8 exhibited significant microcracks parallel to the bedding plane. Thus, for this sample a second stage of preparation following extraction was required. Using a binocular microscope, microtweezers, and a razor knife it was possible to carve out apparently microcrack-free regions of the original slabs of this coal.

Sample preparation and solvent swelling protocol applied for bulk volumetric solvent swelling analysis is identical to that described by Liotta et al. (4). Approximately 1.0 g of finely ground, extracted coal is charged into a calibrated centrifuge

tube. An excess of solvent is added and the sample is vigorously shaken to ensure free volumn expansion. After 24 hr the equilibrium swelled volume of the sample was measured from the increase in height of the coal-pyridine interface.

The actual solvent swelling analysis using the microdilatometer is straightforward. The prepared sample is placed in the sample cavity and the dialotometer head is placed on top of of the sample. From the point that solvent is charged into the probe via a syringe, linear expansion data is continuously recorded. When no further expansion takes place this maximum value is taken to equal the cube root of the coal's equilibrium swelled volume.

Results and Discussion

The size of samples in this study varied from 1.3 to 1.9 mm in the direction parallel to the dilatometer probe. Expansions due to solvent swelling are, therefore, on the order of a 100 to 400 μm. Table 2 gives the comparative results. It is clear that in all cases the linear expansion ratios obtained using microsamples of coal in the microdilatometer are comparable to the cube root of the bulk swelling ratio obtained using the bulk volumetric method. Thus for solvent swelling analysis of small amounts of sample the dilatometer is a reliable tool.

Implications derived from the comparison between the two sets of data are 1) the assumption implicit in volumetric swelling that the increase in the interparticle volume with swelling is proportional to an increase in swelled particle volume is reasonable, 2) the assumption that for vitrinite rich coals the bulk swelling behavior is dominated by the swelling behavior of vitrinite is also supported by this comparison.

The microdilatometer can accurately and precisely measure the dilation of coal during solvent swelling. For cases where only a very small amount of sample is available for analysis this instrument is invaluable. For example, solvent swelling analysis of phytoclasts (organic particles) liberated from organic rich rocks is now readily possible.

References

1) Sanada, Y., Honda, H., Fuel, 1966, 48, 295
2) Flory, P.J., Rehner, J., J. Chem. Phys., 1944, 12, No.10, 412
3) Winans, R., Thiyagarjan, P., Energy Fuels, 1988, 2, 358
4) Liotta, R., Brown, G., Isaacs, J., Fuel, 1983, 62, 781
5) Green, T.K., Kovac, J., Larsen, J.W., Fuel, 1984, 63,935
6) Aida, T., Squires, T.G., ACS Chem. Preprt., Div. of Fuel, 1986, 30, No.1, p.95
7) Cody, G.D., Larsen, J.W., Siskin, M., Energy Fuels, 1988, 2, 340
8) Brenner, D., Fuel, 1984, 63, 1324.
9) Khan, M.R., PhD Thesis, 1985, Pennsylania State University
10) Brenner, D., ACS Chem. Preprt., Div. of Fuel, 1986, 31, No.1, p.17

11) Treloar, L. R. G., The Physics of Rubbery Elasticity, 3rd Edition, Clarendon Press, Oxford, 1975

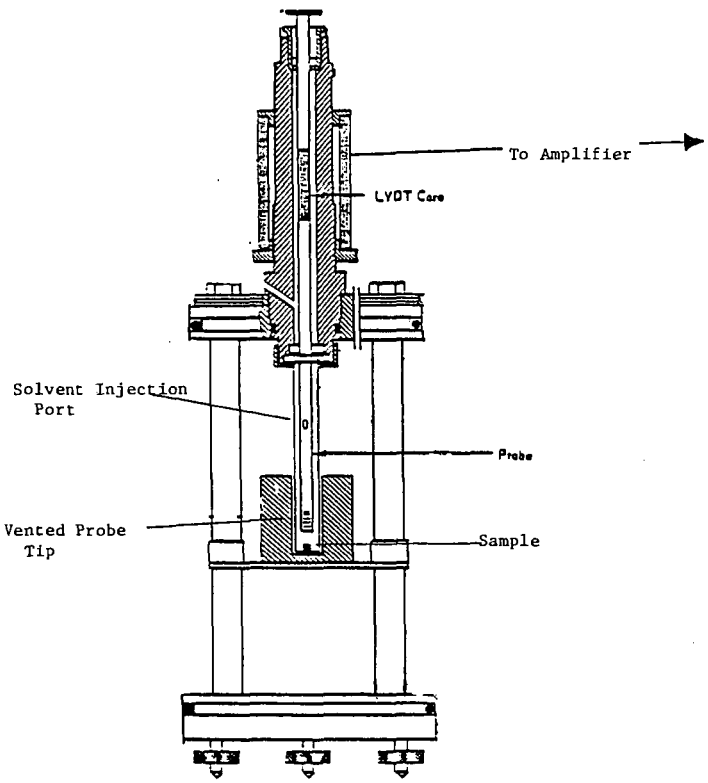

Figure 1: Schematic of microdilatometer modified after Khan, 1985

Table 1 - Coal Samples Studied

SAMPLE	% C	% H	% O	% N	% S	RANK
Smith Seam	70.8	5.0	22.8	0.9	0.5	subbit C
Illinois No. 6	81.9	5.5	9.4	1.4	2.2	Hvb C
Pittsburgh No.8	84.8	5.7	7.4	1.4	0.8	Hvb A
Wyodack/Anderson*	-	-	-	-	-	subbit
Ferron*	78.0	5.3	14.0	1.0	1.7	subbit

* = coalified log

Table 2 - Comparison of Solvent Swelling Results

SAMPLE	Q_f/Q_i	L_f/L_i(calc)*	L_f/L_i**
Smith Seam	1.26	1.08	1.10
Illinois No.6	2.30	1.32	1.29
Pittsburgh No.8	2.30	1.32	1.29
Wyodack/Anderson	1.67	1.19	1.22
Ferron	1.67	1.19	1.19

*linear expansion ratio, the cube root of the bulk swelling ratio Q_f/Q_i.
**linear expansion ratio, measured with microdilatometer

New Applications of Differential Scanning Calorimetry and Solvent Swelling for Studies of Coal Structure

Yongseung Yun, Yoshinobu Otake[1] and Eric M. Suuberg
Division of Engineering, Brown University
Providence, RI 02912

Keywords: Solvent swelling, Differential Scanning Calorimetry, Coal macromolecular structure

Introduction

There have been several reports of structural changes in coal at low temperature (<400°C) indicated by increased mobility of the coal [1] or by crosslinking (associated with the evolution of water and carbon dioxide [2,3]). Since no significant weight loss is normally observed in this low temperature range except moisture and small amount of CO_2, glass transition and/or physical melting have been suspected as responsible for the increased mobility observed in bituminous coals. Some bituminous coals, e.g., Pittsburgh No. 8 coal, are known to contain a considerable amount of thermally extractable mobile phase at temperatures below 400°C [4,5] and thus the role of physical structural changes in releasing this material cannot be ruled out. Recent results on pretreatment of coal for liquefaction by steam, solvent swelling, and preheating have proved that elevated temperatures below those needed for thermal decomposition help enhance the efficacy of the pretreatments, perhaps by promoting greater accessibility of the structure in coal.

Many analytical tools ,e.g., GC, MS, TG/FTIR, TG/MS, which focus on gas phase volatiles, are useful for studies involving thermally induced changes in some functional groups of coal whereas FTIR, NMR, Gieseler Plastometry, Dilatometry, and TMA (Thermomechanical Analysis) focus on the study of the char residue with the first two again directed mainly at obtaining functional group information and the last three at obtaining physical structural data. Differential Scanning Calorimetry (DSC) has been used less for the latter purpose, but as will be seen, can be a suitable tool for studying the structural changes involved at low temperatures.

DSC has earlier been used for measurements of the heats of pyrolysis and hydropyrolysis [6-10], as well as for the determination of glass transition temperatures of coal [11,12]. Because of its sensitive nature, DSC is an ideal tool for investigating the thermal changes associated with softening as well as glass transition and thus for identifying the temperatures of significant structural changes. Therefore, DSC has been heavily applied in polymer science and many commercial devices are available. The application of DSC to coal has been hampered by problems caused by weight loss that accompanies most heat effects and also by tar condensation in the DSC cell. Although hermetic sealing of the coal sample is possible, the pressure build-up inside the cell can easily exceed the maximum allowable pressure of the normal sealed capsules (usually 10 atm). This is apparent, considering that at 200°C the vapor pressure of water is already 15.3 atm. Thus it is difficult to measure well-defined heat effects, partly for this reason. Moreover, water evolution can continue up to 300°C, depending on heating rate and sample, and thus overshadow the heat effects due to structural changes below 300°C.

In this paper, we applied DSC in a way such that minute heat effects could be identified by subtracting consecutive DSC scans. Several groups have already applied this type of methodology in helping identify problems with heat capacity measurement [13,14], but did not draw any conclusions concerning the role of structural changes in heat effects. In combination with solvent swelling, which has been also extensively used for characterizing the density of crosslinking in the macromolecular structure of coal, DSC appears to be a powerful tool for evaluating the extent of

[1]Present address: Osaka Gas Company, Ltd., Research Center, Osaka, Japan.

thermally induced structural changes.

Experimental

Aliquots of several coal samples, obtained from the Argonne National Laboratory - Premium Coal Sample Program, were analyzed by DSC and solvent swelling techniques. These samples included Pittsburgh No. 8 (-20 mesh), Illinois No. 6 (-20 mesh), Blind Canyon (-20 mesh), Upper Freeport (-100 mesh), and Pocahontas No. 3 (-20 mesh) coals. They were used as-received. Detailed petrographic, chemical, and physical analysis data on these coals can be found elsewhere [15].

Differential Scanning Calorimetry

A DuPont 2910 DSC system with a liquid nitrogen cooling accessory (LNCA-II) was employed in this study. The sample cell was operated under a nitrogen flow rate of 90 ml/min in order to keep the cell free of oxygen during measurement. Aluminum sample pans were generally used in an unsealed mode. This was done by just pushing down the top sample pan cover gently onto the bottom pan containing the coal. Samples were heated from 30°C at 8 °C/min or 30 °C/min. Typically 22-28 mg of sample was used in an experiment. Cooling of the cell between consecutive heating scans normally involved air convection, but several runs were cooled at a controlled rate of 20 °C/min with liquid nitrogen as a cooling medium.

Solvent Swelling

The details of this technique were described earlier [16]. In short, coal samples were placed in constant diameter tubes (3 mm i.d., ca. 5 cm high) and centrifuged at 7500 rpm for 3 min in a roughly 30 cm horizontal rotor (SAVANT HSC-10K high speed centrifuge), after which the initial height of the sample was measured by a caliper. The choice of 7500 rpm was rather arbitrary and selected only to be as high as could be comfortably tolerated by the equipment. Solvent was then added and stirred until a visual check showed the total submergence of coal in solvent. The stirring was repeated frequently (normally 3 times) during the first 30 min following solvent addition. At the desired measurement times, the sample tubes were centrifuged again (7500 rpm for 3 min), the swollen coal height measured, and the solvent replaced with the clean solvent. This assured that the concentration of extractable was not so high as to interfere with the measurement.

Samples (22-28 mg) for solvent swelling were prepared in the DSC at a heating rate of 8 °C/min under a nitrogen flowrate of 90 ml/min. After reaching the desired temperature, each sample was cooled immediately by contacting the bottom of the sample pan with ice or cold water.

Swelling solvents employed (tetrahydrofuran(THF), pyridine) were all reagent grade and were used without any further purification.

Results and Discussion

DSC is a very sensitive technique for determining the difference in heat flow between a sample and a reference material, both heated (or cooled) at a controlled rate. The main purpose in employing DSC here was to determine whether DSC can be used more effectively than it has been, as a tool for examining structural changes in coal, particularly those that occur before pyrolysis. One of the phenomena we were concerned with was the so-called glass transition. The glass transition temperature, T_g, is defined as the temperature at which amorphous polymers transform in structure from the glassy state to liquid/rubbery state. In coal, this transformation has been suggested to appear just before thermal degradation begins [11,12]. Due to the heterogeneity and complexity of constituents involved in coal, a clear-cut determination of T_g in coal has been difficult, as might be

expected.

Figures 1-3 show blank background-subtracted DSC thermograms for three high volatile bituminous coals, i.e., Pittsburgh No. 8, Illinois No. 6, and Blind Canyon coals. Samples were predried inside the DSC up to 150°C just before the first run in Figures 1(a)-3(a). The drying occurred at the same experimental conditions as the following DSC runs. Intermediate oxygen exposure was avoided. Figures 1 through 3 also show difference DSC thermograms for three consecutive scans of the same sample. The general trend for three consecutive scans of a sample in Figures 1(a)-3(a) is that the earlier scans show a slightly more endothermic response above 250°C than do later scans. The sharp initial peaks at ca. 40°C on initial heating do not represent any physically significant heat effects. The general downward direction of the thermograms upon heating represent the effect of heat capacity of coal. The subtraction of a first or second thermogram from a second or third one (as a reference) allows very subtle irreversible changes to be examined. If no irreversible changes were involved, the subtracted spectra would be flat, at a value of zero. In Pittsburgh No. 8 coal, the (1st-3rd) difference thermogram shows significant change in 200-300°C range, while the (2nd-3rd) shows much less change. The reasons for this are discussed below.

Illinois No. 6 and Blind Canyon coals also demonstrate the same behaviors, described above. The peak around 110-120°C in the third scan of Illinois No. 6 coal was due to inadvertent water vapor readsorption from ambient air, which occurred while cooling the sample for the 3rd run in the DSC. This water readsorption peak (up to 150-200°C) helps define the temperature range at which moisture would have influenced the DSC thermogram. The distinct downward peak around 190°C in Blind Canyon coal (Figure 3) was also found to be related to incomplete drying; drying was performed inside the DSC cell at a heating rate of 8 °C/min up to 150°C, which was apparently not sufficient to completely drive off all moisture.

The observations in Figure 1 appear to confirm an earlier suggestion [17] that Pittsburgh No. 8 coal has an irreversible heat effect associated with glass transition around 275°C, while Illinois No. 6 and Blind Canyon coals have a T_g value higher than Pittsburgh No. 8 coal. The transition in Illinois No. 6 coal appears to be centered at around 300°C and that in Blind Canyon coal at 275-300°C. The irreversible heat effect was endothermic (downward in the figures) which is an indication of structural relaxation in the first scan. It must be noted that the transition is irreversible, otherwise it would not be visible in the subtractive technique. We earlier saw an irreversible change in THF swellability at this temperature [17]. This in no way suggests that the glass transition itself is irreversible, but rather that the relaxations that occur with glass transition, are irreversible (vide infra). All three coals exhibited initial agglomeration behavior from ca. 340°C, as observed visually from the coal sample after cooling. Thus the softening of coals, leading to gross agglomeration, has not yet commenced at the observed temperature range of the structural transition that we hypothesize to be a glass transition.

Another noteworthy fact observed in Figures 1(a)-3(a) is the reproducibility of small peaks in the thermograms starting from around 150°C, indicating that more or less reversible transitions occur along with the irreversible processes (reversible because the peaks always reappear). These thermograms were reproducible in several independent runs. There may be a wealth of information in the small reproducible peaks, which probably reflect different melting processes.

It is well known that higher heating rates will increase the "intensity" of heat flow at any temperature while decreasing the sensitivity. This is obvious considering that at higher heating rates, thermograms of kinetic events will be broadened in terms of temperature scale although the shape will be comparable in time scale regardless of heating rates. In other words, if peaks are overlapped in a narrow temperature range, slower heating rate run will enhance the separation of peaks. When peaks exhibit low intensity, higher heating rate runs will sharpen them and make them more obvious. The effect of heating rate on DSC thermograms is illustrated in Figures 4, 5 and considerably

simplified thermograms, compared to Figures 1 and 2, can be noted.

Samples for Figures 4 and 5 were not dried and the initial endothermic peaks observed at 60-240°C range were caused by water desorption. In Pittsburgh No. 8 coal, the irreversible transition in the 270-310°C range is more apparent than that observed at lower heating rate of 8 °C/min (Figure 1) and the temperature region of transition is increased by ca. 15°C at high heating rate of 30 °C/min, suggesting that the irreversible transition is an activated process. This would be expected for a glass transition. In Illinois No. 6 coal containing 7.97% moisture, the initial water endothermic peak is the dominant feature of the thermogram as could be expected from the high moisture content of this coal. Subtle changes in the subsequent runs for Illinois No. 6 coal are still visible in the difference DSC thermograms, as shown in Figure 5(b) for which temperature range 250-350°C was chosen for clarity. The downward (endothermic) trend above 300°C is most distinct in the (1st-2nd) and (1st-3rd) runs whereas the (2nd-3rd) run exhibits a smaller transition. Again, this shows the irreversible change occurs mainly during first heating.

The interpretation of the transitions revealed by in the DSC is aided greatly by a knowledge of the solvent swelling behavior of the coal as a function of temperature. Figure 6 shows a comparison of pyridine and THF swelling behavior of the Pittsburgh No. 8 coal obtained on the samples after DSC analysis (a single scan only). It is noted that there is an irreversible increase in THF swellability achieved in heating the coal to the range of temperatures 200-300°C. This is not accompanied by any significant weight loss. Nor is this change accompanied by any increase in pyridine swellability (in fact, a small decrease is seen, if anything). Pyridine is a stronger solvent, and can be expected to disrupt all noncovalent interactions in the coal. Pyridine reveals the extent to which the covalent network structure has been altered (or not altered) in the range of temperature cited above, since it is believed to be the most effective solvent for disrupting non-covalent interactions in the coal. The weaker THF is not as effective in removing all noncovalent crosslinks, as is evident in that it does not swell the coal as much (note the molecular sizes are quite similar for pyridine and THF). For Pittsburgh No. 8 coal, heating the coal to the range of temperatures 200-300°C apparently results in an irreversible removal of noncovalent crosslinks, but not much change in covalent crosslinks. This observation was reported previously by us [17]. This presumably occurs because the coal structure undergoes a glass to rubber transition in this temperature range, and once the structure is more flexible, it can relax to a new equilibrium configuration which is more easily swelled by THF. This effect is presumably related to the observation made by Larsen and coworkers [18] that the first cycle of a swelling in a good solvent such as pyridine normally involves an irreversible expansion of the network structure, due to structural relaxation. This transition is not evident in post-heating pyridine swelling of coals because the solvent alone is already effective at relaxing the structure without the need for heating. This is consistent with the results of Sakurovs [19], which showed pyridine to be as effective as heating with respect to creating "mobility"(at least in bituminous coals up to 86% C content).

The thermally induced relaxation during the first cycle of heating is thus taken to refer the T_g of the raw coal. The fact that repeated DSC scans reveal the transition to be stronger in the first scan than in any subsequent scans confirms the irreversible nature of the process that accompanies the glass transition. Again, a glass transition itself should, of course, not be irreversible. It is the release of stored strain energy that is irreversible. One can imagine that the thermally induced transition involves the disruption of aromatic stacking interactions formed under geological pressure. Since there is no comparable pressure applied when the sample is cooled in a DSC, the same interactions will not be restored; the thermodynamics has been changed.

Interestingly, Figure 6 shows that more time is required to reach THF swelling equilibrium for heat treatment temperatures below 300°C. This indicates that the accessibility of the coal is also irreversibly altered (increased) by heat treatment above this temperature (the structure swells more

readily to final equilibrium value above 300°C). Pyridine swelling ratio slightly decreased with time presumably by weight loss due to extraction of the coal by pyridine.

Figure 7 shows changes of the swelling ratio in THF against pyrolysis temperature for Illinois No. 6 coal along with the weight loss profile (the determination of the pyridine swelling profile against pyrolysis temperature for Illinois No. 6 coal is under way). In contrast to Pittsburgh No. 8 coal, Illinois No. 6 coal exhibits a drastically different THF swelling behavior with heat treatment temperature. Higher swelling ratio was obtained in the low temperature region (<300°C). The fact that Illinois No. 6 coal can swell significantly in THF without any heat treatment reflects a much different starting structure than that of Pittsburgh No. 8 coal. This clearly demonstrates the importance of coal composition in swelling. The swelling evidence to support the DSC interpretation is thus not as clear in Illinois No. 6 coal. The relatively small increase in swellability above 250°C is all that accompanies the transition identified by DSC. The swelling dynamics also suggest a small change at 250°C. Note that the highest swelling ratio is observed in 5 hours, and the ratio decreases with time. This is again presumably associated with a sudden increase in extractability at this temperature, and the swelling decreases as mass is removed. Presumably the increase in both swellability and extractability implies greater accessibility of the structure. From 350°C, pyrolytic crosslinking is clearly dominant as illustrated in the drop of THF swelling ratio and the increase in weight loss. Several pyridine swelling studies on bituminous coals [20] noted that pyridine swelling ratio starts to fall when the pyrolytic bond breakage commences. It should be noted from Figure 7 that the weight loss in the 150-300°C range was 10.3-10.9 wt%, which is clearly higher than the moisture content 7.97 wt% of this coal. This shows either that something other than moisture is being lost, or that an arbitrary drying procedure, such as the ASTM procedure, does not give the correct picture regarding possible moisture loss. This is also suggested by Figure 5(a), which shows "drying" well above 150°C.

Figures 8 and 9 illustrate the correlation between DSC thermograms obtained at 30 °C/min and solvent swelling profiles in two other coals. For Upper Freeport medium volatile bituminous coal, the main endothermic relaxation process starts from ca. 310°C (Figure 8(a)) while THF swelling ratio starts to shoot up around the same temperature (Figure 8(b)). Note that samples for swelling ratio experiments were in this case prepared in a wire-mesh pyrolyzer at 8 °C/min under nitrogen environment [17]. On the other hand, in Pocahontas No. 3 low volatile bituminous coal, the DSC difference thermogram exhibits a rather wider endothermic profile from ca. 230°C, which coincides with dramatic changes in pyridine and THF swelling profiles.

In the case of both the Upper Freeport and Pocahontas coals, swellability increases are difficult to separate from the onset of pyrolytic bond cleavage processes, as evidenced by rapid mass loss. The data certainly suggest that significant increases in swellability precede the period of rapid mass loss, which actually always seems to coincide with swellability decrease. It is difficult to unambiguously say that the data in hand argue for a physical transition prior to the commencement of bond cleavage processes. More work is planned to address this question. In any case, the solvent swelling data do correlate reasonably with the DSC data in terms of predicting increased structural mobility.

In summary, DSC confirms what was suspected from THF solvent swelling in the high volatile bituminous coals - that there is a glass transition in the range of temperature from about 230 to 300°C. This is lower than earlier reported values [11], but it is understandable that some variation might be due to sample differences, heating rates, and the difficulty of interpreting simple DSC scans without additional confirming data such as solvent swelling.

Conclusions

- DSC and solvent swelling techniques were applied to evaluate structural changes at low

temperature (<350°C) before any major pyrolytic bond breakage occurs. The results reveal the existence of reversible structural changes together with an irreversible transition, centered around 200-300°C in three high volatile bituminous coals.

- DSC thermograms appear to correlate with THF swelling ratio profiles, with regard to the information they convey on structural relaxation.

Acknowledgement

The work reported here was financially supported by the Department of Energy Contract No. DE-AC22-91PC91027. EMS also acknowledges the support of the Exxon Education Foundation.

References

1. Lynch, L.J.; Sakurovs,R.; Webster, D.S. *Fuel* **1988**, *67*, 1036.
2. Suuberg, E.M.; Lee, D.; Larsen, J.W. *Fuel* **1985**, *64*, 1668
3. Solomon, P.R.; Serio, M.A.; Despande, G.V.; Kroo, E. *Energy & Fuels* **1990**, *4*, 42.
4. Yun, Y.; Meuzelaar, H.L.C.; Simmleit, N.; Schulten, H.-R. In *Coal Science II*; Schobert, H.H., Bartle, K.D., Lynch, L.J., Ed.; ACS Symposium Series 461; ACS: Washington, DC, 1991; Chapter 8, p 89.
5. Yun, Y.; Meuzelaar, H.L.C.; Simmleit, N.; Schulten, H.-R. *Energy & Fuels* **1991**, *5*, 22.
6. Mahajan, O.P.; Tomita, A.; Walker, P.L., Jr. *Fuel* **1976**, *55*, 63.
7. Mahajan, O.P.; Tomita, A,; Nelson, J.R.; Walker, P.L., Jr. *Fuel* **1977**, *56*, 33.
8. Hefta, R.S.; Schobert, H.H.; Kube, W.R. *Fuel* **1986**, *65*, 1196.
9. Janikowski, S.K.; Stenberg, V.I. *Fuel* **1989**, *68*, 95.
10. Elder, J.P.; Harris, M.B. *Fuel* **1984**, *63*, 262.
11. Lucht, L.M.; Larson, J.M.; Peppas, N.A. *Energy & Fuels* **1987**, *1*, 56.
12. Hall, P.J.; Larsen, J.W. *Energy & Fuels* **1991**, *5*, 228.
13. Isaacs, L.L.; Tsafantakis, E. *Prepr. Pap.- Am. Chem. Soc., Div. Fuel Chem.* **1987**, *32(4)*, 243.
14. MacDonald, R.A.; Callanan, J.E.; McDermott, K.M. *Energy & Fuels* **1987**, *1*, 535.
15. Vorres, K.S. *User's Handbook for the Argonne Premium Coal Sample Program*: Argonne, Illinois, 1989.
16. Otake, Y.; Suuberg, E.M. *Fuel* **1989**, *68*, 1609.
17. Suuberg, E.M.; Otake, Y.; Deevi, S.C. *Prepr. Pap.- Am. Chem. Soc., Div. Fuel Chem.* **1991**,*36(1)*, 258.
18. Larsen, J.W.; Mohammadi, M. *Energy & Fuels* **1990**, *4*, 107.
19. Sakurovs, R.; Lynch, L.J.; Barton, W.A. *Prepr. Pap.- Am. Chem. Soc., Div. Fuel Chem.* **1989**, *34(3)*, 702.
20. Ibarra, J.V.; Moliner, R.; Gavilan, M.P. *Fuel* **1991**, *70*, 408.

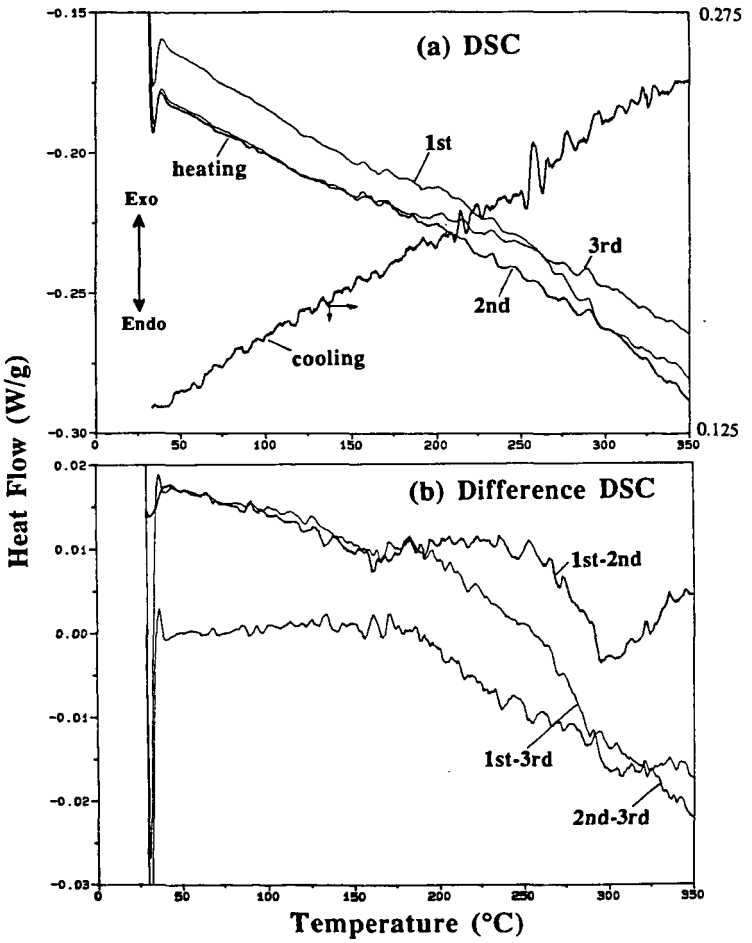

Figure 1. DSC and difference DSC thermograms for Pittsburgh No. 8 coal. After drying coal at 150°C in the DSC, DSC runs were repeated three times at 8 °C/min for the same sample. Difference thermograms in (b) were obtained by subtracting two thermograms in (a).

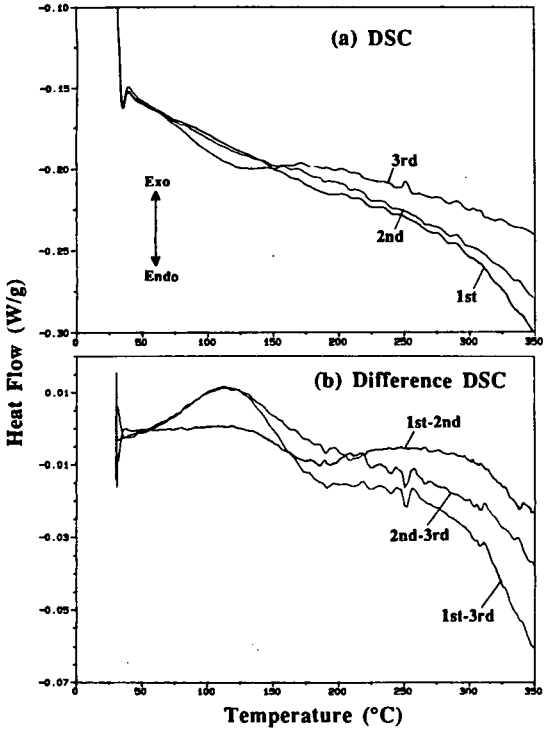

Figure 2. DSC and difference DSC thermograms for Illinois No. 6 coal. After drying coal at 150°C in the DSC, DSC runs were repeated three times at 8 °C/min for the same sample. Difference thermograms in (b) were obtained by subtracting two thermograms in (a).

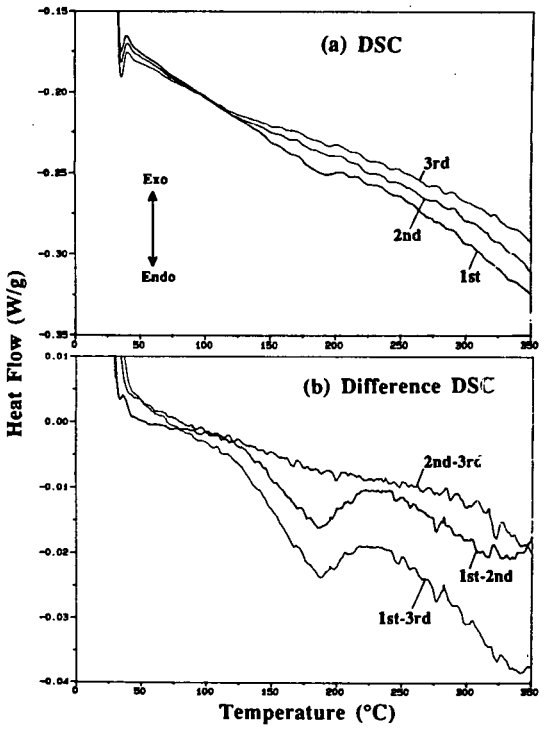

Figure 3. DSC and difference DSC thermograms for Blind Canyon coal. After drying coal at 150°C in the DSC, DSC runs were repeated three times at 8 °C/min for the same sample. Difference thermograms in (b) were obtained by subtracting two thermograms in (a).

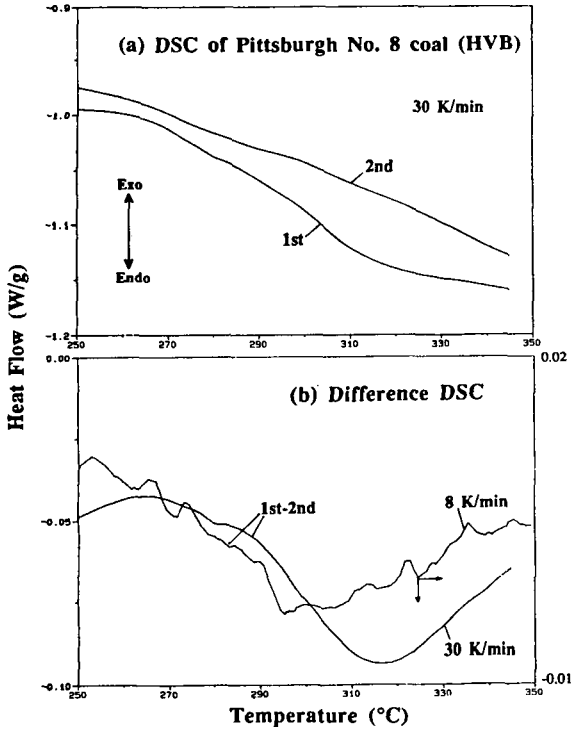

Figure 4. DSC and difference DSC thermograms for undried Pittsburgh No. 8 coal obtained at 8 °C/min and 30 °C/min.

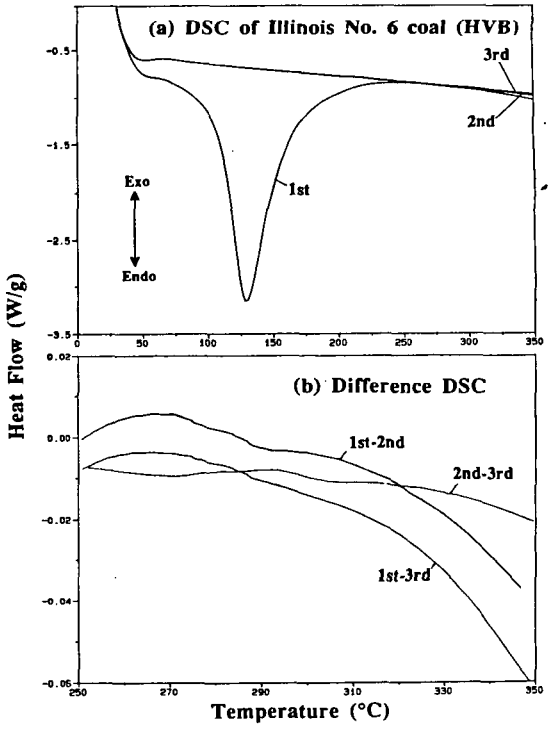

Figure 5. DSC and difference DSC thermograms for undried Illinois No. 6 coal obtained at 30 °C/min.

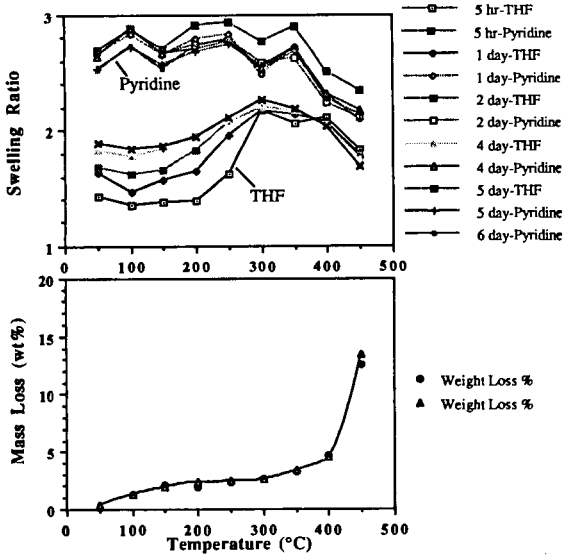

Figure 6. Changes of swelling ratio in tetrahydrofuran and pyridine as well as weight loss profile against pyrolysis temperature for Pittsburgh No. 8 coal (-20 mesh). Undried samples were placed in the DSC cell and heated at 8 °C/min under 90 ml/min nitrogen flow up to the specified temperature.

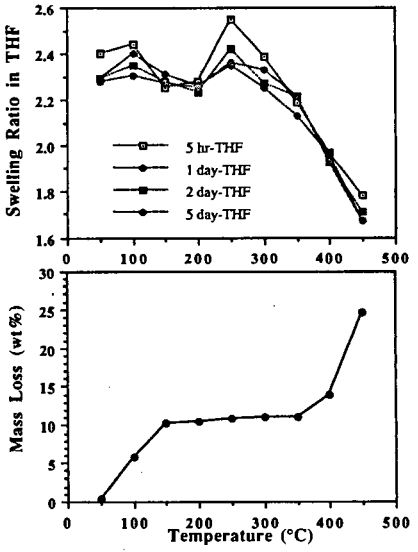

Figure 7. Changes of swelling ratio in tetrahydrofuran as well as weight loss profile against pyrolysis temperature for Illinois No. 6 coal (-20 mesh). Undried samples were placed in the DSC cell and heated at 8 °C/min under 90 ml/min nitrogen flow up to the specified temperature.

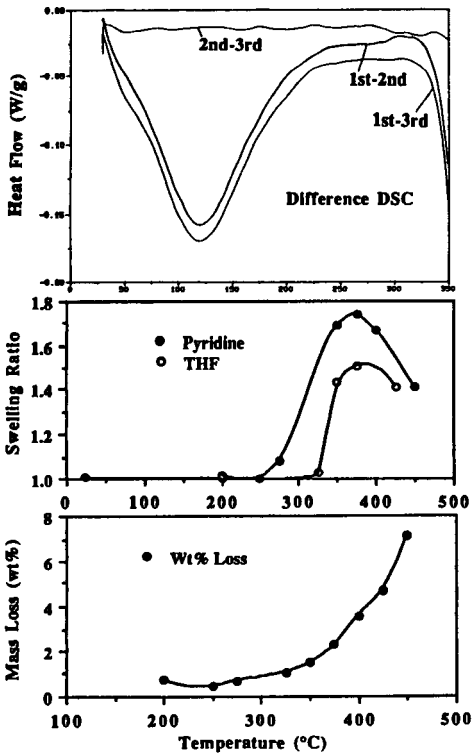

Figure 8. DSC difference thermograms as well as profiles of swelling ratio and weight loss for Upper Freeport medium volatile bituminous coal (-100 mesh). Note that DSC was performed at 30 °C/min whereas samples for swelling were obtained from wire-mesh reactor at 8 °C/min.

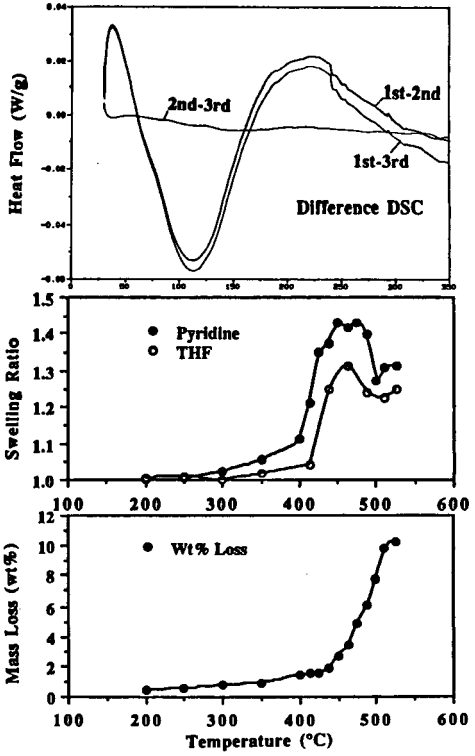

Figure 9. DSC difference thermograms as well as profiles of swelling ratio and weigh loss for Pocahontas low volatile bituminous coal (-20 mesh). Note that DSC was performed at 30 °C/min whereas samples for swelling were obtained from the wire-mesh reactor at 8 °C/min.

Characterization of Coal-Derived Materials by Laser Desorption Mass Spectrometry*

J. E. Hunt, K. R. Lykke, and R. E. Winans
Chemistry Division
Argonne National Laboratory
Argonne, IL 60439

Keywords: laser desorption mass spectrometry, coal, maceral

ABSTRACT

Laser desorption time-of-flight mass spectrometry (LD/TOF MS) is used to characterize complex mixtures of large molecules derived from coals and separated coal macerals. Three groups of macerals, namely liptinite, vitrinite, and inertinite from Argonne Premium Coal Sample 7 were separated by a density gradient technique and subjected to small scale liquefaction. Samples of the maceral products were exposed to laser pulses from a XeCl-Excimer laser or the fourth harmonic output of a Nd:YAG laser. The general features of this method are the virtual absence of ion signal below m/z 200, a distribution of masses from m/z 200 to beyond m/z 1000 and reduced mass fragmentation in contrast to EI and FAB, where much fragmentation is present below m/z 200.

INTRODUCTION

The chemically and physically heterogeneous nature of coals dictates that their structure and reactivity patterns be complicated. The determination of the structural building blocks in coals is of crucial importance in research on their reactivity. The problem is complicated by the fact that the molecular structure of the organic part of coal is not dependent on a single molecule, but on a complex mixture of molecules that vary according to the type of coal. A number of complementary approaches have been used to investigate the structure of coal. Mass spectrometry has played an increasing role in characterizing the organic part of coals and coal-related materials. The approaches have varied from pyrolysis MS (pyMS) to fast atom bombardment (FABMS) to desorption chemical ionization mass spectrometry (DCIMS). Each of these approaches has particular strengths. For example, pyMS has shown heteroatom containing molecules and field ionization MS (FIMS) has produced molecular weight distributions of volatile tars[1,2].

Laser ablation techniques have been applied to coal characterization resulting in small molecules and in some cases fullerenes at high laser powers[3-5]. Our laser desorption (LDMS) study differs from previous laser ionization mass spectrometry studies. Our goal is to desorb ions characteristic of the molecular weight distribution present in the coal sample rather than to pyrolytically ablate material from the coal surface. The desorption laser is intentionally operated close to the ionization threshold to minimize any chance for fragmenting the desorbing material. In this paper the LD/TOF mass spectrometer is described and results on the molecular weight

*This work was performed under the auspices of the Office of Basic Energy Sciences, Division of Chemical Sciences, U.S. Department of Energy, under contract number W-31-109-ENG-38.

distributions of coal derived materials are presented. These data are also compared to other mass spectral methods.

EXPERIMENTAL

Coals

A complete discussion of the characteristics of the coals used in this study has been reported. Vacuum pyrolysis tars of Upper Freeport mv bituminous coal (APCS 1) are used to compare with other ionization techniques[6]. A coal selected for a second study was a high-volatile West Virginia bituminous coal from the Lewiston-Stockton Seam (APCS 7)[7]. In this study, three groups of macerals, namely liptinite, vitrinite, and inertinite were separated by a density gradient technique and subjected to small-scale liquefaction in tetralin. The products of the liquefaction were separated into light gases and hexane-soluble (oils), toluene-soluble (asphaltenes), and tetrahydrofuran-soluble (preasphaltenes) fractions. The LD/TOF data for the toluene solubles is presented here.

Lasers

The laser light source used for laser desorption is either a XeCl-excimer laser (308 nm, 10 ns pulse-width) or a Nd:YAG laser (266 nm, 200 ps pulse-width). The lasers are operated at a 1 to 100-Hz repetition rate at a constant fluence of approximately 10-100 mJ/cm^2, close to the ionization threshold to minimize fragmentation on the surface or in the gas phase. Focusing is accomplished with a 300-mm spherical lens for the desorption laser. Positioning of the desorption laser on the 1.5 cm diameter sample is aided by a He-Ne laser collinear with the desorption laser and a closed-circuit video image of the sample surface.

Mass Spectrometer

The instrument used here is a time-of-flight mass spectrometer constructed in-house. The mass spectrometer is established by a sample surface (a stainless steel polished surface), an acceleration field, x- and y-deflection fields, and field-free region with an ion detector at the end (Figure 1).

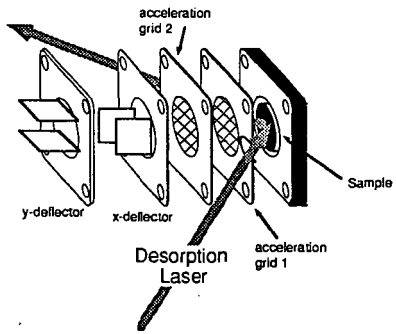

Figure 1. Schematic diagram of the ion-source region of the LD/TOF mass spectrometer.

This design is simpler than in conventional TOF instruments as the ionization source is already pulsed and therefore no pulsed acceleration voltage is needed. The resolution of the mass spectrometer is laser-pulse width limited with m/Δm of approximately 400 FWHM for the 308 nm-pulse and 1500 for the 266 nm-pulse. The mass spectrometer includes vertical and horizontal deflection plates for ion beam steering, a set of pulsed-deflection plates for eliminating high-intensity low-mass ions and an Einzel lens system. The overall flight path length is 120 cm with acceleration distances of 4 mm for each of the two acceleration regions. Ions are produced at threshold irradiances to minimize fragmentation of the desorbing molecules. The ions thus formed are accelerated to 10 keV and detected using a dual-channelplate detector with a modest post-acceleration potential. Ion currents are recorded in a LeCroy 8828 transient recorder with a maximum time resolution of 5 ns or by single-pulse counting in a LeCroy 4208 time-to-digital converter with a time resolution of 1 ns. Further processing of the data is accomplished in a PC-based software system. The typical operating vacuum is 5×10^{-9} Torr.

The samples are prepared in a nitrogen-purged isolation box by allowing solutions of the soluble coal material to evaporate as thin films on the stainless steel sample probe. Approximately 50μg of sample is placed on the probe. Less than 10^{-4} of the sample is consumed in a typical measurement. The remainder of the sample may be recovered intact following the measurement. LDMS spectra are produced by exposing the samples distributed as a thin layer on a stainless steel sample holder to the laser beam.

RESULTS AND DISCUSSION

The LD/TOF mass spectrum obtained from an Upper Freeport mv bituminous coal tar is shown in Fig. 2.

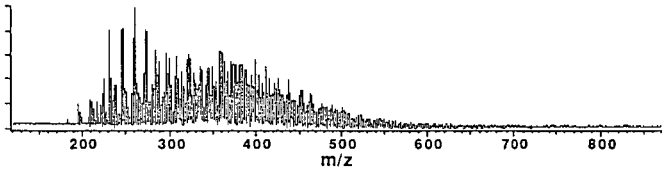

Figure 2. LD/TOF mass spectrum of Upper Freeport (APCS 1) vacuum pyrolysis tars.

The mass spectrum shows a virtual absence of ion signal below m/z 200. This is in contrast to EI and FAB, where much fragmentation is present below m/z 200. Several homologous ion series are present in the spectrum. A possible structure can be assigned to each of these series based on PyHRMS results from the same coal sample. The prominent series at m/z=230 to 272 with a Δm of 14 is assigned to alkyl-pyrenes or fluoranthenes. Another major series contains two different species, alkylphenylnaphthalenes and alkylhydroxy-pyrenes or fluoranthenes. In FAB MS the major cluster ions do not coincide with clusters seen in LD. The number average

molecular weight in the LD spectrum is 350. This compares favorably with DCI (325), while both FAB and FIMS show higher molecular weight distributions[8]. FAB and FIMS are known to be efficient in ionizing polar molecules and the higher molecular weight distributions may reflect a distribution skewed by minor amounts of higher molecular weight polar molecules.

The LD mass spectra of the toluene-soluble (asphaltenes) macerals are shown in Fig. 3.

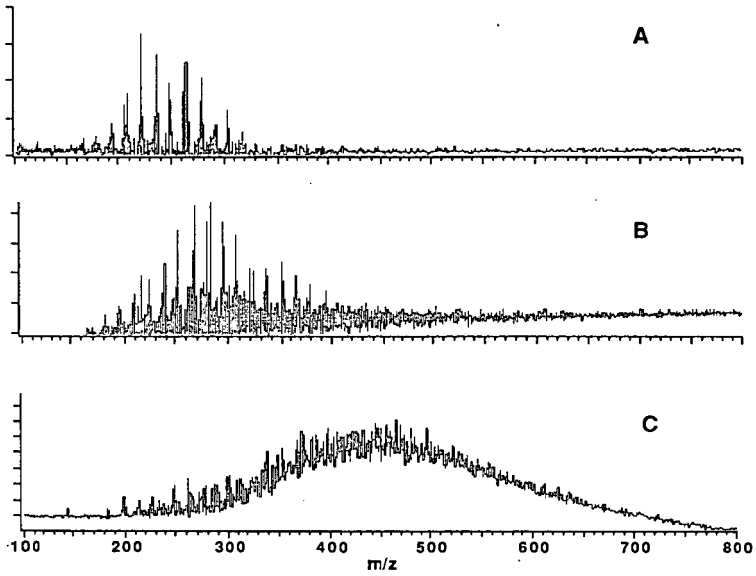

Figure 3. The LD/TOF mass spectra of toluene soluble (asphaltenes) macerals. A, liptinites; B, vitrinites; C, inertinites.

The three different maceral groups were placed in well-defined areas on a single sample probe for the mass measurement. The 200-ps 266-nm laser beam was then translated to each spot to ensure identical irradiance and desorption conditions. The first striking feature is that the LD/TOF data is consistent with carbon aromaticity and hydrogen content data. The most significant differences among the macerals are known to be their hydrogen content and carbon aromaticity[7]. The hydrogen content and the hydrogen/carbon ratio decrease in the order liptinite>vitrinite>inertinite, while the aromaticity shows the opposite trend. The inertinite, which is the least reactive maceral, is often thought to contain char-like material. It contains large multinuclear aromatic clusters. There is a clear trend of increasing average molecular weight of the ions with increasing carbon content (rank). This suggests that for a given irradiance LD/TOF is a good indicator of coal rank.

The LD/TOF MS of the liptinite (Fig. 3A) shows a single ion series separated by 14 amu extending from m/z 180 to 350. This alkyl type separation suggests a strong aliphatic methyl group content. This is supported by IR measurements. The number average molecular weight for the liptinite is 239. The vitrinite (3B) and the inertinite (3C) show increasing average molecular weights of 281 and 453. Note that the inertinite, which is thought to contain large multinuclear aromatic clusters, shows the broadest and least well-resolved spectrum. This implies a relatively low aliphatic content for the inertinite.

CONCLUSIONS

The mechanism at work in laser desorption of ions from surfaces is a subject of much speculation and conjecture. In spite of the complexity of the ionization mechanism, the fact remains that mass spectra of a large number of volatile organic compounds can be generated by laser desorption at threshold powers and that fragmentation of the parent molecule is minimal at best. Higher laser fluences may alter the ionization process to result in destructive fragmentation, in structurally significant fragmentation, or even ion-molecule reactions. Our goal here is to produce ions from the surface of coal-related samples with minimal fragmentation. For the coal products examined here, the LD/TOF mass spectra show no low m/z fragment ions and show molecular weight distributions that increase with rank. Although these are only preliminary experiments, the LD/TOF mass spectrometry approach to coal characterization looks promising with many variables in laser desorption conditions remaining to be explored.

REFERENCES

(1) Winans, R. E.; Neill, P. H..; *Multiple-heteroatom-containing sulfur compounds in a high sulfur coal*, ACS Symposium Series 429: Washington, DC, 1990; Chapter 15, pp 249-259.
(2) Schulten, H.-R.; Marzec, A. *Fuel* 1986, *65*, 855-860.
(3) Greenwood, P. F.; Strachan, M. G.; Willett, G. D.; Wilson, M. A. *Org. Mass Spectrom.* 1990, *25*, 353-362.
(4) Vastola, F. J.; Pirone, A. J. *Amer. Chem. Soc., Div. Fuel Chem., Preprints* 1966, *10*, C53-C58.
(5) Vastola, F. J.; McGahan, L. J. *Fuel* 1987, *66*, 886-889.
(6) Vorres, K. S. *Energy Fuels* 1990, *4*, 420-425.
(7) Joseph, J. T.; Fisher, R. B.; Masin, C. A.; Dyrkacz, G. R.; Bloomquist, C. A. A.; Winans, R. E. *Energy Fuels* 1991, *Submitted*.
(8) Winans, R. E.; McBeth, R. L.; Hunt, J. E.; Melnikov, P. E. In *1991 International Conference on Coal Science*; University of Newcastle upon Tyne, UK, September 16-20, 1991, *Submitted*.

RAPID ANALYSIS USING DIRECT SAMPLING MASS SPECTROMETRY*

Michelle V. Buchanan, Robert L. Hettich, and Marcus B. Wise
Analytical Chemistry Division, Building 4500-S
Oak Ridge National Laboratory
Oak Ridge, TN 37831-6120

Key Words: Ion trap mass spectrometry; crude oil characterization; rapid analysis

INTRODUCTION

Mass spectrometry instrumentation has undergone substantial changes recently due to the advent of trapped ion techniques such as Fourier transform ion cyclotron resonance mass spectrometry[1] (commonly referred to as FTMS) and rf quadrupole mass spectrometers[2]. The introduction of these highly versatile instruments have opened up exciting new applications of mass spectrometry to environmental measurements, biomolecule characterization, molecular dosimetry, materials science, and others. We have been investigating the use of quadrupole ion traps for the rapid, sensitive detection of compounds in a variety of matrices, including water, soil, air, oils, food, and physiological media. In these studies, methods for the direct introduction of the analyte into the quadrupole ion trap have been developed which require little or no sample preparation steps, resulting in analysis times of about 3 minutes and detection limits commonly in the low picogram range. In this paper, applications of this new analytical approach to the characterization of fossil-derived fuels will be described.

EXPERIMENTAL

A Finnigan ion trap mass spectrometer (ITMS) was used in these studies and was specially modified with an electropolished vacuum chamber and two 330 L/sec turbomolecular pumps to increase pumping speed and reduce background signals. Samples are placed in a 40 mL glass vial and closed with a teflon-lined septum screw cap fitted with two lengths of 1/16 inch tubing. One length of tubing extends to near the bottom of the vial and is used to introduce a flow of helium purge gas. The other length of tubing extends just beneath the vial cap and is used to transport the purged materials into the ITMS. The oil samples were diluted in methylene chloride/methanol and a few microliters of the resulting solution was spiked into distilled water. Water was used as the chemical ionization reagent.

For the gas chromatographic studies, a Hewlett-Packard 5990 GC was employed with a flame ionization detector. An aliquot of each oil sample diluted in methylene chloride was injected onto a 40 meter, DB-5 capillary column programmed to hold at 50 °C for 10 minutes, and then ramp to 280 °C at 5 °C/minute. Each chromatographic run took approximately 100 minutes.

For the combined gas chromatography/mass spectrometry studies, a Hewlett-Packard 5985 GC/MS was used. An aliquot of each oil sample in methylene chloride was injected onto a 30 meter, DB-5 capillary column programmed to hold at 50 °C for 5 minutes and then ramp to 280 °C at 20 °C/minute. Methanol was used as a chemical ionization (CI) reagent and was introduced through the direct insertion probe. A mass spectrum was taken every 3 seconds during the chromatographic run, with the entire GC run taking approximately 30 minutes.

Crude oil samples were obtained from the National Institute for Petroleum and Energy Research, Bartlesville, OK.

RESULTS AND DISCUSSION

A gas chromatograph equipped with a flame ionization detector was initially used to profile the twelve crude oil samples. Figure 1 shows chromatographic profiles of two oils, 90SPR53 (Iraq) and 75047 (Iran), and illustrates the hydrocarbon patterns observed for most of the oil samples. As expected, these oils consist mainly of aliphatic hydrocarbons (paraffins), with other minor components present. The chromatograms from

all of the samples were qualitatively quite similar and differed primarily in the abundance of the paraffins. Small differences in the minor components were observed in some cases, although the ability to differentiate the oils based only on this information was very difficult. In addition, the chromatographic analysis required 100 minutes.

In order to selectively examine the non-paraffin components of these oil samples, methanol chemical ionization GC/MS was used. Methanol chemical ionization permitted selective protonation of the alkyl aromatic hydrocarbons, alkenes, and heteroatom-containing hydrocarbons present in the samples, while eliminating ionization of the more abundant paraffins. The resulting mass spectra for these oils consisted primarily of alkyl aromatics, C_2- to C_7-benzenes and C_0- to C_4-naphthalenes, as shown in Figures 2 and 3, respectively. Selected ion chromatograms of the alkyl benzenes and alkyl naphthalenes revealed differences in the relative and absolute abundances of these components in the various oil samples, but the ion signal levels were quite low in most cases and may be difficult to reproducibly quantitate. In these GC/MS studies, because the alkyl aromatics were selectively detected and only classes of compounds were quantitated, less chromatographic resolution was required than in the GC FID studies and a faster column program was employed. However, the GC/MS analysis still required approximately 30 minutes.

Previous research in our laboratory has demonstrated the capability of purging volatile samples from an aqueous matrix directly into an ion trap mass spectrometer without chromatographic separation[3]. This method, called direct sampling ion trap mass spectrometry (DS ITMS) has been used as a rapid, sensitive means of differentiating a series of fuels, including gasoline, diesel, and jet fuels. The volatile components from the oil are then purged from the solution with helium directly into the transfer line of the ITMS (no chromatographic separation is used). The effluent entering the ITMS is ionized using water chemical ionization (the water purged from the sample is used as the chemical ionization reagent). This method allows selective ionization of alkyl aromatics and heteroatom-containing hydrocarbons but not the paraffins. Using this approach, all the volatile components from the oils could be characterized with the total analysis requiring approximately 3 minutes, as compared to 30-100 minutes for the chromatographic analysis. In addition, the remarkable sensitivity and versatility of the ITMS provided detailed information on trace levels of compounds that are characteristic of each oil.

This same DS ITMS approach was adapted to differentiate the crude oil samples. Figure 4 illustrates the total ion purge profile and extracted ion profiles for C_2-benzenes (m/z 107) and C_3-benzenes (m/z 121) for oil 90SPR53. The entire experiment required approximately three minutes. Figure 5 represents the mass spectrum obtained approximately 2 minutes into the purge and reveals the ions observed from this sample. Ions at m/z 83, 85, and 96 originate from the solvent and are present in the blank. The ions with m/z 93, 107, 121, 135, and 149 arise from C_1- to C_5-alkyl benzenes present in the oil sample.

Table 1 is the resulting compilation of relative ion abundances for the alkyl aromatics from the 12 crude oils studied thus far by ITMS. Because the signal from C_2-benzenes at m/z 107 was usually the most abundant, all other ion abundances were normalized to its intensity. The samples were run in duplicate (some were acquired in triplicate), and the precision of the measurements are also included in Table 1. From these data, it may be seen that differentiation of many crude oils is possible using these ion ratios. Note that oils 74023 and 69080 yield similar ion abundance ratios and that they are from the same oil field, but sampled in different years, 1974 and 1969, respectively. In some cases, however, even though the relative ion ratios are similar, the absolute abundances of the alkyl aromatics vary considerably. This is shown in the bar graph in Figure 6, where absolute abundances of the ion with m/z 107 is illustrated. In the case of 90SPR53 and 75047, where the ion abundance ratios in Table 1 prohibit clear distinction of the crude oils, the differences in the absolute abundances of m/z 107 permit their differentiation. In order to quantitatively compare absolute ion abundances, an internal standard (possibly deuterated xylene) should be added to the oil samples prior to analysis to provide a standard ion for comparison.

These low molecular weight alkyl aromatics may not be the best components for the identification process, however, because "weathering" of the oils could lead to losses from volatilization, changing the relative and absolute abundances of the monitored ions. Thermal desorption ITMS, another type of DS ITMS technique developed in our laboratory, could be used to examine the less volatile, higher molecular weight constituents

of the oils (e.g., naphthalenes, phenanthrenes, etc.), which should be less susceptible to "weathering". The thermal desorption method employs rapid heating of a small aliquot of the neat sample to analyze compounds with lower volatilities by ITMS.

CONCLUSIONS

In this study, the potential of DS ITMS for the rapid differentiation of crude oils was examined. Twelve Middle Eastern crude oils were analyzed by GC FID, GC/MS, and DS ITMS. The GC FID chromatograms, which required approximately 100 minutes each to acquire, were qualitatively quite similar, making differentiation of various oils difficult. GC/MS using methanol chemical ionization provided selective ionization of alkyl aromatics and heteroatom-containing hydrocarbons in the presence of aliphatic compounds. However, this technique requires approximately 30 minutes per analysis and generated ion signal levels which were quite low and were difficult to reproducibly quantitate. Some differences in the alkyl aromatic hydrocarbons ratios of the different oils were observed, however. Direct sampling ITMS, using water chemical ionization, of oil samples provided a rapid, sensitive method of examining the abundances of volatile components in the samples. Examination of the ion ratios of the alkyl aromatics provided differentiation for most of the oil samples. Further differentiation could be obtained by comparing absolute ion abundances. Addition of an internal standard, such as a deuterated xylene, would allow the absolute ion abundances to be determined more accurately. The DS ITMS technique required a total analysis time of only three minutes compared with 30 to 100 minutes for chromatography-based techniques.

REFERENCES

[1]M. V. Buchanan and M. B. Comisarow, in "Fourier Transform Mass Spectrometry",American Chemical Society, ed. M. V. Buchanan, American Chemical Society, Washington, 1987, pp.1-20.

[2]R. G. Cooks and R. E. Kaiser, Jr., Acc. of Chem. Res., **23**, 213 (1990).

[3]M. B. Wise, M. V. Buchanan, and M. R. Guerin, "Rapid Determination of Target Compounds in Environmental Samples Using Direct Sampling Ion Trap Mass Spectrometry," Proceedings, 38th ASMS Conference on Mass Spectrometry and Allied Topics, June 3-8, 1990, Tucson, AZ, pp. 619-620.

*Research sponsored by the Space and Defense Technology Program, Martin Marietta Energy Systems, Inc., under contract DE-AC05-84OR21400 with the U.S. Department of Energy.

Table 1. Low Abundance Ratios for Twelve Middle Eastern Crudes Determined by DS ITMS

Oil Sample ID*	121/107	135/107	149/107	93/107
90SPR53[a]	0.90 ± .02	0.49 ± .03	0.09 ± .01	0.58 ± .02
75047[b]	0.89 ± .02	0.51 ± .02	0.15 ± .01	0.68 ± .05
70007[c]	0.91 ± .03	0.51 ± .02	0.11 ± .006	0.62 ± .05
67066[d]	0.91 ± .03	0.61 ± .01	0.15 ± .004	0.71 ± .05
70070[d]	0.85 ± .002	0.50 ± .01	0.09 ± .01	0.75 ± .003
69068[e]	0.87 ± .02	0.52 ± .01	0.12 ± .02	0.66 ± .04
72022[e]	1.23 ± .02	0.85 ± .02	0.23 ± .02	0.73 ± .001
74023[b**]	0.82 ± .02	0.47 ± .02	0.11 ± .001	0.68 ± .03
69080[b**]	0.80 ± .01	0.45 ± .03	0.10 ± .002	0.73 ± .01
69085[b]	0.76 ± .01	0.35 ± .01	0.07 ± .004	0.74 ± .02
69086[b]	0.72 ± .01	0.40 ± .02	0.11 ± .03	0.87 ± .10
70113[b]	0.83 ± .001	0.42 ± .02	0.10 ± .02	0.68 ± .02

Country of Origin: [a]Iraq, [b]Iran, [c]United Arab Emirates, [d]Saudi Arabia, [e]Kuwait

*Identities assigned by National Institute for Petroleum and Energy Research, Bartlesville, OK.

**Oil from same field, but one sampled in 1974 and other in 1969.

Figure 1. Gas Chromatographic Profiles of Two Crudes. Total Analysis Time 100 Minutes.

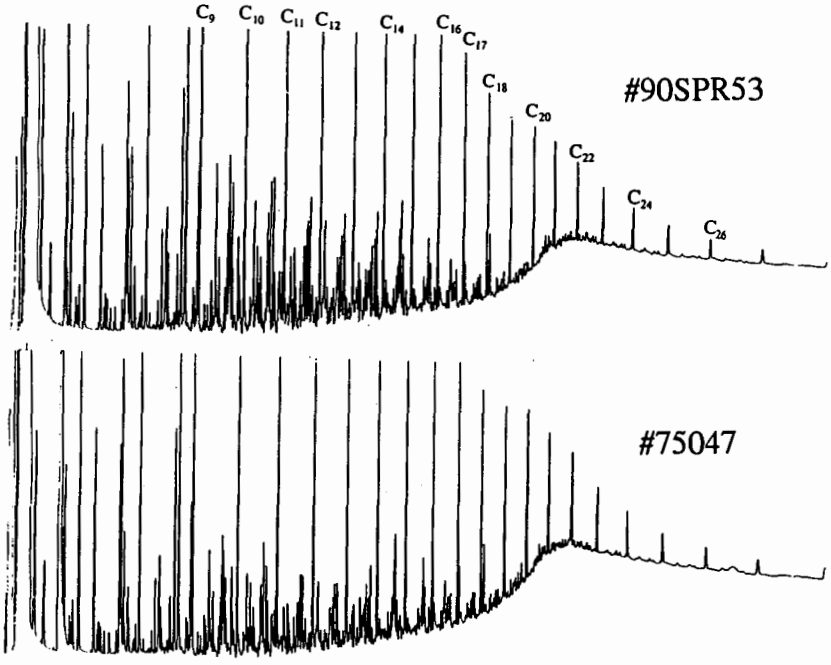

Figure 2. Extracted Ion Chromatograms for C2-C7 Alkyl Benzenes from Oil #90SPR53 Obtained by Methanol CI GC/MS.

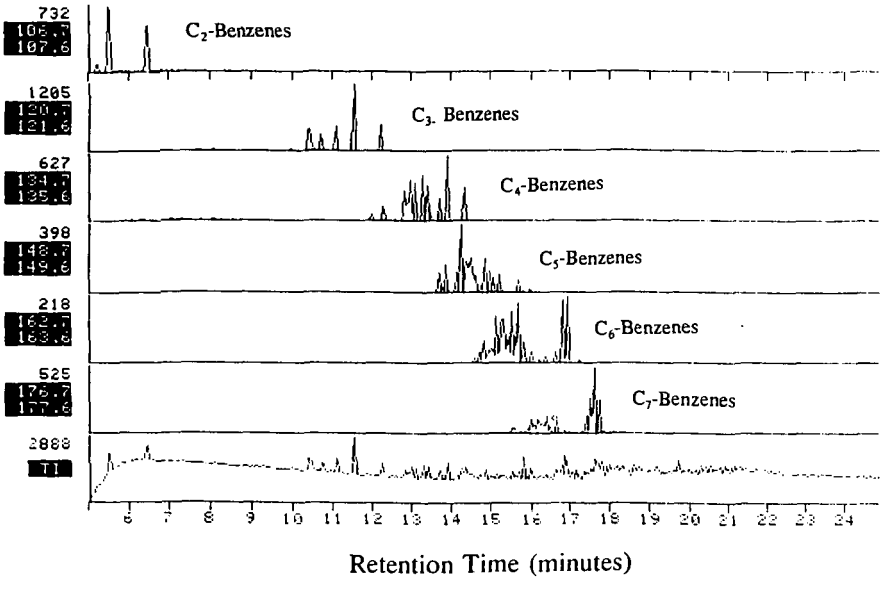

Figure 3. Extracted Ion Chromatograms for CO-C4 Alkyl Naphthalenes from Oil #90SPR53 Obtained by Methanol CI GC/MS.

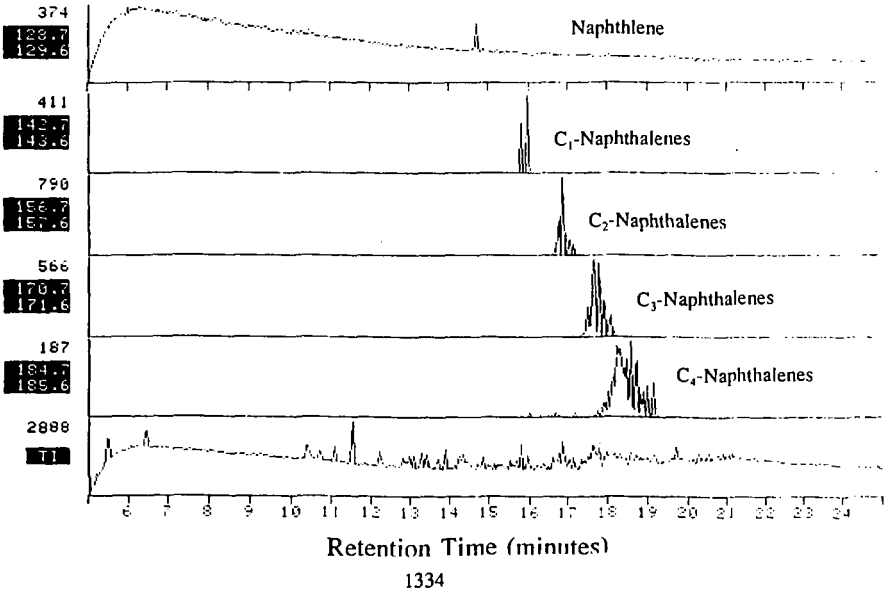

Figure 4. DS ITMS Purge Profile for Oil 90SPR531, Water CI.

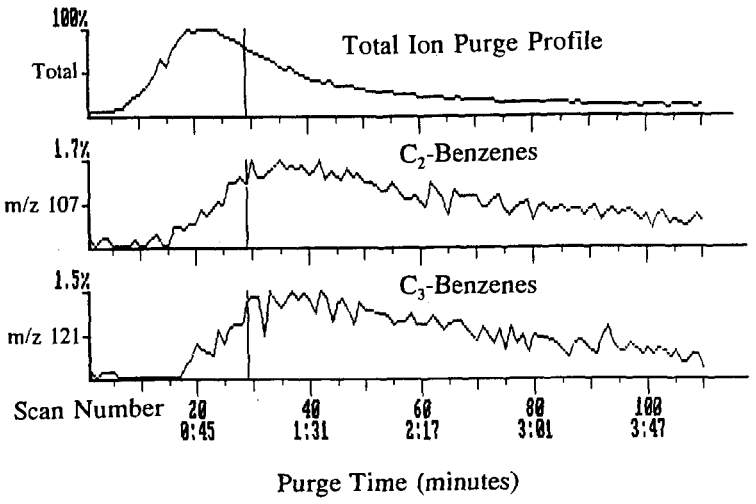

Figure 5. Water CI Mass Spectrum Taken 2 Minutes Into Purge Shown Above.

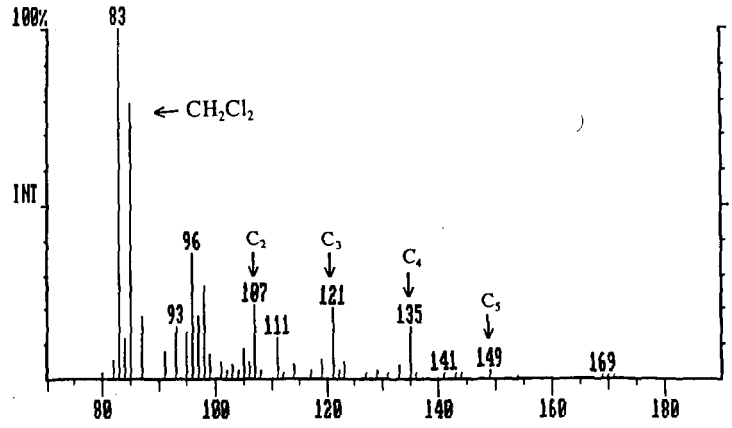

Figure 6. Absolute Abundance m/z 107. Direct Purge ITMS.

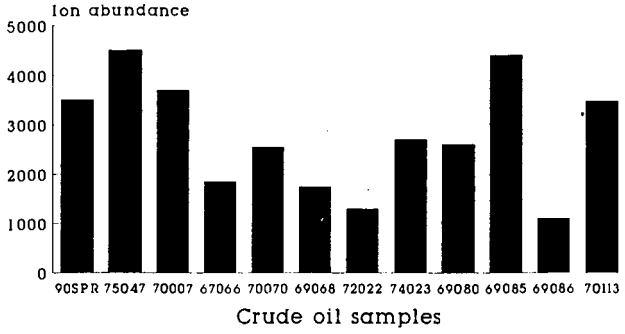

MECHANISM OF SUCCESSIVE SOLVOLYTIC EXTRACTION OF COAL

D. K. Sharma and S. K. Singh
Centre for Energy Studies,
Indian Institute of Technology, Delhi
Hauz Khas, New Delhi-110016, INDIA

KEYWORDS: Coal, Extraction, Solvents

Coal macromolecules are associated (interlocked and intermeshed) with each other so strongly that it generally requires stronger conditions for extraction or solubilization of more than 10-20% of coal. Extraction of coal in an organic solvent is an essential requirement for the conversion of coal to value added fuels and chemicals without a significant loss in original coal constitution and its energy. As a part of our large program on development of convenient and cost effective techniques for solvent extraction of coal under atmospheric pressure conditions using coal derived chemicals, work on successive extraction of coal using anthracene oil-quinoline (Qn) - liquid paraffin (LP) and anthracene oil (AO) - ethylenediamine (EDA) - liquid paraffin was undertaken. The procedure for the successive extraction of coal using different solvents for 24h extraction, has been reported earlier (1). In fact, Assam coal, Talcher coal and Neyveli lignite (analysis shown in Table 1) when subjected to successive solvent extraction (for 24h in each solvent), i.e., anthracene oil-ethylenediamine-liquid paraffin solvents showed 70% extraction of Assam coal, 59% extraction of Talcher coal, and 63% of Neyveli lignite. This was more than that observed using AO-Qn-LP solvents in successive extractions (Table-2) (1).

Table - 1: Analysis of Coals and Lignite

Proximate Analysis: On Dry Basis (%)

Coal	Moisture	Mineral Matter	Volatile Matter	Fixed Carbon
Assam Coal	2.8	8.3	42.0	46.9
Talcher Coal	2.1	16.9	38.8	42.2
Neyveli Lignite	8.7	6.1	46.6	38.6

Ultimate Analysis (% on Dry Mineral Matter Free Basis)

Coal	Carbon	Hydrogen	Sulfur	Nitrogen	Oxygen	Atomic H/C	Atomic O/C
Assam Coal	77.0	5.7	3.8	1.5	12.0	0.88	0.12
Talcher Coal	74.8	5.3	1.0	1.6	17.3	0.87	0.17
Neyveli-Lignite	62.0	5.3	1.4	0.9	30.4	1.02	0.37

The observations showed that there are solvents which are capable of successively extracting coal resulting in 60-70% extraction of coal. In fact, maximum extraction of Assam coal was found to be in AO and this was 36%. This showed that a major portion of coal (64%) remains unextracted. The reason for this could be that the concentration gradient created by AO inside the solid coal and outside in the coal extract reaches a saturation stage and further

extraction in AO is not possible. This is the limit to which coal molecules can be associated with AO. Some of AO also gets into solid coal that is, it gets dissolved in coal. This mutual solubility is because of the reason that like dissolves like, as the major part of macromolecular and polyaromatic heterogeneous structure of coal resembles that of the constituents present in AO, especially phenanthrene and carbazole.

Table - 2: Successive Solvolytic Extraction of Coals Using AO-EDA-LP and AO-Qn-LP Solvent Systems

Coal Sample	Extractability (%) AO	EDA	QN	LP	Total Extraction Yield On Original Coal Wt. Basis	On DMMF Basis
Assam Coal	33	26	*	28	65	70
Assam Coal	33	*	23	22	60	65
Talcher Coal	22	25	*	10	48	59
Talcher Coal	22	*	15	9	40	48
Neyveli Lignite	30	30	*	21	61	63
Neyveli Lignite	30	*	22	23	58	60

* This particular solvent was not used in the successive extraction
DMMF - Dry mineral matter free
Wt. - Weight

These studies showed that the structure of coal is flexible so as to hold solvent molecules between its molecules. In fact, this flexibility of intra and intermolecular bondings in coal molecules renders further extractable the residual coal obtained after AO extraction, in solvents such as Qn, EDA or LP. High boiling solvents such as LP (boiling range 330-350°C) are capable of energizing and stretching the coal macromolecules to such limits that these molecules are disintegrated and thus, reorient and repolymerize after extraction.

Flexibility of coal structure and mobility of loosened molecules is responsible for the successive extraction of coal in solvents having different chemical characteristics. In fact, coal has a heterogeneous structure having different structural units i.e., polyaromatic, hydroaromatic and paraffinic units linked through C-C, C-N-C, C-O-C and C-S-C linkages. The solvents having structural similarities with the structural units present in coal can easily dissociate and mobilize the coal molecules for their solution in that solvent. The extent of similarity between the structures of coal and that of the solvent and the boiling point of the solvent were generally found to determine the extent of extractability of coal.

The swelling ratio in Qn of the residual coal obtained after AO extraction was found to be more than that of the original coal (1). This showed that AO extraction results in reducing the degree of cross-linking in the structure of coal. However, extraction of coal in EDA or LP was found to result in an increase in the degree of cross-linking in the structure of coal, as revealed by the swelling studies. Probably, entrapment of EDA in coal would have resulted in the increase in the cross-linking in the structure of coal. LP extraction, being a high temperature extraction in a nonreactive and less interactive solvent, would result in the residual coal having a repolymerized cross-linked structure. The IR spectral studies of the residual coal obtained after the extraction of coal in AO or EDA or LP were found to show an increase in the aromatic character and a decrease in aliphatic character. The absorptions due to C=O group were missing in all the extracted coal residues obtained using AO or EDA or LP as a solvent. The percentage carbon and the atomic H/C ratios of the residual coals obtained after extraction in different solvents were also found to have been decreased in

comparison to those of the starting coal. This showed that coal might have undergone depolymerization, degradation and dehydrogenation as a result of extraction in AO, EDA or LP.

If the extraction results obtained after successive extraction in AO-EDA-LP solvents are analyzed then it can be seen that each solvent can extract its share of coal products that is structural moieties from coal which resemble its structure or properties. In fact, each solvent would extract the coal and would chemically depolymerize or degrade the coal for rendering it extractable in the next solvent of the successive extraction sequence to allow the extraction of increased amount of coal. The depolymerizing, degrading and molecular dispersing or dissociating ability of AO and EDA was found to be more than that of LP. In fact, preextraction with LP had an adverse effect on the successive extraction in AO or in Qn (1) or in EDA.

The point or position of attack i.e. chemical depolymerization or physical dissociation or dispersion of coal, by different solvents can be different depending upon the bond strength or the particular structural similarities between the coal and the solvent and of course, depending on boiling point of the solvent. Anthracene oil was found to be a wonder solvent for extraction of coal and for depolymerizing the coal (both chemically and physically) to render the enhanced amount of the (AO treated) residual coal in the next solvent, i.e., EDA, QN or LP. Orchin et al. (2) have reported the extraction studies on coals using different polynuclear aromatic compound such as phenanthrene, carbazole, pyrene, anthracene, fluoranthene, phenanthridine, fluorene, and diphenyl, etc. The actual three dimensional shape and size of the solvent molecule (especially angular arrangement of condensed aromatic rings instead of linear) were reported to be important factors for the ability of solvents to dissolve and disperse coal. Similarity of coal structure with angular ring phenanthrene type molecules (present in AO) allows the free passage (inside and outside) to these molecules inside the solid coal. This similarity of structures also helps in breaking the coal-coal (molecular) physical interactions such as London, vander Waals forces and H-bondings, by the solvents such as AO.

Since the coal structure is heterogeneous, therefore, a successive multiple solvent attack has been found to be a good way to loosen, unleash, unlock inter and intramolecular forces and disperse and to physically and chemically depolymerize the three-dimensional cross-linked gel structure of coal macromolecules for getting enhanced extraction without using any high pressure technique involving hydrogenation at elevated temperatures. Successive solvolytic extraction of coal affords a convenient and cost effective technique for solvent refining of coal under ambient pressure conditions.

Acknowledgements

The authors thank the Council of Scientific and Industrial Research, New Delhi, India for financial support.

References

1. Sharma, D.K. and Mishra, S., Energy and Fuels, 3, 641 (1989).

2. Orchin, M., Golumbic, C., Anderson, J.E., and Storch, H.H., Bulletin 505, Bureau of Mines, United States Govt. Printing Office, Washington 1951.

EFFECT OF MOISTURE ON THE SORPTION OF CO_2 BY COAL

V. C. Menon, C. A. Leon y Leon, T. Kyotani and L. R. Radovic
Fuel Science Program
Department of Materials Science and Engineering
The Pennsylvania State University, University Park, PA 16802

Keywords: CO_2 Adsorption, Coal Swelling, Moisture Effects

INTRODUCTION

It is well known that coal deposits contain varying amounts of moisture adsorbed or occluded within void spaces [1]. Coal seams are also known to contain varying amounts of gases such as methane and CO_2 [2]. Even though the presence of moisture is likely to reduce the gas storage capacity of coals [3,4], the reasons for such an occurrence are not well understood. Knowledge of the gas storage capacity of coals is of fundamental importance for coalbed methane studies. Therefore, it is of interest to investigate in detail the role of moisture in affecting the sorption of gases by coals. The presence of moisture in coals can affect the sorption of gases in the following ways: (a) gas dissolution; (b) pore blockage/filling; and (c) structural changes due to coal swelling. These effects have been addressed by (a) using CO_2 as sorbing gas (since it is present in coalbeds, it dissolves in water and it is often used to characterize the coal structure), and (b) using two coals having different swelling tendencies in water.

EXPERIMENTAL

Table 1 shows the ASTM proximate and elemental analyses of the coals used in this study. In both cases, coal powders (-20 Tyler mesh) were studied under dry and moist conditions. Dry conditions were achieved by subjecting the samples to evacuation at ca. 10^{-3} torr and 115°C overnight. Moist coals were prepared using an "incipient wetness" technique [5], which consisted in adding drops of distilled/deionized water to 1 g of coal and stirring until a muddy material remained. The amounts of water required

for achieving incipient wetness (Table 2) were 1.9 and 6.6 times greater than the equilibrium moisture contents for Mary Lee and (the more easily wetted) New Mexico coals, respectively.

Low pressure (0-830 torr) volumetric CO_2 sorption experiments were performed at 25°C using a Carlo Erba Sorptomatic 1800 apparatus. When moist samples were used, it was necessary to correct the equilibrium pressures for the contribution due to water evaporation. This was done by assuming that water evaporation reached equilibrium well within the time frame of the measurements. In addition, a further correction was applied to the CO_2 equilibrium pressure data to account for the amount of CO_2 dissolved in the water contained by the coal. In this case, both equilibrium CO_2 dissolution and the applicability of Henry's Law were assumed.

Moisture-induced swelling effects were assessed by performing experiments following a procedure described by Green et al. [6]. In essence, the volume expansion caused by the addition of water to 1 g of -100 Tyler Mesh coals (after centrifugation) was measured, and was expressed as swelling ratios (Table 2).

RESULTS AND DISCUSSION

CO_2 Sorption Capacity of Dry vs. Moist Coals. Figure 1 shows the CO_2 sorption isotherms for both dry and moist samples of Mary Lee and New Mexico coals. For both coals it is shown that the CO_2 adsorption capacity decreases in the presence of moisture. Similar results were reported for CO_2 sorption on lignites [3] and for CH_4 sorption on bituminous coals [4]. At very low relative pressures, the (typically concave downwards) shapes of the isotherms are affected by nonequilibrium conditions, as evidenced by the shapes of the respective Dubinin-Radushkevich (D-R) plots (Figure 2) [7]. The corresponding D-R equivalent surface areas for both dry coals (Table 2) are of reasonable magnitude compared to reported values [8]. Moist coals also provide D-R surface area estimates in close agreement with those of their dry counterparts (Table 2). Therefore, the equivalent CO_2 D-R

surface areas appear to be independent of the presence of moisture in the coals. Similarly, micropore volumes (obtained by extrapolation of D-R plots to saturation pressure) are comparable for both moist and dry samples of each coal. Hence, at pressures close to saturation the presence of moisture appears to have little bearing on the CO_2 sorption capacity of coals. On the other hand, at low pressures there are clear differences in CO_2 sorption capacity between dry and moist samples of each coal, with the latter taking up less CO_2 than the former.

Contribution by CO_2 Dissolution to CO_2 Sorption. Figure 3 shows the variation in the calculated equilibrium amounts of CO_2 dissolved in the moisture of each coal (assuming that the moisture consists of pure water) with CO_2 partial pressure. These values, obtained using the amounts of water required to reach incipient wetness (Table 2), are seen to be very small in comparison with the total CO_2 uptakes of each coal (Figure 3). Incipient wetness water values provide upper limits for the moisture contents of these coals, and are presumably comparable to the maximum moisture holding capacities of similar coals. Therefore, it is concluded that the dissolution of CO_2 does not contribute significantly to the CO_2 sorption by bituminous coals, at least at low relative pressures.

Contribution by Pore Blockage/Filling to CO_2 Sorption. To account for the moisture-related decrease in CH_4 sorption by bituminous coals, Joubert et al. suggested that some water molecules can effectively block pore entrances through specific interaction with oxygen functional groups in the coals [4]. These authors based their reasoning on the observation that the moisture-induced suppression in CH_4 sorption (and in Langmuir equivalent CH_4 surface area) was proportional to the oxygen content of the coals [4]. The same trend is observed for CO_2 sorption in the present study (see Table 2 and Figure 1). However, the moisture-induced decrease in CO_2 sorption in our case is independent of the D-R equivalent CO_2 surface areas and, especially, the D-R micropore volumes of these coals (Table 2). The latter

observation suggests that the access of CO_2 to the coal pores is not restricted by the presence of moisture.

Contribution by Coal Swelling to CO_2 Sorption. Swelling ratios for the coals investigated differ significantly (Table 2), and are comparable to those reported for low rank coals [3,9]. In the presence of moisture, the more swelling coal, New Mexico, was found to experience a much more drastic reduction in CO_2 sorption capacity than the relatively non-swelling coal, Mary Lee (Figure 1). Studies of swelling-related structural changes in lignites using N_2 sorption [3] indicate that drying induces a collapse of macro- and mesopores, as well as undetectable changes in microporosity which parallel an increase in CO_2 sorption. The latter is in agreement with our observations at low relative pressures (Figure 1). Since CO_2 sorption at low pressures occurs by the preferential volume filling of the narrowest micropores (i.e., those with the highest sorption potentials) [7], the above results are best interpreted by postulating that the micropore diameters decrease upon drying. It follows that micropore diameters should increase when in contact with moisture, especially for swelling coals. This would explain why moisture limits the CO_2 sorption capacity of coals in the following way: (a) in the absence of moisture, CO_2 can penetrate and fill all accessible micropores; (b) in the presence of moisture, average micropore diameters increase, without necessarily involving a loss in micropore volumes (Table 2); (c) the increase in average micropore diameters limits the number of narrower pores that serve as sorption sites for CO_2 at low relative pressures, and hence causes a decrease in the low-pressure CO_2 sorption capacity of the coals (Figure 1); (d) the increase in average micropore diameters is more marked for swelling coals (Table 2), and consequently their CO_2 sorption capacity is more sensitive to the presence of moisture; (e) at higher relative CO_2 pressures, enough CO_2 is available to populate the wider micropores (i.e., those with lower adsorption potentials), and eventually at saturation conditions all accessible micropore volume is filled with CO_2 regardless of the presence of moisture.

CONCLUSIONS

The CO_2 sorption capacity of two bituminous coals at low pressures (up to 830 torr) decreases in the presence of moisture. This contrasts the fact that their micropore volumes, obtained from the corresponding D-R plots, are comparable for both moist and dry coals. The contribution of CO_2 dissolution to its sorption was found to be negligible. The reduction in CO_2 sorption capacity is very significant for the more swelling coal compared to that of the less swelling coal. This remarkable reduction is possibly related to an increase in the average diameter of micropores as a result of swelling, rather than to blockage of pores by moisture.

ACKNOWLEDGEMENTS

Support for this work was provided by the Gas Research Institute, Contract No. 5090-260-1987. The authors also thank Prof. B. McEnaney (University of Bath, U.K.) for helpful comments.

REFERENCES

1. Nelson, C.R., in "Chemistry of Coal Weathering" (C.R. Nelson, Ed.), Elsevier, Amsterdam (1989), Ch.1.
2. Thimons, E.D. and Kissell, F.N., Fuel 52, 274 (1973).
3. Deevi, S.C. and Suuberg, E.M., Fuel 66, 454 (1987).
4. Joubert, J.I., Grein, C.T. and Bienstock, D., Fuel 52, 181 (1973).
5. Solar, J.M., Leon y Leon, C.A., Osseo-Asare, K. and Radovic, L.R., Carbon 28, 369 (1990).
6. Green, T.K., Kovak, J. and Larsen, J.W., Fuel 63, 935 (1984).
7. Linares-Solano, A., in "Carbon and Coal Gasification" (J.L. Figueiredo and J.A. Moulijn, Ed.), NATO ASI Series E-105, Dordretch (1986), p. 167.
8. Mahajan, O.P., in "Coal Structure," Academic Press, New York (1982), p. 51.
9. Yost, R.S. and Creasy, D.E., Fuel 69, 648 (1990).

Table 1. Proximate and Ultimate Analyses of Coals Used

PSU NUMBER	PSOC 1469	PSOC 1446
SEAM NAME	MARY LEE	NEW MEXICO # 8
STATE	ALABAMA	NEW MEXICO
COUNTY	WALKER	SAN JUAN
TOWNSHIP / CITY	GOODSPRINGS	FRUITLAND
RANK	HV bit. A	HV bit. C
PROXIMATE ANALYSIS		
% MOISTURE	1.9	11.2
% ASH	20.6	18.5
% VOLATILES	27.3	33.5
% FIXED CARBON	50.2	36.8
ULTIMATE ANALYSIS (daf)		
% CARBON	84.9	77.3
% HYDROGEN	5.7	5.0
% NITROGEN	1.8	1.6
% SULPHUR	1.0	1.1
% OXYGEN (diff.)	6.6	15.0

Table 2. Properties of Coals Used

PSU NUMBER	PSOC 1469	PSOC 1446
% OXYGEN (daf, diff.)	6.6	15.0
% EQUILIBRIUM MOISTURE	7.2	12.1
INCIPIENT WETNESS VOLUME (cc/g)	0.14	0.80
MICROPORE VOLUME (cc/g)		
DRY	0.14	0.07
MOIST (CORRECTED)	0.15	0.08
BET N_2 SURFACE AREA (m^2/g)		
DRY	26	16
CO_2 SURFACE AREA (m^2/g)		
DRY	162	105
MOIST (CORRECTED)	156	93
MICROPORE SLIT WIDTH (nm)		
DRY	1.8	1.4
MOIST (CORRECTED)	1.9	1.8
SWELLING RATIO	1.09	1.29

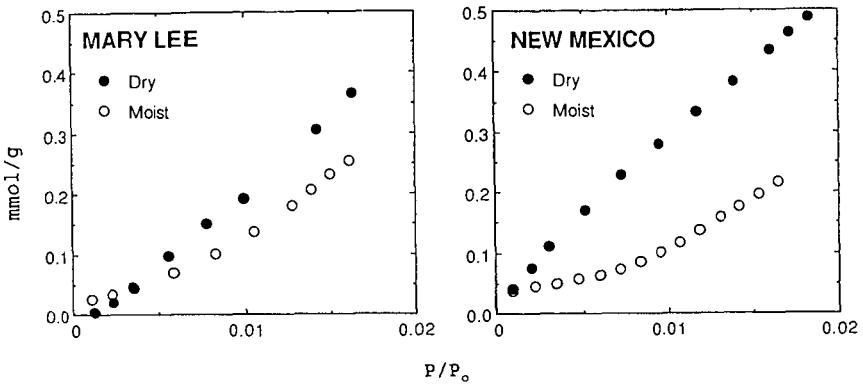

Figure 1. CO_2 adsorption isotherms.

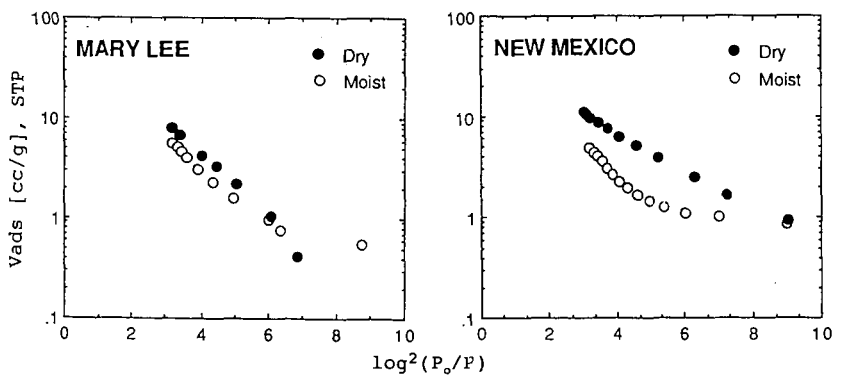

Figure 2. Dubinin-Radushkevich plots.

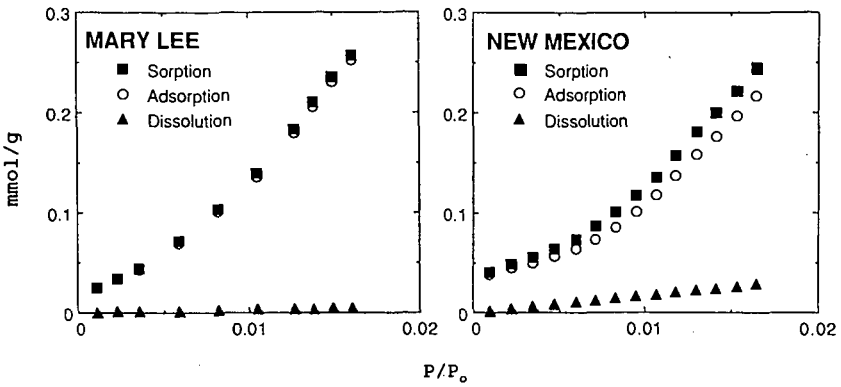

Figure 3. Contribution by dissolution to CO_2 sorption isotherms.

CHARACTERIZATION OF INSOLUBLE ORGANIC MATTER ASSOCIATED WITH CLAY MINERALS FROM SYNCRUDE SLUDGE POND TAILINGS*

Abdul Majid, Bryan D. Sparks and John A. Ripmeester
National Research Council of Canada
Institute for Environmental Chemistry
Ottawa, Ontario, K1A 0R9, CANADA

Keywords: Syncrude Sludge, Insoluble Organic Matter, Humic Matter

Hot water extraction of bitumen from Alberta oil sands generates large quantities of tailings slurry. The fine grained sludge component of this waste is the most troublesome because of its stability and poor compaction potential. Dispersed bitumen, and organic matter that is insoluble in common solvents (IOM), are associated with the fines contained in these clay slimes. This organic matter is believed to be partly responsible for the intractability of the sludge, and it could therefore play an important role in determining the behavioural characteristics of oil sand slimes. In previous investigations we had attempted to enrich the insoluble organic matter by dissolving the minerals in concentrated HCl/HF. As a result of this treatment the inorganic material is decomposed, but the organic constituents are also likely to undergo significant changes. In the present work we have attempted a milder HCl/HF treatment for mineral dissolution. The results from the current investigation are compared with the results of the previous study to assess the chemical alterations of the organic matter resulting from the two treatments.

INTRODUCTION

Hot water extraction of bitumen from Alberta oil sands generates large quantities of tailings slurry.[1-4] These tailings consist mainly of sand and an aqueous dispersion of various clay minerals, some of which are associated with significant amounts of insoluble organic matter (IOM).[5-10] This IOM is believed to be partly responsible for the intractibility of the sludge and could therefore play an important role in determining the nature of slime stability.[1,5] It is believed that the IOM causes the clay particle surfaces to develop a hydrophobic character, allowing particle bridging, by means of residual bitumen, thereby setting up a weak gel structure.

In previous work, IOM from a number of oil sands tailing streams as well as oil sand feedstock samples has been isolated and characterized.[5,7-9,11] IOM was enriched by decomposing the inorganic material with concentrated HCl/HF, which might have resulted in the chemical alterations of the organic constituents. In this investigation we have attempted a milder HCl/HF treatment for mineral dissolution. The results from the studies using mild or severe extraction conditions have been compared in order to assess any chemical alterations that might have occurred during the deashing procedure.

EXPERIMENTAL

Sample description and isolation procedure for organic rich solids fraction have been reported previously.[9]

HCl/HF Treatment Procedure. The general procedure for mineral dissolution and IOM enrichment is shown in Figure 1.

* Issued as NRCC No. 32541

NMR Measurements. The solid state ^{13}C NMR spectra were obtained at 75.47 MHz on a Bruker MSL-300 spectrometer, using a magic angle spinning (MAS) probe. For all samples a cross polarization technique was used with a contact time of 2 ms, and a repetition time of 1 s. Each spectrum was the Fourier transform of 1500-40,000 free induction decay curves.

RESULTS AND DISCUSSION

Table 1 lists the yields for IOM and volatiles obtained during the mild as well as concentrated acid treatments. The ash content of the IOM is also listed.

Table 1. Yields of IOM and Volatiles

Treatment	Yield $^{w}/_{w}$ %		Ash Content of IOM $^{w}/_{w}$ %
	IOM	Volatiles	
Mild Acid	9.6	41	9
Concentrated Acid			
A	24.7	60	35
B	2.1	55	29

Comparison of the results of mild acid treatment with those from the concentrated acid treatment indicates that the organic concentrate obtained from the former exhibited lower ash levels when compared to the concentrates produced by the latter treatment. This observation could result from a greater possibility of forming insoluble fluorosilicates during severe rather than mild acid treatment. Lower weight loss because of the volatiles in the mild acid treatment case as compared to the severe acid treatment case is also consistent with this interpretation.

Elemental Analyses. Elemental compositions of a sample of humic acid and IOM fractions obtained from both mild and severe acid treatments are compared in Table 2.

Table 2. Elemental Analyses (dry, ash free basis)

Sample	Treatment Scheme	Elemental Analyses					Atomic Ratios	
		C	H	N	S	O***	H:C	O:C
Solids, 1-6*	Mild Acid	70.3	5.7	1.3	3.8	18.9	0.97	0.20
Solids, 1-8*	Mild Acid	55.8	4.0	1.0	5.1	34.1	0.86	0.46
IOM**	Conc. Acid	69.1	6.5	0.7	5.6	18.1	1.12	0.20
Humic Acid-1	2% NaOH	71.3	6.8	1.2	2.8	17.9	1.14	0.19

* Figure - 1; ** Previous study ref. 9; *** By difference

The two IOM fractions obtained after mild acid treatment (solids, 1-6 and 1-8) had significantly different elemental compositions. Solids 1-6, the organic concentrate obtained from fraction 1-3, had an elemental composition resembling humic acid-1 and organic concentrate obtained previously[9] using severe acid treatment. The average elemental composition of these fractions (humic acid-1, solids 1-6 and IOM from severe acid treatment) are identical to those of the solvent extractable humic acids from Australian brown coal and benzene/methanol extracts from oil phase solids reported previously.[5,12] Elemental composition of the organic concentrate 1-8, obtained from fraction 1-4, appears to be similar to those reported for peat and soil humic matter.[13,14] Unlike the findings for the samples subjected to severe acid treatment[5,9] the present samples showed no trace of halogens.

Figure 2 is a van Krevelen diagram showing the humic acid and IOM fractions from both mild and severe acid treatments. All samples fall in the region of type III kerogen. Organic matter of type III kerogens is usually derived from plants of terrestrial origin and is rich in polyaromatic nuclei and heteroatomic ketone and carboxylic acid groups.[15] This type of organic matter is not considered to have any potential for hydrocarbon generation and usually matures to give coal. It is comparable in maturity to humic acids from lignite or subbituminous coals and is relatively immature when considered in light of its oil generation potential.[7]

^{13}C NMR Spectra. The CP/MAS ^{13}C NMR spectra for a number of samples are shown on Figure 3. A comparison of these spectra indicates that resolution is equally improved for all samples, regardless of the carbon concentration. However, the spectral resolution in the carbohydrate region (50-100 ppm) is much better for solids 1-8 as compared with that for IOM, obtained using concentrated HCl/HF. This suggests that carbohydrates are less susceptible to attack by mild HCl/HF. Also, the peaks for aromatic carbons were sharper for solids 1-6 and 1-8 than in the spectrum for IOM obtained from concentrated acid treatment.

The aromaticity (f_a) values for fractions 1-6 and 1-8 obtained using mild acid treatment are comparable to those for the IOM obtained from severe acid treatment (0.4 and 0.47 respectively Vs 0.44). These values are considerably higher than those reported for soil and aquatic humic acids and are comparable to those reported for humic acids from subbituminous coal and Victorian brown coal lithotypes.[5,12] As higher aromaticity is characteristic of a contribution from vascular plants[16], it is likely that the humic matter associated with oil sands is largely derived from terrestrial sources.

CONCLUSIONS

The results of this investigation are indicative of the presence of at least two different types of organic matter associated with oil sands solids. The two organic types had significantly different elemental compositions, with one fraction being almost identical to coal humic acids while the other was similar to peat and soil humic matter.

ACKNOWLEDGEMENTS

The authors would like to thank H. Séguin and Ann Web for technical assistance with elemental analyses, and Dr. R. Schutte of Syncrude Canada Ltd. for providing a sample of sludge pond tailings.

REFERENCES

1. Kessick, M.A. J. Can. Pet. Techn. 77, 49 (1979).
2. Camp, F.W. in 'The Tar Sands of Alberta, Canada', Cameron Engineering Inc., Denver, CO, USA, 1969.
3. Bakshi, N.N., Gillies, R.G. and Khare, P., Env. Sci. Techn. 9, 363 (1975).
4. Young, R.N. and Sethi, A.J., J. Can. Pet. Techn. 76, 76 (1978).
5. Majid, A. and Ripmeester J.A., Fuel 65, 1726 (1986).
6. Majid, A., Sirianni, A.F. and Ripmeester, J.A., Fuel 61, 477 (1982).
7. Majid, A. and Ripmeester J.A., 'Metal Complexes in Fossil Fuels: Geochemistry, Characterization and Processing', ACS Symposium Series 344, 290-306 (1987).
8. Majid, A. and Ripmeester J.A., Fuel 69, 1527 (1990).
9. Majid, A., Sparks, B.D. and Ripmeester J.A., Fuel 69, 145 (1990).
10. Ignasiak, T.M., Zhang, Q., Kratochvil, B. et al., AOSTRA J. Res. 2, 21 (1985).
11. Majid, A., Sparks, B.D. and Ripmeester, J.A., Fuel 70, 78 (1991).
12. Verheyen, T.V., Johns, R.B. and Blackburn, D.T., Geochim. Cosmochim Acta, 46, 269 (1982).
13. Schnitzer, M. and Khan, S.U., "Humic Substances in the Environment", Marcell Dekker, New York, 1972.
14. Hartenstein, R., Science, 212, 743 (1981).
15. Tissot, B.P. and Welte, D.H. in "Petroleum Formation and Occurrence", Springer-Verlag, New York, USA, 1984.
16. Christman, R.F. and Gjessing, E.T., "Aquatic and Terrestrial Humic Materials", Ann Arbor Sci. Pub., Ann Arbor, 1983.

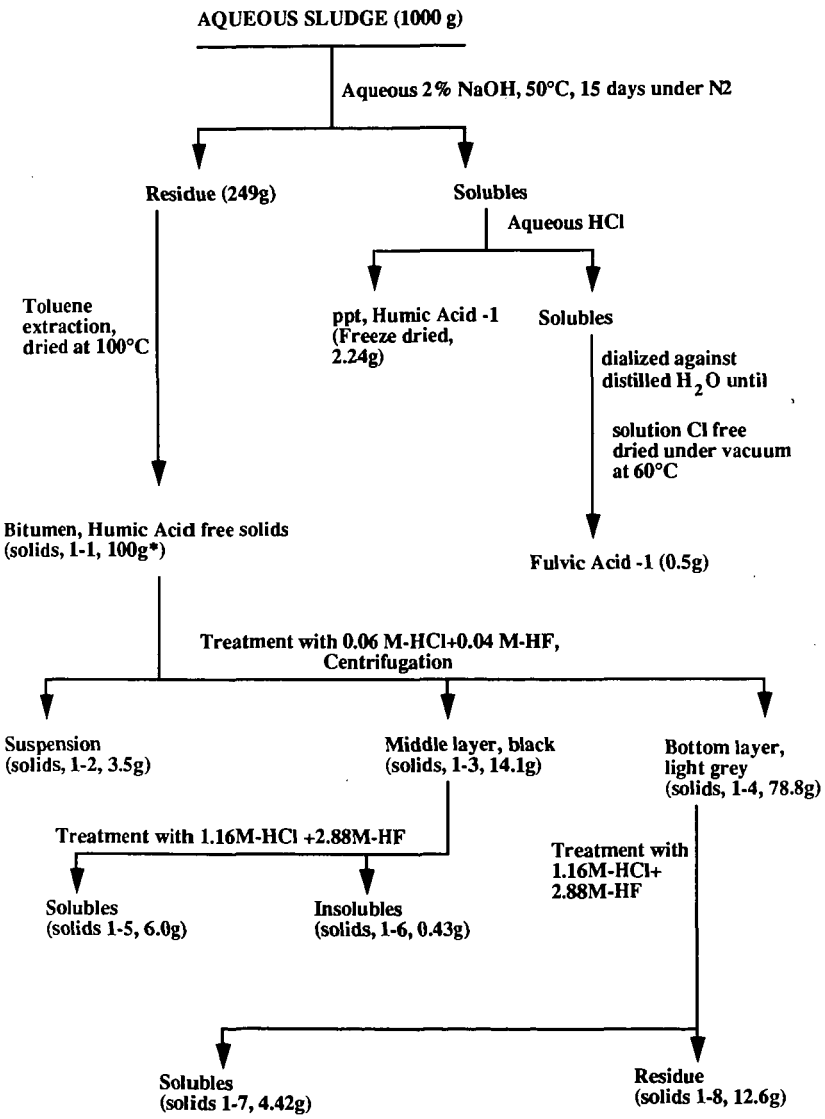

Figure 1. Separation and mild HCl/HF acid treatment scheme
* Represents amount taken for further treatment and not actual yield.

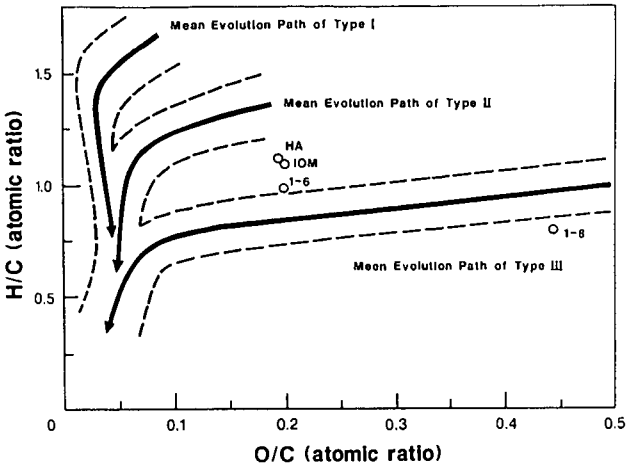

Figure 2. van Krevelen diagram showing the elemental composition of humic acid and organic matter concentrate fractions

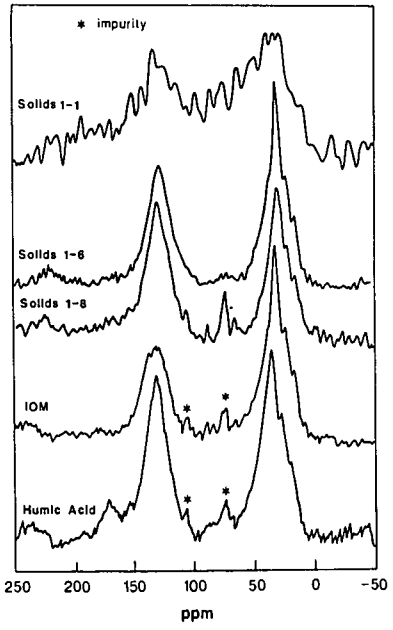

Figure 3. CP/MAS - 13C NMR spectra of various fractions from syncrude sludge pond tailings shown in Table 2

Characterization of Humic Acids from Sludge Pond Solids*

Abdul Majid, Bryan D. Sparks and John A. Ripmeester
National Research Council of Canada
Institute for Environmental Chemistry
Ottawa, Ontario, K1A 0R9, Canada

Keywords: Humic Acids, Oil Sands, Sludge

Considerable quantities of organic material, insoluble in common organic solvents, are known to be associated with the inorganic minerals present in oil sands. This insoluble organic matter (IOM) consists of both humic and non-humic components. This organic matter is believed to be partly responsible for the intractability of the sludge. In our previous work we have successfully isolated non-extractable residual organic matter from oil sand tailings using oil phase agglomeration and acid dissolution techniques. In this investigation we have isolated humic acids from a number of samples of mineral solids obtained from Syncrude sludge pond tailings. These solids were obtained from sludge using different experimental conditions such as soxhlet extraction followed by air drying of solids and centrifugation followed by air drying or vacuum drying of solids. Humic matter was extracted from these solids using a mixture of $Na_4P_2O_7$ and NaOH which extracts both humic acids as well as organometallic compounds. Extraction with NaOH yielded humic acids from this composite organic material. The various samples of humic acids isolated were studied using elemental analysis and ^{13}C NMR spectroscopy.

INTRODUCTION

Athabasca oil sand is a complex, variable mixture of bitumen, sand, water and clays. The hot water process used for the extraction of bitumen from oil sands produces large volumes of tailings, consisting mainly of sand and a dispersion of various clay minerals. Some of these clay minerals are associated with significant amounts of insoluble organic matter (IOM).[1-7] This insoluble organic matter consists of both humic and non-humic components and is believed to be partly responsible for the intractability of the sludge.

* Issued as NRCC No. 32540

In our previous work we have successfully isolated non-extractable (toluene insoluble) residual organic matter from oil sand tailings using oil phase agglomeration and HCl/HF mineral dissolution techniques.[4,8] Characterisation of this organic material using elemental analysis and spectroscopic techniques was reported recently.[3-5] Based on those investigations it was suggested that the non-extractable organic material associated with oil sand minerals was mostly humic matter. This conclusion was also supported by the work of Ignasiak et al[7] who have reported that this organic matter consists of humic and non-humic components containing numerous oxygen functions.

In this investigation we have extracted humic acids from a number of samples of Syncrude sludge pond solids which had been treated under different experimental conditions. The various samples of humic acids isolated were studied using elemental analyses and ^{13}C NMR spectroscopy. The results of this study have been compared with the results obtained for the humic acids from oil sands feedstocks.[9]

EXPERIMENTAL METHODS

Materials. The tailings pond sludge was provided by Syncrude Canada Ltd. A list describing the various samples subjected to humic acid extraction is shown in Table I.

Table I. Feedstocks description

Sample ID	Sample Description	Ash (w/w %)	C (w/w %)
UTS	Untreated sludge	-	-
TEODS	Toluene extracted oven dried solids from sludge	94.5	2.6
ODS	Oven dried untreated sludge	85.4	5.3
CWS	Centrifuged wet solids from sludge	-	-
CVDS	Centrifuged vacuum dried solids from sludge	81.7	4.7

Humic Acid Extraction. Samples were first extracted using a mixture of 0.5 N NaOH + 0.1 M $Na_4P_2O_7$ to isolate composite organic matter consisting of a mixture of humic acids and organometallic compounds. This composite organic matter was then extracted with 0.1 N NaOH to isolate humic acids.

Elemental Analyses. Elemental analyses were performed using standard procedures reported previously.[9]

NMR Measurements. The solid state ^{13}C NMR spectra were obtained either at 45.28 MHz or at 75.47 MHz, using a magic angle spinning probe. For all samples a cross polarization technique was used with a contact time of 2-3 ms, and a repetition time of 1 s. Each spectrum was the Fourier transform of 1500-40,000 free induction decay curves.

RESULTS AND DISCUSSION

Humic acids were extracted from a number of Syncrude sludge pond tailings samples that had been pretreated in accordance with the list shown in Table I. In Table II are listed the yield and ash content for each humic acid sample. The yield was calculated as weight percent of the total insoluble

Table II. The yield and ash content of humic acids

Feedstock	Humic Acid Yield (w/w % of IOC*)	Ash Content of Humic Acid (w/w %)
UTS	21.7	8.9
TEODS	18.5	55.3
ODS	18.4	1.6
CWS	15.6	2.8
CVDS	19.7	51.2
Oil sands (Ref. 9)	15.4 ± 9.4	6.8 ± 5.8

* Insoluble organic carbon

organic carbon of the solids in the various samples. The amount of humic acid that could be extracted from various samples did not vary significantly (18.8±2%). Also, the amount of humic acids extracted from sludge samples compared with that extracted from oil sand feedstocks. This suggests that no significant quantities of humic matter could have been formed during oil sands processing or sludge storage and that the humic acids extracted from sludge solids could have been part of the humic matter associated with clay minerals of oil sands feedstock.

Ash content of the humic acid samples varied considerably. Humic acid samples extracted from TEODS and CVDS had the highest ash content of all the samples.

Elemental Analyses. The elemental analyses data are listed in Table III and can be summarized as follows:

Table III. Elemental Analyses of Humic Acids (w/w % dry, ash free)

Feedstock	Elemental Analysis					Atomic Ratios	
	C	H	N	S	O*	H:C	O:C
UTS	71.3	6.8	1.2	2.8	17.9	1.14	0.19
TEODS	56.3	5.8	0.8	1.3	35.8	1.24	0.48
ODS	75.4	7.5	1.0	4.1	12.0	1.19	0.12
CWS	66.6	4.5	1.5	1.6	25.8	0.81	0.29
CVDS	66.2	6.9	1.7	2.8	22.4	1.25	0.25
Oil Sands (Ref. 9)	66±1.5	5.2±0.7	1.2±0.2	3.1±0.6	24.5±1.7	0.95±0.1	0.28±0.02

1. There was more variation in the elemental composition of humic acids extracted from Syncrude sludge pond tailings than those extracted from the oil sand samples reported previously.[9] This suggests that either the treatment of the samples of Syncrude sludge pond tailings has altered the humic matter eg. by oxidation or that the proportion of humic matter components extracted by a solution of $Na_4P_2O_7$/NaOH varies from sample to sample.

2. The average elemental composition of these samples resemble those derived from coal and oil sand rather than those extracted from soil or marine sediments.[9-11]

^{13}C NMR spectra. The solid state ^{13}C NMR spectra of the five humic acid samples extracted in this investigation are shown in Figure 1. The main features of these spectra are summarized below:

1. The NMR spectra of the samples derived from UTS and ODS have better spectral resolution than those of the other three samples. However, the spectral resolution does not appear to depend on the ash content of the samples.

2. None of the spectra showed any noticeable resonance in the carbohydrate region.

3. Only samples derived from ODS and CVDS had well defined resonances in the carboxylic region. Non-uniform distribution of carboxylic carbon could be due to the difficulties associated with its detection in these types of samples.

4. The aromaticities (f_a) of the five humic acid samples ranged from 0.47 to 0.62. These values were comparable with previously reported values for humic matter fractions from oil sands.[4,5,9] However, these values are considerably higher than those reported for soil or aquatic humic acids. The higher values are closer to those reported for humic acids from victorian coal lithotypes.

ACKNOWLEDGEMENTS

The authors would like to thank Ann Webb and V. Clancy for technical assistance with elemental analysis and R. Schutte of Syncrude Canada Ltd. for providing a sample of sludge pond tailings.

REFERENCES

1. Kessick, M.A., J. Can. Pet. Techn., **77**, 49 (1979).

2. Majid, A., Sirianni, A.F. and Ripmeester, J.A., Fuel, **61**, 477 (1982).

3. Majid, A. and Ripmeester, J.A., Fuel, **65**, 1726 (1986).

4. Majid, A. and Ripmeester, J.A. 'Metal Complexes in Fossil Fuels: Geochemistry, Characterization and Processing', ACS Symposium Series 344, 1987, pp. 290-306.

5. Majid, A. Sparks, B.D. and Ripmeester, J.A., Fuel, **69**, 145 (1990).

6. Majid, A., Sparks, B.D. and Ripmeester, J.A., Fuel, **70**, 78 (1991).

7. Ignasiak, T.M., Zhang, Q., et al, AOSTRA J. Res., **2**, 21 (1985).

8. Ripmeester, J.A. and Sirianni, A.F., J. Can. Pet. Techn., **79**, 131 (1981).

9. Majid, A. and Ripmeester, J.A., Fuel, **69**, 1527 (1990).

10. Mossop, G.D. in 'Facts and principles of World Petroleum Occurrence', (Ed. A.D. Miall), Can. Soc. Pet. Geol. Memoir, **6**, 609-632 (1980).

11. Mossop, G.D., Science, **207**, 145 (1980).

12. Verheyen, T.V., John, R.B. and Blackburn, D.T., Geochim. Cosmochim. Acta, **46**, 269 (1982).

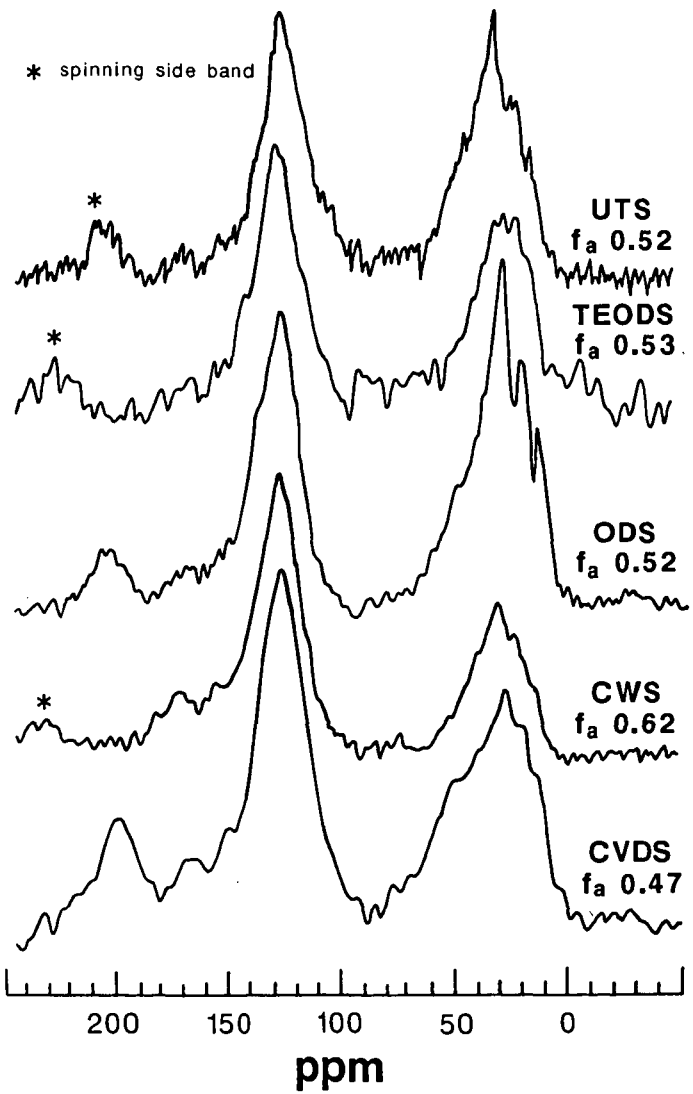

Figure 1. CP/MAS - ^{13}C NMR spectra of humic acids

A Thermal Swing Absorption Process for Production of Oxygen-Enriched Combustion Air

S. Park, C. McLarnon, V.K. Mathur,
S.A. Tomellini and R.P. Planalp*

Chemistry and Chemical Engineering Departments
University of New Hampshire
Durham, NH 03824

Keywords: Oxygen separation, cobalt complex, thermal swing absorption

Abstract. A thermal swing absorption (TSA) process for the production of oxygen-enriched combustion air is described. The process is designed to achieve a ca. 50% fuel efficiency savings by the use of greater than 50% oxygen-enriched air in coal-fired boilers. The TSA process described has three components: an inorganic oxygen-carrying compound (carrier), a solution formulation of the carrier (with supports, promoters, and solvents), and a flow-system reactor with oxygen concentration monitoring. Criteria necessary to success of the process are identified. A literature search for appropriate compounds is summarized. Two compounds are identified, synthesized, formulated and tested in the TSA process. The compounds performed successfully over four absorption/desorption cycles. Goals for further improvements are stated.

Introduction

It is reported[1] that oxygen enriched combustion can substantially improve the thermal efficiency of a combustion system. Union Carbide found that in furnaces with combustion temperatures above 1100°C, an oxygen enrichment of 50 to 100% would result in a 40 to 60% fuel savings. The cost savings and thus economic feasibility of oxygen enriched combustion is sensitive to both fuel prices and the cost of producing oxygen. As an added advantage, the use of oxygen enriched combustion air (OECA) will also minimize NO_x formation.

In a recent study[2] it is reported that thermal swing absorption (TSA) using a solution absorbent offers a potentially viable option for producing low cost OECA for industrial use. The TSA process consists of using a chemical in solution which is capable of absorbing oxygen at low temperature (say 23°C) and desorbing it at higher temperature (say 65°C). These temperatures can be obtained by cooling with ambient air and heating with flue gases. The use of waste heat from combustion gases would make this process economically very attractive.

A solution absorbent system consists of a reversible oxygen-binding chemical compound dissolved in a formulation of solvents and promoters. Four major criteria may be applied to the

absorbent solution. First, it should have a high, reversible and selective affinity for oxygen at room temperature or slightly above, and a lower affinity at a higher temperature (generally greater than 50°C), so that it will absorb and desorb oxygen. Second, the absorption process should happen at a reasonable rate. The solution should have a reasonable lifetime (i.e. it should be possible to cycle the absorbent many times without experiencing degradation). Finally, it should absorb the maximum weight of oxygen per unit weight of solution; this generally implies that the compound be quite soluble in the solvent and promoters.

It is important to note that while many compounds have been observed to have a reversible affinity for oxygen,[3] many physical properties of the compounds which affect their suitability for a TSA formulation are not known. Indeed, few solution absorbent TSA systems have been described.[4]

In this paper, we describe a literature survey of compounds for TSA formulation, and the identification of two compounds for study. The preparation, formulation, and testing of these two in a TSA apparatus is reported. Finally, the significance of the oxygen absorption performance and plans for the future are mentioned.

Experimental

General. Reagents and solvents were obtained from commercial sources (analytical reagent grade) and used as received. *N,N'*-bis(salicylidene) *o*-phenylenediimino cobalt(II) (also known as Salcophen or CoSalophen) was purchased from Aldrich Chemical Co. and used as received. NMR spectra were obtained on a Bruker AM-360 spectrometer. Infrared spectra were obtained on Perkin-Elmer 283B spectrometer.

Preparation of *N,N'*-bis(salicylidene) ethylenediimino cobalt(II).[5] **I. *N,N'*-bis(salicylidene)ethylenediimine (salen).** Freshly distilled salicylaldehyde (7.1 mL, 0.067 mol) in 95% ethanol (33 mL) was heated to a boil with stirring. Ethylenediamine (2.2 mL, 0.0335 mol) was added and the solution was let cool. The resulting yellow precipitate (5.51 g, 61% yield) was filtered and dried under vacuum for 3 h. Proton NMR and elemental analysis (C, H, N) agreed with expected values.[3]

II. *N,N'*-bis(salicylidene) ethylenediimino cobalt(II) (Salcomine or CoSalen). Salen (2.74 g, 0.0102 mol) and sodium acetate (0.031 g) were dissolved in ethanol (31 mL), water (6.7 mL) and 1.0 M aqueous sodium hydroxide (24.3 mL). The mixture was brought to a boil with stirring and cobalt (II) chloride hexahydrate (2.43 g, 0.0102 mol) was added precipitating CoSalen as a brown product which was separated by filtration and washed with water until the washings were colorless. The cake was dried at 110°C for 3 h under reduced pressure, yield 2.75 g (83%). The elemental analysis (C, H, N) and IR spectrum (KBr pellet) agreed with expected values.

Measurement of Oxygen Absorption Under TSA Conditions. The measurement system is shown in Figure 1. Air (A) was passed through a needle valve and a calibrated Hastings mass-flow meter (B) to establish and measure the air flow rate. The air was bubbled through the reactor (D) where absorption and desorption take place. The effluent of the reactor was passed through an Infrared Industries IR-2200 Oxygen Analyzer (E) and then exhausted into a hood. A bypass line (C) around the reactor allowed for calibration and check of the analyzer. The reactor consists of an outer metal jacket around a glass rection vessel fitted with a rubber stopper through which the gas inlet, gas outlet, thermometer and thermocouple were passed. The reactor was alternately cooled in each absorption cycle and heated in each desorption cycle. The gas inlet consisted of a glass line with a frit attached to promote contact of the gas with the liquid.

The data from the oxygen analyzer, mass flow meter, and thermocouple were collected using an IBM PC/XT with the labtech/Notebook data acquisition system. The amount of oxygen absorbed and desorbed was calculated by integrating the product of the oxygen concentration and flow rate over the cycle.

Results and Discussion

Selection of Candidate Compounds. The literature was surveyed based on the above criteria, resulting in a tabulation of cobalt (II) compounds considered candidates for the TSA process. Table I is partial listing of these compounds.

Parameters found in the literature include the solvent and concentration of the formulation (columns 6 and 4). These are important to the fourth criterion above, because they provide information on the solubility of the cobalt complex. Clearly, those oxygen-binding compounds which are more soluble may produce a solution which contains more of the oxygen-binding ingredient and therefore has a greater oxygen absorbing capacity.

The nature of the axial base (column 5) affects the oxygen affinity of the complex (first criterion), by changing the electron density at cobalt, which is the active site for oxygen binding. Other parameters important to the first criterion are the temperature, binding ratio (mol Co:mol O_2), and oxygen affinity (log KO_2). These parameters all provide information on how well the complex would hold and release oxygen during a TSA cycle.

These data are insufficient to determine if the compounds are suitable for the TSA process, however. Some of the data needed are oxygen affinities at higher temperatures (first criterion), maximum solubilities in a range of solvents (fourth criterion), rate of oxygen binding (second criterion), and stability to oxidative degradation (third criterion).

Compounds #1 and #2, CoSalen and CoSalophen (also referred to as salcomine and salcophen, respectively), were selected for further study to obtain some of the above data. They were chosen due to their relatively high oxygen affinities and reasonably

high solubilities. While DiCobalt-*o*-bistren, #4, has a higher oxygen affinity, its low concentration value of 2×10^{-4} M is not practical.

Synthesis and Testing. CoSalen was prepared by modification of a literature procedure while CoSalophen was purchased. CoSalen and CoSalophen were tested for solubility in various solvents. Dimethylsulfoxide (DMSO) was found to be most suitable, giving a high concentration, 0.03 M.

The formulations were tested in the TSA system, giving the results of Table II. In Table II, the first cycle for each compound may be disregarded, as the solutions were prepared in air so that the oxygen content of each solution at the start was unknown. Subsequent cycles give similar oxygen capacities in the absorption and desorption cycles, indicating that all oxygen bound is released. Thus, oxidative degradation is not occurring, because no oxygen is consumed in the cycles. Further, the oxygen capacities are similar from cycle to cycle, indicating that no other deterioration of the absorber is occurring over these cycles.

The utilization value indicates what fraction of the cobalt complex carries oxygen. This value is determined by the difference between the oxygen affinities at 65°C and 25°C, for CoSalophen (between the affinities at 65°C and 22°C for CoSalen). These are related to the log (Ko_2) values of the complex.

Sample plots of oxygen absorption/desorption versus time are shown in Figures 2 (CoSalen) and 3 (CoSalophen), for the fourth cycle of each measurement. From these the rate of oxygen absorption and desorption may be approximated. For CoSalen, the absorption time is ca. 3 min and the desorption time ca. 4 min, while for CoSalophen it is ca. 4 min for absorption and 3.5 for desorption.

Future work will concentrate on improving the oxygen capacity of these TSA compounds. Several approaches will be taken. The solubility of the oxygen absorbing compound will be increased allowing a higher concentration of oxygen absorber per gram of solution. The utilization will be increased by increasing the desorption temperature and increasing the oxygen affinity of the compounds. Finally, the number of cycles will be increased to determine the lifetime of the compounds.

Conclusion

The thermal swing absorption process has been demonstrated using cobalt (II) Schiff-base complexes formulated as solution absorbents in a flow system. Parameters of the system have been determined for two cobalt complexes over four absorption/desorption cycles.

References

1. Kobayashi, H., "Oxygen Enriched Combustion System Performance Study," Vol. 1, Technical and Economic Analysis, by Union Carbide Corp. for US DOE, March 1987.

2. Jain, R.C.; Keller, J.G.; Haq, Z. "Assessment of Thermal Swing Absorption Alternatives for Producing Oxygen Enriched Combustion Air," US DOE Office of Industrial Programs report, April 1990.

3. (a) Gubelmann, M.H.; Williams, A.F. *Struct. Bonding* 1983 *55*, 1. (b) Niederhoffer, E.C.; Timmons, J.H.; Martell, A.E. *Chem. Rev.* 1984 *84*, 137.

4. (a) Roman, I.C. "Absorption Process for Producing Oxygen and Nitrogen and Solution Therefor," U.S. Patent 4,451,270, May 1984 to Bend Research, Inc.; (b) Yamauchi, T. "Method for Oxygen Concentration," Japanese Patent JP 62-83302, issued April 16, 1987 to Taiho Industry Co. Ltd., Tokyo, Japan.

5. This preparation is adapted from the literature: Diehl, H.; Hach, C.C. *Inorg. Syn.* 1950 *3*, 196.

Table I. Candidate Compounds for Oxygen Production by the TSA Process

No	Chemical (A) (Mol.Wt.)	Structure (A)	Conc. of (A)	Axial base (B)	Solvent (C)	Temp (°C)	Ratio ($Co:O_2$)	gO_2/ g(A)	gO_2/g soln. (A+B+C)	log KO_2	Ref. #
1	CoSalen (325)	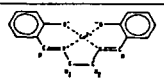	0.01M	4-Methyl pyridine (2M)	diglyme	25°	2:1	0.0492	$1.7x10^{-4}$	0.91	1,2
2	CoSalophen (377)	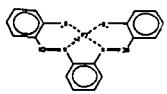	0.012M	4-Mepy (2M) 4-CNpy (1M) py (2M) DMAP (2M)	"	25	1:1 2:1	0.0849 0.0424	$4.098x10^{-4}$ $2.05x10^{-4}$	-2.74 -2.82 -2.81 +1.04	"
3	CoαCH_3Salen (355)	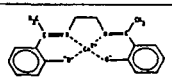	0.010M	4-MePy (3M)	"	10	1:1	0.0901	$3.4x10^{-4}$	-1.68	"
4	DiCobalt-*o*-Bistren (645)		$2x10^{-4}$M	NaOH	H_2O	25	1:1	0.0496	$6.4x10^{-6}$	4.57	3
5	Co(*S*-Me_2en)$(NO_3)_2$ (358.8)	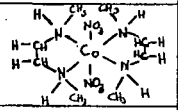	0.075M	Et_2-en (2M)	Formamide	25	1:1	0.0892	$3.49x10^{-4}$	No data	4
6	2,4,6-Tri (mesityl)-phenol (448)	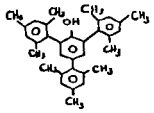	0.0372M	0.3g K-*i*-butanolate	*i*-butanol	20	1:1	0.07142	$1.47x10^{-3}$ theo-retical	No data	5

References: 1. Martell, A.E. Inorg. Chem. 1987 26, 1026-1030; 2. Martell, A.E. Inorg. Chem. 1989 28, 2647-2652; 3. Motekaitis, R.J.; Martell, A.E. J. Am. Chem. Soc. 1988, 110, 7715; 4. Roman, I.C. "Absorption Process for Producing Oxygen and Nitrogen and Solution Therefor," U.S. Pat. #4,451,270, issued May 29, 1984 to Bend Research, Inc., Bend, OR; 5. Yamauchi, T. "Method for Oxygen Concentration," Japanese Patent JP 62-83302, issued April 16, 1987 to Taiho Industry Co. Ltd., Tokyo, Japan.

Table II. Oxygen Absorption Data

Compound	Conc. mol/L	Solution Mass, g	Cycle No.	Bath Temperature, °C		Oxygen Capacity, $g(O_2)/g(soln), \times 10^{-4}$		Utilization, $mol(O_2)/mol(compound)$	
				Absorp	Desorp	Absorp	Desorp	Absorp	Desorp
CoSalen	0.03	218	1	22	65	0.890	1.54	.110	.191
CoSalen	0.03	218	2	22	65	1.81	2.00	.225	.249
CoSalen	0.03	218	3	22	65	1.80	1.90	.224	.235
CoSalen	0.03	218	4	22	65	1.81	1.83	.225	.227
CoSalophen	0.03	219	1	25	65	5.05	1.15	.063	.144
CoSalophen	0.03	219	2	25	65	1.26	1.29	.158	.162
CoSalphen	0.03	219	3	25	65	1.16	1.30	.145	.163
CoSalphen	0.03	219	4	25	65	1.15	1.23	.142	.153

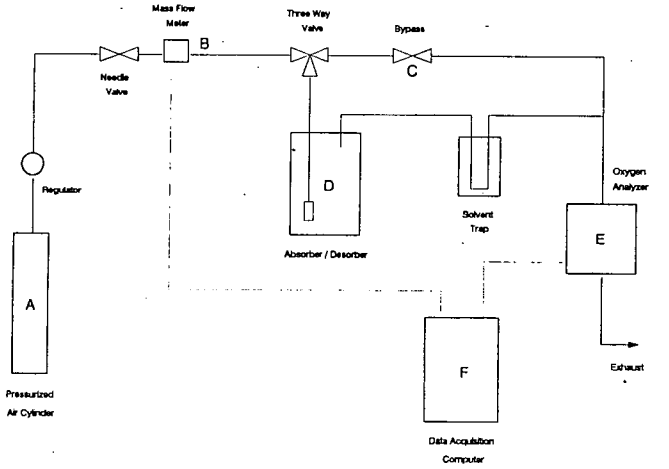

Fig. 1: Oxygen Absorption / Desorption Experimental Set-up

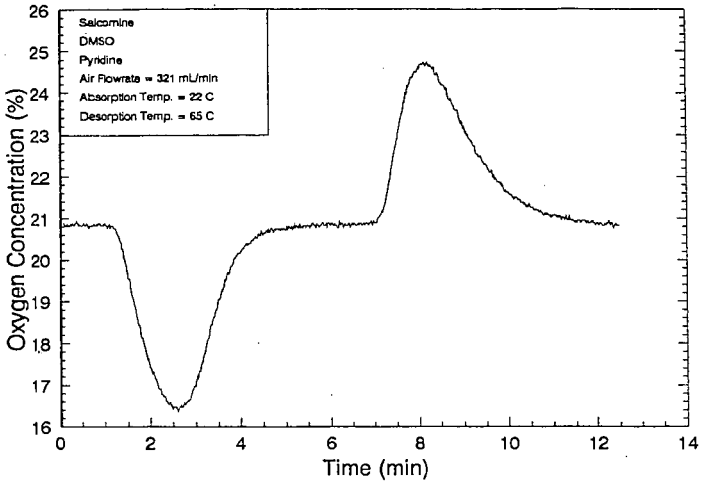

Fig. 2: Oxygen Absorption / Desorption for Salcomine

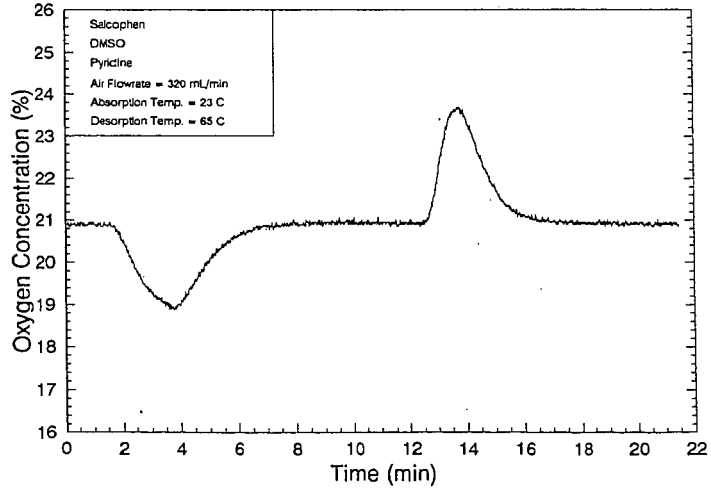

Fig. 3: Oxygen Absorption / Desorption for Salcophen

Methanol and Carbon Monoxide Production from Natural Gas

Terry E. Helton, Jin-Woo Chun and Rayford G. Anthony
Department of Chemical Engineering
Kinetics, Catalysis and Reaction Engineering Laboratory
Texas A&M University
College Station, TX 77843

INTRODUCTION

Partial oxidation of methane to methanol and formaldehyde holds considerable potential for producing liquid fuels and petrochemicals from natural gas. Several groups (Burch et al., 1989; Gesser et al., 1985 and 1987; Hunter et al., 1990; Yarlagadda et al. 1988) have investigated homogeneous partial oxidation. Various sensitizers were capable of lowering the partial oxidation reaction temperature (Hunter et al., 1987,1990). For most of the literature cited, the methanol selectivity varies from 20 to 80 percent. Some research groups have stated that it is difficult to obtain consistent results for the direct conversion of methane into methanol. In this study we present data illustrating the importance of the closure of the oxygen balance, the effect of materials of construction and type of reactor on the yields and selectivity of methanol. A kinetic model containing 175 homogeneous free radical reactions was developed and is used to simulate the performance of a plug flow reactor. Helton (1991) presents additional details on this study.

EQUIPMENT

Two reactor systems are utilized research to study the effects of reactor design on methane activity and product selectivity. Reactor system I can be operated from 1 - 100 atmospheres at temperatures between 25 and 450 °C. Non-selective catalytic wall effects are minimized by using a Pyrex liner. The tubular reactor and Pyrex liner is described in Figure 1. All tubing, exposed to temperatures above 180 °C contains an inner lining of fused silica in order to minimize the potential for surface reaction. For this system the feed is mixed and flows over several feet prior to entering the heated reactor zone of 400+ °C. In the reactor zone it is partial heated prior to entering the reactor tube through the 90 ° elbows. The elbows are 316 stainless steel and a portion of the SS is exposed to the reactants at high temperatures. Some or possibly even substantial reaction may have occurred in this section of the reactor.

Reactor system II is a commercial unit constructed by Autoclave Engineers, and is the Model 900 Micro-Scale Bench-Top Reaction System including the chromatographic system. Three basic modules comprise the reactor system: reactor, control, and analytical modules. A temperature controlled oven encloses the reactor system. Figure 2 provides a detailed description of the tubular reactor. For this system the gases are mixed at 180 °C and pass through an array of valves prior to entering the end of the reactor tube at 180 °C. No reaction occurs below 300 °C. As the fluid flows through the reactor tube it is heated by the three zone heater. The reaction is not conducted under isothermal conditions in either system, so that temperatures reported herein are the maximum temperatures of the reaction mixture. The analytical system

consists of an AE computer-controlled high-performance gas chromatograph containing a capillary and three packed columns along with a palladium transfer tube for hydrogen detection. Detailed operating procedures for the AE 900 Micro-Scale Bench-Top Reaction System exists in the manufacturer's operations manual.

The differences in the two reactor systems is the exposure of SS in the inlet elbows of Reactor System I and the possibility of reaction in this inlet section. Reactor System II has a straight section and no exposure of the reactants to SS as the reactants are heated to the reaction temperature. Also, with the AE-MSBTR instantaneous instead of time average material balances could be obtained.

RESULTS AND DISCUSSION

Burch et al. (1989) concluded the reason the high selectivity work of Gesser et al. (1987) could not be reproduced was due to small, but possibly important, differences in the design of the reactor. Burch and co-workers believed the methane to methanol gas-phase reaction operated within essentially unsteady-state conditions. Gesser et al. (1987) states that the reaction can occur under cool flame conditions in certain temperature and pressure regions. Also, the degree of pre-mixing of the reactant gases may have influenced the high selectivities reported.

Although the product distribution may be affected by the type of experimental apparatus, non-steady state conditions, or gas pre-mixing, failure to close the atom balances may explain the discrepancies in the range of selectivities observed in previous work. Figure 3, which was generated by using Monte Carlo simulation for a feed containing methane and 2.3% and 9.4% oxygen, respectively, illustrates the importance in closing carbon and oxygen atomic balances. For a feed containing 2.3% oxygen and 97.7% methane, a deviation in the carbon atom balance closure of 1% could result in 12 percentage points error in the methanol selectivity.
Table 1 illustrates that the addition of 5 percent ethane to the reaction mixture does not alter the methanol selectivity. However, the reaction temperature is lowered approximately 20 °C. Thus, ethane is capable of initiating the generation of free radicals more readily than methane which leads to further oxidation and enhances the formation of methanol at a lower temperature.

Figure 4 compares the methanol selectivity for the TEHBTR and AE-MSBTR reactor systems. The initial oxygen concentration was varied from 4.3 percent to 10.0 percent. Table 2 lists the gas hourly space velocity and reactor residence time for each reactor system. Except for one experiment, the residence time was maintained at approximately 17 seconds by varying the space velocity at each reaction pressure. The total pressure ranged from 20 to 50 atmospheres. Figure 4 indicates that methanol reaches a maximum after 20 percent of the oxygen is converted. The methanol selectivity could not be increased above 35 percent despite the range of oxygen concentrations and total pressures studied. There is an increase in methanol selectivity to 42 percent for reactor system TEHBTR, but this only occurred at an oxygen concentration of 4.3 percent, 20 atmospheres pressure, and a residence time of approximately 6 seconds.

The walls of the TEHBTR system appear to be catalytically active. When the total pressure is increased from 20 to 50 atmospheres the methanol selectivity decreases drastically from 30 to approximately 10 percent. If the partial oxidation of natural gas was purely homogeneous an increase in reactor pressure should minimize any surface reactions since the gas density to reactor wall surface is greater. Since the opposite is observed, the walls in the TEHBTR system must be catalytically active.

Few kinetic models for the homogeneous partial oxidation of methane to methanol have appeared in the literature. Onsager et al. (1989) and Durante et al. (1989) presented gas phase models at the International Chemical Congress of Pacific Basin Societies for the low temperature partial oxidation of methane to methanol. Onsager's reactor consisted of a one-chamber reactor with an alumina and stainless steel inner surface. The main part of the reaction rate parameters were taken from Tsang (1987) and Tsang and Hampson (1986). Some reactions were generated by Onsager et al. (1989) without any reference to literature values. The rate parameters of these reactions were estimated on the basis of analogous reactions.

Durante et al. (1989) constructed a kinetic model for the homogeneous gas phase reactions involved in methane partial oxidation utilizing published rate constants and activation parameters by Bedeneev et al. (1988). The model predicted the experimental findings of Yarlagadda et al. (1988) for runs at low temperature and oxygen partial pressures, but it could not reproduce the high methanol selectivities (exceeding 80 percent) reported at an 8 percent methane conversion. Onsager et al. (1989) and Durante et al. (1989) limited their models to the reaction of methane and oxygen. Thus, it was necessary to develop a model which incorporated the combined reactions of methane and ethane with molecular oxygen.

A kinetic model consisting of 175 free radical reactions was developed to simulate the reported experimental results. Pre-exponential constants for five reaction steps were increased above the recommended literature values in order to predict the experimental data. The pre-exponential constants were multiplied by the factors illustrated in Table 3. The published rate constants for these two reactions were estimated from the analogous reaction of formaldehyde with molecular oxygen. The increased pre-exponential constants for the formation of carbon dioxide is within the uncertainty of the literature values. Figure 5 shows a comparison of model predictions with experimental data. The kinetic model predicts the experimental data with remarkable accuracy.

CONCLUSIONS

Oxygen atom balance closure is needed to insure a minimum error in the calculated methanol selectivities, because it is the limiting reactant when excess methane is used. Large deviations in products selectivities can occur even though the overall material and the carbon atom balance closures are satisfied to a ± 2%.

The proposed kinetic reaction mechanism is capable of predicting the homogeneous reaction of methane and ethane with molecular oxygen. The model accurately predicts the product selectivities and conversions for the range of experiments in this investigation.

Additional cracking reactions need to be added to the mechanism in order to predict higher ethylene selectivities at low oxygen conversions (less than 10 percent). This would lower the predicted formaldehyde selectivity at low conversions and help in predicting the formaldehyde selectivity more accurately. Also, some spectroscopic work could be performed to determine the free radical concentrations during the reaction. Since the free radicals appear to reach a pseudo steady state, spectroscopic instruments may be able to observe and quantify these species. This would help in improving the kinetic model.

ACKNOWLEDGEMENT

This research was supported in part by a grant from the Texas Advanced Technology Program.

LITERATURE CITED

Bedeneev, V.I., M.Y. Gol'denberg, N.I. Gorban, and M.A. Teitel'boim, *Kinetika i Kataliz*, 29(7), 1 (1988).

Burch, R., G.D. Squire, and S.C. Tsang, *Journal of the Chemical Society, Faraday Transactions I*, 85(10), 3561, (1989).

Durante, V.A., D.W. Walker, W.H. Seitzer, and J.E. Lyons, *1989 International Chemical Congress of Pacific Basin Societies, Preprints of 3B Symposium on Methane Activation, Conversion, and Utilization*, Honolulu, Hawaii, (1989).

Gesser, H.D., N.R. Hunter and C.B. Prakash, *Chemical Reviews*, 85(4), 235 (1985).

Gesser, H.D., N.R. Hunter, L.A. Morton, P.S. Yarlagadda and D.P.C. Fung, *American Chemical Society Preprints*, 32(3), 255 (1987).

Helton, T.E., Ph. D. Dissertation, Department of Chemical Engineering, Texas A&M University (1991), Research Advisor: R. G. Anthony.

Hunter, N.R., H.D. Gesser, L.A. Morton and P.S. Yarlagadda, *American Chemical Society, Division of Petroleum Chemistry Preprints*, 779 (1987).

Hunter, N.R., H.D. Gesser, L.A. Morton, P.S. Yarlagadda and D.P.C. Fung, *Applied Catalysis*, 57(1), 45 (1990).

Onsager, O.T., P. Soraker, and R. Lodeng, *1989 International Chemical Congress of Pacific Basin Societies, Preprints of 3B Symposium on Methane Activation, Conversion, and Utilization*, Honolulu, Hawaii (1989).

Tsang, W., *Journal of Physical and Chemical Reference Data*, 16(3), 471, (1987).

Tsang, W. and R.F. Hampson, *Journal of Physical and Chemical Reference Data*, 15(3), 1087, (1986).

Yarlagadda, P.S., L.A. Morton, N.R. Hunter and H.D. Gesser, *Industrial and Engineering Chemical Research*, 27, 252 (1988).

Table 1: Effect of Ethane on Reaction Temperature and Methanol Selectivity

94 % Methane		89 % Methane - 5 % Ethane	
Reaction Temperature (°C)	Methanol Selectivity	Reaction Temperature (°C)	Methanol Selectivity
413	33.3	388	36.1
421	33.4	390	34.7
429	31.8	398	31.0
421	33.9	401	32.5
414	34.3	405	32.0

Table 2: Experimental Conditions for TEHBTR and AE-MSBTR

Reactor Conditions	Unit	Space Velocity,hr^{-1}	Space Time, seconds
4.3% Oxygen 20 atm	TEHBTR	4652	5.9 - 6.3
6.35% Oxygen 50 atm	AE-MBTR	4165	16.4 - 17.9
8.20% Oxygen 20 atm	AE-MBTR	1573	17.9 - 18.8
9.40% Oxygen 50 atm	AE-MBTR	4165	17.2 - 17.6
9.70% Oxygen 50 atm	TEHBTR	4200	18.0 - 18.9
9.70% Oxygen 50 atm	AE-MBTR	4165	17.5 - 17.7
10.0% Oxygen 50 atm	TEHBTR	4104	18.2-19.0

Table 3: Enhancement Factors for the Pre-exponential Constants

Reaction	Enhancement Factor
$CH_4 + O_2 = CH_3 + HO_2$	1.0×10^7
$C_2H_6 + O_2 = C_2H_5 + HO_2$	7.0×10^6
$CO + CH_3O = CH_3 + CO_2$	3.5
$CO + OH = CO_2 + H$	3.5
$CO + HO_2 = CO_2 + OH$	3.5

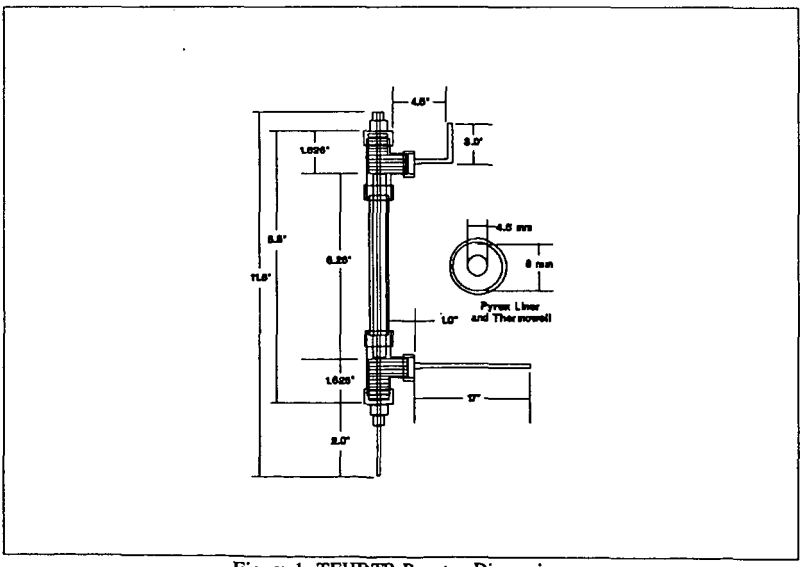

Figure 1: TEHBTR-Reactor Dimensions

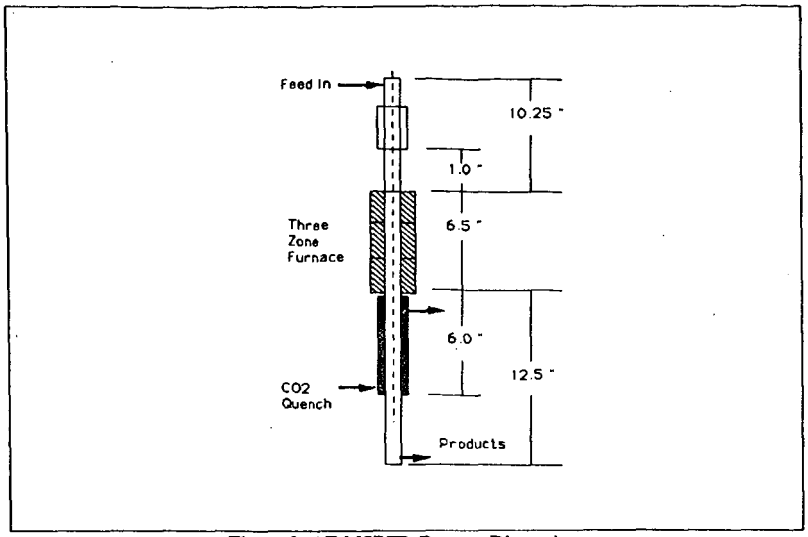

Figure 2: AE-MSBTR-Reactor Dimensions

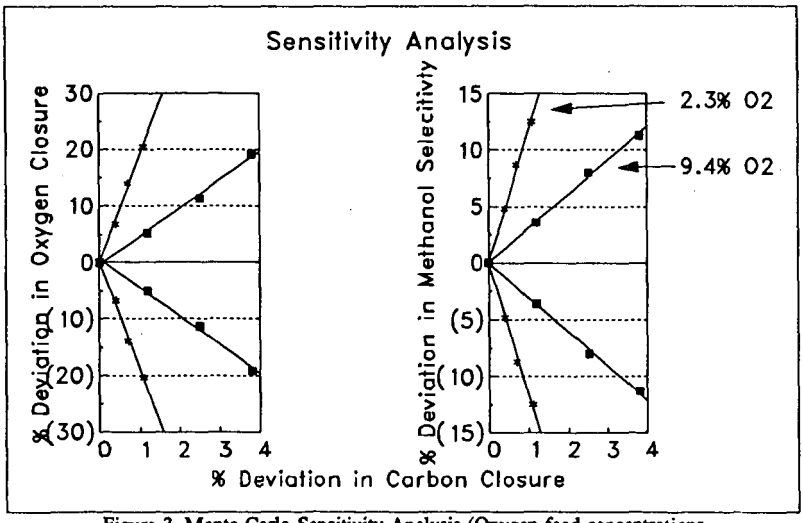

Figure 3. Monte Carlo Sensitivity Analysis (Oxygen feed concentrations of 2.3% and 9.4%)

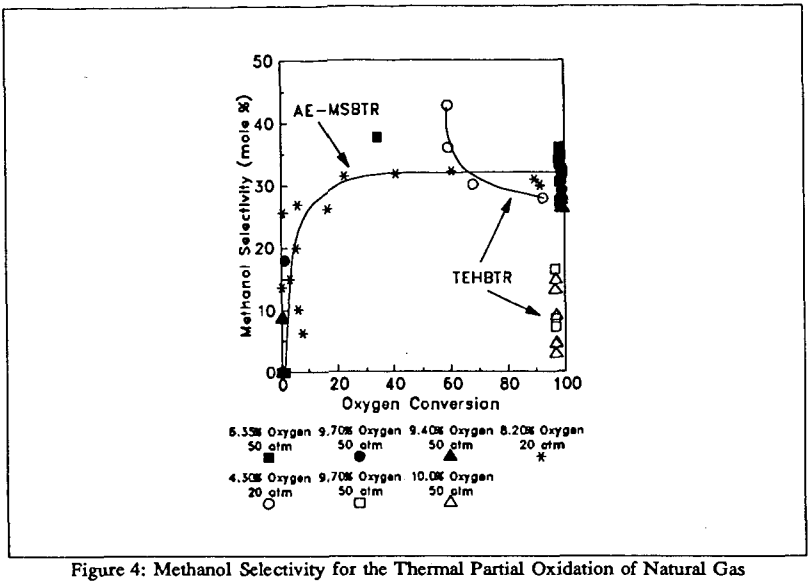

Figure 4: Methanol Selectivity for the Thermal Partial Oxidation of Natural Gas

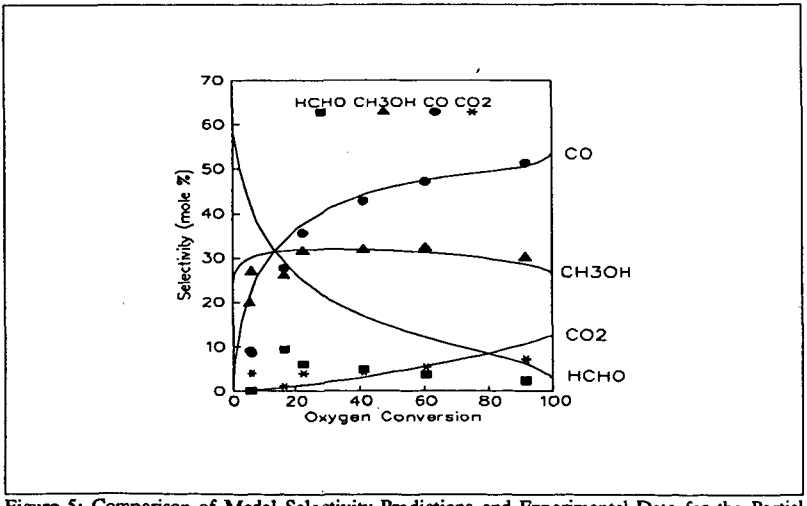

Figure 5: Comparison of Model Selectivity Predictions and Experimental Data for the Partial Oxidation of Natural Gas (8.2 % Oxygen, 5.1 % Ethane, 86.7 % Methane, Pressure = 20 atmospheres, Space Velocity = 1573 hr^{-1})

SURFACE CHEMICAL STUDIES OF "HOT CORROSION LIFE PREDICTION MODEL FOR MARINE GAS TURBINE BLADES AND GUIDE VANES"

Dasara V.Rathnamma,
Code 2842, David Taylor Research Center
Annapolis, MD, 21402-5067

R.Nagarajan
IBM Corp, 5600 Cottle Road, San Jose, CA 95193

Key words: Hot Corrosion, chemical equillibrium, chemically frozen boundary layer,

ABSTRACT

The results of a theoretical program of research directed towards the study of hot corrosion in the hot gas pathways of marine gas turbines burning vanadium contaminated liquid fuels are presented here. A life prediction model,Life, is developed for turbine blades and guide vanes based on the application of fundamental heat, mass, and momentum transfer principles to the chemically reactive non-isothermal combustion environment. The corrosion rate is assumed to be limited by high Schmidt number diffusional dissolution of a protective oxide species into the condensed molten salt solution (equilibrium composition is predicted by means of free energy minimization by the computer program). Alloy surface effects are included to quantitatively relate predicted coating removal rate to hot corrosion data which are used to verify the validity of our theoretical approach. The physical insight into the mechanism of hot corrosion obtained through the study is expected to provide far reaching implications for the future design and protection of marine turbine components.

INTRODUCTION

Fuel composition, among other things, controls the corrosion and hence the life of airfoil material in the marine gas turbine engine. The use of fuels containing contaminants like sulfur, sodium, vanadium and sea salts, is known to cause rapid degradation of alloy coatings as well as substrate alloys of the blades and vanes. Molten salt mixtures of sulfates, vanadates and other hot corrosive species such as oxides of vanadium and sulfur formed as fuel combustion products dissolve the protective oxide on the blade surface. During fluxing a variety of complex chemical reactions take place which required analysis by computer-based multicomponent equilibrium algorithms. The high-Schmidt number Brownian diffusion limited oxide dissolution by the deposited liquid has been assumed to be the rate-limiting process in hot corrosion. Each of these processes has been characterized thoroughly and rigorously. The corrosion rate increases with the salt deposition rate, but the relationship is nonlinear and depends on the composition of the salt and the

substrate alloy or coating. Sodium as a fuel impurity or as airborne sea salts in the marine atmosphere condenses as sodium sulfate (Na_2SO_4) and causes corrosion. In the temperature range 600-800°C, low temperature, hot corrosion is very sensitive to SO_3 partial pressures in the gas phase. In the range 800-950°C, high temperature, hot corrosion is not quite as sensitive to SO_3 levels. A theoretical model (1,2) for hot corrosion limited blade life based on the rates at which oxide formation and dissolution phenomena proceed, has been developed from theoretical considerations by the use of computer programs (3,4,5). The predictive computer program is called Life. The predicted effect of variations in operating parameters and surface coating oxides on predicted blade life has been studied.

Blade surfaces are usually coated with metal alloys that form an adherent, refractory and corrosion-resistant oxide layer on the gas side of the coating. Rosner and Nagarajan (6) have proposed the following mechanism for initiation and propagation of hot corrosion: at locations where the protective oxide scale is partially leached or completely dissolved by the condensed molten salt-'solvent', the metal substrate is more accessible, and hence vulnerable to catastrophic corrosion. Local saturation of the liquid layer is prevented by dynamic fluxing due to aerodynamic-and centrifugal-shear forces which convey dissolved oxide from the site of dissolution to the tip and trailing-edge regions of the blade. The oxide dissolution rate is taken to be limited by high-Schmidt number Brownian diffusion of the oxide species in the melt (as well as by salt/oxide interfacial detachment kinetics). Other parameters that play a role in the oxide dissolution rate include aerodynamic variables such as the convective flux of the gas phase alkali contaminants, and material integrity characteristics of the blade alloy surface.

Many studies have been concerned in the literature with deposition mechanisms, the composition of the salt deposits (7) and mechanisms of low temperature hot corrosion (8). But our model for predicting the life of air foils, is based on fundamental principles. Objective of the present work is to understand the interfacial chemistry of the deposition and corrosion processes approach.

STEPS IN THE ANALYSIS

1. Equilibrium thermodynamic prediction of condensed liquid and vapor phase compositions (3).
2. Chemically Frozen Boundary Layer (CFBL) model prediction of deposition rates (4,5).
3. Estimation of physico-chemical properties of the molten salt solution.
4. Estimation of physical properties and parabolic oxidation rate constants of coating alloys.
5. Prediction of protective oxide coating dissolution rates into the condensed liquid 'solvent'.
6. Prediction of blade 'life' based on the competing dynamics of

oxide layer formation and dissolution.
Each of these steps, along with the assumptions inherent in each was previously addressed (1).

RESULTS AND DISCUSSION

High temperature hot corrosion mechanisms reported in literature (7,8) are not based on rate studies. Model reported in this paper is a rate study model and it uses the multicomponent chemical vapor deposition (CVD) theory (9,10).

Local thermochemical equilibrium calculations by use of solution capable free energy minimization computer programs i.e.,Complex Chemical Equilibria Calculations (CEC) of the National Aeronautics and Space Administration(NASA) and Package code of the Department of Energy (DOE) are shown in figures 1 and 2. Mole fractions of the product species depend upon the impurity concentrations in the fuels (table 1).

Figure 1. CEC predicted dominant vapor species.

Figure 2. Condensed liquid solution comprising principally of $Na_2SO_4(l)$, $Na_2V_2O_6(l)$, and $V_2O_5(l)$.

Figure 3. Shows dependence of the CFBL computed deposition rate on surface temperature and fuel/air ratio.

At sufficiently low surface temperatures, the solution deposition rate is insensitive to surface temperature. As the solution dew point is approached, deposition rate drops to zero at the dew point. The dew point of the solution is in general, higher than that for any of the individual species. This dew point elevation effect, in combination with the freezing point depression effect and eutectic formation, considerably broaden the unsafe temperature range in which the deposit remains molten. For this reason, solution condensates are typically corrosive over a wider operating regime than pure condensates.

Molten salt deposition rate increases with an increasing fuel-to-air ratio, increasing gas main stream temperature, and with increasing sodium/vanadium concentrations in the combustion mixture. Pressure and sulfur level are predicted to have relatively insignificant effects on the computed deposition rate.

Figure 4. Shows dependence of oxide dissolution rate on blade surface temperature. Oxide dissolution rate can actually increase with temperature, even though the salt deposition rate drops rapidly. Oxide dissolution rate is predicted to increase with increasing fuel-to-air ratio, increasing gas mainstream temperature, and increasing sodium/vanadium gas phase concentrations. The rate as with deposition is insensitive to

pressure and sulfur level under normal turbine operating conditions.

Figure 5. Shows for pure metallic oxide coated turbine blades there is a monotonic increase in blade life with temperature since sulfidation corrosion only is considered as the life limiting factor. This inconsistency is due to omission of oxidation corrosion as also life limiting.

Figure 6. Predicts maximum blade life at the temperature when the sulfidation corrosion and oxidation corrosion intersect approximately at 1120K.

Figure 7. Shows evaluation of three Navy test fuels with regard to their corrosion potential. Below 1200 K, use of GT 10 would result in longer blade life than GT 12. NSFO (Navy special fuel oil) is a highly contaminated fuel not used in gas turbine engine.

Figures 8 and 9. Show life of blade material coated with several single metal oxides mostly.

Figure 10. Shows life of blade coated with typical metallic alloys and dependence of life on temperature.

CONCLUSIONS

Objective, central to the preliminary approach was accomplished. There is reasonable agreement between the model predictions and some of the experimental results reported in literature (11). The model needs improvement. Thermodynamic data on vanadium-oxygen gaseous species is lacking (12) in the thermodynamic data base (13,14). Ideal solution calculations are to be replaced by real solution calculations using the SAGE program which is a modified and improved version of sol-gas-mix program.

REFERENCES

1. Rathnamma, D. V. and R. Nagarajan, "Hot Corrosion Life Prediction Model for Marine Gas Turbine Blades and Guide Vanes" paper presented at the Fourth International Symposium on Frontiers of Electrochemistry (Science & Technology), Madras, India, 14-16 Nov 1989.

2. Rathnamma, D. V. and R. Nagarajan, "High Temperature Hot corrosion Control by Fuel additives (Contaminated Fuels), in:Proc.10th International congress on Metallic Corrosion, 7-11 Nov 1987, Madras, India, Oxford and IBH Publishing, Vol IV, pp. 3651-3664.

3. Zelenznik, Frank, "Solution Capable Complex Chemical Equilibrium Calculations Program," NASA, Lewis, Cleveland, Ohio (1985).

4. Gokoglu, S. A., B. K. Chen, and D. E. Rosner, "Calculation of Multicomponent Convective Diffusion Deposition Rates From Chemically Frozen Boundary Layer Theory, " NASA CR-168329 (computer program) (1984).

5. Rosner, D. E., B. K. Chen, G. C. Fryburg, and F. J. Kohl, "Chemically Frozen Multicomponent Boundary Layer Theory of Salt and/or Ash Deposition Rates from Combustion Gases," Combustion Science Technology, 20, pp. 87-106 (1979).

6. Rosner, D.E. and R.Nagarajan, "Vapor Deposition and Condensate Flow on Combustion Turbine Blades: Theoretical Model to Predict/Understand Some Corrosion Rate Consequences of Molten Alkali Sulfate Deposition in the Field or Laboratory," Int.J.Turbo Jet Engines, 1987.

7. Luthra, K. L. and H. S. Spacil, "Impurity Deposits in Gas Turbines From Fuels Containing Sodium and Vanadium," J. Electrochem.Soc.129 (1982) pp. 649-656.

8. Shores, David A., "New Perspectives on Hot Corrosion Mechanisms," pp. 493-501, NACE-6, 1983. Ed R.A.Rapp.

9. Rosner, D. E. and R. Nagarajan, "Transport-Induced Shifts in Condensate Dew-Point and Composition i Multicomponent Systems With Chemical Reaction," Chem.Eng.Sci.,40,pp. 177-186 (1985).

10. Nagarajan, R., "Theory of Multicomponent Chemical Vapor Deposition (CVD) Boundary Layers and Their Coupled Deposits," Ph.D. Thesis, Chemical Engineering Department, Yale University (May 1986).

11. Natesan, K., "Oxidation-Sulfidation Behavior of Nickel-Base Superalloys and M-Cr-Al Coatings," Materials Science Eng., 87, pp. 9-106 (1987).

12. Cook, L. P. and D. W. Bonnell, "Model for Molten Salt Corrosion of (Co,Cr)-Based Superalloys," NBSIR 87-3628, Final Report Prepared for the Department of the Navy-DTRC by the National Bureau of Standards (Dec 1987).

13. Annen, K. D., "Preparation of a Vanadate Thermodynamic Data Base," JANA-NEW, Final Report Prepared for the Department of the Navy-DTRC by Aerodyne Research, Inc., Billerica, Mass. (1985).

14. Gordon, S. and B. J. McBride, "Calculation of Complex Chemical Equilibrium Compositions, Rocket Performance, Incident and Reflected Shocks, and Chapman-Jouguet Detonations," NASA SP-273 (computer program), interim revision (Mar 1976).

Table 1. Impurity concentrations in three Navy test fuels.

Impurity	Fuel		
	GT 10	GT 12	NSFO
Sodium (wt. ppm)	1	2	22
Vanadium (wt. ppm)	–	5	170
Sulfur (wt. %)	1	2	2
Nickel (wt. ppm)	–	–	34
Zinc (wt. ppm)	–	–	2
Iron (wt. ppm)	–	–	11

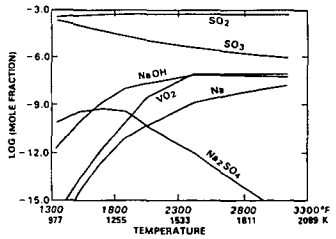

Fig. 1. CEC-predicted vapor phase composition; fuel GT 12, pressure = 1 atmosphere, fuel/air = 1/30.

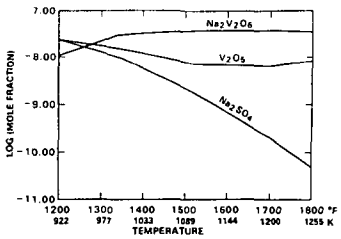

Fig. 2. CEC-predicted liquid phase composition; fuel GT 12, pressure = 1 atmosphere, fuel/air = 1/30.

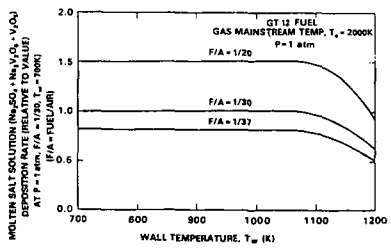

Fig. 3. CRBL deposition rate calculations: predicted dependence on fuel/air (F/A) ratio and blade surface temperature T_w (K).

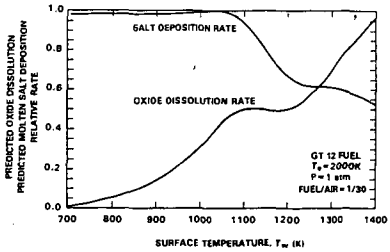

Fig. 4. Predicted effect of blade surface temperature on molten salt deposition and relative oxide (NiO) dissolution rates.

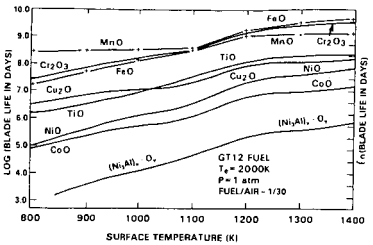

Fig. 5. Predicted hot corrosion-limited life of oxide-coated turbine blades; effect of surface temperature changes.

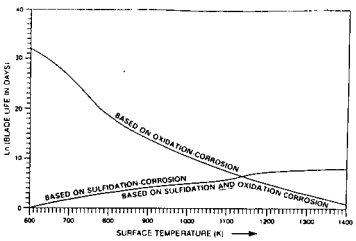

Fig. 6. Predicted surface temperature dependence of Cr_2O_3-coated blade life limited by sulfidation, oxidation, and a combination of the two; fuel GT 12, T_g = 2,000 K, P = 1 atmosphere, fuel/air = 0.0333.

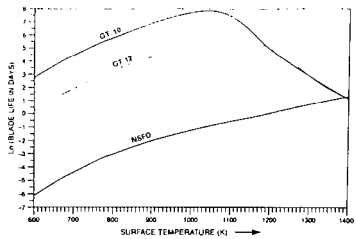

Fig. 7. Evaluation of three Navy test fuels with respect to their corrosion potential; protective coating Cr_2O_3; fuels GT 10, GT 12, NSFO, T_g = 2,000 K, P = 1 atmosphere, fuel/air = 0.0333.

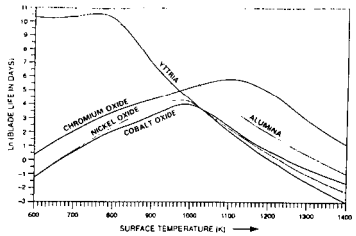

Fig. 8. Computed surface temperature dependence of corrosion-limited life of blades coated with several pure metallic oxides; fuel GT 12, T_g = 2,000 K, P = 1 atmosphere, fuel/air = 0.0333.

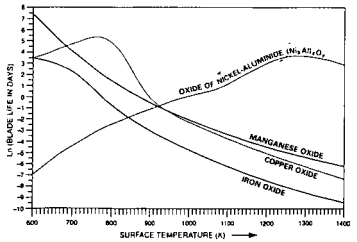

Fig. 9. Predicted surface temperature dependence of corrosion-limited life of blades coated with several metallic and alloy oxides; fuel GT 12, T_g = 2,000 K, P = 1 atmosphere, fuel air = 0.0333.

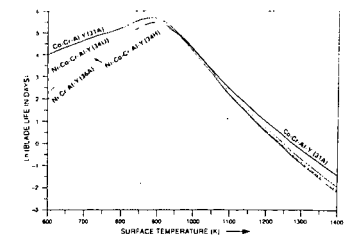

Fig. 10. Predicted surface temperature dependence of corrosion-limited life of blades coated with typical protective alloys; fuel GT 12, T_g = 2,000 K, P = 1 atmosphere, fuel/air = 0.0333.